CERN–2014–004
17 July 2014

ORGANISATION EUROPÉENNE POUR LA RECHERCHE NUCLÉAIRE
CERN EUROPEAN ORGANIZATION FOR NUCLEAR RESEARCH

ICFA Mini-Workshop on Beam–Beam Effects in Hadron Colliders

CERN, Geneva, Switzerland, 18–22 March 2013

Proceedings

Editors: W. Herr
G. Papotti

GENEVA
2014

ISBN 978–92–9083–404–5
ISSN 0007–8328

This reports in indexed in: CERN Document Server (CDS), INSPIRE.

This report should be cited as:

Proceedings of the ICFA Mini-Worskshop on Beam–Beam Effects in Hadron Colliders,
CERN, Geneva, Switzerland, 18–22 March 2013, edited by W. Herr and G. Papotti, CERN-2014-004 (CERN, Geneva, 2014), DOI: 10.5170/CERN–2014–004

A contribution in this report should be cited as:

[Author name(s)], in Proceedings of ICFA Mini-Workshop on Beam–Beam Effect in Hadron Colliders,
CERN, Geneva, Switzerland, 18–22 March 2013, edited by W. Herr and G. Papotti, CERN-2014-004 (CERN, Geneva, 2014), pp. [first page] – [lastpage], DOI: 10.5170/CERN–2014–004. [first page]

Abstract

This report contains the Proceedings of the ICFA Mini-Workshop on Beam-Beam Effects in Hadron Colliders held at CERN from 18 to 22 March 2013. It was the first of its kind after the successful start of LHC operation where a vast amount of beam-beam observations emerged. It brought together 58 international experts in the field and the purpose of this workshop was to review the present knowledge in the fields of beam-beam theory, simulations and observations. In the summary session the participants acknowledged the enormous progress made in recent years and the introduction of new concepts and tools. The workshop was concluded by a discussion on future research work with emphasis on the LHC operation and future circular colliders.

Preface

The ICFA Mini Workshop on Beam-Beam effects in Hadron Colliders was held at CERN from March 18-22. 2013. It was attended by 58 participants from sixteen different institutes and universities. The workshop was motivated by the need to review and collect the present knowledge and progress since the previous workshops, of which this is a successor. The successful start of the LHC provided a vast amount of beam-beam observations, including head-on as well as long range beam-beam interactions, and coherent beam-beam effects. Together with experience from other colliders the observations have been addressed in sessions on weak-strong and strong-strong beam-beam effects. New developments in the fields of beam-beam theory and simulation techniques emerged since the last beam-beam workshop and proved to be essential for the analysis and understanding of the experimental results. Discussions on beam-beam compensation schemes and the impact of beam-beam effects on the successful operation have deserved dedicated sessions. Finally, a session was organized to present and discuss future projects such as the LHC upgrade, lepton-lepton and lepton-hadron colliders. All these project will face new challenges and enter a new territory of beam-beam effects. These problems have been addressed by the participants in talks and discussions organized in nine plenary session:

1 Observations in existing hadron Colliders, chaired by O. Brüning (CERN)

2 Observations in existing lepton Colliders, chaired by J. Seeman (SLAC)

3 Theory and Simulations, chaired by T. Pieloni (CERN)

4 Head-on single particle effects, chaired by K. Oide (KEK)

5 Long range single particle effects, chaired by V. Shiltsev (Fermilab)

6 Beam-beam compensation schemes, chaired by W. Fisher (BNL)

7 Operational aspects of beam-beam interactions, chaired by G. Papotti (CERN)

8 Strong-strong beam-beam interactions, chaired by L. Rivkin (PSI and EPFL)

9 Future projects, chaired by A. Valishev, (Fermilab)

The chairs of the nine session summarized the outcome of the presentations and discussions in a concluding session, chaired by A. Chao (Stanford University and SLAC)
Further information and the presentations are available in electronic form at the workshop web site:
https://indico.cern.ch/conferenceDisplay.py?confId=189544
For papers not submitted to the proceedings, the slides are available at the web site above.
We should like to thank all participants and chairs for their contributions that made this workshop stimulating and successful. The workshop was organized under the sponsorship of the ICFA beam dynamics panel and we also thank the CERN management for the support that made this workshop possible. Further we thank the LHC high luminosity project and the EPFL, Lausanne for the financial support. Finally, it is a pleasure to thank the workshop secretaries D. Rivoiron and L. Hemery for their administrative work and a smooth running of the workshop.

Werner Herr and Giulia Papotti
Editors

Contents

[1] A paper was not submitted to the proceedings. However, the slides presented are available in electronic form at https://indico.cern.ch/event/189544/.

[2] PhD Thesis at: https://cds.cern.ch/record/1670675/.
[3] PhD Thesis at: https://cds.cern.ch/record/1637966/.

Published by CERN in the Proceedings of the ICFA Mini-Workshop on Beam–Beam Effects in Hadron Colliders,
CERN, Geneva, Switzerland, 18–22 March 2013, edited by W. Herr and G. Papotti, CERN–2014–004 (CERN, Geneva, 2014)

OBSERVATIONS OF BEAM–BEAM EFFECTS AT THE LHC

G. Papotti, X. Buffat, W. Herr, R. Giachino, T. Pieloni
CERN, Geneva, Switzerland

Abstract

This paper introduces a list of observations related to the beam–beam interaction that were collected over the first years of LHC proton physics operation (2010–12). Beam–beam related effects not only have been extensively observed and recorded, but have also shaped the operation of the LHC for high-intensity proton running in a number of ways: the construction of the filling scheme, the choice of luminosity levelling techniques, measures to mitigate instabilities, and the choice of settings for improving performance (e.g. to reduce losses), among others.

INTRODUCTION

The Large Hadron Collider (LHC) at CERN, Geneva, is a 27 km long circular accelerator [1]. It is based on a superconducting two-in-one magnet design, with dipoles that allow it to reach a design energy of 7 TeV per beam. It features eight straight sections: four Interaction Points (IPs) are reserved for accelerator equipment and four house particle physics experiments. IP3 and IP7 are dedicated to the collimation system, IP4 houses the RF system and most of the beam instrumentation, while IP6 is reserved for the beam dump system. IP1 and IP5 contain the high-luminosity experiments ATLAS and CMS, while IP2 and IP8 accommodate the Alice and LHCb experiments, together with beam injection (Beam 1 through IP2, clockwise; Beam 2 through IP8, counterclockwise).

The luminosity requirements of the four experiments are very different [2]. Two high-luminosity experiments and the discovery of a new boson are the reason for the push towards high-intensity proton physics performance. This is detailed in the next section, where the beam parameters are compared between the Design Report and 2012 operation.

Alice and LHCb have luminosity limitations, and thus techniques of luminosity levelling have been applied consistently during proton physics production and will be described next. The different luminosity requirements also impact the construction of the filling schemes. Various collision patterns have been used for physics production and during 2012 a change was required to overcome recurrent loss of Landau damping.

The beam parameters were pushed much further during single-bunch Machine Development (MD) sessions, achieving very high beam–beam tune shifts. Similar conditions were used for high pile-up studies for the experiments [3].

Scans of the crossing angle were done during MD sessions to evaluate the effect of long-range interactions in bunch trains, allowing the onset of losses for scaling laws to be measured [4]. The description of these studies and of the observation of orbit effects conclude this paper.

BEAM PARAMETERS AND PERFORMANCE

In these first years of luminosity production, the operation of the LHC has exceeded all expectations. The year 2010 was mostly a commissioning year, and the instantaneous luminosity target was exceeded by a factor of 2, as $2.1 \times 10^{32}\,\mathrm{cm}^{-2}\cdot\mathrm{s}^{-1}$ was achieved. The years 2011 and 2012 were dedicated to luminosity production in search for new physics, and 5.5 fb^{-1} and 23.2 fb^{-1} were collected in each year, respectively. Table 1 shows the machine and beam parameters as defined in [1] compared to the ones used in 2012 operation. Despite the beam energy being about half the design value, the achieved peak luminosity was over 75% of the design value of $10^{34}\,\mathrm{cm}^{-2}\cdot\mathrm{s}^{-1}$. The β^* at the high luminosity experiments in IP1 and IP5 almost reached design values thanks to the excellent physical aperture and the use of 'tight collimators' [5].

The key ingredient in the excellent luminosity performance is the fact that the LHC injectors can deliver much brighter beams with a bunch spacing of 50 ns compared to the nominal 25 ns. At 4 TeV beam energy, the pile-up μ (the number of inelastic collisions per bunch crossing) is at most 30–35, and this is still acceptable for the high-luminosity experiments. This contributed to the choice, for 2012 operation, of 50 ns spaced beams, which have the additional advantage of being much less affected by electron cloud than 25 ns spaced beams (this allowed less beam time to be sacrificed to electron-cloud scrubbing, as 3 days were needed for 50 ns versus the 2 weeks that would have been required for 25 ns). Note also that the smaller emittance

Table 1: A comparison of parameters between design values [1] and what was achieved in 2012 operation

Parameter	Design	2012
Beam injection energy [TeV]	0.45	0.45
Beam energy at collisions [TeV]	7	4
Number of bunches	2808	1380
Bunch spacing [ns]	25	50
β^* [m]	0.55	0.6
Intensity [10^{11} p/bunch]	1.15	1.65
Norm. transv. emittance [μm]	3.75	2.5
Beam size [μm]	16	19
Peak luminosity [$10^{34}\,\mathrm{cm}^{-2}\cdot\mathrm{s}^{-1}$]	1	0.77
Stored energy [MJ]	362	145

978-92-9083-404-5, 0007-8328 –
http://dx.doi.org/10.5170/CERN–2014–004.1

of the 50 ns beams allowed squeezing to proceed further (for comparison, $\beta^*_{25} = 80$ cm) and the use of a smaller crossing angle, both of which contributed directly to the excellent performance.

For operation after the Long Shutdown of 2013–14 (LS1), the pile-up μ will increase due to the energy increase, and thus 25 ns is the preferred choice (for 50 ns beams, $\mu_{50} \approx 80$–120). It is worth pointing out that luminosity levelling techniques might be needed even with 25 ns spaced bunches as $\mu_{25} \approx 25$–45.

LUMINOSITY LEVELLING

The Alice and LHCb experiments run with strong pile-up limitations: Alice at $\mu \approx 0.02$ and LHCb at $\mu \approx 2.5$. The limitations come from various factors that range from detector damage through event size limitations to data-taking optimization [2]. In addition to a less aggressive β^* (in 2012, $\beta^* = 3$ m was used for IP2 and IP8), various techniques of luminosity control and levelling have been used operationally or tested in special runs at the LHC so far.

The luminosity was levelled operationally at LHCb so that the experiment could run at a constant luminosity of $4 \times 10^{32}\,\mathrm{cm}^{-2}\cdot\mathrm{s}^{-1}$. This was achieved by transversely offsetting the beams at the IP. During the fill, the offset was adjusted in small steps so to modulate the overlap between the two beams to obtain the desired rates [6]. No real limitations to this technique were found, as long as the offset bunch pair had enough tune spread due to head-on collisions elsewhere (i.e. in IP1 and IP5).

Given that the limitations in Alice are even stronger, the experiment ran for most of 2012 based on collision with so-called 'satellite' bunches ('main-satellite' collisions). Satellite bunches have a much lower charge (about a factor of 1000 lower than the main bunches), contained in buckets at 25 ns from the main ones (which are at a 50 ns spacing). Note that this technique is not applicable with 25 ns spaced bunches.

During MD sessions, techniques for β^* levelling were also tested, verifying the feasibility and quality of the orbit control while squeezing IP1 and IP5. The squeeze of IP1 and IP5 was done in steps until the operational value of 60 cm [7, 8, 9].

FILLING SCHEMES AND COLLISION PATTERNS

Here, we recall a few of the constraints that have to be taken into account in the creation of a filling scheme:

- *Experiment location*: ATLAS, Alice, CMS are located at the IP symmetry point, while LHCb is 11.25 m away from it; ATLAS and CMS are diametrically opposed.

- *Kicker gaps*: the injection and extraction kickers require part of the ring not to contain beam (e.g. 925 ns for the LHC injection kicker, and 3000 ns for the dump kicker).

- *The 400 MHz RF system*: this gives 2.5 ns long buckets and a harmonic number $h = 35\,640$, but 25 ns bunch spacing is the minimum that the experiments' readout can handle (for a maximum of $\approx$ 2800 bunches per ring, taking the kicker gaps into account).

- *Bunch spacings*: the spacings that can be created in the LHC injector chain are 25 ns, 50 ns, 75 ns, 150 ns, or >250 ns.

- *PS batch injections*: the number of injections into the SPS can be varied dynamically (i.e. from one to four injections).

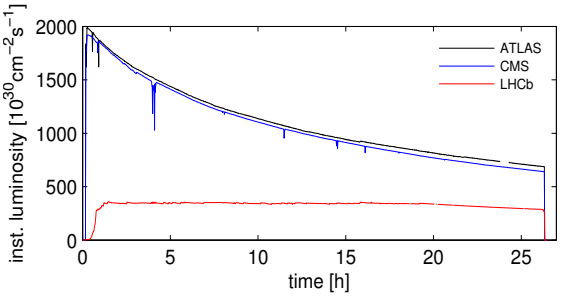

Figure 1: Examples of ATLAS, CMS, and LHCb instantaneous luminosities during fill 2006 (in 2011). Note that while the luminosities of IP1/5 decrease with time, the luminosity of IP8 is kept constant by reducing the transverse offset and starts to decay only after about 20 h into production.

Table 2: The numbers of collisions per IP for three filling schemes used in 2012

Scheme	IP1/5	IP2	IP8
1	1331	0	1320
2	1380	0	1274
3	1377	0	1274

Different numbers of colliding pairs are provided to the different experiments by shifting the injection buckets appropriately. In Table 2, three examples of filling schemes used in 2012 for physics production are shown. All three schemes are based on 50 ns spaced bunches and main-satellite collisions for Alice (thus zero main–main collisions in IP2). The first scheme was the baseline for 2012 operation, and it aimed at giving the same number of colliding pairs to IP1/5 and IP8. Scheme 2 was designed to have all bunches colliding in IP1 and IP5, and was obtained by shifting four injections in scheme 1. Scheme 3 is a minor modification with respect to scheme 2, designed to include three bunches with no collisions in IP1/5 for systematic background studies for ATLAS and CMS.

Loss of Landau Damping

The change from scheme 1 to scheme 2 in Table 2 was dictated by the fact that fills were often terminated prematurely due to instabilities. Some bunches in ring 1 were losing intensity very quickly and an interlock kicked in at $\approx 4 \times 10^{10}$ p/bunch, effectively determining that the length of the fill was much shorter than desirable.

The affected bunches had the peculiarity of colliding only in IP8 (levelled by separation). The lack of Landau damping with respect to the other bunches that collide in IP1/5 was identified to be the reason for the development of the instability [10]. The filling scheme was thus changed to have head-on collisions in IP1/5 for all bunches, so that the head-on beam–beam tune spread would provide the necessary damping.

During the second part of the 2012 run, selected bunches frequently became unstable at the end of the squeeze, before collisions. The instability was visible on loss measurements and as emittance growth, but it is not yet fully understood at the time of writing and studies are still ongoing [10]. Improvements in beam instrumentation, and in particular for the detection of instabilities, are needed [11]: for example, calibrated bunch-by-bunch emittance measurements, headtail monitors to understand the intra-bunch motion, and Schottky monitors for bunch-by-bunch tunes and chromaticity, among others. They will help greatly at restart after LS1.

HIGH HEAD-ON TUNE SHIFT AND HIGH PILE-UP

Single bunches characterized by very high brightness were collided during dedicated MD sessions in 2011 and 2012 [3]. First, in 2011, a possible head-on beam–beam limit was probed, with bunches characterized by $\epsilon \approx 1.3\,\mu$m and $N \approx 1.9 \times 10^{11}$ p/bunch [12]. No significant losses or emittance effects were observed after having performed a tune adjustment to avoid emittance blow-up ($Q_{\mathrm{H}} = Q_{\mathrm{V}} = 0.31$). The linear head-on beam–beam parameter ξ is defined as

$$\xi = \frac{N r_0}{4\pi\epsilon_n}, \qquad (1)$$

where N is the number of protons in the bunch, ϵ_n is the normalized emittance, and $r_0 = 1.54 \times 10^{-18}$ m is the classical proton radius. During the 2011 experiments at injection energy, at most $\xi = 0.02$/IP and $\xi = 0.034$ total (for two IPs) were achieved, to be compared with the Design Report value of $\xi = 0.0033$/IP for (for three head-on IPs [1]).

Given the success of the studies at injection, bunches with similar parameters were put into collisions according to the operational cycle, so that the experiments could use such beams to study their own pile-up limitations [2, 3]. The pile-up is $\mu \approx 19$ in the Design Report [1], but a pile-up of $\mu_{max} \approx 31$ was achieved in 2011 [13] and $\mu_{max} \approx 70$ in 2012 [14]. The very high value achieved in 2012 was reached due to the very bright single bunches that could be produced as a result of the use of the Q20 optics in the SPS ($N = 3 \times 10^{11}$ p/bunch and $\epsilon = 2.2\,\mu$m [15]), and is well beyond what the experiments can handle for efficient data taking. Even higher values would have been achieved had the beams not suffered from instabilities during the acceleration ramp and the betatron squeeze (despite the increase in chromaticity and longitudinal size). Only one beam could be brought cleanly into collisions in the time scheduled for the study.

Coherent Modes

Coherent beam–beam modes, σ and π, could be measured during the 2011 experiments with single bunches [16].

It is also worth recalling that in 2010 a tune split had been used to cure instabilities, possibly from coherent modes, with single-bunch intensities of $\approx 0.9 \times 10^{11}$ p/bunch ($\Delta Q_1 = -0.0025$; $\Delta Q_2 = +0.0025$). The tune split was later removed [17] when more bunches were colliding and after observing that the lifetime of one beam was significantly worse than that of the other beam (the worse lifetime being for the beam with reduced tune).

SCANS OF THE CROSSING ANGLE

In successive MD sessions [4], the machine settings were changed starting from the nominal configuration by reducing the crossing angle in steps until losses or lifetime reduction were observed. This allowed the separation that corresponded to the onset of beam losses to be recorded. Bunch-by-bunch differences depending on the number of LR interactions were highlighted (PACMAN effects), with a higher number of LR interactions leading to higher integrated losses, starting at a larger separation. These experiments were repeated for different β^* and bunch intensities; the different machine settings and beam parameters in each experiment are shown in Table 3. The results were used to confirm simulations [18] and to predict the required separation for different scenarios that might possibly be used in future operation. It has been proven that this is a dynamic aperture effect, as no effects of the scans were observed on the emittance evolution, and as the losses recovered if a sufficient crossing angle was restored.

As an example, Fig. 2 shows the losses in the case of Beam 1 for the first scan in Table 3, when the crossing angle in IP1 was reduced from 120 μrad, or 100%, to a minimum of 40% (corresponding to 4 σ beam separation [19]). It can be seen that the onset of strong losses is between 4 and 5 σ separation, depending on the number of LR interactions experienced by the bunch (shown in Fig. 3).

The scans served as evidence for the effectiveness of the alternate crossing scheme, since when scanning IP5 after IP1, the lifetime seemed best when the separation and the crossing angles were equal for the two IPs (we recall that the crossing plane is vertical in IP1 and horizontal in IP5,

Table 3: Machine settings and beam parameters for crossing angle scans (α is the half crossing angle; ϵ is the transverse emittance; Δt is the bunch spacing; E is the beam energy)

β^* [m]	α [μrad]	Intensity [10^{11} p/bu.]	ϵ [μm]	Δt [ns]	E [TeV]
1.5	120	1.2	2–2.5	50	3.5
0.6	145	1.6	2–2.5	50	4
0.6	145	1.2	2–2.5	50	4
1	145	1.0	3.1	25	4

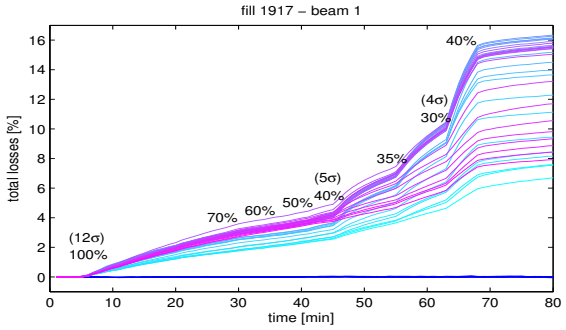

Figure 2: Bunch losses versus time for Beam 1; blue curves for non-colliding bunches, and cyan to magenta for the 36 bunches in the 50 ns spaced bunch train. The separation is indicated in the plot as a percentage of the initial crossing angle, or in the number of σ.

to compensate for first-order LR effects). A dependence on the number of head-on collisions was also shown.

A scan was also performed for 25 ns spaced beams – that is, with twice the number of LR interactions – as it was expected that a bigger separation will be needed, and the information will be useful in deciding the settings for future operation. An asymmetry between Beams 1 and 2 was observed but is not yet fully understood (it is possibly related to electron cloud effects).

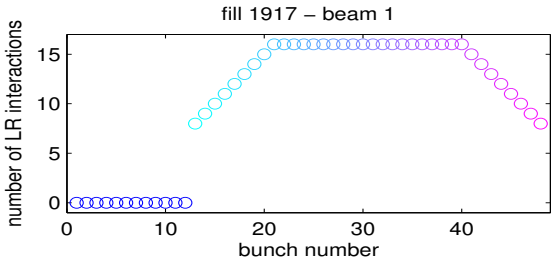

Figure 3: The number of LR encounters per bunch: in blue, the 12 non-colliding bunches; in cyan fading to magenta, the 36 50 ns spaced bunches.

ORBIT EFFECTS

It has been predicted that PACMAN bunches will have different orbits due to LR collisions, and a fully self-consistent treatment was developed to compute those different orbits [20]. The LHC orbit measurement cannot resolve these effects, but the ATLAS vertex centroid measurement [21, 22] was used to qualitatively verify the agreement [19, 23, 24].

Missing LR Deflection

The beam dump of a single beam in collisions leads to a transient effect due to missing LR deflections, resulting in a single-turn trajectory perturbation of the other beam. An end-of-fill test was performed with 72 25 ns spaced bunches ($\approx 1.1 \times 10^{11}$ p/bunch, $\approx 65\,\mu$rad half crossing angle [25]). The horizontal perturbation of the Beam 1 orbit in the arc is ≈ 230 mm = $0.6\,\sigma_{\rm nom}$ (with $\sigma_{\rm nom} = 3.5\,\mu$m). This leads to beam losses above dump thresholds with the physics beam. The effect was observed on beam losses throughout 2012.

CONCLUSIONS

The operation and performance of the LHC are strongly influenced by beam–beam effects, which, already in these first years of physics production, have driven the choice of beam parameters, machine settings, and filling schemes, so to improve performance and mitigate instabilities. A list of observations from routine operation and dedicated studies has been presented in this paper to give an overview of the extent to which beam–beam related effects have shaped LHC operation for high-intensity proton physics.

ACKNOWLEDGEMENTS

The authors would like to acknowledge the operation teams of the LHC and its injectors for their observations during beam operation and their help and support during dedicated studies. The LHC experiments are also acknowledged for providing luminosity and other beam-related data in a productive and collaborative way.

REFERENCES

[1] O.S. Brüning, P. Collier, P. Lebrun, S. Myers, R. Ostojic, J. Poole, and P. Proudlock, LHC Design Report, CERN-2004-003-V-1 (2004).

[2] R. Jacobsson, "Needs and Requirements from the LHC Physics Experiments," these proceedings.

[3] G. Trad, "Beam–Beam Effects with a High Pile-up Test in the LHC," these proceedings.

[4] W. Herr, "Long Range Beam–Beam Effects and Experience in the LHC," these proceedings.

[5] R. Bruce et al., "Collimation Settings and Performance," LHC Performance Workshop, Chamonix (6–10 February 2012).

[6] D. Jacquet and F. Follin, "Implementation and Experience with Luminosity Levelling with Offset Beams," these proceedings.

[7] X. Buffat, W. Herr, M. Lamont, T. Pieloni, S. Redaelli, and J. Wenninger, "Results of β^* luminosity levelling MD," CERN-ATS-Note-2012-071 MD (2012).

[8] X. Buffat, W. Herr, T. Pieloni, L. Ponce, S. Redaelli, and J. Wenninger, "MD on Squeeze with Colliding Beams," CERN-ATS-Note-2013-002 MD (2013).

[9] B. Muratori and T. Pieloni, "Luminosity Levelling Techniques: Implications for Beam–Beam Interactions," these proceedings.

[10] X. Buffat, "Consequences of Missing Collisions, Beam Stability and Landau Damping," these proceedings.

[11] R. Giachino, "Diagnostics Needs for Beam–Beam Studies and Optimization," these proceedings.

[12] R. Alemany et al., "Head-on Beam–Beam Tune Shifts with High Brightness Beams in the LHC," CERN-ATS-Note-2011-029 MD (2011).

[13] G. Trad et al., "Beam Parameters Observations during a High Pile-up Collisions Fill," CERN-ATS-Note-2011-105 MD (2011).

[14] G. Trad, R. Alemany, X. Buffat, R. Calaga, K. Cornelis, W. Herr, D. Jacquet, G. Papotti, M. Schaumann, and W. Venturini Delsolaro, "Beam Parameters Observations during the Second High Pile-up Collisions Fill in 2011," CERN-ATS-Note-2012-010 MD (2012).

[15] Y. Papaphilippou et al., "Operational Performance of the LHC Proton Beams with the SPS Low Transition Energy Optics," THPWO080, these proceedings.

[16] X. Buffat, "Coherent Beam–Beam Modes in the LHC," these proceedings.

[17] G. Papotti and W. Herr, "Observations of Bunch-by-Bunch Losses in the 2010 LHC Proton Physics Operation," CERN-ATS-Note-2011-073 PERF (2011).

[18] D. Kaltchev, "Analysis of Long Range Studies in the LHC – Comparison with the Model," these proceedings.

[19] M. Albert et al., "Head-on Beam–Beam Collisions with High Intensities and Long Range Beam–Beam Studies in the LHC," CERN-ATS-Note-2011-058 MD (2011).

[20] W. Herr and H. Grote, "Self-consistent Orbits with Beam–Beam Effects in the LHC," Proc. 2001 Workshop on Beam–Beam Effects, FNAL (25–27 June 2001).

[21] W. Kozanecki and J. Cogan, private communication (2011).

[22] R. Bartoldus, "Online Determination of the LHC Luminous Region with the ATLAS High Level trigger," TIPP 2011, Int. Conf. on Tech. and Instrum. in Particle Physics, Chicago (2011).

[23] R. Alemany et al., "Observed Orbit Effects during Long Range Beam–Beam Studies," CERN-ATS-Note-2012-021 MD (2012).

[24] M. Schaumann, "Observed Beam–Beam Induced Orbit Effects at LHC," these proceedings.

[25] T. Baer, "Beam–Beam Effects during the Beam Dump Process," these proceedings.

Published by CERN in the Proceedings of the ICFA Mini-Workshop on Beam–Beam Effects in Hadron Colliders,
CERN, Geneva, Switzerland, 18–22 March 2013, edited by W. Herr and G. Papotti, CERN–2014–004 (CERN, Geneva, 2014)

BEAM-BEAM EFFECTS IN THE SPS PROTON-ANTI PROTON COLLIDER

K. Cornelis, CERN, Geneva, Switzerland

Abstract

During the proton-anti proton collider run several experiments were carried out in order to understand the effect of the beam-beam interaction on backgrounds and lifetimes. In this talk a selection of these experiments will be presented. From these experiments, the importance of relative beam sizes and tune ripple could be demonstrated.

GENERAL LAYOUT OF SPS COLLIDER OPERATIONS

In the first collider runs, the Super Proton Synchrotron (SPS) was operated with three proton bunches against three anti-proton bunches, colliding in six collision points. The proton bunch intensity at that time was close to 2×10^{11} and the anti-proton intensities were about ten times less. In this configuration, total tune shifts of 0.028 were sometimes obtained but the anti-proton lifetimes in the beginning of the coast were poor. A horizontal pretzel scheme was introduced to separate the beams in the unwanted collision points (Fig. 1) and the SPS could then profit from the upgraded anti-proton accumulation facility, operating with six against six bunches. In this scheme the beams were separated in 9 of the 12 crossing points.

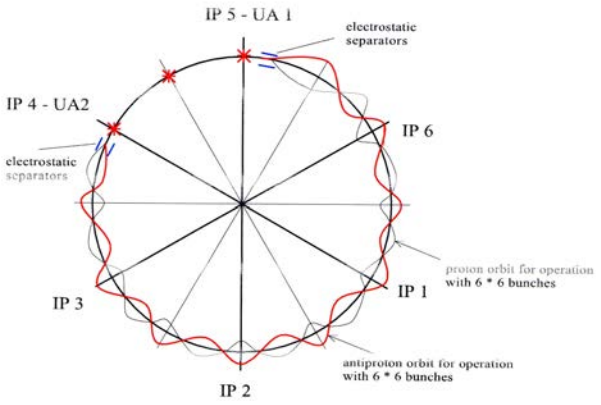

Figure 1: Schematic layout of the SPS pretzel scheme.

The beam separation was 6 σ or better in all the crossing points, except for one, where the separation was only 3.5 σ (Fig. 2).

The same electrostatic separators were used during injection to separate the beams at all crossing points, in order to keep emittances small during the injection and acceleration process. The parameters of the SPS collider in the final six-on-six operation are listed in Table 1.

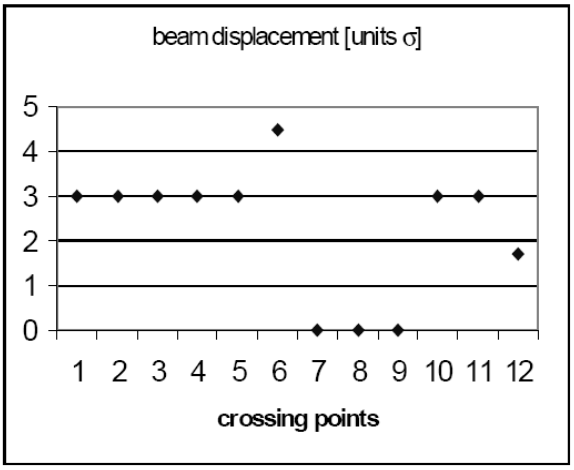

Figure 2: Beam half-separation in the 12 crossing points.

Table 1: General parameters during the SPS collider run with six protons on six anti-protons. The beam emittance ϵ is defined as $\epsilon = 4\gamma\sigma^2/\beta$.

Parameter	**value**
Beam injection energy	26 GeV
Beam coast energy	315 GeV
Proton intensity	1.7×10^{11} p/bunch, 6 bunches
Anti-proton intensity	0.8×10^{11} $\overline{\text{p}}$/bunch, 6 bunches
ϵ_x, ϵ_y	15–20 mm mrad
$\xi_{x,y}$	0.015–0.020(total)

The tune diagram with typical proton and anti-proton footprints during physics runs is shown in Fig.3. The tune difference between protons and anti-protons could be trimmed with sextupoles, placed where the beams were separated. The core of the beam is at the higher tune values.

THE INFLUENCE OF BEAM SIZE

In some of the runs, where the machine went into coast with substantially smaller pbar emittances, the protons had a substantially shorter lifetime and gave a lot of proton background, and was in spite of the fact that the pbar intensity was 10 times less than the proton intensity. This phenomenon could be artificially reproduced by scraping one of the beams with a collimator at a place where they are separated and observing the background and/or the lifetime

978-92-9083-404-5, 0007-8328 –
http://dx.doi.org/10.5170/CERN–2014–004.7

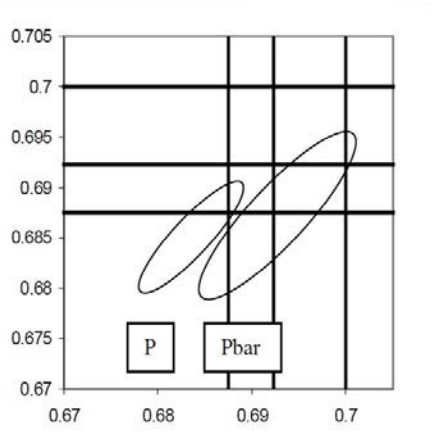

Figure 3: Working point during physics runs. The horizontal and vertical lines represent respectively the 16th (.6875), the 13th (.6923) and the 10th (.700) order resonance.

of the other beam. In Fig.4 a horizontal tune scan is shown looking at the proton background before and after the pbar emittance was reduced by 30%. Although the intensity of the anti-protons was reduced by the scraping process, the protons seem to suffer much more from the beam-beam interaction. This experiment is showing that the high amplitude particles (amplitude measured in units of σ of the other beam) suffer from the high-order resonances.

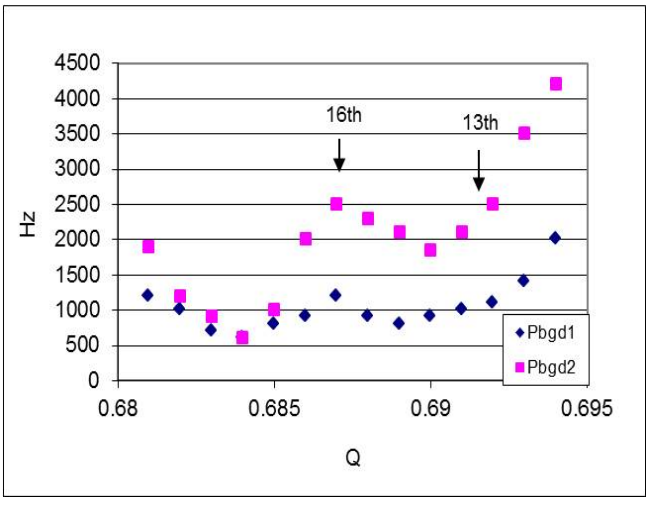

Figure 4: Proton background as a function of tune, before (Pbgd1) and after (Pbgd2) the pbar emittance was reduced by 30%.

In fact it turned out to be very important for the lifetime and background that the two beams had the same size. In case of unequal beam sizes, the bigger beam would loose all the particles sitting outside the other beam mainly, creating a low lifetime and high background in the beginning of the coast. This is illustrated in Fig.5, where the evolution of the proton and anti-proton emittances is plotted during a normal physics coast. By accident the protons are smaller than the anti-protons at the beginning, but throughout the coast the anti-protons mainly lose high amplitude particles and after three to four hours the anti-proton emittance is reduced and matches the proton emittance. The small growth of the proton emittance is due to intra-beam scattering.

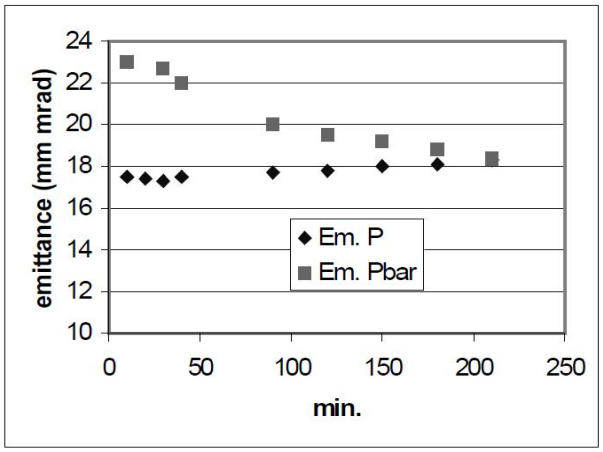

Figure 5: Evolution of the proton and anti-proton emittance during the first 200 min. of a coast.

THE INFLUENCE OF SEPARATION

Tune scans were also performed for different separations. Reducing the separation in the parasitic crossing from $6\,\sigma$ to $3\,\sigma$, increases the background on the 16th as well as on the 13th order resonance as can be seen in Fig. 6. In another experiment only one bunch of protons was colliding head-on with one bunch of anti-protons at two collision points. The beam was then separated at one of the two points in steps of $0.1\,\sigma$. The result is shown in Fig. 7. The background rises very quickly as a function of separation, reaching a maximum at $0.3\,\sigma$. The background then decreases very slowly as a function of further separation.

THE EFFECT OF TUNE MODULATION

High-order resonances in non-linear fields manifest themselves as stable islands in phase space. Most of the particles will have a varying amplitude but the motion stays periodic and stable. Tune modulation will make islands move inward and outward. For small frequencies, the particles will stay trapped in the islands and they can be transported to very high amplitudes due to tune variation. If the tune is varied fast enough there will be passages created between the islands through which the particles can move very quickly inward or outward (cf. empty bucket acceleration). At even higher frequencies the separatrices of the

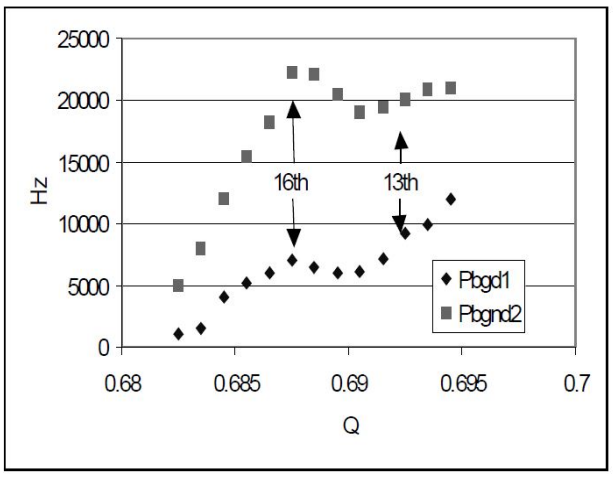

Figure 6: Tune scans with full (Pbgd1) and half separation (Pbgd2).

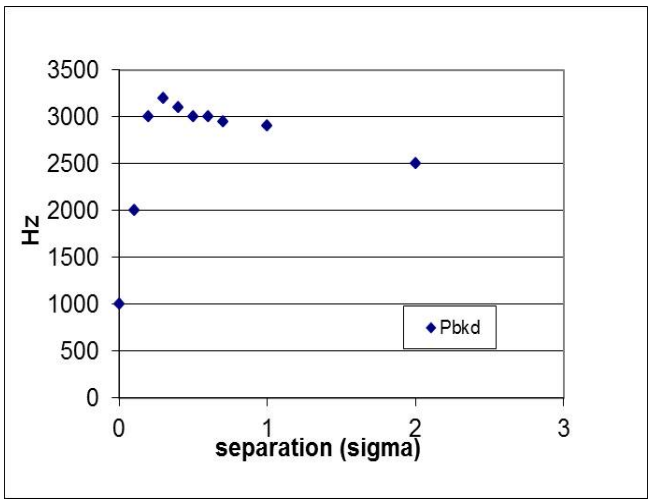

Figure 7: Proton background as a function of the separation.

island become transparent. Particles can be trapped in an island at a low amplitude and leave the island again at a high amplitude. Whatever the mechanism, tune modulation, together with non-linear resonances, creates the possibilities for particles to move to higher amplitudes. This could be very clearly observed in the SPS: in order to have good lifetimes with colliding beams, the chromaticity had to be tuned as close as possible to zero. Also, the noise on the main magnets had be reduced to a minimum in order to preserve good lifetimes during collision. The effect of tune modulation can be easily demonstrated by simulation. In Fig. 8 the results are shown of a simple simulation using a head-on beam-beam kick separated by a linear transfer matrix in which the phase advance is modulated with a frequency of 200 Hz. In the first case the tune modulation is 5×10^{-5} and in the second case it is 3×10^{-4}. The diffusion rate (z-axis) is shown as a function of the unperturbed tune (x-axis) and the initial amplitude (y-axis) ranging from 0 to $10\,\sigma$. In both cases the 16th and 19th order resonance can clearly be seen. In the first case, the particles on the 10th order resonance move out with a diffusion time constant of 1 minute or faster only from $4\,\sigma$ onwards and on the 16th order only from $7\,\sigma$ onwards. In the second case, with the stronger tune modulation, the particles on the 10th order move out with the same speed already at $2.5\,\sigma$ and on the 16th order already at $5\,\sigma$.

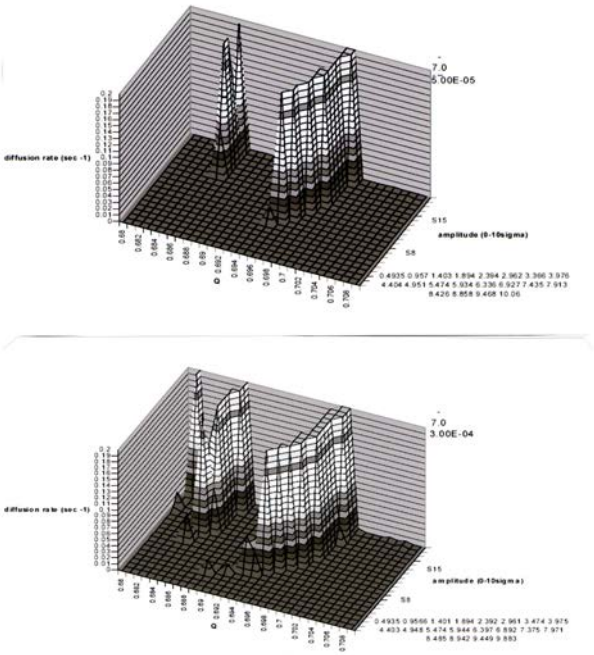

Figure 8: Diffusion rates (z) as function of tune (x) and initial amplitude (y: 0 to $10\,\sigma$). Total tune shift 0.012. Tune modulation 200 Hz, modulation amplitude 0.000 05 (above) and 0.0003 (below).

CONCLUSIONS

- Experience with the SPS proton anti-proton collider showed that it is very important to have the same beam sizes for both beams in order to obtain good lifetimes and backgrounds;
- The high order resonances have almost no effect on the particles with small amplitudes;
- The 'bad' effect of miss-crossing reaches a maximum at a separation of 0.2 to $0.3\,\sigma$.
- All tune modulation (chromaticity, power supply ripple, etc.) should be reduced to a minimum.

Published by CERN in the Proceedings of the ICFA Mini-Workshop on Beam–Beam Effects in Hadron Colliders,
CERN, Geneva, Switzerland, 18–22 March 2013, edited by W. Herr and G. Papotti, CERN–2014–004 (CERN, Geneva, 2014)

OVERVIEW OF BEAM–BEAM EFFECTS IN THE TEVATRON*

V. Shiltsev# for the Tevatron Beam–Beam Team, FNAL, Batavia, IL, USA

Abstract

For almost a quarter of a century the Tevatron proton–antiproton collider was the centrepiece of the world's high-energy physics program, from the start of operation in December 1985 until it was overtaken by the LHC in 2011. The initial design luminosity of the Tevatron was 10^{30} cm^{-2} s^{-1}; however, as a result of two decades of upgrades, the accelerator has been able to deliver 430-times higher luminosities to each of two high-luminosity experiments, Collider Detector at Fermilab (CDF) and D0. On the way to record high luminosities, many issues related to the electromagnetic beam–beam interaction of colliding beams have been addressed. Below we present a short overview of the beam–beam effects in the Tevatron.

BEAM–BEAM EFFECTS IN RUN I

For a detail history of the Tevatron accelerators, performance, and upgrades see Ref. [1]. In 1978 Fermilab decided that proton–antiproton collisions would be supported in the Tevatron, at a centre-of-mass energy of 1800 GeV, and that an Antiproton Source facility would be constructed to supply the flux of antiprotons needed for a design luminosity of 1×10^{30} cm^{-2} s^{-1}.

The Tevatron as a fixed target accelerator was completed in 1983. The Antiproton Source was completed in 1985 and the first collisions were observed in the Tevatron using operational elements of the CDF detector (then under construction) in October 1985. Initial operations of the collider for data-taking took place during a period from February to May 1987. A more extensive run took place between June 1988 and June 1989, representing the first sustained operation at the design luminosity. In this period of operation a total of 5 pb^{-1} were delivered to CDF at 1800 GeV (centre-of-mass).

The initial operational goal of 1×10^{30} cm^{-2} s^{-1} luminosity was exceeded during this run.

Collider Run I took place from August 1992 through February 1996 and employed six bunches in each beam on separated orbits (22 electrostatic separators aimed at mitigating the beam–beam limitations were installed by 1992). Antiproton source improvements supported an accumulation rate of 7×10^{10} antiprotons h^{-1}. Run I ultimately delivered a total integrated luminosity of 180 pb^{-1} to both the CDF and D0 experiments at $\sqrt{s} = 1800$ GeV. By the end of the run the typical luminosity at the beginning of a store was about 1.6×10^{31} cm^{-2} s^{-1}, a 60% increase over the Run I goal.

*Fermi Research Alliance, LLC operates Fermilab under contract No. DE-AC02-07CH11359 with the US Department of Energy.
#shiltsev@fnal.gov

Even at the initial stages of the colliding beam operation, very high beam–beam tune shift parameters were achieved for both protons and antiprotons:

$$\xi = N_{IP}\frac{N_p r_p}{4\pi\varepsilon} \approx 0.018 - 0.025 \quad (1)$$

where r_p denotes the classical proton radius, N_p and ε are the opposite bunch intensity and emittance, respectively, and $N_{IP} = 12$ was the total number of head-on collisions per turn with six-on-six bunches operation. It was realized that the beam–beam footprint covers almost all available tune space between the 3/7th and 2/5th resonances (see Fig. 1) (note that later, after installation of the low-beta insertions for Run I, the working point (WP) was established above half-integer); that the beam loss rates are strongly dependent on the tunes and ξ (see Fig. 2); and the luminosity lifetime significantly deteriorates at the highest beam–beam parameters (see Fig. 3).

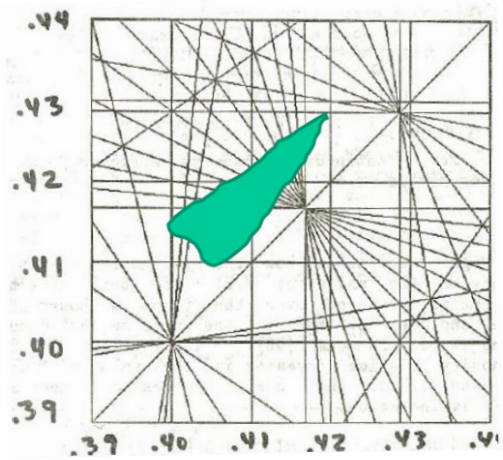

Figure 1: The Tevatron working point in Run I [2].

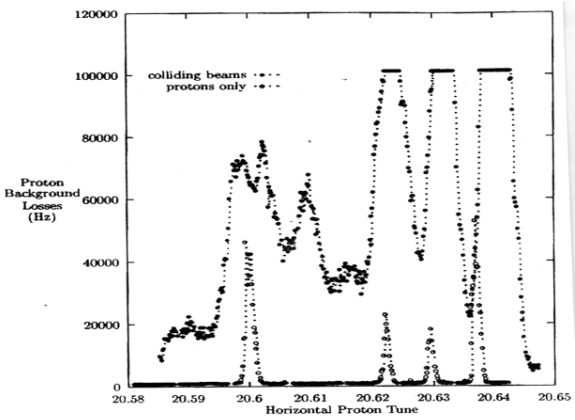

Figure 2: Proton background loss rate in the detectors vs. proton tune Q_x with and without collisions [3].

978-92-9083-404-5, 0007-8328 – © CERN, 2014. Published under the Creative Common Attribution CC BY 4.0 Licence.
http://dx.doi.org/10.5170/CERN–2014–004.11

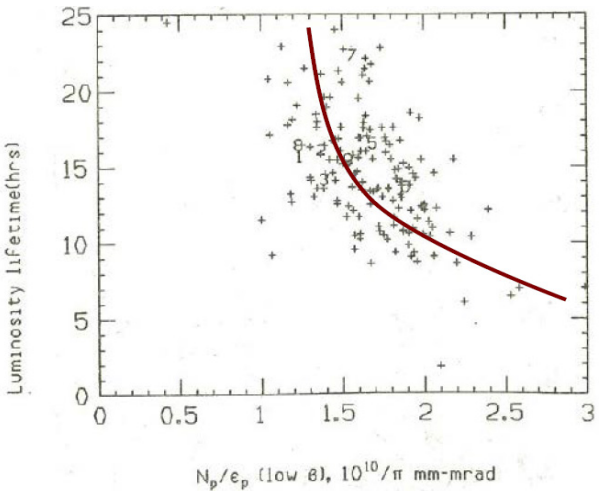

Figure 3: Initial luminosity lifetime as a function of proton brightness N_p/ε_p [2].

Other effects observed were antiproton emittance blowup, transverse halo growth in antiprotons, and high losses in both beams [2, 3]. It was expected that in Collider Run II operation with 36 bunches in each beam, with a much higher antiproton intensity (and, consequently, luminosity) the antiproton helical orbits and tunes would vary significantly from bunch to bunch. The distribution of the antiproton tunes vs. longitudinal bunch position has been measured in a dedicated study and found to be in agreement with theory [4] (Fig. 4). The scale of the expected beam–beam effect was not very clear at that time, and as a safety measure the project for beam–beam compensation with electron lenses was started [5].

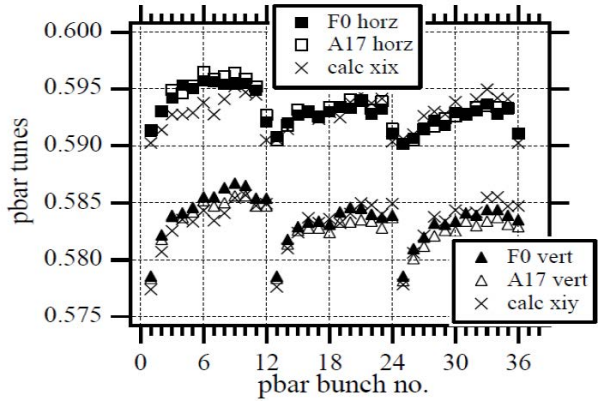

Figure 4: Measured and calculated antiproton tunes for colliding beam conditions (from Ref. [4]). Base pbar (antiproton) tunes were $Q_x/Q_y = 0.5855/0.5755$. A scale factor of ~0.65 was assumed for the tune shift from the head-on beam–beam interaction.

BEAM–BEAM EFFECTS IN RUN II

For the most comprehensive reviews of the beam–beam effects in the Tevatron Collider Run II see Refs. [6, 7]. Collider Run II (2001 to 2011) had employed two new accelerators in the injector chain—the Main Injector (for a significant increase in the number of protons on the antiproton target and beam quality for the collider) and the Recycler (to provide storage for very large numbers of antiprotons—up to 6×10^{12}—and their cooling with stochastic and electron cooling systems). Four additional separators were installed to improve separation at the nearest parasitic crossings. At the end of Run II, typical Tevatron luminosities were well in excess of 3.4×10^{32} cm^{-2} s^{-1}, with record stores exceeding 4.3×10^{32} cm^{-2} s^{-1} (or more than five times above the Run II goal) (see Table 1).

Table 1: Achieved performance parameters for Collider Runs I and II (typical values at the beginning of a store)

	1988 to 1989 Run	**Run Ib**	**Run II**
Energy (com) (GeV)	1800	1800	1960
Protons/bunch ($\times 10^{10}$)	7.0	23	29
Antiprotons/bunch ($\times 10^{10}$)	2.9	5.5	8.1
Bunches/beam	6	6	36
Total antiprotons ($\times 10^{10}$)	17	33	290
P-emittance (rms, *n*) (π μm)	4.2	3.8	3.0
Pbar emittance (rms, *n*) (π μm)	3	2.1	1.5
β^* (cm)	55	35	28
Luminosity (typical) (10^{30} cm^{-2} s^{-1})	1.6	16	350
Luminosity integral (fb^{-1})	$5 \cdot 10^{-3}$	0.18	11.9

During Collider Run II, beam losses during injection, ramp, and squeeze phases were mostly caused by the long-range beam–beam effects. Early in Run II, the combined beam losses in the Tevatron alone (the last accelerator out of a total of seven in the accelerator chain) claimed significantly more than half of the integrated luminosity (see Fig. 5). Due to various improvements, the losses have been reduced significantly down to some 20–30% in 2008 to 2009, paving the road to a many-fold increase of the luminosity. In 'proton-only' or 'antiproton-only' stores, the losses do not exceed 2–3% per specie. So, the remaining 8–10% proton loss and 2–3% antiproton loss is caused by beam–beam effects, as well as some 5–10% reduction of the luminosity lifetime through collision.

Figure 5: A typical plot of the collider 'shot' shows significant beam losses early in Run II (2002).

The particle losses for both beams *on the separated orbit* were driven by diffusion and exacerbated by limited longitudinal and/or transverse apertures. The intensity decay (see Fig.6) was well approximated by [6]:

$$\frac{\Delta N_{a,p}}{N_{a,p}} = 1 - \frac{N(t)}{N(t=0)} \propto \sqrt{t} \cdot \varepsilon_{a,p}^2 \frac{N_{p,a}}{\varepsilon_{p,a}} Q'^2_{a,p} \cdot F(\varepsilon_L, Q_{x,y}, S_{a-p}) \quad . \qquad (2)$$

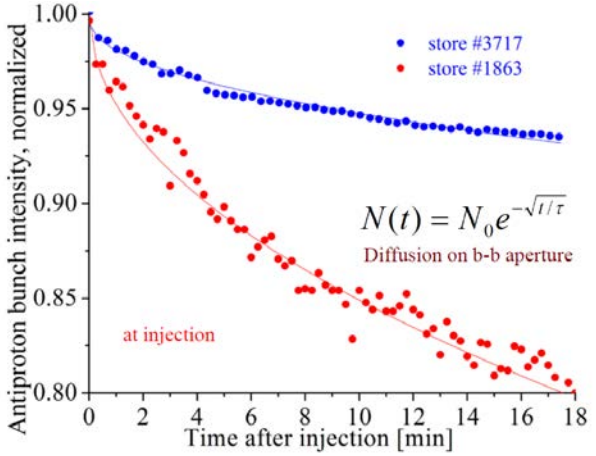

Figure 6: Decay of (normalized) intensity for antiproton bunch #1 at injection. The red dots are for store #1863 (16 October 2002) and the blue dots are store #3717 (8 August 2004). The blue and red lines represent fits according to $N(t) = N_0 e^{-\sqrt{t/\tau}}$ with parameters $N_0 = 32.5 \times 10^9$, $\tau = 7.4$ h and $N_0 = 55.7 \times 10^9$, $\tau = 69.8$ h, respectively [6].

The $\sqrt{t}$-dependence has also been observed for bunch length 'shaving' (slow reduction of the rms bunch length), while transverse emittances do not exhibit such dependence and usually either stay flat or grow slightly. Notably, the proton inefficiencies were higher than the antiproton ones, despite the factor of 3–5 higher proton intensity. That was due to significantly smaller antiproton emittances (see Eq. (2)). Due to the strong dependence of the losses on the chromaticities $Q'_{x,y}$ and beam separation:

$$S = \sqrt{(\Delta x/\sigma_{x\beta})^2 + (\Delta y/\sigma_{y\beta})^2} \quad . \qquad (3)$$

special measures were taken to reduce the former (octupoles and feedback systems allowed Q' to decrease to almost zero) and increase the latter via the increase of limiting physical apertures followed by the increase of the helix size and/or optimization of the HV separator voltages (see Fig. 7).

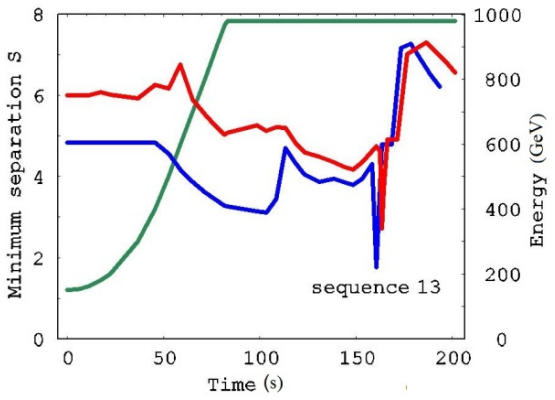

Figure 7: Minimum radial separation (see Eq. (3)) on ramp and during the low-beta squeeze. The green line represents the beam energy on the ramp. The blue and red lines represent $S(t)$ for the helix configurations used ca. January 2002 and August 2004, respectively (from Ref. [6]).

The *head-on beam–beam effects* during the colliding beams stores had been significantly amplified by the presence of the parasitic long-range interactions and unequal beam sizes at the main interaction points (IPs). They were characterized by the record high beam–beam parameters for both protons and antiprotons (the head-on tune shifts up to about $\xi = 0.020$–0.025 for both protons and antiprotons (see Fig. 8), in addition to the long-range tune shifts of $\Delta Q^p = 0.003$ and $\Delta Q^a = 0.006$, respectively (see Fig. 9)), and remarkable differences in the beam dynamics of individual bunches.

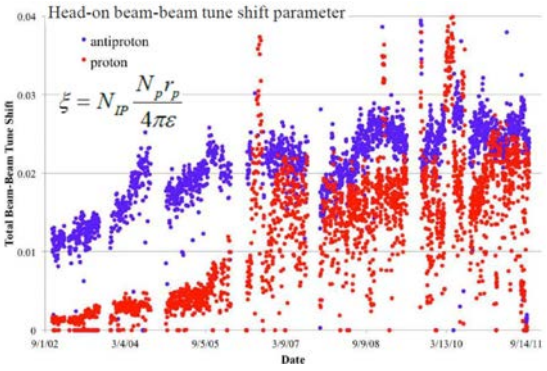

Figure 8: Proton (red) and antiproton (blue) head-on beam–beam tune shifts early in high energy physics (HEP) stores calculated from the measured beam parameters from 2002 to 2011.

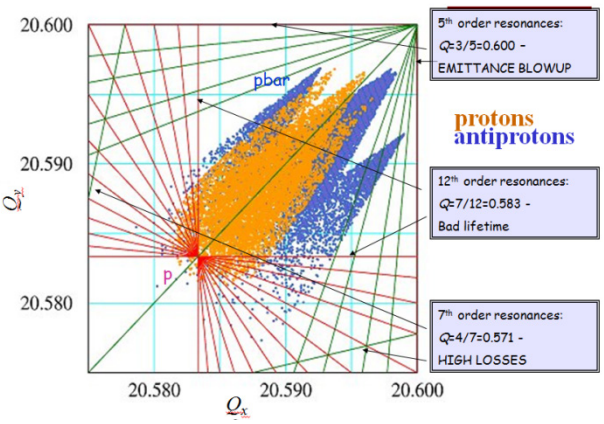

Figure 9: Tevatron proton and antiproton tune distributions superimposed onto a resonance line plot. The red and green lines are various sum and difference tune resonances of up to twelfth order. The blue dots represent calculation of the tune distributions for all 36 antiproton bunches; yellow dots represent the protons. The tune spread for each bunch is calculated for particles up to 6σ amplitude taking into account the *measured* intensities and emittances (from Ref. [6]). The most detrimental effects occur when particle tunes approach the resonances. For example, an emittance growth of the core of the beam is observed near the fifth-order resonances (defined as $nQ_x + mQ_y = 5$, such as $Q_{x,y} = 3/5 = 0.6$) or fast halo particle loss near twelfth-order resonances (for example, $Q_{x,y} = 7/12 \approx 0.583$).

The proton loss rate was also strongly affected by transverse size mismatch for head-on collisions of larger size proton bunches with smaller size antiproton bunches (see Fig. 10). Our studies of the phenomenon in 2003 to 2005 can be summarized as [6]:

$$\frac{1}{\tau_p} = \frac{1}{N_p}\frac{\mathrm{d}N_p}{\mathrm{d}t} \propto N_a \cdot \left(\frac{\varepsilon_p}{\varepsilon_a}\right)^2 F_2(Q_{x,y}, Q', Q'', M) \quad . \quad (4)$$

where M stands for bunch position in the bunch train (see Fig. 11). In order to avoid a large emittance ratio $\varepsilon_p/\varepsilon_a$, the antiproton emittances are routinely diffused at the beginning of HEP stores by a wide band transverse noise to a directional strip line, so the ratio is kept to about 2.6–3.

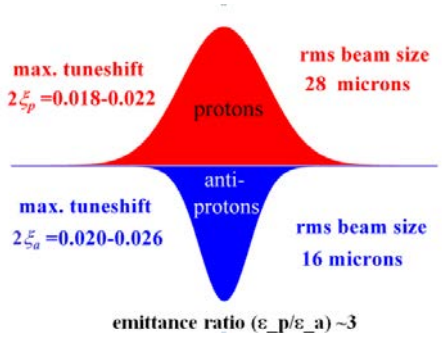

Figure 10: Mismatch of the proton and antiproton transverse beam sizes at the Tevatron IPs.

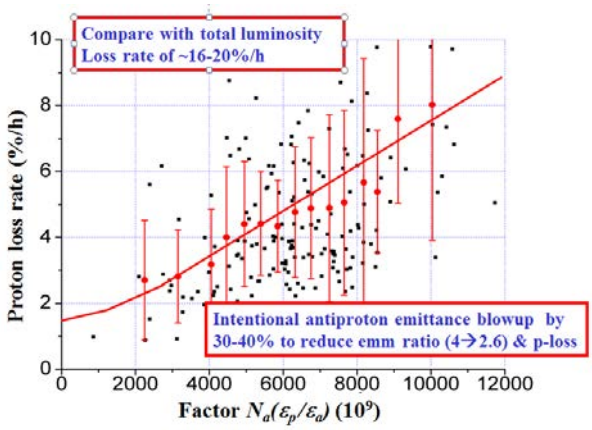

Figure 21: Measured proton loss rates at the beginning of HEP stores vs. factor $N_a(\varepsilon_p/\varepsilon_a)$.

The factor F in Eq. (4) is to indicate strong dependence of the losses on the second order betatron tune chromaticity $Q'' = \mathrm{d}^2Q/\mathrm{d}(\Delta p/p)^2$. Numerical modelling [7]—that was later confirmed by experiments—showed that the deterioration of the proton lifetime was caused by a decrease of the dynamical aperture for off-momentum particles due to head-on collisions (Fig. 12).

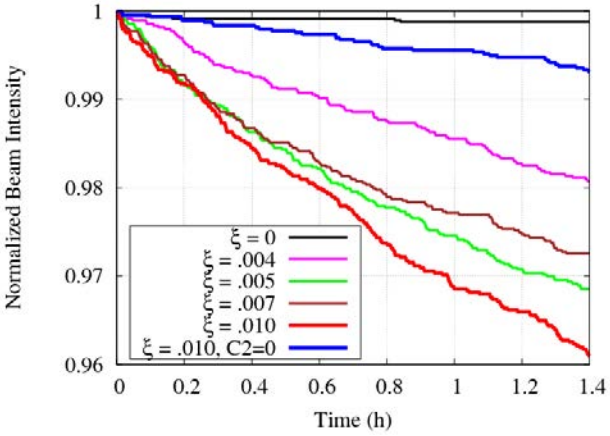

Figure 12: Proton intensity evolution for different values of the beam–beam tune shift parameter per IP from $\xi = 0$ to $\xi = 0.01$; without and with compensation of the chromaticity of β^* ($C2 = 0$) (from Ref. [7]).

It was discovered that the Tevatron optics had large chromatic perturbations, e.g. the value of β^* for off-momentum particles could differ from that of the reference particle by as much as 20%. Also, the high value of second-order betatron tune chromaticity $Q'' = \mathrm{d}^2Q/\mathrm{d}(\Delta p/p)^2$ generated a tune spread of ~0.002. A rearrangement of the sextupole magnet circuits in order to correct the second order chromaticity was planned and implemented before the 2007 shutdown and led to some 10% increase in the luminosity integral/store for 2009 operations (see Fig. 13).

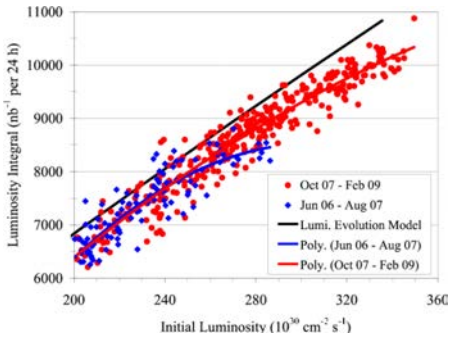

Figure 13: Luminosity integral normalized for 24 h store vs. initial luminosity. Blue points and curve, before the second-order chromaticity correction; red, after the correction. The black line represents the maximum possible luminosity integral for the given beam parameters in the absence of beam–beam effects [7].

The collider luminosity lifetime is determined by the speed of the emittance growth, beam intensity loss rates and bunch lengthening (which affects hour-glass factor H):

$$\tau_L^{-1} = \frac{\mathrm{d}L(t)}{L(t)\mathrm{d}t} = |\,\tau_\varepsilon^{-1}\,| + \tau_{Na}^{-1} + \tau_{Np}^{-1} + \tau_H^{-1}. \quad (5)$$

At the end of Tevatron Collider Run II, the luminosity loss rates were in the range 19–21%/h at the beginning of storage. For the 2010 to 2011 HEP stores with a range of initial luminosities between 3.0 and 4.3×10^{32} cm^{-2} s^{-1}, the largest contribution to luminosity decay came from beam emittance growth with a typical time of $\tau_\varepsilon \sim 9$–11 h. The growth is dominated by intrabeam scattering (IBS) in the proton bunches, with small contributions from the IBS in antiprotons and external noises. Beam–beam effects, if noticeable, usually manifest themselves in reduction of the beam emittances or their growth rates rather than in increases.

The antiproton bunch intensity lifetime $\tau_a \sim 16$–18 h is dominated by the luminosity burn rate, which accounts for 80–85% of the lifetime, while the remaining 10–15% comes from parasitic beam–beam interactions with protons. Proton intensity loss varies in a wide range $\tau_p \sim 25$–45 h and is driven mostly (~50%) by the head-on beam–beam interactions with smaller size antiprotons at the main IPs. The proton lifetime caused by inelastic interactions with antiprotons in collisions and with residual gas molecules varies from 300–400 h. The hourglass factor decays with $\tau_H \sim 70$–80 h due to the IBS, again, mostly in proton bunches. Beam–beam effects may lead to reduction of the proton bunch length growth (longitudinal 'shaving') in a poorly tuned machine. Combining all of these loss rates together, one can estimate the hit on the luminosity lifetime τ_L due to the beam–beam effects as 12–17% (which is equal to (2.5–3.5%/h)/(19–21%/h)).

The luminosity integral $I = \int L\mathrm{d}t$—the sole critical parameter for HEP experiments—depends on the product of peak luminosity and the luminosity lifetime, e.g. for a single store with initial luminosity L_0 and duration $T \sim 16$ h, the integral is $I \approx L_0 \tau_L \ln(1 + T/\tau_L)$. Therefore, the full impact of the beam–beam effects on the luminosity integral should include beam–beam driven proton and antiproton losses at the injection energy (about 5% and 1%, respectively), on the energy ramp (2% and 3%), and in the low-beta squeeze (1–2% and 0.5%), which proportionally reduce the initial luminosity L_0. So, altogether, at the last operational stage of the Tevatron collider present, the beam–beam effects reduce the luminosity integral by 23–33% (see Fig. 14).

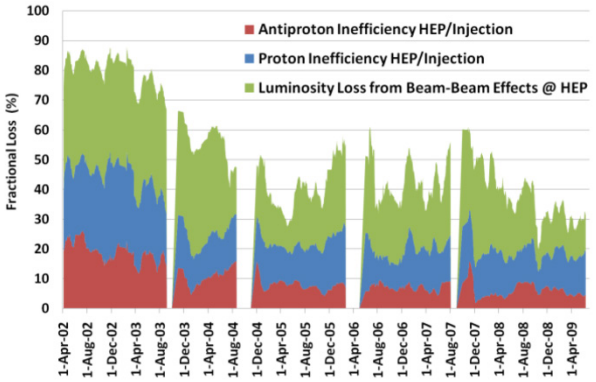

Figure 14: Evolution of beam losses in 2002 to 2009. the red band shows fractional losses of antiprotons between injection into the Tevatron and the start of collisions; the blue band is for the loss of protons; the green band is for the fractional reduction of the luminosity integral caused by beam–beam effects in collisions (from Ref. [8]).

The Tevatron Collider performance history analysis [9] shows that the luminosity increases occurred after numerous improvements; some were implemented during operation and others were introduced during regular shutdown periods. The actions that helped us to keep the beam–beam effects under control during the Run II operations included: i) *at injection, ramp and low-beta squeeze*: opened apertures (replaced magnets), increased helix size S, chromaticity Q' reduction (with help of the transverse dampers and octupoles), optimization of the helices (many times), improved emittances from the injectors; ii) *at low beta (in collision stores)*: the use of additional separators, helix optimization (increased separation at the first long-range IPs), reduction of the chromaticity Q', pbar transverse blowup, tune stabilization; reduction of the chromatism of beta-function (Q''); iii) *trustable beam-beam simulations*; iv) *operational machine stabilization*: stable (repeatable) intensities and emittances from injectors, drastically stabilized Tevatron; v) *outstanding development of the beam diagnostics*: there were three cross-calibrated instruments for the tune measurements, three types of emittance monitors, three intensity monitors, two luminosity monitors, and several types of beam position monitors [10].

BEAM–BEAM COMPENSATION, TELS

Detailed description of the Tevatron Electron Lenses (TELs) and results of the beam–beam compensation studies can be found in Refs. [5, 11–13]. Electron lenses (e-lenses) employ electromagnetic fields of strongly magnetized high-intensity electron beams and were originally proposed for the compensation of head-on and long-range beam–beam effects in the Tevatron [5] (see Fig. 15). The lens employs a low-energy beam of electrons that collides with the high-energy proton or antiproton bunches over an extended length. Electron space charge forces are linear at distances smaller than the characteristic beam radius $r < a_e$ but scale as $1/r$ for $r > a_e$. Correspondingly, such a lens can be used for linear long-range beam–beam and nonlinear head-on beam–beam force compensation depending on the beam-size ratio a_e/σ and the current-density distribution $j_e(r)$.

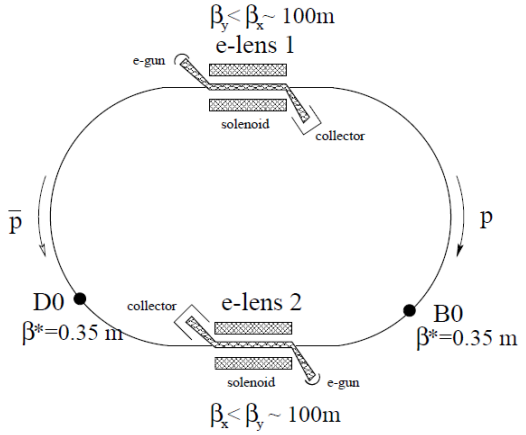

Figure 15: Schematic Tevatron layout with two electron lenses [5].

Main advantages of the e-lenses are: i) the electron beam acts on high-energy beams only through EM forces, with no nuclear interactions; ii) fresh electrons interact with the high-energy particles each turn, leaving no possibility for coherent instabilities; iii) the electron current profile (and, thus, the EM field profiles) can easily be changed for different applications (see Fig. 16); iv) the electron-beam current can be quickly varied, e.g. on a timescale of bunch spacing in accelerators (see Fig. 17).

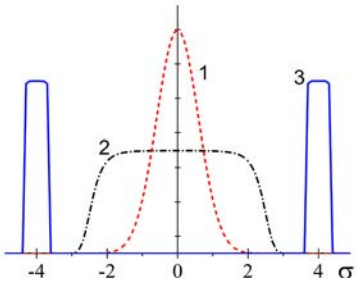

Figure 16: The transverse electron current profiles in electron lenses for: (1) space charge and head-on beam-beam compensation; (2) for bunch-by-bunch tune spread compensation; (3) halo collimation.

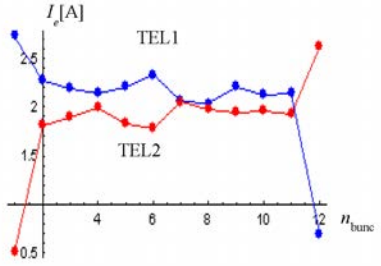

Figure 17: Variation of the currents in two electron lenses needed for long-range tune shift compensation in the Tevatron (bunch spacing is 396 ns).

Two electron lenses were built and installed in the A11 and F48 locations of the Tevatron ring. They use a 1–3 A, 6–10 kV e-beam generated at the 10–15 mm diameter thermionic cathodes immersed in a 0.3 T longitudinal magnetic field and aligned onto the (anti)proton beam orbit over ~2 m length inside a 6 T SC solenoid [11] (see Fig. 18).

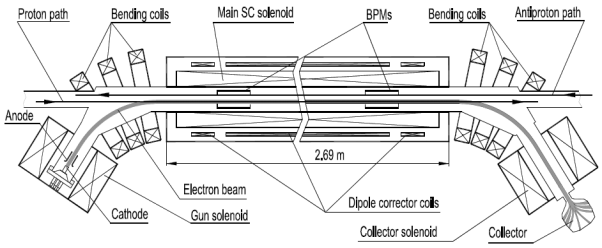

Figure 18: General layout of the Tevatron Electron Lens.

The high-energy protons are focused by the TEL and experience a positive betatron tune shift:

$$\mathrm{d}Q_{x,y} = +\frac{\beta_{x,y} L_e r_p}{2\gamma e c} \cdot j_e \cdot \left(\frac{1-\beta_e}{\beta_e}\right) \qquad (6)$$

In the long-range beam–beam compensation (BBC) experiments [12], a large-radius electron beam was generated $a_e \approx 3\sigma$, therefore the tune shift was about the same for most protons in the bunch. The tune shift for the antiprotons is of about the same magnitude, but negative. Maximum measured tune shift for 980 GeV protons was about 0.01 (see Fig. 19).

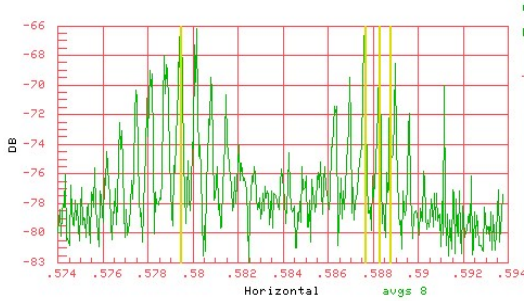

Figure 19: Horizontal tune shift of the 980 GeV proton beam induced by TEL-1 [13].

In the BBC demonstration experiment [12], the electron beam of TEL-2, which was installed at the A11 location with a large vertical beta-function of $\beta_y = 150\text{m}$, was centred and timed onto bunch #12 without affecting any other bunches. When the TEL peak current was increased to $J_e = 0.6\ \text{A}$, the lifetime $\tau = N/(\text{d}N/\text{d}t)$ of bunch #12 went from about 12 h up to 26.6 h (see Fig. 20.)

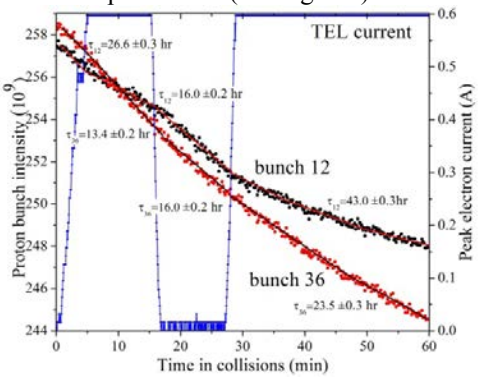

Figure 20: Intensities of proton bunches #12 and #36 early in store #5119 with $L_0 = 1.6 \times 10^{32}\ \text{cm}^{-2}\ \text{s}^{-1}$ (see the text) [12, 13].

At the same time, the lifetime of bunch #36, an equivalent bunch in the third bunch train, remained low and did not change significantly (at 13.4 h lifetime). When the TEL current was turned off for fifteen minutes, the lifetimes of both bunches were, as expected, nearly identical (16 h). The TEL was then turned on again, and once again the lifetime for bunch #12 improved significantly to 43 h while bunch #36 stayed poor at 23.5 h. This experiment demonstrates a factor of two improvement in the proton lifetime due to compensation of beam–beam effects with the TEL.

Proton lifetime, dominated by beam–beam effects, gradually improves and reaches roughly 100 h after 6 h to 8 h of collisions; this is explained by a decrease in antiproton population and an increase in antiproton emittance, both contributing to a reduction of the proton beam–beam parameter. To study the effectiveness of BBC later in the store, the TEL was repeatedly turned on and off every half hour for 16 h, again on bunch #12. The relative improvement R, defined as the ratio of the proton lifetime with the TEL and without, dropped from $R = 2.03$ to $R = 1.0$ in about 10 h. At this point, the beam–beam effects have become very small, providing little to compensate. Similar experiments in several other stores with initial luminosities ranging from $L_0 = 1.5 \times 10^{32}\ \text{cm}^{-2}\ \text{s}^{-1}$ to $2.5 \times 10^{32}\ \text{cm}^{-2}\ \text{s}^{-1}$ repeated these results [13].

Results of many experiments with TELs are reported in Ref. [13], and studies of non-linear BBC with a Gaussian electron beam current profile are presented in Ref. [14]. TELs were not used routinely for the BBC in the Tevatron because beam–beam losses were effectively controlled by other means, as described above. Numerical simulations [15] predict a beneficial effect of electron lenses upon the ultimate intensity LHC beam lifetime.

Besides the BB compensation, the TELs were used for operational abort gap beam removal [16] (see Fig. 21) and for beam halo collimation [17] (see Fig. 22).

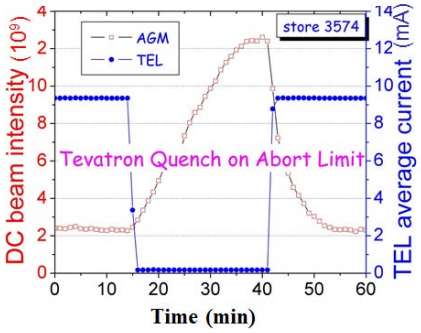

Figure 21: Effective removal of the DC beam from the Tevatron abort gaps by TEL [16].

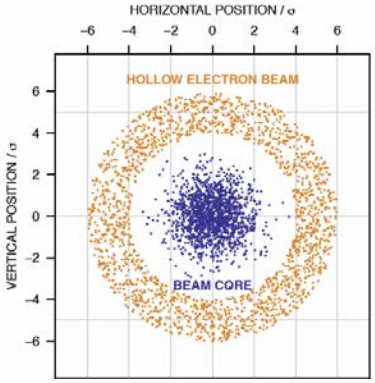

Figure 22: Geometry of the beams for the transverse beam halo removal experiment in the Tevatron [17].

SUMMARY

The beam–beam effects in the Tevatron turned from 'tolerable' (in Collider Run I) to 'very detrimental' (early Collider Run II). We experienced a broad variety of the effects—in both beams, at all stages of the cycle, long-range, and head-on. The Tevatron team has been able to address them and provide critical contribution to a more than 30-fold luminosity increase by the end of Run II (see Fig. 23). We have also enriched beam physics by experimental studies, development of advanced theory, and trustable modelling tools to simulate the beam–beam effects, development of the electron lenses, and the first demonstration of active beam–beam compensation.

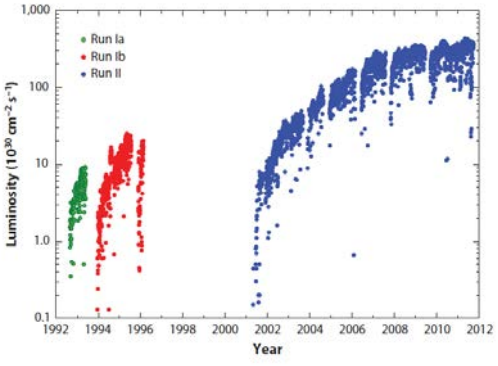

Figure 23: Initial luminosity for all collider stores [1].

The Tevatron collider program ended on 30 September 2011. The machine has worked extremely well for 25 years and has greatly advanced accelerator technology and beam physics. Its success is a great tribute to the Fermilab staff. Among those who contributed to the exploration of the beam–beam effects in the Tevatron were: (*Tevatron Collider Run I*) J. Annala, S. Assadi, P. Bagley, D. Finley, G. Goderre, D.A. Herrup, R. Johnson, J. Johnstone, E. Malamud, M. Martens, L. Michelotti, S. Mishra, G. Jackson, S. Peggs, S. Saritepe, D. Siergiej, P. Zhang; (*Beam–beam effects in the Collider Run II*) Yu. Alexahin, J. Annala, D. Bollinger, V. Boocha, J. Ellison, B. Erdelyi, N. Gelfand, B. Hanna, H.J. Kim, P. Ivanov, A. Jansson, A. Kabel, V. Lebedev, P. Lebrun, M. Martens, R.S. Moore, V. Nagaslaev, R. Pasquinelli, V. Sajaev, T. Sen, E. Stern, D. Shatilov, V. Shiltsev, G. Stancari, D. Still, M. Syphers, A. Tollestrup, A. Valishev, M. Xiao; (*Beam–beam compensation*) A. Aleksandrov, Y. Alexahin, L. Arapov, K. Bishofberger, A. Burov, C. Crawford, V. Danilov, B. Fellenz, D. Finley R. Hively, V. Kamerdzhiev, S. Kozub, M. Kufer, G. Kuznetsov, P. Logatchov, A. Martinez, F. Niell, M. Olson, V. Parkhomchuk, H. Pfeffer, V. Reva, G. Saewert, V. Scarpine, A. Seryi, A. Shemyakin, V. Shiltsev, N. Solyak, G. Stancari, B. Sukhina, V. Sytnik, M. Tiunov, L. Tkachnko, A. Valishev, D. Wildman, D. Wolff, X. Zhang, F. Zimmermann, A. Zinchenko. All the credits for the fascinating results presented above in this review should go to these dedicated researchers. Eight further related presentations have been made at this Workshop [18–25].

REFERENCES

[1] S.D. Holmes and V. Shiltsev, Ann. Rev. Nucl. Part. Sci. 63 (2013); arXiv:1302.2587.
[2] D. Finley, Proc. ICFA Workshop on Beam–Beam Effects (Novosibirsk, Russia), p. 34 (1989).
[3] D. Siergiej, PRE 55 (1997) 3521.
[4] P. Bagley et al., FNAL preprint Conf'96 (1996) 392.
[5] V. Shiltsev et al., PRSTAB 2 (1999) 071001.
[6] V. Shiltsev et al., PRSTAB 8 (2005) 101001.
[7] A. Valishev et al., JINST 7 (2012) P12002.
[8] S.D. Holmes et al., JINST 6 (2011) P08001.
[9] V. Shiltsev, Mod. Phys. Lett. A 27 (2012) 1230001-1.
[10] A. Jansson et al., JINST 4 (2009) P12018.
[11] V. Shiltsev et al., Phys. Rev. ST Accel. Beams 11 (2008) 103501.
[12] V. Shiltsev et al., Phys. Rev. Lett. 99 (2007) 244801.
[13] V. Shitsev et al., New Jour. Phys. 10 (2008) 043042.
[14] A. Valishev et al., Proc. IPAC, p. 2084 (2010).
[15] A. Valishev and V. Shiltsev, Proc. PAC, p. 2567 (2009).
[16] X.-L. Zhang et al., PRSTAB 11 (2008) 051002.
[17] G. Stancari et al., Phys. Rev. Lett. 107 (2011) 084802.
[18] A. Valishev, "Modeling Beam–Beam in the Tevatron," presented at this workshop.
[19] A. Burov, "Beam–Beam, Impedance and Damper,"presented at this workshop.
[20] G. Stancari, "Measurements of the Effect of Collisions on Transverse Beam Halo Diffusion in Tevatron and LHC," these proceedings.
[21] V. Shiltsev, "Experience with Long Range Beam–Beam Effects in the Tevatron," these proceedings.
[22] G. Stancari, "Beam–Beam Compensation Studies in the Tevatron," these proceedings.
[23] G. Stancari, "Detection of Coherent Beam–Beam Modes with Digitized BPM," these proceedings.
[24] A. Valishev, "Beam–Beam for the HL-LHC," presented at this workshop.
[25] A. Burov, "Circular Modes," presented at this workshop.

Published by CERN in the Proceedings of the ICFA Mini-Workshop on Beam–Beam Effects in Hadron Colliders,
CERN, Geneva, Switzerland, 18–22 March 2013, edited by W. Herr and G. Papotti, CERN–2014–004 (CERN, Geneva, 2014)

BEAM–BEAM OBSERVATIONS IN THE RHIC*

Y. Luo, W. Fischer, BNL, Upton, NY, USA

Abstract

The Relativistic Heavy Ion Collider (RHIC) at Brookhaven National Laboratory has been in operation since 2000. Over the past decade, the luminosity in the polarized proton (p-p) operations has increased by more than one order of magnitude. The maximum total beam–beam tune shift with two collisions has reached 0.018. The beam–beam interaction leads to large tune spread, emittance growth, and short beam and luminosity lifetimes. In this article, we review the beam–beam observations during the previous RHIC p-p runs. The mechanism for particle loss is presented. The intra-beam scattering (IBS) contributions to emittance and bunch length growths are calculated and compared with the measurements. Finally, we will discuss current limits in the RHIC p-p operations and their solutions.

INTRODUCTION

RHIC consists of two superconducting rings, the Blue ring and the Yellow ring. They intersect at six locations around the ring circumference. The beam in the Blue ring circulates clockwise and the beam in the Yellow ring circulates counterclockwise. The two beams collide at two interaction points (IPs), IPI6 and IP8. Figure 1 shows the layout of the RHIC. The RHIC is capable of colliding heavy ions and polarized protons (p-p). The maximum achieved total beam–beam parameter with two collisions was 0.003 in the 100 GeV Au–Au collision and 0.018 in the p-p collision. In this article, we only discuss the beam–beam effects in the p-p runs.

The working point in the RHIC p-p runs is chosen to provide a good beam–beam lifetime and to maintain the proton polarization during the energy ramp and physics store. The current working point is constrained between 2/3 and 7/10: 2/3 is a strong third-order betatron resonance; 7/10 is a 10th-order betatron resonance and also a spin depolarization resonance [1]. Experiments and simulations have shown that the beam lifetime and the proton polarization are reduced when the vertical tune of the proton beam is close to $7/10$.

The main limits to the beam lifetime in the RHIC p-p runs are the beam–beam interaction, the non-linear magnetic field errors in the interaction regions (IRs), the non-linear chromaticities with low β^*s, the horizontal and vertical third-order betatron resonances, and the machine and beam parameter modulations.

*This work was supported by Brookhaven Science Associates, LLC under Contract No. DE-AC02-98CH10886 with the US Department of Energy.

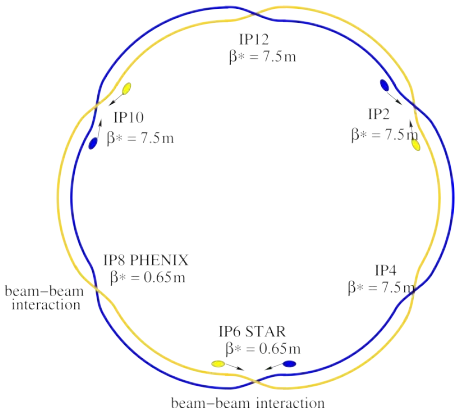

Figure 1: The layout of the RHIC. Two beams collide at IP6 and IP8.

To further increase the luminosity, we can either increase the bunch intensity or reduce β^*. Figure 2 shows the proton tune footprints including beam–beam interactions. In this calculation, the proton bunch intensity is 2.0×10^{11} and the 95% normalized transverse emittance is 15π mm·mrad. The total beam–beam parameter with two collisions is 0.02. From Fig. 2, there is not enough tune space to hold the large beam–beam tune spread when the proton bunch intensity is larger than 2.0×10^{11}.

To minimize the beam–beam tune spread and to compensate the non-linear beam–beam resonance driving terms, head-on beam–beam compensation with electron lenses (e-lenses) is adopted for the RHIC [2, 3, 4]. Two e-lenses are being installed on either side of IP10, one for the Blue ring and one for the Yellow ring. The goal of head-on beam–beam compensation is to double the current RHIC luminosity in the p-p operations.

OBSERVATIONS

Previous p-p Runs

The luminosity in the p-p collision is given by

$$L = \frac{3N_{\mathrm{p}}^2 N_{\mathrm{b}} \gamma f_{\mathrm{rev}}}{2\pi\epsilon_{\mathrm{n}}\beta^*} H(\frac{\beta^*}{\sigma_{\mathrm{l}}}). \quad (1)$$

Here, N_{p} is the proton bunch intensity, N_{b} is the number of bunches, γ is the Lorentz factor, and f_{rev} the revolution frequency. ϵ_{n} is the 95% normalized emittance and σ_{l} the r.m.s. bunch length. $H(\frac{\beta^*}{\sigma_{\mathrm{l}}})$ is the luminosity reduction due to the hourglass effect. The total beam–beam parameter, or the total linear incoherent beam–beam tune shift with two

978-92-9083-404-5, 0007-8328 – © CERN, 2014. Published under the Creative Common Attribution CC BY 4.0 Licence.
http://dx.doi.org/10.5170/CERN–2014–004.19

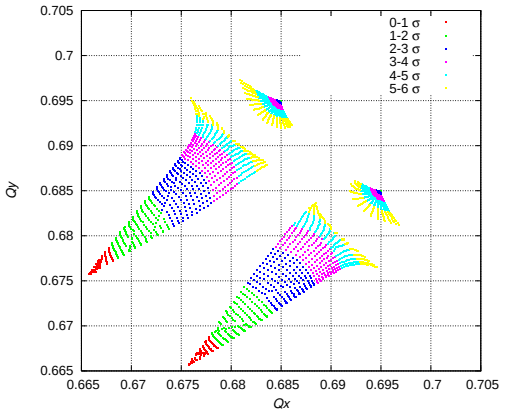

Figure 2: Tune footprints without and with beam–beam. The bunch intensity is 2.0×10^{11}.

collisions, is

$$\xi = \frac{3N_{\rm p}r_{\rm p}}{\pi\epsilon_{\rm n}}. \qquad (2)$$

Here, $r_{\rm p}$ is the classical radius of a proton. We have assumed two collisions, at IP6 and IP8.

In the 2009 RHIC 100 GeV p-p run, with β^*=0.7 m and a bunch intensity of 1.5×10^{11}, we observed a shorter beam lifetime of 7 h compared to 12 h in the 2008 RHIC 100 GeV p-p run with $\beta^* = 1.0$ m [5, 6, 7, 8]. In the 2012 RHIC 100 GeV p-p run, $\beta^* = 0.85$ m lattices were adopted, and the beam lifetime was 16 h with a typical bunch intensity of 1.65×10^{11} [9].

In the 2011 250 GeV and 2012 255 GeV p-p runs, a common 9 MHz RF system was used to produce a long bunch length on the energy acceleration to maintain both transverse and longitudinal emittances [9, 10]. When the beams reached store energy, the bunches were re-bucketed to the 28 MHz RF system. To achieve an even shorter bunch length, we added 300 kV 197 MHz RF voltages at store. In these two runs, β^* at the collision points was 0.65 m. The maximum bunch intensity reached 1.7×10^{11}. The store length was 8 h. Table 1 shows the lattice and typical beam parameters in the 2012 RHIC 255 GeV p-p runs.

Beam Lifetime

In the previous RHIC p-p runs, after the beams were brought into collision, we normally observed a large beam loss in the first hour, followed by a slow beam loss in the rest of store. At the beginning, the instant maximum beam loss rate could reach 30% per hour. The beam loss rate of the slow loss was typically 1-2% per hour. The burn-off contribution to the beam loss rate is less than 1% per hour.

Empirically, the total beam intensity can be fitted with double exponentials [11]:

$$N_p(t) = A_1 \exp(-t/\tau_1) + A_2 \exp(-t/\tau_2), \qquad (3)$$

where $N_p(t)$ is the bunch intensity, and $A_{1,2}$ and $\tau_{1,2}$ are fit parameters. Figure 3 shows an example of beam intensity evolution at store that was fitted with Eq. (3). Figure 4 shows (τ_1,τ_2) of the physics stores in the past three 250 GeV or 255 GeV p-p runs. The reasons for the fast and slow beam losses will be discussed in the next section.

Table 1: Parameters in 2012 255 GeV p-p Runs

Parameter	Unit	Value
No. of colliding bunches	-	107
Protons per bunch	10^{11}	1.7
Transverse emittances	mm.mrad	20
β^* at IP6/IP8	m	0.65
Longitudinal emittances	eV.s	2
Voltage of 28 MHz RF	kV	360
Voltage of 197 MHz RF	kV	300
R.m.s. momentum spread	10^{-4}	1.7
R.m.s. bunch length	m	0.45
Beam–beam parameter per IP	-	0.007
Hourglass factor	-	0.85
Peak luminosity	10^{30}cm^{-2}s^{-1}	165

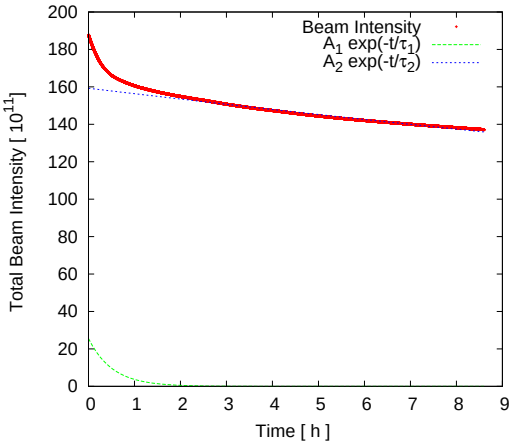

Figure 3: An example of the Blue ring beam intensity evolution at store that was fitted with Eq. (3). The fill number is 16697.

Transverse Emittance and Bunch Length

The transverse emittances are routinely measured with Ionization Profile Monitors (IPMs) in the RHIC. Figure 5 shows an example of the IPM-measured emittances at store. IPMs require knowledge of β functions and need periodic calibrations of micro-channels. An averaged all-plane emittance of both rings can be derived from luminosity based on Eq. (1). In the previous RHIC p-p runs, after beams were brought into collision, the measured emittances decreased in the first hour and then slowly increased in the rest of store. The early emittance reduction was related to the large beam loss at the beginning of store. Experiments showed that the emittance growth with beam–beam was smaller than that without beam–beam.

Bunch length was measured with a Wall Current Moni-

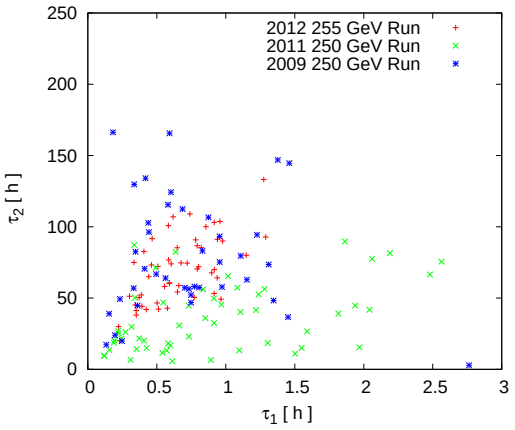

Figure 4: The Blue ring beam loss fit parameters τ_1 and τ_2 in the previous 250 GeV runs.

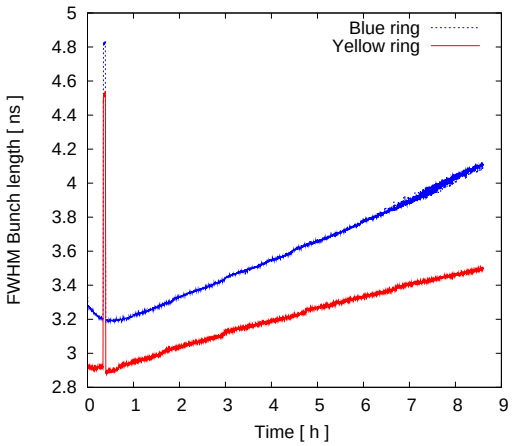

Figure 6: WCM-measured FWHM bunch length at store for fill 16697.

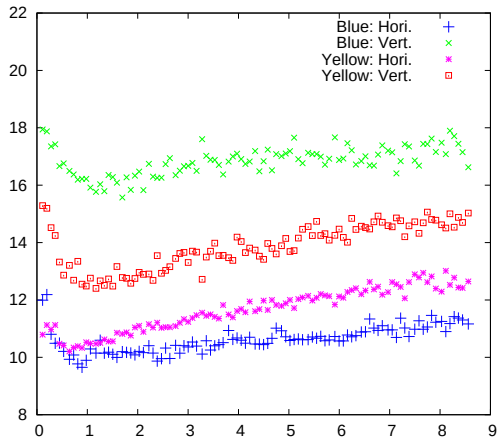

Figure 5: IPM-measured transverse emittances at store for fill 16697.

tor (WCM). Figure 6 shows one example of averaged Full Width Half Maximum (FWHM) bunch lengths at store. The spikes around 0.4 h in the plot were due to polarization measurement. To improve the signal-to-noise ratio during the polarization measurement, the voltages of the 197 MHz RF cavities were temporarily reduced to 20 kV. After the beams were brought into collision, the bunch length decreased in the first hour and then slowly increased in the rest of store. The early bunch length reduction was related to the large beam loss at the beginning of store, and the bunch length growth with beam–beam was less than that without beam–beam interaction.

EXPLANATIONS

The Beam Loss Rate and Beam-Beam

The store beam loss rate was mainly determined by the beam–beam interaction. Without beam–beam interaction, the beam loss rate can be better than 1% per hour, depending on the machine tuning. After the beams were brought into collision, the instant beam loss rate could reach a maximum of 30% per hour. The beam loss rates for bunches with one and two collisions were different. In the RHIC, 10 out of 109 bunches have only one collision instead of two collisions. For example, for fill 15386, for bunches with one collision, the fitted (τ_1, τ_2) are (1.5 h, 100 h), while for the bunches with two collisions, they are (0.8 h, 30 h).

The Particle Loss Mechanism

The WCM profile is actually the particle population distribution in the longitudinal plane. For a given period, we can calculate the number of particles leaking out of the central bunch area. Figure 7 shows each bunch's particle leakage percentage out of the $[-5$ ns, 5 ns] area during the first 0.5 h in the Blue ring in fill 15386, together with the actual particle loss percentage in the same period. The patterns of particle leakage and particle loss show a strong linear correlation, as shown in Fig. 8.

The strong linear correlation between particle leakage and particle loss is also true for the rest of store. During the RHIC p-p runs, there was no de-bunched beam observed from the WCM profiles. Considering that particles in the bunch tail have larger off-momentum deviation, we conclude that the particles got lost in the transverse plane due to a small transverse off-momentum dynamic aperture with beam–beam interaction.

The Off-momentum Dynamic Aperture

To achieve a short bunch length at physics store, 197 MHz RF cavities were used besides the acceleration RF cavities of 28 MHz. Figure 9 shows a typical longitudinal bunch profile. With 197 MHz cavities, the relative momentum spread for the centre bucket between $[-2.5$ ns, 2.5 ns] increases to 5×10^{-4}. And for the tail particles

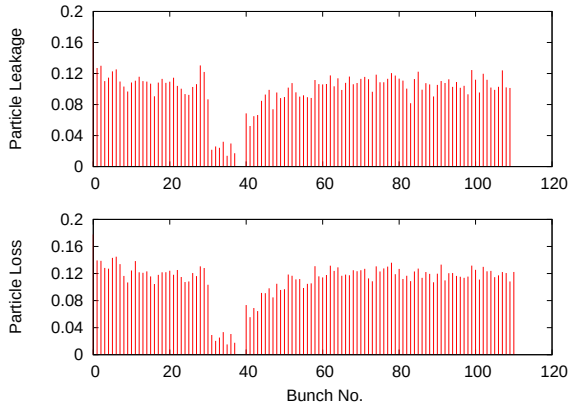

Figure 7: The particle leakage and particle loss of all bunches in fill 15386.

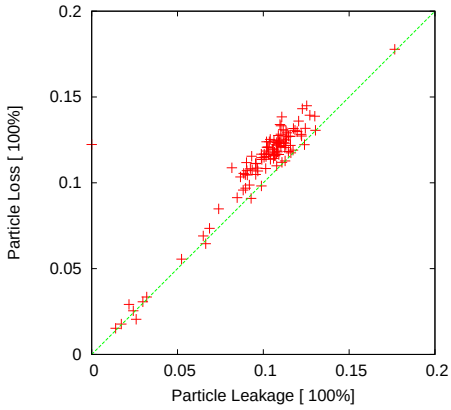

Figure 8: Correlation of the particle leakage and particle loss of all bunches in fill 15386.

out of [−6 ns, 6 ns] (full width), the relative momentum deviation is greater than 6×10^{-4}.

Figure 10 shows the calculated off-momentum dynamic aperture without and with beam–beam interaction from a 10^6-turn particle tracking. The 2012 255 GeV Yellow ring lattice is used. The off-momentum dynamic aperture with beam–beam is much smaller than that without beam–beam when the relative off-momentum deviation $\mathrm{d}p/p_0 > 4 \times 10^{-4}$. For the tail particles with $\mathrm{d}p/p_0 > 6 \times 10^{-4}$, the dynamic aperture is less than 5 σ.

The large beam loss at the beginning of store was related to the initial large number of particles with large momentum deviation. Those particles were generated during RF re-bucketing and 197 MHz RF cavity voltage ramp-up. From WCM profiles, large-momentum particles were observed on both sides of the centre bunch area after re-bucketing. We also observed beam loss shortly after RF re-bucketing without beam–beam. When beams were brought into collision, the transverse off-momentum aperture was reduced. Those particles would get lost sooner or later in the first hour, depending on how close their $(\mathrm{d}p/p_0)_{max}$ to the off-momentum aperture and the longitudinal diffusion rate.

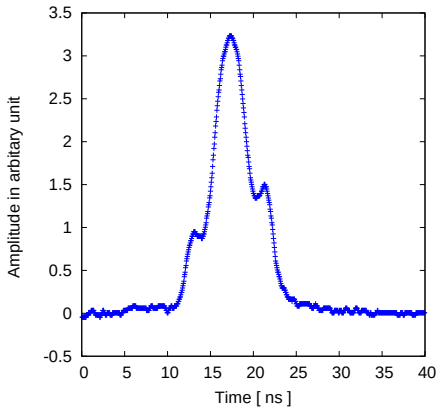

Figure 9: Longitudinal bunch profiles with RF re-bucketing and 197 MHz RF voltages.

Intra-beam Scattering Effects

The slow loss after the first hour into store was linked to slow diffusion processes. Here, we calculate the effects of Intra-Beam Scattering (IBS) on the proton beam emittance and bunch length growth. With a smooth ring approximation, the longitudinal and transverse IBS growth rates can be calculated as follows [12]:

$$\tau_{||}^{-1} = \frac{1}{\sigma_p^2}\frac{\mathrm{d}\sigma_p^2}{\mathrm{d}t}\frac{r_i^2 c N_i \Lambda}{8\beta\gamma^3\epsilon_x^{3/2} < \beta_x^{1/2} > \sqrt{\pi/2}\sigma_l\sigma_p^2}, \quad (4)$$

$$\tau_{\perp} = \frac{\sigma_p^2}{\epsilon_x} < \frac{H_x}{\beta_x} > \tau_{||}^{-1}. \quad (5)$$

Here, σ_l and σ_p are the r.m.s. bunch length and the r.m.s. relative momentum spread. $H_x = \gamma_x D_x^2 + 2\alpha_x D_x D_x' +$

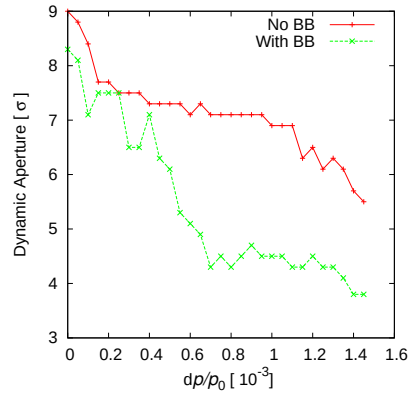

Figure 10: Calculated off-momentum apertures without and with beam–beam interaction.

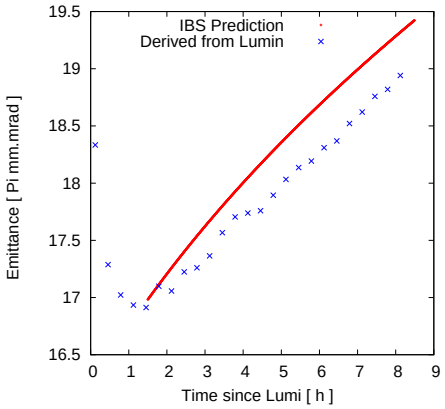

Figure 11: Emittance modelling with IBS for fill 16697, compared to the emittance derived from luminosity.

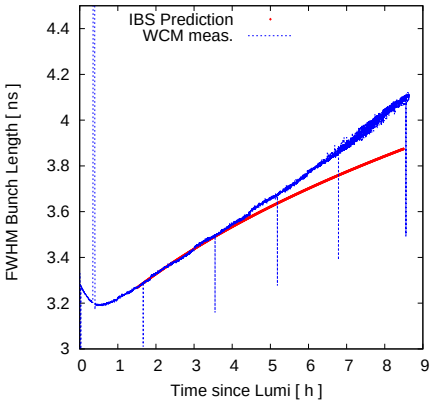

Figure 12: Bunch length modelling with IBS for fill 16697, compared to the WCM bunch length measurement.

$\beta_x D_x'^2$, where $\alpha_x, \beta_x, and \gamma_x$ are Twiss parameters. D_x and D_x' are the horizontal dispersion and its derivative. Λ is the Coulomb logarithm.

Based on Eqs. (2) and (3), Figs. 11 and 12 show an example of the IBS contributions to the emittance and bunch length for fill 16697. We took the bunch intensity evolution, the initial emittance, and the bunch length from the real measurements. Comparing the calculated IBS contributions to the luminosity-derived emittance and the WCM-measured bunch length, the emittance and bunch length growth after 1.5 h into store are largely consistent with IBS.

LIMITS

Low-β^* Lattices

In order to further increase the luminosity, we can either increase the bunch intensity or reduce β^*. A low-β^* lattice increases the β functions in the triplet quadrupoles, and therefore the particles will sample large non-linear magnetic field errors at these locations. As a result, the dynamic aperture will be reduced [13]. For example, in the 2009

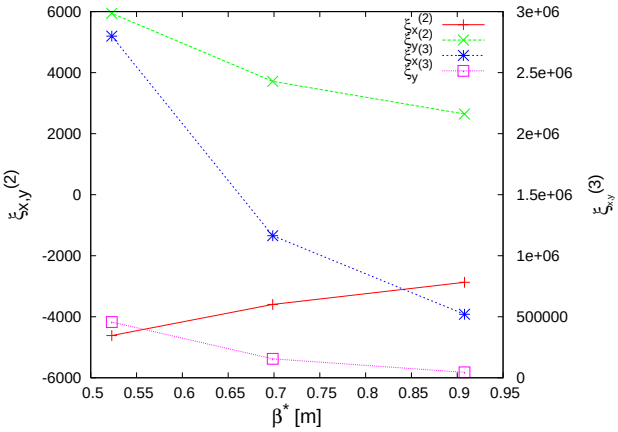

Figure 13: Calculated second- and third-order chromaticities versus β^* in the p-p runs.

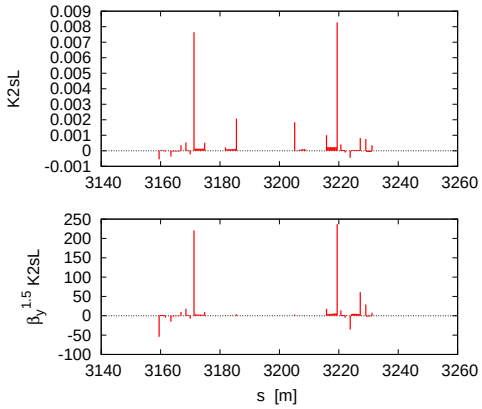

Figure 14: $K_{2s}L$ and $\beta_y^{1.5}K_{2s}L$ in IR8 in the Yellow ring, based on the offline non-linear IR model.

100 GeV p-p run, we used a lattice with $\beta^* = 0.7$ m, which gave a short beam lifetime [8]. At 250 GeV, we achieved $\beta^* = 0.65$ m. The reason is that the transverse beam size is smaller at 250 GeV than at 100 GeV [14].

A low-β^* lattice also increases the non-linear chromaticity and reduces the off-momentum dynamic aperture. Chromatic analysis shows that the non-linear chromaticities are mostly originating from the low-β insertions IR6 and IR8 [15]. The non-linear chromaticities increase dramatically with the decreased β^*. Figure 13 shows the calculated second- and third-order chromaticities as functions of β^*. Large second-order chromaticities push the particles with large momentum errors to the third- or 10th-order resonances. Several correction techniques for non-linear chromaticities have been tested and implemented in the RHIC [16]. To further reduce β^*, we need to balance the hourglass effect, beam lifetime reduction, and the luminosity increase.

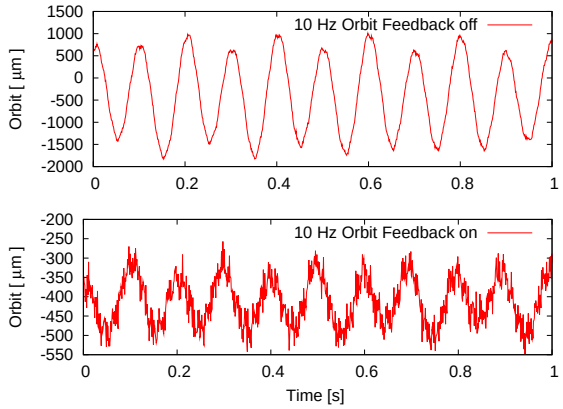

Figure 15: Orbit oscillation without and with 10 Hz orbit feedback. The fill number is 15257.

$3Q_{x,y}$ *Resonances*

To mitigate the coupling between two beams, we would like to mirror the working points of the two RHIC rings on both sides of the diagonal in the tune space. However, in the operation we had to operate with both working points below the diagonal for better beam lifetimes. It was understood in the 2006 100 GeV p-p run that the strong $3Q_x$ resonances at $Q_x = 2/3$ prevented a working point above the diagonal [6]. At that time, the proton bunch intensity was 1.3×10^{11}.

In the 2012 100 GeV run, even with both working points below the diagonal, when the bunch intensity was higher than 1.7×10^{11}, we observed a larger beam loss due to the $3Q_y$ resonance, which is located at $Q_y = 2/3$ [9]. The main contributions to the third-order resonances are from the sextupole and skew sextupole components in IR6 and IR8. As an example, Fig. 14 shows $K_{2s}L$ and $\beta_y^{1.5}K_{2s}L$ in IR8 in the Yellow ring. To reduce the resonance stop-bands, we routinely correct the local sextupole and skew sextupole errors with IR orbit bumps by minimizing the feed-down tune shifts [17], which improved the beam losses experimentally. Measurement and correction of the global third-order resonance driving terms with a.c. dipole excitation were also applied [18, 19].

The 10 Hz Orbit Oscillation

At the beginning of the 2008 100 GeV p-p run, we tested a near-integer working point (0.96, 0.95) in the Blue ring while keeping the working point in the Yellow ring at (0.695, 0.685). Weak–strong beam–beam simulation shows that there is a wider tune space with good dynamic apertures than the working point (0.695, 0.685) [20]. The spin simulation shows that there are weaker spin depolarization resonances in this region as well.

However, operating at near-integer tunes turned out to be very challenging [7]. With such tunes, we found that it was difficult to correct the closed orbit and to control the β-beat. Moreover, both detectors reported high background rates from the beam in the Blue ring when two beams were brought into collision. These backgrounds were caused by horizontal orbit vibrations around 10 Hz, which originated from mechanical vibrations of the low-β triplets driven by the cryogenic flow [21].

We were able to correct the 10 Hz orbit oscillations in the 2011 p-p run by developing a local 10 Hz orbit feedback system [22]. Figure 15 shows an example of horizontal Beam Position Monitor (BPM) readings in the triplet without and with the 10 Hz orbit feedback. The peak-to-peak amplitude of the 10 Hz orbit oscillation was reduced by the feedback system from 2500 μm down to 250 μm. We plan to revisit the near-integer working point in future beam experiment sessions.

SUMMARY

In this article, we have reviewed the beam–beam observations in the previous polarized proton runs in the RHIC. Particle loss happened in the transverse plane, and was due to the limited transverse off-momentum dynamic aperture. Beam–beam interaction, IR non-linear multipole field errors, non-linear chromaticities with low β^*s, and $3Q_{x,y}$ resonances reduce the transverse dynamic aperture. Measures had been implemented in the RHIC to correct the non-linear chromaticities and $3Q_{x,y}$ resonance driving terms. The 10 Hz orbit modulation was reduced by means of a 10 Hz orbit feedback. To further increase the luminosity in the RHIC p-p operations, we plan to increase the bunch intensity and to reduce β^* at collisional IPs. To reduce the large beam–beam tune spread from high bunch intensities, head-on beam–beam compensation with electron lenses is being installed in the RHIC.

ACKNOWLEDGEMENTS

The authors would like to thank M. Bai, M. Blaskiewicz, H. Huang, M. Minty, C. Montag, V. Ptitsyn, V. Scheoffer, and S. White for stimulating discussions during this work.

REFERENCES

[1] M. Bai et al., Phys. Rev. Lett. 96 (2006) 174801.

[2] Y. Luo et al., Phys. Rev. ST Accel. Beams 15 (2012) 051004.

[3] A. Zelenski, Rev. Sci. Instrum. 81 (2010) 02B308.

[4] W. Fischer, "Head-on Beam–Beam Compensation in RHIC," these proceedings.

[5] M. Bai et al., TUODKI04, Proc. PAC'2007.

[6] V. Ptitsyn et al., MOPLS024, Proc. EPAC'2006.

[7] C. Montag et al., WEPP018, Proc. EPAC'2008.

[8] C. Montag et al., MOPEC033, Proc. IPAC'2010.

[9] V. Schoefer et al., MOPPC25, Proc. IPAC'2012.

[10] H. Huang et al., TUPZ035, Proc. IPAC'2011.

[11] W. Fischer et al., BNL C-AD AP Note 235 (2006).

[12] A. Fedotov, BNL RHIC/AP/168 (2009).

[13] Y. Luo et al., WE6PFP007, Proc. PAC'2009.

[14] Y. Luo et al., BNL C-AD AP Note 235 (2006).

[15] Y. Luo et al., THP059, Proc. PAC'2011.

[16] Y. Luo et al., WE6PFP006, Proc. PAC'2009.

[17] F. Pilat et al., WOAC007, Proc. PAC05.

[18] R. Tomas et al., Phys. Rev. ST Accel. Beams 8 (2005) 024001.

[19] Y. Luo et al., FRPMS109, Proc. PAC'2007.

[20] C. Montag et al., TUPAS099, Proc. EPAC'2008.

[21] C. Montag et al., Nucl. Instrum. Methods Phys. A 564 (2006) 26–31.

[22] R. Michnoff et al., MOP268, Proc. PAC'2011.

Published by CERN in the Proceedings of the ICFA Mini-Workshop on Beam–Beam Effects in Hadron Colliders,
CERN, Geneva, Switzerland, 18–22 March 2013, edited by W. Herr and G. Papotti, CERN–2014–004 (CERN, Geneva, 2014)

OPERATIONAL EXPERIENCE WITH CRAB CAVITIES AT KEKB

Y. Funakoshi for the KEKB Commissioning Group
KEK, Ibaraki, Japan

Abstract

KEKB was in operation from December 1988 to June 2010. The crab cavities were installed at KEKB in February 2007 and worked very stably until the end of KEKB operation. Operational experience of the crab cavities with beams is described.

KEKB B-FACTORY

KEKB B-Factory [1] was an energy-asymmetric double-ring e^+e^- collider at KEK in operation from December 1998 to June 2010. KEKB was operated mainly at the $\Upsilon(4S)$ resonance. It was composed of the low-energy positron ring (LER) operated at 3.5 GeV, the high-energy electron ring (HER) operated at 8 GeV, and an injector linac. Two beams collided at the physics detector called 'Belle'. The machine parameters of KEKB with the crab cavities are listed in Table 1 together with the design parameters. The highest luminosity, 2.108×10^{34} cm^{-2} s^{-1}, was achieved in June 2009. The peak luminosity is twice as high as the design value and is the highest value in the world so far.

The HER beam current exceeded the design value, but the LER beam current was lower than the design. This is not attributable to hardware limits; the luminosity saturated at around 1.6 A, and a higher beam current did not bring a higher luminosity. We believe that this is due to electron cloud instability. The bunch spacing is also much longer than the design, to mitigate the electron cloud instability. As a result, the bunch currents were much higher than the design. The vertical beta function at the interaction point (IP), β_y^*, was 5.9 mm, much lower than the design value. Because of the crab cavities, the vertical beam–beam parameter (ξ_y) was as high as 0.09, much higher than the design. Another feature of KEKB is that the horizontal tune was very close to a half-integer; this also contributed to the high luminosity. The daily integrated luminosity was twice as high as the design because of the continuous injection mode and the acceleration of two bunches per radio-frequency (RF) pulse at the linac.

Figure 1 shows the history of KEKB. The crab cavities were installed at KEKB in February 2007 and worked stably until the end of KEKB operation. After installation of the crab cavities, the luminosity was somewhat lower than before the crab cavities were installed. Although the specific luminosity was higher, the beam currents, particularly in HER, were much lower and the luminosity was also lower. This was not due to a hardware limitation; as described below, it was caused by the dynamic beam–beam effects. Upon overcoming this problem, the luminosity increased. In addition, the skew-sextupole magnets, which were installed in the winter shutdown of 2009, contributed to a higher luminosity.

Table 2: Comparison of KEKB machine parameters before and after installation of crab cavities.

	May 2008		Nov 2006		
	LER	HER	LER	HER	
Energy	3.5	8.0	3.5	8.0	GeV
Circum.	— 3016 —		— 3016 —		m
$\phi_{\rm cross}$	Crab crossing		— 22 —		mrad
$I_{\rm beam}$	1619	854	1662	1340	mA
$N_{\rm bunches}$	— 1584 —		— 1387 —		
$I_{\rm bunch}$	1.02	0.539	1.20	0.965	mA
ε_x	15	24	18	24	nm
β_x^*	90	90	59	56	cm
β_y^*	5.9	5.9	6.5	5.9	mm
σ_y^*	1.1	1,1	1.9	1.9	μm
$V_{\rm C}$	8.0	13.0	8.0	15.0	MV
ν_x	0.505	0.509	0.505	0.509	
ν_y	0.567	0.596	0.534	0.565	
ν_s	−0.0240	−0.0204	−0.0246	−0.0226	
ξ_x	0.099	0.119	0.117	0.070	
ξ_y	0.097	0.092	0.105	0.056	
Lifetime	94	158	110	180	min.
Luminosity	— 16.10 —		— 17.12 —		/nb/s
Lum/day	— 1.092 —		— 1.232 —		/fb

CRAB CROSSING SCHEME

Motivation of Crab Cavities

One of the design features of KEKB is the horizontal crossing angle of ± 11 mrad at the IP. Although the crossing angle scheme has many merits, the beam–beam performance may degrade. In the design of KEKB it was predicted that the vertical beam–beam parameter ξ_y could be as high as 0.05 if betatron tunes are chosen properly. The crab crossing scheme was proposed by R. Palmer in 1988 [2] as an approach to recovering the head-on collision with the crossing angle for linear colliders. It has also been shown that the synchro-betatron coupling terms associated with the crossing angle in ring colliders are cancelled by crab crossing [3]. The crab crossing scheme has been considered in the design of KEKB as a back-up measure to guard against possible problems with the crossing angle. Previously the crab cavities had seemed not to be urgently necessary, as KEKB achieved $\xi_y > 0.05$ at the early stage of its operation in 2003. Later, however, interesting beam–beam simulation results appeared [4–6], predicting

978-92-9083-404-5, 0007-8328 –
http://dx.doi.org/10.5170/CERN–2014–004.27

Table 1: Machine parameters of KEKB (27 June 2009). Parameters in parentheses are the design parameters.

	LER	HER	Unit
Energy	3.5	8.0	GeV
Circumference	— 3016 —		m
RF frequency	— 508.88 —		MHz
Horizontal emittance	18 (18)	24 (18)	nm
Beam current	1637 (2600)	1188 (1100)	mA
Number of bunches	— 1585[a] ($\sim$ 4600[b]) —		
Bunch current	1.03 (0.57)	0.75 (0.24)	mA
Bunch spacing	— 1.84 (0.59) —		m
Total RF voltage	8.0 (5–10)	13.0 (10–20)	MV
Synchrotron tune ν_s	-0.0246 (-0.1 to -0.2)	-0.0209 (-0.1 to -0.2)	
Horizontal tune ν_x	45.506(45.52)	44.511 (47.52)	
Vertical tune ν_y	43.561 (45.08)	41.585 (43.08)	
Betas at IP β_x^*/β_y^*	120/0.59 (33/1)	120/0.59 (33/1)	cm
Momentum compaction α	3.31 (1–2)	3.43 (1–2)	$\times 10^{-4}$
Beam–beam parameter ξ_x	0.127 (0.039)	0.102(0.039)	
Beam–beam parameter ξ_y	0.129 (0.052)	0.090 (0.052)	
Vertical beam size at IP σ_y^*	0.94[c] (1.34)	0.94[c] (1.34)	μm
Beam lifetime	133@1637	200@1188	min@mA
Luminosity (Belle CsI)	— 2.108 (1.0) —		10^{34} cm^{-2} s^{-1}
Total integrated luminosity	— 1041 —		fb^{-1}

[a] With 5% bunch gap.
[b] With 10% bunch gap.
[c] Value estimated from the luminosity, assuming that the horizontal beam size is equal to the calculated value.

that the head-on collision or crab crossing provides a higher value of ξ_y, around 0.15, if combined with a horizontal tune that is very close to a half-integer, such as 0.508. Figure 2 shows the comparison of ξ_y for the head-on collision (crab crossing) with that for the crossing angle, obtained by a strong–strong beam–beam simulation. Afterwards, the development of crab cavities was revitalized, and they were finally installed at KEKB in February 2007.

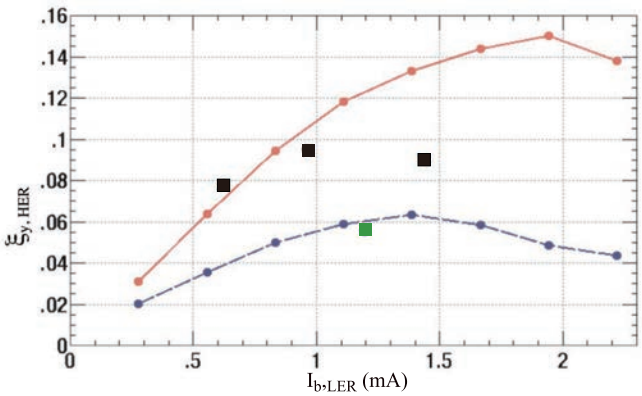

Figure 2: Predicted beam–beam parameters obtained from strong–strong beam–beam simulations with crossing angle 22 mrad (purple) and for head-on or crab crossing (red). Some experimental data are also shown (squares), with black and green squares representing data with and without the crab cavities, respectively.

Single Crab Cavity Scheme

In the original design of KEKB, we had planned to install two crab cavities for each ring on both sides of the IP, so that the crab kick excited by the first cavity would be absorbed by another one. The single crab cavity scheme extends the region with crab orbit until the two cavities eventually merge with each other at a particular location in the ring. Thus it needs only one cavity per ring. The layout is shown in Fig. 3. This scheme not only saved us the cost of the cavities but also made it possible to use the existing cryogenic system in the Nikko region, which has been utilized for the superconducting accelerating cavities.

In the single crab cavity scheme, the following equation should be satisfied for the two beams to achieve a head-on collision:

$$\frac{\phi_x}{2} = \frac{\sqrt{\beta_x^{\mathrm{C}}\beta_x^*}\,\cos\bigl(\pi\nu_x - |\Delta\psi_x^{\mathrm{C}}|\bigr)}{2\sin\pi\nu_x}\,\frac{V_{\mathrm{C}}\,\omega_{\mathrm{RF}}}{Ec}.$$

Here ϕ_x is the full crossing angle; β_x^{C} and β_x^* are the beta functions at the crab cavity and the IP, respectively; $\Delta\psi_x^{\mathrm{C}}$ denotes the horizontal betatron phase advance between the crab cavity and the IP; ν_x is the horizontal tune; and V_{C} and ω_{RF} are the crab voltage and the angular RF frequency, respectively. Typical values for these parameters are shown

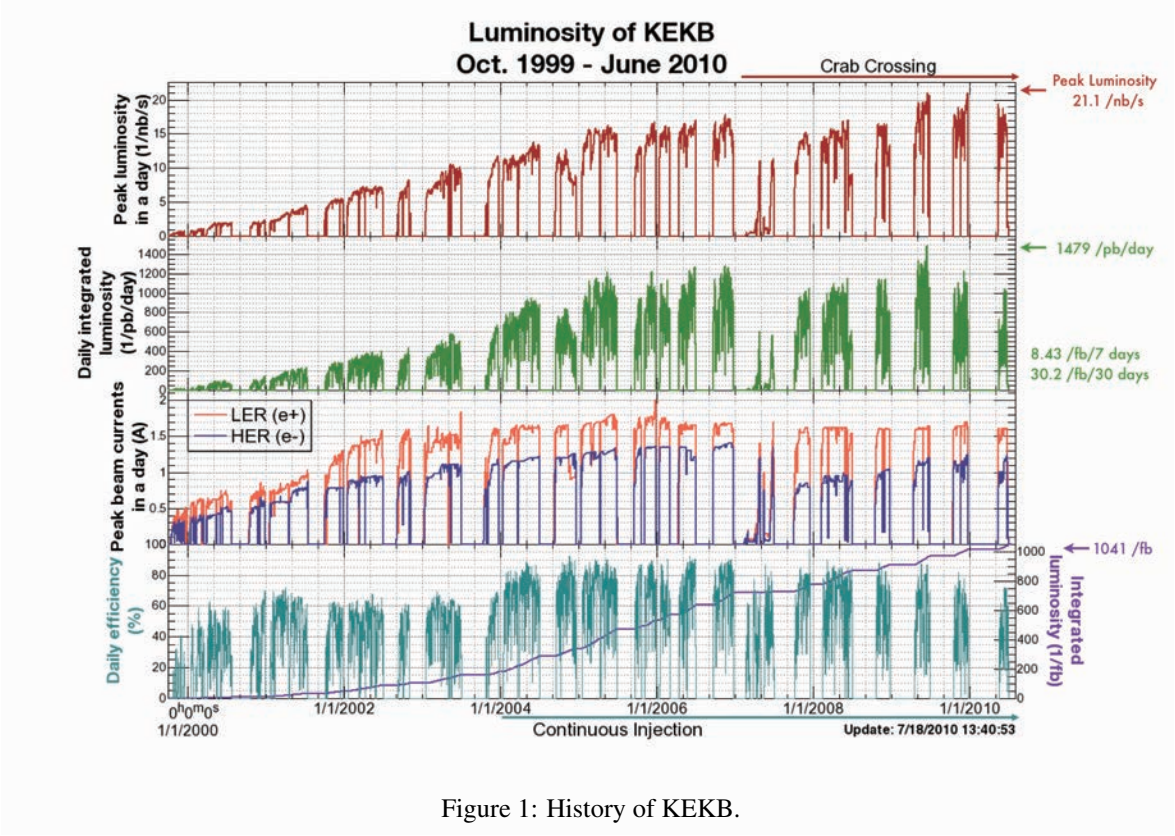

Figure 1: History of KEKB.

in Table 3.

Table 3: Typical parameters for the crab cavities. The crossing angle, the horizontal beta functions at the IP and crab cavities, the horizontal tunes, the horizontal phase advance from the cavities to the IP, the crab voltage, and the RF frequency are shown.

	LER	HER	Unit
ϕ_x	— 22 —		mrad
β_x^*	1.2	1.2	m
$\beta_x^{\rm C}$	51	122	m
ν_x	45.506	44.511	
$\psi_x^{\rm C}/2\pi$	0.25	0.25	
$V_{\rm C}$	0.97	1.45	MV
$f_{\rm RF}$	— 508.89 —		MHz

The beam optics was modified for the crab cavities to give the necessary magnitude of the beta functions at the cavities and the proper phase advance between the cavities and IP. A number of quadrupoles have switched polarity and come to have independent power supplies.

OPERATION WITH CRAB CAVITIES

Tuning Method for Crab Cavity Parameters with Beams, and Beam Tuning with Crab Cavities

Crab voltage Prior to beam operation, calibration of the crab voltage was done by using the klystron output power and the loaded Q values of the crab cavities without actual beams. The crab voltage was also calibrated by using beams. If a bunch passes by the crab cavity at the zero-cross timing of the crab RF voltage, the centre of the bunch receives no dipole kick. When the crab phase shifts from this condition, the bunch receives a net dipole kick from the cavity as in the case of a steering magnet. This dipole kick makes a closed orbit distortion (COD), and its size depends on the crab phase. From the CODs around the ring created by the crab cavity, the dipole kick angle can be estimated. By scanning the crab phase by more than 360° and fitting the kick angle estimated at each data point as a function of the crab phase, the crab voltage can be determined. The crab voltage thus determined is consistent with that calibrated from the klystron power and the Q value to within a few percent. From the crab phase scan and the fit, the phase shifter of the crab cavity system can also be calibrated. For the actual beam operation in the physics run mode, the crab voltages of both rings are scanned to maximize the luminosity, as shown below.

Crab phase In principle, the crab phase should be set so that the centre of the bunch passes by at the zero-cross

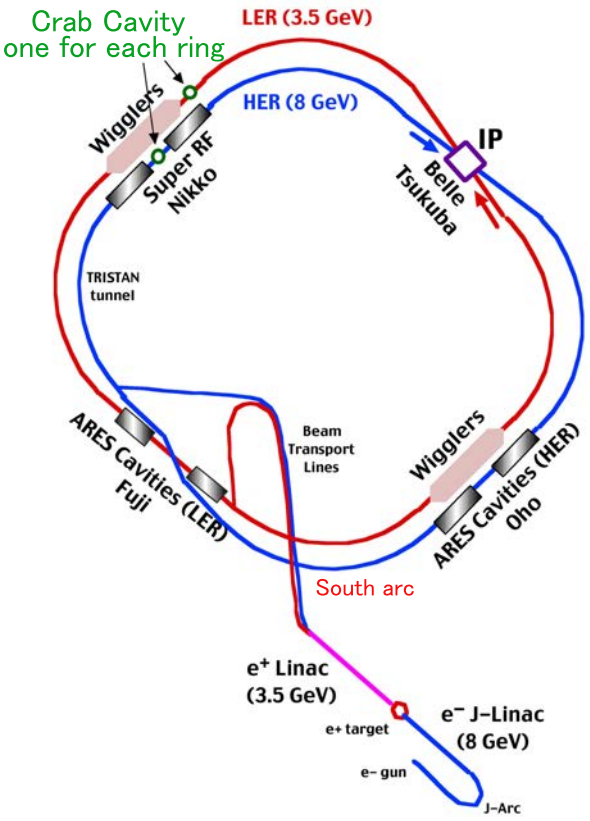

Figure 3: Layout of the KEKB rings and crab cavities.

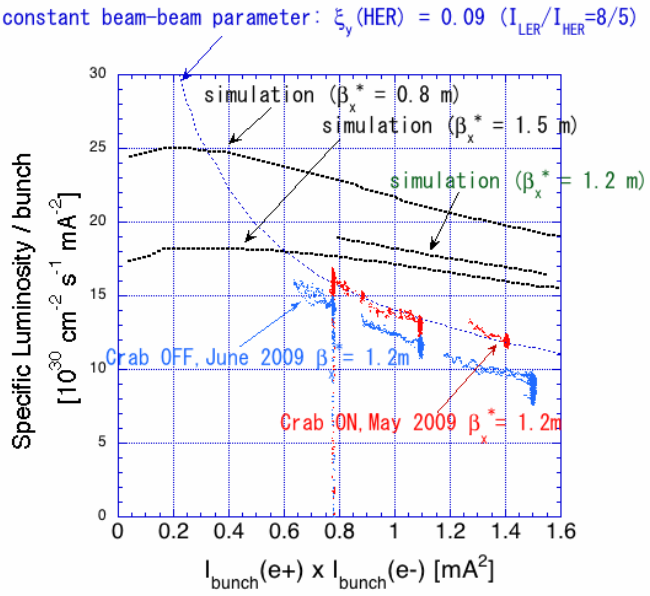

Figure 4: Comparison of the specific luminosity per bunch with and without the crab cavities, as a function of the bunch current product of the two beams. The specific luminosity is defined as the luminosity divided by the bunch current product of the two beams, further divided by the number of bunches. In addition, three different lines from the beam–beam simulation are shown, corresponding to different values of the IP horizontal beta function, β_x^*. The simulations predicted that a smaller β_x^* (smaller σ_x^*) would give a higher luminosity. Also shown is a line that corresponds to a constant vertical beam–beam parameter for an HER of 0.09, assuming that the bunch current ratio between LER and HER is 8 : 5. The data with crab cavities are aligned on this line, which means that the HER vertical beam–beam parameter, $\xi_y(\mathrm{HER})$, is saturated at around 0.09.

timing of the crab cavity. In this situation, the bunch receives no net dipole kick. This condition can be found by scanning the crab phase as described above; however, the method is rather time-consuming and so a easier approach is used in the usual operation. This alternative method involves searching by trial and error for the crab phase that brings no change in the COD between the crab on and off. Although there are two zero-cross phases, we can choose the correct phase by observing the phase of the COD. In the actual physics run, where high beam currents are needed, the crab phase is shifted by a certain amount (typically 10°) to suppress the dipole oscillation observed at high-current crab collision. The COD induced by the net dipole kick from the crab cavity can be compensated for by employing steering magnets in the ring.

Beam orbits at the crab cavities The beam loading for the crabbing mode increases linearly with a horizontal orbit displacement from the centre of the crab cavity. If the RF power to operate the cavity is too sensitive to the beam orbit, the cavity operation under the existence of the beams could be difficult. To avoid this situation, we have chosen the loaded Q value of the cavity to be $Q_\mathrm{L} = 1\text{–}2 \times 10^5$. With this relatively low Q value, the RF power for the operation is relatively high (typically 100 kW at 1.4 MV); however, the RF power becomes less sensitive to the beam orbit (with a typical 20% change per 1 mm orbit change). When we condition the cavity, we need a higher power; but with this Q value, 200 kW is sufficient for conditioning the cavity up to 2 MV. In addition, we have developed an orbit feedback system to keep the horizontal beam orbit at the crab cavity stable [7]. This system is composed of four horizontal steering magnets to make an offset bump for each ring, together with four beam position monitors (BPMs) for each ring to monitor the beam orbit at the crab cavity. The design system speed is 1 Hz, and the target accuracy of the orbit is within 0.1 mm. However, in the actual beam operation, we found that the beam orbit is stable enough even without the orbit feedback system. Therefore, we usually do not use the orbit feedback system. At the beginning of the beam operation with the crab cavities, we searched for the field centre in the cavities by measuring the amplitude of the crabbing mode excited by beams when the cavities were detuned. In this search, the field centre of the HER crab cavity was found to be shifted by about 7 mm from

the assumed centre position of the crab cavity. A possible reason for this large displacement is a misalignment of the cavity. We feel that there could be such a large misalignment, as precise alignment of the crab cavity to the cryostat is very difficult.

Luminosity tuning with crab cavities Luminosity tuning in general is described above. Here we describe the method of luminosity tuning related to the crab cavities. In the following, we discuss two tuning items: the crab V_c (crab voltage) scan, and the tuning on the x–y coupling at the crab cavities. For the crab V_c, the calibration can be done with a single beam as mentioned above; this, however, is not enough for the beam collision operation, since optics errors like those for the beta functions or the phase advance between the crab cavity and IP could shift the optimum crab V_c. In the actual tuning, we first tune the balance of the crab V_c between the two rings. For this purpose, we employ a trick to change the crab phase slightly and observe the orbit offset at the IP. The IP orbit feedback system [8] can detect the orbit offset at the IP precisely. Changing the crab phases of both rings by a certain amount (typically 10–15°), we tune the balance of the crab V_c between the two rings so that the IP orbit offset becomes the same for both rings. In this tuning, we rely on the accuracy of the phase shifter of the crab cavity system. Keeping this balance (the ratio of the crab V_c), we scan the crab V_c for both rings and set the values that give the maximum luminosity. In our experience, the optimum set of the crab V_c thus found is not much different from the calibrated values with the single beam. The difference is usually within 5%.

The motivation for controlling the x–y coupling at the crab cavities is to handle the vertical crabbing. In principle, the crab cavity kicks the beam horizontally; but if there is x–y coupling at the crab cavity or if the crab cavity has some rotational misalignment, the beam could receive a vertical crab kick, and this may degrade the luminosity. The local x–y coupling is expressed with four parameters, $R1$, $R2$, $R3$, and $R4$, as described above. In the actual beam operation, these coupling parameters are scanned one by one to maximize the luminosity. We have found that the tuning with these knobs has some effect on the luminosity and that the luminosity gain with the knobs is typically 5%. We expected that $R2$ and $R4$ might have an effect on the luminosity, since these parameters are related to the vertical crab at the IP. In reality, however, there is no big difference in the effectiveness of the four parameters with respect to luminosity tuning.

Specific Luminosity With and Without the Crab Cavities

Since the introduction of the crab cavities, we have made efforts [9, 10] to realize the beam–beam performance predicted by the beam–beam simulation. As a result of those efforts, we have achieved a relatively high beam–beam parameter of about 0.09, as shown in Table 4. We have found the correction of the chromaticity of the x–y coupling at IP to be effective in increasing the luminosity [11]. This correction increased the vertical beam–beam parameter from about 0.08 to around 0.09. However, even with this improvement, the beam–beam parameter 0.09 is still much lower than the value of around 0.15 predicted by simulation. We do not yet understand the cause of this discrepancy.

Table 4: Comparison of KEKB machine parameters with and without crab crossing.

	Jun 2010 With crab		**Nov 2006** Without crab		
	LER	HER	LER	HER	Unit
Energy	3.5	8.0	3.5	8.0	GeV
Circum.	— 3016 —		— 3016 —		m
$I_{\rm beam}$	1637	1188	1662	1340	mA
# bunches	— 1585 —		— 1387 —		
$I_{\rm bunch}$	1.03	0.75	1.20	0.965	mA
Avg. spacing	— 1.8 —		— 2.1 —		m
Emittance	18	24	18	24	nm
β_x^*	120	120	59	56	cm
β_y^*	5.9	5.9	6.5	5.9	mm
Ver. size @ IP	0.94	0.94	1.8	1.8	μm
RF voltage	8.0	13.0	8.0	15.0	MV
ν_x	0.506	0.511	0.505	0.509	
ν_y	0.561	0.585	0.534	0.565	
ξ_x	0.127	0.102	0.117	0.071	
ξ_y	0.129	0.090	0.108	0.057	
Lifetime	133	200	110	180	min.
Luminosity	2.108×10^{34}		1.760×10^{34}		$/\mathrm{cm}^2/\mathrm{s}$
Lum/day	— 1.479 —		— 1.232 —		fb^{-1}

Figure 4 compares the specific luminosity per bunch with the crab cavities on and off. The specific luminosity is defined as the luminosity divided by the bunch current product of the two beams, further divided by the number of bunches. If the beam sizes are constant with respect to the beam currents, the specific luminosity per bunch should be constant. As seen in Fig. 4, the specific luminosity is not constant. This means that the beam sizes are enlarged as functions of the beam currents. In the experiment to obtain data in Fig. 4, the number of bunches was reduced to 99 to avoid the possible effects of the electron clouds. In the usual physics operation, the number of bunches was 1585. For this experiment, the IP horizontal beta function, β_x^*, was changed from 0.8 m to 1.2 m to avoid the physical aperture problem and to increase the bunch currents. In the usual physics operation, the bunch current product was around 0.8 mA^2. The specific luminosity per bunch with the crab on is about 20% higher than that with the crab off. Since the geometrical loss of the luminosity due to the crossing angle is calculated to be about 11%, there is definitely some gain in the luminosity by the crab cavities other than recovery of the geometrical loss. However, the effectiveness of the crab cavities is much smaller than in the beam–beam simulation, as can be seen in Fig. 4. The

beam–beam parameter is strictly constrained for some unknown reasons.

Efforts to Increase Specific Luminosity with Crab Cavities

Performance with the crab cavities has been considered very important not only for KEKB but also for SuperKEKB in the so-called high-current scheme. Therefore, we have been making every effort to understand the discrepancy between the beam–beam simulation and the experiments on beam–beam performance with the crab cavities. Although we have not identified the cause, we summarize our efforts as follows.

Short beam lifetime related to physical aperture around crab cavities In beam operation with the crab cavities, we encountered a situation where we could not increase the bunch current of one beam due to poor beam lifetime of the other beam. We took this issue seriously and made efforts to overcome it, since it is a possible cause of degradation of the beam–beam performance with the crab crossing. We were able to identify the process responsible for the lifetime decrease: dynamic beam–beam effects, i.e. the dynamic beta effect and the dynamic emittance effect. Since the horizontal tune of KEKB is very close to a half-integer, the effects are very large. In Fig. 5, the beta functions around the LER ring are depicted with and without the dynamic beam–beam effect before we solved the problem. The horizontal beta function around the crab cavity becomes very large. Here, the horizontal tune was 0.506 and the unperturbed horizontal beam–beam parameter was around 0.127, with the operation bunch current of HER. Without the beam–beam perturbation, the horizontal beta functions at the IP and at a quadrupole magnet next to the crab cavity were 0.9 m and 161 m, respectively. With the beam–beam effect, the beta functions were calculated to be 0.138 m and 1060 m at the IP and the quadrupole magnet, respectively. To meet the crab condition, the horizontal phase advance between the crab cavity and the IP was chosen to be $\pi/2$ times an odd integer. With this phase advance, the horizontal beta function becomes very large around the crab cavity. Also, due to the dynamic beam–beam effect, the horizontal emittance (ε_x) was enlarged from 18 nm to around 52 nm. In this situation, we have found that the horizontal beam size around the crab cavity is very large (typically 7 mm) at the operation bunch currents, and the physical aperture there is only around $5\sigma_x$. Therefore, the physical aperture around the crab cavities could seriously affect the beam lifetime. The same problem is also observed at HER, although the effect is less serious because the horizontal tune of HER is further away from the half-integer than in the LER case.

To mitigate this problem, we have taken several countermeasures. In the original optics of LER, the horizontal beta function around the crab cavity took the local maximum value not at the crab cavity but at the quadrupole magnets closest to the crab cavity. To satisfy the crab condition, the horizontal beta function at the crab cavity should be set at the target value. If we can decrease the beta function at the quadrupole magnet while keeping the beta function at the crab cavity unchanged, we can widen the physical acceptance around the crab cavity. During the summer shutdown

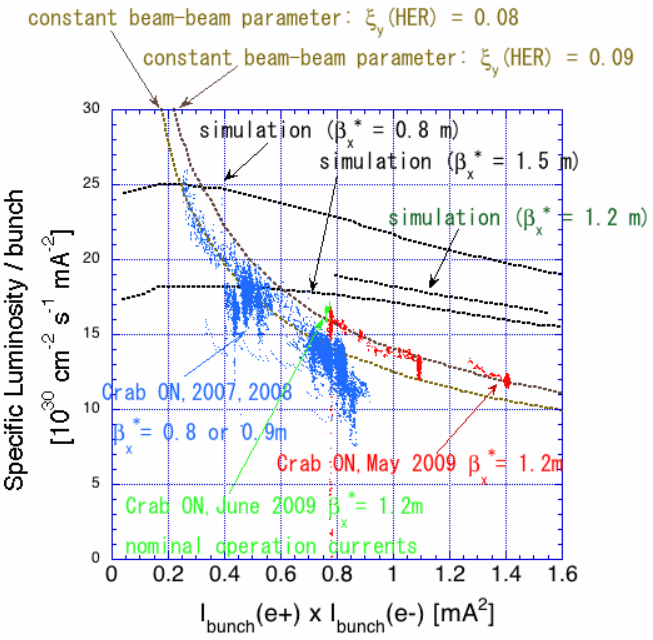

Figure 6: Specific luminosity per bunch as a function of the bunch current product of the two beams, for different values of β_x^*. In addition, three different lines from the beam–beam simulation are shown, corresponding to different values of the IP horizontal beta function, β_x^*. The simulations predicted that a smaller β_x^* (smaller σ_x^*) would give a higher luminosity. Also shown are lines that correspond to constant vertical beam–beam parameters for HER values of 0.08 and 0.09, assuming that the bunch current ratio between LER and HER is 8 : 5. The data with crab cavities are aligned on those lines, which means that the HER vertical beam–beam parameter, $\xi_y(\mathrm{HER})$, was saturated at around 0.08 or 0.09. In the experiment, we found that the luminosity did not depend on the IP horizontal beta functions β_x^*, in contrast to the simulation. The data with $\beta_x^* = 0.8$ or 0.9 m (blue dots) was collected before we introduced the skew-sextupole magnets. The data obtained after introduction of the skew-sextupoles (green and red dots) are aligned on the line corresponding to $\xi_y(\mathrm{HER}) = 0.09$. This means that the maximum beam–beam parameter increased from 0.08 to 0.09 because of the skew-sextupoles. We changed β_x^* from 0.8 or 0.9 m to 1.2 m to increase the bunch currents by mitigating the physical aperture problem at the crab cavities and to be able to compare the data with simulations at a higher bunch current region. Even upon solving the physical aperture problem, a large discrepancy persisted between the simulation and the experiment.

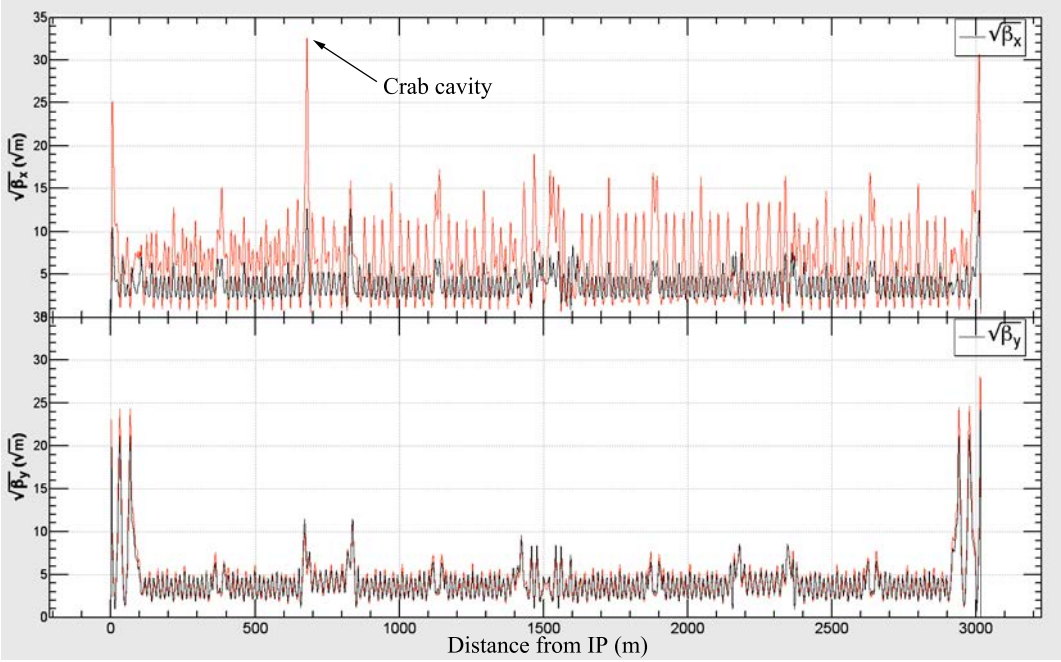

Figure 5: Beating of beta functions due to dynamic beam–beam effects in LER before we took measures to counter this problem, with a ν_x of 0.506 and an unperturbed beam–beam parameter ξ_{x0} of 0.127. The red and black lines are the beta functions with and without the dynamic beam–beam effects, respectively.

of 2008, we changed the optics around the crab cavity by adding some power supplies for the quadrupole magnets and changing the wiring of the power supplies. As a result, the horizontal beta function at the quadrupole magnets next to the crab cavity was reduced to the same value as at the crab cavity. Before this change, the horizontal beta function at the quadrupoles was about twice as large as that at the crab cavity. With this change, the beam lifetime problem was alleviated to some extent; however, when we increased the bunch currents beyond the usual operation values, the lifetime problem appeared again. To investigate the specific luminosity at higher bunch currents, we decided to increase the horizontal beta function at the IP. By enlarging the IP beta function, we can lower the beta function at the crab cavity and enlarge the physical acceptance. We enlarged β_x^* from 0.8 m or 0.9 m to 1.2 m or 1.5 m. With this change, we were able to increase the bunch currents up to the value shown in Fig. 4, and the discrepancy between the simulation and the experiment became more evident. Figure 6 shows a comparison of the specific luminosity with different values of β_x^*. In the beam–beam simulations, as shown in the figure, the specific luminosity with $\beta_x^* = 0.8$ m is much higher than that with $\beta_x^* = 1.5$ m. In the experiment, however, such a change in β_x^* did not make any difference to the specific luminosity. The specific luminosity with $\beta_x^* = 0.8$ m or 0.9 m in Fig. 6 is lower than that with $\beta_x^* = 1.2$ m. This is because the data with $\beta_x^* = 0.8$ m or 0.9 m was taken before the introduction of the skew-sextupole magnets. In Fig. 6, the specific luminosity with the nominal operation bunch currents is also shown (as green dots) for reference. In addition to these counter-measures for the lifetime problem, we also tried to raise the crab voltage. If this were successful, we could have lowered the horizontal beta function at the crab cavity while keeping β_x^* the same. We tried to operate the He refrigerator with lower pressure to lower the He temperature. From the data in the R&D stage, it was expected that we can operate the crab cavity stably with a higher voltage, if the He temperature was lowered. We actually succeeded in lowering the He temperature from 4.4 K to 3.85 K in April 2009. Nevertheless, the maximum crab voltage turned out to be unchanged even with this lower He temperature. Therefore, we gave up this trial.

With these counter-measures in place, we also expected to improve the specific luminosity by solving the lifetime problem, since we sometimes encountered a situation where we could not move some machine parameter, such as a horizontal orbital offset at IP, in the direction giving a higher luminosity because of poor beam lifetime. We found, however, that the lifetime problem has almost nothing to do with the specific luminosity, except in the region of high bunch current where the lifetime problem was particularly serious.

For the short lifetime problem, we have developed another counter-measure of e^+/e^- simultaneous injection. The injector linac is shared by four accelerators: two are the KEKB rings, and the other two are the PF ring and an SR ring called PF-AR. Before the successful introduction of the simultaneous injection scheme, there were four injection modes corresponding to the four rings. Switching

from one mode to another took from about 30 s to around 3 minutes. The idea of simultaneous injection is to switch the injection modes pulse-to-pulse. In the period of KEKB operation, we successfully implemented simultaneous injection for three rings (the two KEKB rings and the PF ring) [12,13]. With this new injection scheme, beam operation with shorter beam lifetime became possible. However, as mentioned above, we found that the lifetime problem has almost nothing to do with the specific luminosity, even though the machine parameter scan at KEKB has become much faster with constant beam currents stored in the rings and it has become possible to find better machine parameters much faster than before.

Synchro-betatron resonance In the KEKB operation, we found that the synchro-betatron resonance of ($2\nu_x + \nu_s$ = integer) or ($2\nu_x + 2\nu_s$ = integer) seriously affects KEKB performance. The nature of the resonance lines was examined in detail during the machine study on crab crossing. We found that the resonances affect (1) single-beam lifetime, (2) single-beam beam sizes (in both horizontal and vertical directions), (3) two-beam lifetime, and (4) two-beam beam sizes (in both horizontal and vertical directions); moreover, the effects are beam-current dependent. The effects lower the luminosity directly or indirectly through beam size blow-up, beam current limitation due to poor beam lifetime, or a smaller variable range of the tunes. The strength of the resonance lines can be weakened by suitably choosing a set of sextupole magnets. KEKB adopted the non-interleaved sextupole scheme to minimize nonlinearity of the sextupoles. LER and HER have 54 pairs and 52 pairs of sextupoles, respectively. With so many degrees of freedom in the number of the sextupoles, optimization of the sextupole setting is not an easy task even with current computing power. Prior to the beam operation, the candidates for the sextupole setting are searched for by computer simulation. Usually, dynamic aperture and an anomalous emittance growth are optimized on the synchro-betatron resonance. A setting of sextupoles that gives good performance in the computer simulation does not necessarily bring good performance in the real machine, and most candidates for the sextupole setting do not yield satisfactory performance. When we changed linear optics, we usually needed to try many candidates before finally obtaining a setting with adequate performance. The single-beam beam size and beam lifetime are criteria for sextupole performance. Alternatively, as an easier method for estimating sextupole performance, a beam loss was observed when the horizontal tune was jumped down across the resonance line. The resonance line in HER is stronger than that in LER, since there is no local chromaticity correction in HER. In usual operation, we could operate the machine with the horizontal tune below the resonance line in the LER case, whereas we could not lower the horizontal tune of HER below the resonance line. The beam–beam simulation predicts a higher luminosity with the lower horizontal tune in HER. To weaken the strength of the resonance line in HER, we tried to change the sign of α (momentum compaction factor). Since ν_s is negative for positive α, the resonance is a sum resonance ($2\nu_x + \nu_s$ = integer). By switching the sign of α, we can change it to a difference resonance ($2\nu_x - \nu_s$ = integer). The trial was undertaken in June 2007; it was successful and we were able to lower the horizontal tune below the resonance. However, when we tried the negative α in LER, an unexpectedly large synchrotron oscillation due to the microwave instability occurred. Because of this oscillation, we gave up the trial of the negative-α optics. So far, we have no definite conclusion about the effect of the synchro-betatron resonance on the specific luminosity.

Machine errors The method of luminosity tuning was described earlier. In the conventional method of tuning at KEKB, most parameters (except for those optimized by observing their own observables) are scanned one at a time just by observing the luminosity and beam sizes. One possible explanation for the low specific luminosity is that we have not yet reached an optimum parameter set, due to the parameter space being too wide. As a more efficient method of parameter search, we introduced in autumn 2007 the downhill simplex method for 12 parameters, consisting of the x–y coupling parameters at the IP as well as the vertical dispersions at IP and their slopes, which from the experience of KEKB operation are very important for luminosity tuning. These 12 parameters can be searched for at the same time with this method. We have been using the method ever since. Nevertheless, even with this method we have not managed to achieve an improvement in specific luminosity, although the speed of parameter search seems to be rather enhanced.

Another possible reason for not being able to achieve a higher luminosity with the above tuning method is the side effects of the large tuning knobs. Although machine errors can be compensated for by using the tuning knobs, too-large tuning knobs bring side effects that would degrade the luminosity. Therefore, if the machine errors are too large, the luminosity predicted by the simulation cannot be achieved by using the usual tuning knobs. We have actually confirmed that large tuning knobs on the x–y coupling at the IP can degrade single-beam performance. The question is how large are the machine errors that exist at KEKB. According to the simulation, with reasonable machine errors such as misalignments of magnets and BPMs, offsets of BPMs, and strength errors of the magnets, large errors of the x–y coupling or the dispersion at IP are not created, as the luminosity cannot be recovered by the knobs because of their side effects. One possibility would be the error related to the detector solenoid. The Belle detector is equipped with the 1.4 T solenoid. The field is locally compensated for by the compensation solenoid magnets installed near the IP, so that the integral of the solenoid field is zero on both sides of the IP. The remaining effects of the solenoid field are compensated for by the skew-quadrupole magnets located close to the IP. If the compensation is not enough

(or if it over-compensates), a large error of the x–y coupling would remain. Although there is no direct evidence that the compensation of the Belle solenoid is not enough, the effect of the Belle solenoid on the luminosity has been doubted, as for the beam-energy dependence of the luminosity. KEKB was designed to operate on the $\Upsilon(4S)$ resonance ($E_{\rm CM} = 10.58$ GeV). KEKB was also operated on $\Upsilon(1S)$ ($E_{\rm CM} = 9.46$ GeV), $\Upsilon(2S)$ ($E_{\rm CM} = 10.02$ GeV), and $\Upsilon(5S)$ ($E_{\rm CM} = 10.87$ GeV). We found that the luminosity on $\Upsilon(5S)$ is almost the same as that on $\Upsilon(4S)$. However, the luminosity on $\Upsilon(1S)$ and $\Upsilon(2S)$ is lower than that on $\Upsilon(4S)$ by about 50% and 20%, respectively. The design beam energy of KEKB is that of $\Upsilon(4S)$, and the x–y coupling due to the Belle solenoid is compensated for completely at this design energy. When we change the beam energy, we do not change the strength of the Belle solenoid and the compensation solenoids. Thus, the x–y coupling correction for the Belle solenoid is not complete on the resonance other than $\Upsilon(4S)$, and the luminosity would be affected by the remaining x–y coupling. To investigate this issue, a machine study was done on $\Upsilon(2S)$ in October 2009 with the Belle solenoid and the compensation solenoid tracked to the beam energy. Contrary to the initial expectation, the luminosity in this condition was even worse than the usual 2S run. We gave up this trial after about two days, since the Belle experiment could not use the data with the different strength of the detector solenoid. Therefore, the correlation between the detector solenoid and the luminosity was not confirmed in this experiment.

We also tried to measure the x–y coupling at the IP directly by using the injection kicker magnets and the BPMs around IP. Although some data showed a very large value of the x–y coupling at IP, we have obtained no conclusive results because of the poor accuracy of the measurements.

Vertical emittance in a single-beam mode The beam–beam simulation showed that the attainable luminosity depends strongly on the single-beam vertical emittance. If the actual vertical emittance is much larger than the assumed value, it could create the discrepancy. We carefully checked the calibration of the beam size measurement system. We found some errors in the calibration of the HER beam size measurement system, and the actual vertical emittance was somewhat smaller than the value considered before. However, the latest values of the global x–y coupling of the two beams are around 1.3%, and these values of the coupling do not explain the discrepancy in specific luminosity between the experiment and the simulation shown in Fig. 6, where the x–y coupling in the simulation is assumed to be 1%.

Vertical crabbing motion The vertical crab at the IP could degrade the luminosity. It may be created by some errors related to the crab kick, such as a misalignment of the crab cavity and the local x–y coupling at the crab cavity. The x–y coupling parameters at the crab cavities give a tuning knob to adjust the vertical crab at the IP. By such tuning, we can eliminate the vertical crab at the IP even if it is created by other sources such as a misalignment of accelerating cavities. Nevertheless, the tuning of these parameters does not suffice to increase the luminosity, as discussed above.

Off-momentum optics It has been shown by beam–beam simulation that the chromaticity of the x–y coupling at the IP could reduce the luminosity largely through the beam–beam interaction, if the residual chromatic coupling is large [14, 15]. While even an ideal lattice has such a chromatic coupling, the alignment errors of the sextupole magnets could create a large chromatic coupling. It has been thought that this kind of chromatic coupling might be one factor responsible for the serious luminosity degradation with crab crossing. Parallel to trials for measuring such chromatic couplings directly, we introduced tuning knobs to control them. For this purpose, we installed 14 pairs of skew-sextupole magnets (10 pairs for HER and 4 pairs for LER) in early 2009. The maximum strength of the magnets (bipolar) is $K_2 \sim 0.1/\mathrm{m}^2$ for HER and $K_2 \sim 0.22/\mathrm{m}^2$ for LER. By using these magnets, the tuning knobs were introduced to the beam operation at the beginning of May 2009. The luminosity gain due to these knobs is about 15%. Even with the improvement in the luminosity obtained by the use of skew-sextupole magnets, there is still a large discrepancy between the experiment and the simulation.

Fast noise Fast noise could lead to a loss in the luminosity. According to the beam–beam simulation, the allowable phase error of the crab cavities for N-turn correlation is $0.1 \times \sqrt{N}$ degrees. On the other hand, the measured error in the presence of the beams was less than ± 0.01 degree for fast fluctuation (1 kHz or faster) and less than ± 0.1 degree for slow fluctuation (from 10 to several hundred hertz). The measured phase error is then much smaller than the allowable values given by the beam–beam simulation. Besides the noise from the crab cavities, any fast noise could degrade the luminosity. For example, a phenomenon we encountered in 2005 is that the luminosity depends on the gain of the bunch-by-bunch feedback system. With a higher gain of about 6 dB, the luminosity decreased by about 20% [16]. This seems to indicate that some noise in the feedback system degraded the luminosity; this phenomenon disappeared, however, after the system adjustment, which included replacement of an amplifier for the feedback system. Although we confirmed that some artificially strong noise introduced to the crab cavities or to the feedback system can decrease the luminosity [17], there is no evidence that the achievable luminosity at KEKB was limited by fast noise.

EXPERIENCE OF CRAB CAVITY OPERATION WITH BEAMS

The initial goal of the beam study of the crab cavities was to show that the high beam–beam parameters predicted by

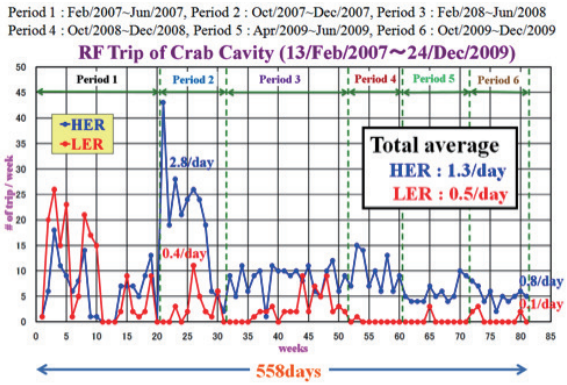

Figure 7: Trip rate of crab cavity system.

the simulation are actually achievable in a real machine. This study could be done with relatively low beam currents and with a smaller number of bunches. High beam current operation of the crab cavities was the second priority, as the tolerance of the crab cavities for high beam currents was unknown. However, they have been working much more stably than initially expected and are currently being used in the usual physics run. Figure 7 shows a history of the trip rate of the crab cavities. Period 1 was a dedicated machine time for the study of the crab cavities and the crab crossing. In most cases the beam currents are rather low, typically 100 mA for LER and 50 mA for HER. Around the sixth week, the maximum attainable kick voltage of the LER crab cavity dropped suddenly from 1.5 MV to about 1.1 MV for an unknown reason. In the middle of this period, we had to warm up the system to room temperature to recover from frequent trips of LER crab cavities. It was also expected that the performance degradation of the LER crab cavity would be recovered with the warm-up; however, the performance was not improved and this problem remains unsolved since then. In the summer shutdown following Period 1, the cavities were warmed up again to room temperature. From Period 2, the use of the crab cavities in the usual physics run started. At the beginning of this period, we were troubled with frequent trips of the HER crab cavity. This problem was solved by lowering the crab voltage, which was possible by enlarging the horizontal beta function at the crab cavity and by RF conditioning. In the winter shutdown following Period 2, the cavities were warmed up once again to room temperature. During Period 3, the trip rate of the HER crab cavity seemed to be more or less stable, while that of the LER crab had a tendency to increase slowly after the warm-up. Generally speaking, the HER crab cavity shows a higher trip rate than that of LER, corresponding to the higher crab voltage as shown in Table 2. It seems that the situation with the trip rate has reached a more or less steady state and will continue in a similar manner from now on. As for the causes of the trips, most of the HER cases are attributable to breakdowns of superconductivity due to discharge in the cavity; causes for the LER cavity include discharge in the coaxial coupler or at the input coupler.

REFERENCES

[1] KEKB B-Factory Design Report, KEK-Report-95-7 (1995).

[2] R.B. Palmer, SLAC PUB-4707 (1988), Proc. DPF Summer Study Snowmass '88, Snowmass, Colorado, USA, Ed. S. Jensen (Singapore: World Scientific, 1988), 613.

[3] K. Oide and K. Yokoya, Phys. Rev. A 40 (1989) 315.

[4] K. Ohmi, M. Tawada, Y. Cai, S. Kamada, K. Oide, and J. Qiang, Phys. Rev. ST Accel. Beams 7 (2004) 104401.

[5] K. Ohmi, M. Tawada, Y. Cai, S. Kamada, K. Oide, and J. Qiang, Phys. Rev. Lett. 92 (2004) 214801.

[6] K. Ohmi and K. Oide, Proc. EPAC'06, Edinburgh, Scotland, p. 616 (2006).

[7] M. Masuzawa, Y. Funakoshi, T. Nakamura, and J. Odagiri, Proc. EPAC'06, Edinburgh, Scotland, p. 613 (2006).

[8] Y. Funakoshi, M. Masuzawa, K. Oide, J. Flanagan, M. Tawada, T. Ieiri, M. Tejima, M. Tobiyama, K. Ohmi, and H. Koiso, Phys. Rev. ST Accel. Beams 10 (2007) 101001.

[9] Y. Funakoshi et al., Proc. EPAC'08, Genoa, Italy, p. 1893 (2008).

[10] T. Abe et al., Prog. Theor. Exp. Phys. 2013 (2013) 03A0010.

[11] T. Abe et al., Prog. Theor. Exp. Phys. 2013 (2013) 03A001.

[12] M. Akemoto et al., Prog. Theor. Exp. Phys. 2013 (2013) 03A002.

[13] N. Iida et al., Prog. Theor. Exp. Phys. 2013 (2013) 03A003.

[14] D. Zhou, K. Ohmi, Y. Seimiya, Y. Ohnishi, A. Morita, and H. Koiso, Phys. Rev. ST Accel. Beams 13 (2010) 021001.

[15] Y. Seimiya, K. Ohmi, D. Zhou, J.W. Flanagan, and Y. Ohnishi, Prog. Theor. Phys. 127 (2012) 1099.

[16] M. Arinaga et al., Prog. Theor. Exp. Phys. 2013 (2013) 03A007.

[17] K. Ohmi et al., Phys. Rev. ST Accel. Beams 14 (2011) 111003.

Published by CERN in the Proceedings of the ICFA Mini-Workshop on Beam–Beam Effects in Hadron Colliders,
CERN, Geneva, Switzerland, 18–22 March 2013, edited by W. Herr and G. Papotti, CERN–2014–004 (CERN, Geneva, 2014)

BEAM–BEAM EFFECTS IN BEPCII

Y. Zhang
Institute of High Energy Physics, Beijing, China

Abstract

We first introduce the design parameters of the Beijing Electron–Positron Collider II (BEPCII) and the simulation study of beam–beam effects during the design process of the machine. The main advances since 2007 are briefly introduced and reviewed. The longitudinal feedback system was installed to suppress the coupled bunch instability in January 2010. The horizontal tune decreased from 6.53 to 6.508 during the course of data taken in December, 2010. The saturation of the beam–beam parameter was found in 2011, and the vacuum chambers and magnets near the north crossing point were moved 15 cm in order to mitigate the long range beam–beam interaction. At the beginning of 2013, the beam–beam parameter achieved 0.04 with the new lower α_p lattice and the peak luminosity achieved 7×10^{32} cm^{-2} s^{-1}.

INTRODUCTION

The Beijing Electron–Positron Collider (BEPC) was constructed for both high energy physics and Synchrotron Radiation (SR) research. As a unique e^+e^- collider operating in the τ-charm region and the first SR source in China, the machine has been operated for well over 16 years since it was put into operation in 1989.

BEPCII is an upgrade project from BEPC. It is a double ring machine. Following the success of KEKB, the crossing scheme was adopted in BEPCII, where two beams collide with a horizontal crossing angle of 2×11 mrad. The design luminosity of BEPCII is 1.0×10^{33} cm^{-2} s^{-1} at 1.89 GeV, which is about 100 times higher than BEPC [1]. The main design collision parameters are shown in Table 1. In March 2013, the peak luminosity achieved 7.0×10^{32} cm^{-2} s^{-1} with 120 bunches and beam current 730 mA, where a lower α_p lattice was used.

Table 1: Design Parameters of BEPCII.

E	1.89 GeV	ν_s	0.034
I	910 mA	α_p	0.024
I_b	9.8 mA	σ_{z0}	0.0135 m
n_b	93	σ_z	0.015 m
V_{rf}	1.5 MV	ϵ_x	144 nmrad
β_x^*/β_y^*	1.0/0.015 m	Coupling	1.5%
ν_x/ν_y	6.53/5.58	ξ_y	0.04
θ_c	22 mrad	$\tau_x/\tau_y/\tau_z$	3.0e4/3.0e4/1.5e4

In the following, we first introduce the simulation study of the beam–beam interaction during the design course of the machine. Then we review the performance and optimization of the real machine.

SIMULATION STUDY DURING DESIGN

Code Development

We have developed new parallel strong–strong beam–beam code, which is used to study the effects in BEPCII [2]. The main characteristics of the code are listed below.

- Particle-in-cell. The Triangular Shaped Cloud (TSC) method is employed for the charge assignment, where the charge of each macroparticle is assigned to its nine nearest points by weight.
- Synchrotron motion is included. The transportation through the arc is same as that of Hirata's BBC code [3].
- The beam–beam potential is calculated by solving the Poisson equation with open boundary.
- Bunch length effect is included by longitudinal slices and the interpolation of beam–beam potential is done when the collision between two slices is considered, which helps to reduce the required slice number.
- It is assumed that a particle in one slice will not jump into non-adjacent ones on the next turn. It seems that this assumption has been valid so far, especially in the ordinary collision scheme (where the required slice number is only about 5).
- Lorentz boost is used to consider the crossing angle effect [4].

Code Check

- The geometrical factor of luminosity reduction for head-on collision. The loss in luminosity due to geometrical effect for nominal BEPCII parameters is 86%, and the code tracking result agrees well.
- The geometrical factor of luminosity reduction for collision with finite crossing angle. The loss in luminosity due to geometrical effect for design BEPCII parameters is 80%, and the code tracking result agrees well.
- The beam–beam field calculated by the code for the Gaussian beam distribution agrees well with the Bassetti–Erskine formula.
- The synchro-betatron mode agrees well with that predicted by the hollow beam matrix model [5].
- The luminosity result for BEPCII agrees well with that of K. Ohmi's code [6].

978-92-9083-404-5, 0007-8328 –
http://dx.doi.org/10.5170/CERN–2014–004.37

Simulation Result

The achieved beam–beam parameter ξ with collision is defined as

$$\xi_u = \frac{N r_e}{2\pi\gamma} \frac{\beta_u^0}{\sigma_u(\sigma_x + \sigma_y)} \quad (1)$$

where β^0 is the nominal beta function without collision, and σ is the disturbed beam size with collision. If we don't consider the finite bunch length and finite crossing angle, the bunch luminosity can be represented as

$$L = \frac{N^2 f_0}{4\pi\sigma_x\sigma_y} \quad (2)$$

where σ is the disturbed beam size with collision. In the normal case, $\sigma_y \ll \sigma_x$, the achieved ξ_y can be represented by luminosity,

$$\xi_y = \frac{2 r_e \beta_y^0}{N\gamma} \frac{L}{f_0}. \quad (3)$$

With the design parameters, the maximum ξ_y only achieves 0.025, which is shown in Fig. 1. This is bad news for the BEPCII team, since ξ_y needs to achieve 0.04 if we want to achieve the designed luminosity with the designed beam current. We therefore did some estimation to determine if it would be feasible to inject more bunches, and it seems that this would be possible.

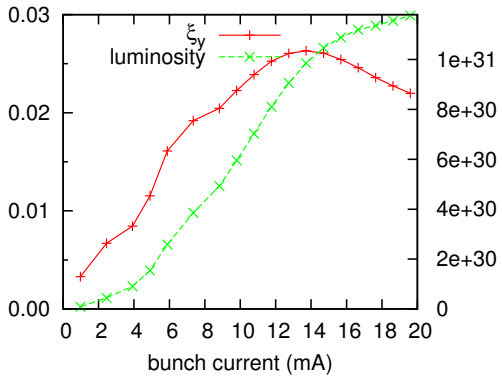

Figure 1: The achieved ξ_y and bunch luminosity versus bunch current with design parameters.

The beam–beam performance is very sensitive to the working point. The normalized luminosity versus tune is depicted in Fig. 2. The best working point is near (0.505,0.570), where the luminosity is about 80% of the design value. That is to say, we could achieve 8×10^{32} cm^{-2} s^{-1} with the designed bunch current, bunch number and optimized working point.

The full horizontal crossing angle between colliding beams is 22 mrad. The luminosity reduction factor is less than 10% at (0.53,0.58), however it is about 30% at (0.51,0.57). It seems that the luminosity loss due to a finite crossing angle is more serious the closer the horizontal tune is to 0.5, the high luminosity working point region.

We also tried to analyze the coupling contribution and carried out some simulations at different working points.

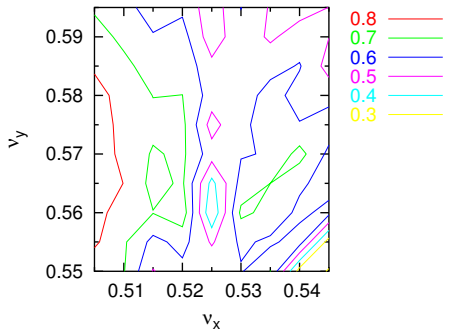

Figure 2: Tune survey of luminosity. The luminosity is normalized to the design value.

Table 2: Coupling contribution at different working point.

Tune	Coupling	Max ξ_y	Lum
(0.510, 0.575)	0.5%	0.041@11 mA	12.3e30
	1.0%	0.037@12 mA	12.1e30
	1.5%	0.034@13 mA	12.1e30
(0.530, 0.580)	0.5%	0.026@7 mA	5.0e30
	1.5%	0.026@13 mA	9.2e30
(0.535, 0.575)	0.5%	0.031@9 mA	7.6e30
	1.0%	0.027@9 mA	6.6e30
	1.5%	0.023@9 mA	5.6e30
(0.540, 0.590)	0.5%	0.025@11 mA	7.6e30
	1.0%	0.024@11 mA	7.2e30

The results are summarized in Table 2. It seems that we have to move the horizontal tune closer to 0.5 and ensure that the emittance coupling is less than 0.5% if ξ_y is expected to achieve 0.04.

PERFORMANCE AND OPTIMIZATION

The first electron beam was stored in the SR ring in November 2006. Optics measurement and correction was studied at that time. The backup collision mode was first tuned in the spring of 2007, during the course of which we learned the collision tuning. The superconducting final focus magnet was installed in the summer of 2007. The detector was installed in June 2008, and this completed the construction of the machine. Here, we review the machine tuning history in chronological order.

Phase I: Autumn of 2008 to Summer of 2010

The big events in this period are listed below.

- January 2009. Profile monitor, which caused very strong longitudinal multibunch instability, was removed from the positron ring.
- May 2009. Horizontal tune was moved to 0.51 from 0.53. Luminosity reached 3×10^{32} cm^{-2} s^{-1}, which is the 'design goal' of the government funding agency.
- January 2010. Longitudinal feedback system was installed and began to work.

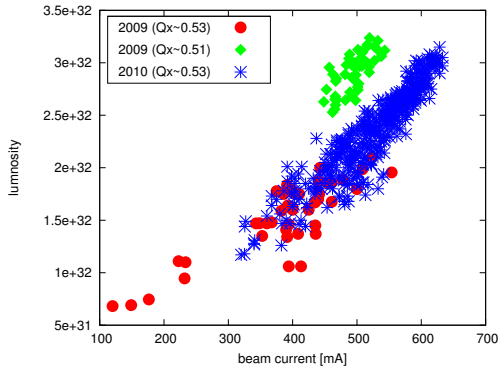

Figure 3: Luminosity versus beam current in 2009 and 2010. The difference between the red (2009) and blue (2010) dots comes from the suppression of longitudinal multibunch instability.

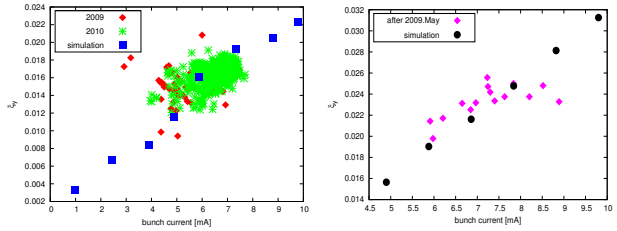

(a) (b)

Figure 4: Beam–beam parameter versus bunch current. The left figure shows that $Q_x \sim 0.53$ and the right shows that $Q_x \sim 0.51$. The longitudinal feedback system begins to work in 2010.

Figure 3 shows the luminosity versus beam current and Fig. 4 shows the beam–beam parameter versus bunch current. The longitudinal coupled bunch instability still reduced the luminosity performance even after the removal of the profile monitor, which caused very strong instability, from the positron ring. In order to increase the luminosity with the same beam current, we tried to move the horizontal tune closer to 0.5 in May 2009. The peak luminosity increased from 2 to 3×10^{32} cm^{-2} s^{-1}. Since the detector background is too high to take data with $Q_x \sim 0.51$, the machine continued to run with $Q_x \sim 0.53$ in the following normal data collection run. In the first half of 2010, the longitudinal feedback system began to work and the peak luminosity achieved 3×10^{32} cm^{-2} s^{-1} with $Q_x \sim 0.53$. The maximum ξ_y is about 0.02 when $Q_x \sim 0.53$, which is less than the simulated 30% percent (see Table 2).

Phase II: Autumn of 2010 to Summer of 2011

The big events in this period are listed below.

- July 2010. It was found that the final focus magnet and vacuum chamber on one side of the detector was displaced by about 10 mm in the horizontal direction. It was aligned in the summer shutdown.
- December 2010. Detector background was reduced with $Q_x \sim 0.51$. The physics people could take data near the 0.51 working point.

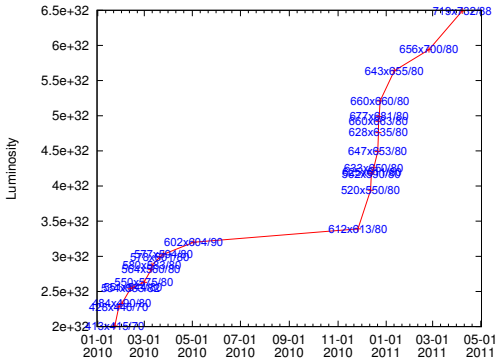

Figure 5: Peak luminosity record from the beginning of 2010 to the summer of 2011. The colliding beam current and bunch number is also shown in the figure.

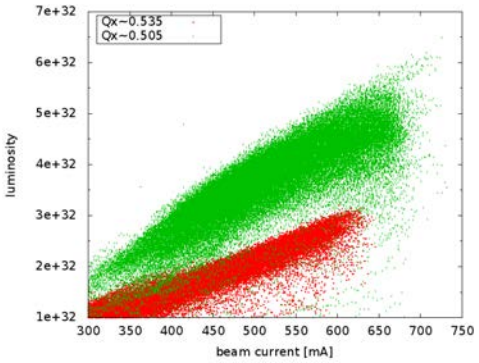

Figure 6: Luminosity performance at different working points.

The most important advance in this period is the reduction of the detector background with $Q_x \sim 0.51$, since the physics people could take data at the working point and the accelerator people had enough time to do the luminosity tuning. The detector background is mainly optimized by the closed orbit tuning along the ring. Figure 5 shows the peak luminosity record from the beginning of 2010 to the summer of 2011. It was very exciting near the start of 2011 since a new record would be born only in a few days. The peak luminosity was 6.5×10^{32} cm^{-2} s^{-1} in 2011. The comparison of luminosity at different working points is shown in Fig. 6, which very obviously shows that a working point closer to 0.5 means a higher luminosity.

The 2010–2011 commissioning year was very successful and exciting, but there was some confusion when we saw the beam–beam performance. The achieved ξ_y is shown in Fig. 7. There exist clear saturation phenomenon for ξ_y and the maximum is about 0.033. We should explain what caused the saturation.

Figure 8 shows the bunch lengthening effect. It seems this effect does not bring very much luminosity loss, and the maximum beam–beam parameter is still above 0.04.

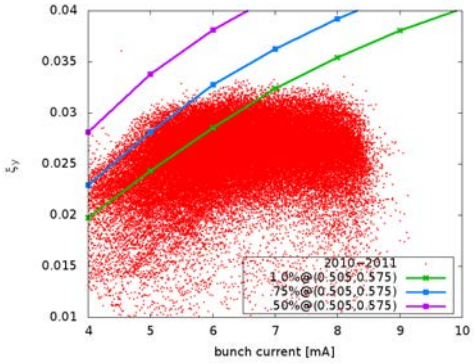

Figure 7: Achieved beam–beam parameter in 2010–2011. The lines shows the simulation result with different coupling.

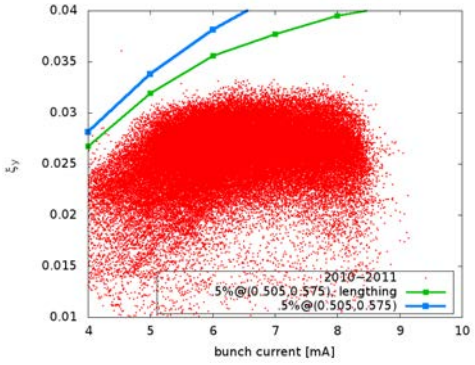

Figure 8: Beam–beam loss due to bunch lengthening, which does not explain the beam–beam parameter saturation in real machine.

The nonlinear arc may also reduce the luminosity performance. We use Hirata's BBC [3] code as a pass method in Accelerator Toolbox (AT) [7] to simulate the weak–strong beam–beam interaction. The map in the arc is implemented using the element-by-element symplectic tracking in AT. Figure 9 shows the comparison between the ideal transfer matrix map and element-by-element tracking in arc. The lattice really reduces the beam–beam performance, but we did not believe that the saturation was mainly caused by the crosstalk between nonlinear arc and beam–beam force. On the other hand, we could not ignore the simulation result, which told us that we should put more emphasis on the sexupole optimization.

There is another crossing point (NCP) in the north of the two rings, where the colliding beams are separated vertically by about 8 mm and the full horizontal angle is about 2×0.15 rad (17.7°). We still use the weak–strong code (AT and BBC) to study the parasitic beam–beam effect, which is shown in Fig. 10. The achieved ξ_y is only about 0.035 with 8 mm separation at NCP

Phase III: Autumn of 2011 to Summer of 2012

The big events in this period are listed below.

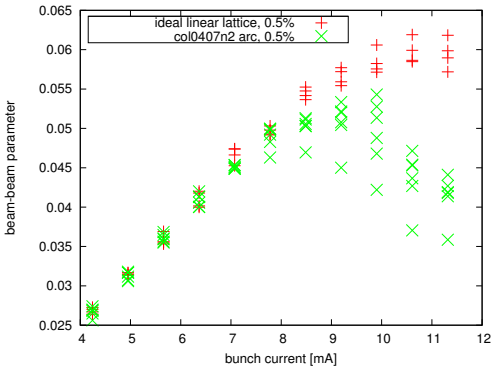

Figure 9: The luminosity loss due to the realistic arc. The arc map is implemented using element-by-element tracking. The ideal linear lattice means the map is represented by a transfer matrix.

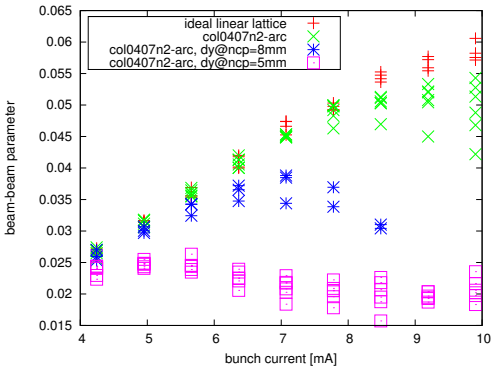

Figure 10: The luminosity loss due to nonlinear arc and long range beam–beam interaction at NCP.

- In the summer shutdown of 2011, the NCP chambers and magnets were moved 15 cm, 1/4 of the rf bucket. The horizontal separation between colliding bunches is greater than $30\sigma_x$.

After the hardware modification, the beam–beam performance did not increase as expected, which is shown in Fig. 11. This could be explained to some extent by the large longitudinal offset of the collision point. In 2011–2012 commissioning year, the offset is about 3 mm, and it is about 6 mm in February 2012. We did not put enough emphasis on monitoring the parameter during collision at that time.

Phase IV: Autumn of 2012 to March 2013

The big events in this period are listed below.

- Lower α_p mode was first tested at 2.18 GeV in February 2013. The ξ_y record 0.033 was broken after about two years.
- One bunch every three buckets, and even one bunch every two buckets, injection was tested in the machine study of March 2013. The peak luminosity achieved 7.0×10^{32} cm^{-2} s^{-1} at 1.89 GeV.

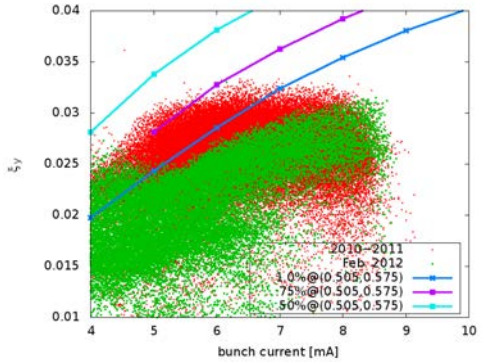

Figure 11: Beam–beam parameter achieved in 2011 and 2012. The mitigation of long range beam–beam interaction at NCP did not bring any improvements.

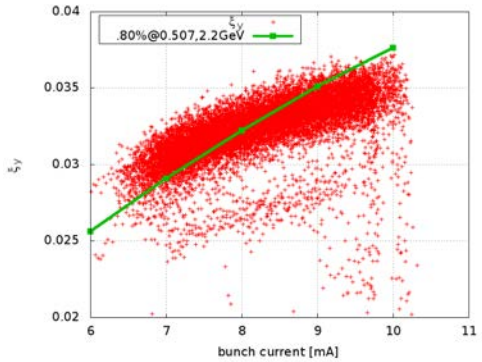

Figure 12: Achieved beam–beam parameter at 2.18 GeV with new lattice in 2013.

The momentum compaction factor of the new lattice is about 0.017, and the old one is 0.024. The reduction of α_p is achieved by increasing the horizontal tune from 6.5 to 7.5. During the lattice design, we also optimized the chromatic distortion and some nonlinear resonance driving terms. However we still did not establish a so-called 'standard' that could tell us if the lattice is good enough.

The achieved beam–beam performance at 2.18 GeV is shown in Fig. 12. We also did some machine study in order to increase the peak luminosity at 1.89 GeV. The achieved beam–beam parameter with different bunch pattern is shown in Fig. 13. The maximum ξ_y is above 0.04. It seems that the multibunch effect reduces the beam–beam performance, which would be a serious limitation if we were to continue to increase the luminosity.

SUMMARY

We review the collision optimization history of BEPCII. The suppression of multibunch longitudinal instability and moving the horizontal tune close to 0.5 helped us to increase the luminosity. The mitigation of long range beam–beam interaction seems not so effective as expected, indicating that maybe the real vertical separation is greater than estimated. The lower α_p lattice helped us to achieve the ξ_y record of 0.04 at 1.89 GeV.

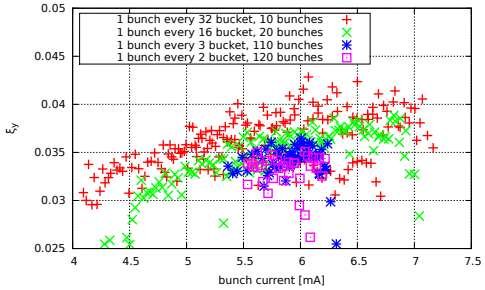

Figure 13: Achieved beam–beam parameter at 1.89 GeV with different bunch pattern in 2013.

The simulation study is very important both in the design and the daily commissioning. It gives a benchmark in normal operation and lets us know if the status is optimized enough, even though we could approach the simulation result and never go beyond it. The difference between the simulation and the optimized result is about 10–20%. It should also be emphasized that we would like to use the maximum achieved ξ_y in the simulation as the beam–beam limit in the simulation.

Increasing beam current is a must to increasing the luminosity. However, it seems the multibunch effect is very serious. The study to cure the instability and even find the instability source will be very important in the future. In the near future, we'll test a new lattice with $alpha_p$ about 0.017, larger emittance (100 nm→130 nm) and lower β_y (1.5 cm→1.35 cm). The colliding bunch current could be higher with the new mode and the beam current could be higher with same bunch number. It is expected that this could help us to increase the luminosity.

REFERENCES

[1] Design Report of BEPCII–Accelerator Part (2nd ed) (2003).

[2] Y. Zhang, K. Ohmi and L. Chen, Phys. Rev. ST Accel. Beams 8 (2005) 074402.

[3] BBC: Program for Beam–Beam Interaction with Crossing Angle. http://wwwslap.cern.ch/collective/hirata/

[4] K. Hirata, Phys. Rev. Lett. 74 (1995) 2228-2231.

[5] E.G. Stern, J.F. Amundson, P.G. Spentzouris, and A.A. Valishev, Phys. Rev. ST Accel. Beams 13 (2010) 024401.

[6] K. Ohmi, Phys. Rev. E 62 (2000) 7287.

[7] A.Terebilo, SLAC-PUB-8732 (2001).

Published by CERN in the Proceedings of the ICFA Mini-Workshop on Beam–Beam Effects in Hadron Colliders,
CERN, Geneva, Switzerland, 18–22 March 2013, edited by W. Herr and G. Papotti, CERN–2014–004 (CERN, Geneva, 2014)

RECENT BEAM–BEAM EFFECTS AT VEPP-2000 AND VEPP-4M*

D. B. Shwartz, D. E. Berkaev, I. A. Koop, E. A. Perevedentsev,
Yu. A. Rogovsky, Yu. M. Shatunov, Budker Institute of Nuclear Physics, Novosibirsk State University, Novosibirsk, Russia
E. B. Levichev, A.L. Romanov, D. N. Shatilov, P. Yu. Shatunov, Budker Institute of Nuclear Physics, Novosibirsk, Russia

Abstract

Budker INP hosts two e^+e^- colliders, VEPP-4M operating in the beam energy range of 1–5.5 GeV and the low-energy machine VEPP-2000, collecting data at 160–1000 MeV per beam. The latter uses a novel concept of round colliding beams. The paper presents an overview of observed beam–beam effects and obtained luminosities.

VEPP-4M

Being a rather old machine with a moderate luminosity, VEPP-4M has several unique features, firstly a very low beam-energy spread, and a system for precise energy measurement, providing an interesting particle physics program for the KEDR detector. Over recent years VEPP-4M was taking data at a low energy range with two bunches in each beam. The luminosity at this range is limited by beam–beam effects with the threshold beam–beam parameter $\xi_y \le 0.04$ [1]. In this case the luminosity depends on energy as $L \propto \gamma^4$ (see Fig. 1).

The main parameters of the VEPP-4M collider are listed in Table 1.

ROUND COLLIDING BEAMS

The VEPP-2000 collider [2] exploits the round beam concept (RBC) [3]. The idea of round-beam collisions was proposed more than 20 years ago for the Novosibirsk Phi-factory design [4]. This approach, in addition to the geometrical factor gain, should yield the beam–beam limit enhancement. An axial symmetry of the counter-beam force together with the X–Y symmetry of the transfer matrix between the two IPs provide an additional integral of motion, namely, the longitudinal component of angular momentum $M_z = x'y - xy'$. Although the particles' dynamics remain strongly nonlinear due to beam–beam interaction, it becomes effectively one-dimensional. Thus there are several demands upon the storage ring lattice suitable for the RBC:

*Work supported by the Ministry of Education and Science of the Russian Federation, grant N 14.518.11.7003.

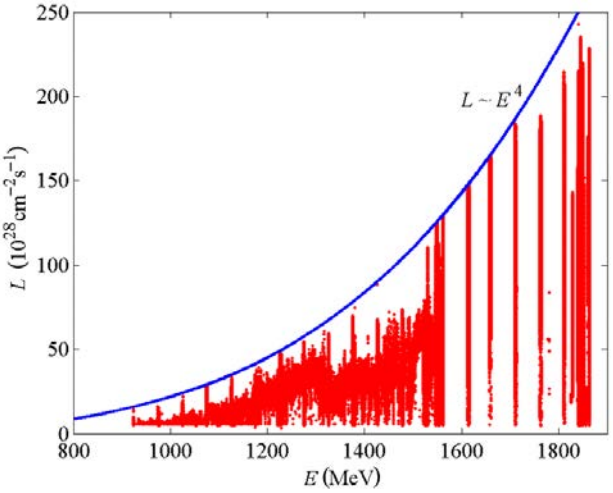

Figure 1: VEPP-4M luminosity dependence on beam energy.

Table 1: VEPP-4M main parameters.

Parameter	**Value**
Circumference (C)	366 m
Energy range (E)	1–5.5 GeV
Number of bunches	2 × 2
Betas and dispersion at IP (β^*_x, β^*_y, η^*)	75, 5, 80 cm
Betatron tunes ($\nu_{x,y}$)	8.54, 7.57
Beam–beam parameters (ξ_x, ξ_y)	0.025, 0.04
Luminosity at 1.85 GeV (L)	2.3×10^{30} cm^{-2} s^{-1}

i) head-on collisions (zero crossing angle);

ii) small and equal β functions at IP ($\beta^*_x = \beta^*_y$);

iii) equal beam emittances ($\varepsilon_x = \varepsilon_y$);

iv) equal fractional parts of betatron tunes ($\nu_x = \nu_x$).

The first three requirements provide the axial symmetry of collisions while requirements (ii) and (iv) are needed for X–Y symmetry preservation between the IPs.

978-92-9083-404-5, 0007-8328 –
http://dx.doi.org/10.5170/CERN–2014–004.43

A series of beam–beam simulations in the weak–strong [5] and strong–strong [6] regimes were done. Simulations showed the achievable values of beam–beam parameters as large as $\xi \sim 0.15$ without any significant blow-up of the beam emittances.

VEPP-2000 OVERVIEW

The layout of the VEPP-2000 complex is presented in Fig. 2. The complex consists of the injection chain (including the old beam production system and Booster of Electrons and Positrons (BEP) with an energy limit of 800 MeV) and the collider itself with two particle detectors, Spherical Neutral Detector (SND) and Cryogenic Magnetic Detector (CMD-3), placed into dispersion-free low-beta straights. The final focusing is realized using superconducting 13 T solenoids. The main design collider parameters are listed in Table 2.

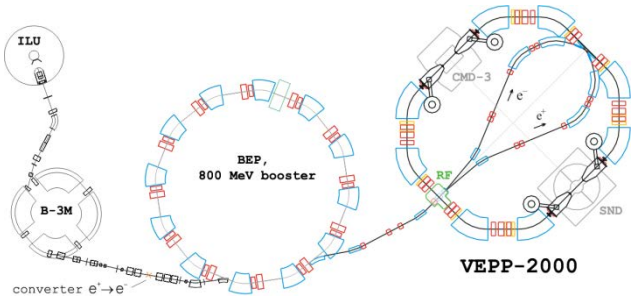

Figure 2: VEPP-2000 complex layout.

Table 2: VEPP-2000 main parameters (at E = 1 GeV).

Parameter	Value
Circumference (C)	24.3883 m
Energy range (E)	200–1000 MeV
Number of bunches	1 × 1
Number of particles per bunch (N)	1×10^{11}
Betatron functions at IP ($\beta^*_{x,y}$)	8.5 cm
Betatron tunes ($\nu_{x,y}$)	4.1, 2.1
Beam emittance ($\varepsilon_{x,y}$)	1.4×10^{-7} m rad
Beam–beam parameters ($\xi_{x,z}$)	0.1
Luminosity (L)	1×10^{32} cm^{-2} s^{-1}

The density of magnet system and detectors components is so high that it is impossible to arrange a beam separation in the arcs. As a result, only a one-by-one bunch collision mode is allowed at VEPP-2000.

BEAM DIAGNOSTICS

Beam diagnostics is based on 16 optical CCD cameras that register the visible part of synchrotron light from either end of the bending magnets and give full information about beam positions, intensities, and profiles (see Fig. 3). In addition to optical beam position monitors (BPM), there are also four pick-up stations in the technical straight sections, two photomultipliers for beam current measurements via the synchrotron light intensity, and one beam current transformer as an absolute current monitor.

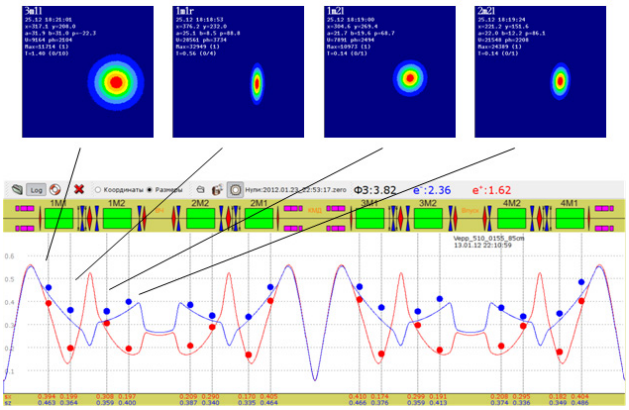

Figure 3: Beam profile measurements.

CIRCULAR MODE OPTIONS

The RBC at VEPP-2000 was implemented by placing two pairs of superconducting focusing solenoids into two interaction regions (IR) symmetrically with respect to collision points. There are several combinations of solenoid polarities that satisfy the round beams' requirements: 'normal round' (++ −−), 'Möbius' (M) (++ −+) and 'double Möbius' (DM) (++ ++) options rotate the betatron oscillation plane by ±90° and give alternating horizontal orientation of the normal betatron modes outside the solenoid insertions.

Two 'flat' combinations (+− +− or +− −+) are more simple and also satisfy the RBC approach if the betatron tunes lie on the coupling resonance $\nu_1 - \nu_2 = 2$ to provide equal emittances via eigenmodes coupling.

All combinations are equivalent in focusing and give the same lattice functions. But the tunes for M and DM options are different due to additional clockwise and counter-clockwise circular mode rotations (see Fig. 4).

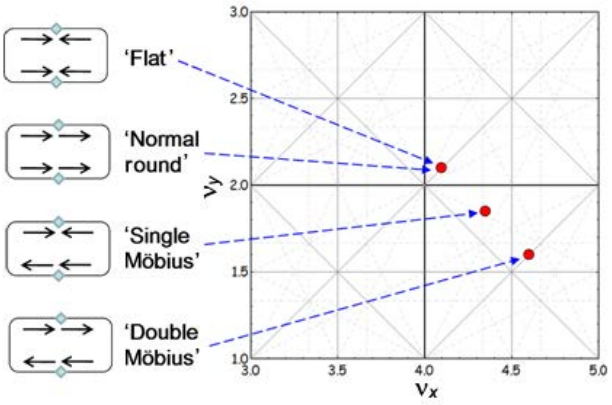

Figure 4: VEPP-2000 round beam options.

Unfortunately, computer simulations showed a serious limitation of the dynamic aperture (DA) for options with mode rotations. A brief experimental study was carried out upon the DM option. At first glance, this case could

be preferable, because the tune is a little above 0.5 instead of an integer for the 'flat' mode. However, both the simulation and measurement gave a DA of only ~10 $\sigma_{x,y}$. Such studies should probably be continued for other options.

LINEAR CONSIDERATIONS

An important feature of the VEPP-2000 lattice is the strong dependence of radiative emittance on the value of β^*. The decrease of β^* causes emittance growth in such a way that $\sigma^{*2} = \beta^* \varepsilon = \mathrm{inv}(\beta^*)$. The expression for luminosity can be written in this case as

$$L = \frac{N^- N^+ f_0}{4\pi\sigma^{*2}} = \frac{4\pi\gamma^2\xi^2\sigma^{*2} f_0}{r_e^2 \beta^{*2}} \quad . \qquad (1)$$

One can now see that, although the specific luminosity does not depend on the choice of the value of β^*, the maximum luminosity limited by the beam–beam interaction with a given threshold ξ_{th} can be higher for a lower β^*. The β^* once optimized for a given aperture value at the top energy of 1 GeV should be decreased for lower energies corresponding to smaller radiative emittance to minimize the luminosity roll-off. Instead of ($\beta^* = \mathrm{const}$, $\varepsilon \propto \gamma^2$, $\sigma^* \propto \gamma$, $L \propto \gamma^4$), the energy scaling can be done as ($\beta^* \propto \gamma$, $\varepsilon \propto \gamma$, $\sigma^* \propto \gamma$, $L \propto \gamma^2$) (see the dashed blue and solid red lines in Fig. 7, respectively). Of course, this approach is very optimistic since it does not take into account the intrabeam scattering (IBS) emittance growth at a low energy as well as DA problems for a low β^*.

Similarly to the variation of β^* caused by lattice tuning, the linear beam–beam simulation as well as weak–strong beam–beam simulations (LIFETRAC software program [7]) predict the inverse variation of the dynamic beta and dynamic emittance so that the beam sizes at IP are left unchanged by the linear beam–beam effect. At the same time, the size of the beam at the profile monitors around the ring varies strongly with the counter beam current (see Fig. 5).

LUMINOSITY MEASUREMENTS

At VEPP-2000 luminosity monitoring is available from both detectors. Electrons and positrons from elastic scattering are easily detected in coincidence by the detector's calorimeters with an efficiency near 100% and counting rates of about 1 kHz at $L = 1 \times 10^{31}$ cm^{-2} s^{-1}.

For prompt collision tuning a method for making luminosity measurements was developed based on the beam size data from the optical diagnostics. To calculate the luminosity one need know only the beam currents and sizes at the IP. As discussed above, due to the beam–beam effects the lattice functions and beam emittances show a significant current-dependent difference from their design values.

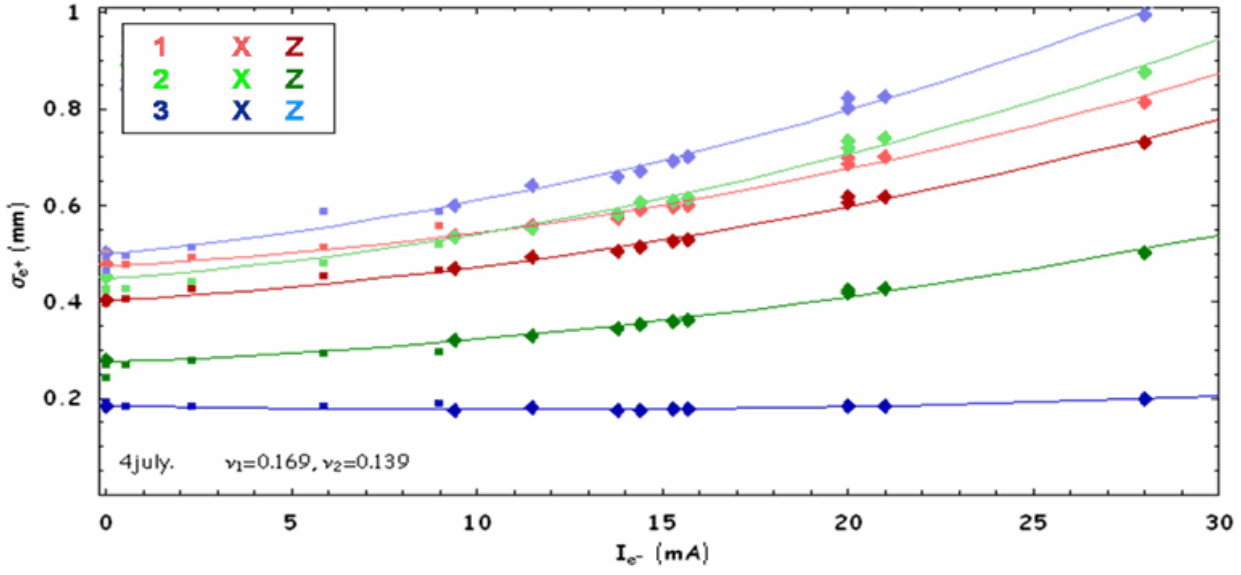

Figure 5: Weak–strong test of beam sizes growth with the counter beam current.

Assuming no focusing perturbations in the lattice other than those caused by the collision, and thus located at the IP, one can use transport matrices verified by the arc optics model to evaluate the beam sizes at the IP from the beam size measurements made by CCD cameras placed around the ring. Eight measurements for each betatron mode of the both beams are more than enough to evaluate the dynamic beta functions and dynamic emittances of the modes.

The accuracy of the method degrades at high beam intensities close to beam–beam threshold, where the beam distribution deviates from the Gaussian. Data from this luminometer, taken regularly during two hours at an energy E = 800 MeV, is presented in Fig. 6.

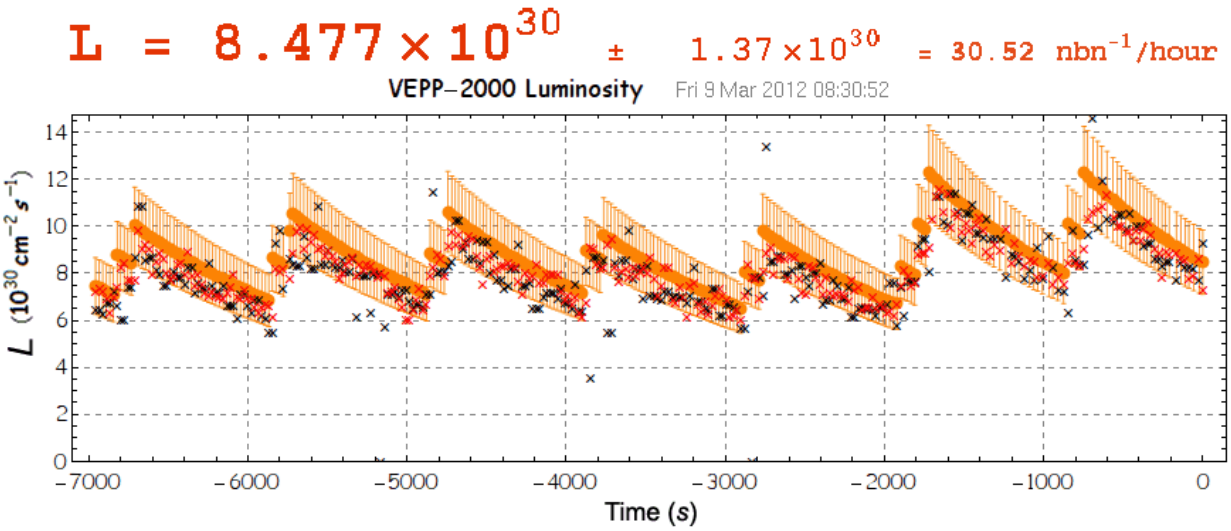

Figure 6: Luminosity at the energy E = 800 MeV. Black and red crosses, detectors; orange dots, luminometer.

The advantages of this technique over the SND and CMD-3 luminosity monitors are the higher measurement speed and lower statistical jitter. The accuracy of the new method is nominally about 3–4% and it does not depend on the luminosity level, in contrast to the detector's data. On the other hand, the new technique is not sensitive to any possible focusing difference in two IPs. Generally, those three monitors give results coinciding within 10% accuracy.

EXPERIMENTAL RUNS

VEPP-2000 started data-taking with both detectors installed in 2009 [8]. The first runs were dedicated to experiments in the high-energy range, while during the last 2012 to 2013 run an energy scan to the lowest energy limit was done. Apart from partial integrability in beam–beam interaction the RBC gives a significant benefit in the Touschek lifetime when compared to traditional flat beams. This results in the ability of VEPP-2000 to operate at an energy as low as 160 MeV — the lowest energy ever obtained in e^+e^- colliders. The luminosity obtained during the last three seasons is shown in Fig. 7 with olive, magenta, and blue points. The red line is a naive estimate of the maximum achievable peak luminosity (jumps correspond to different commutation of the solenoid coils available at low energy). The blue dashed line shows the beam–beam limited luminosity for a fixed machine lattice. Black triangles and squares depict the peak and average luminosity achieved by the previous collider VEPP-2M [9]. Black circles indicate VEPP-2M luminosity without the superconducting wiggler.

For different energies the luminosity is limited for different reasons. At high energies (>500 MeV) it is limited mostly by an insufficient positron production rate. At energies over 800 MeV the necessity of energy ramping in the collider storage ring additionally restricts the luminosity. For lower energies the luminosity is limited by the beam–beam effects, especially by the flip-flop effect (see below). At the lowest energies the main limiting factors are the small DA, IBS, and low beam lifetime.

In Fig. 8 the obtained beam current is presented as a function of machine operation energy. Although the current is limited not by the beam–beam effects for energies over 500 MeV but by the limited and constant positron production rate, it continues to increase with energy due to the beam's lifetime growth. The decrease of current at the highest energies is caused by the time and beam losses during energy ramping in the collider ring.

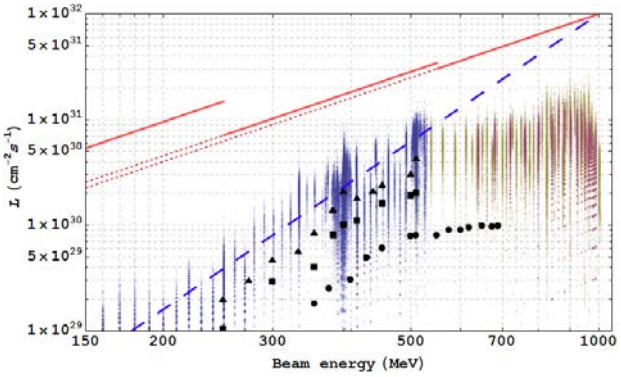

Figure 7: Luminosity scan.

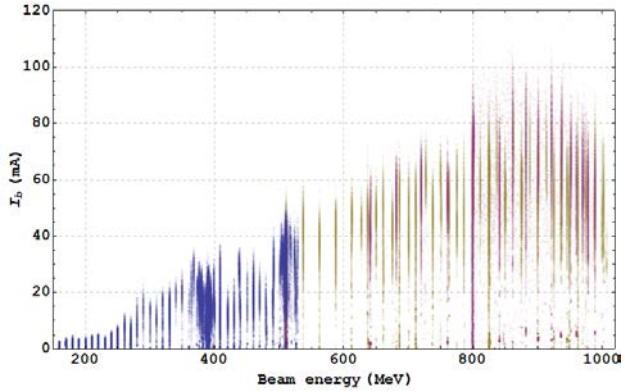

Figure 8: Beams current vs. energy.

BEAM–BEAM EFFECTS

The real beam size can be easily obtained from the luminosity measurements. Contrary to what the simulations predict, the beam sizes grow significantly with beam current increase (see Fig. 9). However, the emittance grows monotonically, without any blow-up threshold.

In Fig. 9 the 'nominal' beam–beam parameter is used for the horizontal axis, which has nothing to do with a real tune shift. This parameter is a normalized measure of the beam current:

$$\xi_{\text{nom}} = \frac{N^- r_e \beta^*_{\text{nom}}}{4\pi\gamma\sigma^{*2}_{\text{nom}}}. \qquad (2)$$

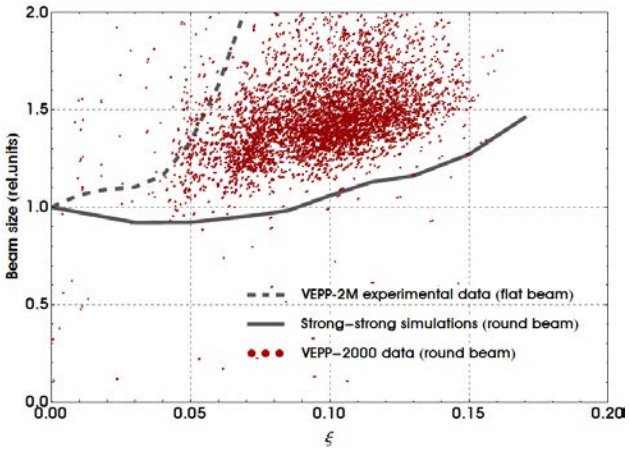

Figure 9: Beam size growth at IP (E = 537 MeV).

BEAM–BEAM PARAMETER EXTRACTED FROM LUMINOSITY

We can also define the 'achieved' beam–beam parameter as:

$$\xi_{\text{lumi}} = \frac{N^- r_e \beta^*_{\text{nom}}}{4\pi\gamma\sigma^{*2}_{\text{lumi}}}, \qquad (3)$$

where the beta function is nominal while the beam size is extracted from the measured luminosity. With this definition, the range of the beam–beam parameter actually achieved during experimental runs can be seen in Fig. 10.

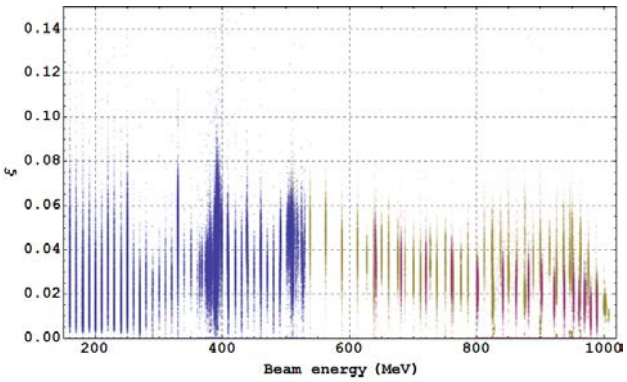

Figure 10: Achieved beam–beam parameter vs. beam energy.

The bulky data accumulated during three experimental seasons is strongly thinned out to produce Fig. 10. For this reason the top points corresponding to the peak luminosity and best-tuned machine can hardly be seen. In Figure 11 the correlation between achieved and nominal beam–beam parameters is shown for the full data at the given energy E = 392.5 MeV. The beam–beam parameter achieves the maximal value of $\xi \sim 0.09$ during regular work (magenta dots in Fig. 11).

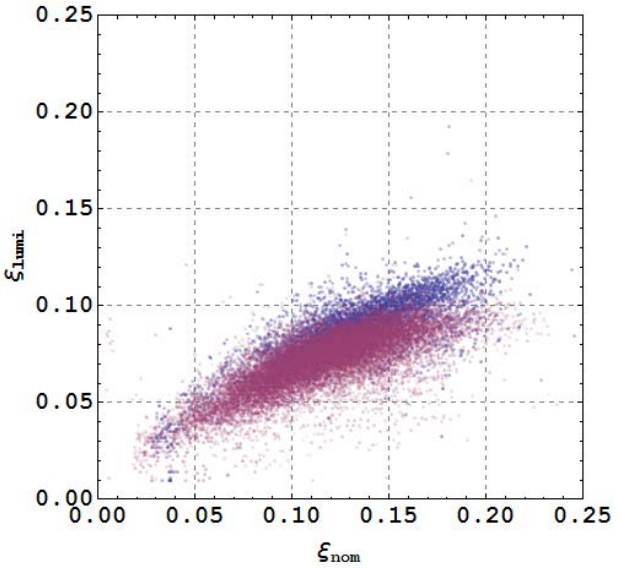

Figure 11: Achieved beam–beam parameter at 392.5 MeV.

While studying the dependence of beam–beam threshold on bunch length it was found that the RF voltage decrease from 30 kV to 17 kV gives a significant benefit in the maximal value of ξ (blue dots in Fig. 11) up to $\xi \sim 0.12$ per IP. This phenomena is not yet fully explained but some predictions of beam–beam interaction mitigation can be found in Ref. [10] for the bunch slightly longer than β^*. The bunch lengthening in our particular case comes not only from the RF voltage decrease itself, but also from microwave instability, which was observed at low energies with a low RF voltage above a certain bunch intensity.

BEAM–BEAM PARAMETER EXTRACTED FROM COHERENT OSCILLATIONS

Another independent instrument for beam–beam parameter measurement is the analysis of the coherent beam oscillation spectrum. In Fig. 12 one can find two pairs of σ- and π-modes tunes equal to 0.165 and 0.34, respectively. The total tune shift of $\Delta\nu = 0.165$ corresponds to ξ per one IP equal to:

$$\xi = \frac{\cos(\pi\nu_\sigma) - \cos(\pi\nu_\pi)}{2\pi\sin(\pi\nu_\sigma)} = 0.124\,. \qquad (4)$$

The Yokoya factor here is taken to be equal to 1 due to the fact that oscillations with very small amplitude (~10 μm = 0.2 σ^*) were excited by a fast kick and the spectrum was investigated for only 8000 turns. During this short time beam distribution is probably not deformed by an oscillating counter beam and remains Gaussian [11].

FLIP-FLOP EFFECT

The beam–beam limit of $\xi_{lumi} \sim 0.1$ usually corresponds to the onset of a flip-flop effect: the self-consistent situation when one beam's sizes are blown-up while another beam's sizes are almost unperturbed. This flip-flop is probably caused by an interplay of beam–beam effects and nonlinear lattice resonances. One can see in the spectra of a slightly kicked bunch that the shifted tunes (π-mode) jumped to the 1/5 resonance in the case of a flip-flop (Fig. 13).

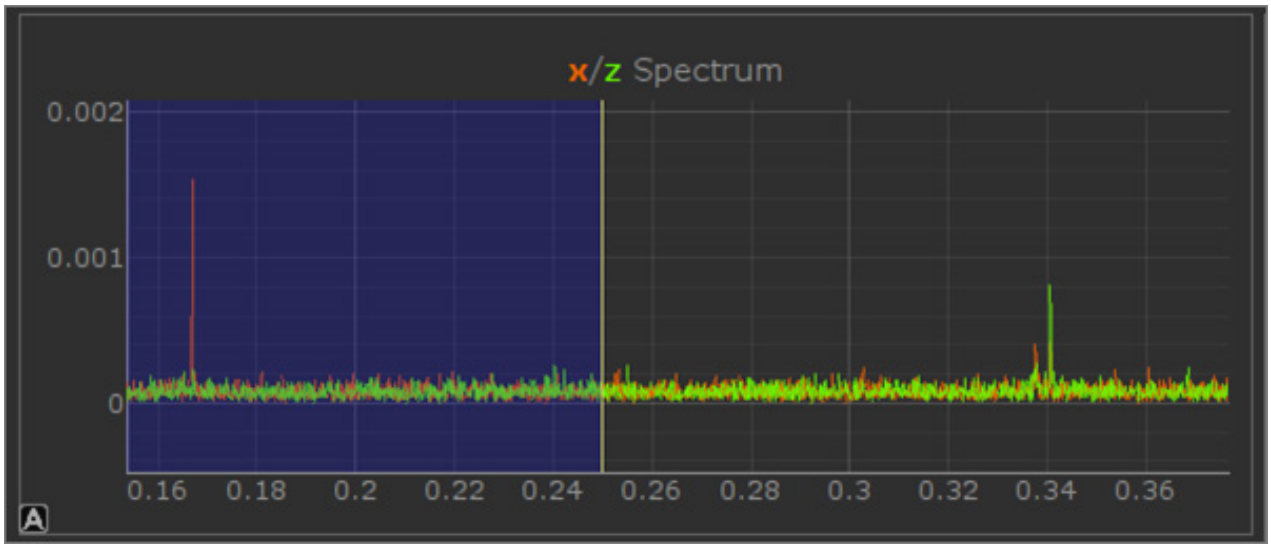

Figure 12: Coherent beam–beam oscillations spectrum at 479 MeV. The vertical axis corresponds to oscillation harmonic amplitude (mm).

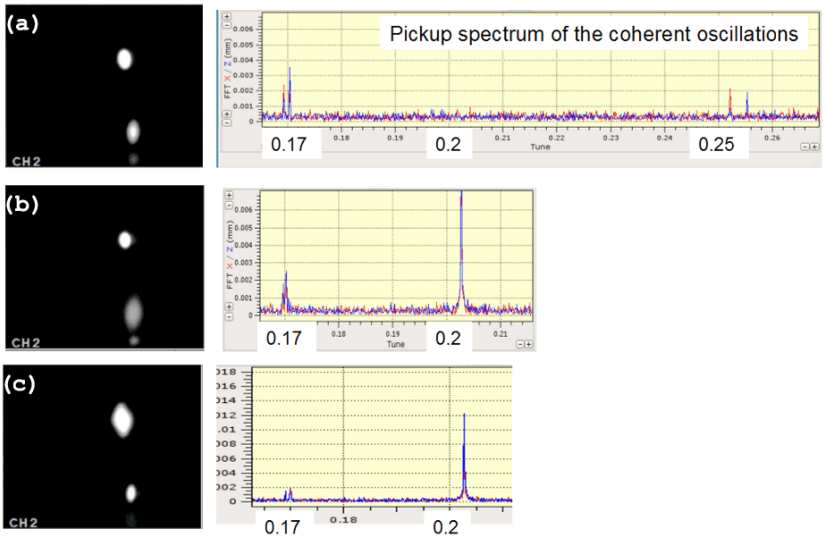

Figure 13: Flip-flop effect. 240 MeV, 5 × 5 mA. (a) Regular beams; (b) flipped electron beam; (c) positron beam.

The type of flip-flop effect that has been observed seems to be avoidable by suppressing the resonance driving terms, as well as by tuning down the working point. Unexpected problems with DA prevent us from currently using the design working point. The acceptable bunch stacking rate and beam lifetime at collision is available only for the betatron tunes of $\{\nu\} \sim 0.13$–0.18.

In Figure 13 the images from the online control TV camera are presented for the cases of regular beams, flipped electron beams or positron beams. The corresponding spectra are shown on the left.

CONCLUSION

Round beams give a serious luminosity enhancement. The achieved beam–beam parameter value at low energy amounts to $\xi \sim 0.1$–0.12. VEPP-2000 is successfully taking data with two detectors across the whole designed energy range of 160–1000 MeV with a luminosity value two to five times higher than that achieved by its predecessor, VEPP-2M. To reach the target luminosity, more positrons and the upgrade of the BEP booster are needed.

REFERENCES

[1] S. Karnaev et al. “Low Energy Luminosity at VEPP-4M Collider,” Proc. APAC’01, Beijing, p. 201 (2001).

[2] Yu.M. Shatunov et al. “Project of a New Electron-Positron Collider VEPP-2000,” Proc. EPAC’00, Vienna, p. 439 (2000).

[3] V.V. Danilov et al. “The Concept of Round Colliding Beams,” Proc. EPAC’96, Sitges, p. 1149 (1996).

[4] L.M. Barkov et al. “Phi-Factory Project in Novosibirsk,” Proc. 14th HEACC’89, Tsukuba, p. 1385 (1989).

[5] I. Nesterenko, D. Shatilov, E. Simonov, “Beam–Beam Effects Simulation for VEPP-2M With Flat and Round Beams,” Proc. PAC’97, Vancouver, p. 1762 (1997).
I.A. Koop, “VEPP-2000 Project,” Proc. e+e− Physics at Intermediate Energies Workshop, Stanford, p. 110 (2001).

[6] A.A. Valishev, E.A. Perevedentsev, K. Ohmi “Strong–Strong Simulation of Beam–Beam Interaction for Round Beams,” Proc. PAC’03, Portland, p. 3398 (2003).

[7] D. Shatilov et al., “LIFETRAC Code for the Weak–Strong Simulation of the Beam–Beam Effects in Tevatron,” Proc. PAC’05, Knoxville, USA, p. 4138 (2005).

[8] M.N. Achasov et al., “First Experience with SND Calorimeter at VEPP-2000 Collider,” Nucl. Instrum. Meth. A 598 (2009) 31–32.

[9] P.M. Ivanov et al., “Luminosity and the Beam–Beam Effects on the Electron–Positron Storage Ring VEPP-2M with Superconducting Wiggler Magnet,” Proc. 3rd Advanced ICFA Beam Dynamics Workshop on Beam–Beam Effects in Circular Colliders, Novosibirsk, p.26 (1989).

[10] V.V. Danilov and E.A. Perevedentsev. “Two Examples of Integrable Systems with Round Colliding Beams,” Proc. PAC’1997, Vancouver, Canada, p. 1759 (1997).

[11] P.M. Ivanov et al. “Experimental Studies of Beam–Beam Effects at VEPP-2M,” Proc. Workshop on Beam–Beam Effects in Circular Colliders, Fermilab, p. 36 (2001).

Published by CERN in the Proceedings of the ICFA Mini-Workshop on Beam–Beam Effects in Hadron Colliders,
CERN, Geneva, Switzerland, 18–22 March 2013, edited by W. Herr and G. Papotti, CERN–2014–004 (CERN, Geneva, 2014)

POISSON SOLVERS FOR SELF-CONSISTENT MULTI-PARTICLE SIMULATIONS*

J. Qiang, S. Paret, LBNL, Berkeley, USA

Abstract

Self-consistent multi-particle simulation plays an important role in studying beam–beam effects and space charge effects in high-intensity beams. The Poisson equation has to be solved at each time-step based on the particle density distribution in the multi-particle simulation. In this paper, we review a number of numerical methods that can be used to solve the Poisson equation efficiently. The computational complexity of those numerical methods will be $O(N\log(N))$ or $O(N)$ instead of $O(N^2)$, where N is the total number of grid points used to solve the Poisson equation.

INTRODUCTION

The self-consistent multi-particle simulation based on the particle-in-cell method has been widely used in studying beam–beam effects in high-energy ring colliders and space charge effects in high-intensity/brightness accelerators. A schematic plot of a single step of the multi-particle simulation for the strong–strong (self-consistent) beam–beam simulation is given in Fig. 1.

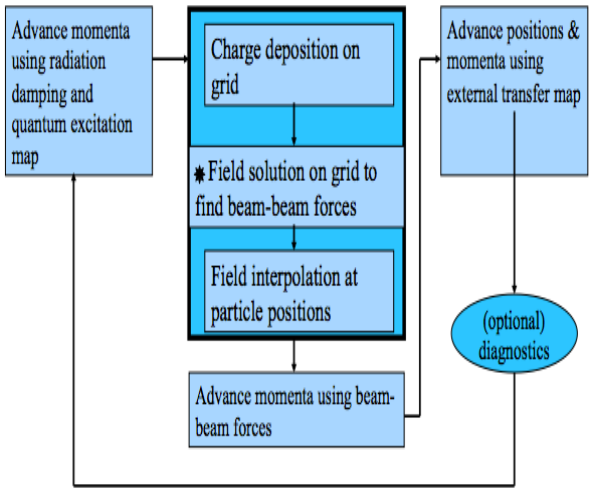

Figure 1: A schematic plot of a single step in the multi-particle simulation.

Here, we assume that a number of macro-particles have been initially generated from a given initial 6D phase space distribution. Within this step, these macro-particles are deposited onto a 2D computational grid for each slice to obtain the spatial charge density distribution. The Poisson equation is solved on the grid and the electromagnetic fields are calculated from the solution of the Poisson equation. Those fields are interpolated back to individual particle positions to calculate the beam–beam forces. Momenta of each particle are updated using the beam–beam forces. Positions and momenta of each particle are advanced using a transfer map. For a lepton accelerator, particle momenta are further advanced using a radiation damping and quantum excitation map to finish the single step. This single-step loop is repeated many times in the multi-particle simulation. Since the charge density will be updated during every step, the Poisson equation has to be solved for every step. The speed of the Poisson solver could become the bottleneck for the whole simulation. In the following section we review a number of efficient numerical methods (FFT-based method, spectral-finite difference method, and multigrid spectral-finite difference method) used to solve the Poisson equation in multi-particle beam–beam and space charge simulations.

FFT-BASED GREEN FUNCTION METHOD

The FFT-based Green function method is mostly used to solve the Poisson equation subject to an open boundary condition. This is true if the pipe radius in an accelerator is much larger than the beam bunch transverse size. Given the Poisson equation:

$$\nabla^2\phi = -\frac{\rho}{\varepsilon} \tag{1}$$

subject to the open boundary conditions, the solution of the electric potential can be written as:

$$\phi(r) = \int G(r-r')\rho(r')dr' \tag{2}$$

where the Green function is given by:

$$G(r) = \begin{cases} -\log(r): & in\,2D \\ \frac{1}{r}: & in\,3D \end{cases} . \tag{3}$$

Integral Eq. (2) can be written as a numerical summation for each grid point in a 2D problem:

*Work supported by the US Department of Energy under contract No. DE-AC02- 05CH11231.

978-92-9083-404-5, 0007-8328 –
http://dx.doi.org/10.5170/CERN–2014–004.51

$$\phi(x_i,y_j)=h_xh_y\sum_{i'=1}^{N_x}\sum_{j'=1}^{N_y}G(x_i-x_{i'},y_j-y_{j'})\rho(x_{i'},y_{j'}) \quad (4)$$

A direct calculation of the above summation will have a computational cost of $O(N^2)$, where $N = N_xN_y$. For a grid of 100×100 points in each dimension, this yields an operation of 10^8 in a 2D problem and 10^{12} in a 3D problem to solve the Poisson equation for each step.

The direct calculation is very inefficient and will significantly slow down the computational speed of the multi-particle simulation. Fortunately, Eq. (4) can be calculated using an FFT-based method by turning it into a cyclic summation. The idea behind this method is to construct a discrete periodic system so that the FFT can be used to calculate this discrete cyclic summation. In this new periodic system, the original computational domain is doubled in each dimension within a period of computational domain. A new Green function and a new charge density function are defined in this new computational domain so that the cyclic summation will yield the same results as the original summation in Eq. (4) inside the original computational domain. Outside the original computational domain, the two summation results will be different but irrelevant since we are only interested in the field inside the original domain. The detailed expression for the Green's function and the charge density inside the new computational domain can be found in Refs. [1, 2].

The computational cost for the cyclic summation will be $O(N \log(N))$. Figure 2 shows a comparison of the electric field as a function of the radius from the FFT-based numerical solution and from the analytical solution of a 2D Gaussian density distribution. The agreement between those two solutions is excellent.

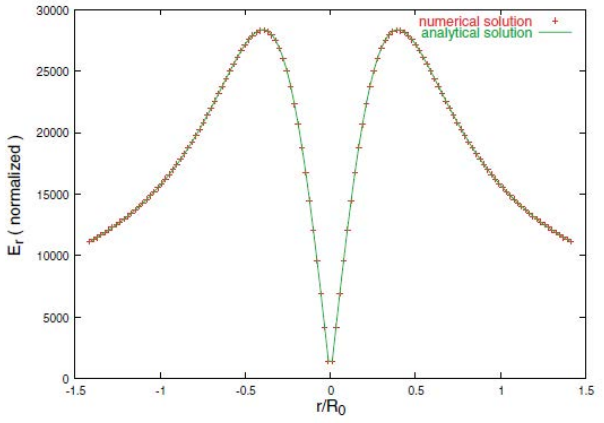

Figure 2: Electric field as a function radius within a 2D Gaussian distribution from the numerical solution (red) and the analytical solution (green).

The FFT-based method described above works well for a beam with a small aspect ratio. For a beam with a large aspect ratio, which is the case for an electron or positron beam inside a lepton collider, the direct use of the above FFT-based method will be inefficient since a large number of grid points are needed to resolve the variation of the Green function inside a grid cell. Assuming a slow variation of the charge density inside a grid cell, a new Green function can be defined as:

$$G_i(r,r')=\int_{r'-\Delta/2}^{r'+\Delta/2}G(r,r')dr' \quad (5)$$

where Δ is the size of the grid cell. This integrated Green function can be used in the original FFT-based method to calculate the cyclic summation of the electric potential. The detailed expression of the integrated Green function in 2D can be found in Refs. [3–5] and in 3D can be found in Refs. [6–8].

The above method calculates the electric potential inside the beam itself. In some applications, one might also be interested in the fields outside the beam such as in the case of long-range beam–beam interaction or the image space charge forces from a flat conducting plate. Under these situations, the direct use of the above method will be inefficient since it requires using a computational domain that contains both the domain of the beam and the domain of the field that could be far from the beam. It is wasteful to define such a large computational domain since one is only interested in the fields inside the field domain. A more efficient method is to define a computational domain that is large enough to contain either the particle beam domain or the field domain and a new shifted Green function as [9]:

$$G_s(r,r')=G(r+r_s,r') \quad (6)$$

where r_s is the separation distance between the particle beam domain and the field domain. This shifted Green function can be used in the above FFT-based method to calculate the cyclic summation.

The FFT-based methods above assume a uniform computational grid. In some applications, the particle density distribution is not uniform and a non-uniform grid might be preferred. For the 2D Poisson equation with open boundary condition, the solution of electric potential can be written as:

$$\phi(r,\theta)=\int G(r,r',\theta,\theta')\rho(r',\theta')r'dr'd\theta' \quad (7)$$

in a polar coordinate system, where:

$$G(r,r',\theta,\theta')=-\frac{1}{2}\log(r^2-2rr'\cos(\theta-\theta')+r'^2)$$

.

The above convolution cannot be directly calculated using the FFT-based method. Instead, we define a new variable:

$$s = \frac{1}{k_1}\log\left(\frac{r}{k_2}\right) \tag{8}$$

Under this new variable, the Green function can be rewritten as

$$G(s,s',\theta,\theta') = -\frac{1}{2}\log(e^{2k_1(s-s')} - 2e^{k_1(s-s')}\cos(\theta-\theta') + 1)$$

The new Green function on the uniform grid of s and θ can be calculated using the FFT-based method discussed above. This yields a non-uniform grid along the radial direction r. Figure 3 shows the electric field error calculated for a round beam with a Gaussian density distribution [10]. It is seen that in this case the non-uniform grid Green function method yields a factor of three less errors than the uniform grid Green function method.

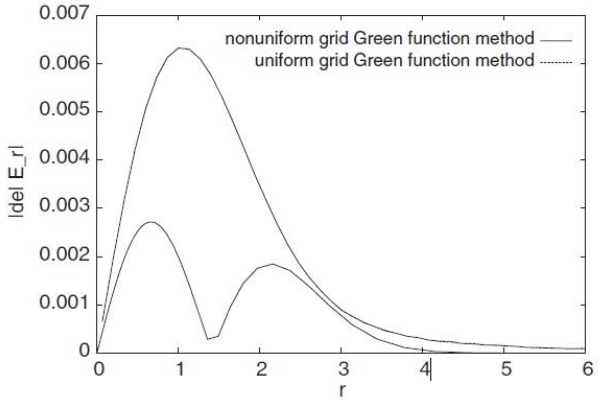

Figure 3: Electrical field error as a function of radius using the non-uniform grid Green method and the uniform grid Green function method.

SPECTRAL FINITE DIFFERENCE METHOD

In some applications, the Poisson equation might be subject to simple regular shape boundary conditions. If an analytical eigenfunction can be found to satisfy both the Poisson equation and the boundary condition in a dimension, one can use the spectral method in that dimension and combine it with the finite difference method in the other dimensions. For example, a 2D Poisson equation subject to open boundary conditions can be written in cylindrical coordinates as:

$$\frac{1}{r}\frac{\partial}{\partial r}\left(r\frac{\partial}{\partial r}\phi\right) + \frac{1}{r^2}\left(\frac{\partial^2}{\partial\theta^2}\phi\right) = -\frac{\rho}{\varepsilon_0} \tag{9}$$

Making use of the periodic boundary condition in the azimuthal direction, the electric potential and the charge density can be written as:

$$\phi(r,\theta) = \sum \phi_m(r)e^{-im\theta}$$

$$\rho(r,\theta) = \sum \rho_m(r)e^{-im\theta}$$

Substituting those expressions into the Poisson's equation above yields:

$$\frac{1}{r}\frac{\partial}{\partial r}\left(r\frac{\partial}{\partial r}\phi_m\right) - \frac{m^2}{r^2}\phi_m = -\frac{\rho_m}{\varepsilon_0} \quad for \quad r \le a \tag{9a}$$

$$\frac{1}{r}\frac{\partial}{\partial r}\left(r\frac{\partial}{\partial r}\phi_m\right) - \frac{m^2}{r^2}\phi_m = 0 \quad for \quad r > a \tag{9b}$$

for each mode m. The ordinary differential equation for each mode inside the beam boundary can be solved using the finite difference method:

$$\left(\frac{1}{h^2}+\frac{1}{hr}\right)\phi_m^{n+1} - \left(\frac{2}{h^2}+\frac{m^2}{r^2}\right)\phi_m^{n} + \left(\frac{1}{h^2}-\frac{1}{hr}\right)\phi_m^{n-1} = -\frac{\rho_m}{\varepsilon_0} \tag{10}$$

subject to the boundary conditions:

$$\frac{\partial}{\partial r}\phi_m = 0 \quad for \quad r = 0 \quad and \quad m = 0$$

$$\phi_m = 0 \quad for \quad r = 0 \quad and \quad m > 0$$

For the ordinary differential equation outside the beam, the electric potential solution can be written as:

$$\phi = c\,r^{-m} \qquad m > 0$$

$$\phi = c\ln(r) \qquad m = 0$$

The above solutions can be used as a boundary condition to match the electric solution inside the beam. This solution together with the boundary condition at the origin will close the N algebra equations for N unknowns at each mode m. This group of linear algebra equations form a tri-diagonal equation that can be solved by direct elimination method with a computational cost of $O(N)$ where N is the number of grid points inside the beam. Figure 4 shows the electric field as a function of radius for a round Gaussian beam from the numerical solution and the analytical solution. It is seen that the agreement between those two solutions is excellent.

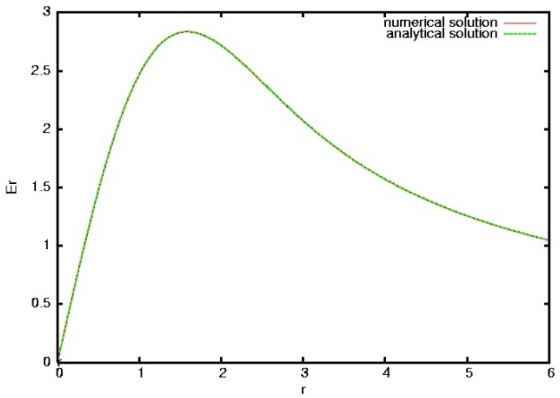

Figure 4: Electric field as a function of radius from the numerical solution and the analytical solution.

The above boundary matching method uses the computational domain to contain only the beam instead of the large empty space where the electric potential vanishes at the boundary. A similar numerical method was also used to solve the 3D Poisson equation subject to the transverse finite round and rectangular boundary conditions and the longitudinal open boundary condition [11].

MULTIGRID SPECTRAL FINITE DIFFERENCE METHOD

In applications where the transverse boundary geometry is not regular, e.g. with an electrode, the simple spectral finite difference method above might not be applicable. In this case, a multigrid spectral method can be used. Given the 3D Poisson equation in a cylindrical coordinate system:

$$\frac{\partial^2\phi}{\partial r^2}+\frac{1}{r}\frac{\partial\phi}{\partial r}+\frac{1}{r^2}\frac{\partial^2\phi}{\partial\theta^2}+\frac{\partial^2\phi}{\partial z^2}=-\frac{\rho}{\varepsilon} \qquad (11)$$

subject to an azimuthally symmetric boundary condition, the charge density and electrical potential can be written as:

$$\rho(r,\theta,z)=\sum\rho^m(r,z)\exp(-im\theta)$$

$$\phi(r,\theta,z)=\sum\phi^m(r,z)\exp(-im\theta).$$

Substituting the above solutions into the Poisson equation yields:

$$\frac{\partial^2\phi^m}{\partial r^2}+\frac{1}{r}\frac{\partial\phi^m}{\partial r}-\frac{m^2}{r^2}\phi^m+\frac{\partial^2\phi^m}{\partial z^2}=-\frac{\rho^m}{\varepsilon}. \qquad (12)$$

The above group of partial differential equations can be solved for each mode m using a finite difference method with appropriate boundary geometry shape, which results in a group of algebraic equations. These algebraic equations form a sparse matrix equation and can be solved using an iterative method. Directly solving the above sparse matrix equation on the original grid using a classical iterative matrix-vector multiplication method such as the successive over-relaxation method (SOR) has a slow convergence rate. This is because the low-frequency errors during the iteration decrease slowly after the first few iterations. The classical iteration method moves the information one grid per iteration and will take a large number of iterations ($O(N^{1/d})$) (where d is the dimension of the problem) to move the information across the full grid. Since the operation is done on the full grid, this results in a large number of operations to solve the linear algebraic equations.

The multigrid method smoothes out the numerical errors of different frequencies on different scales using multiple grids. It moves the information across the grid using $O(\log(N))$ steps. Most matrix-vector multiplications are done on the coarser grid with a much smaller number of operations so that the total number of operations in the multigrid method scales as $O(N)$. It replaces the error correction on the finer grid by an approximation on the coarser grid. It solves the coarser grid problem recursively by using a still coarser approximation until the direct solutions can be found on the coarsest grid. The solution from the coarser grid is then interpolated back to the finer grid and is used as a new starting solution on the finer grid until the final finest grid is reached. A detailed discussion of the multigrid method can be found in Refs. [12, 13] and an application to the simulation of the ion beam formation from an ECR ion source can be found in reference [14].

REFERENCES

[1] R.W. Hockney and J.W. Eastwood, Computer Simulation Using Particles (New York: McGraw-Hill Book Company, 1985).
[2] W.H. Press et al., Numerical Recipes in FORTRAN: The Art of Scientific Computing, 2nd ed. (Cambridge: Cambridge University Press, 1992).
[3] K. Ohmi, Phys. Rev. E 62 (2000) 7287.
[4] R.D. Ryne, ICFA Beam Dynamics Mini Workshop on Space Charge Simulation, Trinity College, Oxford (2003).
[5] J. Qiang, M. Furman, and R. Ryne, J. Comp. Phys. 198 (2004) 278.
[6] J. Qiang et al., PRST-AB 9, (2006) 044204.
[7] J. Qiang et al., PRST-AB 10, (2007) 129901.
[8] V. Ivanov, Int. J. Mod. Phys. A, 24, (2009) 869.
[9] J. Qiang, M. Furman, and R. Ryne, PRST-AB 5, (2002) 104402.
[10] J. Qiang et al., NIM-A, 558, (2006) 351.
[11] J. Qiang and R. Ryne, Comput. Phys. Comm. 138 (2001) 18.

[12] W. Hackbusch, Multi-Grid Methods and Applications (New York: Springer-Verlag, 1985).
[13] P. Wesseling, An Introduction to Multigrid Methods (Chichester: John Wiley& Sons, 1992).
[14] J. Qiang, D. Todd, and D. Leitner, Comput. Phys. Comm. 175 (2006) 416.

Published by CERN in the Proceedings of the ICFA Mini-Workshop on Beam–Beam Effects in Hadron Colliders,
CERN, Geneva, Switzerland, 18–22 March 2013, edited by W. Herr and G. Papotti, CERN–2014–004 (CERN, Geneva, 2014)

STABILITY DIAGRAM OF COLLIDING BEAMS

X. Buffat, EPFL, Lausanne; CERN, Geneva, Switzerland
W. Herr, N. Mounet, T. Pieloni, CERN, Geneva, Switzerland

Abstract

The effect of the beam–beam interactions on the stability of impedance mode is discussed. The detuning is evaluated by the means of single particle tracking in arbitrarily complex collision configurations, including lattice non-linearities, and used to numerically evaluate the dispersion integral. This approach also allows the effect of non-Gaussian distributions to be considered. Distributions modified by the action of external noise are discussed.

INTRODUCTION

The stability of impedance driven modes is usually ensured by non-linearities via Landau damping. The strength of the Landau damping is represented in a stability diagram, defining the area of complex tune shifts which can be kept stable [1]. The computation of the stability diagram is a crucial element for the evaluation of the non-linearity required for the beam stability. It can be done analytically in many simple cases, in particular considering lattice non-linearities and a limited number of beam–beam interactions. Facing the complexity of the LHC collision scheme, a numerical approach seems more appropriate. In particular, the dispersion integral is solved numerically using the amplitude detuning provided by single particle tracking, thus allowing the computation of stability diagrams in arbitrarily complex cases.

Following the same approach, the effect of non-Gaussian distribution functions can be introduced in the computation. Previous studies have shown that the distribution function plays a crucial role in the stability diagram [2] and, being usually poorly known, greatly diminishes the predicting power of such a consideration. The numerical evaluation of the stability diagram allows us to go further in the understanding of this effect by using a non-analytical distribution function. In particular, coloured external noise is known to enhance diffusion of resonant particles [3], greatly modifying the distribution and therefore the stability diagram.

STABILITY OF MULTIBUNCH COHERENT BEAM–BEAM MODES

The method to derive the stability of impedance driven multibunch modes by placing their tune shifts in the stability diagram derived using the lattice non-linearities, as described in [4], considers bunches with identical detuning. In the LHC, this assumption is no longer valid once beam–beam effects are considered. Indeed, the asymmetric layout of the interaction points as well as the asymmetric filling scheme lead to a variety of bunches having significantly different detuning. Theoretical treatment of the beam stability in such configurations is currently lacking. It is however possible to assess these cases using multiparticle tracking simulation [5], at the expense of large computational power.

The beam–beam interactions do not only introduce bunch dependent detuning, they also change the nature of the coherent modes. The Landau damping of beam–beam modes in the single bunch regime is addressed in [6], the extension to multibunch coherent beam–beam mode is, however, not trivial. Preliminary studies by the means of multiparticle tracking simulation are presented in [5]. Such an approach is well suited to studying the LHC in its full complexity, however it is very demanding in terms of computing power. It is therefore interesting to consider simplified cases. In this paper, we address the stability of single bunch impedance modes with detuning from the lattice and beam–beam interactions, in other words, multibunch effects from the impedance as well as beam–beam coherent mode are neglected. These drastic assumptions are motivated by the observation, in the LHC, of single bunch instabilities, while operating in the multibunch regime. Figure 1 shows such an instability at the end of the squeeze during operation of the LHC in 2012. In particular, the measurement of the beam oscillation amplitude provided by the BBQ system indicates a coherent instability on Beam 1. The observation of bunch intensities indicates that only one bunch lost its intensity in an abnormal way, with respect to the other bunches, suggesting that only this bunch had undergone the instability.

NUMERICAL EVALUATION OF STABILITY DIAGRAMS

Considering a case without coupling, the stability diagram of each plane is obtained by solving the dispersion relation for a given detuning $q(J_x, J_y)$ and distribution function $\psi(J_x, J_y)$ where J_x and J_y are the unperturbed actions in each plane,

$$\frac{-1}{\Delta Q_i} = \iint_0^\infty \frac{J_i \frac{\mathrm{d}\psi}{\mathrm{d}J_i}}{Q - q(J_x, J_y)} \mathrm{d}J_x \mathrm{d}J_y,\ Q \in \mathbb{R},\ i = 1, 2. \tag{1}$$

The ΔQ_i found for different values of Q are the tune shifts at the limit of stability, therefore, they define an area in which the tune shifts are stable. In cases where the denominator is strictly non-zero, the tune shift is purely real, which indicates the absence of Landau damping. In the relevant cases, the integral possesses poles, and can be evaluated using various techniques. Whereas it is difficult to obtain

978-92-9083-404-5, 0007-8328 –
http://dx.doi.org/10.5170/CERN–2014–004.57

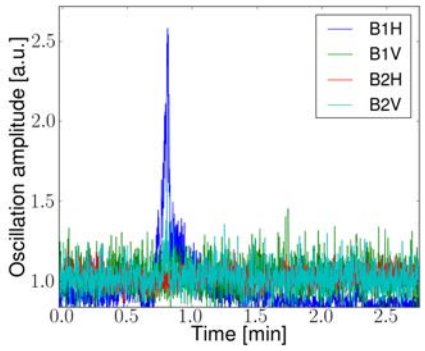

(a) BBQ

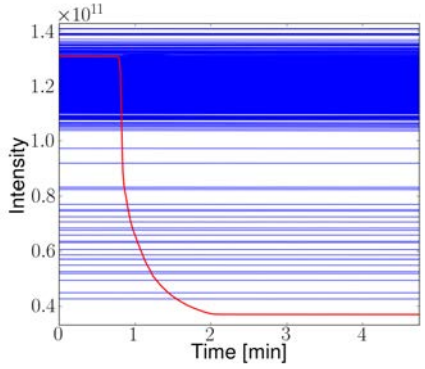

(b) FBCT

Figure 1: Observation of an instability during luminosity production in the LHC (fill 2644). The beam oscillation amplitude shows a coherent excitation in the horizontal plane of Beam 1. The bunch by bunch intensity of both beams shows that all bunches (in blue) except one (in red) are stable.

analytically in complex configurations, the detuning is easily obtainable numerically. The dispersion integral can then be evaluated by standard numerical techniques, in our case by adding a vanishing complex part to the denominator.

Detuning

The detuning is obtained numerically from tracking simulation with MAD-X [7–9]. Particles with different actions are tracked for 1024 turns from which the tunes can be evaluated, the result is represented in the tune diagram as a tune footprint (Fig. 2). A significant number of particles is required to reduce the noise in the evaluation of the integrals. In particular, the effect of resonant driving term on the tracking can have a significant effect on the evaluation of the footprint. This effect is reduced by an automatic removal of faulty points and interpolation from the closest non-faulty points. As illustrated in Fig. 2, this technique does not allow us to fully remove distortions due to strong non-linearities, in particular from coupling resonances. In the cases of practical interests, however, the effect on the

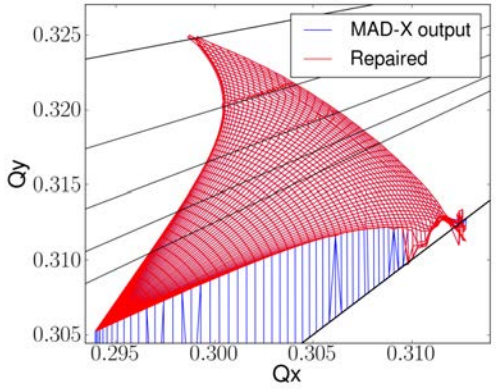

Figure 2: Illustration of a typical tune footprint with octupoles (positive polarity) and long-range beam–beam interactions at the end of the squeeze in the LHC. The tracking result is often distorted by the presence of resonances; using a fine mesh and a repairing algorithm allows us to get a footprint suitable for the computation of stability diagrams.

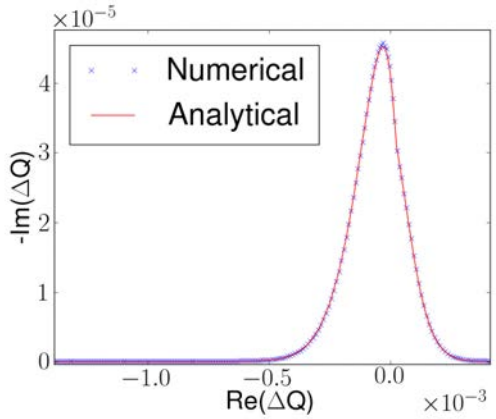

Figure 3: Comparison of analytical and numerical derivation of a stability diagram with LHC octupoles powered with -100 A for a 4 TeV beam with a normalized emittance of 2 μm.

footprint, and consequently on the stability diagram, is tolerable. The integrity of the footprint is nevertheless systematically checked before deriving a stability diagram.

Benchmarking

Figure 3 shows a good agreement between stability diagrams computed analytically and numerically in the case of octupolar detuning using a Gaussian distribution.

Practical applications of this code for the LHC can be found in [10].

THE EFFECT OF EXTERNAL NOISE

External coloured noise enhances the diffusion of resonant particles. In the presence of amplitude detuning, this results in a depletion of certain parts of the distribution. This effect is illustrated with a simple model, using a multiparticle code that tracks particles through a lattice with amplitude detuning described by

$$Q_x = Q_{x,0} + a \cdot J_x + b \cdot J_y, \quad (2)$$
$$Q_y = Q_{y,0} + b \cdot J_x + a \cdot J_y. \quad (3)$$

The noise is modelled with a sinusoidal excitation with finite correlation time. The relative difference to the initial distribution in action space after $2 \cdot 10^4$ turns is shown in Fig. 4(a). The depletion of the distribution at the position of resonant particles is visible. This effect was already studied for different purposes in [11]. The measurable effect on the distribution in real space is very small (Fig. 4(c)), the effect on the stability diagram is, however, significant, as illustrated by the comparison of the stability diagrams obtained using the initial and perturbed distributions (Fig. 4(b)).

The effect illustrated by this simple model can be simulated in more realistic scenarios. In particular, the COMBI code [12], extended with an impedance model, was used to model the action of external noise on a beam stabilized by both amplitude detuning and a transverse feedback. We consider a study case, where a single bunch is rendered unstable by negative chromaticity. This study case intends to mimic a situation similar to the LHC at the end of the squeeze where the beams have to be stabilized by high damper gain and high octupole current, while relaxing significantly the need for computational power due to the large number of bunches in this case. The results are therefore not meant to be compared to measurements, but rather to illustrate an effect that should be studied in more realistic cases in the future. The upper dot in Fig. 5(a) shows the coherent tune shift of the most unstable mode, with a large positive imaginary part. The imaginary part is brought down to the lower dot using a transverse feedback. The line represents the stability diagram provided by an octupolar amplitude detuning. In this configuration, this analysis suggests that both the damper and the octupoles are required to stabilize the beam, which is confirmed by tracking (Fig. 5(b)), showing the oscillation amplitude as a function of time for the different scenarios. The stable configuration can, however, be rendered unstable by a wideband noise, i.e. a random kick is applied every turn, the kick being constant over the bunch length. Indeed, the response to the wideband noise is more important at the mode frequencies as it cannot be entirely damped by a transverse feedback with finite gain. Wideband noise in this configuration has a similar effect on the diffusion as coloured noise, and therefore can compromise the stability from Landau damping, as described above. In particular, in Fig. 6, the simulation of the stable case for different noise amplitude shows that the latency time before the instability takes off depends on the noise amplitude.

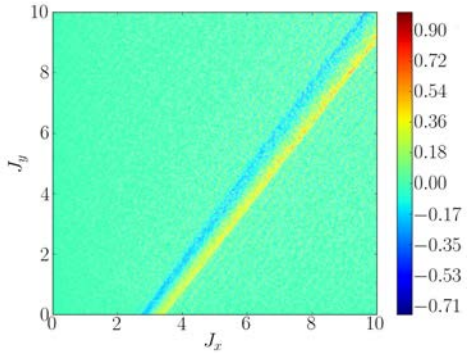

(a) Relative difference to initial distribution in action space after $2 \cdot 10^4$ turns

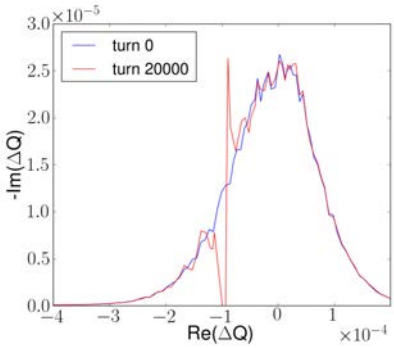

(b) (Un)perturbed stability diagrams

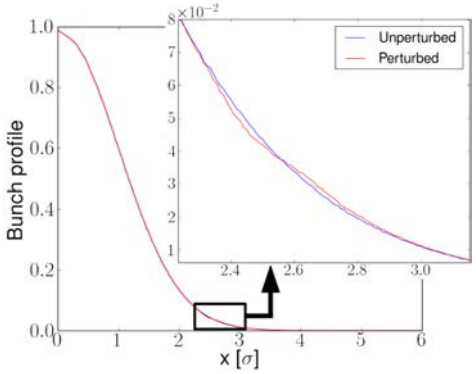

(c) Real space bunch profile

Figure 4: Stability diagram derived from a distribution perturbed by external noise in the presence of amplitude detuning $a = 1.64 \cdot 10^{-4}, b = -1.16 \cdot 10^{-4}$. The noise has an amplitude of $10^{-4}\sigma_{x'}$ and a frequency of $Q_{x,0} + 0.05$ with a correlation time of 100 turns.

The extension of this study case to more realistic configurations including multibunch impedance and beam–beam interactions promises great challenges from the computational point of view, but is however not out of reach with current resources. In particular, one could expect that other sources of diffusion may counterbalance the effect described. Nevertheless, this analysis suggests that the external noise could play a critical role in configurations where both a transverse feedback and amplitude detuning are required to stabilize the beams.

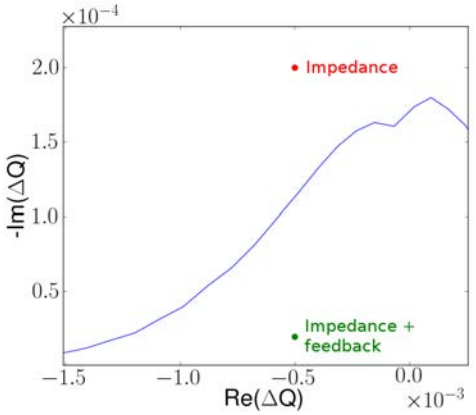

(a) Stability diagram and tune shifts

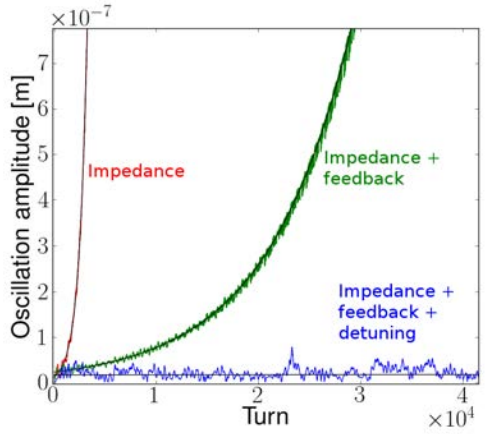

(b) Tracking without external noise

Figure 5: Analysis of a single bunch with intensity $1.5{\cdot}10^{11}$ in the LHC, chromaticity of -10 units, stabilized with a transverse damper with gain $\sim$ 700 turns and amplitude detuning $a = -2.05 \cdot 10^{-4}, b = 1.45 \cdot 10^{-4}$.

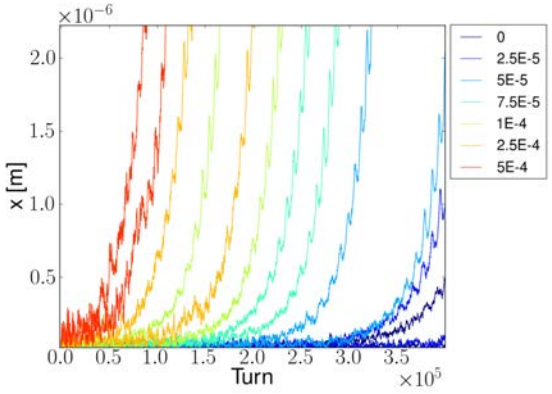

(a) Tracking in the stable configuration with different noise amplitude

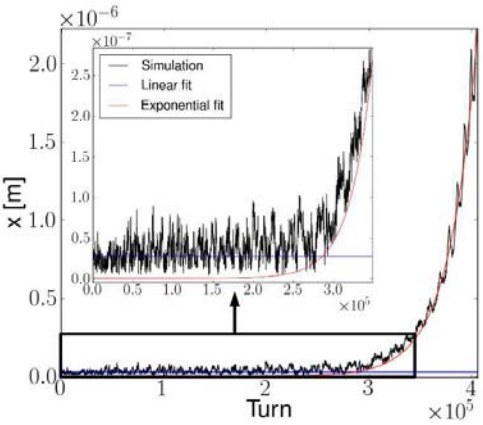

(b) Latency time with a noise amplitude of $5 \cdot 10^{-5}$ $\sigma_{x'}$

Figure 6: Tracking simulations in the stable configuration (Fig. 5) rendered unstable by wideband noise. The linear fit is done on the first part, and the exponential fit during the instability, which indicates a latency of $2.8 \cdot 10^5$ turns before an instability of rise time $2.7 \cdot 10^4$ turns.

CONCLUSION

Single bunch stability of beams colliding in arbitrary complex configurations can be investigated by numerically solving the dispersion integral, using amplitude detuning derived from single particle tracking simulations. A new code, based on MAD-X output, has been developed to assess the stability of the LHC beams in any operational configuration. This approach is however not suited to studying the stability of multibunch coherent modes.

The effect of distributions perturbed by external noise on the stability diagram has been investigated using the code mentioned above, and revealed very strong effects for modifications of the distributions well below the sensitivity of current measurements. It has been shown using multiparticle tracking codes that, indeed, a beam well stabilized by both amplitude detuning and transverse damper could be rendered unstable by the introduction of wideband noise.

ACKNOWLEDGMENTS

The authors would like to acknowledge S. White and E. Métral for fruitful discussions.

REFERENCES

[1] A.W. Chao, *Physics of Collective Beams Instabilities in High Energy Accelerators*, (John Wiley and Sons, New York, 1993).

[2] E. Métral *et al.*, "Stability Diagram for Landau Damping with a Beam Collimated at an Arbitrary Number of Sigmas," CERN-AB-2004-019-ABP (2004).

[3] A. Bazzani *et al.*, "Diffusion in Hamiltonian Systems Driven by Harmonic Noise," J. Phys. A: Math. Gen. 31 (1998).

[4] J.P. Koutchouk and F. Ruggiero, "A Summary on Landau Octupoles for the LHC," LHC Project Note 163 (1998).

[5] S. White *et al.*, "Beam–Beam and Impedance," these proceedings.

[6] Y.Alexahin, "On the Landau Damping and Decoherence of Transverse Dipole Oscillations in Colliding Beams," CERN SL-96-064 AP (1996).

[7] http://mad.web.cern.ch/mad/.

[8] W. Herr, "Particle Tracking With MAD-X Including LHC Beam–Beam Interactions," LHC Project Note 344 (2004).

[9] W. Herr, "Tune Shift and Spread Due to Short and Long Range Beam–Beam Interactions in the LHC," CERN SL/90-06 (AP), LHC Note No. 119 (1990).

[10] X. Buffat $et\ al.$, "Operational Considerations on the Stability of Colliding Beams," these proceedings.

[11] A. Bazzani $et\ al.$, "Effect of Colored Noise on the Betatronic Motion: A Possible Mechanism for Slow Extraction," Nonlinear and Stochastic Beam Dynamics in Accelerators - A Challenge to Theoretical and Computational Physics, Lüneburg (1997).

[12] T. Pieloni, "A Study of Beam–Beam Effects in Hadron Colliders with a Large Number of Bunches," EPFL Thèse No 4211 (2008).

Published by CERN in the Proceedings of the ICFA Mini-Workshop on Beam–Beam Effects in Hadron Colliders,
CERN, Geneva, Switzerland, 18–22 March 2013, edited by W. Herr and G. Papotti, CERN–2014–004 (CERN, Geneva, 2014)

BEAM–BEAM EFFECTS IN SPACE CHARGE DOMINATED ION BEAMS *

C. Montag, A. Fedotov, Brookhaven National Laboratory, Upton, NY, USA

Abstract

During low-energy operations below the regular injection energy in the Relativistic Heavy Ion Collider (RHIC), significant beam lifetime reductions due to the beam–beam interaction in conjunction with large space charge tune shifts have been observed. We report on dedicated experiments aimed at understanding this phenomenon as well as preliminary simulation results, and propose alternative working points to improve the beam lifetime in future low-energy RHIC runs.

INTRODUCTION

One of the major physics programmes at the RHIC for the next 5–10 years is the search for the critical point in the Quantum ChromoDynamics (QCD) phase diagram (Fig. 1), which is expected to occur at centre-of-mass energies in the range of $\sqrt{s_{\rm NN}}$ = 5–30 GeV/n. This requires colliding gold beams with energies between 2.5 and 15 GeV/nucleon, which is well below the nominal energy range of 10–100 GeV/n in the RHIC (Fig. 2). In conjunction with the circumference of 3.8 km, this low energy results in a significant direct space charge tune shift up to $\Delta Q_{\rm sc} = 0.1$, which is more than ten times larger than the total beam–beam parameter $\xi_{\rm beam-beam}$ encountered during low-energy operation [1]. Experiments with a large beam–beam parameter comparable with the space charge tune shift have been performed using protons and are reported elsewhere [2]. Table 1 lists space charge and beam–beam parameters achieved in the RHIC for different Au beam energies. However, in spite of the large difference in magnitude of these two effects, and the similar functional dependence of the associated forces on transverse particle coordinates, we have observed a significant deterioration of beam lifetimes once beams are brought into collision.

To gain a better understanding of this phenomenon, we have performed a series of beam experiments and developed a simulation code. In the following sections, we describe our experimental observations during regular low-energy operations with Au ions, as well as those dedicated Au beam experiments. Furthermore, we report on first results obtained from simulations.

EXPERIMENTAL OBSERVATIONS

When the RHIC was operated at a beam energy of $E = 3.85\,\mathrm{GeV/n}$, a tune scan was performed to maximize the beam lifetime. Starting at the regular RHIC heavy ion

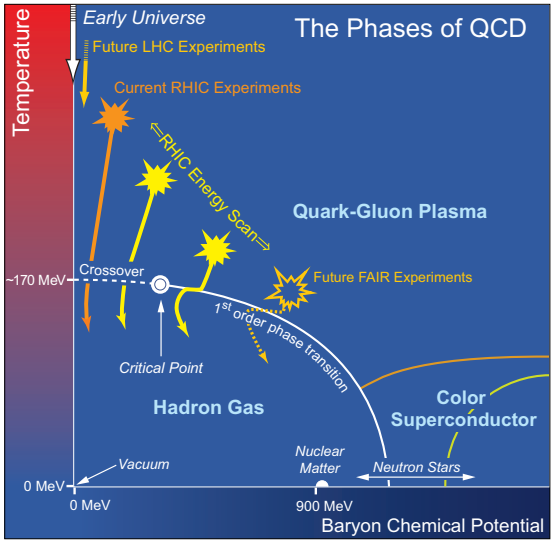

Figure 1: The QCD phase diagram. A lower centre-of-mass energy $\sqrt{s_{\rm NN}}$ corresponds to a higher baryon chemical potential. The critical point is expected to be in the energy range between $\sqrt{s_{\rm NN}} = 5$ and 30 GeV.

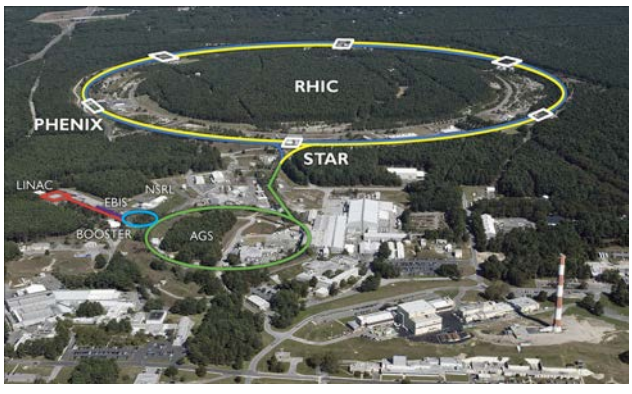

Figure 2: An aerial view of the RHIC accelerator complex, with its two 3.8 km circumference storage rings, 'Blue' and 'Yellow'.

* Work supported under Contract Number DE-AC02-98CH10886 with the auspices of the US Department of Energy

978-92-9083-404-5, 0007-8328 – © CERN, 2014. Published under the Creative Common Attribution CC BY 4.0 Licence.
http://dx.doi.org/10.5170/CERN–2014–004.63

Table 1: Beam Lifetimes τ with and without Collisions at Different Energies in the RHIC, with the Corresponding Space Charge Tune Shifts ΔQ_{sc} and Beam–Beam Parameters $\xi_{\mathrm{beam-beam}}$

E [GeV/n]	ΔQ_{sc}	$\xi_{\mathrm{beam-beam}}$	τ [s]
9.8	0.03	0	2000
9.8	0.03	0.002	600
5.75	0.05	0	1600
5.75	0.05	0.0015	400
5.75	0.09	0	700
5.75	0.09	0.0027	260
3.85	0.11	0	70
3.85	0.08	0.003	70

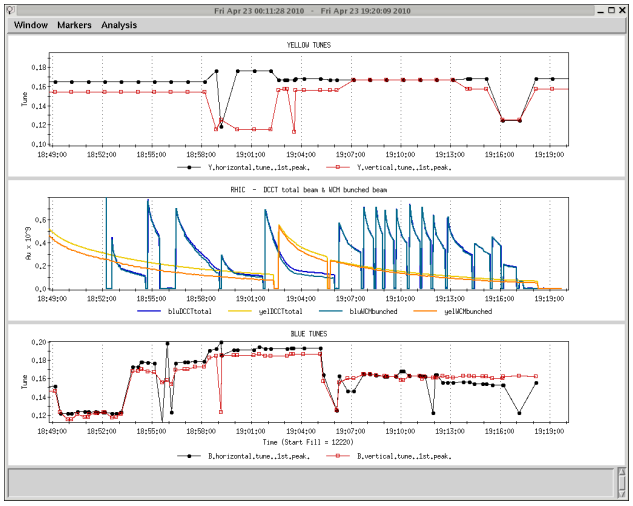

Figure 3: Beam intensities (middle plot) in the Blue and Yellow RHIC rings during a tune scan at $E = 5.75\,\mathrm{GeV/n}$ beam energy. The Yellow tunes are shown in the top part of the plot and the Blue tunes in the bottom third. The best Blue beam lifetime is achieved at a working point of $(Q_x/Q_y) = (28.17/29.16)$.

working point of $(Q_x/Q_y) = (28.23/29.22)$, the tunes were lowered and the beam lifetime in collision was observed (see Fig. 3). This resulted in a new working point of $(Q_x/Q_y) = (28.17/29.16)$; during the course of the run this was further lowered to $(28.13/29.12)$. This latest working point was subsequently used at $E = 5.75\,\mathrm{GeV/n}$ as well.

During the course of the run, a strong effect of beam–beam interactions on the lifetime of the space charge dominated beams was consistently observed, as illustrated in Figs. 4–6. Figure 4 shows the intensity of individual bunches in the Yellow RHIC ring at a beam energy of $E = 3.85\,\mathrm{GeV/n}$. Although the initial intensity drops rather quickly for the first couple of minutes while beams

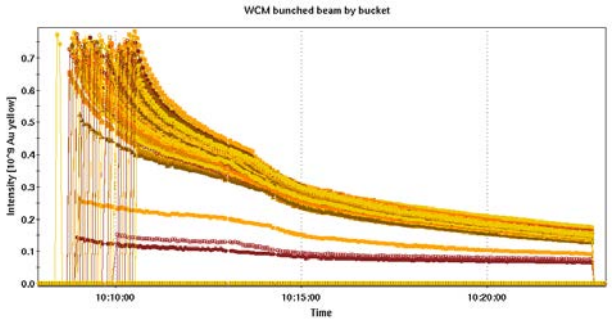

Figure 4: The intensities of individual bunches in the Yellow ring, at $E = 3.85\,\mathrm{GeV/n}$ beam energy. Collisions start at 10:14, resulting in a sudden decrease in the lifetime.

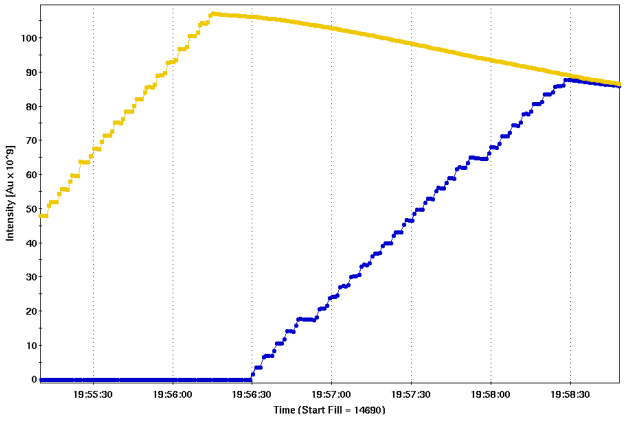

Figure 5: The total beam intensity in the two RHIC rings during injection, without any transverse separation of the two beams. After the Yellow ring has been filled, Blue is being injected, resulting in a gradual decrease of the Yellow beam lifetime due to the beam–beam interaction.

are not colliding, there is a sudden, sharp decrease in beam lifetime, to roughly the same level as at the beginning of store, as soon as the two beams begin colliding. Since the intensity of the Yellow bunch at this time is only about half the initial value, which reduces the space charge tune shift by the same factor of 2, this lifetime deterioration cannot simply be explained by the total tune shift; that is, the sum of the space charge and beam–beam tune shift. Moreover, a significant beam–beam effect is observed for bunches with a much smaller intensity, as can be seen in Fig. 4.

As a second example, we discuss the evolution of the total intensity of the Yellow beam at $E = 5.75\,\mathrm{GeV/n}$ while the Blue ring is being filled (Fig. 5). In this case, there is no transverse separation of the two beams during the injection process, so the injection of each individual Blue bunch results in a Yellow bunch starting to experience beam–beam collisions. As a result, the total Yellow beam lifetime slowly deteriorates the more bunches undergo collisions with the newly injected Blue bunches.

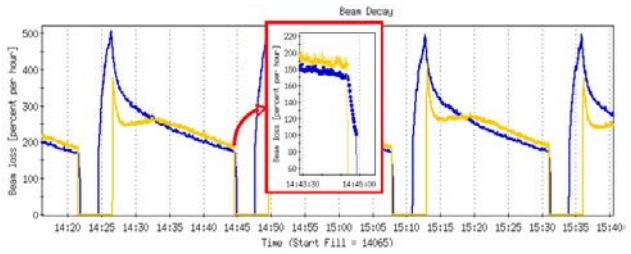

Figure 6: Beam decay rates during several Au beam stores at $5.75\,\mathrm{GeV/n}$ beam energy. The Blue beam decay rate improves dramatically as soon as the Yellow beam is dumped at the end of each store (see insert). Note that the algorithm to calculate the beam decay rate from the measured beam intensity has a time constant of 20 s. Hence, the actual drop in the instantaneous beam decay is even more dramatic than suggested in this picture.

Finally, we focus on the beam decay rate at the end of a Au store with $E = 5.75\,\mathrm{GeV/n}$ beam energy (Fig. 6). When the beam–beam force on the Blue beam disappears due to dumping of the oncoming Yellow beam, its decay rate improves dramatically.

Based on operational experience and the desire to improve beam lifetimes and therefore integrated luminosities in future RHIC low-energy runs, a dedicated beam experiment aimed at searching for a better working point was performed. Since the spacing of non-linear resonances is largest in the vicinity of the integer resonance, fractional tunes below 0.1 were proposed as the most promising candidates. These studies were performed at the regular RHIC injection energy of $9.8\,\mathrm{GeV/n}$, with a space charge tune shift of $\Delta Q_{\mathrm{sc}} = 0.03$ and a beam–beam tune-shift parameter of $\xi_{\mathrm{beam-beam}} = 0.002$.

As already observed during low-energy operations, the beam lifetime deteriorated substantially when the two beams were brought into collision at the regular RHIC working point of $(Q_x/Q_y) = (28.23/29.22)$ (Fig. 7). However, when the experiment was repeated at a near-integer working point of $(Q_x/Q_y) = (28.08/29.09)$ in Yellow and $(Q_x/Q_y) = (28.08/29.07)$ in Blue, there was no discernable effect on the Blue lifetime, while the Yellow lifetime still deteriorated somewhat when beams were brought into collision, as shown in Fig. 8.

The cause of the differing behaviour in the two rings is not yet understood. It may be attributable to parameters such as chromaticity, coupling control, or the different working point above the diagonal, which may have been less than optimal in the Yellow ring during the experiment. However, this result is very encouraging for future low-energy operations, although the space charge tune shift during this injection energy experiment was a factor of 2–3 smaller than at the lower energies.

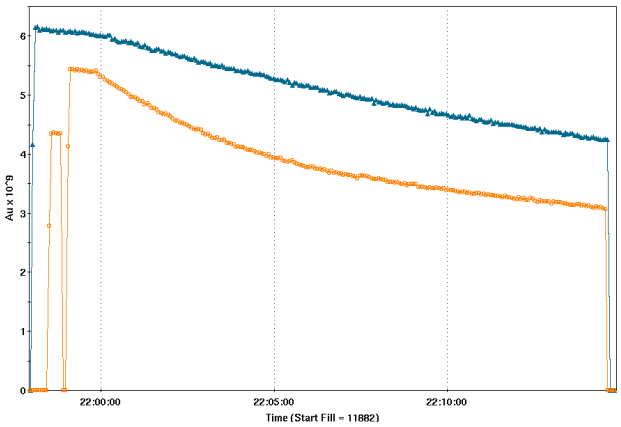

Figure 7: The beam intensities in the two RHIC rings during a beam experiment at regular injection energy ($E = 9.8\,\mathrm{GeV/n}$), at the regular RHIC heavy ion working point of $(Q_x/Q_y) = (28.23/29.22)$. The beams are brought into collision shortly after injection, resulting in significant decrease in the lifetime.

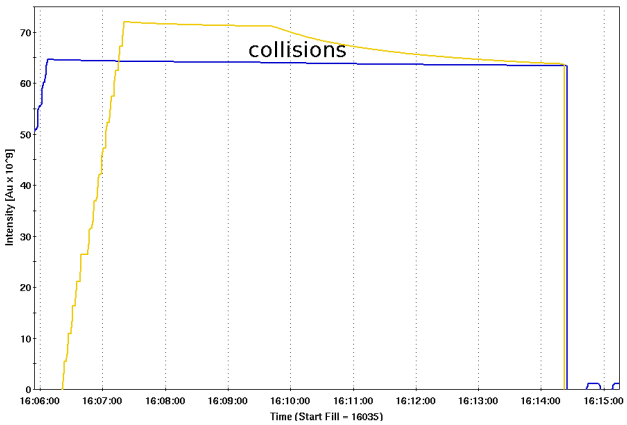

Figure 8: The beam intensities in the RHIC at $E = 9.8\,\mathrm{GeV/n}$, at a near-integer working point of $(Q_x/Q_y) = (28.08/29.09)$ in Yellow and $(Q_x/Q_y) = (28.08/29.07)$ in Blue. When beams are brought into collision, the lifetime of the Yellow beam suffers, while the Blue beam is unaffected.

SIMULATIONS

To investigate the root cause of the lifetime deterioration, we performed tracking simulations with a space charge tune shift of $\Delta Q_{\mathrm{sc}} = 0.06$ and a beam–beam parameter in each of the two RHIC interaction points of $\xi_{\mathrm{beam-beam}} = 0.003$. Using these parameters, tune scans as well as a frequency map analysis at a fixed working point were applied.

The Model

Space charge simulations are usually very CPU-time consuming because of frequent recalculations of the par-

ticle distribution and the associated electromagnetic fields. In the particular problem studied here, however, we can take advantage of the fact that the evolution of the particle distribution is comparatively slow. This is indicated by the beam lifetime of several minutes to tens of minutes. Typical simulations track particles only over a number of turns that corresponds to seconds of real time, so we can safely assume that the distribution of our test particles does not change appreciably over the course of the simulation. This approach, which is equivalent to the weak–strong simulation technique applied in numerical beam–beam studies, significantly speeds up the computation. In addition, no artificial noise is introduced into the simulation by the finite number of particles, since recalculation of the electromagnetic fields from the actual particle distribution is avoided. Instead, we assume that the distribution remains Gaussian during the entire simulation process. The r.m.s. width of this Gaussian distribution is calculated from the beam emittance and the local β function, including the dynamic β-beat introduced by the space charge and beam–beam forces around the machine. The accelerator model is based on the RHIC lattice as described in MAD. So far, no lattice non-linearities except the chromaticity correction sextupoles and the sextupole error in the main dipoles have been included. Particles are tracked element by element, and space charge kicks are applied at every quadrupole around the machine. Two beam–beam interaction points are included in IPs 6 and 8. Synchrotron oscillations are included, and the modulation of the space charge kick due to the resulting longitudinal position oscillations is taken into account.

Results

To study the emittance growth as a function of tune, we launch 1000 particles with a Gaussian distribution in all six phase space coordinates and track them over 20 000 turns. At the end of each turn i, we calculate the 4-D transverse emittance:

$$\epsilon(i) = \left| \begin{array}{cccc} \langle xx \rangle & \langle xx' \rangle & \langle xy \rangle & \langle xy' \rangle \\ \langle x'x \rangle & \langle x'x' \rangle & \langle x'y \rangle & \langle x'y' \rangle \\ \langle yx \rangle & \langle yx' \rangle & \langle yy \rangle & \langle yy' \rangle \\ \langle y'x \rangle & \langle y'x' \rangle & \langle y'y \rangle & \langle y'y' \rangle \end{array} \right|^{\frac{1}{4}}, \qquad (1)$$

where $\langle \cdots \rangle$ indicates the average over all particles. The emittance growth rate

$$\tau_\epsilon^{-1} = \frac{1}{\epsilon} \frac{\mathrm{d}\epsilon}{\mathrm{d}t} \qquad (2)$$

is then computed as a function of tune by a linear fit to this 4-D emittance evolution.

For the initial tune scan, depicted in Fig. 9, we varied the tunes in steps of $\Delta Q_{x,y} = 0.01$, with $Q_y = Q_x - 0.01$. In the absence of the beam–beam interaction, the 4-D emittance growth rate at fractional tunes below 0.2 is significantly lower than above, which qualitatively agrees with experimental observations. Once beam–beam interactions

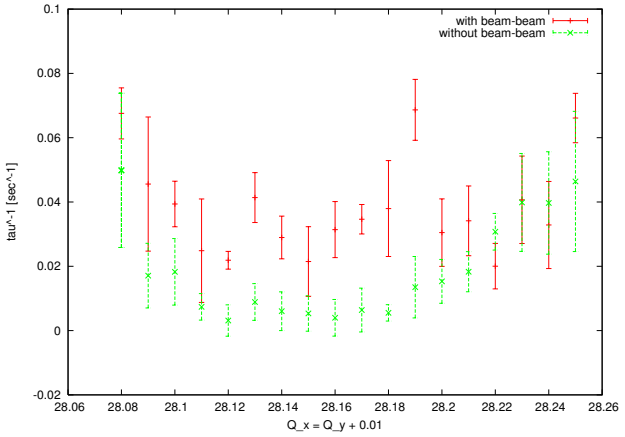

Figure 9: The 4-D emittance growth rate $\tau_\epsilon^{-1} = \frac{1}{\epsilon}\frac{\mathrm{d}\epsilon}{\mathrm{d}t}$ as a function of tune, with the working point (Q_x/Q_y) chosen such that $Q_y = Q_x - 0.01$.

are added, the emittance growth rate increases over most of the tune range; however, the resulting growth rate is, within error bars, independent of tune.

To determine the tune footprint and the tune diffusion frequency, map analysis [3, 4] was applied at a fixed working point of $(Q_x/Q_y) = (28.13/29.12)$ for the two cases with and without beam–beam interaction. For this purpose, we track a single test particle over 2^{14} turns and apply fast Fourier transforms to calculate the horizontal and vertical tunes $(Q_{x,1}/Q_{y,1})$ and $(Q_{x,2}/Q_{y,2})$ for the first and second 2^{13} turns. To increase the tune resolution, we apply an interpolation technique [5].

The tune diffusion is measured as

$$|\Delta Q| = \sqrt{|Q_{x,1} - Q_{x,2}|^2 + |Q_{y,1} - Q_{y,2}|^2}. \qquad (3)$$

The resulting tune footprint and tune diffusion is plotted in Fig. 10. While the tune footprint overlaps the coupling resonance $Q_x = Q_y$ with as well as without beam–beam interaction, the presence of the beam–beam force significantly enhances the tune diffusion around that resonance.

Plotting the same data in the amplitude space (Fig. 11) reveals that this enhanced tune diffusion occurs for amplitudes (A_x, A_y) in the region $\sigma_x < A_x < 2\sigma_x$ and $2\sigma_y < A_y < 4\sigma_y$.

As shown above, the largest tune diffusion occurs around the coupling resonance. This behaviour suggests that it might be beneficial to increase the tune split between the two planes, thus selecting a working point further away from the coupling resonance. To study this hypothesis, we performed a tune scan with $Q_y = Q_x - 0.02$ and determined the 4-D emittance growth rates. As shown in Fig. 12, the effect of the beam–beam interaction on the emittance growth rate is significantly reduced.

This observation is supported by the results of a frequency map analysis for the working point $(Q_x/Q_y) =$

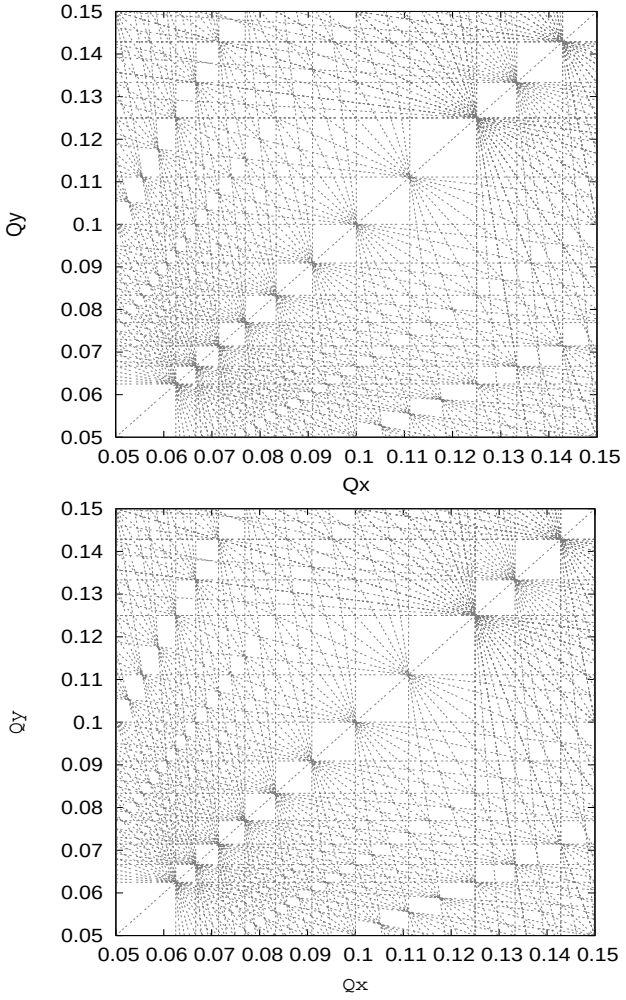

Figure 10: Tune footprints at a nominal working point of $(Q_x/Q_y) = (28.13/29.12)$, without (top) and with (bottom) beam–beam interaction.

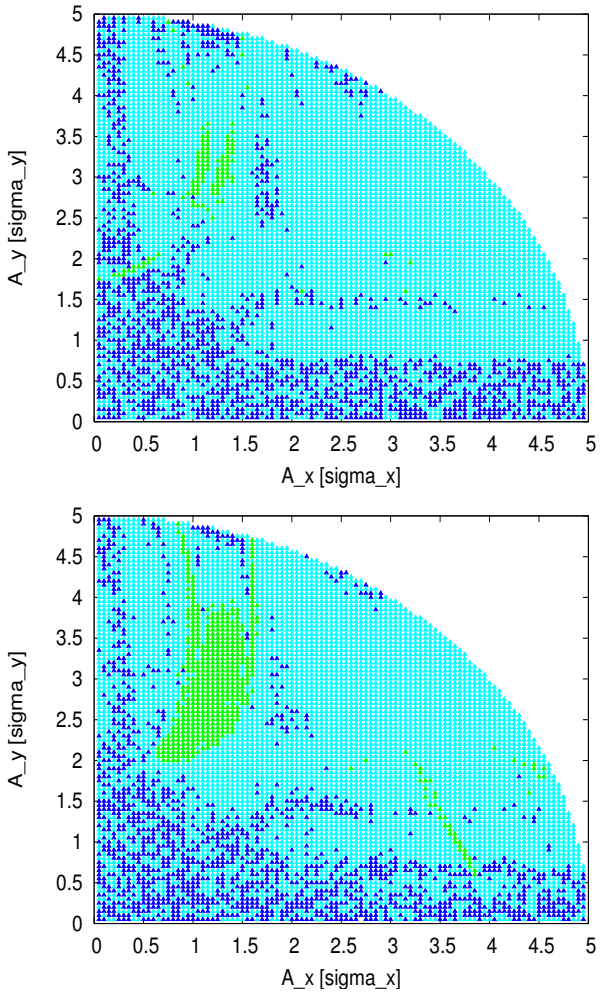

Figure 11: Tune diffusion in the amplitude space, as obtained from the frequency map analysis at a nominal working point of $(Q_x/Q_y) = (28.13/29.12)$, without (top) and with (bottom) beam–beam interaction.

$(28.14/29.12)$ (Figs. 13 and 14), which shows little effect of the beam–beam interaction on tune diffusion.

While this result is certainly very encouraging in terms of improving the machine performance, it is worthwhile repeating that our model so far does not include any magnet non-linearities beyond sextupoles, which may lead to increased tune diffusion around the associated non-linear resonances in the presence of the beam–beam interaction.

SUMMARY

We have studied the effects of beam–beam interactions in colliding beams with large direct space charge parameters up to $\Delta Q_{\rm sc} = 0.1$ both experimentally and through simulations. During RHIC low-energy operations as well as dedicated experiments, we have consistently observed a strong effect of the beam–beam interaction on the lifetime of the stored beam, although the associated beam–beam parameter was about an order of magnitude smaller than the

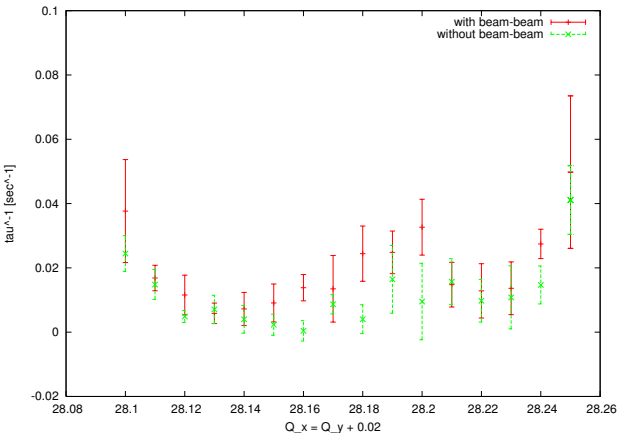

Figure 12: The 4-D emittance growth rate $\tau_\epsilon^-1 = \frac{1}{\epsilon}\frac{\mathrm{d}\epsilon}{\mathrm{d}t}$ as a function of tune, with the working point (Q_x/Q_y) chosen at an increased tune split with $Q_y = Q_x - 0.02$.

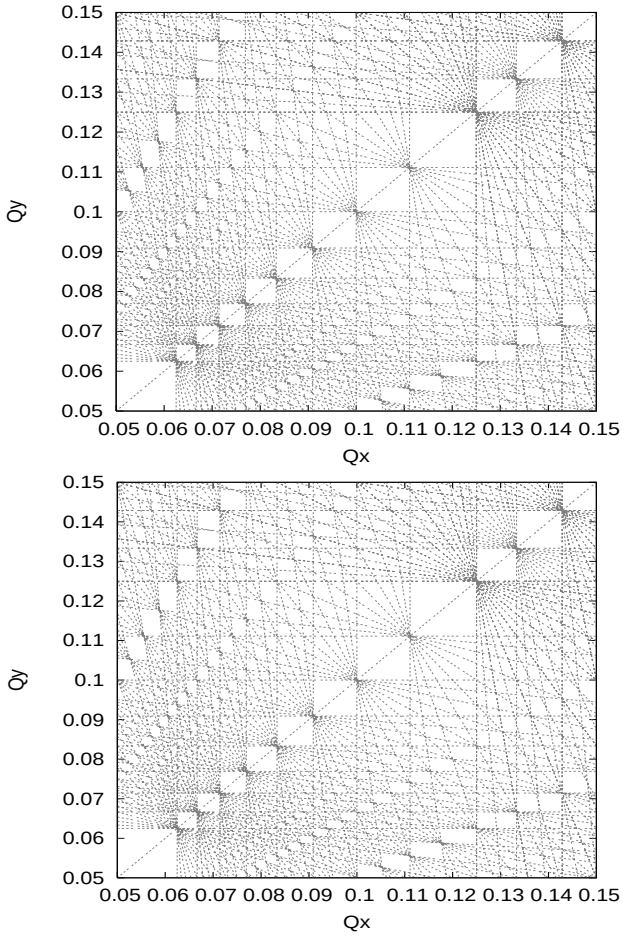

Figure 13: Tune footprints at a nominal working point with an increased tune split between the two planes, $(Q_x/Q_y) = (28.14/29.12)$, without (top) and with (bottom) beam–beam interaction.

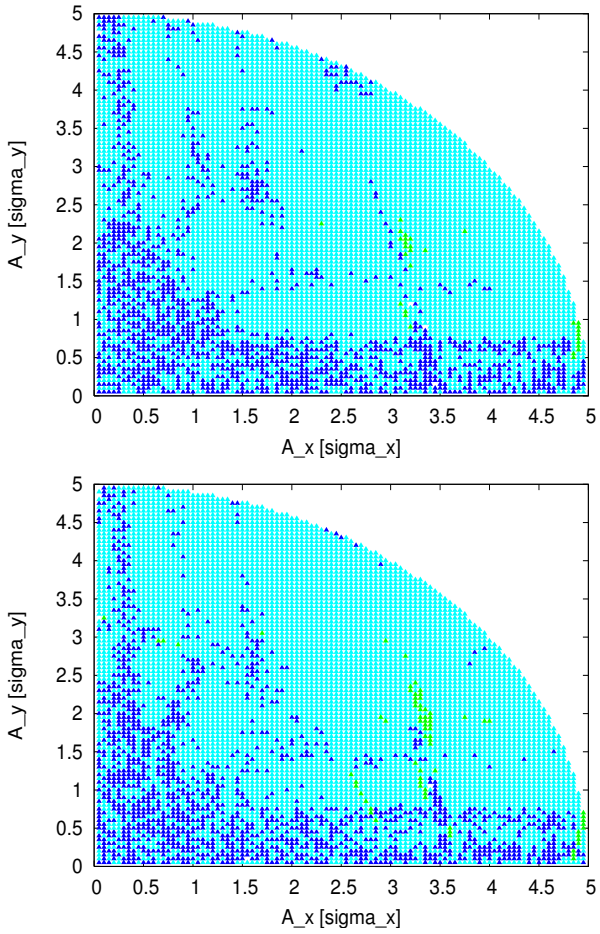

Figure 14: Tune diffusion in the amplitude space, as obtained from the frequency map analysis at a nominal working point with an increased tune split between the two planes, $(Q_x/Q_y) = (28.14/29.12)$, without (top) and with (bottom) beam–beam interaction.

space charge tune shift.

To provide the maximum tune space between non-linear resonances, we have operated the RHIC at a near-integer working point. In this case, we observed no discernable lifetime reduction in the Blue ring, while Yellow still suffered. The root cause of this difference between the two rings is still unknown, and may be related to parameters such as chromaticity and coupling control, or the particular working point during the experiment. However, this result is very encouraging for future low-energy runs, although the corresponding space charge tune shift of $\Delta Q_{\rm sc} = 0.03$ was comparably modest.

Although a quantitative comparison of our simulation results with experimental observations in the RHIC is difficult due to the lack of effects such as intra-beam scattering in the simulation code, the tracking model presented here qualitatively reproduces the main experimental result, namely the strong effect of the beam–beam interaction in the presence of a large space charge tune shift. Based on these simulation results, an alternative working point further away from the coupling resonance $Q_x = Q_y$, which appears to be the main source of emittance growth in our simulations, may be beneficial. However, it is of utmost importance to repeat these simulations after higher-order multipole errors have been added to the tracking model, which may lead to a further reduction of the usable tune space.

REFERENCES

[1] A. Fedotov et al., "Beam Lifetime and Limitations during Low-Energy RHIC Operation," Proc. PAC'11.

[2] A. Fedotov et al., "Interplay of Space Charge and Beam–Beam Effects in a Collider," Proc. HB2010 (Morschach, Switzerland, 2010), p. 634.

[3] J. Laskar, Physica D 67 (1993) 257.

[4] J. Laskar and D. Robin, Part. Accel. 54 (1996) 183.

[5] A. Bazzani et al., Part. Accel. 147 (1996) 147.

Published by CERN in the Proceedings of the ICFA Mini-Workshop on Beam–Beam Effects in Hadron Colliders,
CERN, Geneva, Switzerland, 18–22 March 2013, edited by W. Herr and G. Papotti, CERN–2014–004 (CERN, Geneva, 2014)

BEAM-BEAM EFFECTS UNDER THE INFLUENCE OF EXTERNAL NOISE

K. Ohmi, KEK, Oho, Tsukuba, 305-0801, Japan

Abstract

Fast external noise, which gives fluctuation into the beam orbit, is discussed in connection with beam–beam effects. Phase noise from crab cavities and detection devices (position monitor) and kicker noise from the bunch by bunch feedback system are the sources. Beam-beam collisions with fast orbit fluctuations with turn by turn or multi-turn correlations, cause emittance growth and luminosity degradation. We discuss the tolerance of the noise amplitude for LHC and HL-LHC.

INTRODUCTION

Beam-beam effects under external noise are studied with the weak-strong model in this paper. The strong beam is regarded as a target with a Gaussian charge distribution. In the model, an external noise is introduced into the transverse position of the strong beam at the collision point.

We first discuss an orbit (transverse position) shift of the strong beam given as:

$$\Delta x_{i+1} = (1 - 1/\tau)\Delta x_i + \delta x \cdot \hat{r} \tag{1}$$

where Δx_i is the orbit shift at the ith turn. τ, δx and $\hat{r}$ are the damping times, a constant characterizing the random fluctuation amplitude and a Gaussian random number with unit standard deviation. This is known as the Ornstein-Uhlenbeck process. This type of noise is referred to as first type later.

All particles in the weak beam experience the fluctuation of the strong beam, thus a transverse collective motion is induced. The collective motion results in an emittance growth due to filamentation caused by the nonlinear beam–beam force.

The stable amplitude of the fluctuation of the strong beam is given by:

$$\Delta x^2 = \langle \Delta x^2_{n\to\infty} \rangle = \frac{\tau \delta x^2}{2}. \tag{2}$$

The correlation function between ith and i^{n-th} turns is expressed by the damping time as:

$$\langle \Delta x_\ell \Delta x_{\ell+n} \rangle = \Delta x^2 e^{-|n|/\tau}. \tag{3}$$

The damping time is regarded as the correlation time of the fluctuation. For white noise, which corresponds to $\tau = 1$, the correlation function is expressed as:

$$\langle \Delta x_\ell \Delta x_{\ell+n} \rangle = \Delta x^2 \delta_{n0} \tag{4}$$

where δ_{n0} is the Kronecker delta.

The beam oscillates with the betatron frequency. We consider a second type of noise as:

$$\Delta x_{i+1} = (1 - 1/\tau)(\Delta x_i \cos\mu_o + \Delta p_i \sin\mu_o) + \delta x \hat{r} \tag{5}$$

$$\Delta p_{i+1} = (1 - 1/\tau)(-\Delta x_i \sin\mu_o + \Delta p_i \cos\mu_o) + \delta x \hat{r} \tag{6}$$

where x and p are the coordinate and canonical momentum normalized by the beta function, so that $J = (x^2 + p^2)/2$. $\mu_o = 2\pi\nu_o$ is the betatron tune multiplied by 2π. In collision the offset causes an emittance growth. The stable dipole oscillation amplitude is expressed by the same equation as Eq. (2). The correlation function contains the betatron tune as:

$$\langle \Delta x_\ell \Delta x_{\ell+n} \rangle = \Delta x^2 e^{-|n|/\tau} \cos n\mu_o. \tag{7}$$

We discuss the effect of noise for the cases of the LHC and High Luminosity-LHC. The parameters are listed in Table 1. The phenomena depend on the beam–beam parameter, the noise amplitude normalized by the beam size and the Piwinski angle.

EMITTANCE GROWTH DUE TO THE EXTERNAL NOISE

The emittance growth under an external noise and the non-linear force of the beam–beam interaction is discussed in [1, 2, 3]. Previous work is reviewed in this section.

The beam–beam potential for a bunch population N_p and the transverse size σ_r is expressed as:

$$U(x) = \frac{N_p r_p}{\gamma_p} \int_0^\infty \frac{1 - e^{-x^2/(2\sigma_r^2+q)}}{2\sigma_r^2 + q} dq \tag{8}$$

where r_p and γ_p are the classical radius of the proton and the relativistic factor of the (weak) beam, respectively. The potential is expanded as a Fourier series:

$$U(x) = \frac{N_p r_P}{\gamma_p} \sum_{k=0}^{\infty} U_k(a) \cos 2k\psi \tag{9}$$

where

$$U_k(a) = \int_0^a \left[\delta_{0k} - (2 - \delta_{0k})(-1)^k e^{-w} I_k(w)\right] \frac{dw}{w}, \tag{10}$$

and $a = \beta^* J/2\sigma_r^2 = J/2\varepsilon$. The change of J per revolution is given by the derivative of the beam–beam potential with respect to ψ as:

$$\Delta J = -\frac{\partial U}{\partial \psi} = \frac{N r_p}{\gamma} \sum_{k=0}^{\infty} 2k U_k \sin 2k\psi. \tag{11}$$

978-92-9083-404-5, 0007-8328 –
http://dx.doi.org/10.5170/CERN–2014–004.69

Table 1: Parameters for LHC (50 ns bunch spacing) and HL-LHC (25 ns bunch spacing).

	LHC	HL-LHC(25ns)	HL-LHC(50ns)
Circumference (m)		26 658	
Energy (TeV)		7	
Tunes Q_x, Q_y, Q_s		64.31, 59.32, 0.0019	
Normalized Emittance (μm)	2.0	2.5	3.0
β^* (m)	0.55	0.15	0.15
Bunch length (m)		0.0755	
Bunch population (10^{11})	1.65	2.2	3.5
Number of bunches	1380	2808	1404
Beam-beam parameter/IP	0.0034	0.005-0.011	0.005-0.014

This change, which indicates a stable sinusoidal modulation of the betatron amplitude, does not induce emittance growth.

We consider the case in which the strong beam has a small offset (Δx). The beam–beam potential with the offset is expanded for Δx:

$$U(x+\Delta x) = U(x) + U'(x)\Delta x. \tag{12}$$

Here Δx is a random variable fluctuating described by Eq. (1) or (6).

The potential with the offset is expanded as a Fourier series:

$$U'(J,\psi) = \frac{\partial U}{\partial J}\frac{\partial J}{\partial x} + \frac{\partial U}{\partial \psi}\frac{\partial \psi}{\partial x} \tag{13}$$

$$= \frac{N_p r_p}{2\gamma\sigma_r}\sum_{k=0}^{\infty} G_k(a)\cos(2k+1)\psi. \tag{14}$$

The Fourier coefficients as a function of a are expressed as:

$$G_k(a) = \sqrt{a}\left[U'_{k+1} + U'_k\right] + \frac{1}{\sqrt{a}}\left[(k+1)U_{k+1} - kU_k\right]. \tag{15}$$

where U'_k is the derivative with respect to a.

The diffusion of J^2 after N revolutions is given by:

$$\langle \Delta J^2(N)\rangle = \sum_{\ell=1}^{N}\sum_{n=-\ell+1}^{N-\ell}\frac{\partial U'(\ell)}{\partial\psi}\frac{\partial U'(\ell+n)}{\partial\psi}\langle \Delta x_\ell \Delta x_{\ell+n}\rangle \tag{16}$$

For turn-by-turn white noise, the correlation function is replaced by the Kronecker delta, δ_{n0}. The diffusion of J is expressed by:

$$\langle \Delta J^2\rangle = \frac{\langle \Delta J^2(N)\rangle}{N} \approx \frac{N_p^2 r_p^2}{8\gamma^2\sigma_r^2}\sum_{k=0}^{\infty}(2k+1)^2 G_k(a)^2. \tag{17}$$

The diffusion of J per revolution is given for the fluctuation in Eq. (1) by:

$$\langle \Delta J^2\rangle \approx \frac{N_p^2 r_p^2}{8\gamma^2\sigma_r^2}$$

$$\sum_{n=-\infty}^{\infty}\sum_{k=0}^{\infty}(2k+1)^2 G_k^2\cos[(2k+1)n\mu_o]e^{-|n|/\tau}$$

$$\approx \frac{N_p^2 r_p^2}{8\gamma^2\sigma_r^2}\sum_{k=0}^{\infty}\frac{(2k+1)^2 G_k(a)^2\sinh 1/\tau}{\cosh 1/\tau - \cos(2k+1)\mu_o}. \tag{18}$$

The diffusion of J for the second type of noise (Eq. (6)) is given using the correlation of Eq. (7):

$$\langle \Delta J^2\rangle \approx \frac{N_p^2 r_p^2}{16\gamma^2\sigma_r^2}\sum_{k=0}^{\infty}(2k+1)^2 G_k(a)^2\sinh 1/\tau$$

$$\left[\frac{1}{\cosh 1/\tau - \cos(2k\mu - \delta\mu)} + \right. \tag{19}$$

$$\left.\frac{1}{\cosh 1/\tau - \cos(2(k+1)\mu + \delta\mu)}\right]$$

where $\delta\mu$ is the tune difference between the weak and strong beam oscillations ($\delta\mu = \mu - \mu_o$).

Figure 1 shows the diffusion rate of J as a function of J. The diffusion rate is proportional to the square of the fluctuation amplitude Δx and the square of the beam–beam parameter $\propto N_p$. The rate is normalized by the factor $C = (N_p r_p \Delta x/\gamma\sigma_r)^2/8$ in the figure.

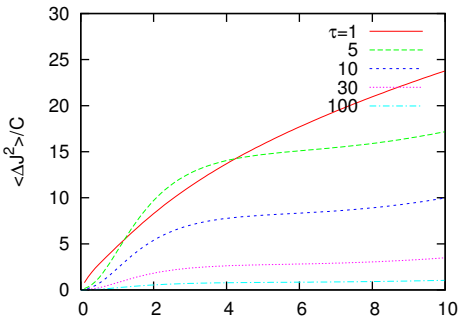

Figure 1: Diffusion rate given by Eq. (18). The rate is normalized by $C = (N_p r_p \Delta x/\gamma\sigma_r)^2/8$.

The emittance growth is evaluated from the diffusion rate, when the rate $\langle \Delta J^2\rangle$ is proportional to J.

$$\frac{\Delta\varepsilon}{\varepsilon} = \frac{\langle \Delta J^2\rangle}{2\varepsilon J} = \frac{1}{4\varepsilon^2}\frac{d\langle \Delta J^2\rangle}{da}. \tag{20}$$

Figure 1 shows that the rate is proportional to J for small $J/2\varepsilon < 2$. The slope of $\langle \Delta J^2 \rangle$ for turn-by-turn noise ($\tau = 1$) is:

$$\frac{\langle \Delta J^2 \rangle}{a} = \frac{N_p^2 r_p^2}{8\gamma^2} \frac{\Delta x^2}{\sigma_r^2} \times 4.4. \quad (21)$$

The luminosity degradation rate per collision is estimated by the emittance growth rate as:

$$\Delta L/L = \left(\xi \frac{\Delta x}{\sigma_r} \right)^2 \times 21.7. \quad (22)$$

For two IPs, the formula is corrected by a factor two, i.e. $21.7 \to 10.8$ and $\xi \to \xi_{tot}$, The tolerance for the noise amplitude is given for a luminosity life time $\Delta L/L = 10^{-9}$:

$$\xi_{tot} \frac{\Delta x}{\sigma_r} = 9.8 \times 10^{-6}. \quad (23)$$

We now discuss the second type of noise given by Eq. (6). Figure 2 shows the diffusion rates. Figures 2 (a) and (b) are given for the beam-orbit oscillation with the same tune ($\delta\mu = 0$) and a difference of $\delta\mu = \xi = 0.01$, respectively. A strong enhancement of the diffusion is seen at small amplitudes at a large correlation time in shown in Fig. 2 (a). This behavior mainly comes from a contribution at $k = 0$.

$$\langle \Delta J^2 \rangle \approx \frac{N_p^2 r_p^2}{16\gamma^2 \sigma_r^2} G_0(a)^2 \tau \quad (24)$$

The strong beam modulation with the same tune gives an external force oscillation to the weak beam particles. For colliding beams, the assumption, that beam-orbit oscillations have the same tune, is not obvious. The diffusion rate for $\delta\mu = \xi$ in Fig. 2 (b) may be better to represent the beam–beam system. The diffusion rate, which is saturated at $J/2\varepsilon = 1$, is similar as that of $\tau = 1$ on the whole. Therefore we study the diffusion rate for $\tau = 1$ in simulations.

It may be better that the noise effects are studied in the framework of a strong-strong model, especially for the second type of noise. The noise induces either coherent σ or π modes or a continuous frequency spectrum. The σ mode does not contribute the emittance growth. Emittance growth based on the strong-strong model had been discussed in [3]. The author discussed that 18% of the dipole motion induced by offset collision into the mode with continuous frequency spectrum. The emittance increases by smearing the dipole motion. The growth rate is expressed by:

$$\frac{\delta\varepsilon}{\varepsilon} \approx \frac{K}{\left(1 + \frac{1}{2\pi\tau|\xi|}\right)^2} \frac{\delta x^2}{\sigma_x^2} = \frac{2K}{\tau \left(1 + \frac{1}{2\pi\tau|\xi|}\right)^2} \frac{\Delta x^2}{\sigma_x^2} \quad (25)$$

where $K = 0.089$ is a form factor for the emittance change induced by a dipole amplitude, and the damping rate $1/\tau$ of the coherent motion. The emittance growth rate is independent of the beam–beam tune shift, when $1/\tau \ll 2\pi|\xi|$, while the rate is proportional to the square of the beam–beam tune shift, when $1/\tau \gg 2\pi|\xi|$.

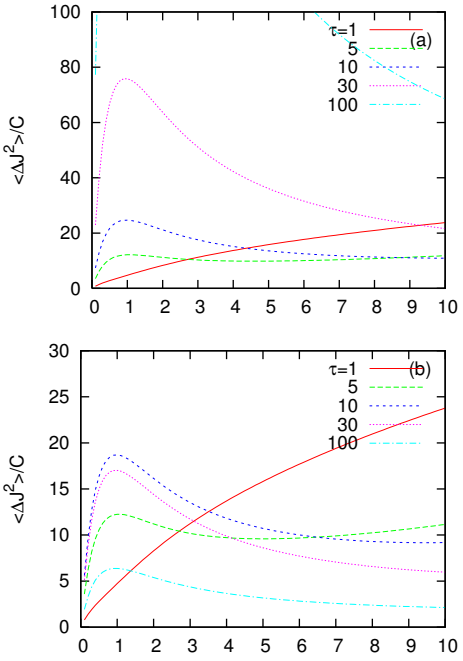

Figure 2: Diffusion rate given by Eq. (19). The rate is normalized by $C = (N_p r_p \Delta x/\gamma\sigma_r)^2/8$.

Figure 3 shows the emittance growth given by Eq. (25) and by a strong-strong beam–beam simulation [4], where the beam–beam tune shift is $\xi = 0.0034/IP$. The results agree fairly well. The strong-strong simulation suffers from numerical noise related to the statistics of macro-particles. One million macro-particles are used in the simulation, thus 0.1% of the offset noise is induced by the statistics.

SIMULATION OF EXTERNAL NOISE

Study based on LHC

The analytical theory is based on the near solvable system far from resonances. There is no such limitation in beam–beam simulations, while simulations take considerable computing time to evaluate a slow emittance growth. Simulations considering external noise are straightforward: a modulation is applied to the strong beam with Eq. (1) or (6). Effects of resonances, longitudinal motion and a crossing angle are taken into account in simulations.

We only discuss weak-strong simulations taking into account external noise. The weak beam is represented by 131072 macro-particles. The particles are tracked one million turns interacting a strong beam located at two interaction points. The luminosity is calculated turn-by-turn, and averaged every 100 turns. Luminosity degradation is evaluated by fitting its evolution.

Figure 4 shows the luminosity degradation for collisions without a crossing angle. The degradation is plotted as a

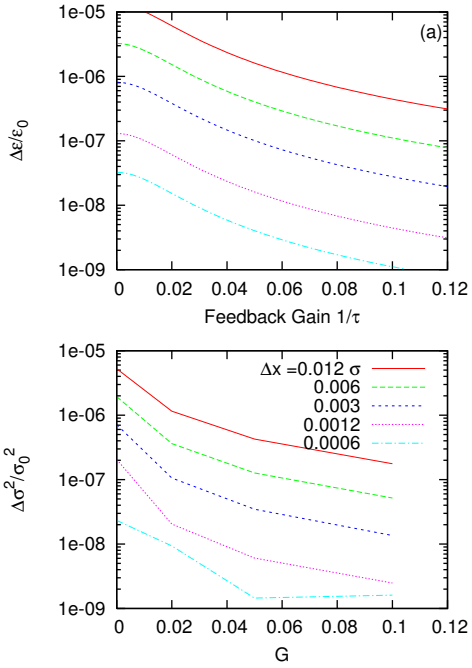

Figure 3: Emittance growth given by Eq. (25) and by a strong-strong beam–beam simulation [4].

function of the fluctuation amplitude for three total beam–beam parameters, $\xi_{tot} = 0.02$, 0.04 and 0.05. Three lines given by the analytical formula Eq. (23) are shown in the figure. The simulation results agree with the formula fairly well.

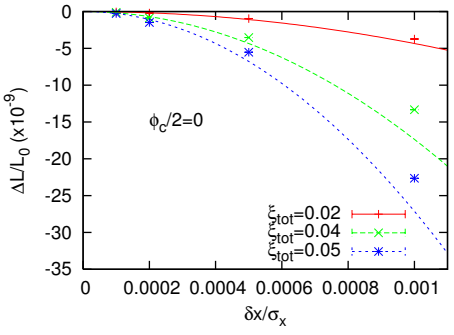

Figure 4: Diffusion rate given by a weak-strong simulation using Eq. (23).

The luminosity degradation for collision with a crossing angle ($\phi_c = 290$ μrad) is shown in Fig. 5. The Piwinski angle is $\phi_c \sigma_z / 2\sigma_r = 0.89$.

Figure 6 shows luminosity degradation as a function of the beam–beam parameter under offset noise. The tune shift is reduced to 70% for the crossing collision. The luminosity degradation for noise is independent of the crossing angle. At high beam–beam parameters > 0.05, the luminosity degradation due to the crossing angle is dominant.

There was no qualitative change for collision without a

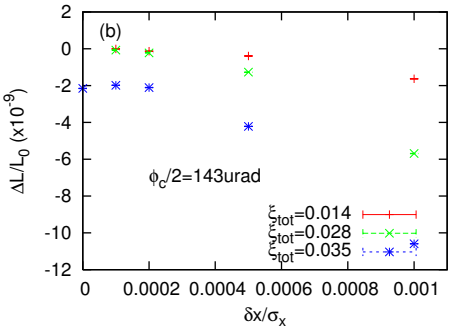

Figure 5: Diffusion rate for crossing collision given by weak-strong simulation.

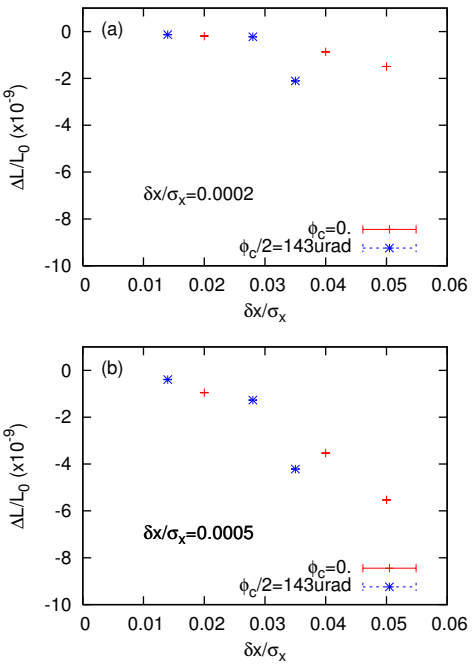

Figure 6: Luminosity degradation as a function of the beam–beam parameter with offset noise.

crossing angle. For $\xi_{tot} = 0.035$, a degradation due to the crossing angle is seen, but a significant cross-talk is not observed. The degradation of the luminosity due to the fluctuation depends on ξ_{tot}, but hardly on the presence of the crossing angle.

High Luminosity LHC (HL-LHC)

For the HL-LHC, a higher luminosity is the target and obtained by increasing the bunch population and squeezing to smaller beta function, while the pile up of collision events sets an upper limit for the luminosity at $L/coll = 2.6 \times 10^{31}$ cm^{-2}s^{-1}. The luminosity at $\beta = 0.15$ m is expected to be $L/coll = 8.6$ or 18×10^{31} cm^{-2}s^{-1} for the bunch population of 2.2 or 3.5×10^{11}, respectively. Therefore luminosity levelling keeping the luminosity constant at $L/coll = 2.6 \times 10^{31}$ cm^{-2}s^{-1} is proposed. The level-

ling can be done by controlling the crab cavity voltage or the beta function at the interaction point (IP). Leveling with the beta function, the total beam–beam parameter (2IP) is $0.011\times2 = 0.022$ (25ns) or $0.014\times2 = 0.028$ (50ns) at the early stage of the collision, where the beta function is 0.49 m or 1.02 m. The results given in the previous subsection are applied for the parameters:

$$\frac{\Delta x}{\sigma_r} = 4.5\times10^{-4} \text{ or } 3.5\times10^{-4}. \quad (26)$$

for 25 ns and 50 ns, respectively.

Using a levelling with crab cavities, the crab voltage increases to keep the luminosity constant while the beam current decreases. At the early stage of collision, the crab voltage is low and two beams collide with a large Piwinski angle, where $\phi_c\sigma_z/2\sigma_r = 3.14$ or 2.87 for 25 ns or 50 ns, respectively. We study the effects of noise for collisions with a large Piwinski angle.

Figure 7 shows the luminosity degradation rate as a function of the offset amplitude. The simulation is performed for two IPs. The tune shift is 0.0015 or 0.0050 in the crossing or orthogonal plane for the design bunch population of $N_p = 2.2\times10^{11}$ (25ns). The tune shift is 0.0065 in both planes, due to the combination of the horizontal and vertical crossing. The fluctuation amplitude 0.2% is a tolerable limit for $\Delta L/L_0 = 10^{-9}$ as shown in the figure. The simple formula Eq. (23) is satisfied for the HL-LHC, $0.0065\times0.002 = 1.3\times10^{-5}$, with 30% difference from the formula.

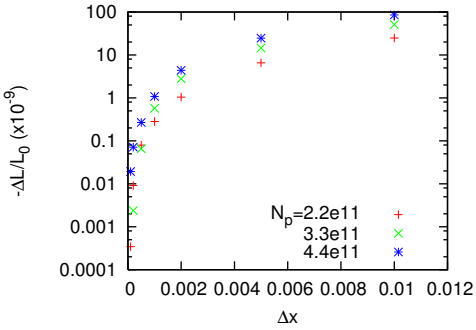

Figure 7: Luminosity degradation as a function of noise amplitude.

Figure 8 shows the luminosity degradation as a function of the correlation time. The luminosity degradation, which scales as $1/\tau$, is consistent with Eq. (18).

The effect of noise on its amplitude and the dependence on the correlation time is similar for collisions with a large Piwinski angle and those for ordinary collisions without a crossing angle. The luminosity degradation depends on the beam–beam parameter and the noise amplitude, but with little dependence on the Piwinski angle.

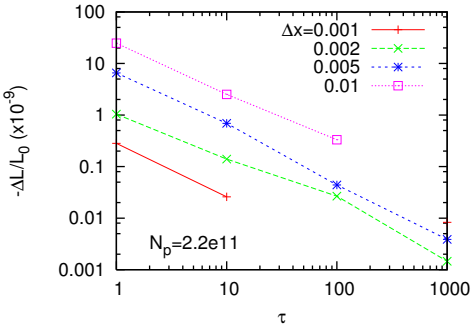

Figure 8: Luminosity degradation as a function of the correlation time.

Tolerance for crab cavity phase noise in HL-LHC

Crab cavities are used to compensate the crossing angle ($\phi_c = 590$ μrad) at IP. The relation of the phase noise and collision offset is given by

$$\Delta\varphi_{cc} = \frac{\omega_{cc}}{c\phi_c/2}\Delta x, \quad (27)$$

where $\Delta\varphi_{cc}$ and ω_{cc} are the phase fluctuation and frequency of the crab cavity.

Using beta function levelling the beam–beam parameter is very high, $\xi_{tot} = 0.022$ or 0.028 for 25 ns or 50 ns, respectively. The tolerance of the noise amplitude is given by Eq. (26). The corresponding phase error is $\Delta\varphi = 1.6\times10^{-4}$ or 2.3×10^{-4} rad.

For the crab cavity levelling, the beam–beam parameter is $\xi_{tot} = 0.0065$. The tolerance of the noise amplitude is $\Delta x/\sigma_r = 0.002$ and the corresponding phase error is $\Delta\varphi = 4\times10^{-3}$, where the crab angle is 10% of the crossing angle $\phi_c = 59$ μrad ($L/coll = 2.7\times10^{31}$ cm^{-2}s^{-1}).

The crab cavity noise was measured at KEKB, 1.7×10^{-4} rad for frequencies above 1 kHz ($\tau < 10$). The value is critical for beta function levelling, because of the large beam–beam parameter. Using four crab cavities, the noise tolerance is twice as large, while for the crab voltage levelling, the measured phase error is tolerable.

Incoherent noise due to intra-beam scattering

Emittance growth times due to intra-beam scattering (IBS) are 105 h and 63 h for the horizontal and longitudinal planes, respectively, in the nominal LHC [13]. The transverse emittance and bunch population in the nominal are 5.0×10^{-10} and 1.15×10^{11}, respectively. The horizontal IBS growth rate is approximately proportional to the particle density in the six dimensional phase space. The growth time is 40 h for ξ_{tot} = 0.02 in this paper ($\varepsilon = 2.7\times10^{-10}$ and $Np = 1.63\times10^{11}$). The fluctuation is $\delta x/\sigma_x = 5.5\times10^{-5}$ for ξ_{tot} = 0.05. The luminosity degradation is determined by geometrical emittance growth $\delta L/L_0 = \delta x^2/\sigma_x^2$ for incoherent noise.

COHERENT BEAM–BEAM EFFECTS UNDER EXTERNAL NOISE

Effects of external noise in crab cavity were performed in KEKB during 2008 and 2009 [6]. Sinusoidal noise is applied to the crab cavity RF system. Near the σ mode tune, a strong luminosity drop of 80 % was seen when suddenly exceeding a threshold excitation amplitude. A smaller luminosity drop ($L = 0.9L_0$) was seen near π mode frequency. Strong-strong simulations reproduced these luminosity drops. A systematic study using the strong-strong simulation showed that these characteristic phenomena for coherent nonlinear beam–beam interactions. A similar phenomenon was observed in Ref.[7]. The detailed analysis is published in Ref.[6].

CONCLUSIONS

Fast noise of the collision offset degrades the luminosity performance in hadron colliders. The luminosity degradation depends on the product of the noise amplitude and the beam–beam parameter as shown in Eq. (23), with little dependence on the crossing angle. A tolerance for the crab cavity phase error was obtained for the HL-LHC.

The crab cavity noise was measured at KEKB, 1.7×10^{-4} rad above 1 kHz ($\tau < 10$). The value is critical for beta function levelling, because of the high beam–beam parameter. For the crab voltage levelling, the measured phase error is tolerable because of the small beam–beam tune shift.

Further studies related to beam–beam modes should be done using strong-strong models.

ACKNOWLEDGEMENT

The author would like to thank Drs. Y. Alexahin, R. Calaga, W. Herr, S. Paret, T. Pieloni, J. Qiang, R. Tomas and F. Zimmermann for fruitful discussions.

REFERENCES

[1] G. Stupakov, SSCL-560 (1991).

[2] T. Sen and J.A. Ellison, Phys. Rev. Lett. **77**, (1996) 1051.

[3] Y. Alexahin, Nucl. Instr. Methods in Phys. Res. **A391**, (1996) 73.

[4] K. Ohmi *et al.*, "Beam-beam effect with an external noise in LHC", Proc. Particle Accelerator Conference, Albuquerque, June, 2007, (2007) p. 1496; http://www.JACoW.org. K. Ohmi *et al.*, CERN-LHC-PROJECT-REPORT-1048.

[5] LHC Design Report, CERN-2004-003-V-1; http://lhc.web.cern.ch/lhc/lhc-designreport.html.

[6] K. Ohmi *et al.*,Phys. Rev. ST-AB, 14, 111003 (2011).

[7] T. Ieiri and K. Hirata, Proc. Particle Accelerator Conference, March, 1989, Chicago, USA.

Published by CERN in the Proceedings of the ICFA Mini-Workshop on Beam–Beam Effects in Hadron Colliders,
CERN, Geneva, Switzerland, 18–22 March 2013, edited by W. Herr and G. Papotti, CERN–2014–004 (CERN, Geneva, 2014)

BEAM–BEAM EFFECTS IN THE HIGH-PILE-UP TESTS OF THE LHC

G. Trad, CERN, Geneva, Switzerland

Abstract

Investigating the beam–beam limit in the LHC is of great importance, since identifying its source is crucial for the luminosity optimization scenario. Several experiments were carried out to search for this limit and check whether it is dominated by the head-on (HO) or the long-range (LR) interactions. In this paper only the HO collision effects will be considered, tracking the evolution of the maximum tune shift achieved during the dedicated machine developments and the special high pile-up fills.

INTRODUCTION

Contrarily to electron machines, hadron machines are mostly limited by non-linear effects and lifetime problems, in particular for beams with high intensities [1]. The limitation appears as a slow emittance increase (over hours) or beam losses (tails and dynamic aperture), bad lifetime or other effects such as coherent beam–beam oscillations.

It is important to note that the head-on (HO) tune shift depends only on the bunch intensity and the normalized emittance, i.e. is independent of the beta function at the interaction point β^* and the energy as shown in Eq. (1). For the long-range (LR) interactions, the tune shift depends on the beam separation $d_{\rm sep}$, thus on the crossing angle α and the beam energy γ, as shown in Eq. (3).

$$\Delta Q_{\rm HO} \propto \frac{N}{\varepsilon_n}, \tag{1}$$

$$L \propto \frac{N^2}{\varepsilon_n} = \Delta Q_{\rm HO} \cdot N, \tag{2}$$

$$\Delta Q_{\rm LR} \propto \frac{N}{d_{\rm sep}^2} = \frac{N \cdot \varepsilon_n}{\alpha^2 \cdot \beta^* \cdot \gamma}. \tag{3}$$

Therefore, identifying the source of these limits has vital significance for the luminosity optimization strategy: if the HO collisions are dominating the beam–beam limit, it is then advantageous to increase the bunch intensity together with the transverse emittance since this would keep the tune shift unaffected and increases the luminosity proportionally to the intensity (see Eq. (2)). The luminosity is further increased by pushing more the focusing at the interaction point (IP) without affecting the beam–beam parameter ξ:

$$\xi_{21x,y} = \frac{N_1 r_p}{2\pi\sqrt{\varepsilon_{x,y_{n1}}}\left(\sqrt{\varepsilon_{x,y_{n1}}} + \sqrt{\varepsilon_{y,x_{n1}}}\right)}. \tag{4}$$

On the other hand, when the machine is limited by the LR interactions, a large number of bunches with a moderate β^* is preferred. Since ΔQ_{LR} depends on β^*, any change of the optical function at the IP requires one to adjust the crossing angle α to keep the LR tune shift constant,

$$\alpha \propto \sqrt{\frac{N \cdot \varepsilon_n}{\Delta Q_{\rm max} \cdot \beta^* \cdot \gamma}}. \tag{5}$$

Some confusion is related to the maximum expected HO beam–beam tune shift for the LHC. The nominal HO tune shift was derived from the experience of the Super Proton Synchrotron (SPS), taking into account possible contributions from the lattice non-linearities and significant LR contributions. The nominal value of $\xi = 0.0037$ was defined to provide a coherent set of parameters to reach the target luminosity, $L = 10^{34}\,{\rm cm}^{-2}\,{\rm s}^{-1}$ [2, 3]. Therefore, it should be considered as a conservative value and not as a real upper limit, in particular in the absence of strong LR interactions.

IS THE 'NOMINAL' BEAM–BEAM HO TUNE SHIFT REACHABLE?

Early in 2010, even if no show-stoppers were expected, dedicated experiments and observations during normal operation were planned to check the feasibility of colliding beams with the nominal tune shift estimated in the design report. In the following, we briefly list a few of these fills including the important results observed [4].

Fill 1069 (May 2010)

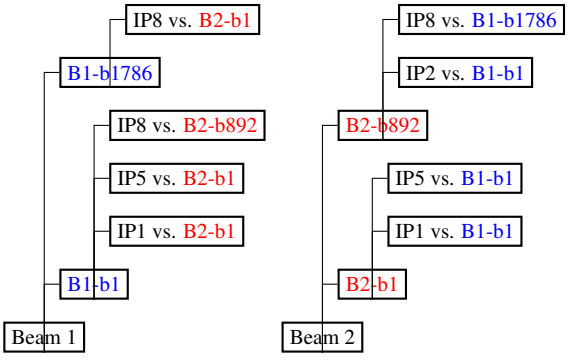

Figure 1: Collision scheme of the injected bunches in Fill 1069. Shown are the colliding bunch pairs in the two beams in the four interaction points. The slot numbers are given to specify a bunch position.

Experimental setup For the LHC fill in study (Fill 1069), two 'almost' nominal bunches of intensity

978-92-9083-404-5, 0007-8328 –
http://dx.doi.org/10.5170/CERN–2014–004.75

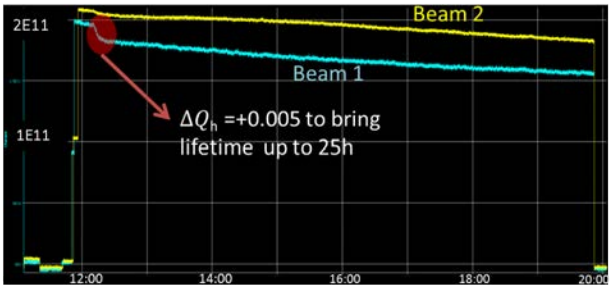

Figure 2: Total beam intensity evolution during Fill 1069. Beam 1 is shown in blue while Beam 2 is shown in yellow.

$\sim 1 \times 10^{11}$ ppb and normalized emittance of 3 μm were injected in each ring.
The bunches were put in collision according to the standard operational cycle, with $\beta* = 10$ m in all IPs and the collision tunes ($Q_x = 0.31$, $Q_y = 0.32$), at the injection energy of 450 GeV. The collision scheme is shown in Fig. 1.

Observations When the separation bumps were 'collapsed' simultaneously to bring the beams into collision, the lifetime dropped, especially in Beam 1, but a small tune adjustment ($\Delta Q_h \sim +0.005$) was sufficient to stabilize it at 25 h (Fig. 2). The resulting beam–beam tune shift exceeded the nominal value reaching $\xi = 0.004$ per IP. An increase of the vertical emittance in Beam 2 was observable and thought to be originating from an external excitation not fully understood (the hump). Since the results were encouraging, and no limitations were expected for the HO tune shift, it was decided to increase the intensity of the colliding bunches exploring regions with a higher tune shift.

Fill 1765 (May 2011)

Experimental setup One high-intensity bunch was injected per beam ($\sim 1.6 \times 10^{11}$ ppb); the measured normalized emittance by the wire scanners (WSs) was $\varepsilon_{x,y} = 1.2\,\mu$m. With the collision tunes setting, the beams were brought into collision at injection energy. The IP settings were the following: $\beta* = 11$ m and nominal crossing angles in all IPs, while the spectrometers were off in IP2 and IP8. The transverse damper (ADT) was turned on only at injection and set off afterwards [5, 6].

Observations An increase in the vertical emittance once in collision was observed, resulting in a 2.2 μm emittance and $\xi = 0.009$/IP. Since the bunches were colliding only in IP1 and IP5, a total $\xi = 0.018$ was reached. A small tune scan was tried as well at the end of the fill, to search for a better working point. No lifetime effects were observed, just a minor emittance blow-up for Beam 2.

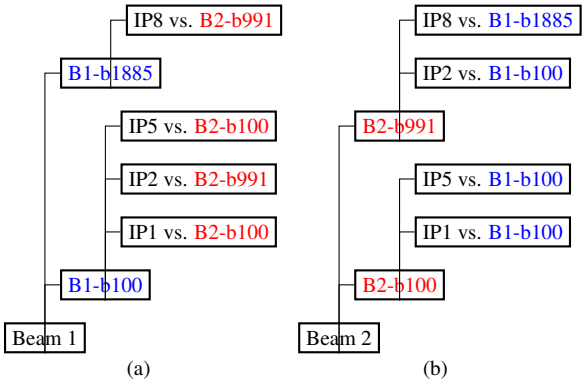

Figure 3: Collision scheme of the injected bunches in Fill 1766.

Fill 1766: Part 1 (May 2011)

Following the encouraging beam–beam parameter reached in Fill 1765, it was decided to maintain the high-intensity bunches and increase the number of collisions. Therefore, two bunches per beam were injected, allowing collisions in all interaction points but with a different collision pattern, as shown in Fig. 3.

Observations A signicant emittance increase was observed when beams started to collide in IP8. This emittance increase is observed on the bunches colliding only in IP8, i.e. with a single collision. The bunch with the largest number of collisions had the smallest emittance increase. The emittances as a function of time measured with the synchrotron light monitor (BSRT) are shown in Figs. 4 and 5.

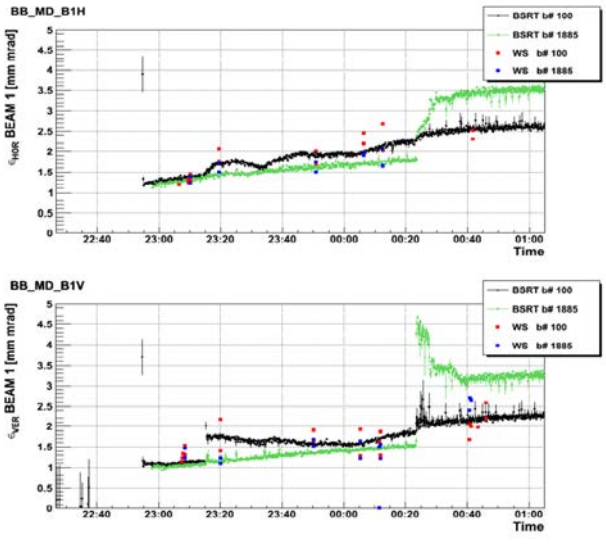

Figure 4: Fill 1766: Beam 1 horizontal (upper plot) and vertical (lower plot) normalized emittance evolution for the bunches $B1-b100$ (black) and $B1-b991$ (green), as measured by the BSRT.

This emittance increase did not start when the bunches

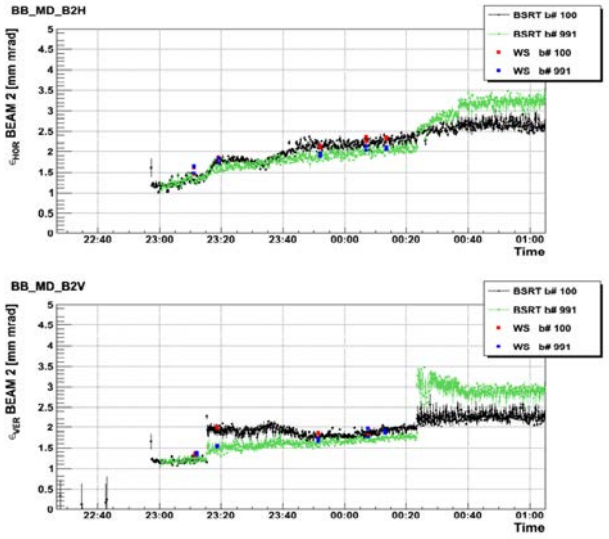

Figure 5: Fill 1766: Beam 2 horizontal (upper plot) and vertical (lower plot) normalized emittance evolution for the bunches $B2-b100$ (black) and $B2-b991$ (green), as measured by the BSRT.

were put into collision, but during the optimization process, i.e. luminosity scan. It was done manually since the automatic procedure did not find an optimum.

Fill 1766: Part 2 (May 2011)

With the same machine configuration as in Fill 1765, again two single bunches colliding only in IP1 and 5 were injected to study in more detail the parameter space, in particular the effect of the working point on the initial emittance growth observed once the beams are put into collision. Two fillings were done using the same filling scheme with roughly the same injected intensities ($\sim$1.8$\times$ 10^{11} ppb) and normalized emittance ($\sim$1.32 μm), but changing the tunes starting working point. As shown in Figs. 6 and 7, it is seen that moving the tune point from (0.31, 0.32) to (0.31, 0.31) helped to increase the beams' lifetime. The initial low lifetime observed was thought to originate from a lattice resonance where the core of the bunch was getting close to the 10th-order resonance; a small negative shift for the vertical tune ($\Delta Q_v = -0.01$) improved the losses and reduced the emittance blow-up since the large tune shift from the collisions will bring the core particles below the resonance.

Once this emittance blow-up was cured, a beam–beam linear parameter of $\xi = 0.017$/IP was achieved resulting in a total value $\xi = 0.034$.

HIGH PILE-UP TESTS: SINGLE BUNCHES

To provide a calibration test for the LHC experiments, tests were performed to generate a high pile-up in the de-

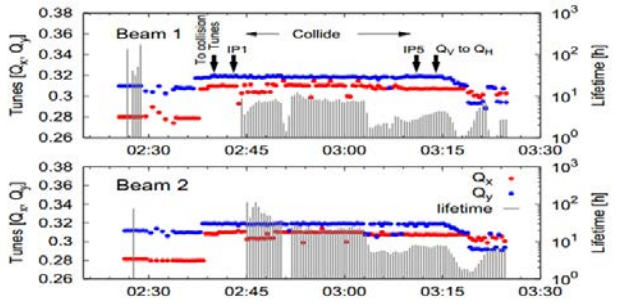

Figure 6: Fill 1766: horizontal (blue) and vertical (red) tune and the lifetime (black) evolution with the (0.31, 0.32) tune working point for Beam 1 (upper plot) and Beam 2 (lower plot).

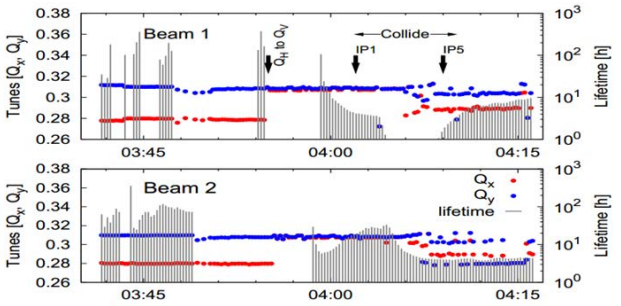

Figure 7: Fill 1766: horizontal (blue) and vertical (red) tune and the lifetime (black) evolution with the (0.31, 0.31) tune working point for Beam 1 (upper plot) and Beam 2 (lower plot).

tectors, i.e. a large number of events per crossing [7, 8]. For this purpose a large number of bunches is not needed and was done with single bunches per beam.

Experimental Setup

For the LHC fill in study (Fill 2201), one high-intensity bunch ($\sim$2.4$\times$ 10^{11} ppb) was injected in the bucket 1001 of both rings. The bunches were accelerated to the flat-top energy (3.5 TeV) and put in collision in ATLAS and CMS according to the standard operational cycle, where the machine was in the standard configuration:
$\beta* = 1$ m in IP1/5 and $\pm$120 μrad crossing angle,
$\beta* = 10$ m in IP2 and $\pm$80 μrad crossing angle,
$\beta* = 3$ m in IP8 and $\pm$250 μrad crossing angle.

Observations

The resulting luminosity was $\sim 4.7 \times 10^{-30}\,\mathrm{cm}^{-2}\,\mathrm{s}^{-1}$ corresponding to a pile-up (number of inelastic interactions per crossing) of $\mu \sim 31$ encounters per turn. The nominal number is $\mu \sim 20$ [2]. Observations of the beam intensity and emittance showed the following:

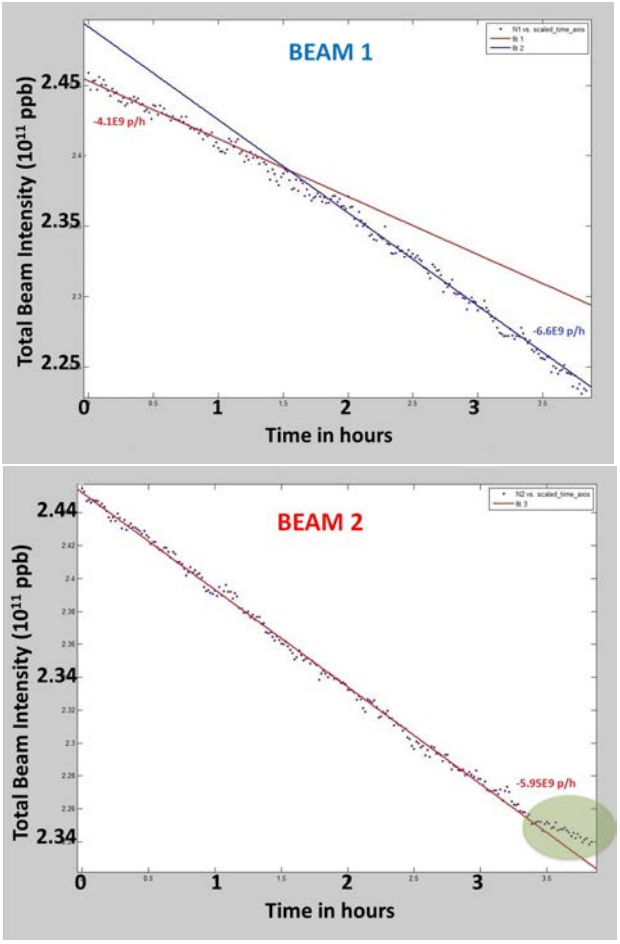

Figure 8: Fill 2201: measured vs. fitted bunch intensity for Beam 1 (upper plot) and Beam 2 (lower plot). The points refer to the fBCT measurement and the lines are the linear fits representing the loss regimes observed. The slopes of the linear fits corresponding to the constant loss rate are also reported.

Emittance The bunch transverse emittances were frequently measured with the WSs throughout the fill. At the injection energy an emittance growth was observed only in the horizontal plane (12% for Beam 1 and 8% for Beam 2). Through the ramp the beams' emittances in both planes steadily grew reaching $\sim$3.1 μm at the beginning of the collisions (a growth of 44% B1 and 27% B2 in the horizontal plane and 30% B1 and 7% B2 in the vertical plane). In about 3 h in collision the horizontal emittances grew by about 20% for both beams while the vertical ones increased by $\sim$ 13%.

Intensity The beam intensity decay was studied and two loss regimes were observed for Beam 1: the first regime ended after 1.5 h in collision with a loss rate of $\sim 4.1 \times 10^9$ p/h followed until the end of the fill with a constant loss regime of $\sim 6.6 \times 10^9$ p/h. For Beam 2, a constant loss rate was recorded throughout all the fill $\sim 6 \times 10^9$ p/h. A correlation was observed between the transition between the two loss regimes in Beam 1 and its bunch length growth [9], where, once the value of ~ 8.95 cm was reached, corresponding to the initial bunch length of Beam 2, the losses settled to their maximum value (Fig. 8).

Luminosity A validation of the measured beam parameters was made through a comparison between the published instantaneous luminosity from the experiments and the analytically calculated one. The observed discrepancy was compatible with the uncertainties in the values of the machine parameters (β^*) and the monitors' accuracy.

In addition, the luminosity evolution model developed for the TEVATRON was applied using the LHC parameters, trying to predict the evolution of the beam parameters. An agreement was only found for the period corresponding to the first loss regime for Beam 1, while for the second loss regime and for the Beam 2 intensity evolution, the longitudinal losses were underestimated almost by a factor of 3.

2011 HIGH-PILE-UP TESTS: MULTIPLE BUNCHES

After the single-bunch high-pile-up tests, the experimenters requested a new test to check whether multiple high-pile-up collisions can be effectively processed.

Experimental Setup

Fill 2252 was dedicated to providing ATLAS and CMS with high-pile-up collisions. A peak pile-up μ of almost 35 was achieved. Part of the test was also to bring the pile-up to values < 0.5 and this was achieved by separating the beams in steps. The head-on collisions were restored after each IP separation to study its effects. The collision scheme during this experiment is shown in Fig. 9. The number of collisions is shown for every bunch.

The bunch parameters (intensity, emittance and length) of high-pile-up colliding bunches were observed while putting beams in collision with the same machine setup as in Fill 2201 but with the following filling scheme:

Observations

After $\sim$100 min in single-bunch mode, the beams were re-separated into three different phases, as shown in Fig. 10:

- Five separation steps in the horizontal plane of IP5 reducing the luminosity from $\sim$44 Hz/μb to $\sim$10 Hz/μb,
- Eleven separation steps in the vertical plane of IP1 reducing the luminosity from $\sim$43 Hz/μb to $\sim$0.08 Hz/μb,

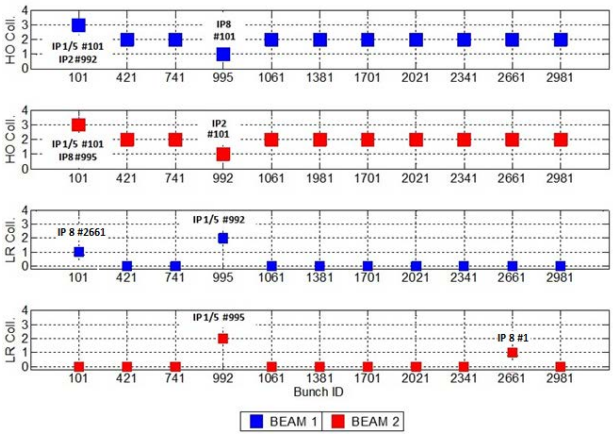

Figure 9: Collision scheme of the injected bunches in Fill 2252. All bunches are colliding HO in IP1 and 5, except for $B1-b995$ and $B2-b992$ colliding respectively in IP8 with $B2-b101$ and in IP2 with $B1-b101$. The number of LR encounters is shown as well.

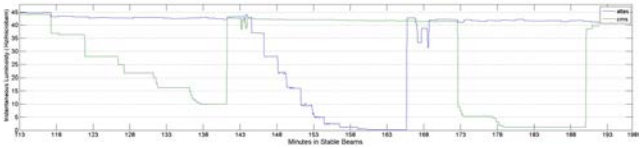

Figure 10: ATLAS and CMS instantaneous luminosity during the separation phases shown respectively in blue and green.

– Two separation steps in the horizontal plane of IP5 reducing the luminosity from $\sim 41\,\mathrm{Hz}/\mu\mathrm{b}$ to $\sim 1.23\,\mathrm{Hz}/\mu\mathrm{b}$.

After each separation, the instantaneous luminosity was re-optimized to its maximum value in the considered IP.

Emittance The bunches can be classified into three categories:

– bunches presenting a higher growth rate in the vertical plane during the separation phases: $B2-b101$, $B2-b421$ and $B1-b1061$ (see Fig. 11),

– bunches presenting sudden blow-up throughout the separation steps: $B1-b101$, $B1-b421$, $B2-b992$ and $B2-b1061$ (see Fig. 12).

– bunches not affected by the separation steps.

The sudden increases in emittance were observed mainly in the vertical plane during the steps of the first CMS separation (recall that in IP5 the vertical plane is the separation plane).

Lifetime Normalizing the bunch intensity curves to the initial value at the start of collisions allows one to identify three groups of behaviours according to the number of

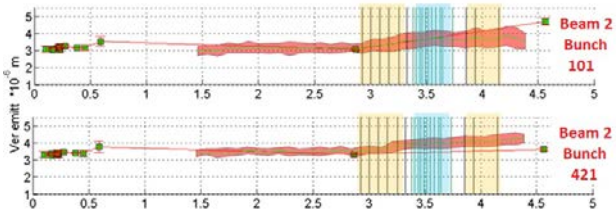

Figure 11: Vertical emittances of bunches 101–421 (Beam 2) showing a continuous smooth increase in the emittance while separating the beams in IP5. The vertical coloured bar delimits the separation steps of every separation phase in both IPs.

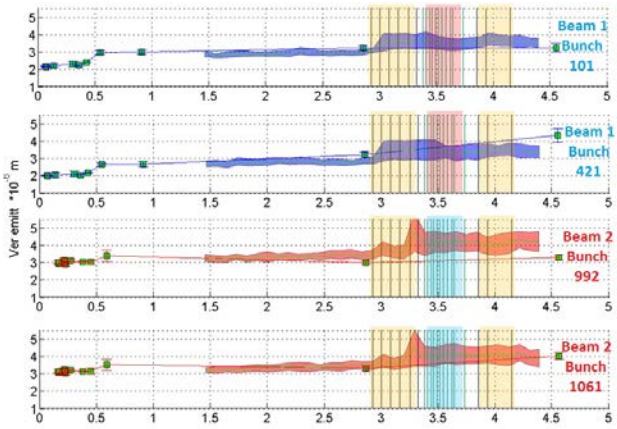

Figure 12: Vertical blow-up of the vertical emittance of bunches 101–421 (Beam 1) and bunches 992–1061 (Beam 2) while separating the beams in IP5. The vertical coloured bar delimits the separation steps of every separation phase in both IPs.

HO collisions the bunches experience (three HO, two HO, one HO).

Analysing the intensity data for the first 1.8 h, it is possible to disentangle the separation effects from the initial evolution of the bunch parameters.

Once in collision, for most bunches a linear decrease in intensity is observed during the considered time period; a linear fit is applied to the measured intensities and the slopes corresponding to the loss rates are shown in Fig. 13.

The highest losses are observed for bunches experiencing three HO collisions while the lowest losses are for bunches with one HO collision only.

We observe the losses for each of the three separation phases mentioned before; the loss trend can be organized into families (according to the collision scheme) for all the steps.

– ***Separation phase 1 (IP5)***
The first separation step in IP5 had an effect on the luminosity in IP1, where a drop of 3.5% was observed. No significant change in the intensity evolution of all the bunches in both beams except for:

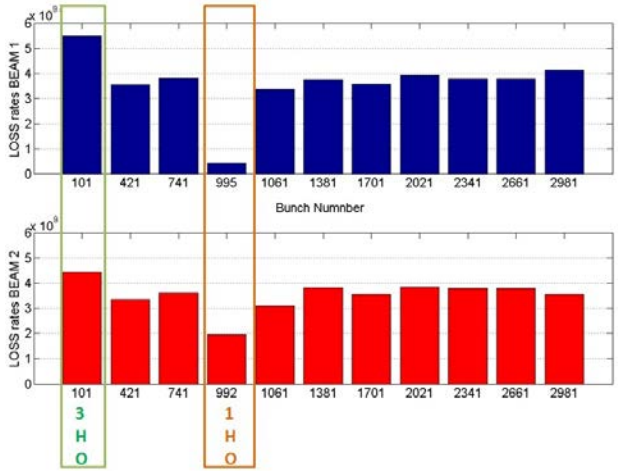

Figure 13: Slopes from linear fits of the bunch intensity decays for the first 100 min.

. bunch 101 in Beam 1 (having three HO: IP1 and 5 with bunch 101 in Beam 2, IP2 with bunch 992 in Beam 2),

. bunch 992 in Beam 2 (having one HO: IP2 with bunch 101 in Beam 1).

An increase in the loss rate is observed for $B1-b101$ after the first separation step as shown in Fig. 14. For $B2-b992$, a sudden increase in losses is seen in the first and last steps of the separation. Note that at the end of the fifth step, once the beams are put back in HO collisions in IP5, the loss rate for $B2-b992$ returned to the value it had before the beams' manipulation as seen in Fig. 14. In order to explain and understand the link between the behaviour of $B2-b992$, colliding only in IP2, and the separations in IP5 it is important to consider the LR collisions this bunch is experiencing in IP5 with $B1-b995B1$.

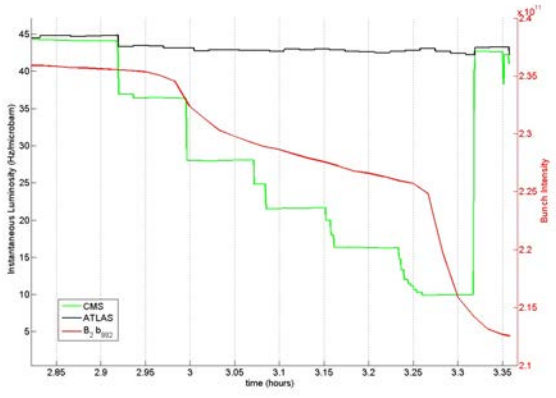

Figure 14: The evolution of the normalized intensity of $B2-b992$ (red) during the first separation phase in IP5. The instantaneous luminosity in IP1 and IP5 is shown respectively in black and green.

– ***Separation phase 2 (IP1)***
$B1-b995$ and $B2-b992$ having one HO collision in IP8 and 2, respectively, were not affected by the steps of this separation. For the three HO collisions family, it can be observed that $B1-b101B1$ experienced higher loss rate at half total separation and kept this loss regime until the beams were brought back into HO collision; bunch $B2$-$b101$ entered a higher loss regime after the first separation step and maintained this rate once back in the initial situation of fully HO collisions. The slopes of the intensity evolution for all the other bunches (two HO families) depend on the value of the separation between the beams: lower losses were observed for higher separations. It is worth observing that the bunch losses for both families in Beam 1 and Beam 2 colliding in IP1 and 5 at zero separation were higher at the end of this phase (especially for Beam 1).

– ***Separation phase 3 (IP5)***
No clear variation in the intensity decay was observed for the bunches having one HO and three HO in both beams, while for all the other bunches, the losses were decreasing for an increasing beam separation. Again for some bunches in Beam 1 having two HO, the initial loss rate was not restored at the end when the beams were brought into HO collisions: higher losses were still observed at the end.

Bunch length We only highlight the bunch length evolution of Beam 2. It is worth pointing out the behaviour of $B2-b992$ (see Fig. 15): a bunch shortening is observed simultaneously to the intensity loss, corresponding to the first separation step in IP5 (first separation phase). For all the other bunches, the bunch length did not bear signs of the losses and the emittance blow-up (horizontal and vertical).

2012 HIGH-PILE-UP

Profiting from the new optics in the SPS (Q20 optics), where the fractional part of the tune was moved to 0.2, very high brightness bunches were put into collision in the LHC aiming to establish a new record pile-up possibly up to 100. High-brightness bunches with intensity of 3×10^{11} ppb and normalized emittance of 2 μm were used for this test. The energy ramp was troublesome; the controlled longitudinal blow-up needed for the beam stability was faulty, as shown in Fig. 16. The bunch length of Beam 2 was brought to the target bunch length of 1.3 ns while Beam 1 bunch length went down to ~ 0.4 ns before reaching a value close to its target value of 1.2 ns. This caused a deterioration in the beam quality throughout the ramp. The bunches were put into collision with more than 10% of losses (end of ramp and at flat-top energy) and a doubled emittance, as shown in Fig. 17.

The resulting pile-up of 58 was the best reached in two tries. Once the issue with the longitudinal blow-up was

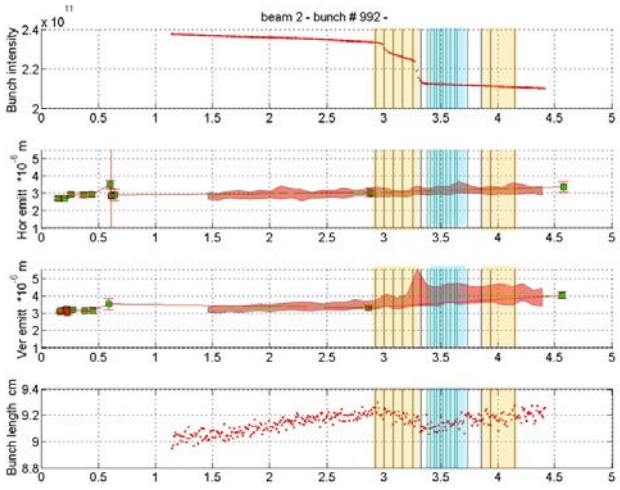

Figure 15: The observed parameters for $B2 - b992$ (intensity, transverse emittances and bunch length) from the start of the fill until the end of the collisions. The vertical coloured bar delimits the separation steps of every separation phase in both IPs.

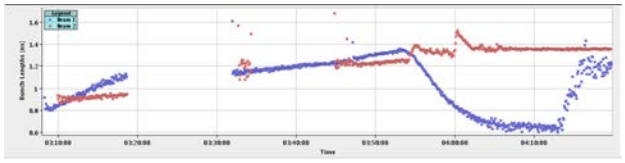

Figure 16: Fill 2824: bunch length evolution for Beam 1 (blue) and Beam 2 (red) during the fill as measured by the beam-quality monitors in the LHC.

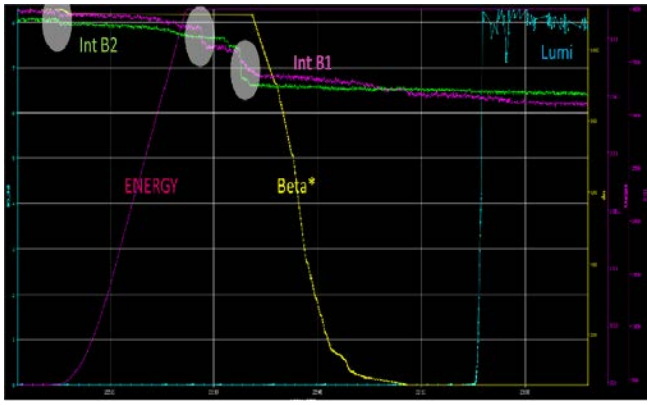

Figure 17: Fill 2824: intensity evolution of Beam 1 (magenta) and Beam 2 (green) along with energy ramp (red). The value of β^* in IP1 is shown as well to indicate the squeeze phase, and the instantaneous luminosity (blue) in IP1 is shown as well as an indication for the start of collisions.

solved, two bunches per beam colliding only in IP1 and IP5 were injected and with difficulty brought into collision at 4 TeV with a β^* of 60 cm in both IPs. An instability arising during the squeeze was observed leading again to some losses along with an emittance increase. The maximum pile-up obtained was 70 in IP1 and 65 in IP5.

SUMMARY

In this paper, we reported the main studies of the HO beam–beam effects in the LHC with nominal, high-intensity, high-brightness single and multiple bunches. It is worth noting that small contributions of the lattice non-linearities as well as good settings of the machine allowed one to quickly reach the nominal head-on beam–beam tune shift; it was also shown that the LHC allows very large head-on tune shifts above nominal.
It has to be seen whether this can be maintained in the presence of many LR interactions. Yet there is no reason to assume that an HO limit has been reached for the moment in the LHC.

ACKNOWLEDGMENTS

I would like to thank all the CERN beam–beam working group members for their contribution, help and advice, especially W. Herr and G. Papotti.

REFERENCES

[1] W. Herr et al., "Observations of Beam–Beam Effects at high intensity at the LHC," Proceedings of International Particle Accelerator Conference 2011, San Sebastian Spain (2011).

[2] LHC Design Report, CERN-2004-003 (2004).

[3] W. Herr, "LHC Beam–Beam Effects – Review and Outlook", Proc. LHC Operations Workshop, Evian, December 2010 (2010).

[4] G. Arduini, W. Herr and J.M. Jowett, "First Observation of Beam–Beam Interactions in High Intensity Collisions at the LHC," CERN-ATS-Note-2010-039 PERF.

[5] W. Herr et al., "Head-on Beam–Beam Tune Shift with High Brightness Beams in the LHC," CERN-ATS-Note-2011-029 MD.

[6] M Albert et al., "Head-on Beam–Beam Collisions with High Intensities and Long Range Beam–Beam Studies in the LHC," CERN-ATS-Note-2011-058 MD.

[7] G. Trad et al., "Beam Parameters Observations During a High Pile-up Collisions fill," CERN-ATS-Note-2011-105 MD.

[8] G. Trad et al., "Beam Parameters Observations During the Second High Pile-up Collisions fill in 2011," CERN-ATS-Note-2012-010 MD.

[9] G. Papotti, T. Bohl, F. Follin, and U. Wehrle, "Longitudinal Beam Measurements at the LHC: the LHC Beam Quality Monitor," IPAC11, San Sebastian, September 2011.

Published by CERN in the Proceedings of the ICFA Mini-Workshop on Beam–Beam Effects in Hadron Colliders,
CERN, Geneva, Switzerland, 18–22 March 2013, edited by W. Herr and G. Papotti, CERN–2014–004 (CERN, Geneva, 2014)

MEASUREMENTS OF THE EFFECT OF COLLISIONS ON TRANSVERSE BEAM HALO DIFFUSION IN THE TEVATRON AND IN THE LHC

G. Stancari*, G. Annala, T.R. Johnson, V. Previtali, D. Still, A. Valishev
Fermi National Accelerator Laboratory, Batavia, IL, USA
R.W. Assmann†, Deutsches Elektronen-Synchrotron, Hamburg, Germany
R. Bruce, F. Burkart, S. Redaelli, B. Salvachua, G. Valentino, CERN, Geneva, Switzerland

Abstract

Beam–beam forces and collision optics can strongly affect beam lifetime, dynamic aperture, and halo formation in particle colliders. Extensive analytical and numerical simulations are carried out in the design and operational stages of a machine to quantify these effects, but experimental data are scarce. The technique of small-step collimator scans was applied to the Fermilab Tevatron collider and to the CERN Large Hadron Collider to study the effect of collisions on transverse beam halo dynamics. We describe the technique and present a summary of the first results on the dependence of the halo diffusion coefficient on betatron amplitude in the Tevatron and in the LHC.

INTRODUCTION

Beam quality and machine performance in circular accelerators depend on global quantities such as beam lifetimes, emittance growth rates, dynamic apertures, and collimation efficiencies. Calculations of these quantities are routinely performed in the design stage of all major accelerators, providing the foundation for the choice of operational machine parameters.

At the microscopic level, the dynamics of particles in an accelerator can be quite complex. Deviation from linear dynamics can be large, especially in the beam halo. Lattice resonances and nonlinearities, coupling, intrabeam and beam-gas scattering, and the beam–beam force in colliders all contribute to the topology of the particles' phase space, which in general includes regular areas with resonant islands and chaotic regions. In addition, various noise sources are present in a real machine, such as ground motion (resulting in orbit and tune jitter) and ripple in the radio-frequency and magnet power supplies. As a result, the macroscopic motion can in some cases acquire a stochastic character, describable in terms of diffusion [1–7].

In studies for the Superconducting Super Collider [8], the concept of diffusive dynamic aperture was discussed, as well as how it is affected by beam–beam forces, lattice nonlinearities, and tune jitter. Detailed theoretical studies of beam–beam effects and particle diffusion can be found, for instance, in Refs. [4–6, 9, 10]. In Ref. [7], the effects of random fluctuations in tunes, collision offsets, and beam sizes were studied. Numerical estimates of diffusion in the Tevatron are given in Refs. [11–13].

Two main considerations lead to the hypothesis that macroscopic motion in a real machine, especially in the halo, may have a stochastic nature: (1) the superposition of the multitude of dynamical effects (some of which are stochastic) acting on the beam; (2) the operational experience during collimator setup, which generates spikes and dips in loss rates that often decay in time as $1/\sqrt{t}$, a typically diffusive behaviour.

It was shown that beam halo diffusion can be measured by observing the time evolution of particle losses during a collimator scan [14]. These phenomena were used to estimate the diffusion rate in the beam halo in the SPS and $S p\bar{p} S$ at CERN [15–17], in HERA at DESY [14], and in RHIC at BNL [18]. An extensive experimental campaign was carried out at the Tevatron in 2011 [19] to characterize the beam dynamics of colliding beams and to study the effects of the novel hollow electron beam collimator concept [20]. Recently, the technique has also been used to measure halo diffusion rates in the LHC at CERN [21]. These measurements shed light on the relationship between halo population and dynamics, emittance growth, beam lifetime, and collimation efficiency. They are also important inputs for collimator system design and upgrades, including new methods such as channelling in bent crystals or hollow electron lenses.

Halo diffusion rates have been measured under various experimental conditions. In this paper, we focus on the comparison between colliding and separated beams, in an attempt to expose the effects of beam–beam forces. After briefly describing the method of small-step collimator scans, we present data on the dependence of the transverse beam halo diffusion coefficient on betatron amplitude in the Tevatron and in the LHC.

EXPERIMENTAL METHOD

A schematic diagram of the apparatus is shown in Fig. 1 (top). All collimators except one are retracted. As the collimator jaw of interest is moved in small steps (inward or outward), the local shower rates are recorded as a function of time. Collimator jaws define the machine aperture. If they are moved towards the beam centre in small steps, typical spikes in the local shower rate are observed, which approach a new steady-state level with a characteristic relaxation time (Fig. 1, bottom). When collimators are retracted,

* stancari@fnal.gov
† Previously at CERN, Geneva, Switzerland.

978-92-9083-404-5, 0007-8328 –
http://dx.doi.org/10.5170/CERN–2014–004.83

on the other hand, a dip in loss rates is observed, which also tends to a new equilibrium level. By using the diffusion model presented below, the time evolution of losses can be related to the diffusion rate at the collimator position. By independently calibrating the loss monitors against the number of lost particles, halo populations and collimation efficiencies can also be estimated. With this technique, the diffusion rate can be measured over a wide range of amplitudes. At large amplitudes, the method is limited by the vanishing beam population and by the fast diffusion times. The limit at small amplitudes is given by the level of tolerable loss spikes.

MODEL

A diffusion model of the time evolution of loss rates caused by a step in collimator position was developed [22]. It builds upon the model of Ref. [14] and its assumptions of (1) constant diffusion rate, and (2) linear halo tails within the range of the step. These hypotheses allow one to obtain analytical expressions for the solutions of the diffusion equation and for the corresponding loss rates versus time. The present model addresses some of the limitations of the previous model and expands it in the following ways: (a) losses before, during, and after the step are predicted; (b) different steady-state rates before and after are explained; (c) determination of the model parameters

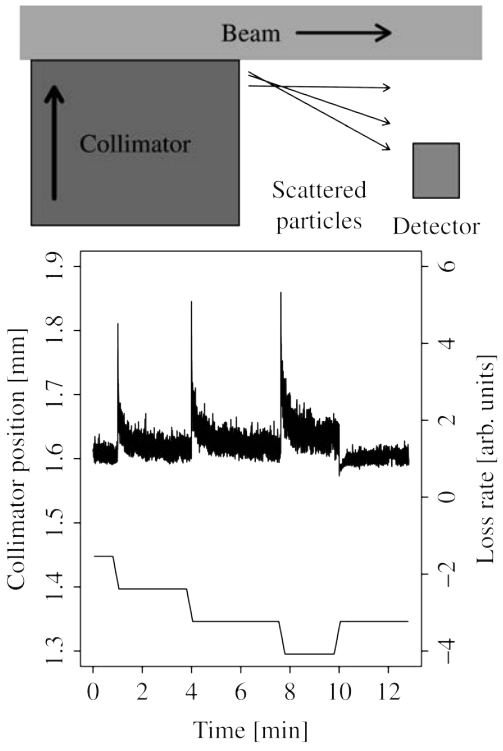

Figure 1: Schematic diagram of the apparatus (top), and an example of the response of local loss rates to inward and outward collimator steps (bottom).

(diffusion coefficient, tail population gradient, detector calibration, and background rate) is more robust and precise.

Following Ref. [14], we consider the evolution in time t of a beam of particles with phase-space density $f(J,t)$, described by the diffusion equation $\partial_t f = \partial_J(D\,\partial_J f)$, where J is the Hamiltonian action and D the diffusion coefficient in action space. The particle flux at a given location $J = J'$ is $\phi = -D\cdot[\partial_J f]_{J=J'}$. During a collimator step, the action $J_c = x_c^2/(2\beta_c)$, corresponding to the collimator half-gap x_c at a ring location where the amplitude function is β_c, changes from its initial value J_{ci} to its final value J_{cf} in a time Δt. The step in action is $\Delta J \equiv J_{cf} - J_{ci}$. In the Tevatron, typical steps in half-gap were 50 μm in 40 ms; smaller steps (10 μm in 5 ms, typically) were possible in the LHC. In both cases, the amplitude function was of the order of a hundred metres. It is assumed that the collimator steps are small enough so that the diffusion coefficient can be treated as a constant in that region. If D is constant, the local diffusion equation becomes $\partial_t f = D\,\partial_{JJ} f$. With these definitions, the particle loss rate at the collimator is equal to the flux at that location:

$$L = -D\cdot[\partial_J f]_{J=J_c}. \tag{1}$$

Particle showers caused by the loss of beam are measured with scintillator counters or ionization chambers placed close to the collimator jaw. The observed shower rate is parametrized as

$$S = kL + B, \tag{2}$$

where k is a calibration constant including detector acceptance and efficiency and B is a background term which includes, for instance, the effect of residual activation. Under the hypotheses described above, the diffusion equation can be solved analytically using the method of Green's functions, subject to the boundary condition of vanishing density at the collimator and beyond. Details are given in Ref. [22].

Local losses are proportional to the gradient of the distribution function at the collimator. The gradients differ in the two cases of inward and outward step, denoted by the I and O subscripts, respectively:

$$\partial_J f_I(J_c,t) = -A_i + 2(A_i - A_c)P\left(\frac{-J_c}{w}\right) + \frac{2}{\sqrt{2\pi}w}\left\{-A_i(J_{ci}-J_c) + (A_i J_{ci} - A_c J_c)e^{-(J_c/w)^2/2}\right\} \tag{3}$$

$$\partial_J f_O(J_c,t) = -2A_i P\left(\frac{J_{ci}-J_c}{w}\right) + 2(A_i - A_c)P\left(\frac{-J_c}{w}\right) + \frac{2}{\sqrt{2\pi}w}\left(A_i J_{ci} - A_c J_c\right)e^{-(J_c/w)^2/2}. \tag{4}$$

The positive parameters $A_i = -[\partial_J f]_{J=J_{ci}}$ and $A_f = -[\partial_J f]_{J=J_{cf}}$ are the opposites of the slopes of the distribution function before and after the step, whereas A_c varies linearly between A_i and A_f as the collimator moves. The parameter w is defined as $w \equiv \sqrt{2Dt}$. The function $P(x)$

is the S-shaped cumulative Gaussian distribution function, such that $P(-\infty) = 0$, $P(0) = 1/2$, and $P(\infty) = 1$.

The above expressions, Eqs. (3) and (4), are used to model the measured shower rates. Parameters are estimated from a fit to the experimental data. The background B is measured before and after the scan when the jaws are retracted. The calibration factor k is in general a function of collimator position, and can be determined independently by comparing the local loss rate with the number of lost particles measured by the beam current transformer. The fit parameters (kDA_{i}) and (kDA_{f}) are the steady-state loss rate levels before and after the step. The diffusion coefficient D depends on the measured relaxation time and on the value of the peak (or dip) in loss rates.

The model explains the data very well when the diffusion time is long compared to the duration of the step. The model can be extended by including a separate drift term (from the Fokker–Planck equation) or a non-vanishing beam distribution at the collimator.

RESULTS

All Tevatron scans were done vertically on antiprotons, either at the end of regular collider stores (0.98 TeV per beam) or with only antiprotons in the machine at the same top energy. Losses were measured with scintillator paddles located near the collimators. (A detailed description of the Tevatron collimation system can be found in Ref. [23].)

The LHC measurements were taken in a special machine study at 4 TeV with only one bunch per beam, first with separated beams and then in collision, with vertical crossing at the first interaction point (IP1) and horizontal crossing at IP5 [21]. Losses were measured with ionization chambers. Because of the negligible cross-talk between loss monitors, it was possible to simultaneously scrape proton beam 1 vertically and proton beam 2 horizontally.

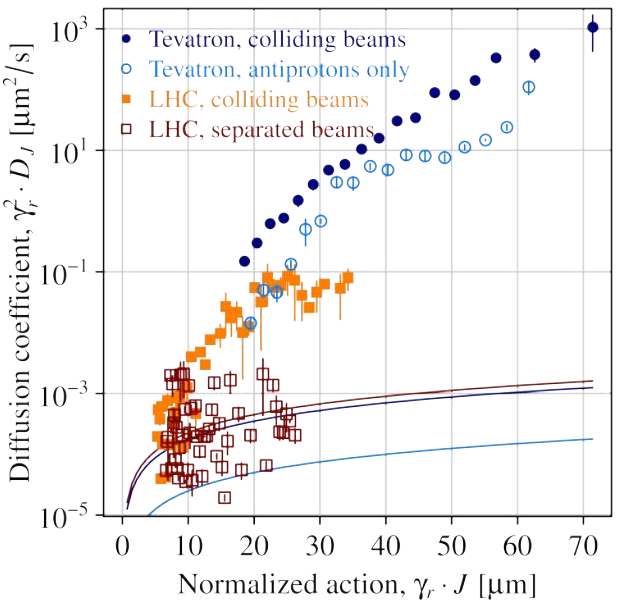

Figure 2: Measurements of vertical halo diffusion in the Tevatron and in the LHC.

Figure 2 shows a comparison of vertical beam halo diffusion measurements in the Tevatron and in the LHC, for inward collimator steps. To account for the different kinetic energies of the two machines, diffusion coefficients are plotted as a function of normalized vertical collimator action $I \equiv \gamma_{\mathrm{r}} J$, where γ_{r} is the relativistic Lorentz factor. On the vertical axis, we plot the diffusion coefficient in normalized action space $D_{\mathrm{I}} \equiv \gamma_{\mathrm{r}}^2 D$, which stems from recasting the diffusion equation as follows: $\partial_t f = \partial_J (D\, \partial_J f) \rightarrow \partial_t f = \partial_I (D_I\, \partial_I f)$.

The dark-blue filled circles refer to the end of Tevatron collider Store 8733 (13 May 2011). The light-blue data (empty circles) were taken during a special antiproton-only fill (Store 8764, 24 May 2011). The LHC data were taken on 22 June 2012 and refer to beam 1 (vertical) with separated beams (empty red squares) and in collision (filled orange squares). The continuous lines represent the diffusion coefficients derived from the measured core geometrical emittance growth rates $\dot{\varepsilon}$: $D = \dot{\varepsilon} \cdot J$. (In this particular dataset, the synchrotron-light measurements were not sufficient for estimating emittance growth rates of colliding beams in the LHC.)

In the LHC, separated beams exibited a slow halo diffusion, comparable with the emittance growth from the core. This fact can be interpreted as a confirmation of the extremely good quality of the magnetic fields in the machine. Collisions enhanced halo diffusion in the vertical plane by about one to two orders of magnitude. No significant diffusion enhancement was observed in the horizontal plane. The reason for this difference is not understood. In the Tevatron, the comparison between halo and core diffusion rates suggests that single-beam diffusion at these large amplitudes is dominated by effects other than residual-gas scattering and intrabeam scattering, pointing towards field nonlinearities and noise (including tune modulation generated by power-supply ripple). At the end of the store, collisions enhance diffusion by about one order of magnitude.

From the measured diffusion coefficients, estimates of impact parameters on the primary collimator jaws are possible [14]. One can also calculate the particle survival time versus the amplitude. The diffusion coefficient is related to the steady-state density of the beam tails, which can therefore be deduced by using a procedure that is complementary to the conventional static model, based on counting the number of lost particles at each collimator step. These and other consequences of beam halo diffusivity will be investigated in separate reports.

CONCLUSIONS

The technique of small-step collimator scans was applied to the Fermilab Tevatron collider and to CERN's Large Hadron Collider to study transverse beam halo dynamics in relation to beam–beam effects and collimation.

We presented the first data on the dependence of transverse beam halo diffusion rates on betatron amplitude. In the Tevatron, vertical antiproton diffusion at the end of a collider store was compared with a special store with only antiprotons in the machine. Even with a reduced beam–beam force, the effect of collisions was dominant. A comparison with core emittance growth indicated that halo diffusion of single beams was driven by nonlinearities and noise, not by residual-gas or intrabeam scattering. In the LHC, horizontal and vertical collimator scans were performed during a special machine study with only one bunch per beam (i.e. no long-range beam–beam interactions). With separated beams, no significant difference was observed between halo and core diffusion, which indicated very low noise levels and nonlinearities. In collision, horizontal diffusion was practically unchanged; the vertical diffusion rate enhancement was a function of action and reached about two orders of magnitude. In general, it was confirmed that collimator scans are a sensitive tool for the study of halo dynamics as a function of transverse betatron amplitude.

ACKNOWLEDGMENTS

The authors thank X. Buffat, R. De Maria, W. Herr, B. Holzer, T. Pieloni, J. Wenninger (CERN), H.J. Kim, N. Mokhov, T. Sen, and V. Shiltsev (Fermilab) for valuable discussions and insights. These measurements would not have been possible without the support of the CERN Operations Group and the Fermilab Accelerator Division personnel. In particular, we would like to thank S. Cettour Cave, A. Macpherson, D. Jacquet, M. Solfaroli Camillocci (CERN), M. Convery, C. Gattuso, and R. Moore (Fermilab).

Fermilab is operated by Fermi Research Alliance, LLC, under contract no. DE-AC02-07CH11359 with the United States Department of Energy. This work was partially supported by the US LHC Accelerator Research Program (LARP).

REFERENCES

[1] A.J. Lichtenberg and M.A. Lieberman, *Regular and Chaotic Dynamics* (New York: Springer, 1992).

[2] T. Chen et al., Phys. Rev. Lett. 68 (1992) 33.

[3] A. Gerasimov, Report No. FERMILAB-PUB-92-185 (1992).

[4] F. Zimmermann, PhD Thesis, Hamburg University, Germany, Report No. DESY-93-059 (1993).

[5] O.S. Brüning, PhD Thesis, Hamburg University, Germany, Report No. DESY-94-085 (1994).

[6] F. Zimmermann, Part. Accel. 49 (1995) 67; Report No. SLAC-PUB-6634 (October 1994).

[7] T. Sen and J.A. Ellison, Phys. Rev. Lett. 77 (1996) 1051.

[8] J. Irwin, Report No. SSC-233 (1989).

[9] Y. Papaphilippou and F. Zimmermann, Phys. Rev. ST Accel. Beams 2 (1999) 104001.

[10] Y. Papaphilippou and F. Zimmermann, Phys. Rev. ST Accel. Beams 5 (2002) 074001.

[11] T. Sen et al., Phys. Rev. ST Accel. Beams 7 (2004) 041001.

[12] E.G. Stern et al., Phys. Rev. ST Accel. Beams 13 (2010) 024401.

[13] V. Previtali et al., Proc. 2012 Int. Particle Accelerator Conf. (IPAC12), New Orleans, Louisiana, USA, 20–25 May 2012, p. 1113.

[14] K.-H. Mess and M. Seidel, Nucl. Instrum. Methods Phys. Res. A 351 (1994) 279; M. Seidel, PhD Thesis, Hamburg University, Report No. DESY-94-103 (June 1994).

[15] L. Burnod, G. Ferioli, and J.B. Jeanneret, Report No. CERN-SL-90-01 (1990).

[16] M. Meddahi, PhD Thesis, Université de Paris VII, France, Report No. CERN-SL-91-30-BI (1991).

[17] W. Fischer, M. Giovannozzi, and F. Schmidt, Phys. Rev. E 55 (1997) 3507.

[18] R.P. Fliller III et al., Proc. 2003 Particle Accelerator Conf. (PAC03), Portland, Oregon, USA, 12–16 May 2003, p. 2904.

[19] G. Stancari et al., Proc. 2011 Int. Particle Accelerator Conf. (IPAC11), San Sebastián, Spain, 4–9 September 2011, p. 1882.

[20] G. Stancari et al., Phys. Rev. Lett. 107 (2011) 084802; arXiv:1105.3256 [phys.acc-ph].

[21] G. Valentino et al., Phys. Rev. ST Accel. Beams 16 (2013) 021003.

[22] G. Stancari, arXiv:1108.5010 [physics.acc-ph], Report No. FERMILAB-FN-0926-APC (2011).

[23] N. Mokhov et al., J. Instrum. 6 (2011) T08005.

Published by CERN in the Proceedings of the ICFA Mini-Workshop on Beam–Beam Effects in Hadron Colliders,
CERN, Geneva, Switzerland, 18–22 March 2013, edited by W. Herr and G. Papotti, CERN–2014–004 (CERN, Geneva, 2014)

LONG-RANGE BEAM–BEAM EFFECTS IN THE LHC

W. Herr, X. Buffat, R. Calaga, R. Giachino, G. Papotti, T. Pieloni,
D. Kaltchev, TRIUMF, Vancouver, Canada

Abstract

We report on the experience with long-range beam–beam effects in the LHC, in dedicated studies as well as the experience from operation. Where possible, we compare the observations with the expectations.

LAYOUT FOR BEAM–BEAM INTERACTIONS

The layout of experimental regions in the LHC is shown in Fig. 1. The beams travel in separate vacuum chambers

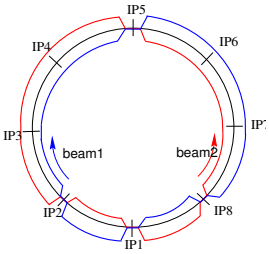

Figure 1: Layout of the experimental collision points in the LHC [1, 2].

and cross in the experimental areas where they share a common beam pipe. In these common regions the beams experience head-on collisions as well as a large number of long-range beam–beam encounters [1–3]. This arrangement together with the bunch filling scheme of the LHC as shown in Fig. 2 [1, 3] leads to very different collision pattern for different bunches, often referred to as "PACMAN" bunches. The number of both, head-on as well as

Figure 2: Bunch filling scheme of the nominal LHC.

long-range encounters, can be very different for different bunches in the bunch trains and lead to a different integrated beam–beam effect [2, 3]. This was always a worry in the LHC design and the effects have been observed in an early stage of the commissioning. Strategies have been provided to minimize these effect, e.g. different planes for the crossing angles [1, 3].

Strength of Long-range Interactions

A key parameter for the effect of long-range interactions is the local beam separation at the parasitic encounters. Usually this separation is measured in units of the transverse beam size at the corresponding encounter. As standard and for comparison between different configurations, we use the normalized separation in the drift space. For small enough β^* and round beams it can be written as a simple expression:

$$d_{sep} \approx \frac{\sqrt{\beta^*} \cdot \alpha \cdot \sqrt{\gamma}}{\sqrt{\epsilon_n}} \,. \tag{1}$$

Beyond the drift space the exact separation has to be computed with an optics program. For a small β^* the phase advance varies fast between the head-on interaction point and the first parasitic encounter from 0 to $\frac{\pi}{2}$. Most of the parasitic encounters occur at similar phases and therefore can add up. This is in strong contrast to other separation schemes such as pretzel separation used in the Super Proton Synchroton (SPS) collider and the Tevatron, where the parasitic encounters are distributed around the whole ring. The separation is easier to control in the case of a crossing angle than for a global separation. A strong, local nonlinearity can be expected to have a strong effect, but opens the possibility of a correction. Possible correction schemes are discussed in a dedicated session at this workshop [4].

STUDIES OF LONG-RANGE INTERACTIONS

Contrary to the head-on beam–beam effects, the long-range beam–beam interactions are expected to play an important role for the LHC performance and the choice of the parameters [5, 6]. To study the effect of long-range beam–beam interactions we have performed two dedicated experiments. In the first experiment, the LHC was set up with single trains of 36 bunches per beam, spaced by 50 ns. The bunch intensities were $\approx 1.2 \times 10^{11}$ protons and the normalized emittances around 2.5 μm. The trains collided in IP1 and IP5, leading to a maximum of 16 long-range encounters per interaction point for nominal bunches. First, the crossing angle (vertical plane) in IP1 was decreased in small steps and the losses of each bunch recorded. The details of this procedure are described in [7].

In the second experiment we injected 3 trains per beam, with 36 bunches per train. The filling scheme was chosen

978-92-9083-404-5, 0007-8328 –
http://dx.doi.org/10.5170/CERN–2014–004.87

such that some trains have collisions in IP1 and IP5 and others collide only in IP2 or IP8.

Losses Due to Long-range Interactions

From simulations [8] we expected a reduction of the dynamic aperture due to the long-range beam–beam encounters and therefore increased losses when the separation is decreased.

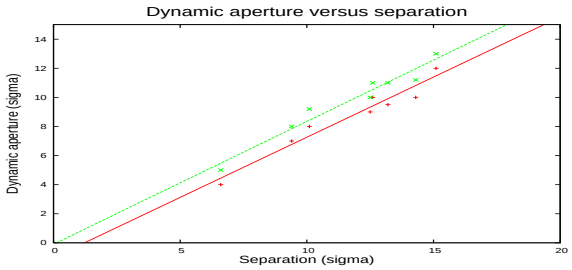

Figure 3: Expected dynamic aperture as function of separation in drift space [8]. Computed for 50 ns and 25 ns separation.

To estimate the losses, we show in Fig. 3 the expected dynamic aperture as a function of the normalized separation [8] for two different bunch spacings (50 ns and 25 ns). The separation was varied by changing the crossing angle as well as β^* . From this figure we can determine that visible (i.e. recordable) losses we can expect for a dynamic aperture around 3 σ and therefore when the separation is reduced to values around 5 σ. For larger separation the dynamic aperture is also decreased but the losses cannot be observed in our experiment.

Losses Due to Long-range Encounters During Operation

Significant losses have also been observed during regular operation. Given that the expected dynamic aperture is closely related to the normalized separation as shown in Fig. 3, this separation should be kept large enough and, if possible, constant during an operation of the machine. From the expression for the normalized separation it is clear that a change of β^* requires a change of the crossing angle α to keep the separation constant.

For the first attempt to squeeze the optical functions from β^* = 1.5 m to β^* = 1.0 m, the crossing angle was decreased to reduce the required aperture, thus reducing the separation at the encounters. During the ramp, an instability occurred which (probably) increased the emittances of all bunches, reducing further the normalized beam separation. When the optics was changed, very significant beam losses occurred (see Fig. 4) for those bunches colliding in interaction points 1 and 5, where the separation was reduced due to smaller β^* . Bunches colliding only in interaction points 2 and 8 are not affected.

This clearly demonstrates the strong effect of long-range encounter and the need for sufficient separation.

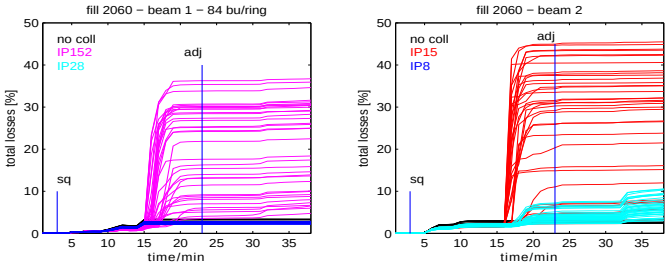

Figure 4: Losses in Beam 1 and Beam 2 with too small separation.

Losses due to Long-range Encounters during Dedicated Experiments

We have performed two measurements, and the results of the first experiment are shown in Fig. 5, where the integrated losses for the 36 bunches in Beam 1 are shown as a function of time and the relative change of the crossing angle is given as a percentage of the nominal (100% $\equiv$ 240 μrad). The nominal value corresponds to a separation of approximately 12 σ at the parasitic encounters.

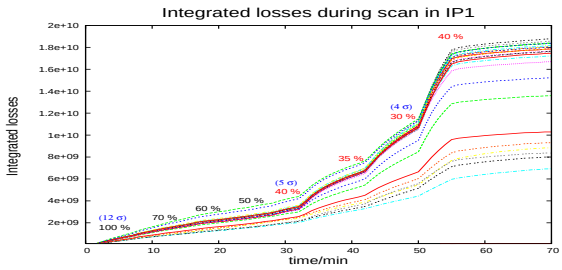

Figure 5: Integrated losses of all bunches as a function of time during scan of beam separation in IP1. Numbers show percentage of full crossing angle.

The losses per bunch observed in the second experiment are shown in Fig. 6. The observed behaviour is very similar.

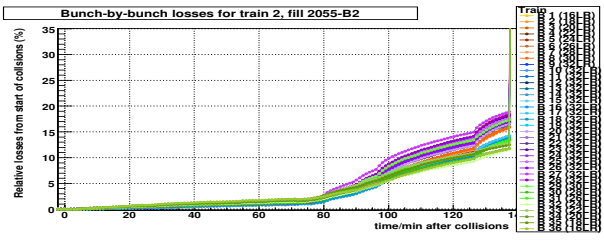

Figure 6: Integrated losses of bunches as a function of time during scan of beam separation in IP1. Bunches colliding in IP1 and IP5. Numbers show percentage of full crossing angle.

In this experiment we have set up several trains with different collision schemes and in Fig. 7 we show the losses in the bunches colliding in IP8, but not in IP1 and IP5 where

the separation was reduced. As expected, this reduction had no effect on the losses of these bunches (please note change of the scale).

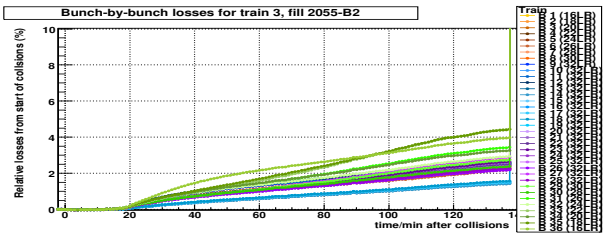

Figure 7: Integrated losses of bunches as a function of time during scan of beam separation in IP1. Bunches without collisions in IP1 and IP5. Numbers show percentage of full crossing angle.

In Fig. 8 we show the vertical emittances for all bunches during this second experiment. Such a measurement was not available in the first study.

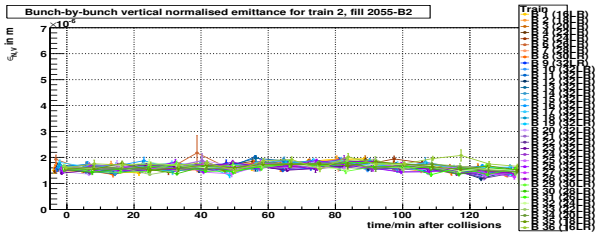

Figure 8: Vertical emittances all bunches as a function of time during scan of beam separation in IP1.

From Fig. 5 and Fig. 6 we observe significantly increased losses for some bunches when the separation is reduced to about 40%, i.e. around 5 σ. The emittances are not affected by the reduced separation (Fig. 8) and we interpret this as a reduction of the dynamic aperture as expected from the theory and simulations. The emittances, mainly determined by the core of the beam, are not affected in this case.

Bunch to Bunch Differences and PACMAN Effects

Not all bunches are equally affected. At a smaller separation of 30%, all bunches experience significant losses ($\approx$4 σ). Returning to a separation of 40% reduces the losses significantly, suggesting that mainly particles at large amplitudes have been lost during the scan due to a reduced dynamic aperture. Such behaviour is expected [8, 9]. The different behaviour is interpreted as a "PACMAN" effect and should depend on the number of long-range encounters, which varies along the train. This is demonstrated in Fig. 9 where we show the integrated losses for the 36 bunches in the train at the end of the experiment.

The maximum loss is clearly observed for the bunches in the centre of the train with the maximum number of long-range interactions (16) and the losses decrease as the

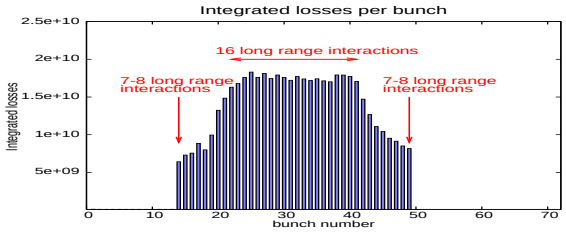

Figure 9: Integrated losses of all bunches along a train of 36 bunches, after reducing the crossing angle in IP1.

number of parasitic encounters decrease. The smallest loss is found for bunches with the minimum number of interactions, i.e. bunches at the beginning and end of the train [1, 3].

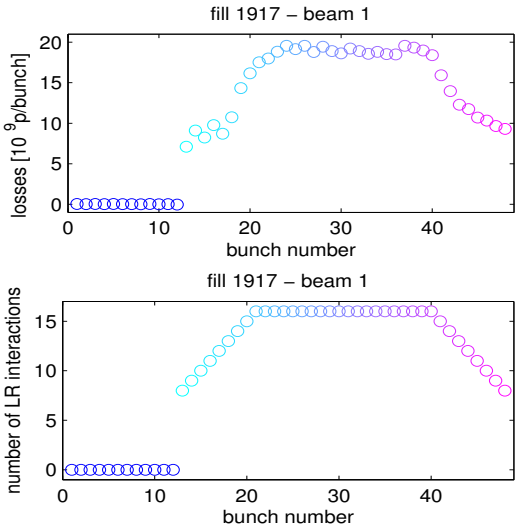

Figure 10: Integrated losses of all bunches along a train of 36 bunches, after reducing the crossing angle in IP1. The second figure shows number of long-range encounters for the same bunches.

This is demonstrated in Fig. 10, where we show the integrated losses, and in the second figure for the same bunches the number of long-range encounters. The agreement is rather obvious. This is a very clear demonstration of the expected different behaviour, depending on the number of interactions.

In the second part of the experiment we kept the separation at 40% in IP1 and started to reduce the crossing angle in the collision point IP5, opposite in azimuth to IP1 (Fig. 1). Due to this geometry, the same pairs of bunches meet at the interaction points, but the long-range separation is in the orthogonal plane. This alternating crossing scheme was designed to compensate first-order effects from long-range interactions [1].

Figure 11 shows the evolution of the luminosity in IP1 as we performed the scan in IP5. The numbers indicate again the relative change of separation, this time the horizontal crossing angle in IP5. The luminosity seems to show

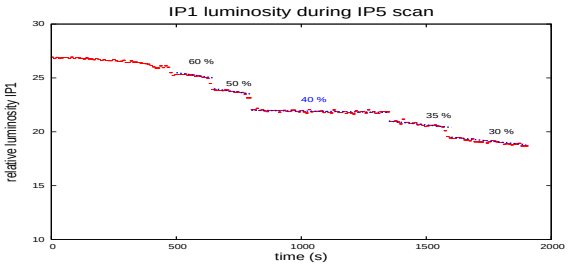

Figure 11: Luminosity in IP1 as a function of time during scan of beam separation in IP5.

that the lifetime is best when the separation and crossing angles are equal for the two collision points. It is worse for smaller as well as for larger separation. This is the expected behaviour for a passive compensation due to alternating crossing planes, although further studies are required to conclude. A more quantitative comparison with the expectations is shown in Fig. 12. The dynamic aperture in units of the beam size is shown as a function of the beam separation [8].

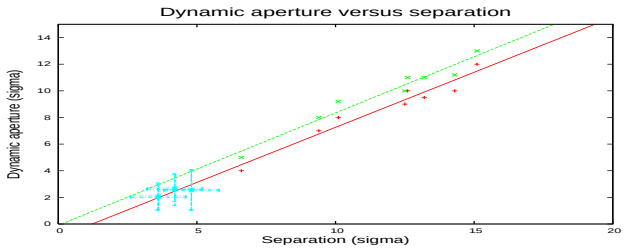

Figure 12: Dynamic aperture versus separation. Comparison with results from experiment.

From the relative losses in the experimental studies, we have tried to estimate the dynamic aperture, assuming a Gaussian beam profile and tails. This measurement can obviously only give a rough estimate, but is in very good agreement with the expectations. At larger separation, the losses are too small to get a reasonable estimate. More information can be obtained from an analytical model [10, 11].

Further Observations of PACMAN Effects

The behaviour of so-called PACMAN bunches [3, 12] was always a concern in the design of the LHC. In order to avoid a tune shift of PACMAN bunches relative to the nominal bunches, an alternating crossing scheme was implemented in the LHC [3]. The effect of the alternating crossing scheme on the tune along a bunch train is shown in Fig. 13. The computation is based on a self-consistent calculation of orbits and all optical beam parameters [13].

Without the alternating crossing, the PACMAN bunches exhibit a strong dependence of their tunes on their position in the bunch train. Depending on the intensity, bunch spacing and separation, this spread can exceed 2×10^{-3}.

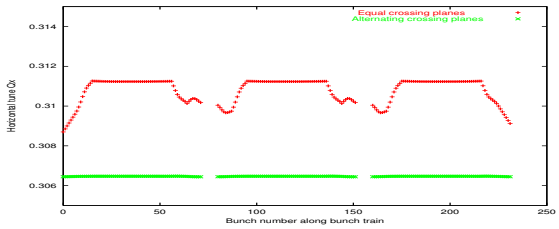

Figure 13: Computed tune along bunch train for equal and alternating crossing planes [1, 3].

The alternating crossing scheme compensates completely for this spread. This compensation is incomplete when bunch to bunch fluctuations are taken into account, but in all cases the compensation is efficient [3]. This compensation is largely helped by the design feature that the two low β^* experimental regions are exactly opposite in azimuth (see Fig. 1) [2] and the same bunch pair collide in the two regions with alternating crossings and the same optical parameters. This requires that the contribution to the long-range beam–beam effects from the other two experiments is small. Due to the larger β^* this is guaranteed under nominal operational conditions.

Another predicted behaviour of PACMAN bunches are the different orbits due to the long-range interactions. The decreased separation, corresponding to stronger dipolar kicks, clearly lead to orbit changes along the corresponding bunch train. The bunches not participating in collisions in IP1 and IP5 are not affected. To study these effects, a fully self-consistent treatment was developed to compute the orbits and tunes for all bunches in the machine under the influence of the strong long-range beam–beam interactions [13]. Figures 14 and 15 show the vertical orbit offsets at IP1 for the two beams in the case of vertical crossings in IP1 and IP5.

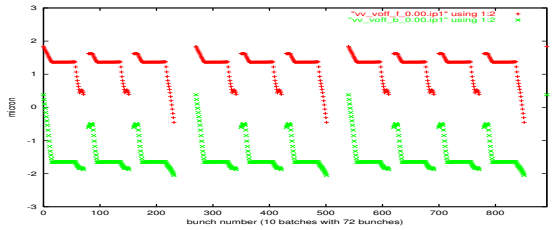

Figure 14: Computed orbit offsets in IP1 for Beam 1 and Beam 2 two vertical crossings [1, 3, 13].

The figures show a significant effect at the interaction point, and, moving the beams, it is not possible to make all bunches overlap.

The effect of alternating crossings (vertical in IP1 and horizontal in IP5) is shown in Fig. 15. Now the bunches from the two beams can be made overlap exactly, although not at the central collision point. In the other plane this complete overlap cannot be obtained, although the offset is small.

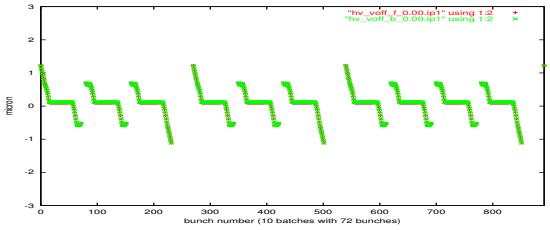

Figure 15: Computed orbit offsets in IP1 for Beam 1 and Beam 2 alternating crossings [1, 3, 13].

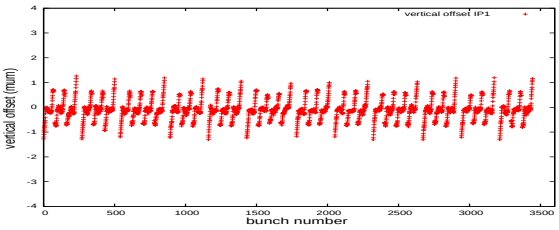

Figure 16: Computed orbit offsets in IP1 along the bunch train [1, 3].

In Fig. 16 we show a prediction for the vertical offsets in IP1 [1, 3]. The offsets should vary along the bunch train. Although the orbit measurement in the LHC is not able to resolve these effects, the vertex centroid can be measured bunch by bunch in the experiment.

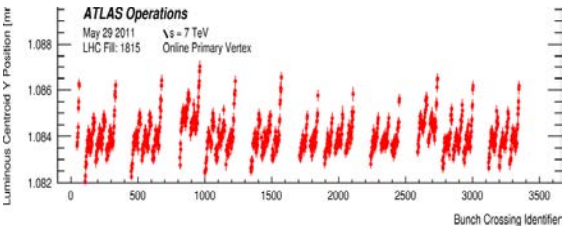

Figure 17: Measured orbit offsets in IP1 along the bunch train [14, 15].

The measured orbit in IP1 (ATLAS experiment) is shown in Fig. 17 and at least the qualitative agreement is excellent. This is a further strong indication that the expected PACMAN effects are present and understood and that our computations are reliable.

PARAMETRIC DEPENDENCE OF LONG-RANGE LOSSES

In order to study the dependence of long-range effects on the parameters of the beam–beam interaction, we have performed the experiments with different parameters, in particular different β^* and intensities. The relevant parameters of the three experiments are found in Table 1.

The experimental procedure was the same as before: the separation (crossing angle) was reduced until visible losses were observed.

Table 1: Parameters for three long-range experiments

Experiment	Emittance	β^*	Intensity
2011 (50 ns)	2.0 - 2.5 μm	1.5 m	1.2 10^{11}
2012 (50 ns)	2.0 - 2.5 μm	0.6 m	1.2 10^{11}
2012 (50 ns)	2.0 - 2.5 μm	0.6 m	1.6 10^{11}

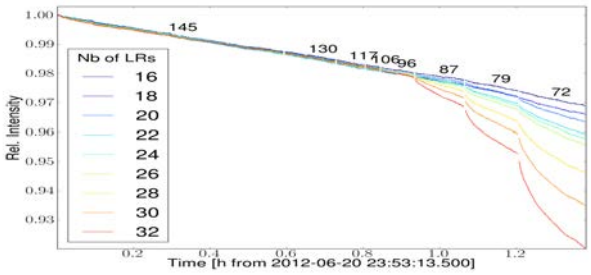

Figure 18: Separation scan with high intensity.

The results of a first separation scan are shown in Fig. 18. The main observations are as follows:

- Recent test (2012) with β^* = 0.60m, intensity: 1.6 10^{11} p/bunch
- Initial beam separation $\approx$ 9 - 9.5 σ
- Losses start at $\approx$ 6 σ separation

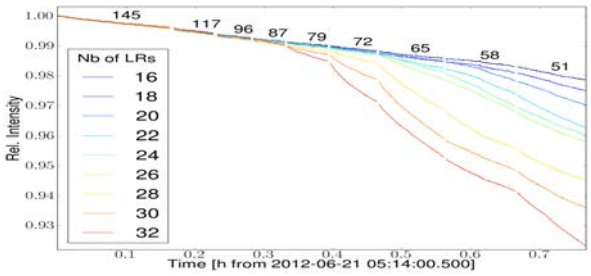

Figure 19: Separation scan with reduced intensity.

The results of a second separation scan are shown in Fig. 19. The main observations are as follows:

- Recent test (2012) with β^* = 0.60 m, intensity: 1.2 10^{11} p/bunch.
- Initial beam separation $\approx$ 9 - 9.5 σ.
- Losses start at $\approx$ 5 σ separation.

The experiments summarized in Tab. 1 have been analysed using a recently developed technique to parametrize the strength of the long-range non-linearity, based on the evaluation of the invariant and the smear [10, 11].

This method is applied to compare different configurations [11] and allows us to derive scaling laws for the dynamic aperture.

SUMMARY

We have reported on the first studies of beam–beam effects in the LHC with high intensity, high brightness beams and can summarize the results as follows.

- The effect of the beam–beam interaction on the beam dynamics is clearly established.
- The effect of long-range interactions on the beam lifetime and losses (dynamic aperture) is clearly visible.
- The number of head-on and/or long-range interactions important for losses and all predicted PACMAN effects are observed.

All observations are in good agreement with the expectations and an analytical model [11]. From this first experience we have confidence that beam–beam effects in the LHC are understood and should allow us to reach the target luminosity for the nominal machine at 7 TeV beam energy. The analytical model [11] should allow us to extrapolate the results to different configurations and allow an optimization of the relevant parameters.

ACKNOWLEDGEMENTS

These studies would have been impossible without the help and support from the operations teams for the LHC and its injectors. We are also grateful to the LHC experiments for the collaboration during our studies and for providing us with luminosity and background data.

REFERENCES

[1] W. Herr, Features and implications of different LHC crossing schemes, CERN LHC Project Report 628 (2003).

[2] G. Papotti *et al.*, "Observations of Beam–Beam Effects in the LHC," these proceedings.

[3] W. Herr, "Dynamic Behaviour of Nominal and PACMAN Bunches for Different LHC Crossing Schemes," CERN LHC Project Report 856 (2005).

[4] W. Fischer, "Beam–Beam Compensation Schemes," these proceedings.

[5] T. Pieloni *et al.*, "Beam–Beam Studies in the LHC and New Projects," these proceedings.

[6] G. Trad *et al.*, "Beam–Beam Effects with a High Pile-up Test in the LHC," these proceedings.

[7] W. Herr *et al.*, "Head-on Beam–Beam Interactions with High Intensities and Long Range Beam–Beam Studies in the LHC," CERN-ATS-Note-2011-058 (2011).

[8] W. Herr and D. Kaltchev, "Results of Dynamic Aperture Studies with Increased β^* with Beam–Beam Interactions," LHC Project Note 416 (2008).

[9] W. Herr *et al.*, "Large Scale Beam–Beam Simulations for the CERN LHC using Distributed Computing," Proc. European Partical Accelerator Conference, Edinburgh, 2006 (published by European Physical Society Accelerator Group, Geneva, 2006).

[10] W. Herr and D. Kaltchev, "Analytical Calculation of the Smear for Long Range Beam–Beam Interactions," Partical Accelerator Conference, Vancouver, 2009, unpublished.

[11] D. Kaltchev, "Analysis of Long Range Studies in the LHC – Comparison with the Model," these proceedings.

[12] D. Neuffer and S. Peggs, "Beam–Beam Tune Shifts and Spreads in the SSC: Head-on, Long Range, and PACMAN Conditions," SSC Report, SSC-63 (1986).

[13] W. Herr and H. Grote, "Self-consistent Orbits with Beam–Beam Effects in the LHC," Proc. Workshop on Beam–Beam Effects, 2001, FNAL 25.6.-27.6.2001 (2001).

[14] W. Kozanecki and J. Cogan, private communication (2011).

[15] R. Bartoldus, "Online Determination of the LHC Luminous Region with the ATLAS High Level Trigger," 2011, International Conference on Technology and Instrumentation in Particle Physics, Chicago 2011, Ed. T. Liu (Elsevier, Chicago, 2012), Vol. 37.

Published by CERN in the Proceedings of the ICFA Mini-Workshop on Beam–Beam Effects in Hadron Colliders,
CERN, Geneva, Switzerland, 18–22 March 2013, edited by W. Herr and G. Papotti, CERN–2014–004 (CERN, Geneva, 2014)

ANALYSIS OF LONG-RANGE STUDIES IN THE LHC – COMPARISON WITH THE MODEL

D. Kaltchev, TRIUMF, Vancouver, Canada, W. Herr, CERN, Geneva, Switzerland

Abstract

We find that the observed dependencies (scaling) of long-range beam–beam effects on the beam separation and intensity are consistent with the simple assumption that, all other parameters being the same, the quantity preserved during different set-ups is the first-order smear as a function of amplitude.

INTRODUCTION

The Proposed Method

In several Machine Development (MD) studies (see Ref. [1] and the references therein), reduced crossing angles have been used to enhance long-range beam–beam effects and thus facilitate their measurement. The basic assumption made in this paper is that under such conditions, a single non-linearity, the one caused by beam–beam, dominates the dynamics. Hence the method followed: we choose some simple low-order dynamical quantity that characterizes phase space distortion and assume that when this quantity is the same, the behaviour of the system is the same. A most obvious candidate is the first-order smear – the r.m.s. deviation of the phase-space ellipse from the perfect one. At a fixed amplitude, smear is defined as the averaged generalized Courant–Snyder invariant over the angle variable [2].

An analytical expression has previously been found [2] for the smear S as a function of amplitude n_σ. Suppose that the parametric dependence of $S(n)$ on several beam–beam related parameters – the relativistic γ, the number of particles per bunch N_b, the crossing angle α, and the normalized separations $n_{\mathrm{l.r.}}$ – is known. According to the above assumption, for two machine configurations *a* and *b* one should have

$$S(n_\sigma; N_b^a, n_{\mathrm{l.r.}}^a, \alpha^a, \gamma^a) = S(n_\sigma; N_b^b, n_{\mathrm{l.r.}}^b, \alpha^b, \gamma^b). \quad (1)$$

As a particular application of Eq. (1), we considered two experiments where the intensities are N_b^a and N_b^b. All other parameters being the same, given α^a, one can compute the expected α^b. Our task will be to show that the result agrees with observations.

Analytical Calculation of Invariant and Smear

Our derivation of $S(n_\sigma)$ is based on the Lie algebraic method – concatenation of Lie-factor maps – and is valid only to first order in the beam–beam parameter and in one-dimension, in either the horizontal or the vertical plane, but for an arbitrary distribution of beam–beam collisions, head-on or long-range, around the ring.

For a ring with a *single head-on collision point*, Hamiltonian perturbation analysis of the beam–beam interaction without or with a crossing angle has been done by a number of authors, mostly in the resonant case. Non-linear invariants of motion, both non-resonant and resonant, were analysed by Dragt [3], with the one-turn map as observed immediately after the kick being

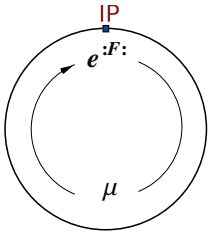

$$R\, \mathrm{e}^{:F:} = \mathrm{e}^{:h:}. \quad (2)$$

Here, $R = \mathrm{e}^{:f_2:}$ is the linear one-turn map and the kick factor F is the beam–beam potential (or Hamiltonian). For small perturbations and far from resonances, particle coordinates in phase space are restricted on the Poincaré surface of section

$$h = \mathrm{const}. \quad (3)$$

A detailed derivation of h to first order in the beam–beam perturbation strength can be found in A. Chao's lectures:

$$h(J,\phi) = -\mu J + \sum_{n=-\infty}^{\infty} c_n^{(\mathrm{ho})}(J) \frac{n\,\mu}{2\sin\frac{n\mu}{2}} \mathrm{e}^{in(\phi+\mu/2)}, \quad (4)$$

where μ is the ring phase advance and $c_n^{(\mathrm{ho})}(J)$ are coefficients in the Fourier expansion of F, when the latter is rewritten in action-angle coordinates J, ϕ. The coefficients are shown to be related to the modified Bessel functions. Analytical expressions for the invariant h, the first-order smear, and the second-order detuning for the case of non-linear multipole kicks distributed in an arbitrary way around the ring have been derived by Irvin and Bengtsson [4]. Smear, the distortion of the ideal phase-space ellipse, is formally defined in Ref. [5]. Finally, note that extracting the smear is a natural step in the procedure that brings the map into its normal form [6].

In Ref. [7], following the Lie algebraic procedure in Refs. [8] and [4], we generalized Eq. (4) to describe multiple head-on kicks (IP1 and IP5) for the case of the LHC. In Ref. [2], an expression was presented that was valid for an arbitrary number of head-on (h.o.) and long-range (l.r.) collisions. This expression, to be derived in detail next, has been used on several occasions to interpret results from SixTrack simulations.

978-92-9083-404-5, 0007-8328 –
http://dx.doi.org/10.5170/CERN–2014–004.93

DERIVATION OF THE INVARIANT

Multiple Collision Points

The horizontal betatronic motion of a weak-beam test particle depends on its initial amplitude n_σ (in units of σ) and the collision set: a set of all h. o. and l. r. collisions, also known as Interaction Points (IPs), that this particle sees over a single revolution. Let us label the set with an index k, limiting ourselves to only IPs located within the main interaction regions IR5 (horizontal crossing) and IR1 (vertical crossing). In the case of 50 ns bunch spacing, k ranges from 1 to 34, which includes 32 long-range IPs ($N_{\text{l. r.}} = 32$).

The Lie map depends on the above-defined collision set through the normalized separations $n_{x,y}^{(k)} = d_{x,y}^{(k)}/\sigma^{(k)}$ and the unperturbed horizontal betatronic phases $\phi^{(k)}$ at the IPs. Here, $d_{x,y}$ is the real-space offset of the strong-beam centroid in the x or y direction, and it has been assumed that both the weak- and strong-beam transverse distributions are round Gaussians of the same r.m.s. That is:

$$\sigma^{(k)} = \sqrt{\beta^{(k)}\epsilon} \quad (\beta_x^{(k)} = \beta_y^{(k)} \equiv \beta^{(k)}). \tag{5}$$

In Eq. (5), $\beta^{(k)}$ are the beta functions and ϵ is the emittance. It will be shown below that off-plane collisions contribute very little to smear; thus after excluding these, the problem becomes one-dimensional and may easily be illustrated (see Fig. 1). Here, $n_x^{(k)}$ are the strong-beam centroids in amplitude space: points $(s^{(k)}, n_x^{(k)})$, with s being the distance to IP5 in metres.

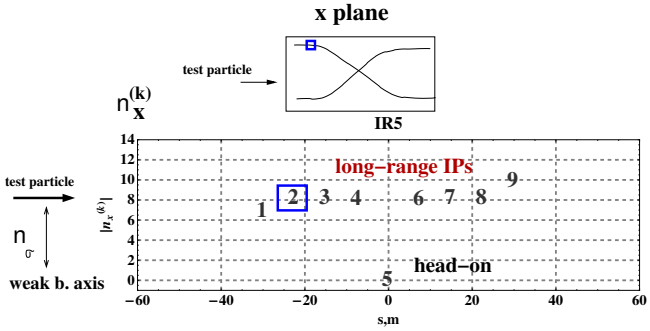

Figure 1: A schematic view of weak- and strong-beam trajectories in real (top) and amplitude (bottom) spaces. A reduced set is used: $N_{\text{l. r.}} = 8 + 8 = 16$ ($k = 1, 18$).

The Beam–Beam Hamiltonian

For a single collision (see Eq. (2)), by omitting the superscript k in σ and $n_{x,y}$, the x-motion is described by a kick factor F (or Hamiltonian H) [2]:

$$F = -H(x) = \int_0^P (1 - \mathrm{e}^{-\alpha})\frac{\mathrm{d}\alpha}{\alpha} = \tag{6}$$

$$= \overline{\gamma} + \Gamma_0(P) + \ln(P)\,, \tag{7}$$

$$P = P(x) = \frac{1}{2}\left[(n_x + \frac{x}{\sigma})^2 + n_y^2\right]\,,$$

where F is in units of $\lambda \equiv \frac{N_b r_0}{\gamma}$, r_0 is the classical particle radius, $\Gamma_s(P) \equiv \Gamma(s, P)$ denotes the upper incomplete gamma function [9], and $\overline{\gamma}$ = 0.577216 is Euler's constant. The corresponding beam–beam kick is as follows:

$$\Delta x' \equiv \frac{\mathrm{d}}{\mathrm{d}x}F(x) = \frac{\partial F}{\partial P}\frac{\mathrm{d}P}{\mathrm{d}x} =$$

$$= \frac{2(x+n_x\sigma)}{(x+n_x\sigma)^2+(n_y\sigma)^2}\left[1 - \mathrm{e}^{-\frac{(x+n_x\sigma)^2+(n_y\sigma)^2}{2\sigma^2}}\right]. \tag{8}$$

The Fourier expansion of H is as follows:

$$H(n_\sigma, \phi) = \sum_m \mathcal{C}_m \mathrm{e}^{im\phi}\,, \tag{9}$$

where $\mathcal{C}_m \equiv \frac{1}{2\pi}\int_0^{2\pi} \mathrm{e}^{-im\phi} H \;\mathrm{d}\phi$. These coefficients are easily computed numerically by using the implementation of Γ in *Mathematica* [2]. Further, analytical expressions in the form of single integrals over Bessel functions have been derived in Ref. [10]. We display these again in the simplified case $n_y = 0$ (no off-plane collisions):

$$\mathcal{C}_m|_{n_y=0} = \int_0^1 \frac{\mathrm{d}t}{t} \times$$

$$\begin{cases} [1 - \mathrm{e}^{-\frac{t}{2}n_x^2}\mathrm{e}^{-\frac{t}{4}n_\sigma^2}\sum_{k=-\infty}^{\infty} I_{-2k}(t\,n_\sigma n_x) I_k(-\frac{t}{4}n_\sigma^2)] \\ \text{if } m = 0 \quad \text{and} \\ -\mathrm{e}^{-\frac{t}{2}n_x^2}\mathrm{e}^{-\frac{t}{4}n_\sigma^2}\sum_{k=-\infty}^{\infty} i^m I_{m-2k}(t\,n_\sigma n_x) I_k(-\frac{t}{4}n_\sigma^2) \\ \text{if } m \neq 0. \end{cases}$$

In the head-on case ($n_x^{(k)} = n_y^{(k)} = 0$), the coefficients $\mathcal{C}_m$ reduce to the $c_m^{(\text{ho})}$ from Ref. [8]. Note that in the most interesting case, amplitudes near the dynamic aperture, both n_σ and n_x and hence the Bessel function arguments are large ($\gg 1$).

Our first step is to remove the linear and quadratic parts $F_{(1)} = \frac{\partial F}{\partial x}\big|_{x=0} x$ and $F_{(2)} = \frac{1}{2}\frac{\partial^2 F}{\partial x^2}\Big|_{x=0} x^2$. The nonlinear kick factor and the corresponding kick are as follows:

$$F_{\text{nonl}} = F - F_{(1)} - F_{(2)}\,, \tag{10}$$

$$\Delta x'_{\text{nonl}} \equiv \frac{d}{dx}F_{\text{nonl}}(x)\,.$$

As a next step, we rewrite Eq. (10) in action-angle coordinates J, ϕ by substituting in it $x = \sqrt{2J\beta}\sin\phi = n_\sigma\sigma\sin\phi$, where $n_\sigma = \sqrt{2I} = \sqrt{2J/\epsilon}$ is the test particle amplitude (Eq. (A.1)). Next, we expand in Fourier series:

$$F_{\text{nonl}}(n_\sigma\,\sigma\,\sin\phi) = c_0 + \sum_{m\neq 0} c_m \mathrm{e}^{im\phi}\,. \tag{11}$$

The coefficients c_m are naturally the same as $\mathcal{C}_m$ above, with the exception of c_1 and c_2, which contain additional sin and $\sin^2$ terms (see Eq. (A.1)).

Lie Map and Invariant

For an arbitrary set of collisions $n_x^{(k)}$, $\phi^{(k)}$ $(k = 1, N)$, we represent the LHC lattice by a combination of linear elements and non-linear kicks. It is shown in the Appendix that, to first order in λ, the Lie map has the same form as the one for a single kick (2) – where, however, the factor F is given by the sum

$$F \equiv \sum_{k=1}^{N} F_{\rm nonl}^{(k)}(n_\sigma, \phi)$$

and $F_{\rm nonl}^{(k)}$ are such that, compared to Eq. (11), the kth IP participates with a phase shifted by $\phi^{(k)}$:

$$F_{\rm nonl}^{(k)}(n_\sigma, \phi) \equiv F_{\rm nonl}^{(k)}(x)\Big|_{x \,\to n_\sigma \,\sigma^{(k)}\, sin(\phi+\phi^{(k)})} = \\ = \sum_{m\neq 0} C_m^{(k)} {\rm e}^{im\phi}\,. \qquad (12)$$

The shift in phase means that the coefficients in Eq. (12) are simply related to $c_m^{(k)}$: $C_m^{(k)} \equiv c_m^{(k)} {\rm e}^{im\phi^{(k)}}$ and still satisfy $C_{-m} = C_m^\star$. Another important property of the expansion is that only the oscillating part is taken (the $m = 0$ term is excluded). The invariant for multiple collision points is as follows (see the Appendix):

$$h(I,\phi) = -\mu J - \lambda \sum_{k=1}^{N}\sum_{m=1}^{\infty} \frac{m\,\mu\, c_m^{(k)}(I)}{2\sin\left(\frac{m\mu}{2}\right)} {\rm e}^{im(\phi+\mu/2+\phi^{(k)})} \\ + c.c.$$

The surface of the section in phase space is given by $h(I, \phi) = {\rm const}$. A natural initial condition is now imposed: that the initial point in phase space for a particle starting at $x_0 = n_\sigma\sigma$ – that is, with an amplitude $I_0 \equiv J_0/\epsilon = n_\sigma^2/2$ – lies on the curve representing the invariant:

$$h(I,\phi) = h(I_0, \pi/2), \qquad (13)$$

For a fixed I_0, this equation implicitly defines I as a function of ϕ. It satisfies the initial condition $I(0) = I_0$:

$$I(\phi) = I_0 + \sum_{k=1}^{N} \left({\rm d}I^{(k)}(\phi) - {\rm d}I^{(k)}(0) \right)\,,$$

$$ {\rm d}I^{(k)}(\phi) = \qquad (14) \\ = \frac{\lambda}{\epsilon} \sum_{m=1}^{M} \left(\frac{m\, c_m^{(k)}(I_0)}{2\sin(m\mu/2)} {\rm e}^{im(\mu/2+\phi-\phi^{(k)}+\pi/2)} + c.c. \right).$$

Note that, to first order, the argument in $c_m^{(k)}$ has been replaced with I_0. We have also separated the two sums so that ${\rm d}I^{(k)}(\phi) - {\rm d}I^{(k)}(0)$ is the individual contribution of the kth IP. In the same way, a different initial condition may be used (more suitable for plots): $I(0) = I_0$, instead of $I(\pi/2) = I_0$.

The smear $S(n_\sigma)$ is now defined as the normalized r.m.s. of the invariant – that is, $\sqrt{V}$, with V being the variance:

$$S(n_\sigma) = \sqrt{V}/\langle\, I\,\rangle\,,$$
$$V = \tfrac{1}{2\pi}\int (I - \langle I\rangle)^2 {\rm d}\phi\,, \quad \langle I\rangle = \tfrac{1}{2\pi}\int I {\rm d}\phi\,.$$

VERIFICATION WITH TRACKING

As an example application, this section studies the very simple collision set that still possesses all the symmetries with the l.r. set at 8 sigma, as depicted in Fig. 2. Both IR5 and IR1 are included. The goal here is to test the invariant $I(\phi)$ by tracking with a simple model built with kicks $\Delta x'_{\rm nonl}$ alternating with linear matrices and SixTrack. The parameters are as follows: energy 3.5 TeV, $N_{\rm b} = 1.2 \times 10^{11}$, and normalized emittance $\epsilon_n = 2.5 \times 10^{-6}$. Tracking single particles at various amplitudes with the

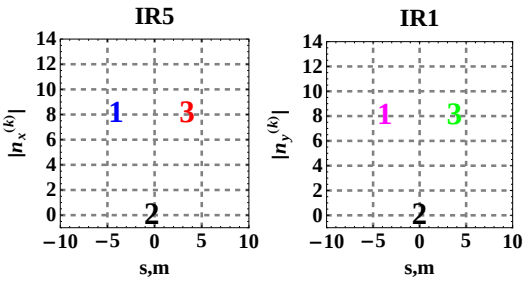

Figure 2: The sample set-up: three collisions in each IR5 and IR1. The l.r. are set at 8 sigma.

simple model produces the results shown in Fig. 3. A particle starts with $n_\sigma = 3$, or 7 ($I_0 = 4.5$, or 24.5). The c_m are computed with an accuracy of 10^{-7} – the value of M in Eq. (15) is about 40. Since the beam–beam poten-

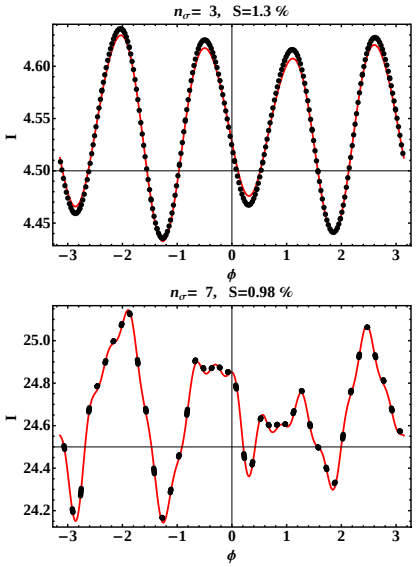

Figure 3: An invariant tested on a simple kick-matrix model. Black points: turn-by-turn coordinates (ϕ, I) for 10^3 turns. Red: invariant $I(\phi)$ (initials chosen so that $I(\pi/2) = I_0$).

tial changes the linear optics, we need to find the linearly perturbed matched β-function value at the initial point for tracking. For the plots in Fig. 3, this is done in a separate run, using a linear kick $(\Delta x')_{\rm lin}$ (only terms $\sim x^2$ in the Hamiltonian). This is similar to what is done in SixTrack. The resultant matched β is used to define the initial coordinate x_0 (through n_σ). The values of the smear are shown at the top of each plot.

Plotting the smear over a range of amplitudes with all three methods – model, SixTrack, and analytical $S(n_\sigma)$ – results in Fig. 4. Note that here the images of the strong-beam centroids (see Fig. 1) are represented by vertical grey lines drawn at 0 and 8 sigma. Let us now look at the individual contributions to $I(\phi)$ of the six IPs at three amplitudes chosen arbitrarily; say, $n_\sigma = 1, 3$, and 7. The excursions (w.r.t. I_0) of the individual invariant surfaces are shown in Fig. 5. Here, $I(0) = I_0$. The colour code is as in Fig. 2, and in addition for the head-ons we use solid black for IP5 and dashed for IP1. Near the axis ($n_\sigma = 1$), only the two head-ons contribute and, being of opposite signs, almost compensate each other. At $n_\sigma = 3$, one begins to see long-range contributions that grow when $n_\sigma = 7$. At such large amplitudes, the compensation is no longer true. Magenta and green are barely seen, meaning that the contribution of off-plane collisions is negligible. Thus in the case of a test particle moving in the horizontal motion, the contribution of all l.r. in IR1 can be neglected, and vice versa for vertical motion and IP5.

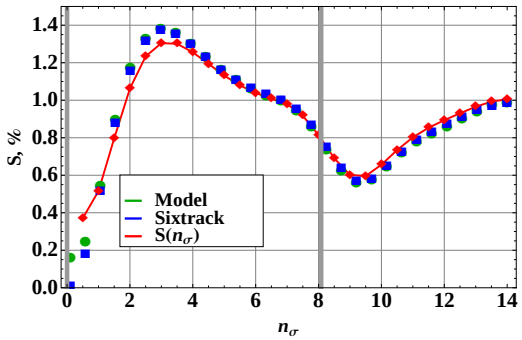

Figure 4: Agreement with SixTrack.

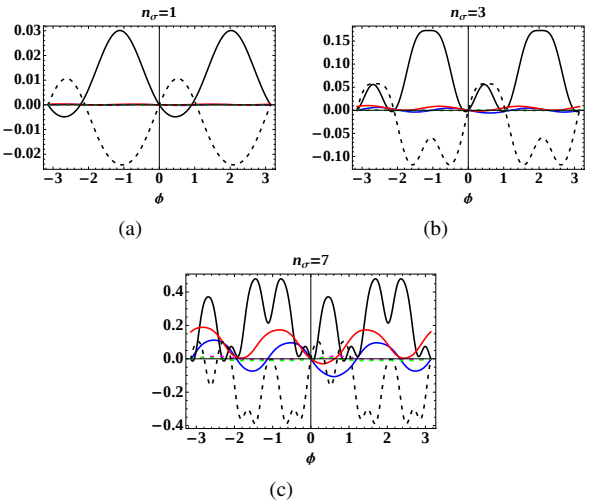

Figure 5: Individual contributions $dI^{(k)}(\phi) - dI^{(k)}(0)$ – color code as in Fig. 2.

THE BEHAVIOUR OF THE SMEAR $S(n_\sigma)$ NEAR THE DYNAMIC APERTURE

Above some critical strength of beam–beam interaction – that is, quantities $N_{\rm l.\,r.}$ and/or $N_{\rm b}$ and/or an inverse crossing angle – the first-order theory is no longer an adequate description of the smear. However, as we will see, the behaviour of $S(n_\sigma)$ may still be used as an indication of the dynamic aperture, since it exhibits a local maximum near it. What happens is that the linear behaviour – that is,

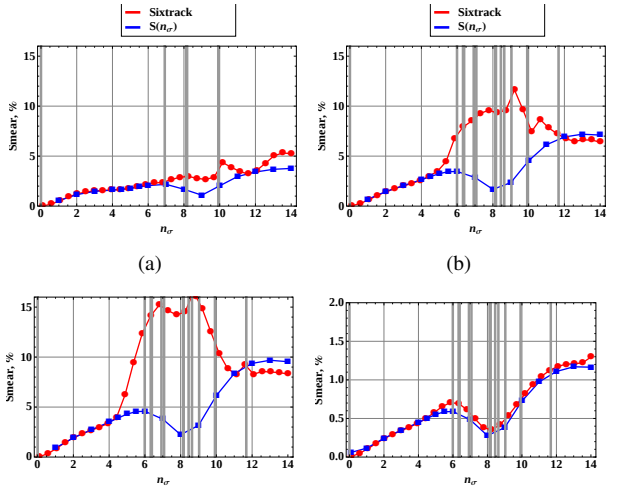

Figure 6: Various combinations of numbers of long-range collisions and bunch intensities to illustrate linear and nonlinear behaviour:

	$N_{\rm l.\,r.}$	$N_{\rm b}$
(a)	16	1.2×10^{11}
(b)	32	1.2×10^{11}
(c)	32	1.6×10^{11}
(d)	32	0.2×10^{11}

the agreement between the first-order S and SixTrack at all amplitudes seen in Fig. 4 – is replaced by what is shown in Figs. 6(a)–(c). The blue ($S(n_\sigma)$) and the red (SixTrack) curves depart from each other once n_σ approaches amplitudes near the strong-beam core, represented by the cluster of vertical grey lines. At this point, the exact smear (red) exhibits a steep growth; thus the dynamic aperture is likely to be close to this point, while S goes through a maximum and then through a minimum, thus forming a dip. Upon exiting the core, past the last grey line, the red and blue curves almost re-merge. It can be shown that the above property of $S(n_\sigma)$ is a consequence of the left–right symmetry of IR5 and IR1. Namely, the individual contributions (such as the

red and blue curves in Fig. 2) change sign or flip about the axis each time n_σ crosses a grey line. At this amplitude, $S(n_\sigma)$ stops growing and goes through a maximum.

ANALYSIS OF LONG-RANGE EXPERIMENTS

Dependence on Intensity and Crossing Angle

We set the parameters as at the MD: energy 3.5 TeV, $\epsilon_n = 2.5 \times 10^{-6}$ [11], and $\beta^\star = 0.6$ m.

Of all the collision sets used at the MD, let us consider three: $N_{\mathrm{l.r.}} = 32$, 24, and 16. For each of them, two parameters, the bunch intensity N_b and the (half) crossing angle α, uniquely define the dependence of the first-order smear on amplitude $S(n_\sigma; N_\mathrm{b}, \alpha)$ through the following procedure. First, being a first-order quantity in λ, the smear is obviously proportional to the intensity: $S \sim N_\mathrm{b}$. Second, the dependence of $n_{x,y}^{(k)}$ on the (half) crossing angle α is given by the well-known scaling law: $n_{x,y}^{(k)} \sim \alpha\sqrt{\beta^\star}$, where $n_{x,y}^{(k)}$ are taken from some sample lattice built for $\beta^\star = 0.55$ m and $\alpha = 125$. Finally, the phases $\phi^{(k)}$ are assumed to be independent of α.

The dependence on the angle is presented in Fig. 7. Each blue branch corresponds to $S(n_\sigma; 1.2{\times}10^{11}, \alpha)$ being taken over an amplitude range where it is monotonically increasing; hence, as we already know, it will remain in agreement with the tracking for any strength of the beam–beam interaction.

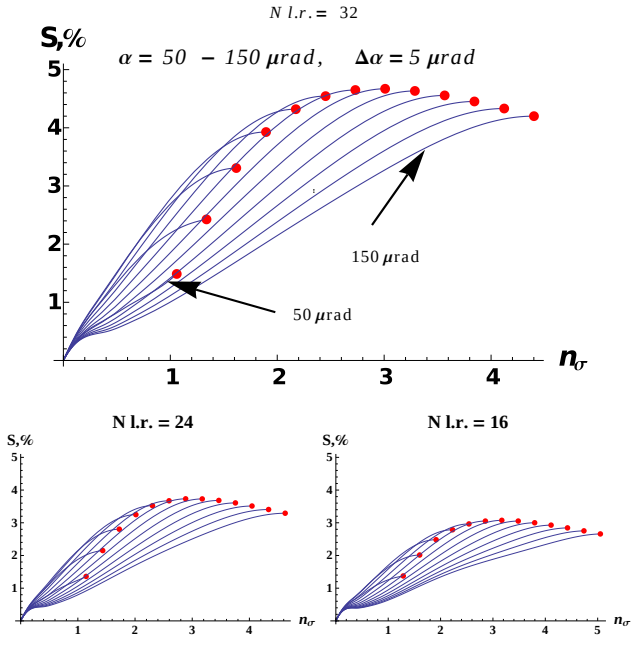

Figure 7: The dependence of the smear(amplitude) graph on the parameter α for $N_{\mathrm{l.r.}} = 32$ (top) and $N_{\mathrm{l.r.}} = 24$, 16 (bottom). Each graph is restricted within a domain extending up to its first maximum (red dot) (the entrance into the strong-beam core).

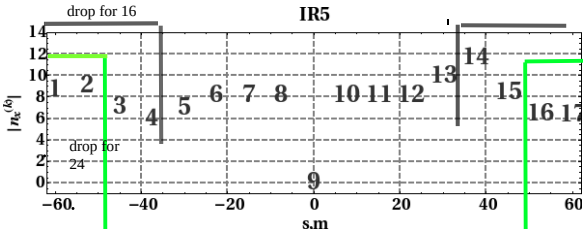

Figure 8: The collision sets for $N_{\mathrm{l.r.}}$ =24 and 16 are built by dropping the first and last two or four elements from the full set ($N_{\mathrm{l.r.}} = 32$).

Coming now to the MD, the observed losses during reduction of the crossing angle in IP1 are shown in Figs. 9 and 10 [1].

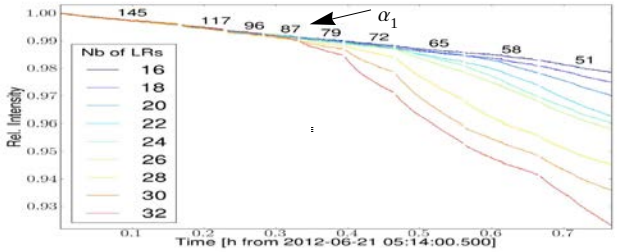

Figure 9: An experiment with $N_\mathrm{b} = 1.2 \times 10^{11}$: losses start at $\alpha_1 \approx 87$ μrad.

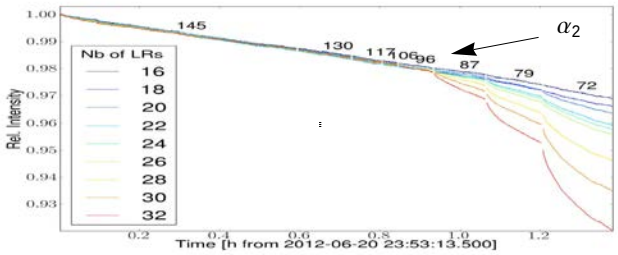

Figure 10: An experiment with $N_\mathrm{b} = 1.6 \times 10^{11}$: losses start at $\alpha_1 \approx 96$ μrad.

An Explanation of the Case $N_{\mathrm{l.r.}} = 32$ (Brown Curves)

For $N_{\mathrm{l.r.}} = 32$ (the full 50-ns collision set shown in Fig. 8), we need to explain the brown curves in Figs. 9 and 10. Here, losses are seen to start at $\alpha_1 \approx 87$ and $\alpha_2 \approx 96$ μrad, respectively.

In view of our previous findings, the off-plane losses (in IR5) are neglected and by using the postulate made in the Introduction (Eq. 1), we have:

$$S(n_\sigma; 1.2 \times 10^{11}, \alpha_1) = S(n_\sigma; 1.6 \times 10^{11}, \alpha_2), \quad (15)$$

which is to be solved for the angles.

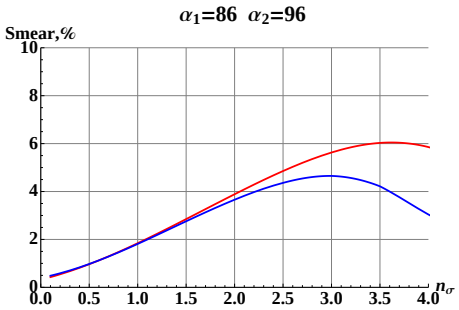

Figure 11: Graphs of $S(n_\sigma; 1.2 \times 10^{11}, 86)$ (red) and $S(n_\sigma; 1.6 \times 10^{11}, 96)$ (blue). The smear is seen to be $\approx 3\%$ at 1.5 σ.

Figure 11 shows that a good solution to Eq. (15) consists of the values $\alpha_1 = 86$, $\alpha_2 = 96$ μrad. Indeed, this figure shows that Eq. (15) is fulfilled not in a single point, but for all amplitudes up to 1.5 σ, where the smear reaches $\approx 3\%$. What has happened, of course, is that scaling by a factor $1.6/1.2$, but reducing the angle from α_2 to α_1, has almost exactly preserved one particular blue branch from Fig. 7. Conversely, small variations about this solution, say ± 5 μrad, lead to deviations of red and blue curves, as shown in Fig. 12.

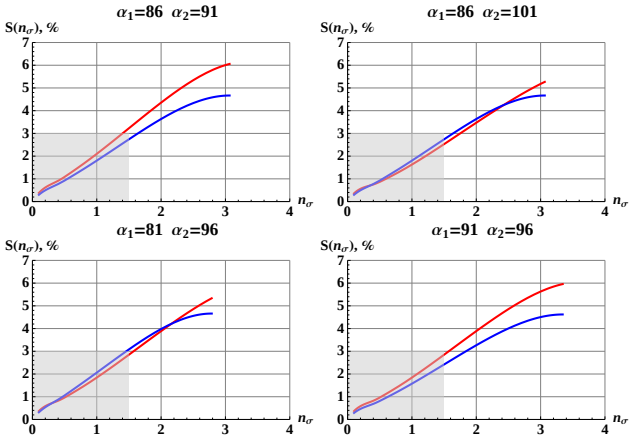

Figure 12: Small variations about the solution ± 5 μrad.

Explanation of Cases $N_{\mathrm{l.r.}}$ =24 and 16 (Green and Black)

For $N_{\mathrm{l.r.}}$ =24 and 16 (reduced collision sets in Fig. 8), one needs to explain the green and black decay curves in Figs. 9 and 10. By looking now at the bottom two plots in Fig. 7, we search for blue branches that pass through the same maximum-smear point as found above: 3% at 1.5 σ. The resultant branches are plotted in Figs. 13 and 14, with solution angles as summarized in Table 1. Again, at least a qualitative agreement is observed to the extent allowed by the resolution of Figs. 9 and 10.

Table 1: Angles of solutions for different intensities.

N_{b}	Green	Black
1.2×10^{11}	65	53
1.6×10^{11}	83	72

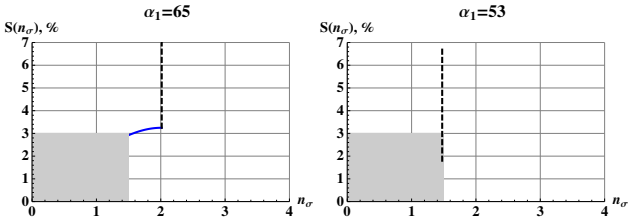

Figure 13: $N_{\mathrm{b}} = 1.2 \times 10^{11}$.

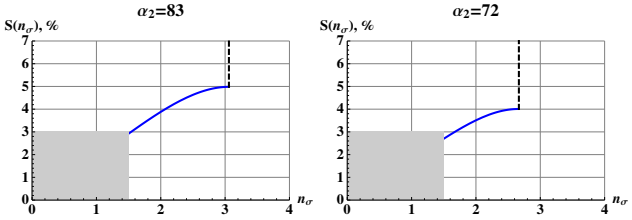

Figure 14: $N_{\mathrm{b}} = 1.6 \times 10^{11}$.

Of the four plots in Figs. 13 and 14, on three occasions the 3%-smear line intersects a monotonic part of $S(n_\sigma)$ where, as we already know from Section 4, there is an exact agreement with SixTrack. The rough indication for the dynamic aperture, as the amplitude corresponding to a maximum of S, has been used in only one case: α=53.

REFERENCES

[1] R. Assmann et al., "Results of Long-Range Beam–Beam Studies – Scaling with Beam Separation and Intensity," CERN-ATS-Note-2012-070 MD (2012).

[2] W. Herr and D. Kaltchev, "Analytical Calculation of the Smear for Long Range Beam–Beam Interactions," Proc. PAC 2009.

[3] A.J. Dragt and O.G. Jakubowicz, "Analysis of the Beam–Beam Interaction Using Transfer Maps," Proc. Beam–Beam Interaction Seminar, Stanford, CA, 22–23 May 1980, SLAC-R-541.

[4] J. Bengtsson and J. Irwin, "Analytical Calculation of Smear and Tune Shift," SSC-232 (February 1990).

[5] M.A. Furman and S.G. Peggs, "A Standard for the Smear," SSC-N-634 (1989).

[6] E. Forest, "Analytical Computation of the Smear," SSC-95 (1986).

[7] D. Kaltchev, "On Beam–Beam Resonances Observed in LHC Tracking," TRI-DN-07-9 (2007).

[8] A. Chao, "Lie Algebra Techniques for Nonlinear Dynamics," http:www.slac.stanford.edu/~achao

[9] M. Abramowitz and I.A. Stegun, *Handbook of Mathematical Functions* (New York: Dover, 1972).

[10] D. Kaltchev, "Hamiltonian for Long-range Beam-Beam, Fourier coefficients," TRIUMF Note (2012).

[11] The use of $\epsilon_n = 2 \times 10^{-6}$ as an alternative does not change any results.

APPENDIX

The non-linear kick factor in Eq. (10) is

$$F_{\rm nonl}(n_\sigma,\phi) = \gamma + \Gamma_0(P) + \ln(P) - F_{(1)} - F_{(2)}\,,$$
$$P = \tfrac{1}{2}\left((n_x + n_\sigma \sin\phi)^2 + n_y^2\right)\,,$$
$$F_{(1)} = \tfrac{2n_x}{(n_x^2+n_y^2)}\left(1 - {\rm e}^{-\frac{n_x^2+n_y^2}{2}}\right) n_\sigma \sin\phi\,,$$
$$F_{(2)} = \frac{-n_x^2+n_y^2+{\rm e}^{-\frac{n_x^2}{2}-\frac{n_y^2}{2}}\left(n_x^2+n_x^4-n_y^2+n_x^2 n_y^2\right)}{\left(n_x^2+n_y^2\right)^2} \times$$
$$\times\, n_\sigma^2 \sin^2\phi. \qquad \text{(A.1)}$$

By following Ref. [4], the Lie map is given by an expression of the following form:

$$M_{N+1}{\rm e}^{:f^{(N)}:}M_N \ldots {\rm e}^{:f^{(2)}:}M_2{\rm e}^{:f^{(1)}:}M_1\,,$$
$$f^{(k)}(x) \equiv F^{(k)}_{\rm nonl}(x).$$

Here, M_k are linear operators and for brevity we have replaced $F^{(k)}_{\rm nonl}(x)$ with $f^{(k)}(x)$. We will show that since $F_{\rm nonl}$ depends only on the normalized coordinate x/σ, once we rewrite it in terms of the eigen-coordinates at the kth kick, the local beta functions $\beta^{(k)}$ disappear, while the phase $\phi^{(k)}$ is simply added to ϕ.

By reversing the order, the map transforming the test particle (x, p_x) for one turn around the ring is

$$\mathcal{M} = M_1{\rm e}^{:f^{(1)}:}M_2{\rm e}^{:f^{(2)}:}\ldots M_N{\rm e}^{:f^{(N)}:}M_{N+1} =$$
$$= {\rm e}^{:\overline{M}_1 f^{(1)}:}{\rm e}^{:\overline{M}_2 f^{(2)}:}\ldots {\rm e}^{:\overline{M}_N f^{(N)}:}\overline{M}_{N+1}.$$

Reversal of the order means that in the first line all $f^{(k)}$ are now functions of the same initial variables (x, p_x). In the second line, accumulated linear maps $\overline{M}_k = M_1 M_2 ... M_k$ have been applied to transform the initial vector to the kick location. Thus, as a first step, we have moved all kicks to the front of the lattice and $\overline{M}_{N+1}$ is the total one-turn linear Lie operator.

Let us denote matrices corresponding to Lie operators with hats; for example, $\widehat{M}_{N+1}$. As a second step, with β, α being matched Twiss parameters at the end of the lattice, one uses an A_0 transform that transforms the ring matrix to a rotation (inserting identities $\mathcal{A}_0\mathcal{A}_0^{-1}$ in between the exponents):

$$\widehat{M}_{N+1} \xrightarrow{\widehat{\mathcal{A}}_0} \widehat{R} = \begin{pmatrix} \cos\mu & \sin\mu \\ -\sin\mu & \cos\mu \end{pmatrix},$$

$$\widehat{\mathcal{A}}_0 = \begin{pmatrix} \sqrt{\beta} & 0 \\ -\alpha/\sqrt{\beta} & 1/\sqrt{\beta} \end{pmatrix}.$$

The two steps above combined are equivalent to replacing the argument of f by $\widetilde{x}_k$ – the eigen-coordinate at the kth location. To see this, apply the $\mathcal{A}_0$ transform to both kick factor and coordinate:

$$\mathcal{A}_0\overline{M}_k f^{(k)}(x) = f^{(k)}(\mathcal{A}_0\overline{M}_k x) = f^{(k)}(\widetilde{x}_k)\,,$$

$$\widetilde{x}_k \equiv \mathcal{A}_0\overline{M}_k x = \sqrt{2\beta^{(k)}J}\sin\left(\phi + \phi^{(k)}\right)\,.$$

One can now drop the $\mathcal{A}_0$ on both sides of $\mathcal{M}$ and consider the map:

$$\mathcal{M} = {\rm e}^{:\widetilde{f}^{(1)}:}{\rm e}^{:\widetilde{f}^{(2)}:}\ldots{\rm e}^{:\widetilde{f}^{(N)}:}R,$$
$$\widetilde{f}^{(k)}(J,\phi) = f^{(k)}(\widetilde{x}_k),$$
$$R = {\rm e}^{:f_2:}, \qquad :f_2: = -\mu J.$$

To first order, one can just sum the Lie factors:

$$\mathcal{M} \approx {\rm e}^{:F:}\,R = {\rm e}^{:h:}, \qquad F \equiv \textstyle\sum_{k=1}^{N}\widetilde{f}^{(k)}.$$

By noting that above, as in Ref. [4], R precedes the kick, while in Eq. (2) and Ref. [8] the kick is assumed to be at the end of the lattice, our map is identical to Eq. (2).

The first-order invariant h is now found with the BCH theorem. Let us write $F = \bar{F} + F^\star$, where $F^\star$ is the oscillating part. By taking only $F^\star$:

$$h(J,\phi) = f_2 + \frac{:f_2:}{1-{\rm e}^{-:f_2:}}F^\star, \quad \text{(A.2)}$$
$$F^\star \equiv \sum_{k=1}^{N}(\widetilde{f}^{(k)})^\star,$$

where according to Eq. (12),

$$(\widetilde{f}^{(k)})^\star = \sum_{m\neq 0} C_m^{(k)}{\rm e}^{im\phi} = \sum_{m=1}^{\infty}\left(C_m^{(k)}{\rm e}^{im\phi} + cc\right)\,.$$

A basic property of $:f_2:$ is to operate in a simple way on functions of J, or eigenvectors ${\rm e}^{in\phi}$. Also, functions $G(f_2)$ can easily be applied to eigenvectors:

$$:f_2:{\rm e}^{in\phi} = i\,n\,\mu\,{\rm e}^{in\phi},$$
$$G(:f_2:){\rm e}^{in\phi} = G(i\,n\,\mu\,){\rm e}^{in\phi}.$$

If we choose $G(:f_2:) \equiv \frac{:f_2:}{1-{\rm e}^{:f_2:}}$, then we have:

$$:G(f_2):{\rm e}^{im\phi} =$$
$$= G(im\mu){\rm e}^{im\phi} =$$
$$= \frac{im\mu}{1-{\rm e}^{-im\mu}}{\rm e}^{im\phi} =$$
$$= \frac{i\,m\,\mu\,{\rm e}^{im\phi}}{{\rm e}^{i\,m\,\mu/2}-{\rm e}^{-i\,m\,\mu/2}}{\rm e}^{i\,m\,\mu/2} =$$
$$= \frac{m\,\mu\,{\rm e}^{im\phi}}{2\,\sin\left(m\,\mu/2\right)}{\rm e}^{i\,m\,\mu/2}.$$

By substituting all these in Eq. (A.2) and using the property $C_m^{(k)} = c_m^{(k)} \mathrm{e}^{im\phi^{(k)}}$, we obtain:

$$\begin{aligned} & h(J,\phi) = \\ = \quad & -\mu J - \lambda \sum_{k=1}^{N} \sum_{m=1}^{\infty} \left(\frac{m\ \mu\ c_m^{(k)}}{2\sin\left(m\mu/2\right)} \mathrm{e}^{im(\mu/2+\phi+\phi^{(k)})} + c.c. \right). \end{aligned}$$

Published by CERN in the Proceedings of the ICFA Mini-Workshop on Beam–Beam Effects in Hadron Colliders,
CERN, Geneva, Switzerland, 18–22 March 2013, edited by W. Herr and G. Papotti, CERN–2014–004 (CERN, Geneva, 2014)

LONG-RANGE BEAM–BEAM EFFECTS IN THE TEVATRON*

V. Shiltsev#, A.Valishev, FNAL, Batavia, IL, USA

Abstract

Long-range beam–beam effects occurred in the Tevatron at all stages (injection, ramp, squeeze, and collisions) and affected both proton and antiproton beams. They resulted in beam losses and emittance blow-ups, which occurred in remarkable bunch-to-bunch dependent patterns. On the way to record-high luminosities of the collider, many issues related to the long-range beam–beam interactions have been addressed. Below we present a short overview of the long-range beam–beam effects in the Tevatron. (For a detailed discussion on the beam–beam effects in the Tevatron please see reviews in Refs. [1–3] and references therein).

HELICAL ORBITS IN TEVATRON

Beam–beam interactions in the Tevatron differ between the injection and collision stages. The helical orbits were introduced to provide sufficient separation between the proton and antiproton beams in order to reduce detrimental beam–beam effects, e.g. tune shifts, coupling, and high-order resonance driving terms. In 36 × 36 bunch operation, each bunch experienced 72 long-range interactions per revolution at injection, but at collision there were 70 long-range interactions and two head-on collisions per bunch at the Collider Detector at Fermilab (CDF) and D0 detectors (see Fig. 1). At a bunch spacing of 396 s^{-9}, the distance between the neighbour interaction points (IPs) was 59 m. In total, there were 138 locations around the ring where beam–beam interactions occurred. The sequence of 72 interactions out of the 138 possible ones differed for each bunch, hence the effects varied from bunch to bunch. The locations of these interactions and the beam separations change from injection to collision because of the antiproton cogging (relative timing between antiprotons and protons).

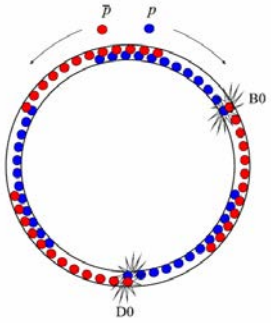

Figure 1: Schematic of proton (blue) and antiproton (red) bunches in the Tevatron and the two head-on collision locations B0 and D0.

*Fermi Research Alliance, LLC operates Fermilab under contract No. DE-AC02-07CH11359 with the US Department of Energy.
#shiltsev@fnal.gov

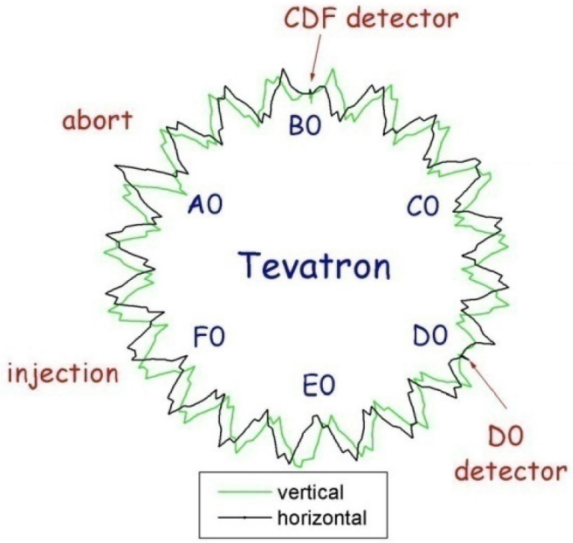

Figure 2: The pattern of the Tevatron helical orbits at the collision stage.

Initially, there were six separator groups (three horizontal and three vertical) in the arcs between the two main interaction points, B0 (CDF) and D0. During collisions, these separators form closed 3-bumps in each plane (see Fig. 2). However, the condition of orbit closure prevented running the separators at maximum voltages with the exception of horizontal separators in the short arc from B0 to D0. This limited separation at the nearest parasitic crossings 59 m away from the main IPs, aggravating the long-range beam–beam interaction. To increase separation at these parasitic crossings, three additional separators were installed to create closed 4-bumps both in the horizontal and vertical planes in the long arc (from D0 to B0) and in the vertical plane in the short arc. Each 3 m long HV separator (of which there were 24) was rated to operate with up to 300 kV over a 50 mm gap (horizontal/vertical) (see Fig. 3).

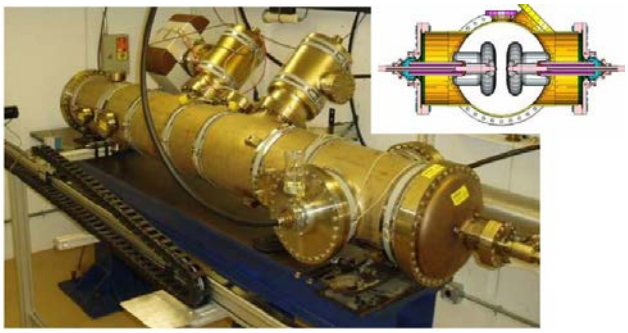

Figure 3: The Tevatron electrostatic HV separator.

There was some flexibility in the helix design for the preceding stages (injection, ramp, and squeeze). There were still some difficulties at these stages, including:

978-92-9083-404-5, 0007-8328 –
http://dx.doi.org/10.5170/CERN–2014–004.101

i) irregularities in betatron phase advance over the straight sections, especially A0;

ii) aperture restrictions (physical as well as dynamic) that limit the helix amplitude at injection and at the beginning of the ramp (see Fig. 4);

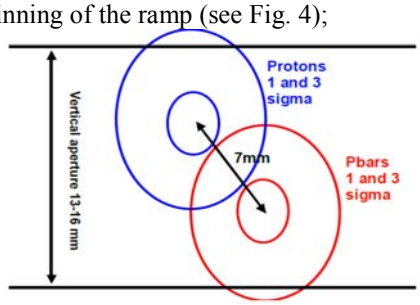

Figure 4: Schematic representation of one of the smallest separation locations at the C0 region inside the 16 mm aperture magnets. Long-range interaction at the spot caused significant beam losses and the small aperture magnets were taken out and replaced with 40 mm aperture dipoles in 2003.

iii) the maximum separator gradient of 48 kV/cm (limited by the separator spark rate) leads to a faster drop in separation, $d \sim 1/E$, than in the beam size, $\sigma \sim 1/E^{1/2}$, during the second part of the ramp above an energy of $E = 500$ GeV;

iv) the polarity reversal of the horizontal separation during the squeeze (to satisfy the needs of high energy physics (HEP) experiments) that leads to a short partial collapse of the helix.

Helical orbits were optimized many times over the course of Collider Run II in order to improve the performance of the machine. Our experience has shown that less than $S \sim 6\ \sigma$ separation resulted in unsatisfactory losses. Figure 5 shows the minimum radial separation S during the ramp and squeeze with the initial helix design (blue, ca. January 2002) and an improved helix (red, ca. August 2004). The long-range interactions contribute a tune spread [1] of about:

$$\Delta Q \approx \sum_{\text{parasitic encounters}} \frac{2\xi}{S^2} \approx 0.008 \qquad (1)$$

as well as several units of chromaticity [4, 5]. For comparison, the head-on beam–beam tune shift parameters for both protons and antiprotons were about:

$$\xi = N_{IP} \frac{N_p r_p}{4\pi\varepsilon} \approx 0.018 - 0.025 \qquad (2)$$

where r_p denotes the classical proton radius, N_p and ε are the opposite bunch intensity and emittance, respectively, and $N_{IP} = 2$ is the total number of head-on collisions per turn.

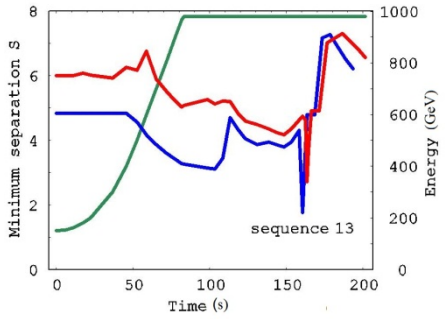

Figure 5: Minimum radial separation, Eq. (3), on ramp and during the low-beta squeeze. The green line represents the beam energy on the ramp. The blue and red lines represent $S(t)$ for the helix configurations used ca. January 2002 and August 2004, respectively (from Ref. [1]).

BEAM–BEAM INDUCED LOSSES

As reported elsewhere, the beam–beam interactions had very detrimental effects on Collider performance early in Run II, but were eventually controlled via a number of improvements [1–3] (see Fig. 6).

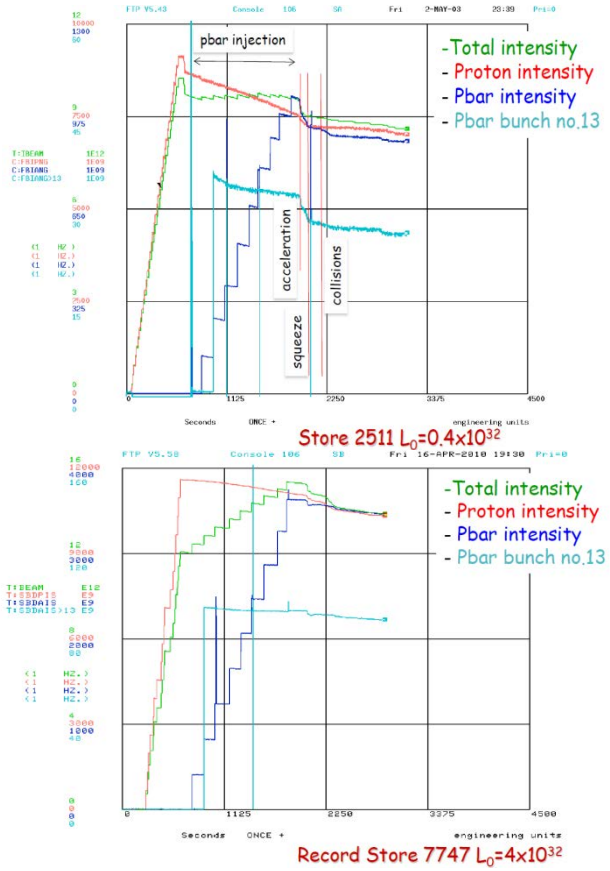

Figure 6: A typical plot of the collider 'shot' shows significant beam losses at all stages of the Tevatron cycle early in Run II (2003). A similar plot taken later in Run II shows greatly reduced inefficiencies and excellent performance in 2010.

Long-range beam-beam effects usually manifested themselves in reduction of beam lifetime and accelerated emittance growth. This accounted for as much as 50% luminosity loss early in Run II, down to ~10% loss at the end of the Run II. We observed no coherent effects that could be attributed to the LR beam–beam interactions.

At injection energy, LR beam-beam was the dominant factor for intensity losses both in proton and antiproton beams. This was especially noticeable for off-momentum particles, and strongly related to the tune chromaticity Q' (strength of sextupoles). Figure 7 shows an interesting feature in the behaviour of two adjacent proton bunches (nos. 3 and 4). Spikes in the measured values are instrumental effects labelling the time when the beams are cogged (moved longitudinally with respect to each other). Initially, the bunches have approximately equal lifetimes. After injection of the second batch of antiprotons (four bunches each), the loss rate of bunch 4 greatly increased. After the first cogging, bunch 3 started to exhibit faster decay. Analysis of the collision patterns for these bunches allowed the pinpointing of a particular collision point responsible for the lifetime degradation [2].

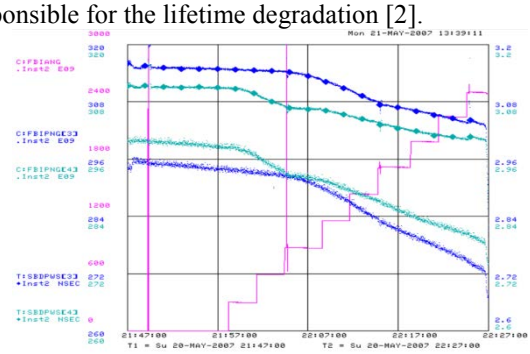

Figure 7: Intensity and rms length (s^{-9}) of proton bunches nos. 3 and 4 during injection of antiprotons (red line).

The particle losses for both beams on the separated orbits were larger at the higher intensities of the opposite beam (see Fig. 8) or, to be precise, larger at a higher brightness of the opposite beam (see Fig. 9), and were usually accompanied by longitudinal 'shaving' (preferential loss of particles with large momentum offset and corresponding reduction of the rms bunch length (see Fig. 10)).

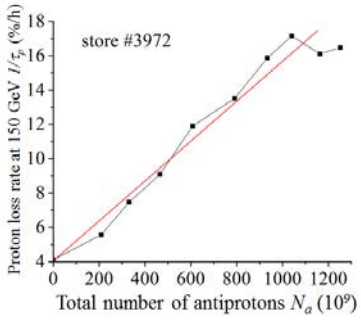

Figure 8: Proton loss rates at the energy of 150 GeV vs. the total number of injected antiprotons [1].

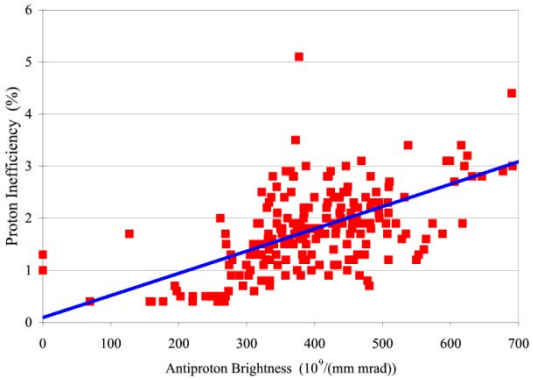

Figure 9: Proton losses on the energy ramp vs. antiproton brightness N_a/ε_a [1].

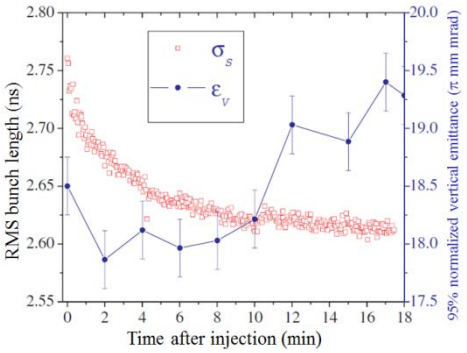

Figure 10: Time evolution of rms bunch length (red squares) and 95% normalized vertical emittance of antiproton bunch 1 (blue dots) after injection in store #3717 (8 August 2004). The error bars represent an rms systematic error in the flying wire emittance measurements [1].

The intensity decay was well approximated by [1]:

$$\frac{\Delta N_{a,p}}{N_{a,p}} = 1 - \frac{N(t)}{N(t=0)} \propto \sqrt{t} \cdot \varepsilon_{a,p}^2 \frac{N_{p,a}}{\varepsilon_{p,a}} Q'^2_{a,p} \cdot F(\varepsilon_L, Q_{x,y}, S_{a-p}) \quad . \quad (3)$$

The observed $\sqrt{t}$ dependence of beam intensity decay and bunch length is believed to be due to particle diffusion that leads to particle loss at physical or dynamic apertures (see Fig. 11). The major diffusion mechanisms are intrabeam scattering (IBS), scattering on the residual gas, and diffusion caused by RF phase noise. For example, if the available machine aperture is smaller than the beam size of the injected beam, the beam is clipped on the first turn, with an instantaneous particle loss. Such a clipping creates a step-like discontinuity at the boundary of the beam distribution that causes very fast particle loss due to diffusion. The diffusion wave propagates inward, so that the effective distance is proportional to $\sqrt{t}$. Consequently, the particle loss is also proportional to $\sqrt{t}$. To estimate such a 'worst-case loss', consider an initially uniform beam distribution: $f(I) = f_0 \equiv 1/I_0$, where I_0 is the action at the boundary. For sufficiently small time:

$t << I_0 / D$, where D is the diffusion coefficient, the diffusion can be considered one-dimensional in the vicinity of the beam boundary. Solving the diffusion equation:

$$\frac{\partial f}{\partial t} = D \frac{\partial}{\partial I}\left(I \frac{\partial f}{\partial I} \right) \qquad (4)$$

gives the result:

$$f(I,t) = \frac{2 f_0}{\sqrt{\pi}} \int_0^{(I_0 - I)/\sqrt{4 I_0 D t}} \mathrm{e}^{-\xi^2} \mathrm{d}\xi \quad . \qquad (5)$$

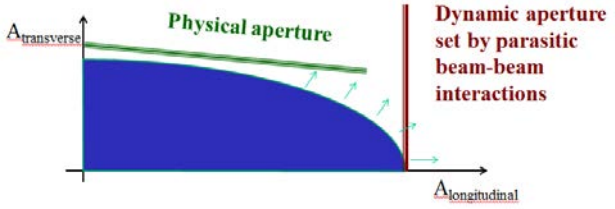

Figure 11: Schematic representation of the loss mechanism due to diffusion onto dynamic aperture set by the LR beam–beam interactions in the longitudinal–transverse action plane.

By integrating it over I, one obtains the dependence of particle population on time:

$$\frac{N(t)}{N_0} \approx 1 - \sqrt{\frac{t}{\tau}}, \quad \tau = \frac{\pi I_0}{4D}, \quad t << \tau \quad . \qquad (6)$$

In the transverse degree of freedom, the Tevatron acceptance at 150 GeV on the helical orbit is about $I^{tr}{}_0 \approx$ 8–13 π mm mrad, depending on the pre-shot machine tune-up, while the emittance growth rate is about $D^{tr} \approx$ 0.15–0.25 π mm mrad/h, chiefly from external noises and scattering on the residual gas. From Eq. (6), one can obtain a lifetime of $\tau \approx$ 30–80 h. In addition, diffusion in the longitudinal plane with a rate $D^{long} \approx$ 0.03–0.3 rad^2/h can lead to lifetimes of $\tau \approx$ 10–100 h in the case where the longitudinal aperture is limited only by the RF bucket size $\sqrt{I_0^{long}} \approx 2$ rad. Not all the numbers used above are well known, but we believe they are in the indicated ranges.

In reality, the machine acceptance is determined by the interplay between the physical and dynamic apertures. The latter is a strong function of the synchrotron action, and beam–beam interactions drastically reduce the dynamic aperture for synchrotron oscillation amplitudes close to the bucket size. Naturally, such an aperture reduction is stronger for larger values of chromaticity.

Notably, the proton inefficiencies were higher than the antiproton ones, despite a factor of 3–5 higher proton intensity. That was due to significantly smaller antiproton emittances (see Eq. (3) above).

During low-beta squeeze the beams briefly (for ~2 s) came within 2–2.5 σ at 1 parasitic IP. This caused sharp loss spikes. In general, the beam intensity losses were dependent on:

i) the chromaticities $Q'_{x,y}$, and special measures were taken for their reduction (reduction of impedance and implementation of octupoles and feedback systems allowed Q' to decrease to almost zero);

ii) beam separation:
$$S = \sqrt{(\Delta x / \sigma_{x\beta})^2 + (\Delta y / \sigma_{y\beta})^2} \qquad (7)$$
e.g. at collisions there were four crossings at 5.8–6 σ separation that were essential, the remaining LR's were at 8–10 σ;

iii) during the colliding beams stores—complex interplay between the head-on and parasitic long-range interactions (the head-on tune shifts up to about $\xi = 0.020$–0.025 for both protons and antiprotons, in addition to the long-range tune shifts of $\Delta Q^p = 0.003$ and $\Delta Q^a = 0.006$, respectively, see Ref. [3]);

iv) on the second order betatron tune chromaticity $Q'' = \mathrm{d}^2 Q / \mathrm{d}(\Delta p/p)^2$ (numerical modelling [2] indicated, and it was later confirmed by experiments that the deterioration of the proton life time was caused by a decrease of the dynamical aperture for off-momentum particles at high Q'');

v) on the bunch position in the train (there were remarkable differences in the dynamics of individual bunches—see below).

At the end of Run II, the antiproton intensity lifetime deterioration due to the beam–beam effects was much smaller than the proton one, and was found to scale approximately as [1]:

$$\left(\frac{1}{\tau_a} \right)_{BB} = \left(\frac{\mathrm{d}N_a}{N_a \mathrm{d}t} \right)_{BB} \propto N_p \frac{\varepsilon_a^2}{S^3}, \qquad (8)$$

where S stands for the beam–beam separation (helix size).

PATTERNS OF BEAM–BEAM EFFECTS

All beam dynamics indicators were dependent on the bunch position in the train of bunches (there were three train of 12 bunches in each beam)—beam orbits and coupling (of about 40 microns (see Fig. 12)), tunes (by as much 0.005 as shown in Fig. 13) and chromaticities (up to six units (see Fig. 14)).

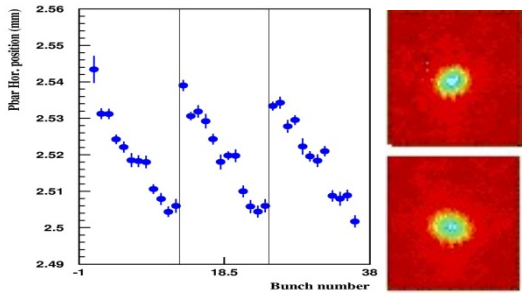

Figure 22: Antiproton horizontal orbit variations along the bunch train for comparison. The pbar rms horizontal betatron size at the location of the synchrotron light monitor [6] is equal to ~0.3 mm. 2D beam images on the right are for bunches #1 (top) and #8 (bottom). Different tilts of the images indicate a significant difference in local coupling.

Similar type differences (though smaller—proportional to the intensity of the opposite beam) took place for the proton bunches. The observed variations data are in good agreement with analytical calculations [1, 2, 5].

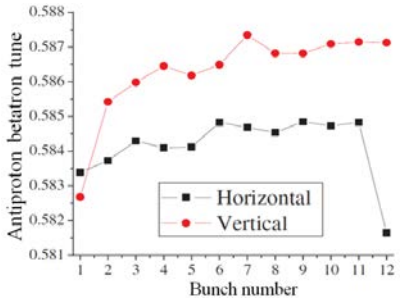

Figure 13: Horizontal and vertical antiproton tunes vs. bunch number in the bunch train measured by 1.7 GHz Schottky monitor [4] ~3 h into store #3678 (27 July 2004) [1].

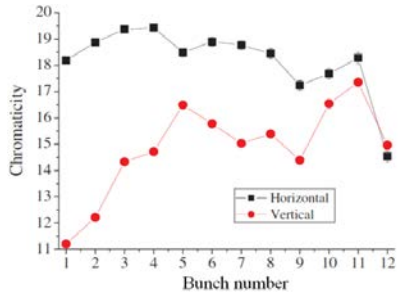

Figure 14: Antiproton chromaticities measured by the 1.7 GHz Schottky monitor vs. bunch number for store #3678 (27 to 28 July 2004) [1].

It is not surprising that with such significant differences in tunes and chromaticities, the antiproton and proton bunch intensity lifetime and emittance growth rates vary considerably from bunch to bunch. The orbit difference did not produce adverse effects on the performance. As an illustration, Fig. 15 shows the vertical emittance blow-up early in an HEP store for all three trains of antiproton bunches.

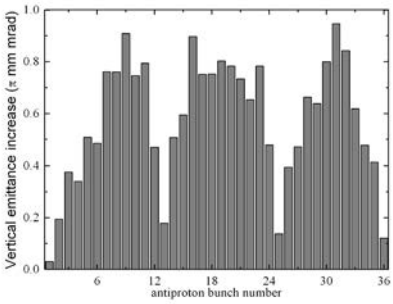

Figure 15: Antiproton bunch emittance increase over the first 10 minutes after initiating collisions for HEP store #3231 with an initial luminosity $L = 48 \times 10^{30}$ cm^{-2} s^{-1}.

One can see a remarkable distribution along the bunch train, which gave rise to the term 'scallops' (three scallops in three trains of 12 bunches) for this phenomenon—the end bunches of each train exhibit lower emittance growth than the bunches in the middle of the train. Because of the three-fold symmetry of the proton loading, the antiproton emittance growth rates are the same within 5–20% for corresponding bunches in different trains (in other words, bunches #1, #13, and #25 have similar emittance growths). The effect is dependent on the antiproton tunes, particularly on how close each bunch is to some important resonances—in the case of the Tevatron working point, these are fifth-order (0.600), seventh-order (0.5714), and twelfth-order (0.583) resonances. For example, the scallops occur near the fifth-order resonances $nQ_x + mQ_y = 5$, such as $Q_{x,y} = 3/5 = 0.6$. Smaller but still definite scallops were also seen for protons if the proton tunes are not optimally set. After the initial 0.5–1 h of each store, the growth rate of each bunch decreased significantly. Various methods have been employed to minimize the development of scallops (including a successful attempt to compensate one bunch's emittance growth with a Tevatron electron lens (TEL), see Ref. [7]), but carefully optimizing the machine tunes was found to be the most effective, e.g. the vertical tune changes as small as −0.002 resulted in significant reduction of the amplitude of the scallops.

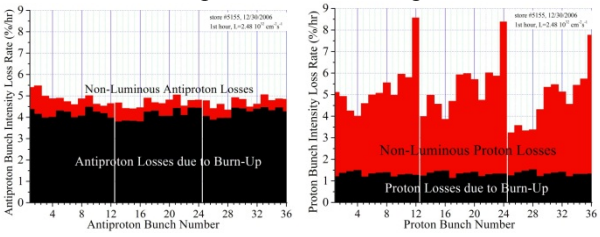

Figure 16: (a - left) proton-bunch intensity loss rates and (b - right) antiproton-bunch intensity loss rates at the beginning of Tevatron store #5155, 30 December 2006, with an initial luminosity $L = 250 \times 10^{30}$ cm^{-2} s^{-1} (from Ref. [7]).

The attrition rate of protons and antiprotons due to their interaction with the opposite beam varied bunch-by-bunch and is especially large at the beginning of the HEP

stores where the total proton beam–beam tune shift parameter peaks. Figure 16(a) shows a typical distribution of proton loss rates $(dN_p/N_p)/dt$ at the beginning of a high-luminosity HEP store. Bunches #12, 24, and 36 at the end of each bunch train typically lost about 9% of their intensity per hour while other bunches lost only 4–6%/h. These losses were a very significant part of the total luminosity decay rate of about 20% per hour (again, at the beginning of the high luminosity HEP stores). The losses due to inelastic proton–antiproton interactions $dN_p/dt = \sigma_{int} L$ at the two main IPs ($\sigma_{int} = 0.07$ barn) were small (1–1.5%/h) compared to the total losses. Losses due to inelastic interaction with the residual vacuum and due to leakage from the RF buckets were less than 0.3%/h. The single largest source of proton losses is the beam–beam interaction with the antiprotons. Such a conclusion is also supported by Fig. 16(a), which shows a large bunch-to-bunch variation in the proton loss rates within each bunch train, but very similar rates for equivalent bunches, e.g. bunches #12, 24, and 36. On the contrary, antiproton intensity losses dN_a/dt were about the same for all of the bunches (see Fig. 16(b)) as they are mostly due to luminosity burn-up and not determined by beam–beam effects (the latter are labelled as a 'non-luminous' component of the loss rate).

The remarkable distribution of the proton losses seen in Fig. 16, e.g. the particularly high loss rates for bunches #12, 24, and 36, is usually thought to be linked to the distribution of betatron tunes along the bunch trains. Bunches at the end of the trains have their vertical tunes closer to the $7/12 \approx 0.583$ resonance lines and, therefore, have higher losses. The average Tevatron proton tune Q_y of about 0.588–0.589 lies just above this resonance, and the bunches at the end of each train, whose vertical tunes are lower by $\Delta Q_y = -(0.002–0.003)$ due to the unique pattern of long-range interactions, are subject to stronger beam–beam effects. The tunes Q_y, Q_x were carefully optimized by the operation crew to minimize the overall losses of intensity and luminosity. For example, an increase of the average vertical tune by quadrupole correctors is not possible because it usually results in higher losses and scallops as small amplitude particle tunes move dangerously close to the $3/5 = 0.600$ resonance. The Tevatron electron lenses did reduce by a factor of >2 the proton losses out of bunches #12, 24, and 36 (see Fig. 17) (for more details please refer to Refs. [3, 7, 8]).

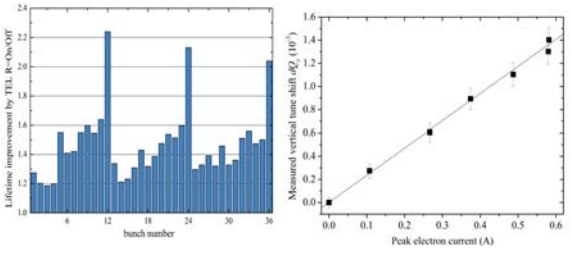

Figure 17: Proton bunch lifetime improvement factor due to (a - left) TEL), and (b - right) tuneshift vs. the TEL current [7].

NOTE ON BEAM–BEAM SIMULATIONS

We would like to draw attention to the fact that for most of Collider Run II we had trustable numerical models and simulation tools for stored beam physics analysis and weak–strong beam–beam modelling, which were used to study the beam–beam effects in the Tevatron [2]. Our simulations correctly described many observed features of the beam dynamics, had predictive power, and have been particularly useful for supporting and planning changes of the machine configuration (see Figs. 18 and 19). We also had very practical computations of the resonant driving terms [9].

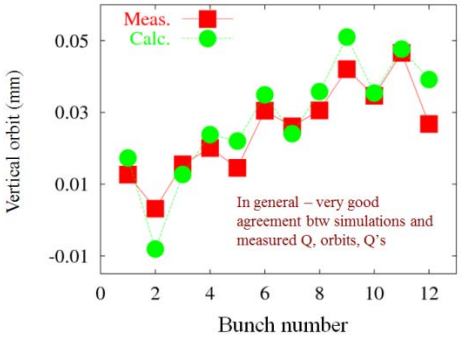

Figure 18: Bunch by bunch antiproton vertical orbits. Squares, measurements; circles, Lifetrac simulations [2].

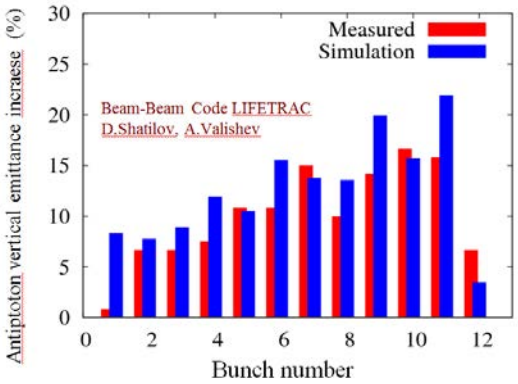

Figure 19: Bunch-by-bunch antiproton emittance growth. Measured in store 3554 (red) and simulated with Lifetrac (blue) [2].

SUMMARY

Long-range beam–beam effects occurred in the Tevatron at all stages (injection, ramp, squeeze, and collisions) and in both beams. They resulted in beam losses and emittance blow-ups—with bunch-to-bunch dependent patterns. Careful optimization of helical orbit separation and many operational tune-ups and upgrades have led essentially to putting the effects upon the luminosity under control by the mid to end of Run II. Trustable weak–strong simulations had helped us a lot. Compensation of the LR beam–beam effects by TELs has been demonstrated.

REFERENCES

[1] V. Shiltsev et al., PRSTAB 8 (2005) 101001.
[2] A. Valishev et al., JINST 7 (2012) P12002.

[3] V. Shiltsev, these proceedings.
[4] R. Pasquinelli and A. Jansson, PRSTAB 14 (2011) 072803.
[5] T. Sen et al., PRSTAB 7 (2004) 041001.
[6] R. Thurman-Keup et al., JINST 6 (2011) T10004.
[7] V. Shiltsev et al., New Jour.Phys., 10 (2008) 043042.
[8] V. Shiltsev et al., Phys.Rev.Lett. 99 (2007) 244801.
[9] Yu. Alexahin, FERMILAB-TM-2148 (2001).

Published by CERN in the Proceedings of the ICFA Mini-Workshop on Beam–Beam Effects in Hadron Colliders,
CERN, Geneva, Switzerland, 18–22 March 2013, edited by W. Herr and G. Papotti, CERN–2014–004 (CERN, Geneva, 2014)

STATUS OF HEAD-ON BEAM–BEAM COMPENSATION IN RHIC *

W. Fischer†, Z. Altinbas, M. Anerella, M. Blaskiewicz, D. Bruno, M. Costanzo, W.C. Dawson, D.M. Gassner, X. Gu, R.C. Gupta, K. Hamdi, J. Hock, L.T. Hoff, R. Hulsart, A.K. Jain, R. Lambiase, Y. Luo, M. Mapes, A. Marone, R. Michnoff, T.A. Miller, M. Minty, C. Montag, J. Muratore, S. Nemesure, D. Phillips, A.I. Pikin, S.R. Plate, P. Rosas, L. Snydstrup, Y. Tan, C. Theisen, P. Thieberger, J. Tuozzolo, P. Wanderer, S.M. White, W. Zhang
BNL, Upton, NY, USA

Abstract

In polarized proton operation, the performance of the Relativistic Heavy Ion Collider (RHIC) is limited by the head-on beam–beam effect. To overcome this limitation, two electron lenses are under commissioning. We give an overview of head-on beam–beam compensation in general and in the specific design for RHIC, which is based on electron lenses. The status of installation and commissioning are presented along with plans for the future.

INTRODUCTION

Head-on beam–beam compensation was first proposed as a four-beam $e^+e^-e^+e^-$ scheme for COPPELIA [1] and implemented for Dispositif de Collisions dans l'Igloo (DCI) [2]. The DCI experience, however, fell short of expectations; luminosities with two, three, or four beams were about the same. The shortfall is generally attributed to coherent beam–beam instabilities [3–5], and head-on beam–beam compensation has not been tested again since.

Nevertheless, various proposals have been made, such as for the SSC [6, 7], Tevatron [8], LHC [6, 7, 9–11], and B-factories [12]. In hadron colliders, the compensation can be achieved by colliding positively charged beams with a negatively charged low-energy electron beam, in a device usually referred to as an electron lens. Doing so avoids the coherent instabilities seen in DCI, as the electron beam will not couple back to the hadron beam, except for single-pass effects; these can be significant [13, 14] and may require the addition of a transverse damper in RHIC. Two electron lenses were installed in the Tevatron [8, 13, 15–19], where they were routinely used as a gap cleaner, but not for head-on beam–beam compensation. The Tevatron experience is valuable for several reasons: (i) the reliability of the technology was demonstrated, as no store was ever lost because of the lenses [20]; (ii) the tune shift of selected bunches due to PACMAN effects was corrected, leading to lifetime improvements [16]; (iii) the sensitivity to positioning errors, transverse profile shape, and electron beam current fluctuations was explored [21]; (iv) experiments with a Gaussian profile electron beam were performed; and (v) a hollow electron beam was tested in a collimation scheme [19]. For the design of the RHIC electron lenses we have benefited greatly from the Tevatron experience. We have also drawn on the expertise gained in the construction and operation of an Electron Beam Ion Source (EBIS) at Brookhaven National Laboratory (BNL) [22, 23], which is a device similar to an electron lens but with a different purpose.

In RHIC there are two head-on beam–beam interactions at interaction points IP6 and IP8 (Fig. 1), as well as four long-range beam–beam interactions with large separation (about 10 mm) between the beams at the other interaction points. The luminosity is limited by the head-on effect in polarized proton operation [24–30], as can be seen in Fig. 2. Bunches with two collisions experience a larger proton loss throughout the store than bunches with only one collision. The enhanced loss is particularly strong at the beginning of a store. Beam–beam effects in other hadron colliders are reported in Refs. [31–36].

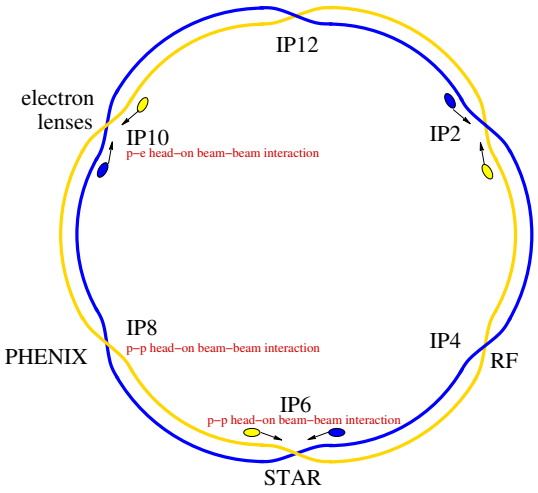

Figure 1: General layout of RHIC with locations of the head-on beam–beam interactions and electron lenses.

We consider the partial indirect compensation of the head-on beam–beam effect with one electron lens in each ring. Together with intensity and emittance upgrades [37], our goal is to approximately double the luminosity over what can be achieved without these upgrades.

This article gives a summary of previous studies and progress reports on head-on beam–beam compensation in RHIC with electron lenses [38–74], updated with the latest available information.

* Work supported by Brookhaven Science Associates LLC under Contract no. DE-AC02-98CH10886 with the U.S. Department of Energy.
† Wolfram.Fischer@bnl.gov

978-92-9083-404-5, 0007-8328 –
http://dx.doi.org/10.5170/CERN–2014–004.109

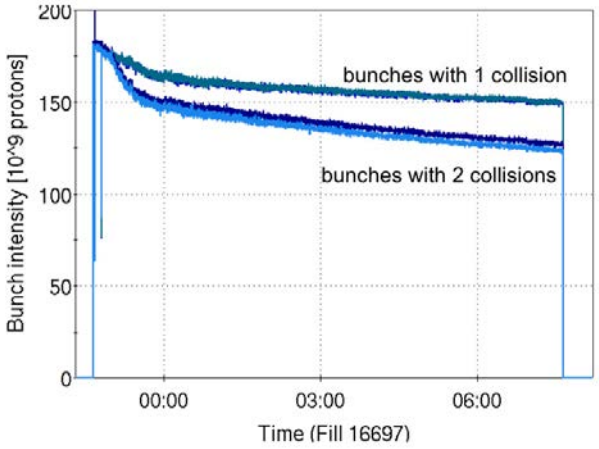

Figure 2: Time-dependent intensity of polarized proton bunches with one or two head-on collisions during the 2012 run.

HEAD-ON BEAM–BEAM COMPENSATION

If a collision of a proton beam with another proton beam is followed by a collision with an electron beam, the head-on beam–beam kick can in principle be reversed. For simplicity we consider only the horizontal plane and beams with a Gaussian transverse distribution. Figure 3 shows the beam line layout for head-on compensation, and Fig. 4 shows the normalized phase space view.

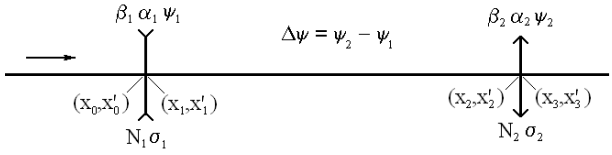

Figure 3: Schematic of head-on beam–beam compensation in a beam line view. At the first location, with lattice parameters $(\beta_1, \alpha_1, \psi_1)$, a proton experiences a beam–beam kick from another proton bunch with intensity N_1 and root-mean-square beam size σ_1. At the second location, with lattice parameters $(\beta_2, \alpha_2, \psi_2)$, another beam–beam kick is generated by the electron beam with effective bunch intensity N_2 and root-mean-square beam size σ_2.

Before experiencing a beam–beam kick from another proton beam at location 1, a proton has transverse phase space coordinates (x_0, x_0'). The proton then receives a kick from the other proton beam [75],

$$\Delta x_0' = \frac{2N_1 r_0}{\gamma x_0}\left[1 - \exp\left(-\frac{x_0^2}{2\sigma_1^2}\right)\right],$$

where N_1 is the bunch intensity of the second proton beam, γ is the relativistic factor of the proton receiving the kick, r_0 is the classical proton radius, and σ_1 is the root-mean-square (rms) beam size of the second proton beam. The

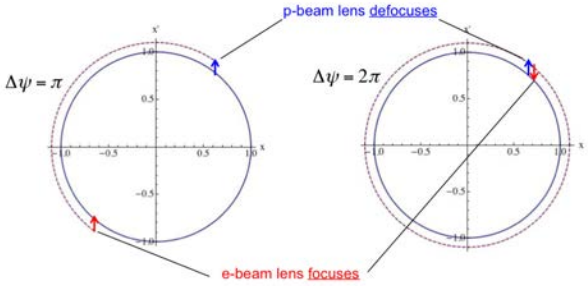

Figure 4: Schematic of head-on beam–beam compensation in a normalized phase space view.

new coordinates are then

$$x_1 = x_0,$$
$$x_1' = x_0' + \Delta x_0'.$$

After transport through the linear beam line, the coordinates are

$$x_2 = M_{11}x_1 + M_{12}x_1',$$
$$x_2' = M_{21}x_1 + M_{22}x_1',$$

with (see [76, 77])

$$M_{11} = \sqrt{\frac{\beta_2}{\beta_1}}\,(\cos\Delta\psi + \alpha_1 \sin\Delta\psi),$$
$$M_{12} = \sqrt{\beta_1\beta_2}\,\sin\Delta\psi,$$
$$M_{21} = -\frac{1+\alpha_1\alpha_2}{\sqrt{\beta_1\beta_2}}\sin\Delta\psi + \frac{\alpha_1-\alpha_2}{\sqrt{\beta_1\beta_2}}\cos\Delta\psi,$$
$$M_{22} = \sqrt{\frac{\beta_1}{\beta_2}}\,(\cos\Delta\psi - \alpha_2 \sin\Delta\psi)$$

where $\Delta\psi = \psi_2 - \psi_1$. In the electron lens, the proton receives the kick

$$\Delta x_2' = -\frac{2N_2 r_0}{\gamma x_2}\left[1 - \exp\left(-\frac{x_2^2}{2\sigma_2^2}\right)\right],$$

where N_2 is the effective bunch intensity of the electron lens beam (i.e. the number of electrons the proton passes in the lens) and σ_2 is the rms beam size of the electron lens beam. The coordinates after passing the electron lens are then

$$x_3 = x_2,$$
$$x_3' = x_2' + \Delta x_2'.$$

One can now express the final coordinates (x_3, x_3') as a function of the intensities (N_1, N_2) and require, for exact compensation, that

$$x_3(N_1, N_2) = x_3(0, 0) \quad (1)$$

and

$$x_3'(N_1, N_2) = x_3'(0, 0), \quad (2)$$

i.e. that the final coordinates are the same with and without beam–beam interaction and compensation. From the condition (1) it follows that $M_{12} = 0$ and hence $\Delta\psi = k \cdot \pi$, where k is an integer. From the condition (2) it follows that $N_1 = N_2$ and $\sigma_1^2/\sigma_2^2 = \beta_1/\beta_2$.

Therefore, if the following three conditions are met, the beam–beam kicks are cancelled exactly.

1. The ion beam and electron beam produce the same amplitude-dependent force by having the same effective charge and profile.
2. The phase advance between the two beam–beam collisions is a multiple of π in both transverse planes.
3. There are no nonlinearities between the two collisions.

In practice the above can be achieved only approximately. Deviations from condition 1 include:

- an electron current that does not match the proton bunch intensity;
- a non-Gaussian electron beam profile (assuming that the proton beam transverse profile is Gaussian);
- an electron beam size that differs from the proton beam size;
- time-dependence of the electron and proton beam parameters.

Deviations from condition 2 include:

- a phase advance $\Delta\psi \neq k\pi$ between the head-on collision and the electron lens;
- long bunches, i.e. $\sigma_\mathrm{s} \gtrsim \beta^*$.

Deviations from condition 3 include:

- lattice sextupoles and octupoles, as well as multipole error between the head-on collision and the electron lens.

Tolerances were studied extensively in simulations and reported in Ref. [70], and bunch length effects have been investigated in Refs. [47, 48]. The Tevatron experience also provides tolerances for positioning errors, transverse shape and size mismatches, and electron current variations. We give the tolerances for all devices below.

We plan to compensate for only one of the two head-on collisions in RHIC, since a full compensation would lead to a small tune spread and could give rise to instabilities.

RHIC ELECTRON LENS DESIGN

In designing the electron lens, we were aiming for a technically feasible implementation that would come as close as possible to the ideal compensation scheme outlined above. In addition, a major design consideration was ease of commissioning and operation. Our goal is a commissioning that is largely parasitic to the RHIC operation for physics. The main design process can be summarized as follows.

Condition 1 (same amplitude-dependent forces from the proton beam and electron lens) has a number of implications. Since both proton beams are round in the beam–beam interactions ($\beta_x^* = \beta_y^*$ and $\epsilon_x = \epsilon_y = \epsilon_n$), we also require that $\beta_x = \beta_y$ at the electron lens location, and require matched transverse proton and electron beam profiles, i.e. that the electron beam profile is also Gaussian with $\sigma_{\mathrm{p},x} = \sigma_{\mathrm{e},x} = \sigma$ and $\sigma_{\mathrm{p},y} = \sigma_{\mathrm{e},y} = \sigma$. The condition $\beta_x = \beta_y$ limits the electron lens locations to the space between the DX magnets; in these locations the RHIC lattice also has a small dispersion.

Table 1: Reference cases for RHIC beam–beam and beam-lens interactions. Bunch intensities without electron lenses are expected to saturate at about 2×10^{11} because of head-on beam–beam effects [30, 70].

Quantity	Unit	Value		
Proton beam parameters				
Total energy E_p	GeV	100	255	255
Bunch intensity N_p	10^{11}	2.5	2.5	3.0
$\beta^*_{x,y}$ at IP6, IP8 (p–p)	m	0.85	0.5	0.5
$\beta^*_{x,y}$ at IP10 (p–e)	m	10.0	10.0	10.0
Lattice tunes (Q_x, Q_y)	–	— (0.695, 0.685) —		
rms emittance ϵ_n, initial	mm mrad	— 2.5 —		
rms beam size at IP6, IP8 σ^*_p	μm	140	70	70
rms beam size at IP10 σ^*_p	μm	485	310	310
rms bunch length σ_s	m	0.50	0.40	0.20
Hourglass factor F, initial	–	0.88	0.85	0.93
Beam–beam parameter ξ/IP	–	0.012	0.012	0.015
Number of beam–beam IPs	–	— 2 + 1[a] —		
Electron lens parameters				
Distance of centre from IP	m	— 2.0 —		
Effective length L_e	m	— 2.1 —		
Kinetic energy E_e	keV	7.8	7.8	9.3
Relativistic factor β_e	–	0.18	0.18	0.19
Electron line density n_e	$10^{11}\,\mathrm{m}^{-1}$	1.0	1.0	1.2
Electrons in lens N_e1	10^{11}	2.1	2.1	2.5
Electrons encountered N_e2	10^{11}	2.5	2.5	3.0
Current I_e	A	0.85	0.85	1.10

[a] One head-on collision in IP6 and IP8 each, plus a compensating head-on collision in IP10.

The tolerances for the main solenoid field straightness and for the relative beam alignment are easier to meet with a larger proton beam. A larger beam is also less susceptible to coherent instabilities [13, 71]. The β-function at IP10 cannot be larger than 10 m at 250 GeV proton energy without modifications to the buses and feedthroughs of the IR10 superconducting magnets. Such modifications are currently not under consideration because of costs, but could be implemented if coherent instabilities occur and cannot be mitigated by other means.

With a fully magnetized electron beam, the beam size σ_e in the main solenoid is given by its size at the cathode, σ_ec, together with the solenoid fields B_sc at the cathode and B_s in the main solenoid as $\sigma_\mathrm{e} = \sigma_\mathrm{ec}\sqrt{B_\mathrm{sc}/B_\mathrm{s}}$. For technological and cost reasons, the field B_s cannot be much larger than 6 T, and a strong field makes a correction of the field straightness more difficult. The field B_sc has to be large enough to suppress space charge effects. With the limits in the B_sc and B_s fields and a given beam size σ_e, the electron beam size and current density at the cathode follow, and they must be technically feasible. Unlike the Tevatron elec-

tron lenses, we use a DC electron beam to avoid the noise possibly introduced through the high-voltage switches. A DC beam requires the removal of ions created in the electron lens through residual gas ionization.

Condition 2 (phase advance of multiples of π between p–p and p–e interaction) can be achieved through lattice modifications. We have installed four phase-shifter power supplies for both transverse planes of both rings so that the betatron phase between IP8 and the electron lenses in IR10 can be adjusted. To have $\Delta\psi = k\pi$ in both planes of both rings, it is also necessary to change the integer tunes from $(28, 29)$ to $(27, 29)$ in the Blue ring and from $(28, 29)$ to $(29, 30)$ in the Yellow ring to find a solution. With the new lattices, higher luminosities were reached in 2013 than in previous years, but the polarization was lower. The lower polarization is still being investigated and may not have resulted from the new lattices. Other lattice options are also under study: (i) a solution was found for the Yellow ring that maintains the integer tunes of $(28, 29)$ and has the correct phase advances; (ii) the phase advance of a multiple of π may also be realized between IP6 and the electron lenses.

Condition 3 (no nonlinearities between the p–p and p–e interactions) is best achieved when the p–e interaction is as close as possible to the p–p interaction. With the location in IR10 (Fig. 1), there is only one arc between the p–p interaction at IP8 and the p–e interaction at IR10. In this configuration, a proton, after receiving a beam–beam kick at IP8, passes a triplet with nonlinear magnetic fields from field errors, an arc with chromaticity sextupoles and dodecapoles in the quadrupoles as dominating nonlinear field errors, and another triplet in IR10. To avoid bunch length effects, the parameter β^* cannot be too small [47, 48]. In simulations, a value as low as $\beta^* = 0.5$ m was found to be acceptable [70].

The location of both the Blue and the Yellow electron lenses in IR10, in a section common to both beams (Fig. 5), allows local compensation of the main solenoid effect on both linear coupling and spin orientation by having the two main solenoids with opposing field orientations. At 255 GeV proton energy, one superconducting solenoid with a 6 T field introduces coupling that leads to $\Delta Q_{\min} = 0.0023$ [51] and increases all spin resonance strengths by 0.003 [78]. In this configuration it is also possible to ramp the magnets together during RHIC stores without affecting the beam lifetime or spin orientation.

The instrumentation must allow for monitoring of the electron beam current and shape as well as the relative position and angle of the electron and proton beams in the electron lens. Two modes are foreseen: a setup mode in which the electron beam current is modulated and affects only a single bunch in RHIC, and a compensation mode with a DC electron beam. The main parameters of the electron beams are presented in Table 1.

A RHIC electron lens consists of (see Fig. 6) an electron gun, an electron beam transport to the main solenoid, the superconducting main solenoid in which the interaction with the hadron beam occurs, an electron beam transport to the collector, an electron collector, and instrumentation.

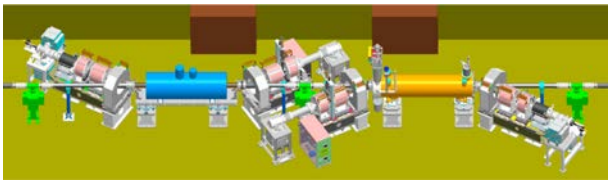

Figure 5: Layout of the two electron lenses in IR10. In 2013 the Blue lens (left) had the EBIS spare solenoid installed instead of the superconducting solenoid designed for the electron lens. In each lens three beams are present, the two proton beams and the electron beam acting on one of the proton beams; the proton beams are vertically separated.

Electron Gun

The electron gun (see Fig. 7 and Table 2) [59] has to provide a beam with a transverse profile that is close to Gaussian. Considering the magnetic compression of the electron beam into the main solenoid centre with a maximum magnetic field of 6.0 T, a cathode radius of 4.1 mm gives a Gaussian profile with 2.8 rms beam sizes. The perveance of the gun is $P_{\rm gun} = 1.0 \times 10^{-6}$ AV$^{-1.5}$. The current density of the electron beam on its radial periphery can be changed with the control electrode voltage (Fig. 7, top), while the general shape of the beam profile remains Gaussian. The cathodes (LB_6 and IrCe) were produced at BINP in Novosibirsk [79]. With a nominal current density of 12 A/cm^2, IrCe was chosen as the cathode material for its long lifetime (greater than 10 000 h).

An assembled gun is shown in the bottom panel of Fig. 7. The gun has three operating modes: (i) DC for continuous compensation; (ii) 100 Hz for electron beam positioning with BPMs, such that the electron current rises between the last two RHIC bunches and falls in the abort gap; (iii) 78 kHz for single-bunch compensation, with rise and fall time as in the 100 Hz mode.

The gun and collector vacuum is UHV compatible, with a design pressure of 10^{-10} Torr and a nominal pressure of 10^{-11} Torr for the interface to the RHIC warm bore. For this reason, all of the components are bakeable to 250°C. The gun and collector chambers will have a confined gas load by using a conductance-limiting aperture and enough installed pumping speed. All vacuum chambers interfacing with the RHIC warm bore will be made from stainless steel.

Electron Collector

The collector spreads the electrons on the inside of a cylindrical surface that is water-cooled on the outside (see Fig. 8). Simulations give a power density of 10 W/cm^2 for a 10 A electron beam, decelerated to 4 keV. The collector can absorb up to four times this power density [59]. The design is dictated primarily by the UHV requirements of RHIC. It separates the heavily bombarded area from the rest of

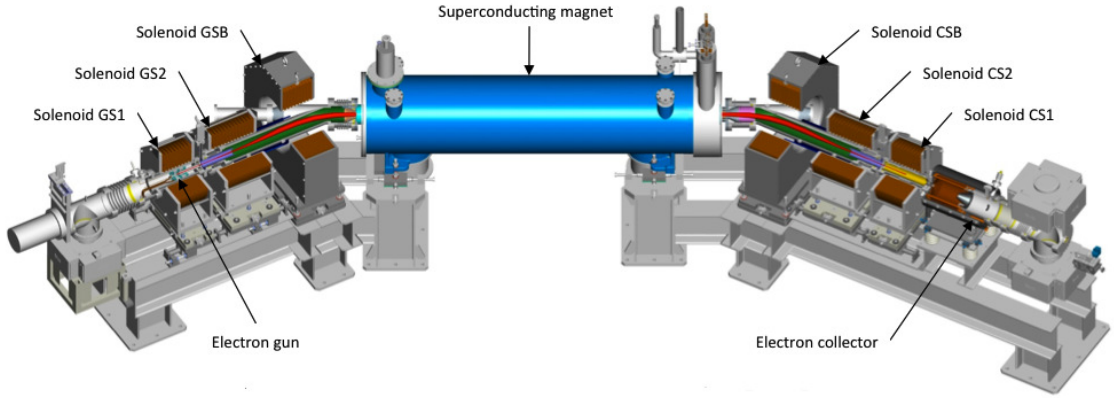

Figure 6: RHIC electron lens. The electrons in the DC beam move from left to right and interact with the protons, which move in the opposite direction, inside the superconducting solenoid.

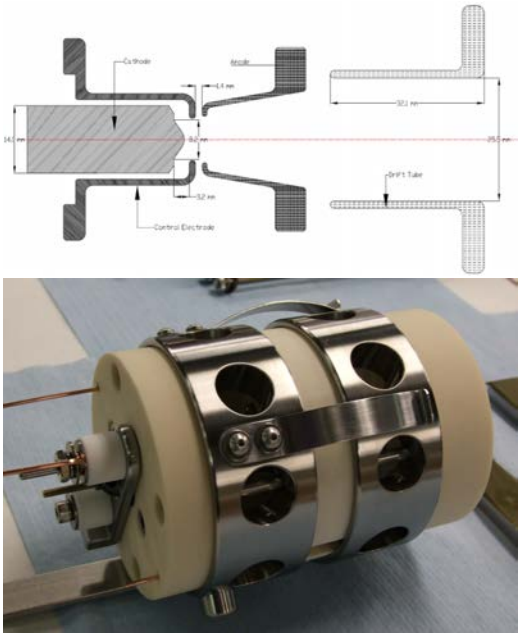

Figure 7: Gun schematic (top) and manufactured gun (bottom).

the electron lens by using a small diaphragm. A magnetic shield leads to fast diverting electrons inside the collector. The reflector has a potential lower than the cathode and pushes electrons outwards to the water-cooled cylindrical surface. Under a load twice as high as expected from a 2 A electron beam, the maximum temperature on the inner surface of the shell is 102°C. This temperature is acceptable for the material (copper) and for UHV conditions in RHIC. Twenty tubes with an ID = 8.0 mm are brazed to the outside of the cylindrical shell and are connected in parallel for water flow (Fig. 8).

The collector design also limits the flow of secondary and backscattered electrons from the collector towards the interaction region because the volume is magnetically shielded.

Table 2: Main parameters of the thermionic electron gun.

Quantity	Unit	Value
Perveance	μA V$^{-3/2}$	1.0
Voltage	kV	10
Current	A	1.0
Profile	–	Gaussian
Cathode radius	mm / σ	4.1 / 2.8
Max B-field	T	0.8
Modes	–	DC, 100 Hz, 78 kHz

The gun and collector power supplies are referenced to the cathode. The gun supplies include the cathode bias supply, the cathode heater, the beam-forming supply, and two anode supplies (DC and pulsed). The collector power supply is rated with 10 kV at 2 A, and will limit the energy deposited in the device should an arc occur. An ion reflector is powered with respect to the cathode potential. A suppressor element is powered with respect to the collector.

Superconducting Main Solenoid

A superconducting solenoid guides and stabilizes the low-energy electron beam during the interaction with the proton beam, and allows for magnetic compression of the electron beam size to the proton beam size. The superconducting main solenoid is a warm bore magnet with an operating field of 1–6 T (Fig. 9). The cryostat includes a number of additional magnets for a total of 17 [62]. The main parameters are given in Table 3.

Fringe field (FF) solenoid coils at both ends are included to allow for a guiding and focusing solenoid field for the electrons of no less than 0.3 T between the superconducting magnet and the warm transport solenoids GSB and CSB (see Fig. 6). To achieve the desired field uniformity over a range of field strengths B_s, anti-fringe field (AFF) coils are placed next to the FF coils. The FF and AFF coils on

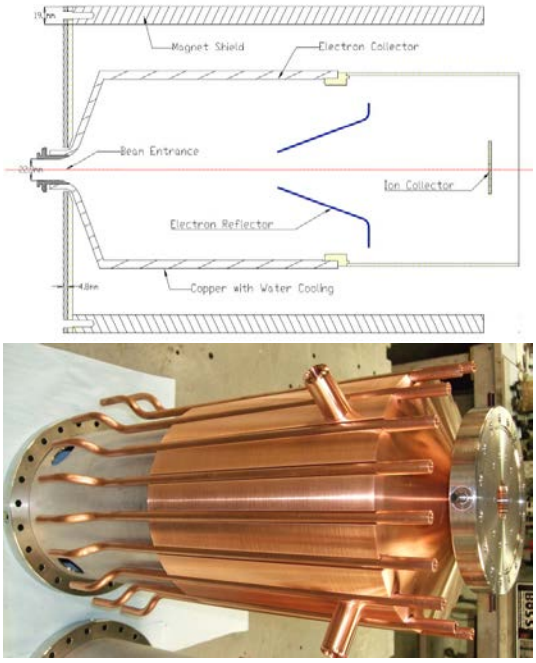

Figure 8: Collector schematic (top) and collector during manufacturing (bottom).

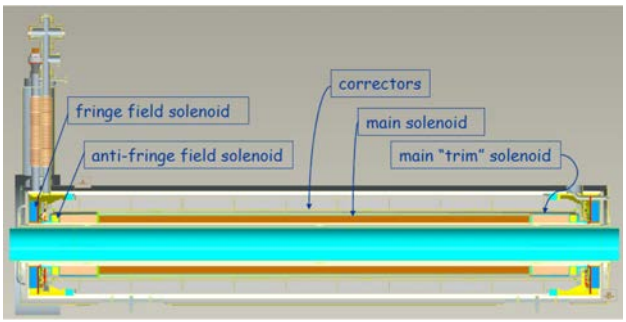

Figure 9: Superconducting main solenoid with fringe and anti-fringe solenoids, and straightness and angle correctors.

both ends can be powered independently to avoid forming a magnetic bottle with a low main field B_s, which would trap backscattered electrons. Extraction of scattered electrons is also possible by using a split electrode [69].

Included in the cryostat are five short (0.5 m) dipole correctors in both the horizontal and the vertical planes, to correct the solenoid field straightness to ± 50 μm. A long (2.5 m) dipole corrector in each transverse plane allows the angle of the electron beam inside the main magnet to be changed by ± 1 mrad (at 6 T) to align the electron and proton beams.

To reduce the number of layers in the main, FF, and AFF coils, and thereby the manufacturing time, a relatively large conductor was chosen, and the current in these coils was 430 A, 470 A, and 330 A, respectively [62]. A total of 17 individual coils (main coil, two FF coils, two AFF coils, ten straightness dipole correctors, and two angle dipole correctors) can be powered.

Table 3: Main parameters of the superconducting solenoids and corrector magnets in the same cryostat.

Quantity	Unit	Value
Cryostat length	mm	2838
Coil length	mm	2360
Warm bore inner diameter	mm	154
Uniform field region	mm	± 1050
Main coil layers	–	22 (11 double)
Additional trim layers in ends	–	4 (2 double)
Wire I_c specification (4.2 K, 7 T)	A	> 700
Operating main field B_s	T	1–6
Field uniformity $\Delta B_s/B_s$	–	± 0.006 (1–6 T)
Field straightness, after correction	μm	± 50 (1–6 T)
Straightness correctors (5H + 5V)	T m	± 0.010
Angle correctors (1H + 1V)	T m	± 0.015
Inductance	H	14
Stored energy (6 T)	MJ	1.4
Current (6 T)	A	430 (473[a])

[a] First double layer disabled.

The magnet is bath-cooled at a temperature just above 4.5 K, dictated by the operating pressure of RHIC cryogenic system's main warm return header. The current leads are all conventional vapour-cooled leads with individual flow controllers. The magnet's thermal shield and supports intercepts are cooled by the balance of the boil-off vapour not used by the current leads, which also returns to the main warm return header. The total flow rate draw from the RHIC cryogenic system is 1.6 g/s for each solenoid. Liquid helium can be supplied from a local Dewar when the RHIC refrigerator is not running.

Both magnets were tested vertically and reached 6.6 T, 10% above the maximum operating field, after a few training quenches. The magnets are now fully cryostatted. During the vertical test of the first magnet, a short in the first layer was detected, and the first double layer was grounded permanently. This required raising the operating current from 440 A to 473 A.

The field measurement system is under development. With proton rms beam sizes as small as 310 μm in the electron lenses, a deviation by no more than 50 μm of the solenoid field lines from straight lines is targeted. A needle-and-mirror system has been constructed that can be used in the RHIC tunnel to both measure the straightness of the field lines and verify the correction with the integrated short dipole correctors. The needle-and-mirror measurement system is being cross-checked with a vibrating wire system [80] using the second superconducting solenoid.

Warm Magnets

The electron beam is transported from the gun to the main solenoid and from the main solenoid to the collector through three warm solenoids each (Fig. 6) [54, 59]. These provide focusing with a solenoid field of at least 0.3 T along the whole transport channel. Within the GS2 and CS2 solenoids are also horizontal and vertical steering

magnets that can move the beam by ±5 mm in the main solenoid in either plane.

The solenoids are made of pancake coils whose field errors have been optimized [56]. The power consumption of both electron lenses with nominal parameters is limited to a total of 500 kW to avoid upgrades to the electrical and cooling water infrastructure in IR10. The main parameters are given in Table 4. All warm magnets and associated power supplies are installed (Fig. 10).

Table 4: Main parameters of the warm magnets.

Quantity	Unit	GS1 CS1	GS2 CS2	GSB CSB	GSX CSX	GSY CSY
ID	mm	174	234	480	194	210
OD	mm	553	526	860	208	224
Length	mm	262	379	262	500	500
No. layers	–	13	10	13	12	12
No. pancakes	–	9	13	9		
Inductance	mH	20	20	40	0.2	0.2
Resistance	mΩ	40	50	80	20	20
Current	A	1188	731	769	258	271
Power	kW	58	26	45	1.4	1.7
ΔT	K	13.4	3.6	14.2	5.9	6.9
Δp	bar	1.5	1.5	1.5	1.5	1.5
Solenoid field B_s	T	0.8	0.45	0.32		

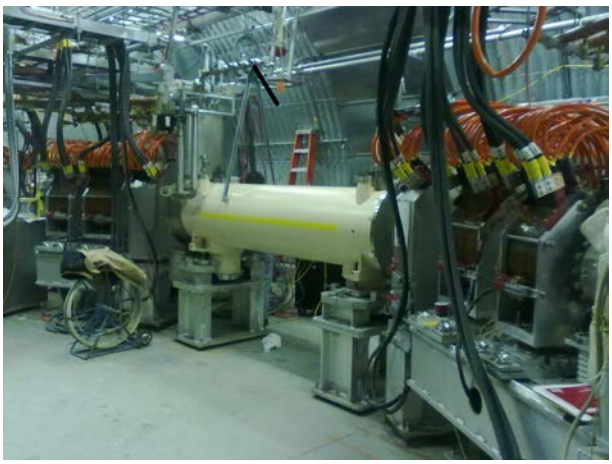

Figure 10: Yellow electron lens as installed in 2013. Visible are the gun side (left), the superconducting main solenoid (centre), and the collector side (right).

Instruments and Vacuum System

The instrumentation monitors the current and shape of the electron beam, the electron beam losses, and the overlap of the electron beam with the proton beam. The following items are included (the quantities given in parentheses are for each lens):

- dual-plane beam position monitors (2);
- e–p beam overlap monitor based on backscattered electrons (1) [65];
- differential current monitor (1);
- beam loss monitor drift tubes (8);
- collector temperature sensor (1);
- profile monitor (YAG screen) (1);
- profile monitor (pin-hole) (1);
- ion collector (1).

The layout of the vacuum system with the drift tubes is shown in Fig. 11. A total of eight drift tubes allow for changes in the electron beam energy and the removal of ions in the interaction region; the split drift tube 4 enables the removal of backscattered electrons [69], which can be trapped with a low main field B_s and high fringe fields. Figure 12 shows the detail of a section containing a beam position monitor (BPM), two drift tubes, cables, feedthroughs, and a heat sink to cool the cables, which can heat up when the proton beam deposits radio-frequency energy in the structure.

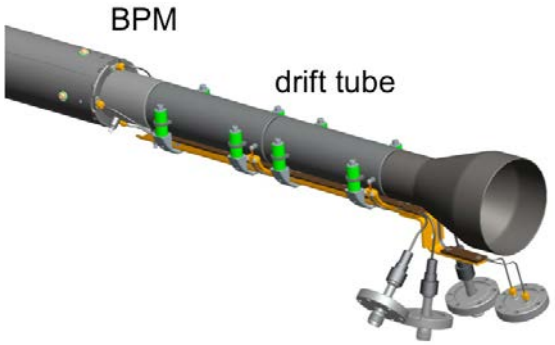

Figure 12: Beam position monitor and drift tubes with high-voltage stand-offs and cable.

The BPMs see only a signal with a pulsed beam. The proton beams are bunched, and a fill pattern can be created so that a bunch in one beam is detected when there is a gap in the other beam. The electron beam needs to be pulsed (at 100 Hz or 80 kHz) to be visible. The BPMs are used to bring the electron and proton beams in close proximity. The final alignment is done with the beam overlap monitor based on backscattered electrons [65]. Alignment was found to be a critical parameter in the Tevatron electron lenses, and the beams have to be aligned to within a fraction of the rms beam size, which can be as small as 310 μm (see Table 1). Figure 13 shows the beam overlap monitor.

The differential current monitor, drift tubes, ion collector, and collector temperature sensor all monitor the electron beam loss in the lens. The YAG screen and pin-hole profile monitors can only be used in a low-power mode. The extracted ion current is monitored in a collector [59].

TEST BENCH RESULTS

The test bench (Figs. 15 and 16) uses the location and the superconducting solenoid of the BNL EBIS test stand. Of the RHIC electron lenses, the following components were installed: a gun and collector, a GS1 solenoid with power supply, a movable pin-hole detector, a movable YAG screen with camera, and an electron halo detector.

The test bench work is complete and the following have been demonstrated [68, 72–74].

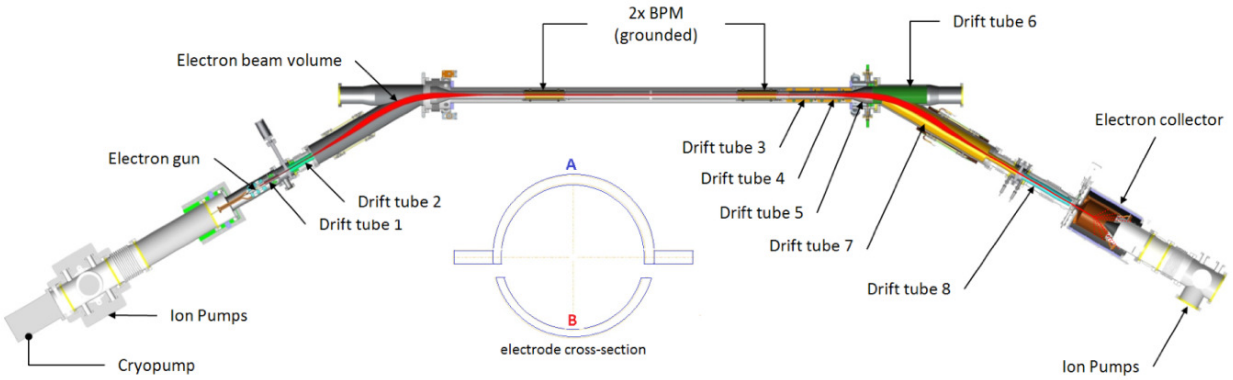

Figure 11: Layout of the drift tube system. The inset shows the cross-section of drift tube 4, which is split for the removal of trapped electrons [69].

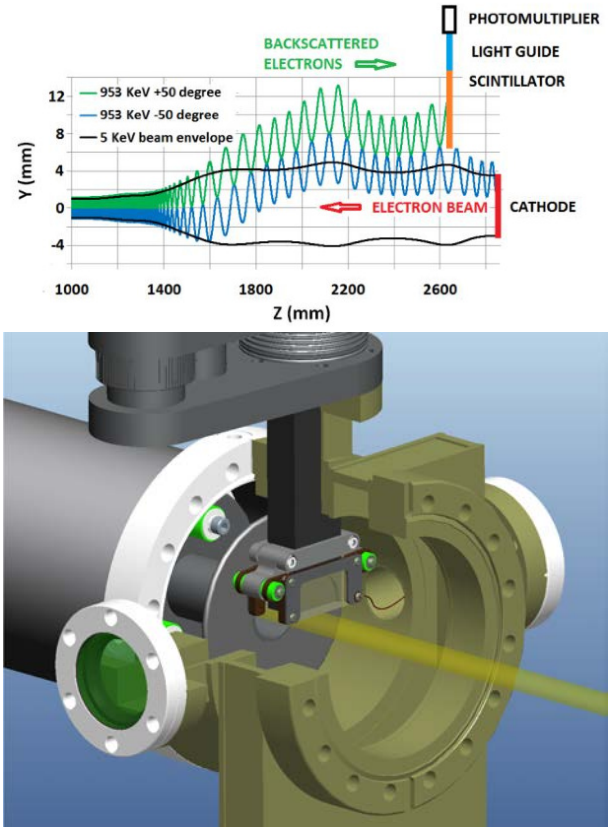

Figure 13: Beam overlap monitor using backscattered electrons [65]. The top view is a schematic showing two trajectories of backscattered electrons arriving at the gun above the primary electron beam; the bottom view shows the positioning mechanism of the detector.

- The gun operated in 80 kHz pulsed mode and DC mode, and reached 1 A of DC current with a current ripple of $\Delta I/I = 0.075\%$.
- The gun perveance with a La_6B cathode was measured to be 0.93 $\mu AV^{-3/2}$.
- The collector temperature and pressure was measured with the 1 A DC current and found to be within expectations.
- The Gaussian transverse electron beam profile was verified.
- The machine protection system was prototyped.
- Part of the controls software was tested.

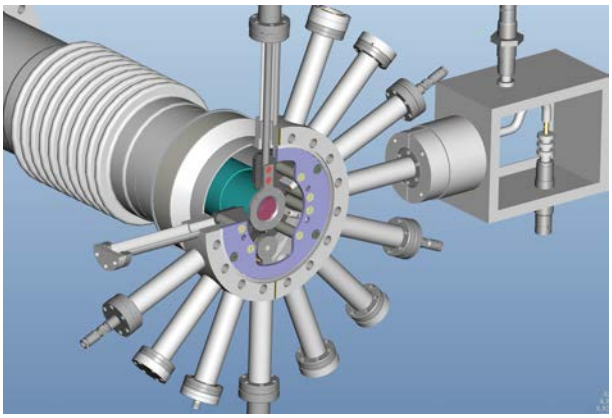

Figure 14: Instrument holder in front of the collector. Visible are the halo detector, YAG screen (inserted), and pinhole detector (retracted).

After completion of the test bench, the components were removed and installed in the RHIC tunnel and service building.

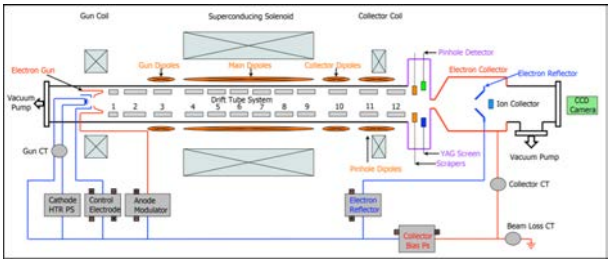

Figure 15: Schematic of the electron lens test bench layout.

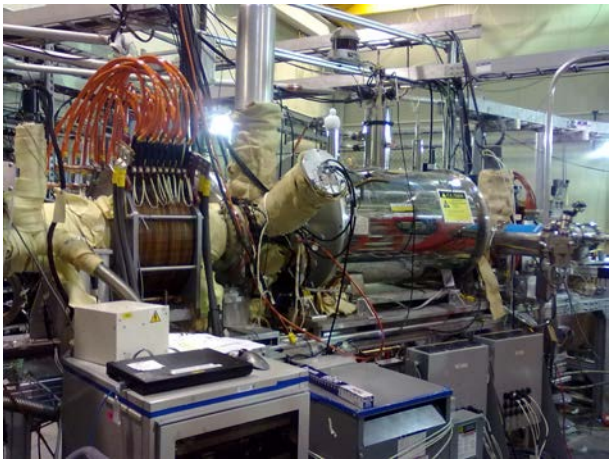

Figure 16: RHIC electron lens test bench. The electron beam travels from left to right, and GS1 is visible.

STATUS AND OUTLOOK

For the ongoing RHIC Run-13, the hardware of both lenses is partially installed (Fig. 5). The Blue lens has a complete electron beam transport system, although instead of the superconducting main solenoid designed for the electron lens a spare solenoid of the BNL EBIS is installed. This magnet is a 2 m-long superconducting solenoid with a maximum field strength of 5 T, but it does not have an iron yoke and therefore the field lines are not straight enough for beam–beam compensation; it does, however, allow for propagation of the electrons from the gun to the collector even at field strengths as low as 1 T. The low field is necessary to minimize the effect on the proton spin, as long as the second superconducting solenoid is not yet powered. The Blue lens also has a full complement of instrumentation, with the exception of the overlap monitor based on backscattered electrons. All drift tubes are grounded. In this configuration, all warm magnets can be commissioned as well as the electron beam in pulsed mode. The two dual-plane BPMs inside the superconducting solenoid, the YAG screen profile monitor, and the pin-hole detector can be tested. Interaction with the proton beam is in principle possible.

The Yellow lens has one of the new superconducting solenoids installed, but with a straight beam pipe that does not have BPMs or drift tubes (i.e. the vacuum system of the electron gun and collector is not connected to the proton beam vacuum system). This configuration allows for commissioning of the superconducting main solenoid and all superconducting correctors, as well as all warm magnets. The Yellow lens is shown in Fig. 10.

The second superconducting solenoid is set up in the Superconducting Magnet Division as a test bed for the field-straightness measurement system. As of the submission of this paper, the following have been achieved. A new lattice was commissioned for both rings that has a phase advance of a multiple of π between IP8 and the electron lens; for this new phase shifter, power supplies were installed in both rings and both transverse planes. A bunch-by-bunch loss monitor has become available, and bunch-by-bunch BTF measurements are being tested. The derivation of the incoherent beam–beam tune spread in the presence of coherent modes from transverse BTF measurements is under investigation [81]. In the Blue lens, a field of 1 T in the superconducting solenoid has been established. All warm solenoids were tested at operating currents, and all GSB and CSB solenoids ran concurrently with RHIC polarized proton operation.

In the summer of 2013 the second superconducting main solenoid will be installed, and the field straightness of both magnets will be measured in place and corrected. After that, the installation will be completed for both lenses, including the overlap detector based on backscattered electrons.

In 2014 RHIC is likely to operate predominantly with heavy ions. The beam–beam effect with heavy ions is too small for compensation, but all electron beam operating modes (pulsed and DC) can be established, and the electron beam can interact with the ion beam. The first compensation test can be done in polarized proton operation.

SUMMARY

Partial head-on beam–beam compensation is being implemented in RHIC. One of two beam–beam interactions is to be compensated with two electron lenses, one for each of the two proton beams. This allows for an increase in the bunch intensity with a new polarized proton source [37], with the goal of doubling the average luminosity in polarized proton operation.

The components of two electron lenses have been manufactured and partially installed. The current installation allows for commissioning of the warm magnets, electron beam, and instrumentation in the Blue lens. In the Yellow lens, the new superconducting solenoid and the warm magnets can be commissioned. First tests with ion beams are anticipated for the next year, after which the compensation can be commissioned for polarized proton operation.

ACKNOWLEDGMENTS

We are grateful to V. Shiltsev, A. Valishev, and G. Stancari of FNAL for many discussions on the Tevatron electron lenses and for the opportunities to participate in electron lens studies at the Tevatron. We also greatly benefited from the experience of the BNL EBIS team, including J. Alessi, E. Beebe, M. Okamura, and D. Raparia. We had many fruitful conversations about beam–beam and compensation problems with V. Shiltsev, A. Valishev, T. Sen, and G. Stancari of FNAL; X. Buffat, R. DeMaria, U. Dorda, W. Herr, J.-P. Koutchouk, T. Pieloni, F. Schmidt, and F. Zimmerman of CERN; K. Ohmi of KEK; V. Kamerdziev of FZ Jülich; A. Kabel of SLAC; and P. Görgen of TU Darmstadt. We are thankful to the U.S. LHC Accelerator Research Program (LARP) for support of beam–beam simulations. We also acknowledge the technical and administrative support received from the BNL Su-

perconducting Magnet Division, as well as from all groups of the Collider-Accelerator Department, in particular K. Mirabella and G. Ganetis.

REFERENCES

[1] G. Arzelia et al., Proc. 8th Int. Conf. High Energy Acc., p. 150 (1971).

[2] M. Bergher et al., "Status Report on D.C.I.," Proc. 1979 Particle Accelerator Conf., San Francisco, Calif., USA, pp. 3559–3561 (1979).

[3] Ya.S. Derbenev, "Collective Instability of Compensated Colliding Beams," Nuclear Physics Institute, Siberian Division, Academy of Sciences USSR, Novosibirsk, Report IYAF 70-72, in Russian (1972); SLAC-TRANS 151 in English.

[4] N.N. Chau and D. Potau, "Stabilité des oscillations transverse dans un anneau à charge d'espace compensée," LAL Orsay (1974 and 1975).

[5] B. Podobedov and R.H. Siemann, "Coherent Beam–Beam Interaction with Four Colliding Beams," Phys. Rev. E 52 (1995) 3066.

[6] E. Tsyganov, R. Meinke, W. Nexsen, and A. Zinchenko, "Compensation of the Beam–Beam Effect in Proton Colliders," SSCL-PREPRINT-519 (1993).

[7] E. Tsyganov, E. Tarantin, and A. Zinchenko, "Compensation of Space Charge Effect at Beam–Beam Interactions in Proton Proton Colliders," JINR-E9-96-4 (1996).

[8] V. Shiltsev, V. Danilov, D. Finley, and A. Sery, "Considerations on Compensation of Beam–Beam effects in the Tevatron with Electron Beams," Phys. Rev. ST Accel. Beams 2 (1999) 071001.

[9] E.N. Tsyganov, A. Taratin, and A.I. Zinchenko, "Beam–Beam Compensation at the LHC," CERN SL-Note-95-116-AP (1995).

[10] W. Scandale and F. Zimmermann, "Head-on Compensation in LHC," presentation at US LARP Mini-Workshop on Beam-Beam Compensation, SLAC (2009).

[11] U. Dorda, F. Zimmermann, W. Fischer, and V. Shiltsev, "LHC Beam–Beam Compensation Using Wires and Electron Lenses," Proc. 2007 Particle Accelerator Conf., Albuquerque, New Mexico, USA; LHC-PROJECT-Report-1023 (2007).

[12] Y. Ohnishi and K. Ohmi, "Beam–Beam Simulations in Four-Beam Scheme for High-Luminosity e+e- Collider," Proc. HALO'03 and Beam-Beam'03, Montauk, New York, AIP Conference Proceedings 693 (2003).

[13] A. Burov, V. Danilov, and V. Shiltsev, "Transverse Beam Stability with an Electron Lens," Phys. Rev. E 59 (1999) 3605.

[14] S. White, M. Blaskiewicz, and W. Fischer, "Coherent Beam–Beam Effects in Experiments and Implications for Head-on Beam–Beam Compensation," these proceedings.

[15] V. Shiltsev and A. Zinchenko, "Electron Beam Distortions in Beam–Beam Compensation Setup," Phys. Rev. ST Accel. Beams 1 (1998) 064001.

[16] V. Shiltsev, Y. Alexahin, K. Bishofberger, V. Kamerdzhiev, G. Kuznetsov, and X.-L. Zhang, "Experimental Demonstration of Colliding-Beam-Lifetime Improvement by Electron Lenses," Phys. Rev. Lett. 99 (2007) 244801.

[17] X.-L. Zhang, K. Bishofberger, V. Kamerdzhiev, V. Lebedev, V. Shiltsev, R. Thurman-Keup, and A. Tollestrup, "Generation and Diagnostics of Uncaptured Beam in the Fermilab Tevatron and its Control by Electron Lenses," Phys. Rev. ST Accel. Beams 11 (2008) 051002.

[18] V. Shiltsev et al., "Tevatron Electron Lenses: Design and Operation," Phys. Rev. ST Accel. Beams 11 (2008) 103501.

[19] G. Stancari, A. Valishev, G. Annala, G. Kuznetsov, V. Shiltsev, D. A. Still, and L. G. Vorobiev, "Collimation with Hollow Electron Beams," Phys. Rev. Lett. 107 (2011) 084802.

[20] V. Shiltsev, private communication.

[21] G. Stancari and A. Valishev, "Beam-Beam Compensation Studies in the Tevatron with Electron Lenses," these proceedings.

[22] J. Alessi (ed.), "Electron Beam Ion Source Pre-Injector Project (EBIS), Conceptual Design Report," BNL-73700-2005-IR (2005).

[23] J.G. Alessi et al., "Commissioning of the EBIS-based Heavy Ion Preinjector at Brookhaven," Proc. LINAC2010, Tsukuba, Japan, pp. 1033–1037 (2010).

[24] C. Montag et al., "RHIC Performance as a 100 GeV Polarized Proton Collider in Run-9," Proc. 2010 Int. Particle Accelerator Conf., Kyoto, Japan, pp. 531–533 (2010).

[25] H. Huang et al., "RHIC Polarized Proton Operation and Highlights," Proc. 2011 Int. Particle Accelerator Conf., San Sebastian, Spain, pp. 1888–1890 (2011).

[26] V. Schoefer et al., "RHIC Polarized Proton Operation in Run 12," Proc. 2012 Int. Particle Accelerator Conf., New Orleans, Louisiana, USA, pp. 184–186 (2012).

[27] Y. Luo, M. Bai, W. Fischer, C. Montag, and S. White, "Beam–Beam Effects in RHIC," BNL C-AD/AP/467 (2012).

[28] Y. Luo, M. Bai, W. Fischer, C. Montag, and S. White, "Beam–Beam Effects in RHIC," Proc. 52th ICFA Advanced Beam Dynamics Workshop on High Intensity High Brightness Hadron Beams (HB2012), Beijing, China (2012).

[29] S.M. White, W. Fischer, and Y. Luo, "Coherent Beam–Beam Effects Observation and Mitigation at the RHIC Collider," Proc. 2012 Int. Particle Accelerator Conf., New Orleans, Louisiana, USA, pp. 193–195 (2012).

[30] Y. Luo and W. Fischer, "Beam–Beam Observations in RHIC," these proceedings.

[31] F. Zimmermann and J. Poole (eds.), Proc. Workshop on Beam-Beam Effects in Large Hadron Colliders, LHC99, CERN, CERN-SL-99-039 AP (1999).

[32] T. Sen and M. Xiao (eds.), Proc. Workshop on Beam–Beam Effects in Circular Colliders, FNAL, FERMILAB-Conf-01/390-T (2001)

[33] W. Fischer and T. Sen (eds.), Proc. HALO'03 and Beam-Beam'03, Montauk, New York, USA, AIP Conference Proceedings 693 (2003).

[34] V. Shiltsev, Y. Alexahin, V. Lebedev, P. Lebrun, R. S. Moore, T. Sen, A. Tollestrup, A. Valishev, and X. L. Zhang, "Beam–Beam Effects in the Tevatron," Phys. Rev. ST Accel. Beams 8 (2005) 101001.

[35] W. Fischer (issue ed.) and W. Chou (exec. ed.), *ICFA Beam Dynamics Newsletter No. 52: Current Beam–Beam Problems* (2010).

[36] W. Herr, E. Metral, and T. Pieloni (eds.), these proceedings.

[37] A. Zelenski, "OPPIS with Fast Atomic Beam Source," presentation at 2011 Particle Accelerator Conf., New York, USA (2011).

[38] Y. Luo and W. Fischer, "Outline of Using an Electron Lens for the RHIC Head-on Beam–Beam Compensation," BNL C-A/AP/286 (2007).

[39] Y. Luo, W. Fischer, and N. Abreu, "Stability of Single Particle Motion with Head-on Beam–Beam Compensation in the RHIC," BNL C-A/AP/310 (2008).

[40] Y. Luo, W. Fischer, N. Abreu, E. Beebe, J. Beebe-Wang, C. Montag, M. Okamura, A. Pikin, and G. Robert-Demolaize, "Head-on Beam–Beam Compensation with Electron Lenses in the Relativistic Heavy Ion Collider," Proc. 2008 European Particle Accelerator Conf., Genoa, Italy, pp. 1616–1618 (2008).

[41] Y. Luo, G. Robert-Demolaize, N. Abreu, and W. Fischer, "Multi-Particle Weak-Strong Simulation of Head-on Beam–Beam Compensation in the RHIC," Proc. 2008 European Particle Accelerator Conf., Genoa, Italy, pp. 3125–3127 (2008).

[42] N.P. Abreu, W. Fischer, Y. Luo, and G. Robert-Demolaize, "The Effect of Head-on Beam–Beam Compensation on the Stochastic Boundaries and Particle Diffusion in RHIC," Proc. 2008 European Particle Accelerator Conf., Genoa, Italy, pp. 2521–2523 (2008).

[43] W. Fischer et al., "Long-range and Head-on Compensation Studies in RHIC with Lessons for the LHC," Proc. Final CARE-HHH Workshop on Scenarios for the LHC Upgrade and Fair (HHH-2008), Chavannes-de-Bogis, Switzerland; W. Scandale and F. Zimmermann (eds.), CERN-2009-004 (2009); CARE-Conf-08-032-HHH (2008).

[44] N.P. Abreu, W. Fischer, Y. Luo, and G. Robert-Demolaize, "Stochastic Boundary, Diffusion, Emittance Growth and Lifetime Calculation for the RHIC e-Lens," BNL C-A/AP/347 (2009).

[45] A. Valishev, Y. Luo, and W. Fischer, "Summary of the LARP Mini-Workshop on Electron Lens Simulations at BNL," BNL C-A/AP/353 (2009).

[46] Y. Luo, N.P. Abreu, R. de Maria, W. Fischer, G. Robert-Demolaize, and E. McIntosh, "Weak-Strong Simulation of Head-on Beam–Beam Compensation in the RHIC," Proc. 2009 Particle Accelerator Conf., Vancouver, Canada, pp. 94–96 (2009).

[47] W. Fischer, Y. Luo, and C. Montag, "Bunch Length Effects in the Beam–Beam Compensation with an Electron Lens," BNL C-AD/AP/359 (2010).

[48] W. Fischer, Y. Luo, and C. Montag, "Bunch Length Effects in the Beam–Beam Compensation with an Electron Lens," Proc. 2010 Int. Particle Accelerator Conf., Kyoto, Japan, pp. 4755–4757 (2010).

[49] C. Montag, W. Fischer, and D.M. Gassner, "Optimizing the Beam–Beam Alignment in an Electron Lens Using Bremsstrahlung," Proc. 2010 Int. Particle Accelerator Conf., Kyoto, Japan, pp. 537–539 (2010).

[50] W. Fischer et al., "Status of the RHIC Head-on Beam–Beam Compensation Project," Proc. 2010 Int. Particle Accelerator Conf., Kyoto, Japan, pp. 513–515 (2010).

[51] Y. Luo and W. Fischer, "6-D Weak-Strong Simulation of Head-on Beam–Beam Compensation in the RHIC," Proc. 2010 Int. Particle Accelerator Conf., Kyoto, Japan, pp. 4758–4760 (2010).

[52] Y. Luo and W. Fischer, "Simulation Study of Dynamic Aperture with Head-on Beam–Beam Compensation in the RHIC," BNL C-AD/AP/392 (2010).

[53] Y. Luo, W. Fischer, and X. Gu, "Coupling Effect on the Proton Optics From the Electron Lenses," BNL C-AD/AP/395 (2010).

[54] X. Gu, A. Pikin, M. Okamura, W. Fischer, Y. Luo, R. Gupta, J. Hock, A. Jain, and D. Raparia, "RHIC Electron Lens Beam Transport System Design Considerations," BNL C-AD/AP/409 (2010).

[55] X. Gu, Y. Luo, A. Pikin, M. Okamura, W. Fischer, C. Montag, R. Gupta, J. Hock, A. Jain, and D. Raparia, "Effect of the Electron Lenses on the RHIC Proton Beam Closed Orbit," BNL C-AD/AP/424 (2011).

[56] X. Gu, M. Okamura, A. Pikin, W. Fischer, and Y. Luo, "The Effects of Realistic Pancake Solenoids on Particle Transport," Nucl. Instrum. Methods A 637 (2011) 190.

[57] W. Fischer et al., "Status of the RHIC Head-on Beam–Beam Compensation Project," Proc. 2011 Particle Accelerator Conf., New York, USA, pp. 2223–2225 (2011).

[58] Y. Luo, W. Fischer, X. Gu, and A.I. Pikin, "Optimizing the Electron Beam Parameters for Head-on Beam–Beam Compensation in RHIC," Proc. 2011 Particle Accelerator Conf., New York, USA, pp. 70–72 (2011).

[59] A.I. Pikin et al., "Structure and Design of the Electron Lens for RHIC," Proc. 2011 Particle Accelerator Conf., New York, USA, pp. 2309–2311 (2011).

[60] X. Gu, W. Fischer, R.C. Gupta, J. Hock, Y. Luo, M. Okamura, A.I. Pikin, and D. Raparia, "Designing a Beam Transport System for RHIC's Electron Lens," Proc. 2011 Particle Accelerator Conf., New York, USA, pp. 1205–1207 (2011).

[61] X. Gu, W. Fischer, R.C. Gupta, J. Hock, Y. Luo, M. Okamura, A.I. Pikin, and D. Raparia, "The Effects of the RHIC e-Lenses' Magnetic Structure Layout on the Proton Beam Trajectory," Proc. 2011 Particle Accelerator Conf., New York, USA, pp. 1202–1204 (2011).

[62] R.C. Gupta et al., "Magnetic Design of e-Lens Solenoid and Corrector System for RHIC," Proc. 2011 Particle Accelerator Conf., New York, USA, pp. 1130–1132 (2011).

[63] P. Thieberger et al., "Proposed Electron Halo Detector System as One of the Beam Overlap Diagnostic Tools for the New RHIC Electron Lens," Proc. 2011 Particle Accelerator Conf., New York, USA, pp. 489–491 (2011).

[64] C. Montag, M. Bai, K.A. Drees, W. Fischer, A. Marusic, and G. Wang, "Beam Experiments Related to the Head-on Beam–Beam Compensation Project at RHIC," Proc. 2011 Particle Accelerator Conf., New York, USA, pp. 2243–2245 (2011).

[65] P. Thieberger et al., "Design of a Proton-Electron Beam Overlap Monitor for the New RHIC Electron Lens, Based on Detecting Energetic Backscattered Electrons," Proc. Beam Instrumentation Workshop BIW12, Newport News, Virginia, USA (2012).

[66] T.A. Miller, J. Aronson, D.M. Gassner, and A. Pikin, "RHIC Electron Lens Beam Profile Monitoring," Proc. Beam Instrumentation Workshop BIW12, Newport News, Virginia, USA (2012).

[67] W. Fischer et al., "Construction Progress of the RHIC Electron Lenses," Proc. 2012 Int. Particle Accelerator Conf., New Orleans, Louisiana, USA, pp. 2125–2127 (2012).

[68] X. Gu et al., "The e-Lens Test Bench for RHIC Beam–Beam Compensation," Proc. 2012 Int. Particle Accelerator Conf., New Orleans, Louisiana, USA, pp. 2720–2722 (2012).

[69] X. Gu, W. Fischer, D.M. Gassner, K. Hamdi, J. Hock, Y. Luo, C. Montag, M. Okamura, A.I. Pikin, and P. Thieberger, "A Split-Electrode for Clearing Scattered Electrons in the RHIC e-Lens," Proc. 2012 Int. Particle Accelerator Conf., New Orleans, Louisiana, USA, pp. 4038–4040 (2012).

[70] Y. Luo, W. Fischer, N.P. Abreu, A. Pikin, and G. Robert-Demolaize, "Six-Dimensional Weak-Strong Simulation of Head-on Beam–Beam Compensation in the Relativistic Heavy Ion Collider," Phys. Rev. ST Accel. Beams 15 (2012) 051004.

[71] S.M. White, W. Fischer, and Y. Luo, "Simulations of Coherent Beam–Beam Effects with Head-on Compensation," Proc. 2012 Int. Particle Accelerator Conf., New Orleans, Louisiana, USA, pp. 187–189 (2012).

[72] T.A. Miller, J.N. Aronson, D.M. Gassner, X. Gu, A.I. Pikin, and P. Thieberger, "Electron Lens Test Stand Instrumentation Progress," Proc. 2012 Int. Beam Instrumentation Conf., Tsukuba, Japan (2012).

[73] X. Gu et al., "RHIC Electron Lens Test Bench – High Intensity Electron Beam Characteristics and Hardware Commissioning," report in preparation (2013).

[74] D.M. Gassner, E. Beebe, W. Fischer, X. Gu, K. Hamdi, J. Hock, C. Liu, T.A. Miller, A. Pikin, and P. Thieberger, "RHIC Electron Lens Test Bench Diagnostics," Proc. DIPAC2011, Hamburg, Germany, pp. 38–40 (2011).

[75] E. Keil, "Beam–Beam Dynamics," in CERN 95-06, pp. 539–555 (1995).

[76] E.D. Courant and H. Snyder, "Theory of the Alternating-Gradient Synchrotron," Ann. Phys. 281 (1957) 360.

[77] D.A. Edwards and M. Syphers, "Linear Betatron Motion," *Handbook of Accelerator Physics and Engineering*, 3rd printing (Singapore: World Scientific, 2006), 65.

[78] M. Bai, private communication (2011).

[79] G. Kuznezov, BINP Novosibirsk (2011).

[80] A. Jain, "Plans for Measurement of Field Straightness in the Solenoids for the Electron Lens System for RHIC," presentation at 17th International Magnetic Measurement Workshop (IMMW17), Barcelona, Spain (2011).

[81] P. Görgen, O. Boine-Frankenheim, and W. Fischer, "BTF Measurements with Beam–Beam Interactions," these proceedings.

Published by CERN in the Proceedings of the ICFA Mini-Workshop on Beam–Beam Effects in Hadron Colliders,
CERN, Geneva, Switzerland, 18–22 March 2013, edited by W. Herr and G. Papotti, CERN–2014–004 (CERN, Geneva, 2014)

BEAM–BEAM COMPENSATION STUDIES IN THE TEVATRON WITH ELECTRON LENSES

G. Stancari*, A. Valishev
Fermi National Accelerator Laboratory, Batavia, IL, USA

Abstract

At the Fermilab Tevatron collider, we studied the feasibility of suppressing the antiproton head-on beam–beam tune spread by using a magnetically confined 5 keV electron beam with Gaussian transverse profile overlapping with the circulating beam. When electron cooling of antiprotons was applied in regular Tevatron operations, the nonlinear head-on beam–beam effect on antiprotons was small. Therefore, we first focused on the operational aspects, such as beam alignment and stability, and on fundamental observations of tune shifts, tune spreads, lifetimes, and emittances. We also attempted two special collider stores with only three proton bunches colliding with three antiproton bunches, to suppress long-range forces and enhance head-on effects. We present here the results of this study and a comparison between numerical simulations and observations. These results contributed to the application of this compensation concept to RHIC at Brookhaven.

INTRODUCTION

The nonlinear forces between colliding beams are one of the main performance limitations in modern colliders. Electron lenses have been proposed as a tool for the mitigation of beam–beam effects [1]. It was demonstrated that the pulsed electron current can produce different betatron tune shifts in different proton or antiproton bunches, thus cancelling bunch-to-bunch differences generated by long-range beam–beam forces [2–4]. In these experiments, the electron beam had a flat transverse current-density distribution, and the beam size was larger than the size of the circulating beam. To first order, the effect of the electron lens was a bunch-by-bunch linear betatron tune shift.

The present research went a step further. We studied the feasibility of using the magnetically confined, nonrelativistic beam in the Tevatron electron lenses to compensate for nonlinear head-on beam–beam effects in the antiproton beam. For this purpose, the transverse density distribution of the electron beam must mimic that of the proton beam, so that the space-charge force acting on the antiprotons is partially cancelled. The betatron phase advance between the interaction points and the electron lens should be close to an integer multiple of π.

During regular Tevatron operations, both stochastic and electron cooling were used to reduce the transverse emittance of antiprotons. Under these conditions, antiprotons were transversely much smaller than protons, making head-on effects essentially linear. Intensity loss rates of antiprotons due to beam–beam effects were caused by long-range interactions and rarely exceeded 5% per hour. While an improvement of the Tevatron performance by head-on beam–beam compensation was not foreseen, we were interested in the feasibility of the concept and in providing an experimental basis for the simulation codes used in the planned application of electron lenses to the RHIC collider at BNL [5–7].

* stancari@fnal.gov

EXPERIMENTAL APPARATUS

An electron gun based on a convex tungsten dispenser cathode operating at a temperature of 1400 K was designed and built [8]. The diameter of the cathode was 10.2 mm (0.4 in.); its shape and the geometry of the electrodes were chosen to produce a current-density profile close to a Gaussian distribution. Figure 1 shows pictures of the electron gun and an example of a current-density measurement. The maximum peak current yield was 0.5 A at a cathode–anode voltage of 4.6 kV. The standard deviation (rms) of the cur-

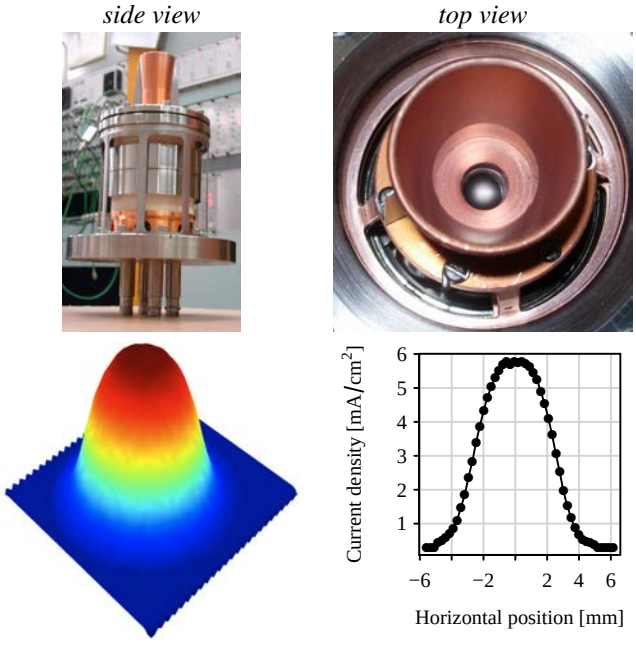

Figure 1: The 10.2 mm (0.4 in.) Gaussian electron gun: the assembled gun (top left); a detail of the copper cylindrical anode and the convex tungsten dispenser cathode surface (top right); and an example of current-density measurements (bottom).

978-92-9083-404-5, 0007-8328 –
http://dx.doi.org/10.5170/CERN–2014–004.121

Table 1: Tevatron lattice functions (amplitude β, dispersion D, and betatron phase ϕ) at the interaction points and at the electron lens.

	β_x	β_y	D_x	D_y	ϕ_x	ϕ_y
	[m]		[m]		[2π]	
CDF	0.30	0.30	0.0	0.0	6.63	6.85
DZero	0.50	0.50	0.0	0.0	13.77	13.85
TEL2	68	153	1.2	−1.0	3.17	3.22

rent profile distribution was $\sigma_g = 2.0$ mm at the gun.

The electron gun was installed in the second Tevatron electron lens (TEL2) in June 2009 (Fig. 2). In the electron lens, the beam was generated inside the gun solenoid (0.1–0.4 T) and guided by a superconducting solenoid (1–6 T) through the 3 m overlap region, where it interacted with the circulating beams (protons or antiprotons) before being extracted and dumped in the collector. The size σ_m of the electron beam in the overlap region was controlled by the ratio between the magnetic field in the gun solenoid, B_g, and the magnetic field in the main solenoid, B_m: $\sigma_m = \sigma_g \cdot \sqrt{B_g/B_m}$. Distortions of the electron beam profile due to its space-charge evolution were mitigated by the large axial field ($B_m > 1$ T).

In the Tevatron, 36 proton bunches (referred to as P1–P36) collided with 36 antiproton bunches (A1–A36) at the centre-of-momentum energy of 1.96 TeV. There were two head-on interaction points (IPs), corresponding to the CDF and the DZero experiments. Protons and antiprotons circulated in the same vacuum pipe on helical orbits. Their separation at TEL2 was 9 mm (about 6 mm both horizontally and vertically). Each particle species was arranged in three trains of 12 bunches each, circulating at a revolution frequency of 47.7 kHz. The bunch spacing within a train was 396 ns, or 21 RF buckets at 53 MHz. The bunch trains were separated by 2.6 μs abort gaps. The synchrotron frequency was 34 Hz, or 7×10^{-4} times the revolution frequency. The machine operated with betatron tunes near 20.58. The relevant lattice functions are reported in Table 1. Thanks to the special 5 kV high-voltage modulator (with 200 ns rise time), the electron beam could be synchronized with any bunch or group of bunches, and its intensity could be varied bunch by bunch [9].

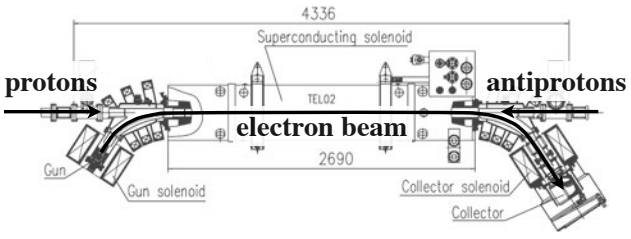

Figure 2: Layout of the beams in the Tevatron electron lens (dimensions are in millimeters).

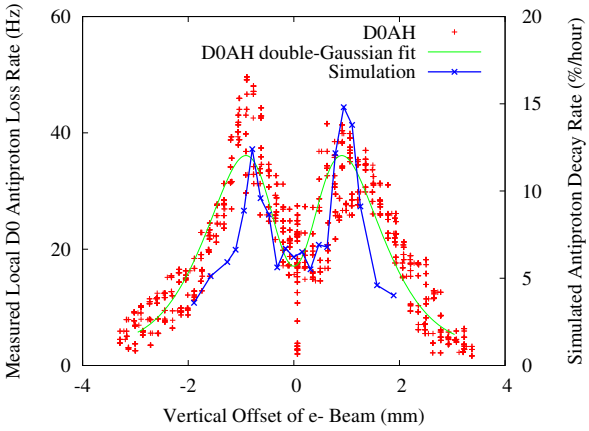

Figure 3: Measured loss rates (red) and calculated intensity decay rates (blue) during a vertical electron beam scan across the antiproton beam. The antiproton vertical tune was lowered by 0.003 to enhance the effect. No losses caused by the electron beam were observed with nominal tunes.

RESULTS

Experiments on beam–beam compensation with Gaussian electron beams were carried out between September 2009 and July 2010. Preliminary results were discussed in Refs. [10, 11].

Beam Alignment and Loss Patterns

Because of the nonlinear fields, alignment between electrons and antiprotons was critical. We performed several position scans to ensure that the response of the beam position monitors was accurate both for fast signals from antiproton bunches and for slower signals from electron pulses. These position scans were also useful for assessing the effects of misalignments on losses and for comparing the experimental results with numerical calculations. We simulated losses during a vertical alignment scan using the weak–strong numerical tracking code Lifetrac [12]. The model included the full collision pattern for the relevant antiproton bunch and a thin-kick Gaussian electron beam implemented via an analytical formula. The beam parameters corresponded to the conditions at the time of the measurement at the end of Store 7718. We tracked a bunch of 5000 macroparticles for 3×10^6 turns for various vertical electron beam misalignments and evaluated the intensity loss rate. The simulation reproduced several features observed in experiments. First, the simulation performed at the nominal antiproton working point (with tunes set to $Q_x = 0.575$ and $Q_y = 0.581$) predicted no losses for any value of the vertical misalignment. This was also observed experimentally: at the nominal working point, the electron beam did not cause any additional beam loss. Similarly to the experiment, the vertical tune in the simulation had to be lowered by 0.003 to produce particle losses. Moreover, the simulation at the modified working point demonstrated

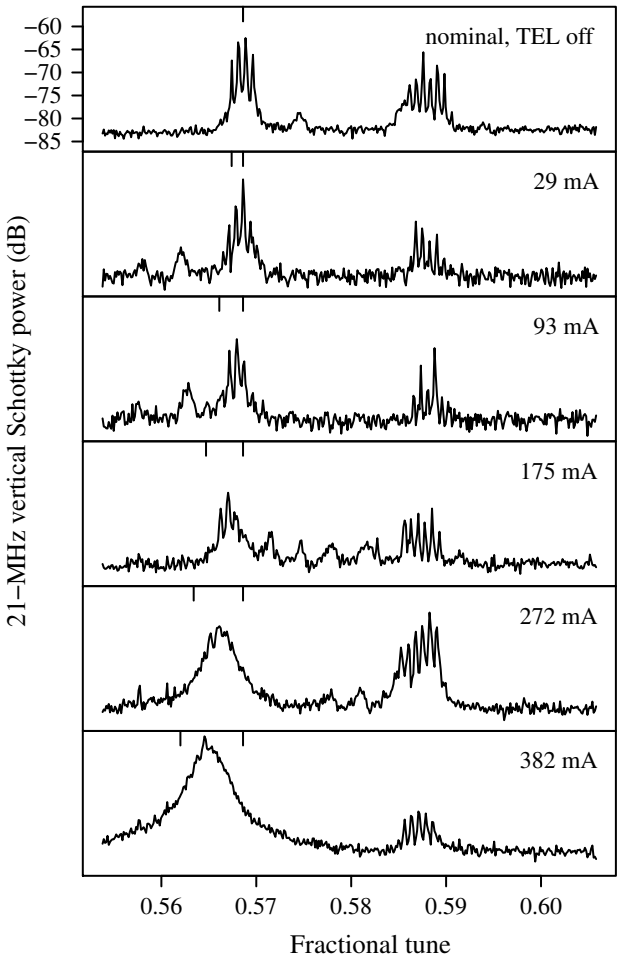

Figure 4: Schottky spectra versus electron lens current.

the characteristic double-hump structure of the loss rate as a function of the offset. The positions of peaks were in good agreement with the measurements. Figure 3 shows the measured loss rates (red crosses) and the simulated decay rates (blue crosses and lines). Both electron and antiproton vertical rms beam sizes in the overlap region were equal to 0.6 mm.

Incoherent Tune Shifts and Tune Spread

The effect of the electron lens on the incoherent tune distribution could be observed directly during dedicated antiproton-only stores, when there was no contamination from protons in the 21 MHz Schottky signal. Figure 4 shows the vertical Schottky signal as a function of electron lens current. The vertical tick marks indicate the expected magnitude of the linear beam–beam parameter ξ_e due to N_e electrons with Gaussian standard deviation σ_e and velocity $\beta_e c$ at a location where the amplitude function is β:

$$\xi_e = -\frac{N_e r_p \beta (1+\beta_e)}{4\pi\gamma_p \sigma_e^2}.$$

Here, r_p represents the classical radius of the proton and γ_p is the relativistic factor of the circulating beam. As expected, a downward shift and widening of the antiproton tune distribution is observed. The width of the vertical tune line agrees well with the hypothesis that ξ_e represents the maximum tune shift.

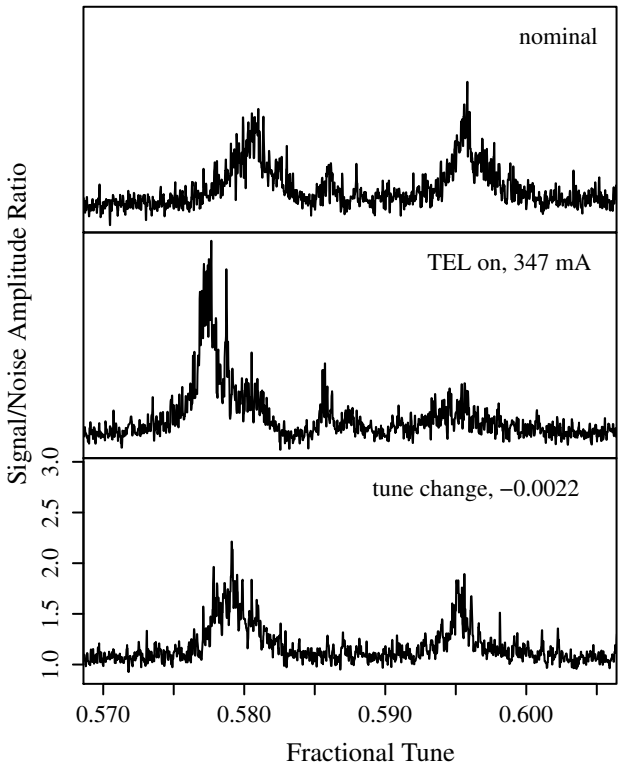

Figure 5: Spectra of transverse coherent modes.

Effects on Coherent Beam–Beam Modes

A system for bunch-by-bunch measurements of transverse coherent beam–beam oscillations was developed [13, 14]. It was based on the signal from a single beam position monitor in a region of the ring with high amplitude functions. Because of its high frequency resolution and its single-bunch capability, this system complemented the Schottky detectors and direct-diode-detection base-band tune monitor. It was conceived as a possible tool for monitoring beam–beam compensation effects.

Figure 5 shows the signal from a single antiproton bunch towards the end of a regular collider store (Store 7719). The top plot shows the spectrum of coherent modes under nominal conditions. The linear beam–beam parameter per interaction point was 0.0050 for antiprotons and 0.0023 for protons. The middle plot corresponds to the electron lens acting on the bunch, with $\xi_e = -0.006$. For comparison, the bottom plot shows the effect of lowering the vertical antiproton tune by 0.0022. In the middle plot, one can see a downward shift of the first eigenmode and a suppression of the second. This suppression could be caused in part by the antiproton tune moving away from the proton tune. A considerable change in the width of the first coherent mode was also observed, but relating the reduced width of

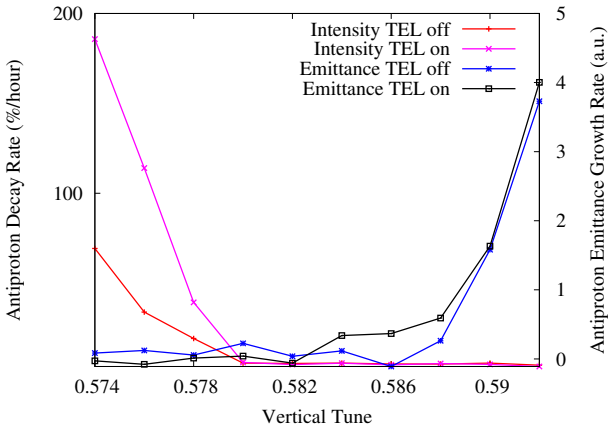

Figure 7: Numerical simulation of a diagonal tune scan.

the coherent mode to a narrower tune distribution (as one would expect if there was beam–beam compensation) requires further investigation and numerical simulations.

Tune Scans with Dedicated Head-on-only Stores

To enhance head-on effects and to suppress long-range forces in the Tevatron, two special 3-on-3 collider stores were attempted. In these stores, three proton bunches collided with three antiproton bunches. The bunches were equally spaced around the machine. Antiprotons were intentionally heated to increase their emittance and approach the size of proton bunches. Unfortunately, during the first experiment, the emittances of two proton bunches increased dramatically between the beta squeeze and collisions, before the beginning of the study. Hence, the store could not be used for our purposes.

A smaller blow-up of proton emittances occurred before the second study as well, making conditions far from ideal: the antiproton beam–beam parameter was less than 0.015, electron sizes could not be matched to proton sizes, and the attempt to increase the size of the electron beam resulted in a reduced compensation strength ($\xi_e = -0.002$). Nevertheless, several tune scans were performed, both vertically and diagonally in the tune diagram.

Figure 6 shows the measured decay rates for the three antiproton bunches as a function of the average tune (from the 1.7 GHz Schottky detector) during a diagonal scan: the bunch affected by the electron lens (A25, magenta), the control bunch (A13, dark blue), and the bunch colliding with the two least-dense proton bunches (A1, green). Lifetimes and tune space were obviously better for A1. The tune shift of the affected bunch with respect to the control bunch is compatible with the expected amount (0.002), but it is too small to be clearly observed. Some resonances (4/7 and 7/12, for instance) appear stronger with the lens on, whereas the 3/5 resonance is weaker (or shifted). One may observe that, as expected, beam–beam forces appear to drive the even resonance 7/12 (large difference between the green and the blue points) but not the odd resonance 4/7 (control bunch and low-beam–beam bunch have similar lifetimes). There are regions of the working point where the bunch affected by the electron lens had better lifetime (0.560–0.568 and 0.592–0.598), but this special 3-on-3 store was not enough to clearly show a reduction in tune spread or an improvement in the available tune space.

Nevertheless, these measurements provided useful information on the available tune space for comparisons with simulation codes. Figure 7 shows the antiproton intensity decay rates and emittance growth rates calculated with Lifetrac as a function of tune in a diagonal scan. The horizontal scale is the bare lattice tune plus half the beam–beam parameter, in order to simulate the average of the incoherent tune distribution. As the tune approaches the 7th-order resonance (0.571) from above, loss rates increase dramatically. Increasing the tune towards the 5th-order resonance (0.6) causes emittance growth. According to this calculation, with the non-ideal experimental conditions described above, the electron lens does not cause harm in the stable region, but it can make things worse outside. The region of available tune space is well reproduced by the simulations.

CONCLUSIONS

The first studies of beam–beam compensation with Gaussian electron lenses were carried out at the Tevatron.

We found that, in spite of the very different time structures of the antiproton bunch and the electron pulse, alignment of the electron beam with the circulating beam using a common beam position monitor was accurate to within 0.1 mm and reproducible from store to store.

We observed the effects of the electron lens on beam lifetimes and tunes. At the nominal working point in tune space, the electron lens did not have any adverse effects on the circulating beam, even when intentionally misaligned. With only antiprotons in the machine, the tune shift and tune spread caused by the electron lens were clearly seen.

Dedicated collider stores with only three bunches per species (no long-range interactions) were attempted, but the experimental conditions were not ideal. The data were used for code benchmarking. Moreover, tune scans conducted during these special stores provided a direct comparison between the lifetimes of a control antiproton bunch, a bunch affected by the electron lens, and a bunch experiencing reduced beam–beam forces.

The machine was not ideal for a direct demonstration of the beam–beam compensation concept for two main reasons: head-on nonlinearities for cooled antiprotons were weak during normal operations; and the lattice requirements (zero dispersion, phase advance close to an integer multiple of π) were not exactly met at the electron lens. Nevertheless, several key experimental observations were made.

ACKNOWLEDGMENTS

The authors thank W. Fischer and C. Montag (BNL) for their suggestions on experiment design and their participation in part of the studies, and V. Shiltsev (Fermilab) for

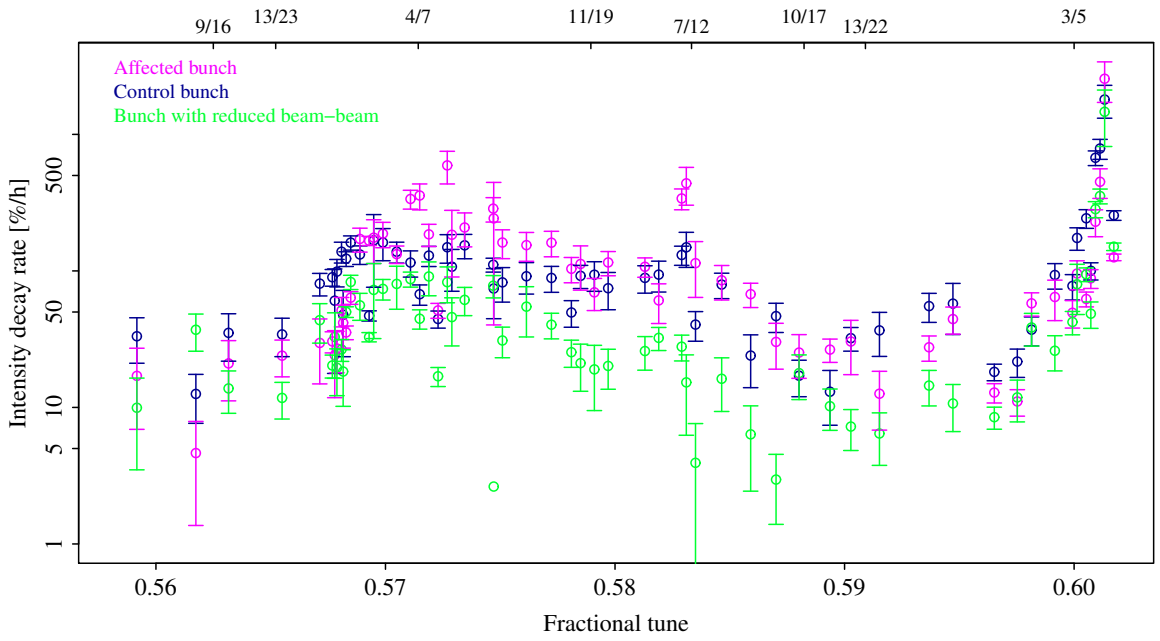

Figure 6: Measured decay rates of the three antiproton bunches during a diagonal tune scan in a special 3-on-3 collider store.

discussions and insights. We are grateful to the Operations Department in Fermilab's Accelerator Division for making these experiments possible.

Fermi Research Alliance, LLC, operates Fermilab under contract no. DE-AC02-07CH11359 with the United States Department of Energy. This work was partially supported by the US LHC Accelerator Research Program (LARP).

REFERENCES

[1] V. Shiltsev et al., Phys. Rev. ST Accel. Beams 2 (1999) 071001.

[2] V. Shiltsev et al., Phys. Rev. Lett. 99 (2007) 244801.

[3] V. Shiltsev et al., New J. Phys. 10 (2008) 043042.

[4] V. Shiltsev et al., Phys. Rev. ST Accel. Beams 11 (2008) 103501.

[5] W. Fischer et al., Proc. 2012 Int. Particle Accelerator Conf. (IPAC12), New Orleans, Louisiana, USA, 20–25 May 2012, p. 2125.

[6] X. Gu et al., Proc. 2012 Int. Particle Accelerator Conf. (IPAC12), New Orleans, Louisiana, USA, 20–25 May 2012, p. 2720.

[7] Y. Luo et al., Phys. Rev. ST Accel. Beams 15 (2012) 051004.

[8] V. Kamerdzhiev et al., Proc. 2008 European Particle Accelerator Conf. (EPAC08), Genoa, Italy, 23–27 June 2008, p. 3500.

[9] H. Pfeffer and G. Saewert, J. Instrum. 6 (2011) P11003.

[10] A. Valishev et al., Proc. 2010 Int. Particle Accelerator Conf. (IPAC10), Kyoto, Japan, 23–28 May 2010, p. 2084.

[11] A. Valishev and G. Stancari, Proc. 2011 Particle Accelerator Conf. (PAC11), New York, USA, 28 March–1 April 2011, p. 67.

[12] D. Shatilov et al., Proc. 2005 Particle Accelerator Conf. (PAC05), Knoxville, Tennessee, USA, 16–20 May 2005, p. 4138.

[13] G. Stancari, A. Valishev, and A. Semenov, Proc. 14th Beam Instrumentation Workshop (BIW10), Santa Fe, New Mexico, USA, 2–6 May 2010, p. 363.

[14] G. Stancari and A. Valishev, Phys. Rev. ST Accel. Beams 15 (2012) 041002.

Published by CERN in the Proceedings of the ICFA Mini-Workshop on Beam–Beam Effects in Hadron Colliders,
CERN, Geneva, Switzerland, 18–22 March 2013, edited by W. Herr and G. Papotti, CERN–2014–004 (CERN, Geneva, 2014)

SIX-DIMENSIONAL WEAK–STRONG SIMULATIONS OF HEAD-ON BEAM–BEAM COMPENSATION IN RHIC*

Y. Luo, W. Fischer, N.P. Abreu, X. Gu, A. Pikin, G. Robert-Demolaize
BNL, Upton, NY, USA

Abstract

To compensate the large beam–beam tune spread and beam–beam resonance driving terms in the polarized proton operation in the Relativistic Heavy Ion Collider (RHIC), we will introduce a low-energy DC electron beam into each ring to collide head-on with the opposing proton beam. The device to provide the electron beam is called an electron lens. In this article, using a 6-D weak–strong beam–beam interaction simulation model, we investigate the effects of head-on beam–beam compensation with electron lenses on the proton beam dynamics in the RHIC 250 GeV polarized proton operation. This article is abridged from the published article [1].

INTRODUCTION

To further increase the luminosity in the RHIC polarized proton (p-p) run, we plan to increase the proton bunch intensity with an upgraded polarized proton source [2]. In the 2012 RHIC 250 GeV p-p run, the maximum bunch intensity at the beginning of physics store was 1.7×10^{11}. With the upgraded polarized proton source, we expect that the maximum bunch intensity will be increased up to 3.0×10^{11}. Assuming the normalized r.m.s. transverse emittance of 15 π mm·mrad, the linear incoherent tune shift or the beam–beam parameter will reach 0.03.

Currently, the working tune space for the RHIC p-p operation is chosen between 2/3 and 7/10 to achieve a good beam lifetime at store with beam–beam interaction and to maintain the proton polarization on the energy ramp and at the physics store [3]. The 7/10 tune space is not only a 10th betatron resonance but also a spin depolarization resonance. Therefore, there is not enough tune space between 2/3 and 7/10 to hold the beam–beam generated tune spread when the bunch intensity is greater than 2×10^{11}.

To reduce the beam–beam tune spread and also to compensate the non-linear beam–beam resonance driving terms, we plan to install head-on beam–beam compensation in the RHIC p-p operation. The proton beams collide at IP6 and IP8. A d.c. low-energy electron beam will be introduced into each ring around IP10 to head-on collide with the proton beam. The electron beam should have the same transverse profile as the proton beam. The device to provide the electron beam for this purpose is called an electron lens (e-lens) [4].

In the following, with the 6-D weak–strong simulation, we study the head-on beam–beam compensation with e-lenses on the proton beam dynamics in the RHIC 250 GeV p-p runs. The results from dynamic aperture and proton beam loss rate calculations are presented. Key beam parameters involved in this scheme are varied to search for the optimum compensation condition. The sensitivity of head-on beam–beam compensation to beam imperfections and beam offsets is also studied.

*This work was supported by Brookhaven Science Associates, LLC under Contract No. DE-AC02-98CH10886 with the US Department of Energy.

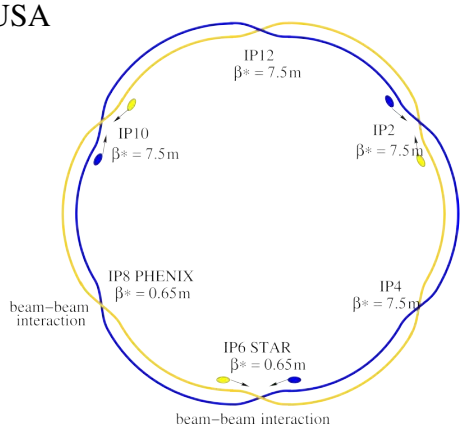

Figure 1: The layout of the head-on beam–beam compensation in the RHIC. E-lenses are to be installed on either side of IP10.

LATTICE AND BEAM PARAMETERS

In the following simulation, we use a proposed Blue ring lattice for 250 GeV RHIC polarized proton operation. Table 1 lists the lattice and beam parameters. The β^* values at IP6 and IP8 are 0.5 m. The β values at the e-lenses are 10 m. The RHIC has not yet operated with $\beta^* = 0.5$ m. In the 2012 RHIC 250 GeV polarized proton run, we achieved $\beta^* = 0.65$ m. In this study, we assume that the r.m.s. transverse emittance is 15 π mm·mrad and the r.m.s. relative momentum spread is 1.4×10^{-4}.

To cancel the non-linear beam–beam Resonance Driving Terms (RDTs) more effectively, the betatron phase advance between the beam–beam interaction and the e-lens should be $k\pi$, where k is an integer. Since we only have one e-lens for each ring in the current design, we would like to have the betatron phase advances between IP8 and the e-lenses set at $k\pi$. For the above lattice, the default phase advances between IP8 and the e-lens are $(8.5\pi, 11.1\pi)$. In the following study, we will insert an artificial phase shifting matrix to bring them to $(9\pi, 11\pi)$.

For simplicity, we define that half and full beam–beam compensation compensate the half and full total linear incoherent beam–beam tune shift. Their compensation strengths are 0.5 and 1, respectively. If the electron beam

978-92-9083-404-5, 0007-8328 –
http://dx.doi.org/10.5170/CERN–2014–004.127

Table 1: The lattice and beam parameters used in this study

Parameter	Value
Circumference	3833.8451 m
Energy	250 GeV
Working point	$(28.67, 29.68)$
Linear chromaticities	$(1, 1)$
Second-order chromaticities	(2800, 2900)
Transverse r.m.s. emittance	2.5 mm·mrad
$\beta^*_{x,y}$ at IP6 and IP8	0.5 m
$\beta_{x,y,e-lens}$ at the e-lens	10 m
Trans. r.m.s. beam size at IP6 and IP8	68 μm
Trans. r.m.s. beam size at e-lens	310 μm
$\Delta\Phi_{x,y}$ between IP6 and IP8	$(10.6\pi, 9.7\pi)$
$\Delta\Phi_{x,y}$ between IP8 and the e-lens	$(8.5\pi, 11.1\pi)$
RF harmonic number	360
RF cavity voltage	300 kV
Longitudinal r.m.s. bunch area	0.17 eV·s
Bucket height	1.1×10^{-3}
Relative r.m.s. momentum spread	1.4×10^{-4}
R.m.s. bunch length	0.45 m

has the same transverse r.m.s. beam size as the proton beam at the e-lens, we have $N^*_{\rm e} = N_{\rm p}$ and $N^*_{\rm e} = 2N_{\rm p}$ for half and full beam–beam compensation, respectively. Here, $N^*_{\rm e}$ and $N_{\rm p}$ are the electron populations in the e-lens and the proton bunch intensity.

THE SIMULATION MODEL

In the following simulation study, we track the proton particles element by element [5]. The non-linear magnetic field errors in the triplets and separation dipoles in the interaction regions are included. Each magnetic element is modelled with a 6-D symplectic transfer map. We have adopted fourth-order symplectic integration [6]. To save time in the long-term particle tracking, we model the magnetic multipoles as thin lens kicks. Tunes and chromaticities are rematched before tracking.

Considering that β^* is comparable to the proton bunch length, we use the 6-D weak–strong synchro-beam map [7] to model the proton-proton beam–beam interaction at IP6 and IP8. The strong bunch is split into 11 slices to achieve good convergence. Considering that the e-lens is working in a d.c. mode, its electric and magnetic fields are static. In the simulation code, we split the 2 m long e-lens into eight slices. Each slice is modelled as a drift – a 4-D weak–strong beam–beam kick. The 4-D weak–strong beam–beam kick is given by Bassetti and Erskine [8].

To fully use the available tune space between 2/3 and 7/10 and for better comparison of the simulation results under different beam–beam conditions, we fix the zero-amplitude particle tunes at (0.67, 0.68) under different beam–beam conditions, except in the proton working point scan. The RHIC polarized proton operational experience shows that a lower working point between 2/3 and 7/10 is preferable to obtain a better beam–beam lifetime and to preserve the proton polarization at store. In the simulation, the linear chromaticities are set to (1,1).

CALCULATION OF THE DYNAMIC APERTURE

In this section, we calculate the proton dynamic aperture with head-on beam–beam compensation in the RHIC. Particles are tracked in 10 phase angles in the (x, y) plane up to 10^6 turns. The initial relative momentum error is 0.42×10^{-4}. We compare the minimum dynamic aperture under different beam and lattice conditions. The dynamic aperture is given in units of r.m.s. transverse beam size σ.

Figure 2 shows the dynamic apertures without, with half, and with full head-on beam–beam compensation. The proton bunch intensity varies from 1.0×10^{11} to 3.0×10^{11}. In this calculation, the betatron phase advances between IP8 and the e-lens are the default ones (8.5π, 11.1π). From Figure 2, half beam–beam compensation increases the dynamic aperture when the proton bunch intensity is bigger than 2.0×10^{11}. Full beam–beam compensation reduces the dynamic aperture for all shown bunch intensities.

Figure 3 shows the dynamic apertures versus the head-on beam compensation strength. In this study, we keep the electron transverse beam size the same as the proton beam size at the e-lens, and adjust the electron beam intensity to change the beam–beam compensation strength. From Figure 3, the proton dynamic apertures drop sharply when the compensation strength is larger than 0.7. The optimized compensation strengths for the bunch intensities 2.5×10^{11} and 3.0×10^{11} are around 0.5–0.6.

Figure 4 shows the dynamic apertures of half head-on beam–beam compensation with $k\pi$ phase advances between IP8 and the e-lens and the second-order chromaticity correction. The second-order chromaticities without correction are around 2800. With correction, they are below 500. The results show that the $k\pi$ phase advances and second-order chromaticity further improve the dynamic aperture of half beam–beam compensation by about 1 σ for all the bunch intensities shown in the plot. In the above calculation, the zero-amplitude tunes of the proton beam are fixed at (0.67, 0.68). With beam–beam compensation, the tune footprint becomes smaller and it is possible to scan the proton working point between 2/3 and 7/10 to maximize the dynamic aperture with a better working point. Figures 5 and 6 show the dynamic apertures of half and full beam–beam compensation in the tune scan. The horizontal axis is the fractional horizontal zero-amplitude tune. The fractional vertical zero-amplitude tune is always 0.01 higher than the horizontal one. Simulation results show that half beam–beam compensation prefers a lower working point, between 2/3 and 7/10, while full beam–beam compensation prefers a higher working point. The maximum dynamic aperture of half beam–beam compensation in the tune scan is higher than that with full beam–beam compensation.

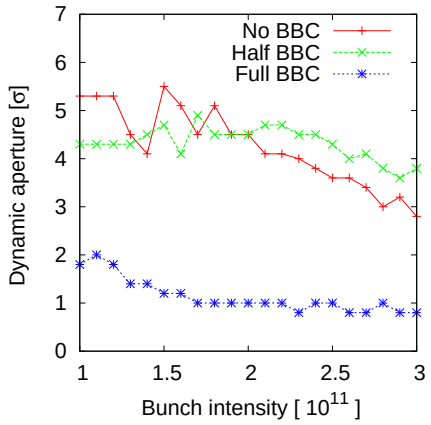

Figure 2: Dynamic apertures without beam–beam compensation and with half and full beam–beam compensation.

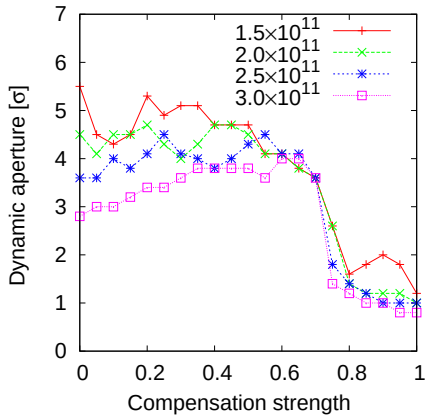

Figure 3: Dynamic apertures of four proton bunch intensities versus the head-on beam–beam compensation strength.

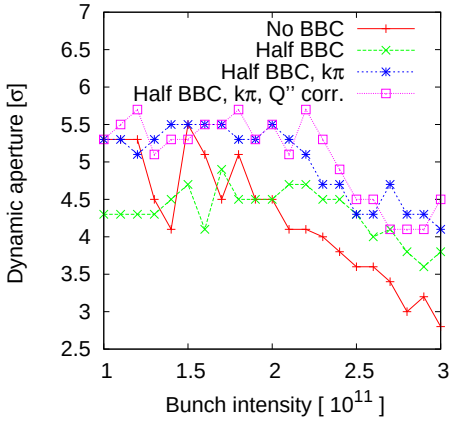

Figure 4: Dynamic apertures of half head-on beam–beam compensation with the betatron phase advance adjustment and the global second-order chromaticity correction.

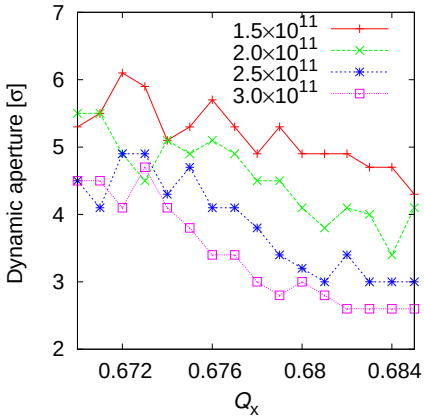

Figure 5: Dynamic apertures of half head-on beam–beam compensation in the scan of the proton working point.

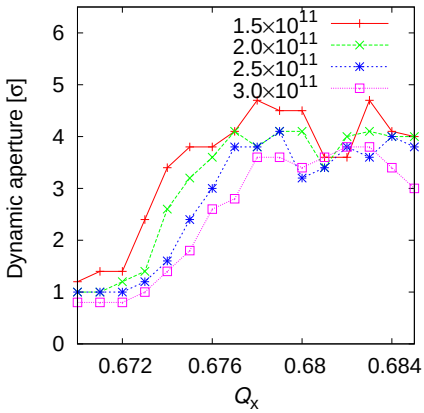

Figure 6: Dynamic apertures of full head-on beam–beam compensation in the scan of the proton working point.

CALCULATION OF THE PARTICLE LOSS RATE

In this section, we calculate the proton beam loss rate with multi-particle tracking in the presence of head-on beam–beam compensation. Limited by computing capacity, in most cases we track 4800 macro-particles up to 2×10^6 turns. 2×10^6 turns are 24 s for the RHIC.

Particles with large transverse amplitudes and large momentum deviations are probably lost in long-term tracking. However, for a limited number of macro-particles sampled from a solid Gaussian distribution, there are only a few macro-particles in the Gaussian bunch tail. To detect a small beam loss in 2×10^6 turns without increasing the number of macro-particles, we track particles with an initially hollow Gaussian distribution.

In this approach, we assume that the particles in the bunch core are stable and will not be lost in 2×10^6 turns. To save computing time, we only track macro-particles the transverse or longitudinal amplitudes of which are bigger than a certain r.m.s. beam size. The boundary between the

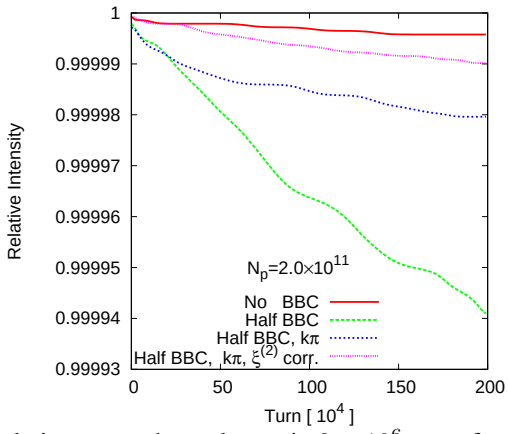

Figure 7: Relative proton beam losses in 2×10^6 turns for the proton bunch intensity 2.0×10^{11}.

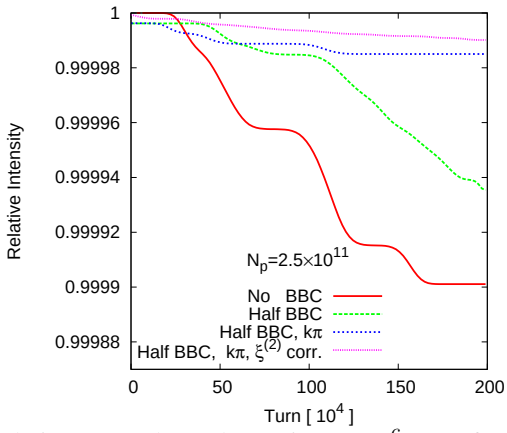

Figure 8: Relative proton beam losses in 2×10^6 turns for the proton bunch intensity 2.5×10^{11}.

stable core and the unstable bunch tail is carefully chosen. We first calculate the dynamic aperture and set the boundary well below it.

Figures 7–9 show the relative proton beam losses in 2×10^6 turns under different beam–beam compensation conditions with proton bunch intensities 2.0×10^{11}, 2.5×10^{11}, and 3.0×10^{11}. Just as in the dynamic aperture calculation, here we set the zero-amplitude tunes of the proton beam to (0.67, 0.68) and the linear chromaticities to (1,1).

For each proton bunch intensity, we compare the relative proton beam losses without beam–beam compensation, with half beam–beam compensation, with the optimized betatron phase advances $k\pi$ between IP8 and the e-lens, and with the global second-order chromaticity correction. For all the three bunch intensities, full head-on beam–beam compensation gives a much bigger beam loss than other beam–beam conditions and therefore its beam loss is not plotted.

From Figs. 7–9, half head-on beam–beam compensation reduces proton particle losses with bunch intensities 2.5×10^{11} and 3.0×10^{11} in 2×10^6 turns. Also, the $k\pi$ phase advances between IP8 and the e-lens and the second-order chromaticity correction further improve the proton beam lifetime, which agrees the results from above dynamic aperture calculations. For the bunch intensity 2.0×10^{11}, simulation shows that head-on beam–beam compensation does not increase the proton lifetime.

SENSITIVITY STUDY

In this section, we study the sensitivity of head-on beam–beam compensation to the beam imperfections and beam noise. We focus on the Gaussian tail truncated electron beam, the random noise in the electron beam current, and the static and random offsets between the electron and proton beams. The baseline for this study is with the proton bunch intensity $N_{\mathrm{p}} = 2.5 \times 10^{11}$ and half beam–beam compensation. The betatron phase advance adjustment and

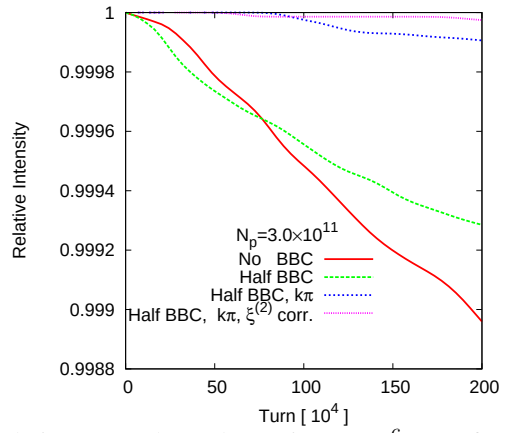

Figure 9: Relative proton beam losses in 2×10^6 turns for the proton bunch intensity 3.0×10^{11}.

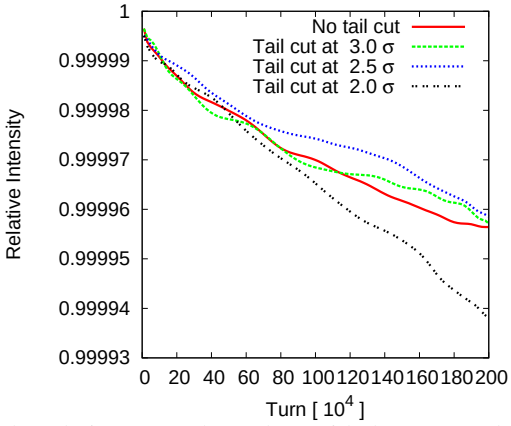

Figure 10: The relative proton beam loss with the truncated Gaussian tail of the electron beam.

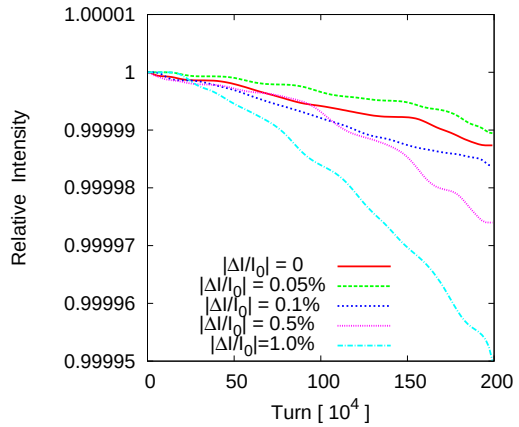

Figure 11: The relative proton beam loss versus the random noise in the electron beam current.

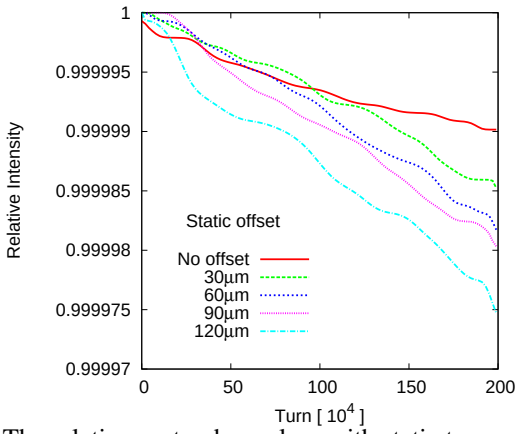

Figure 12: The relative proton beam loss with static transverse offset between the e-lens and the proton beam in the e-lens.

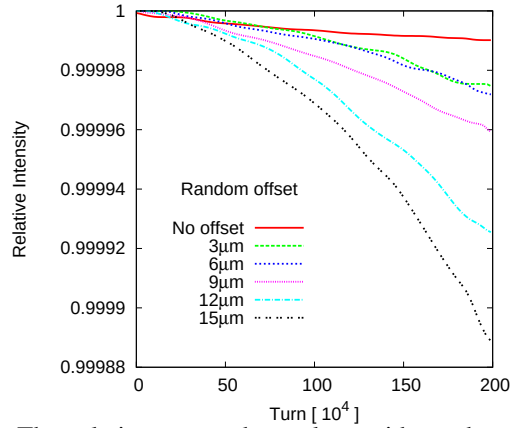

Figure 13: The relative proton beam loss with random transverse offset between the e-lens and the proton beam in the e-lens.

second-order chromaticity correction are included.

In the above simulation study, we assume that the electron beam has a perfect transverse Gaussian distribution. Simulation of the electron gun for the RHIC e-lens system shows that the electron beam has a Gaussian tail cut off at 2.8 σ. Figure 10 shows the calculated relative proton beam loss with the electron beam's Gaussian tail cut off at 3 σ, 2.5 σ and 2 σ. Compared to the baseline with a perfect Gaussian distribution, the Gaussian tail cut at 2.8 σ from the current electron gun design is acceptable.

Due to the instability of the power supplies of the electron gun, there is noise in the electron beam current. Figure 11 shows the relative proton beam loss versus the random electron current noise. The proton beam loss with a random noise below 0.1% in the electron current is comparable to the baseline without current noise. In the design of the RHIC electron gun system, we require that the stability of the power supplies of the electron gun should be better than 0.1%.

Overlapping of the electron and proton beams in the e-lens plays a crucial role in head-on beam–beam compensation. Figures 12 and 13 show the calculated relative proton beam losses with static and random offsets between the electron and proton beams. Based on the simulation results, in the RHIC e-lens design, we set the tolerance of the static offset error to 30 μm, which is a 10th of a r.m.s. beam size in the e-lens, and the random offset to 9 μm, which requires the stability of the bending magnet's power supply to be better than 0.01%.

SUMMARY

In this article, with a 6-D weak–strong beam–beam model, we have investigated the effects of head-on beam–beam compensation with e-lenses on the proton beam dynamics in the RHIC 250 GeV p-p operation. We found that half beam–beam compensation improves the proton dynamic aperture and beam lifetime. The $k\pi$ phase advances between IP8 and the e-lens, and the global second-order chromaticity, further increase the proton dynamic aperture and particle loss rate. The sensitivity of half beam–beam compensation on the electron profile, the electron current, and the overlapping of the electron and proton beams are studied and their tolerances are set.

REFERENCES

[1] Y. Luo et al., Phys. Rev. ST Accel. Beams 15 (2012) 051004.

[2] A. Zelenski, Rev. Sci. Instrum. 81 (2010) 02B308.

[3] M. Bai et al., Phys. Rev. Lett. 96 (2006) 174801.

[4] V. Shiltsev et al., Rev. Lett. 99 (2007) 244801.

[5] Y. Luo, in Proc. 2010 IPAC'10, Kyoto, Japan (2010).

[6] R.D. Ruth, IEEE Trans. Nucl. Sci. NS-30 (1983) 2669–71.

[7] K. Hirata et al., Part. Accel. 40 (1993) 205–28.

[8] M. Bassetti and G.A. Erskine, CERN-ISR-TH/80-06 (2006).

Published by CERN in the Proceedings of the ICFA Mini-Workshop on Beam–Beam Effects in Hadron Colliders,
CERN, Geneva, Switzerland, 18–22 March 2013, edited by W. Herr and G. Papotti, CERN–2014–004 (CERN, Geneva, 2014)

COHERENT BEAM–BEAM EXPERIMENTS AND IMPLICATIONS FOR HEAD-ON COMPENSATION*

S. White, M. Blaskiewicz, W. Fischer, Y. Luo
BNL, Upton, NY, USA

Abstract

In polarized proton operation in the Relativistic Heavy Ion Collider (RHIC) coherent beam–beam modes are routinely observed with beam transfer function measurements. These modes can become unstable under external excitation or in the presence of impedance. This becomes even more relevant in the presence of head-on compensation, which reduces the beam–beam tune spread and hence Landau damping. We report on experiments and simulations carried out to understand the impact of coherent modes on operation with electron lenses.

INTRODUCTION

The Relativistic Heavy Ion Collider (RHIC) is currently operating between the 2/3 and 7/10 resonances with a beam–beam parameter of approximately 0.015 leaving little space for significant increase in luminosity. The RHIC luminosity upgrade program [1] aims at an increase of the luminosity by a factor of 2. In order to accommodate the significant increase in beam–beam tune spread it was decided to install electron lenses to compensate for the beam–beam non-linearities and effectively reduce the tune spread at constant bunch intensity. This technology was first developed at the Tevatron where it was tested for head-on compensation [2] and then successfully used for long-range compensation, abort gap cleaning [3] and collimation studies [4].

The RHIC collider consists of two rings where the beams are colliding in interaction points IP6 and IP8 as shown in Fig. 1. The two electron lenses, one for each ring, will be located close to IP10. Studies regarding dynamic aperture were performed and showed improvements for high beam–beam parameter [5]. The details about the status and construction of the electron lens can be found in Ref. [6]. These simulations however did not cover the coherent beam–beam effects related to the electron lens. The failure in increasing the luminosity in the DCI (Dispositif de Collisions dans l'Igloo) four-beam experiment ($e^+e^-e^+e^-$) was attributed to coherent effects [7], which should therefore be carefully investigated. This paper reports on strong–strong beam–beam simulations performed using the RHIC lattice and upgrade parameters and related beam experiments to understand the impact of the coherent beam–beam effects in the presence of electron lenses.

* Work supported by Brookhaven Science Associates, LLC under Contract No. DE-AC02-98CH10886 with the U.S. Department of Energy, and in part by the U.S. LHC Accelerator Research Program.

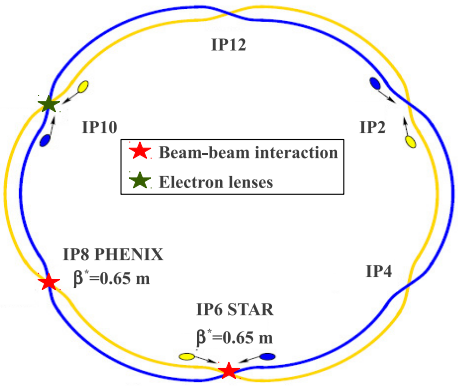

Figure 1: Layout of the RHIC collider. The colliding IPs are denoted by the red stars, the head-on compensation by the green star.

MODEL

The simulation code BeamBeam3D [8] was used for this study. BeamBeam3D is a fully parallelized three-dimensional code allowing for self-consistent field calculation of arbitrary distributions and tracking of multiple bunches. The transport from one IP to the other is done through linear transfer maps. The beam fields are calculated by solving the Poisson equation using a shifted integrated Green function method which is efficiently computed with a FFT-based algorithm on a uniform grid.

In order to correctly model the RHIC lattice the Twiss parameters are extracted at each IP, including the one where the head-on compensation takes place, and used to compute the transfer maps. As shown in Fig. 1, the symmetry of the different colliding IPs allows one to reduce the number of bunches to three per beam to simulate the full collision pattern.

The electron lens is modelled as a thin-lens Gaussian beam located exactly at IP10 for both beams. The size of the electron beam is determined by the lattice parameters. The phase advance between IP8 and IP10 is set exactly to π by artificially shifting the phase between these two IPs and evenly compensating the global tune change with the other arcs.

Figure 2 shows the footprints calculated with BeamBeam3D for an intensity of 3.0×10^{11} protons per bunch without compensation and with half compensation. The footprint with compensation was artificially shifted for better visibility. As expected, we observe a reduction of the

978-92-9083-404-5, 0007-8328 –
http://dx.doi.org/10.5170/CERN–2014–004.133

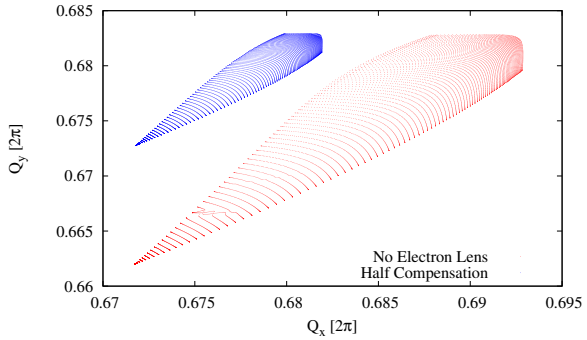

Figure 2: Tune footprint computed with BeamBeam3D for an intensity of 3.0×10^{11} protons per bunch with and without compensation. No compensation in red, half compensation in blue.

tune spread by a factor of 2. One can also see that the footprint without compensation is crossing the $3Q_y$ resonance, indicating that the machine cannot be operated with such high beam–beam parameter.

COHERENT BEAM–BEAM SIMULATIONS

In addition to the single-particle effects described in the previous sections, colliding beams will experience coherent dipole oscillation driven by the beam–beam force. In the simplest case of one interaction point two main modes arise corresponding to the two bunches oscillating in phase (σ-mode) or out of phase (π-mode). The σ-mode will oscillate at the betatron frequency and the π-mode will be shifted, negatively for equally charged beams, with respect to the σ-mode by an amount $Y \cdot \xi$, where Y is the Yokoya factor and ξ the beam–beam parameter [9].

The collision pattern at RHIC can be reduced to three colliding bunches theoretically giving rise to six coherent dipole modes. In reality, only two modes are observed as the other ones are located inside or very close to the incoherent tune spread and are Landau damped.

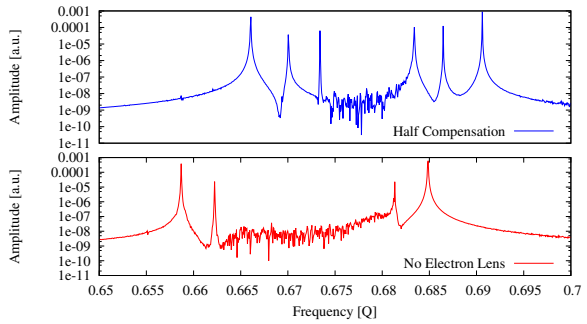

Figure 3: Simulated coherent modes with (top) and without (bottom) half compensation with a bare lattice tune of 0.685.

Figure 3 shows a strong–strong simulation of the RHIC lattice with and without compensation. The bare lattice tunes used for this simulation are (0.695, 0.685) as defined in the design and the beam–beam parameter ξ per IP is 0.011. Only the vertical plane is shown but a similar picture is observed in the horizontal plane. The coherent modes are excited with an initial kick of 0.1 σ.

As predicted by the weak–strong simulations in Fig. 2, the incoherent continuum is reduced by the head-on compensation. The bare lattice tunes, or σ-mode in this plot, are shifted by $\xi/2 \approx 0.005$ corresponding to the coherent beam–beam tune shift induced by the quadrupolar part of the beam–beam force. This effect can be easily predicted and corrected for. The phase advance between IPs is also modified leading to slightly different relative frequencies of the modes.

In the presence of head-on compensation, the distance in tune space covered by the coherent modes therefore remains approximately constant while the incoherent tune spread is significantly reduced. All six coherent modes are now observed as they are moved out of the continuum and not Landau damped any more. Head-on compensation with electron lenses reduces the intrinsic stabilizing properties of the beam–beam interaction. This could give rise to coherent dipole instabilities driven by external sources of excitation or impedance.

EFFECT OF THE 2/3 RESONANCE ON COHERENT MODES

As seen in Fig. 3, even if the incoherent tune spread is reduced, the tune space covered by the coherent modes remains constant and will overlap the 2/3 resonance in the case of the RHIC working point. While it is difficult to experimentally reproduce the reduction of the tune spread induced by the electron lenses, we verified experimentally that driving the π-mode onto this resonance would not excite coherent dipole motion or degrade the beam lifetime.

For this experiment we moved only the two tunes of the Blue beam towards the 2/3 resonance keeping the difference $Q_x - Q_y = 0.004$, see Figs. 4 and 5. This was done with a beam–beam parameter estimated to be 0.011. The onset of losses is observed at (0.687, 0.683); at these tunes the location of the π-mode is 0.669 and the zero-amplitude particles are at 0.672: no emittance blow-up is observed at that point. Losses are observed only in the Blue beam, indicating that the π-mode, which has the same frequency for both beams, is insensitive to the 2/3 resonance. The stop band of the 2/3 resonance with non-colliding beams was estimated to be around 0.005, which is consistent with losses of low-amplitude particles in our case. As we moved the beam closer to the resonance strong losses associated with emittance blow-up were observed only in the Blue beam. In addition, no unusual activity was observed in the tune spectrum during the whole experiment, pointing towards a reduction of the dynamic aperture rather than the excitation of coherent modes.

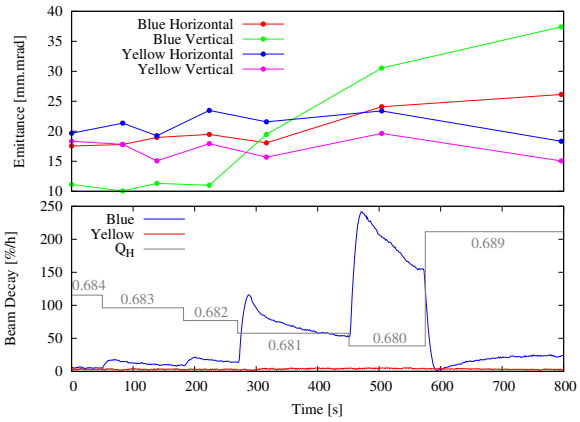

Figure 4: Tune scan towards the 2/3 resonance with colliding beams. The top plot shows the emittance during the scan and the bottom plot the beam decay. The tunes were reconstructed using measurements with non-colliding beams.

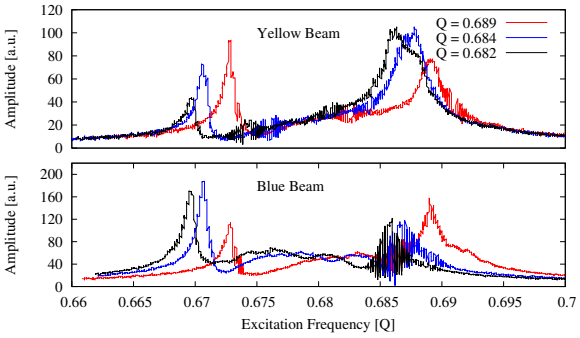

Figure 5: BTF (Beam Transfer Function) data during the tune scan towards the 2/3 resonance.

The tune scan was reproduced in numerical simulations. Figure 6 shows the FFT of the centre of motion during the the tune scan. It is observed that even when the π-mode is on top of the 2/3 resonance it remains stable. Figure 7 shows the vertical emittance growth for both beams. Only the Blue beam, pushed towards the resonance, is affected

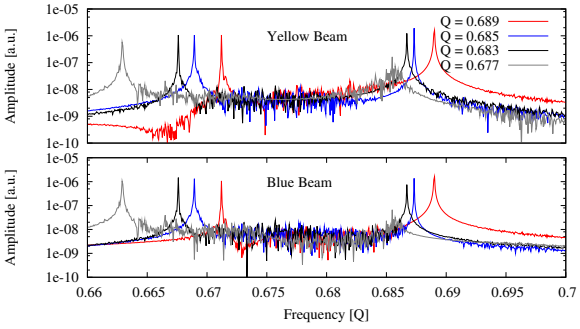

Figure 6: Simulated spectrum reproducing the experiment.

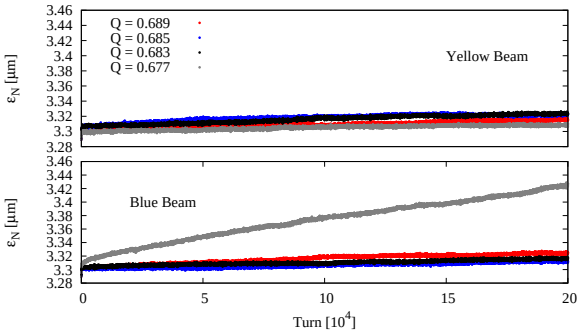

Figure 7: Simulated emittance during the tune scan.

and a blow-up is observed only when the beam–beam tune spread overlaps the resonance. This is very consistent with experimental data and confirms that the 2/3 resonance is not a concern for beam stability. The only non-linear element in the model is the beam–beam interaction. The absence of sextupoles explains why the stop band of the resonance is narrower in the numerical simulation.

COHERENT MODE SUPPRESSION

Coherent beam–beam mode suppression has been investigated in Refs. [10, 11], where it was shown that the following techniques can be used to damp the modes:

- Phase advance adjustment between colliding IPs
- Synchro–betatron coupling. If $\xi \approx Q_s$, the π-mode can be damped by the sidebands of the continuum
- Beams colliding on different working points (tune split)

Although these effects could all be reproduced in simulations, one has to consider the constraints associated with the machine layout and beam parameters. Due to the magnet powering scheme in the RHIC there is very little flexibility to adjust the phase advance between the colliding IPs (IP6 and IP8). The synchrotron tune Q_s is of the order of 5.0×10^{-4}, which is much smaller than the expected beam–beam parameter in the presence of head-on compensation ($\xi \approx 0.02$–0.03) making it impossible to profit from synchro–betatron coupling. This leaves the tune split as the only option for coherent mode suppression in the RHIC.

To fully suppress the coherent modes the tune split between the two beams has to be larger than the beam–beam parameter, in which case the coherent modes will cluster inside the incoherent continuum and experience Landau damping [10]. This can be achieved at the RHIC with tunes of about (0.695, 0.685) for the Blue beam and (0.74, 0.73) for the Yellow beam. Figure 8 shows an example of a BTF measurement with the beams on different tunes. The coherent modes are completely suppressed, as expected from the theory.

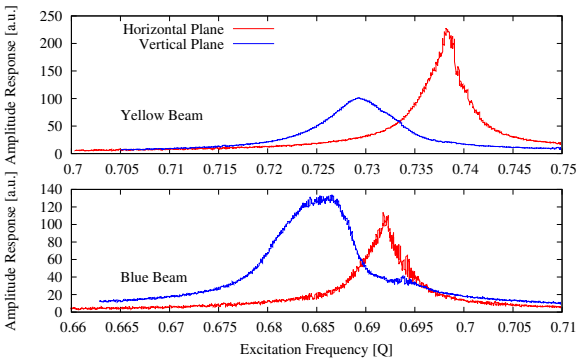

Figure 8: BTF measurement with split tunes.

Figure 9 shows emittance measurements over four consecutive stores with split tunes. A strong emittance blow-up is observed in three fills out of four as soon as the beams are brought into collision, leading to poor luminosity performance. For comparison, the emittance at the beginning of the stores is generally around 15 mm mrad for normal operation. This behaviour for colliding beams with unequal tunes had been predicted in past simulations and theoretical analysis [11], where it was stated that operating a collider with unequal tunes could lead to coherent beam–beam resonance excitation and, providing the modes lie inside the incoherent continuum, emittance blow-up.

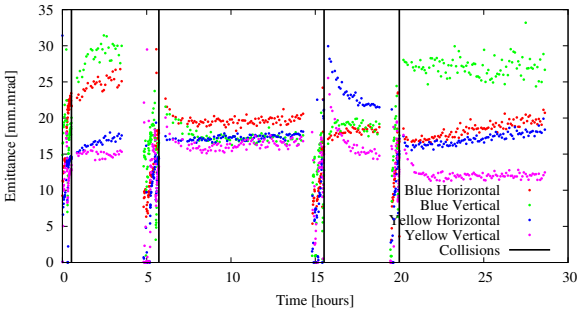

Figure 9: Emittance measurements during fills with split tunes.

Using the estimated working points (0.689, 0.691) and (0.74, 0.73) and beam–beam parameter (0.013) one can compute the frequencies of the coherent modes using a rigid bunch model. In this specific case the machine was operated in the vicinity of a resonance of the form $4Q_1 - Q_2$, which is excited by offset collisions. Numerical simulations were carried out to assess the impact of this resonance on emittance. The results of these simulations are shown in Fig. 10, where three cases were considered:

- Head-on collisions with tunes close to the resonance (experimental conditions)
- Collisions with an offset of 1σ in the horizontal plane with tunes close to the resonance

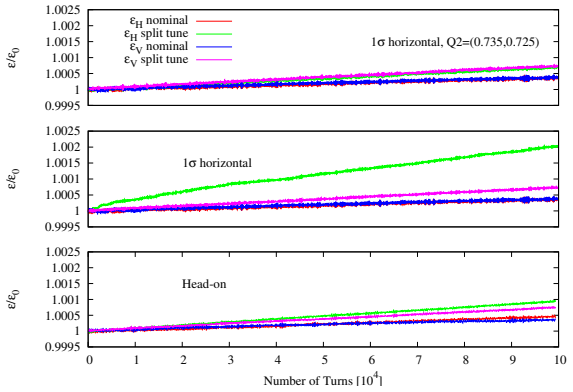

Figure 10: Simulated emittance growth in the vicinity of the resonance for head-on interactions (bottom), separated beams (middle) and separated beams away from the resonance (top).

- Collisions with an offset of 1σ in the horizontal plane with tunes away from the resonance

A strong emittance blow-up is observed in the case of offset collisions with working points close to the resonance condition. When the beams are colliding head-on or the working points are moved away from the resonance the conditions simulated for equal tunes are almost recovered. Simulations appear to confirm the hypothesis of a coherent beam–beam resonance of odd order. We could expect that by properly setting the working points to avoid resonances nominal luminosity performance could be achieved. Another important parameter in the RHIC is the polarization. During the split tune experiment a very poor polarization was measured for the Yellow beam (0.74, 0.73), ruling out the possibility of running the RHIC in this configuration.

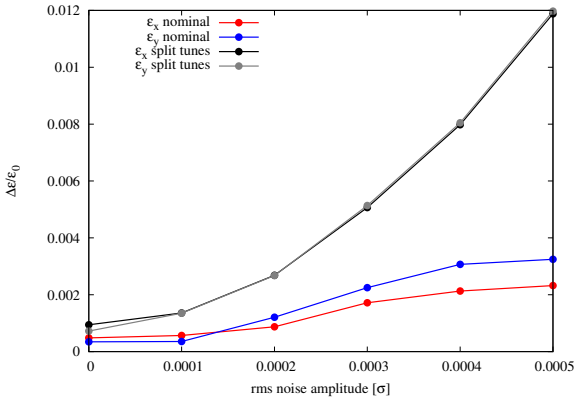

Figure 11: Emittance growth in the presence of white noise for colliding beams with equal and unequal tunes.

Figure 11 shows the emittance growth due to white-noise excitation. In this case, beam parameters were set to be away from any low-order resonance. It is clearly observed

Table 1: Stabilizing detuning coefficients derived from tracking simulation with impedance and RHIC non-linear model.

	$\partial Q_x/\partial\epsilon_x$ m^{-1}	$\partial Q_y/\partial\epsilon_y$ m^{-1}	$\partial Q_y/\partial\epsilon_x$ m^{-1}
Tracking	607	607	417
Non-linear model	314	387	463

that colliding the beams with unequal tunes degrades the situation and makes the beams more sensitive to external excitation. This was not verified experimentally and would need confirmation but could become an issue if operation with split tunes is considered for a collider.

MACHINE IMPEDANCE

Head-on compensation with electron lenses will significantly reduce the beam–beam tune spread and Landau damping. The interplay with machine impedance was studied in numerical simulations using the RHIC impedance model which takes into account the contribution of stripline BPMs (Beam Position Monitor), bellows and resistive wall.

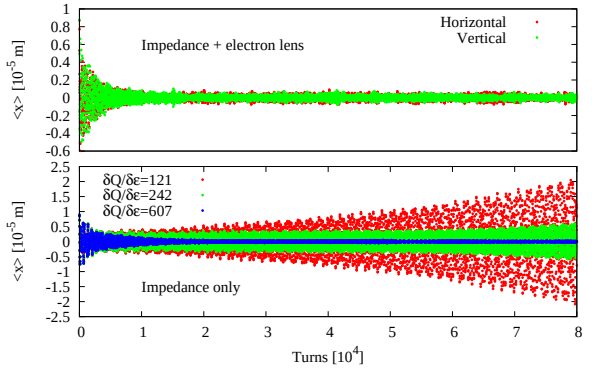

Figure 12: Beam stability with machine impedance only and including electron lens for $Q' = 2.0$.

Figure 12 shows the results of simulations for a chromaticity of 2.0, which corresponds to what is generally used in regular RHIC operation. The bottom plot is a scan in octupolar detuning with impedance only. Stability is achieved for a detuning coefficient $\delta Q_x/\delta\epsilon_x = 607\,\mathrm{m}^{-1}$. Table 1 summarizes the stabilizing coefficient obtained from tracking simulations and the detuning coefficients derived from the RHIC non-linear model. Considering the uncertainties from the impedance model and the difficulty in accurately computing the stability threshold from tracking simulation, it is not unlikely that the machine non-linearities provide sufficient detuning to stabilize the beam. This would be consistent with the fact that instabilities are generally not observed during RHIC polarized proton runs. Even when half-compensated the beam–beam non-linearities will provide significantly larger detuning than the results from Table 1. Machine impedance is therefore not considered to become an issue for stability. This was confirmed by simulations as shown in the top plot of Fig. 12, where the beam is fully stable with electron lenses running at half compensation.

ELECTRON LENS DRIVEN TMCI

When a proton bunch interacts with the electron beam it will drive Larmor oscillations of the electrons along the interaction region resulting in an s-dependent kick onto the proton bunch. This can be interpreted as an electron lens impedance comparable to or larger than the machine impedance. Its strength depends on the electron lens parameters and under certain conditions can lead to transverse mode coupling instabilities (TMCI). This effect was studied in detail in Ref. [12], where it was shown that the s-dependent momentum change of the protons can be modelled with the following wake function:

$$\Delta p_x = W[\Delta x \sin(ks) + \Delta y(1 - \cos(ks))], \quad (1)$$

where Δx and Δy are the offsets of the source in the horizontal and vertical planes respectively and W is a constant depending on both the beam–beam parameters of the electron and proton beams and the solenoid field B. A similar equation is also valid for the vertical plane y. The variable k is defined as

$$k = \frac{\omega_L}{(1+\beta_e)c}, \quad (2)$$

where β_e is the relativistic β of the electron beam, c is the speed of light and ω_L is the Larmor angular frequency defined as

$$\omega_L = \frac{eB}{\gamma_e m}. \quad (3)$$

Using this wake function and considering uniform and equal transverse distributions for the proton and electron beams, it is possible to analytically derive the TMCI threshold and hence the required solenoid field to ensure stability. This threshold can be expressed expressed as [12]

$$B_{\mathrm{th}} = 1.3\frac{eN_p\xi_e}{r^2\sqrt{\Delta Q Q_s}}, \quad (4)$$

where N_p is the proton bunch intensity, ξ_e is the electron lens beam–beam parameter, r is the radius of the beam ($r \approx 2\sigma$ for a Gaussian distribution), ΔQ is the separation between horizontal and vertical tunes and Q_s is the synchrotron tune. Using typical RHIC parameters ($N_p = 3.0 \times 10^{11}$ protons per bunch, $\xi_e = 0.011$, $\Delta Q = 0.01$, $Q_s = 5.0 \times 10^{-4}$ and $r \approx 0.8\,\mathrm{mm}$), a threshold field of 14 T is found, which is approximately a factor 2 above the design field of 6 T. This six-dimensional electron lens interaction was built into the code BeamBeam3D to study

beam stability with an electron lens in multi-particle tracking simulations. Benchmarking with theoretical predictions was done using linearized beam–beam kicks, which allows for direct comparison.

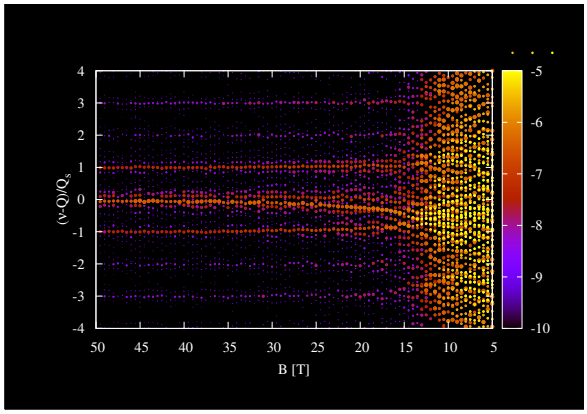

Figure 13: Synchro–betatron mode frequencies and amplitudes (colours) as a function of the solenoid field and using a linearized model (no Landau damping). The transverse mode coupling instability occurs at around 14 T.

Figure 13 shows the results of this benchmarking using the same beam parameters as the field threshold computation from Eq. (4). The transverse mode coupling instability occurs at around 14 T, which is consistent with theoretical expectations. These results only include interactions with an electron lens; in the presence of beam–beam (proton–proton) interactions coherent motion is driven by these additional interactions and the mode frequencies are modified. This is especially true in the presence of strong synchro–betatron coupling from the beam–beam interaction, which, in the case of the RHIC, is a result of the hourglass effect ($\beta^*/\sigma_s \approx 1$, no crossing angle).

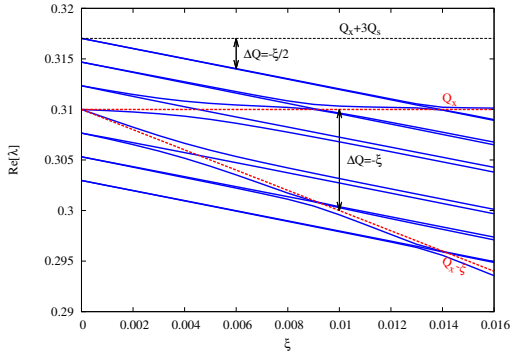

Figure 14: Synchro–betatron mode frequencies as a function of the beam–beam parameter for $Q_s \approx 0.0025$ and $\beta^*/\sigma_s \approx 1$.

This is illustrated in Fig. 14, where it is clearly seen that the synchrotron sidebands are deflected by the beam–beam π and σ modes. In this case the mode frequencies were computed using a linearized model based on the circulant matrix approach [13], in which case the Yokoya factor is equal to 1.

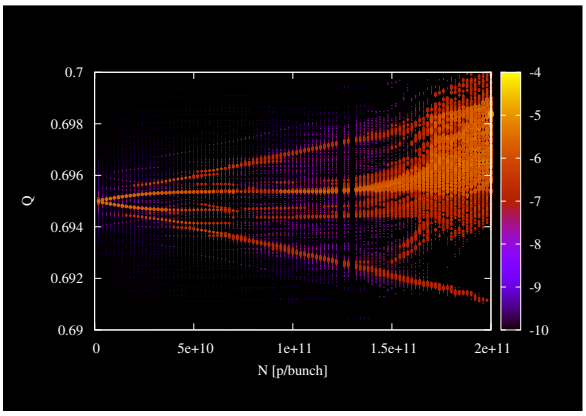

Figure 15: Synchro–betatron mode frequencies and amplitudes (colours) as a function of bunch intensity for a solenoid field of 6 T and using a linearized model (no Landau damping). The transverse mode coupling instability occurs at around 1.0×10^{11} protons per bunch.

Figure 15 shows tracking results including beam–beam and electron lens using linearized beam–beam kicks and RHIC beam parameters. The expected threshold from Eq. (4) is 2.0×10^{11} in this case. The mode coupling instability in the presence of coherent beam–beam effects is reduced by a factor 2 for these parameters with respect to theoretical expectations without coherent beam–beam effects (the threshold in terms of solenoid field scales with N_p^2).

The above simulations were carried out using a linearized model which does not include the amplitude detuning related to the non-linearities of the beam–beam force and hence its contribution to Landau damping. Landau damping could provide additional stability and mitigate the electron lens driven TMCI. In order to include this effect, we carried out tracking simulations using the full nonlinear beam–beam force. The proton–proton interactions are computed using a Poisson solver, making no assumption on the beam distribution, while the interaction with the electron lens is done assuming elliptical Gaussian shapes but allowing for a tilt angle of the phase-space distribution in order to account for the coupling introduced by the solenoid field; more detailed studies would be required to verify the validity of the Gaussian approximation and its impact on Landau damping. The proton bunch is sliced longitudinally into 50 slices, which correspond to 10 times the wavelength of the Larmor oscillations. Although the high-frequency component of the wake function should not have a significant impact on stability, it is necessary to perform systematic studies regarding the effect of the number of slices. This may introduce some aliasing issues when sampling the electron oscillations and eventual smoothing approximations could apply. The importance of these pa-

rameters is under investigation and will not be covered in detail in this paper.

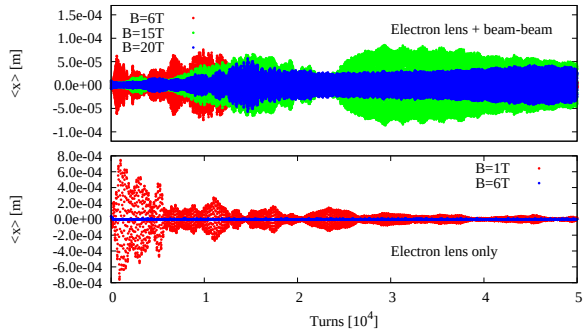

Figure 16: Solenoid field scan including non-linear beam–beam force with (top) and without (bottom) proton–proton interactions.

Figure 16 shows the results of a solenoid field scan including Landau damping for cases with and without proton–proton interactions. The case without proton–proton interactions at the bottom provides a direct comparison with theoretical predictions and illustrates the impact of Landau damping. The theoretical threshold was estimated to be approximately 14 T. Including Landau damping, this threshold is significantly reduced and stability is achieved for a solenoid field between 1 T and 6 T, which is within the RHIC electron lens design. Unfortunately, the degradation due to coherent beam–beam effects is also observed in the presence of Landau damping and the beam could not be stabilized for a field up to 20 T, which is well above design.

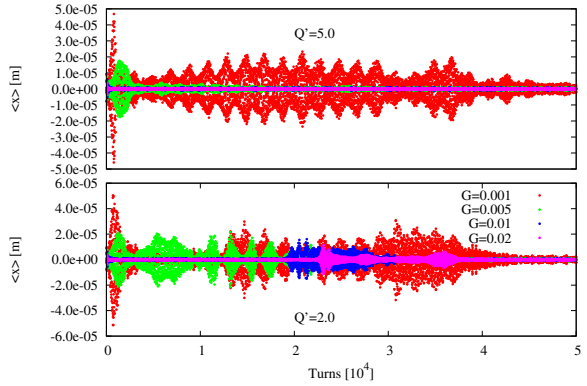

Figure 17: Rigid bunch damper gain scan with $Q' = 2.0$ (bottom) and $Q' = 5.0$ (top).

As demonstrated in Ref. [14], the combination of a strong rigid bunch damper and relatively high chromaticity can provide stability to higher order head–tail modes ($m > 0$) and could even push the TMCI to higher threshold. Figure 17 shows the results of tracking simulations including a rigid bunch damper and chromaticity. At $Q' = 2.0$, which corresponds to normal RHIC running chromaticity, a clear improvement is observed when the damper gain is increased but the beam remains unstable even at high gain. Increasing the chromaticity makes the damper more efficient against the mode coupling instability and the beam can be stabilized with a damper gain of 100 turns.

CONCLUSIONS

Head-on beam–beam compensation with electron lenses reduces the beam–beam tune spread allowing one to accommodate larger bunch intensity at the current RHIC working point. In return, the contribution from the beam–beam tune spread to Landau damping is reduced while the coherent beam–beam modes remain unaffected. This may have some detrimental effects on beam stability and luminosity performance. Beam experiments were conducted at the RHIC to understand the impact of coherent beam–beam effects on beam dynamics:

- **Impact of the 2/3 resonance**: the beam–beam π-mode was driven onto the 2/3 resonance without effect on beam stability or cross talk between beams. Losses and emittance blow-up were observed in the beam moving towards the resonance, which is attributed to incoherent effects when the tune spread overlaps the resonance stop band. This is consistent with theoretical estimates and tracking simulations

- **Coherent mode suppression**: coherent beam–beam mode suppression with tune split was attempted. This resulted in significant luminosity performance degradation due to emittance blow-up when bringing the beams into collision. This effect could be attributed to the excitation of coherent beam–beam resonance as predicted in Ref. [11]. Tracking simulations also support this hypothesis

Numerical simulations were carried out to understand possible limitations coming from machine impedance and electron lens impedance. It was shown that the intrinsic machine non-linearities provide almost sufficient detuning to stabilize instabilities driven by machine impedance. This is consistent with experimental data, as instabilities are generally not observed in regular operation. The electron lenses are foreseen to compensate for only half of the full beam–beam tune spread. The remaining tune spread would still be significantly larger than the simulated stabilizing octupolar detuning, leading to the conclusion that machine impedance is not a limitation for operation with electron lenses. Another aspect investigated in this paper is the electron lens driven TMCI. It was found that the RHIC design field is not sufficient to ensure stability with the current machine layout and beam parameters. A possible solution to overcome this issue would be the implementation of a bunch-by-bunch transverse damper combined with slightly higher than nominal chromaticities. These results are preliminary and more systematic studies and model refinements are required to draw final conclusions. The electron lens driven TMCI could also be mitigated using beam

parameters such as the distance between the horizontal and vertical tunes or the β-function at the electron lens. These alternative solutions should be investigated in future studies.

ACKNOWLEDGMENTS

The authors would like to thank J. Qiang for his help regarding the implementation of the RHIC lattice and electron lenses into the code BeamBeam3D, the RHIC operation and M. Bai and A. Marusic for their support with data acquisition.

REFERENCES

[1] W. Fischer et al., "RHIC Luminosity Upgrade Program," Proceedings of IPAC10, 2010.

[2] V. Shiltsev et al., New J. Phys. 10 (2008) 043042.

[3] V. Shiltsev et al., Phys. Rev. Lett. 99 (2007) 244801.

[4] G. Stancari et al., Phys. Rev. Lett. 107 (2011) 084802.

[5] Y. Luo et al., Phys. Rev. Spec. Top. Accel. Beams 15 (2012) 5-051004.

[6] W. Fischer et al., "Status of Head-on Compensation in RHIC," these proceedings.

[7] B. Podobedov et al., Phys. Rev. E 52 (1995) 3066.

[8] J. Qiang et al., Phys. Rev. Spec. Top. Accel. Beams 5 (2002) 104402.

[9] K. Yokoya et al., Part. Accel. 27 (1990) 181.

[10] A. Hofmann, CERN-SL-99-039 AP (1999).

[11] Y. Alexahin, Nucl. Instrum. Methods A 480 (2002) 253.

[12] A. Burov et al., Phys. Rev. E 59 (1999) 3065.

[13] V.V. Danilov and E.A. Perevedentsev, Nucl. Instrum. Methods A 391 (1997) 77.

[14] A. Burov, CERN AP Forum (2012).

Published by CERN in the Proceedings of the ICFA Mini-Workshop on Beam–Beam Effects in Hadron Colliders,
CERN, Geneva, Switzerland, 18–22 March 2013, edited by W. Herr and G. Papotti, CERN–2014–004 (CERN, Geneva, 2014)

LONG-RANGE BEAM–BEAM EXPERIMENTS IN THE RELATIVISTIC HEAVY ION COLLIDER

(Published in Phys. Rev. ST Accel. Beams 14, 091001)

R. Calaga, CERN, Geneva, Switzerland
W. Fischer, N. Milas, G. Robert-Demolaize, BNL, Upton, NY, USA

Abstract

Long-range beam–beam effects are a potential limit to the LHC performance with the nominal design parameters, and certain upgrade scenarios under discussion. To mitigate long-range effects, current carrying wires parallel to the beam were proposed and space is reserved in the LHC for such wires. Two current carrying wires were installed in RHIC to study the effect of strong long-range beam–beam effects in a collider, as well as test the compensation of a single long-range interaction. The experimental data were used to benchmark simulations. We summarize this work.

INTRODUCTION

The reader should note that this is an identical copy of an article first published in [1]. Beam–beam effects have limited the performance of previous and existing hadron colliders [2–4] such as the ISR [5, 6], Sp$\bar{\text{p}}$S [7–10], Tevatron [11–13] and RHIC [14, 15], and are also expected to limit the performance of the LHC [16–31].

Beam–beam effects can be categorized as either incoherent (dynamic aperture and beam lifetime), PACMAN (bunch-to-bunch variations), or coherent (beam oscillations and instabilities) [25]. These effects can be caused by both head-on and long-range interactions. Head-on effects, leading to tune shifts and spreads, are important in all hadron colliders. Total beam–beam induced tune shifts as large as 0.028 were achieved in the Sp$\bar{\text{p}}$S [10] and Tevatron [13], although operational tune shift values are somewhat lower. The LHC in its early stages of commissioning has already reached a total head-on beam–beam tune shift of 0.02 [32].

Long-range effects, however, differ in previous and existing colliders. In the ISR the beams collided under a large crossing angle of 15 deg [33] that greatly reduced long-range effects. In the Sp$\bar{\text{p}}$S, with both beams in the same aperture and only three bunches per beam, there were a few long-range interactions distributed over the ring circumference. Due to the difference in the bunch intensities, the effect on the anti-protons was stronger. In the Tevatron, also with both beams in the same aperture but 36 bunches per beam, there are more long-range interactions. With increased intensity of the anti-proton bunches, protons can also be affected.

In RHIC (Fig. 1), where both beams share the same aperture only in the interaction regions, there is only one long-range interaction per interaction region without an experiment (a total of four in the current configuration), with a 10 mm separation (corresponding to 30 rms beam sizes for protons at 250 GeV energy). Long-range interactions have affected the RHIC ramp transmission in the past [14].

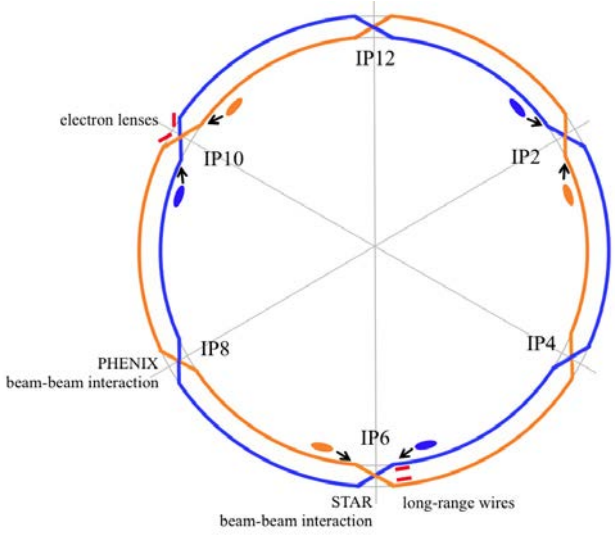

Figure 1: Beam–beam interactions in RHIC and locations of wires and electron lenses.

LONG-RANGE EFFECTS AND COMPENSATION IN THE LHC

In the LHC there are 32 long-range beam–beam interactions localized in each of four interaction regions [25]. A major upgrade of the LHC interactions region is foreseen by the end of the decade with the primary objective to increase the average luminosity of the machine by about a factor of 5 to 10 above the design performance. Among the various upgrade scenarios a crab crossing scheme (CC), an early beam separation scheme (ES), and a large Piwinski angle (LPA) are considered. In the CC scheme, crab cavities placed on either side of the interaction region impart a transverse kick to effectively compensate the crossing angle. This scheme allows for a large crossing angle that greatly reduces long-range beam–beam effects. In the ES scheme [27, 28] the number of long-range interactions is greatly reduced but four parasitic collisions at 4–5 σ per IP remain. In the LPA scheme [26] the small crossing angle will be maintained, and long bunches of intensities up to $4–5 \times 10^{11}$ protons are used. All schemes aim at higher than nominal bunch currents and reduced β^*. Therefore, long-range effects tend to become more problematic and require

978-92-9083-404-5, 0007-8328 –
http://dx.doi.org/10.5170/CERN–2014–004.141

more aperture for larger crossing angles or compensation to mitigate these effects. The LPA scheme would most benefit from long-range beam–beam compensation. The compensation of long-range effects in the Tevatron was proposed with electron lenses [34], and in the LHC with wires [35]. Electron lenses were also considered for the LHC [36], and the use of wires was also studied for the Tevatron [37]. Implementation of long-range beam–beam compensation in the Tevatron is challenging because the effect is distributed over the whole ring. In the LHC the effect is localized in the interaction regions. A partial long-range beam–beam compensation was successfully implemented in the e^+e^- collider DAΦNE [38]. Beam–beam compensation and related issues were reviewed at a workshop in 2007 [39].

RHIC AS A TEST BENCH FOR LONG-RANGE STUDIES

Figures 1 and 2 show the basic layout of the beam–beam interaction and compensation studies in RHIC. At store there are nominally two head-on interactions in points 6 and 8 (IP6 and IP8), and long-range interactions with a large separation in the other interaction points. Three bunches in the Blue ring are coupled to three bunches in the Yellow ring through the head-on beam–beam interaction. For studies, two DC wires were installed in the Blue and Yellow rings respectively in interaction region 6 (IR6). Table 1 shows the main beam parameters for polarized proton operation, both achieved and design. In RHIC the beam–beam effect is strongest in proton operation.

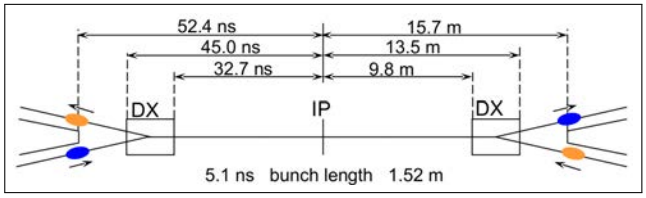

Figure 2: Schematic of the RHIC interaction regions.

Table 1: Main RHIC parameters achieved in polarized proton operation that are relevant for beam–beam effects protons (2009). Note that the polarized proton bunch intensity is also limited by intensity dependent depolarization effects in the AGS.

Quantity	Unit		
Beam energy, E_b	GeV	100	250
Bunch intensity, N_b	10^{11}	1.35	1.1
Norm emittance, ϵ	μm	2.5	3.0
rms bunch length, σ_z	m	0.85	0.60
Beam–beam parameter ξ/IP	...	0.0056	0.0045
No of IPs	...	2	2
β^* at IP6, IP8	m	0.7	0.7

In the LHC locations in warm sections of the interaction regions are reserved to accommodate long-range beam–beam wire compensators (Fig. 3), or electron lenses. These locations have about equal horizontal and vertical β-functions. With the expected strong long-range beam–beam effects in the LHC, and the proposed wire compensation, experimental data and simulations of long-range effects are highly desirable. Operational and experimental data exist from the Sp$\bar{p}$S and the Tevatron. In the SPS, wires were installed to further investigate strong long-range beam–beam interactions, to test the compensation scheme, and to benchmark simulations [30, 40–42].

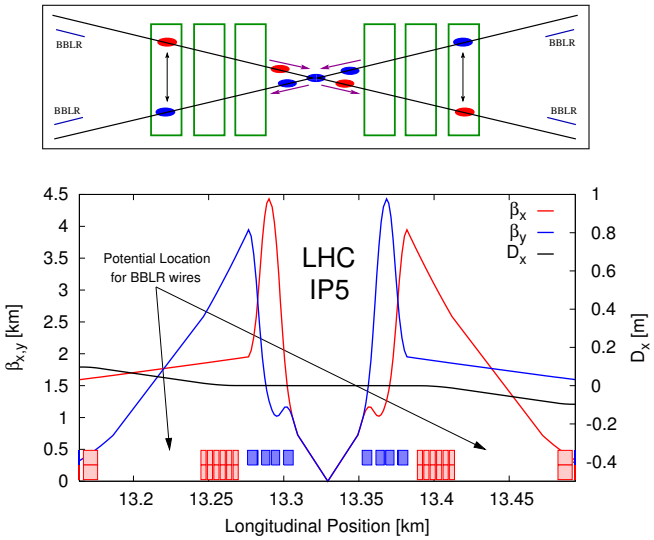

Figure 3: LHC interaction region schematically showing the common focusing channel with the 32 long-range interactions on the left and the right of the collision point (top) and the optics functions in the region.

The wire experiments in RHIC complement these studies. The beam lifetime in RHIC is typical for a collider and better than in the SPS wire experiments. In addition, and unlike in the SPS, head-on effects can be included, and with properly placed long-range interactions and wires, the compensation of a single long-range interaction is possible.

WIRES IN RHIC

The RHIC wire design is based on experience gained with the SPS units. Design considerations are: the location in ring, the integrated strength (IL), the wire temperature T in operation, the positioning range and accuracy, power supply requirements, controls, and diagnostics [43, 44]. The wire parameters are shown in Table 2.

Location in the Ring

For a successful compensation the phase advance between the long-range interaction and the compensator should be no larger than about 10 degrees [45]. Lattices with $\beta^* \leq 1.0$ m have such small phase advances between the entrance to the DX and the exit of Q3. Thus it is possible to place a wire in the warm region after Q3 to compensate for a long-range beam–beam interaction near the DX

Table 2: Parameters for RHIC wires. The wire material is Cu at 20°C. The nominal wire strength is for a single long-range interaction with a proton bunch intensity of 2×10^{11}.

Quantity	Unit	Value
Strength (IL), nominal	A m	9.6
Max. strength $(IL)_{\max}$	A m	125
Length of wire L	m	2.5
Radius of wire r	mm	3.5
Number of heat sinks n	...	3
Electrical resistivity ρ_e	Ω m	1.72×10^{-8}
Ceat conductivity λ	W m^{-1}K^{-1}	384
Thermal expansion coeff.	K^{-1}	1.68×10^{-5}
Radius of existing pipe r_p	mm	60
Current I, nominal	A	3.8
Max. current $I_{\max}$	A	50
Current ripple $\Delta I/I$ (at 50 A)	10^{-4}	< 1.7
Electric resistance R	mΩ	1.12
Max. voltage $U_{\max}$	mV	55.9
Max. power $P_{\max}$	W	2.8
Max. temp. change $\Delta T_{\max}$	K	15
Max. length change $\Delta L_{\max}$	mm	0.4
Vertical position range	mm/σ_y	65/10.6

magnet (Fig. 4). Since the beam paths must cross horizontally, it is easier to control the distance between the beams in an experiment through vertical separation. To compensate for a vertical long-range interaction near the DX magnet, one wire can be installed in each ring (see Fig. 5). In the Blue ring the wire is installed below the beam axis, in the Yellow ring above the beam axis.

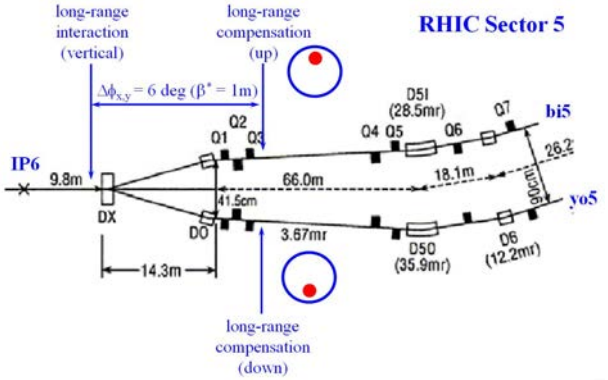

Figure 4: Location of wires in RHIC and location of long-range beam–beam interaction for compensation.

Integrated Strength

To compensate a single long-range interaction, the compensator's integrated strength (IL) must be the same as the opposing bunch's current integrated over its length $(IL) = N_b ec$, where I is the current in the wire, L its length, N_b the bunch intensity, e the elementary charge, and c the speed of light (see Table. 2).

In the LHC, an integrated strength of 80 A m is required to correct for the 16 long-range interactions on either side

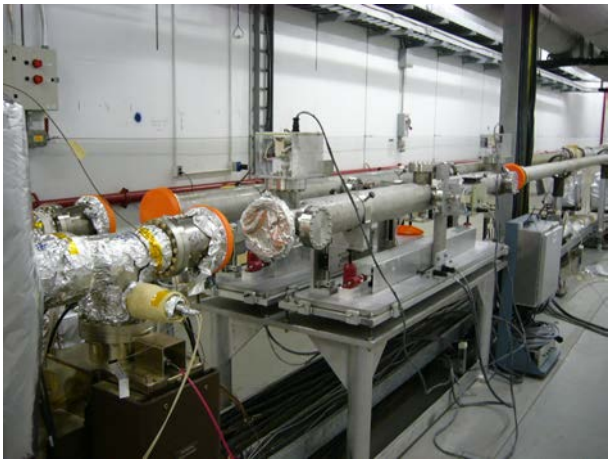

Figure 5: The two long-range beam–beam wires in the RHIC tunnel during installation.

of an IR [35]. Such a strength is also expected to lead to enhanced diffusion at amplitudes larger than 6 rms transverse beam sizes [45]. To study the enhanced diffusion in RHIC, the wire is designed for $(IL)_{\max} = 125$ A m.

Wire Temperature

The wire temperature should not exceed 100°C to avoid increased outgassing of the vacuum components. We use a number of air cooled heat sinks to limit the wire temperature.

Assume first a wire in vacuum of radius r and length l, with electrical resistivity ρ_e and heat conductivity λ. A current I flows through the wire, and at both ends there are heat sinks that maintain the temperature T_0. Further we assume that the temperature rise ΔT in the wire is small enough so that the material coefficients ρ_e and λ are constants. In each length element $\mathrm{d}x$ heat $\mathrm{d}Q$ is produced through the wire's resistivity at the rate

$$\frac{\mathrm{d}Q}{\mathrm{d}t} = \rho_e \frac{\mathrm{d}x}{\pi r^2} I^2, \tag{1}$$

and the heat flow is connected to the temperature gradient $\mathrm{d}T(x)/\mathrm{d}x$ via the heat equation

$$\frac{\mathrm{d}Q}{\mathrm{d}t} = -\lambda \pi r^2 \frac{\mathrm{d}T}{\mathrm{d}x}. \tag{2}$$

Combining Eqs. (1) and (2) yields the differential equation for the temperature

$$\frac{\mathrm{d}T^2(x)}{\mathrm{d}x^2} = -\frac{\rho_e}{\lambda} \frac{I^2}{\pi^2 r^4} \tag{3}$$

with the solution

$$T(x) = -\frac{1}{2\pi^2} \frac{\rho_e}{\lambda} \frac{I^2}{r^4} x^2 + ax + b. \tag{4}$$

The coefficients a and b can be determined from the boundary conditions $T(0) = T(l) = T_0$ yielding

$$T(x) = T_0 + \frac{1}{2\pi^2} \frac{\rho_e}{\lambda} \frac{I^2}{r^4} (xl - x^2). \tag{5}$$

The maximum temperature increase $\Delta T_{\max}$ is in the centre of the wire, $x = l/2$, and is

$$\Delta T_{\max} = \frac{1}{8\pi^2}\frac{\rho_e}{\lambda}\frac{(Il)^2}{r^4}. \quad (6)$$

If we now assume a wire of length L with n heat sinks, we can replace l by $L/(n-1)$ in Eq. (6) and arrive at

$$\Delta T_{\max} = \frac{1}{8\pi^2}\frac{\rho_e}{\lambda}\frac{(IL)^2}{(n-1)^2 r^4}. \quad (7)$$

We use $n = 3$ heat sinks cooled with forced air. To move the wire compensator close to the beam, its radius should not be much larger than an rms transverse beam size. The calculated temperature change is shown in Table 2. Figure 6 shows a drawing of the end of a wire. Visible are the wire support, the electrical feed-through which is also a heat sink, and a connecting loop allowing for thermal expansion of the wire.

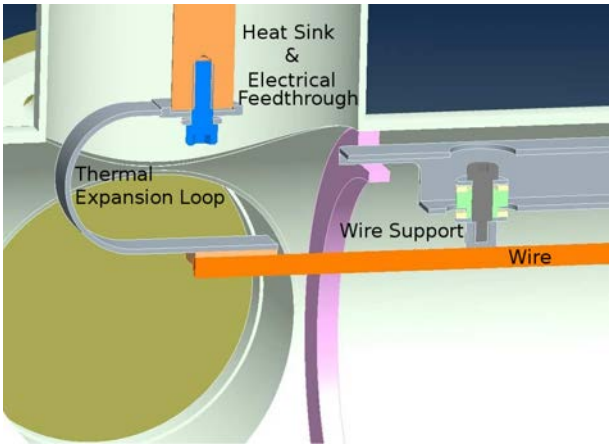

Figure 6: Drawing of the end of a long-range beam–beam wire in RHIC.

Power Supply Requirements

To limit emittance growth, a current ripple of $\Delta I/I < 10^{-4}$ is required [45]. A measurement shows a current ripple of $\Delta I/I < 1.7 \times 10^{-4}$ where the upper limit is given by the noise floor of the current measurement.

LONG-RANGE EXPERIMENTS AT RHIC

More than 30 dedicated Long-Range (LR) beam–beam experiments were performed at different energies, with different species and various machine configurations. They span a variety of long-range conditions which help benchmark simulation tools. The main parameters that were varied were the strength of the long-range interactions (wire current), the distance between the beam and the wire (or other beam), the tune and chromaticity. All experimental sessions to study long-range beam–beam interactions in RHIC can be broadly classified into three categories approximately in chronological order:

- measurement of a single long-range interaction between the two proton bunches at 23 and 100 GeV in IP6;
- effect of the DC wires on a single beam either by varying the current at a fixed distance or varying the distance to the beam with fixed current on both protons at 100 GeV and gold at 100 GeV/nucleon;
- effect of long-range interaction either with a wire in the presence of head-on collisions or long-range interactions between the two beams in IP6 with simultaneous compensation using a wire at 100 GeV.

A summary of all long-range experiments performed in the RHIC accelerator between 2005 to 2009 is listed with corresponding beam conditions in Table 3. The main observables in long-range beam–beam experiments are orbits, tunes, Beam Transfer Functions (BTFs), and the beam lifetime. Several simulations were performed for a subset of measurements which show successful reconstruction of all measurable quantities and the onset of losses [46]. Specific examples for each of the three categories with detailed results are presented in the next sections to summarize all the long-range experiments performed at RHIC.

Single Long-range Measurements

The first set of long-range beam–beam experiments were performed with proton beams in 2006. The motivation of these experiments was to characterize the effect of one parasitic interaction on beam losses for a future compensation demonstration. The Blue and Yellow beams were vertically separated in the IR6 region close to the DX magnet (Fig. 2). The RHIC beams are very stable at the nominal working point and the effect of a single long-range (weak effect) is not visible in the beam lifetime. An effect of a compensation effect will not be possible to detect with the available instrumentation.

Therefore, a finite strength in lattice octupoles and a working point close to the 10^{th} order resonance was used as shown in Fig. 7. At this modified working point, the beams are marginally stable as the introduction of the single parasitic interaction increases the tune spread of the large amplitude particles on to the 10^{th} order resonance, thus enhancing the effect. This setup of marginally stable beams is only used for experiments with single long-range interaction between the two beams. Some relevant lattice and beam parameters are listed in Table 4. The marginally stable beams were essential as the effect of the single long-range interaction on the rather stable RHIC beams is subtle. In one such experiment, the effect on the beam losses on both beams as a function of the separation is shown in Fig. 8. To increase the signal-to-noise ratio the losses are averaged over the 12 bunches.

Note that the Yellow beam was moved while the Blue beam was kept stationary. Therefore, the effect on the Blue beam is of relevance as the losses in the Yellow beam may

Table 3: Summary of long-range beam–beam experiments in RHIC. The wires in the Blue and Yellow ring are named B-BBLR and Y-BBLR respectively. Fields are left blank when the experimental value could not be determined.

fill no	ring	scan	species	rel. γ	bunches per ring	Q_x	Q_y	LR location	LR strength (IL)	LR separation d	fitted exponent p	d for $\tau < 20$ h	comment
...	...	...	...	...	...	...	...	...	A m	σ	...	σ	
2005													
6981	B	1	p	25.963	1	0.7331	0.7223	IP4	5.3	B moved			weak signal
6981	Y	1	p	25.963	1	0.7267	0.7234	IP4	5.3	B moved			weak signal
6981	B	2	p	25.963	1	0.7351	0.7223	IP4	5.8	B moved			weak signal
6981	Y	2	p	25.963	1	0.7282	0.7233	IP4	5.8	B moved			weak signal
6981	B	3	p	25.963	1	0.7383	0.7247	IR4 DX	8.6	Y moved			weak signal
6981	Y	3	p	25.963	1	0.7271	0.7218	IR4 DX	8.6	Y moved			weak signal
6981	B	4	p	25.963	1	0.7394	0.7271	IR4 DX	8.9	Y moved	4.9	6.5	
6981	Y	4	p	25.963	1	0.7264	0.7388	IR4 DX	8.9	Y moved	2.8		
2006													
7707	B	1	p	106.597	10			IR6 DX	6.7	B moved			weak signal
7707	Y	1	p	106.597	10			IR6 DX	6.7	B moved			weak signal
7707	B	2	p	106.597	10			IR6 DX	6.7	Y moved			weak signal
7707	Y	2	p	106.597	10			IR6 DX	6.7	Y moved			weak signal
7747	B	1	p	106.597	8			IR6 DX	7.9	B moved			weak signal
7747	Y	1	p	106.597	10			IR6 DX	7.9	B moved			weak signal
7747	B	2	p	106.597	8			IR6 DX	7.0	Y moved			weak signal
7747	Y	2	p	106.597	10			IR6 DX	7.0	Y moved			weak signal
7807	B	1	p	106.597	12	0.6912	0.6966	IR6 DX	8.2	Y moved	2.5	3.5	additional octupoles
7807	Y	1	p	106.597	12	0.7092	0.6966	IR6 DX	8.2	Y moved	1.5	3.5	additional octupoles
2007													
8231	B	1	Au	10.520	6	0.2327	0.2141	B-BBLR	12.5	B-BBLR moved	7.2	6.5	
8231	B	1	Au	10.520	6	0.2322	0.2140	B-BBLR	125	B-BBLR moved	7.8	9.0	
8405	B	1	Au	107.369	56	0.2260	0.2270	B-BBLR	125	B-BBLR moved	1.7	15.0	background test
8609	B	1	Au	107.369	23	0.2340	0.2260	B-BBLR	12.5	B-BBLR moved	7.4	6.0	
8609	B	2	Au	107.369	23	0.2340	0.2260	B-BBLR	125	B-BBLR moved	16.0	5.5	
8609	Y	1	Au	107.369	23	0.2280	0.2350	Y-BBLR	12.5	Y-BBLR moved	4.8	9.5	
8609	Y	2	Au	107.369	23	0.2280	0.2350	Y-BBLR	125	Y-BBLR moved	4.1	7.5	
8727	B	1	Au	107.369	23	0.2200	0.2320	B-BBLR	12.5	B-BBLR moved	5.2	9.5	
8727	B	2	Au	107.369	23	0.2200	0.2320	B-BBLR	125	B-BBLR moved	8.1	10.0	
8727	B	1	Au	107.369	23	0.2320	0.2280	Y-BBLR	12.5	Y-BBLR moved	6.3	4.5	
8727	B	2	Au	107.369	23	0.2320	0.2280	Y-BBLR	125	Y-BBLR moved	10.8	5.0	
8727	B	3	Au	107.369	23	0.2320	0.2280	Y-BBLR	125-0	-6.5			
8727	B	4	Au	107.369	23	0.2320	0.2280	Y-BBLR	125	-6.5			ver. chromaticity 2-8
8727	B	5	Au	107.369	23	0.2320	0.2280	Y-BBLR	125-0	-6.5			ver. chromaticity 8
2008													
9664	B	1	d	107.369	12	0.2288	0.2248	B-BBLR	125	B-BBLR moved	3.8	17.0	end of physics store
9664	B	2	d	107.369	12	0.2288	0.2248	B-BBLR	75-125	5.8			end of physics store
2009													
10793	B	-	p	106.597	36	0.691	0.688	B-BBLR	125	B-BBLR moved			with head-on collisions
10793	Y	-	p	106.597	36	0.695	0.692	Y-BBLR	125	Y-BBLR moved			with head-on collisions
10793	B	-	p	106.597	36	0.691	0.688	IR6 DX	12.5	B-BBLR moved			LR compensation
10793	Y	-	p	106.597	36	0.695	0.692	IR6 DX	12.5	Y-BBLR moved			LR compensation

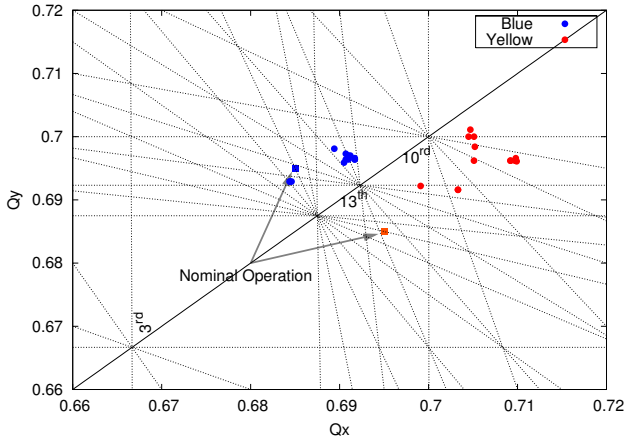

Figure 7: Tunes in the resonance diagram for both beams and both planes during a scan.

Table 4: RHIC parameters for experiments with long-range interactions with proton beams.

Quantity	Enit	Blue	Yellow
Beam energy E	GeV/n	100	
Rigidity ($B\rho$)	T m	831.8	
Number of bunches	...	12	
LR interaction from IP6	m	10.6	
Norm. Emittances ($\epsilon_{x,y}$)	μm	15-20	
β_x at wire location	m	105	
Tunes ($Q_{x,y}$)	...	0.69/0.7	0.71/0.69
β_x at wire location	m	1060	342
β_y at wire location	m	357	1000
Octupole Strength (kl)	m^{-2}	6.3×10^{-3}	

also be affected by orbit and tunes shifts. A small effect is visible when the beams are approximately 5 σ or closer.

Compensation of such small effects is difficult as the losses are smaller than the natural reproducibility of the machine for a given beam setup. Therefore, it was important to significantly enhance the loss due to the long-range interactions to clearly demonstrate compensation with a DC wire. Increased chromaticity and introduction of head-

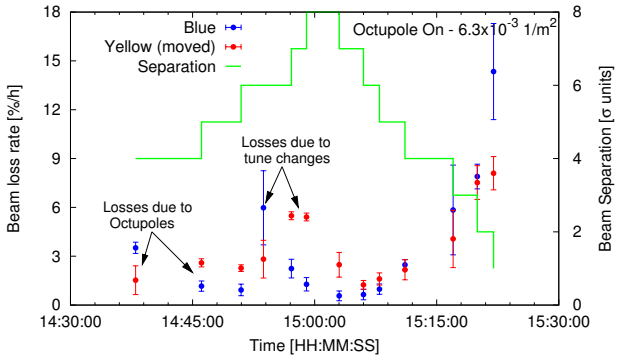

Figure 8: Beam losses due to a single parasitic interaction of the Blue and Yellow beam. The Yellow beam moved closer to the Blue beam from an initially large separation.

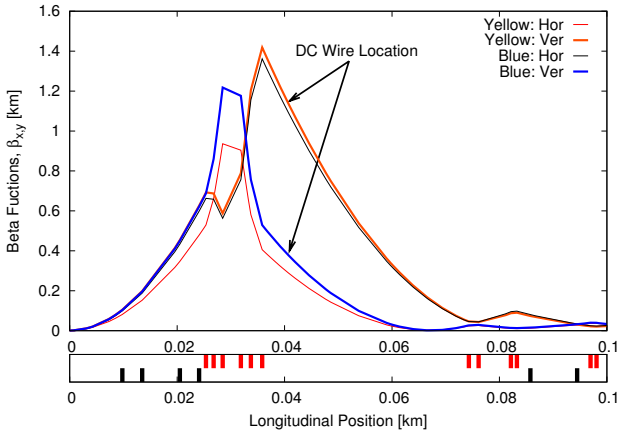

Figure 9: The beta functions from MAD lattice for both rings as a function of longitudinal position.

on collisions were utilized to enhance the effect of the LR interaction with the DC wires [46].

Wire Scans on Single Beam

After the installation of the DC wires in 2007, the majority of the experiments were carried out using the individual wires of the Blue and the Yellow ring to characterize the onset of the losses under certain beam conditions [44, 46]. Most of the wire experiments were done with gold beams. Table 5 shows the main beam parameters for the wire experiments at store with gold beams.

Table 5: RHIC parameters for experiments with DC wires on individual gold beams.

Quantity	Unit	Blue	Yellow
Beam energy E	GeV/nucleon	100	
Rigidity $(B\rho)$	Tm	831.8	
Number of bunches	...	6–56	
Norm. Emittance $\epsilon_{x,y}$	μrad	17	17
Distance IP6 to wire centre	m	40.92	
Parameter K (at 50 A)	nm	-30.1	
Hor. tune Q_x	...	28.234	28.228
Ver. tune Q_y	...	28.226	29.235
β_x at wire location	m	1091	350
β_y at wire location	m	378	1067

The β-functions in Table 5 are the best estimate of the real β-functions in the machine. The design lattice has $\beta^* = 0.8$ m at IP6. To calculate the β-functions at the wire location we use $\beta^* = 0.9$ m, and assume a 10% error. Figure 9 shows the MAD lattice near the interaction region 6 where the wires are located.

The measurements consisted mainly of distance and current scans and simultaneous measurements of the beam loss rate. An overview of the beam losses and wire position for the Blue and the Yellow ring during the course of a scan (Fill 8727) is illustrated in Fig. 10. The beam loss rates are clearly different for the Blue and Yellow beams. This indicates towards different diffusion rates and re-population of tails for the two beams. The exact reason for this difference is not identified. It should be noted that the wire installations are identical.

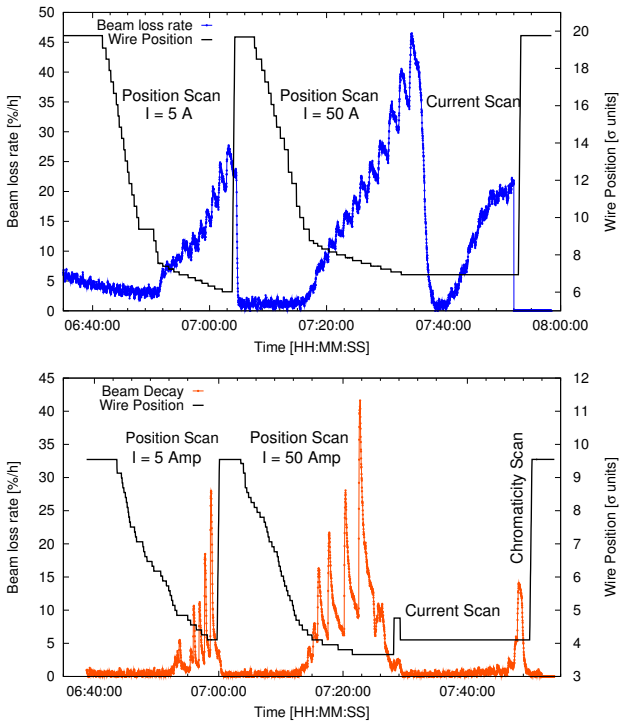

Figure 10: Beam losses and wire position as a function of time during the course of position and current scan (May 2007, Fill 8727).

Orbit, tune and chromaticity changes can be calculated as a function of the long-range strength and distance [47]. These quantities and beam transfer functions are usually recorded to benchmark with theory and simulations. The vertical dipole kick $\Delta y'$ and vertical tune change ΔQ_y due to the wire for a separation d in the vertical plane between the beam and the wire are given by (assume no horizontal

separation)

$$\Delta y' = \frac{K}{d} \quad \text{and} \quad \Delta Q_{x,y} = \pm \frac{K\beta_{x,y}}{4\pi}\frac{1}{d^2} \tag{8}$$

with

$$K = \frac{\mu_0 (IL)}{2\pi (B\rho)}, \tag{9}$$

where d is the distance between the wire and the beam, μ_0 the permeability of the vacuum, (IL) the integrated wire strength, and $(B\rho)$ the beam rigidity.

Note that we take a positive sign for d for a wire above the beam, and a negative sign below the beam. We also assume that the reference vertical orbit position at the location of the wire is zero ($y_{ref} = 0$) for the wire current off. The sign of K depends on the direction of the wire current relative to the beam direction, and the charge of the beam particles. In our case the wire current has the opposite direction to the beam, the Blue wire is above and the Yellow wire below the beam, and the beam particles have positive charges. In this case the sign of K is negative in Blue, and positive in Yellow. The orbit change Δy at the location of the wire due to the dipole kick $\Delta y'$, for $\Delta y \ll d$, is then

$$\Delta y = \frac{K\beta_y}{2d}\frac{\cos(\pi Q_y)}{|\sin(\pi Q_y)|}. \tag{10}$$

If the wire comes close to the beam Eq. (10) becomes inaccurate and needs to be replaced by

$$\Delta y = \frac{d}{2} - \sqrt{\frac{d^2}{4} - \frac{1}{2}K\beta_y \cot(\pi Q_y)} \tag{11}$$

where d is now the distance between the wire and the beam position at zero wire current.

Orbit and tune changes agree with expectations under well controlled experimental circumstances [46, 48]. Figure 11 shows a comparison of the measured beam trajectories to the analytical prediction as a function of the separation between the wire and the Blue beam.

Figure 12 shows a comparison of the measured tunes to the analytical prediction as a function of the separation between the wire and the beam.

The beam lifetime, however, is determined through the nonlinear beam–beam effect and can only be assessed in detailed simulations. Figure 13 (top) shows the beam loss rate as a function of the vertical wire distance to the beam. The onset of losses due to a long-range type interaction between the wire and the beam is visible. Similarly the effect on beam losses due to a current scan at a fixed distance is shown in Fig. 13 (bottom). The approximate separation in the Blue ring is 9 σ and in the Yellow ring is 5 σ. The Yellow ring shows very weak or no effect with a current scan which is probably due to a previous distance scan resulting in a cleaning of the large amplitude particles.

It was speculated that the beam lifetime τ can be expressed as $\tau = Ad^p$ where A is an amplitude, d the distance between wire and beam, and p an exponent that would typically be in a narrow range. For the SPS p had been found to

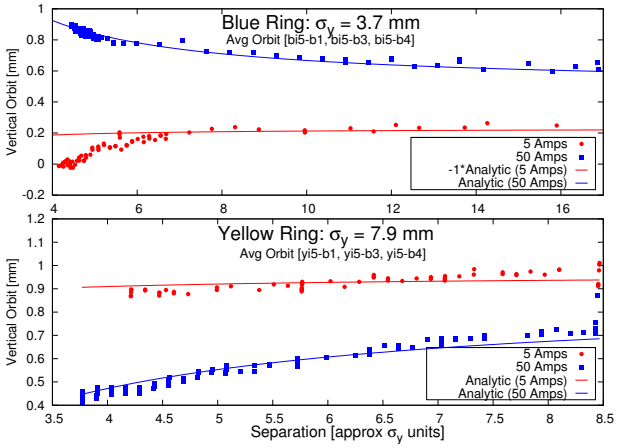

Figure 11: Vertical orbit change (average of 3 BPMs near wire) as a function of vertical distance, in Blue and Yellow ring at 5 A and 50 A. Solid lines in all plots represent the analytical prediction.

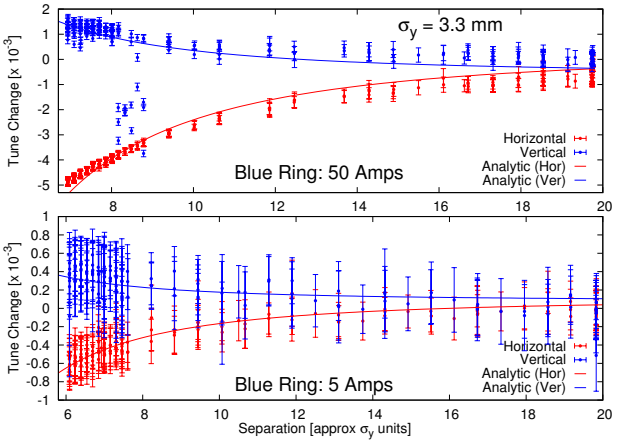

Figure 12: Horizontal and vertical tune change for 50 A and 5 A wire current, for the Blue ring. Solid lines in all plots represent the analytical prediction.

be about 5, and for the Tevatron to be about 3 [49]. In Table 3 the fitted exponents are listed for all cases for which a fit was possible. The fitted exponents range from 1.7 to 16, i.e. p is not constrained within a narrow range. Ten of the thirteen p values are between 4 and 10. Figure 14 shows the fitted exponents p as a function of the ion tunes in the upper part, and the proton tunes in the lower part. Ion tunes near the diagonal and away from either horizontal or vertical resonances show smaller exponents p. The experiments also showed that the beam lifetime is reduced with increased chromaticity [46].

Another simple measure of assessing the long-range beam–beam effect in experiments is the distance between the beam and wire (or other beam) at which the beam lifetime becomes smaller than a certain value. We have chosen this value to be 20 h, which would imply a luminosity lifetime of 10 h or less. Table 3 shows an amplitude range between 3.5 and 17 σ. With the available amount of data

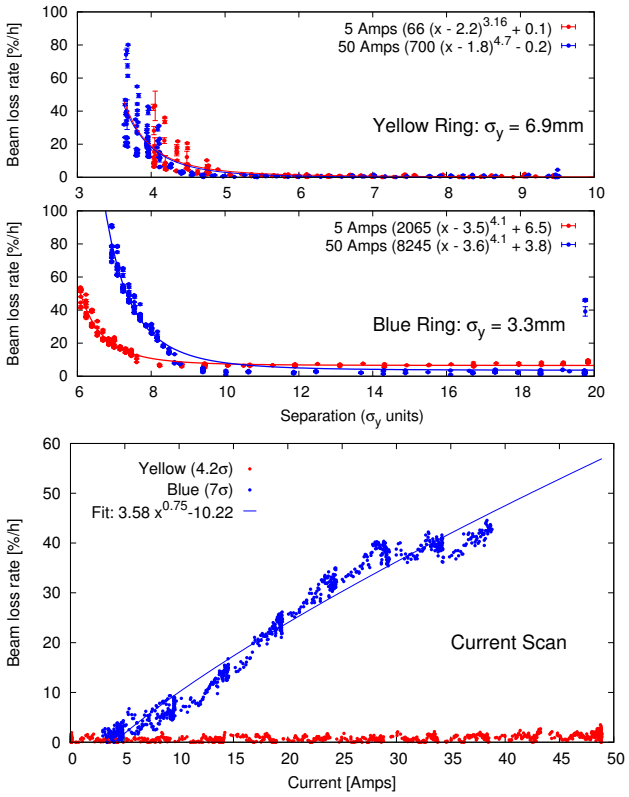

Figure 13: Top: Beam loss as a function of the DC wire separation to the Blue and the Yellow beams at 5 A and 50 A. Bottom: Beam loss due to a current scan in the DC wire fixed at a given distance from the beam. Solid lines in all plots show a power law fit to the losses.

no clear correlation can be established between this distance and the fitted coefficient p. In two cases the distance was found to be as large as or larger than 10 σ, and most cases fall between 4 and 10 σ. Operation with less than 5 σ separation appears to be difficult [50]. Note that the beam is sometimes used for multiple scans and that a large lifetime drop at large distances is more typical for previously unused beams (Table 3).

One important goal of the experiments is to benchmark simulations. In several simulations the onset of large losses as a function of the distance between wire and beam was reproduced within about 1 σ [30, 48, 51–55]. One such comparison is shown in Fig. 15.

Long-range Effects with Head-on Collisions

End of physics fills were initially used to test the effect of the wires on colliding gold and deuteron beams (see Table 3). It should be noted that the beam–beam parameter of proton beams in RHIC is approximately three times larger than the beam–beam parameter of heavy ion beams. The first dedicated experiment with protons to compare the effect of the wire on colliding beams and compensation of a single LR beam–beam interaction was conducted in 2009 at 100 GeV. Due to aperture considerations for decreasing β^*,

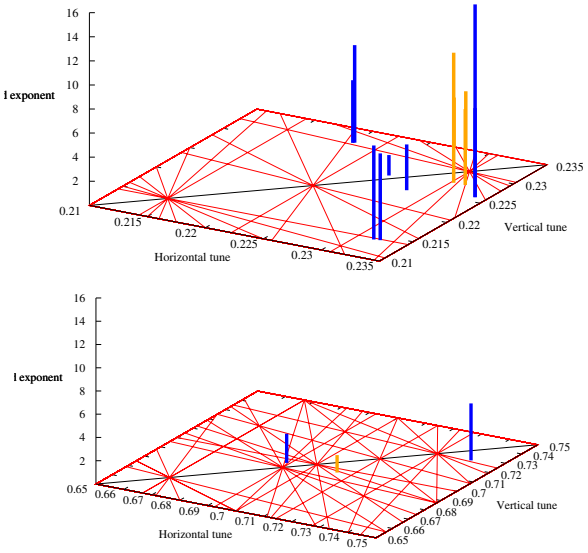

Figure 14: Fitted exponents p for long-range beam–beam experiments as a function of the ion tunes (top) and the proton tunes (bottom). The fitted exponents range from 1.7 to 16.

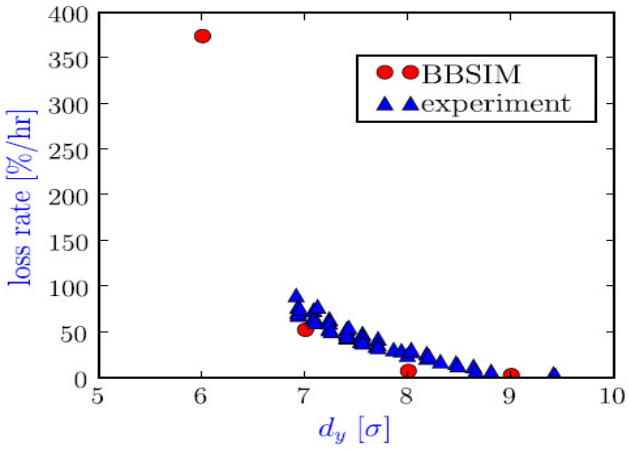

Figure 15: Comparison of measured and simulated beam loss rate as a function of distance between wire and beam. Experiment with gold beam at store, wire strength of 125 Am [51, 53].

the Blue wire was removed during the shutdown after the 2009 run and the Yellow wire was removed subsequently. Therefore, the experiments in 2009 serve as the final set of measurements for LR beam–beam with RHIC as a test bed. The relevant RHIC beam and lattice parameters are listed in Table 6 for the experiments in 2009.

Prior to a long-range compensation attempt, a position scan of the wire on each beam was performed with a wire current of 50 A. A 36×36 bunch pattern with six non-colliding bunches was chosen to enable a comparison of the lifetime in the presence of the wire between single beam

Table 6: Relevant RHIC beam and lattice parameters for experiments with proton beams.

Quantity	Unit	Blue	Yellow
Beam energy E	GeV	100	
Rigidity $(B\rho)$	Tm	333.5	
Number of bunches	-	36	
# of colliding bunches	-	30	
Bunch intensity	10^{11}	1.7	1.7
Norm. Emittance $\epsilon_{x,y}$	μrad	25,24	49,19
Horizontal tune Q_x	...	28.691	28.232
Vertical tune Q_y	...	29.688	29.692
Chromaticities (ξ_x, ξ_y)	...	$(+2, +2)$	
β_x at wire location	m	1566	556
β_y at wire location	m	576	1607

and colliding beams simultaneously. The corresponding beam loss rates as a function of beam to wire separation on both colliding and non-colliding bunches were measured. The initial beam loss rates with colliding beams were stabilized to the nominal 10% per hour. The maximum total beam losses for the wire movements towards the beam at fixed current were constrained to 100–150% per hour for a very short period to avoid disrupting the beam quality significantly for subsequent measurements.

Figure 17 shows the evolution of the intensity between bunches with and without head-on collisions. It is evident that the bunches with the head-on collisions have a more severe effect from the LR forces of the wire. Several hypotheses can be formulated to explain the increased losses for bunches with head-on collision.

- The dynamic aperture for the bunches with head-on is significantly smaller than that of the single beam which could lead to the observed beam losses.
- It was also suggested by an anonymous referee that the addition of the head-on collisions enhances the diffusion leading to enhanced losses in the presence of long-range interactions. Figure 17 clearly shows a larger initial slope for bunch intensities with collisions. However, it is difficult to untangle the contribution from the reduced dynamic aperture as opposed to enhanced diffusion.
- The additional tune shift due to the wire along with large head-on tune shift could lead to beam losses due to very limited tune space available. No tune optimization was performed during the experiment.
- The effect of the wire on the orbit can introduce a static offset between the two beams at the IP which is approximately proportional to the wire distance. A large offset due to the kick from the wire can lead to emittance blow-up and beam losses [31]. The relative offset at the collision point during the wire scan with 50 A (see Fig. 16) is well below the 1 σ level which is very small.

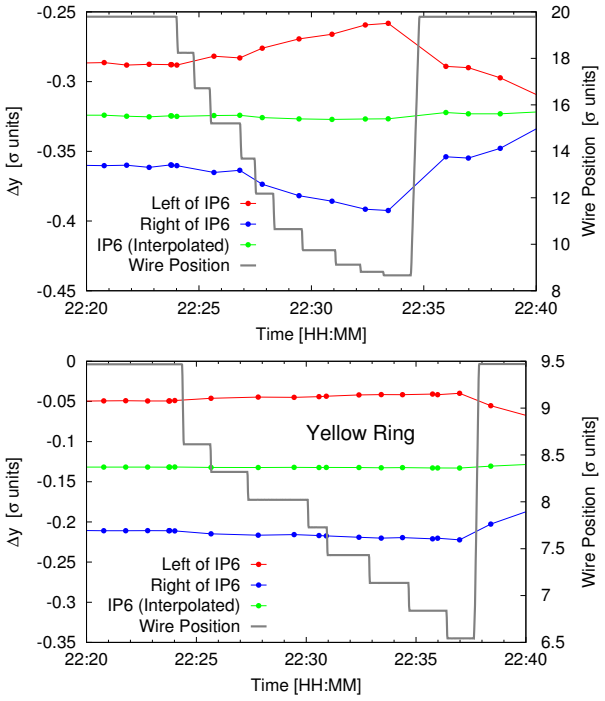

Figure 16: Orbit offset at IP6 as a function of the wire position for Blue (top) and Yellow (bottom) rings with a current of 50 A.

However, simulations to support each of the above hypotheses to explain its contribution towards observed losses is beyond the scope of this paper.

Single Long-range and Wire Compensation

The bunch spacing and the interaction region geometry in RHIC does not inherently have LR beam–beam interactions. It is therefore necessary to shift the collision point towards the DX magnet closest to the DC wires as noted before. This location enables an artificially induced LR interaction between the two beams and simultaneously allows for a minimum phase advance between the LR interaction and DC wires (6 deg). Additionally, this location has sufficient aperture for an orbit scan with the range of interest (3–10 σ). Figure 18 shows the trajectories of the Blue and Yellow rings with the LR interaction set at approximately 3.1 σ.

The individual bunch intensities and beam losses were recorded during the position scan with the LR compensation [56]. Figure 19 shows the beam losses as a function of the wire position. In the Blue ring, the losses are always increasing as the wire approaches the beam. Therefore, no evidence of compensation of the LR interaction from the Blue beam is visible. However, in the Yellow ring, the beam lifetime improved as the beam to wire distance approaches 3 σ (Fig. 19). Consecutive retractions and restoration of the beam to wire distance to 3 σ show similar improvement of the beam lifetime. This indicates a compensation of the effect of LR interaction by the DC wire.

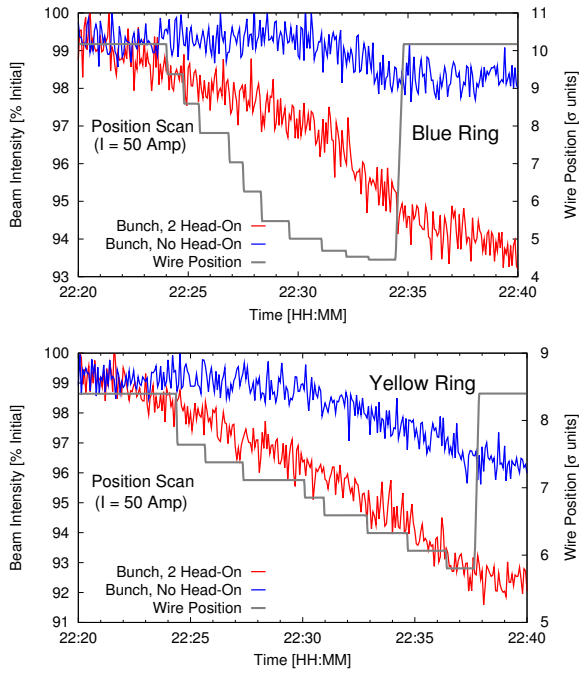

Figure 17: Single bunch intensities as a function of wire position for Blue (top) and Yellow (bottom) rings with a current of 50 A. Comparison between bunches with head-on and no head-on collision is shown.

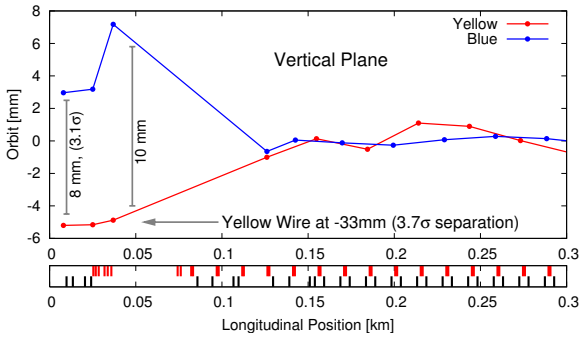

Figure 18: Orbits right of IP6 for the Blue and the Yellow ring with the LR interaction setup near the DX magnet at approximately 3.1 σ.

In addition to beam losses, the individual bunch intensities with and without LR interactions and simultaneous compensation is shown in Fig. 20. Note that all 36 bunches experience the effect of the DC wire, but only 30 bunches experience LR interactions. Therefore, only bunches with an LR interaction can experience a compensation. In the Blue ring, the bunch intensity evolution is similar for bunches with and without LR compensation. Hence, only the effect from the wire is visible. The bunches with LR interaction and simultaneous compensation have reduced beam losses as compared to the bunches that only see the wire. This is consistent with the beam loss measurements (Fig. 19).

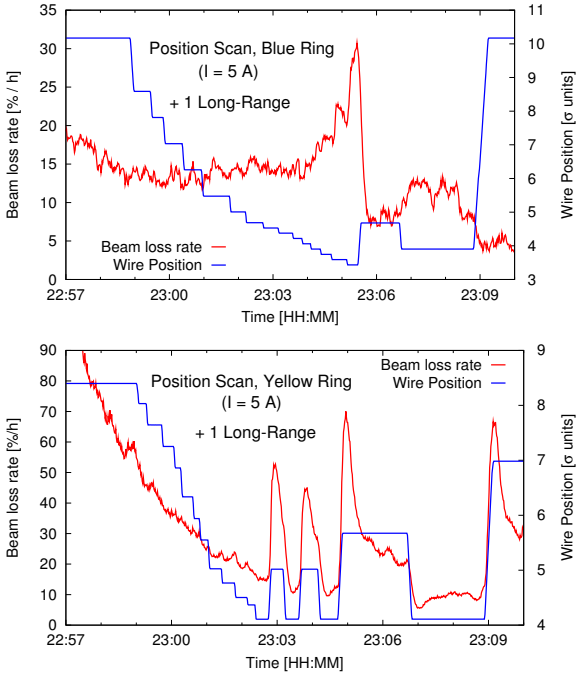

Figure 19: Beam loss rate for a Blue (top) and Yellow (bottom) bunch with one long-range interaction, and an additional wire interaction. The wire position varies, and the wire current is constant at 5 A.

SUMMARY

Long-range beam–beam experiments were conducted in RHIC from 2005 to 2009. The motivation for these were two-fold. First, the experimental data can benchmark simulation codes for situations of strong localized long-range beam–beam interactions as they will exist in the LHC. Second, the compensation of a single long-range beam–beam interaction can be tested in a scheme that is also usable in the LHC.

These experiments complement the experience with long-range beam–beam interactions in the Sp$\bar{p}$S and Tevatron, wire experiments in the SPS, and the partial long-range compensation in DAΦNE. The RHIC wires created strong localized long-range beam–beam effects, comparable in strength to the effect expected in the LHC, with a beam that has a lifetime typical of hadron colliders, and including head-on beam–beam collisions. The observed orbit and tune changes due to the wire were as expected. The effect of the long-range beam–beam interactions on the beam loss rate is sensitive to a number of beam parameters such as the tunes and chromaticities. Fitting the beam lifetime τ to an exponential function $\tau \propto d^p$ as a function of the distance d between the beam and the wire, exponents p in the range between 1.7 and 16 were found. Distances smaller than 5 σ created losses too large for collider operation. The experimentally observed distance from the wire to the beam at which large beam losses set in could be reproduced in simulations within 1 σ. The beam lifetime with long-range interactions created by the wire was de-

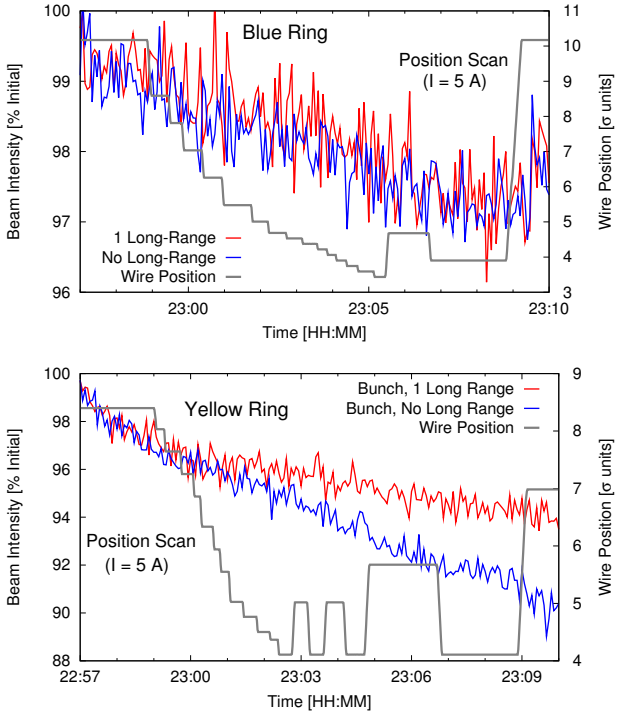

Figure 20: Beam intensity comparison between bunches with a single long-range and no long-range interaction as a function of the wire position for Blue (top) and Yellow (bottom) rings with a wire current of 5 A.

graded further through head-on collisions. A single attempt to compensate long-range beam–beam interaction via a DC wire showed evidence of compensation.

ACKNOWLEDGEMENTS

For discussions and help we are most thankful to collaborators within the US LHC Accelerator Research Program as well as several people at various laboratories. Among these are O. Brüning, R. DeMaria, U. Dorda, W. Herr, A. Kabel, H.-J. Kim, J.-P. Koutchouk, C. Milardi, K. Ohmi, T. Pieloni, J. Qiang, F. Schmidt, T. Sen, G. Sterbini, and F. Zimmermann.

Work supported by Brookhaven Science Associates, LLC under Contract No. DE-AC02-98CH10886 with the US Department of Energy, and in part by the US LHC Accelerator Research Program.

REFERENCES

[1] N. Abreu, R. Calaga, W. Fischer and G. Robert-Demolaize, Phys. Rev. ST Accel. Beams 14 (2011) 091001.

[2] E. Keil, "Beam–Beam Effects in Electron and Proton Colliders," PAC'89, Illinois, March 1989, pp. 1731–1735 (1989).

[3] Y. Alexahin, "Theory and Reality of Beam–Beam Effects at Hadron Colliders," PAC'05, Tennessee, May 2005, pp. 544–548 (2005).

[4] J.-P. Koutchouk, "A Summary on CARE-HHH_APD Presentations on Beam–Beam Effects & Beam–Beam Compensation at the LHC," Final CARE-HHH Workshop on Scenarios for the LHC Upgrade and Fair - HHH-2008 - Chavannes-de-Bogis, Switzerland; W. Scandale and F. Zimmermann (eds.), CERN-2009-004 (2009); CARE-Conf-08-032-HHH (2008).

[5] M. Jacob and K. Johnson (editors), "The Role of the ISR in the Development of Particle Physics," CERN Yellow Report 84-23 (1984).

[6] J.Y. Hémery, A. Hofmann, J.-P. Koutchouk, S. Myers, and L. Vos, "Investigation of the Coherent Beam–Beam Effects in the ISR," IEEE Trans. of Nucl. Sci. NS-28, No. 3 (1981).

[7] L.R. Evans and J. Gareyte, "Beam–Beam and Single Beam Effects in the SPS Proton-Antiproton Collider," PAC'83, Santa Fee, March 1983, pp. 2397–2399 (1983).

[8] L. Evans, J. Gareyte, M. Meddahi, and R. Schmidt, "Beam–Beam Effects in the Strong-Strong Regime at the CERN-SPS," PAC'89, Illinois, March 1989, pp. 1403–1405 (1989).

[9] K. Cornelis, M. Meddahi, and R. Schmidt, "The Beam–Beam Effect in the SPS Proton Antiproton Collider With Unequal Emittances," EPAC'90, Nice, June 1990, pp. 1670–1672 (1990).

[10] K. Cornelis, "Beam–Beam Effects in the SPS Antiproton-Proton Collider," LHC'99, Geneva, June 1999, CERN-SL-99-039 AP (1999).

[11] X. Zhang, T. Sen, V. Shiltsev, M. Xiao, Y. Alexahin, F. Schmidt, and F. Zimmermann, "Experimental Studies of Beam–Beam Effects in the Tevatron", PAC'03, Oregon, 2003, pp. 1757–1759 (2003).

[12] V. Shiltsev, Y. Alexahin, V. Lebedev, P. Lebrun, R. S. Moore, T. Sen, A. Tollestrup, A. Valishev, and X. L. Zhang, Phys. Rev. ST Accel. Beams 8, (2005) 101001.

[13] A. Valishev, "Simulation of Beam–Beam Effects and Tevatron Experience", EPAC'08, Genoa, 2008, pp. 2937–2941 (2008).

[14] W. Fischer et al., "Observation of Strong-Strong and Other Beam–Beam Effects in RHIC," PAC'03, Oregon, 2003, pp. 135–137 (2003).

[15] V. Ptitsyn et al., "RHIC Performance With Polarized Protons in Run-6," EPAC'06, Edinburgh, 2006, pp. 592–594 (2006).

[16] W. Herr, "Computer Simulation of the Coherent Beam–Beam Effect in the LHC," PAC'91, San Francisco, May 1991, pp. 1068–1070 (1991).

[17] N. Gelfand, C. Johnstone, T. Sen, and W. Wan, "Effect of the Beam–Beam Interactions on the Dynamic Aperture of the LHC at Collision," PAC'99, New York, March 1999, pp. 1677–1679 (1999).

[18] J. Gareyte, "Beam–Beam Design Criteria for LHC," LHC'99, Geneva, June 1999, CERN-SL-99-039 AP (1999).

[19] M.A. Furman and W.C. Turner, "Beam–Beam Simulations for Separated Beams in the LHC," EPAC'00, Vienna, June 2000, pp. 1196–1189 (2000).

[20] H. Grote, "Self-Consistent Orbits With Beam–Beam Effect in the LHC," EPAC'00, Vienna, June 2000, pp. 1202–1204 (2000).

[21] L.H.A. Leunissen, H. Grote, and F. Schmidt, "LHC Dynamic Aperture Including the Beam–Beam Force," EPAC'00, Vienna, June 2000, pp. 1208–1210 (2000).

[22] M.P. Zorzano and T. Sen, "Emittance Growth of the LHC Beam Due to the Effect of Head-On Beam–Beam Interaction and Ground Motion," EPAC'00, Vienna, June 2000, pp. 1226–1228 (2000).

[23] M.P. Zorzano and F. Zimmermann, "Simulations of Coherent Beam–Beam Modes at the LHC," EPAC'00, Vienna, June 2000, pp. 1229–1231 (2000).

[24] W. Herr, "Tune Spreads and Shifts Due to the Long-Range Beam–Beam Effect in The LHC," EPAC'00, Vienna, June 2000, pp. 1630–1632 (2000).

[25] O. Brüning, P. Collier, P. Lebrun, S. Myers, R. Ostojic, J. Poole, and P. Proudlock (editors), CERN-2004-003 (2004).

[26] F. Zimmermann, "LHC Upgrade Scenarios," PAC'07, Albuquerque, June 2007, pp. 714–718 (2007).

[27] J.-P. Koutchouk, "A Concept for the Luminosity Upgrade ...," PAC'07, Albuquerque, June 2007, pp. 3387–3389 (2007).

[28] G. Sterbini and G. Tommasini, "A Feasibility Study of Superconducting Dipole for the Early Separation Scheme of SLHC," EPAC'08, Genoa, June 2008, pp. 2461–2463 (2008).

[29] K. Ohmi, "Study of Beam–Beam Effect at Various Collision Schemes in LHC," EPAC'08, Genoa, June 2008, pp. 2593–2595 (2008).

[30] U. Dorda, "Compensation of Long-Range Beam–Beam Interaction at the CERN LHC," PhD thesis, Vienna University of Technology, Austria (2008).

[31] T. Pieloni, "A Study of Beam–Beam Effects in Hadron Colliders With a Large Number of Bunches," PhD thesis, Ecole Polytechnique Federale de Lausanne, Switzerland (2008).

[32] W. Herr, LHC Beam Operation Workshop, Evian (2010).

[33] The CERN study group on new accelerators, CERN AR/Int. SG/64-9 (1964).

[34] V. Shiltsev, V. Danilov, D. Finley, and A. Sery, Phys. Rev. ST Accel. Beams 2 (1999) 071001.

[35] J.-P. Koutchouk, "Correction of the Long-Range Beam–Beam Effect in LHC Using Electro-Magnetic Lenses," PAC'01, Illinois, 2001, pp. 1681–1683 (2004).

[36] U. Dorda, F. Zimmermann, W. Fischer, and V. Shiltsev, "LHC Beam–Beam Compensation Using Wires and Electron Lenses," PAC'07, Albuquerque, June 2007, pp. 1589–1591 (2007).

[37] T. Sen and B. Erdelyi, "Feasibility Study of Beam–Beam Compensation in the Tevatron With Wires," PAC'05, Knoxville, 2005, pp. 2645–2647 (2005).

[38] C. Milardi, D. Alesini, M.A. Pregner, P. Raimondi, M. Zobov, and D. Shatilov, "Wire Compensation of Parasitic Crossing in DAΦNE," EPAC'06, Edinburgh, 2006, pp. 2808–2810 (2006).

[39] W. Fischer, O. Brüning, J.-P. Koutchouk, F. Zimmermann, T. Sen, V. Shiltsev, K. Ohmi, M. Furman, Y. Cai, and A. Chao, informal note BNL C-A/AP/291; ICFA Beam Dynamics Newsletter No. 44, pp. 220-225; proceedings of BEAM'07, CERN-2008-005, CARE-Conf-08-004-HHH (2008).

[40] J.-P. Koutchouk, J. Wenniger, and F. Zimmermann, "Experiments on LHC Long-Range Beam–Beam Compensation in the SPS," proceedings EPAC'04, Lucerne, 2004, pp. 1936–1938 (2004).

[41] F. Zimmermann, J.-P. Koutchouk, F. Roncarolo, J. Wenninger, T. Sen, V. Shiltsev, and Y. Papaphilippou, "Experiments on Long-Range Beam–Beam Compensation and Crossing Schemes at the CERN SPS in 2004," PAC'05, Knoxville, 2005, pp. 686–688 (2005).

[42] U. Dorda, J.-P. Koutchouk, R. Tomas, J. Wenniger, F. Zimmermann, R. Calaga, and W. Fischer, "Wire Excitation Experiments in the CERN SPS," EPAC'08, Genoa, pp. 3176–3178 (2008).

[43] W. Fischer, R. Alforque, H.C. Hseuh, R. Lambiase, C.J. Liaw, G. Miglionico, T. Russo, J.-P. Koutchouk, F. Zimmermann, and T. Sen, informal note BNL C-A/AP/236 (2006).

[44] W. Fischer, R. Calaga, U. Dorda, J.-P. Koutchouk, F. Zimmermann, V. Ranjbar, T. Sen, J. Shi, J. Qiang, and A. Kabel, "Observation of Long-Range Beam–Beam Effect in RHIC and Plans for Compensation," EPAC'06, Edinburgh, 2006, pp. 2158–2160 (2006).

[45] F. Zimmermann, "Weak-Strong Simulation Studies for the LHC Long-Range Beam–Beam Compensation," proceedings of the Beam–Beam Workshop at Fermilab, FERMILAB-Conf-01/390-T, CERN LHC Project Report 502 (2001)

[46] W. Fischer et al., "Experiments With a DC Wire in RHIC," PAC'07, Albuquerque, 2007, pp. 1859–1861 (2007).

[47] T. Sen and B. Erdelyi, "Analytical Studies of the Long-Range Beam–Beam Tune Shifts and Chromaticities," EPAC'02, Paris, 2002, pp. 1247–1249 (2004).

[48] H.J. Kim and T. Sen, "Simulations of Beam-Wire Experiments at RHIC," PAC'07, Albuquerque, 2007, pp. 3492–3494 (2007).

[49] F. Zimmermann, private communication.

[50] N. Abreu, "Beam–Beam With a Few Long-Range Encounters at Long Distance," proceedings BEAM'07, CERN-2008-005, CARE-Conf-08-004-HHH (2008).

[51] H.J. Kim, T. Sen, N.P. Abreu, and W. Fischer, "Simulations of Wire Compensator in RHIC," HB2008, Nashville, 2008, pp. 72 (2008).

[52] H.J. Kim, T. Sen, N.P. Abreu, and W. Fischer, "Studies of Wire Compensation and Beam–Beam Interaction in RHIC," EPAC'08, Genoa, 2008, pp. 3119–3121 (2008).

[53] H.J. Kim and T. Sen, Phys. Rev. ST Accel. Beams 12, 031001 (2009).

[54] H.J. Kim, T. Sen, and W. Fischer, "Long-Range Beam–Beam Compensation in RHIC," IPAC'10, Kyoto, May 2010, pp. 2072–2074 (2010).

[55] A. Kabel, private communication.

[56] R. Calaga, W. Fischer, and G. Robert-Demolaize, "RHIC BBLR Measurements in 2009," IPAC'10, Kyoto, May 2010, pp. 510–512 (2010).

Published by CERN in the Proceedings of the ICFA Mini-Workshop on Beam–Beam Effects in Hadron Colliders,
CERN, Geneva, Switzerland, 18–22 March 2013, edited by W. Herr and G. Papotti, CERN–2014–004 (CERN, Geneva, 2014)

10 YEARS OF WIRE EXCITATION EXPERIMENTS IN THE CERN SPS

F. Zimmermann, CERN, Geneva, Switzerland

Abstract

This paper reviews the set-up, experimental studies, and beam observations with one or two prototype long-range beam-beam 'wire' compensators in the CERN SPS from 2002 to 2012.*

MOTIVATION

Following earlier studies investigating the effect of long-range collisions for the SSC [1] and LHC [2, 3], in 1999 weak-strong beam-beam simulations for the LHC – using the modelling recipe of Ref. [4] – revealed the existence of a diffusive aperture at transverse amplitude of 6-7σ, which is induced by the nominal long-range beam-beam encounters [5]. An example simulation result is illustrated in Fig. 1.

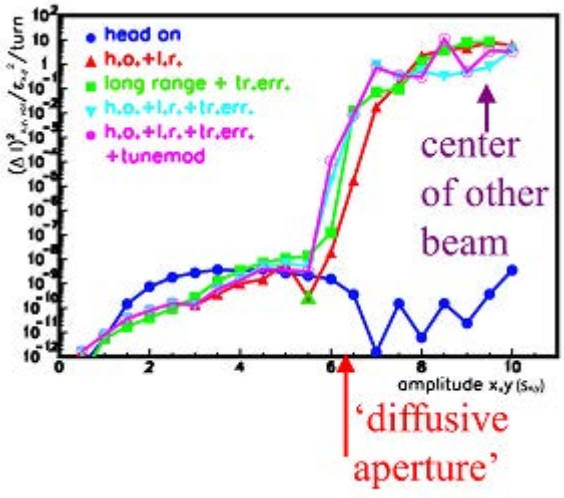

Figure 1: Transverse action diffusion rate $\Delta I^2_{rms}/\varepsilon^2_{x,y}$/turn as a function of transverse amplitude in units of σ under various conditions obtained from a weak-strong beam-beam simulation [5].

COMPENSATION SCHEME

The simulated strong effect of the LHC long-range collisions inspired the search for mitigation, and in 2000 J.-P. Koutchouk proposed a long-range beam-beam compensation for the LHC based on current-carrying wires [6]. At a transverse distance, the wires generate the same transverse force of shape $1/r$, as the field of the opposing beam at the parasitic long-range encounters [6]. In order to correct all non-linear effects the correction must be local. For this reason, there needs to be at least one wire compensator, in the CERN internal naming convention called 'BBLR', on one side of each primary interaction point (IP) for either beam, in a region where the two beams are already physically separated, but otherwise as close as possible to the common region where the long-range encounters occur. The proposed layout features the compensator 41 m upstream of the separation dipole D1, on both sides of IP1 and IP5, where the horizontal and vertical function are equal, as is shown in Fig. 2. Figure 3 illustrates how one wire cancels the effect of all 16 long-range encounters occurring on one side of the IP. The betatron phase difference between the BBLR and the average LR collision is 2.6° (ideally it should be zero).

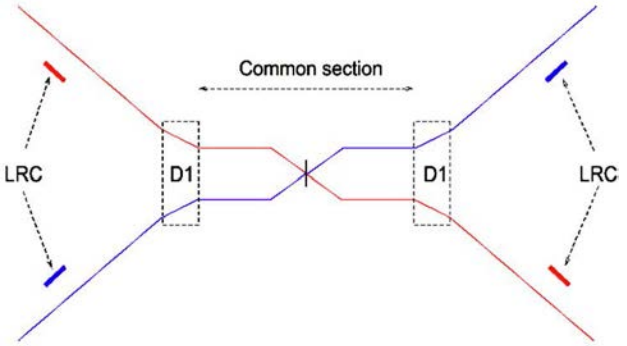

Figure 2: Schematic location of proposed LHC wire compensators [6, 7].

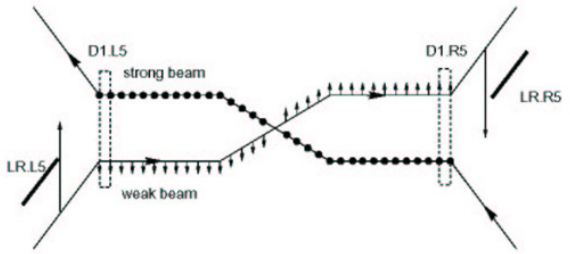

Figure 3: Illustration of the compensation principle [6, 7].

In simulations the wire compensator was shown to effectively shrink the tune spread caused by the long-range collisions to essentially zero [6] (Fig. 4) and to gain about 1.5σ in diffusive aperture [8] (Fig. 5).

Strong-strong beam-beam simulations including wire compensators were reported in Ref. [9], and further analytical studies of the onset of chaos due to the long-range collisions in Ref. [10].

SPS WIRE COMPENSATORS

In order to explore the 'simulated' effect of long-range encounters and to benchmark the simulations with the SPS beam, in 2002 a first prototype compensator was fabricated and installed. This BBLR consisted of two 80-cm long units (each with a wire length equal to 60 cm),

* This work was supported, in parts, by the European Commission under the FP7 Research Infrastructures project EuCARD, grant agreement no. 227579.

978-92-9083-404-5, 0007-8328 – © CERN, 2014. Published under the Creative Common Attribution CC BY 4.0 Licence.
http://dx.doi.org/10.5170/CERN–2014–004.153

installed one behind the other, and each containing a single water-cooled wire, vertically displaced from the beam centre. Two years later, a second BBLR was constructed, equipped with three wires of different transverse orientation. The second BBLR also consisted of two units of the same length, like the first one, but mounted on a movable support so that their vertical position could be varied over a range of 5 mm through remote control. A primary purpose of this second BBLR, installed at a betatron phase advance of about 3° from the first one (hence similar to the phase advance between the proposed location of the LHC wire compensator and the centre of the long-range collisions), was to demonstrate the effectiveness of a realistic compensation scheme, which could be simulated by powering the vertical wire(s) of the two BBLRs with opposite polarity. In addition to the vertical wire, a horizontal wire and a wire at 45° were added to allow for experimental studies and comparisons of various crossing schemes (horizontal-vertical, vertical-vertical, and 45°).

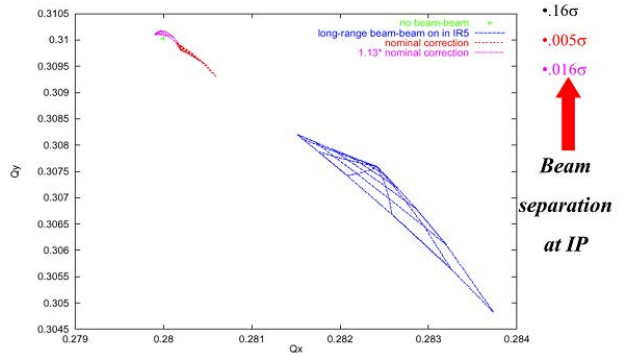

Figure 4: Simulated LHC tune footprint due to long-range collisions with and without wire compensator [6].

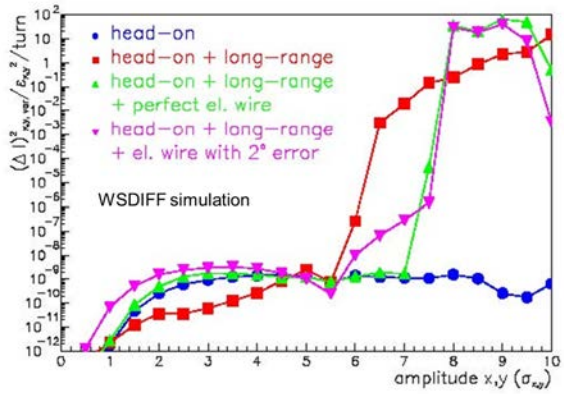

Figure 5: Simulated LHC diffusive aperture with ideal (green) and realistic wire compensator (pink) compared with the case of no compensation (red) and head-on collisions only (blue) [8].

Photographs of both devices are shown in Fig. 6, as well as technical drawings in Figs. 7 and 8. The wire of the first BBLR is mounted at a fixed nominal vertical distance of 19 mm from the centre of the chamber (so that it is in the shadow of the SPS arc aperture). More details and documentation on the SPS wire compensator prototypes (and the experiments conducted in the SPS using these devices) can be found on a dedicated web site [11].

The needed wire current I_w is related to the number of long range collisions to be compensated, the length of the l_w and the bunch population N_b, as $I_w = N_b ec \, \#LR \, / l_w$, where e denotes the elementary charge and c the speed of light. The two 60-cm long wires of one unit can be excited with up to 267 A of current, which, according to the above equation, produces an effect equivalent to 60 LHC LR collisions (e.g., roughly the combined effect of all nominal long-range encounters around IPs 1 and 5).

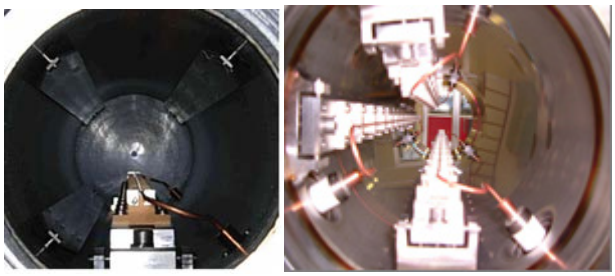

Figure 6: The first (left) and the second prototype wire compensator (right) installed in the CERN SPS in 2002 and 2004, respectively.

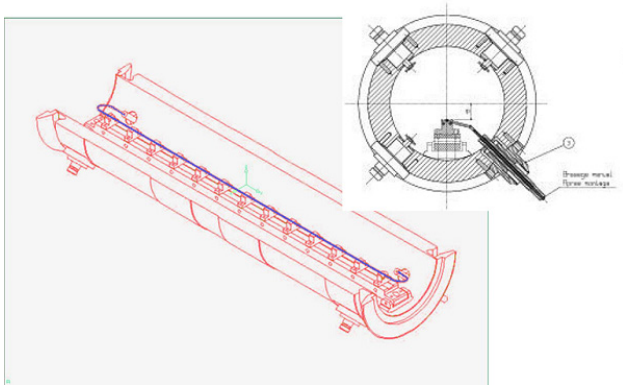

Figure 7: Technical drawings of the first SPS wire compensator (2002).

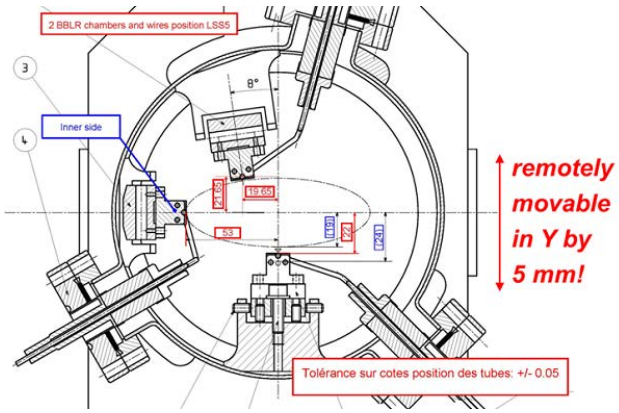

Figure 8: Technical drawing of the second SPS wire compensator (2004).

Figure 9 presents a side view of the first BBLR device. Each BBLR, consisting of two units, has a total length of (2 × 0.8 + 0.25) m = 1.85 m. A photograph shows BBLRs 1 and 2 installed in the SPS tunnel (Fig. 10). Figure 11 illustrates the horizontal and vertical beta functions along the two × two BBLR units. The average value of the beta functions is about 50 m.

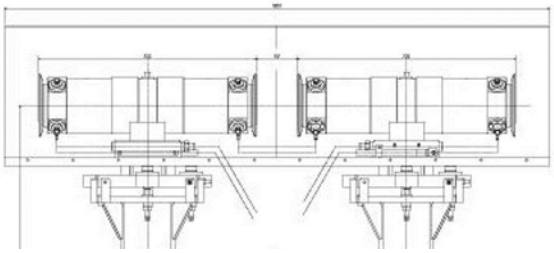

Figure 9: Side view of SPS BBLR #1.

Figure 10: SPS BBLRs no. 1 and 2 (4 boxes) installed in SPS Straight Section 5.

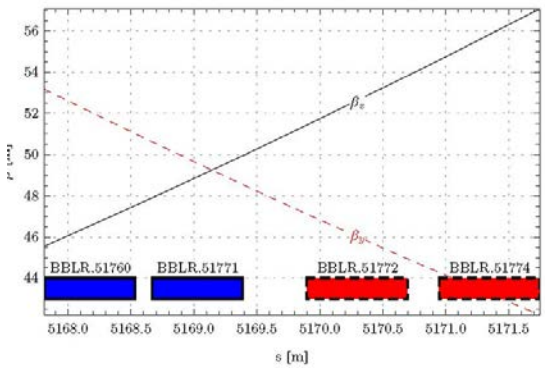

Figure 11: Horizontal and vertical beta functions across the two SPS BBLRs (each consisting of two units).

Additional compensator wire units are available at CERN. A complete BBLR consisting of two units with water-cooling, similar to BBLR no. 2, is ready (repaired after an earlier leak). Two air-cooled BBLRs from the Relativistic Heavy Ion Collider (RHIC) have been shipped from Brookhaven National Laboratory and are in store at CERN [12]. Thus, including the two BBLRs presently installed in the SPS, a total of five sets are (or have been) available.

SCALING LAWS

The perturbation by the wire compensator at distance d from the beam centre is

$$\Delta y' = \frac{2 r_p l_w I_w}{\gamma e c (y - d)} ,$$

from which the relative perturbation at the dynamic aperture becomes

$$\frac{\Delta y'}{\sigma_{y'}} = \left(\frac{2 r_p l_w}{e c} \right) \left(\frac{I_w}{(\gamma \varepsilon) \tilde{n}_{da}} \right) ,$$

where $\tilde{n}_{da}$ denotes the dynamic aperture in units of the rms beam size, l_w the wire length and I_w the wire current. This equation shows that, for constant normalized emittance, the effect in units of sigma is independent of energy and beta function. In *scaled experiments* the wire current is varied in direct proportion to the factor by which the emittance differs from the desired emittance.

HISTORY OF SPS BBLR STUDIES

The SPS BBLRs were used to perform the following beam studies:

- perturbation by single wire as LHC LR simulator (2002 to 2003) [13,14];
- two wire compensation, scaled experiments, distance scan (2004) [15,16];
- tests of crossing schemes (2004) [15,16,17];
- one and two wires at different energies: 26, 37, and 55 GeV/*c*; scans of *Q*', distance, current (2007) [18,19,20];
- two-wire compensation with varying *Q*, I_w, *Q*' scans at 55 GeV/*c* (2008) [21,22];
- two-wire compensation and excitation in coasts at 120 GeV/*c* (2009) [22]; and
- two-wire compensation and excitation in coasts at 55 GeV/*c* (2010) [23].

Figure 12 illustrates typical SPS cycles used towards the end of the last decade for BBLR studies at three different beam energies. During dedicated machine studies, at the target energy the SPS cycle could be stopped and the beam be made to 'coast' for e.g. ten minutes for measurements of the beam lifetime in steady-state conditions and parameter scans.

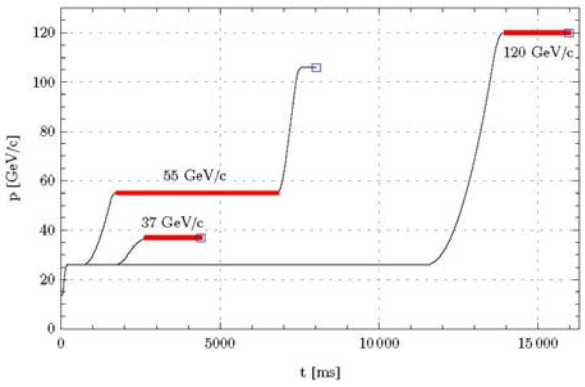

Figure 12: SPS cycles during experiments in 2008 and 2009 [G. Sterbini].

TECHNICAL ISSUESS

A number of technical issues had to be addressed, especially in the early days of the SPS BBLR studies. These included:

- installation of dedicated ion chambers and photomultiplier tubes (PMTs) near the BBLR;
- the addition of an inductive coil to suppress wire-current ripple;
- computation and experimental verification of wire heating;
- emittance blow-up by means of the transverse damper or by injection mismatch together with resonance crossing (equalizing the vertical and horizontal emittances) so as to achieve the nominal LHC parameters or to increase sensitivity;
- use of fast wire scanners and scrapers;
- installation of a dedicated dipole near the BBLR to correct the induced orbit change locally;
- continuous tune corrections;
- preparation and use of multiple superimposed orbit bumps to vary the beam-wire distance;
- (later) choice of higher beam energy: 37, 55 or 120 GeV/*c* (for good lifetime without wire excitation); and
- (later) experiments in coast (to avoid transient data).

Figure 13 illustrates the combination of orbit-corrector bumps used to vary the beam-wire distance at higher beam energy. The resulting minimum normalized distance in units of rms beam size depends on the beam energy and on the normalized emittance as shown in Fig. 14. In case the emittance was too small the beam could be blown-up with transverse feedback and resonance crossing.

The natural SPS beam lifetime was about 30 h at 55 GeV/*c*, but only 5-10 min at 26 GeV/*c* (where the physical aperture was only about 4σ).

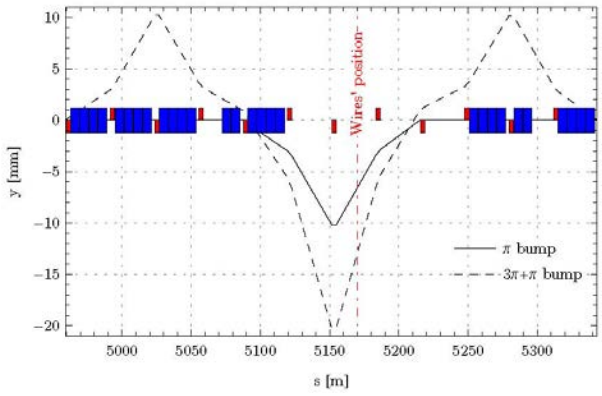

Figure 13: Superimposed 3+5 corrector bumps at the SPS wire compensator [G. Sterbini].

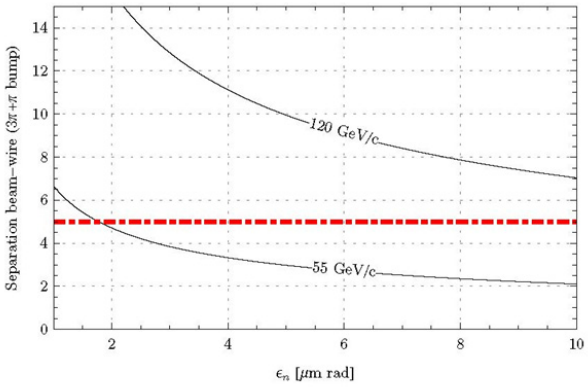

Figure 14: Minimum normalized distance in units of rms beam size as a function of normalized emittance for two beam energies [G. Sterbini].

SINGLE BBLR 'EXCITATION' STUDIES

Changes in orbit and tunes allow for a precise determination of the beam-wire distance. Example data from 2002 are shown in Figs. 15-17.

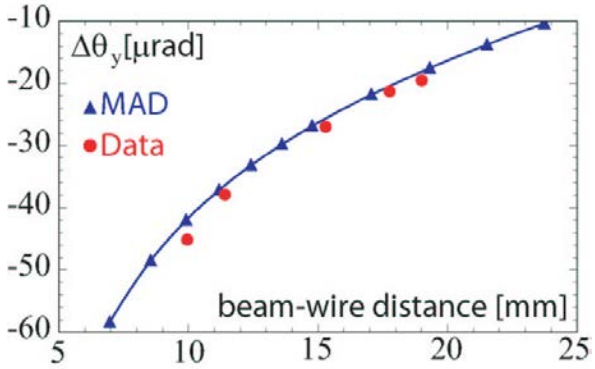

Figure 15: Deflection angle at the wire compensator as a function of beam-wire distance, comparing data and measurements [14] [J. Wenninger].

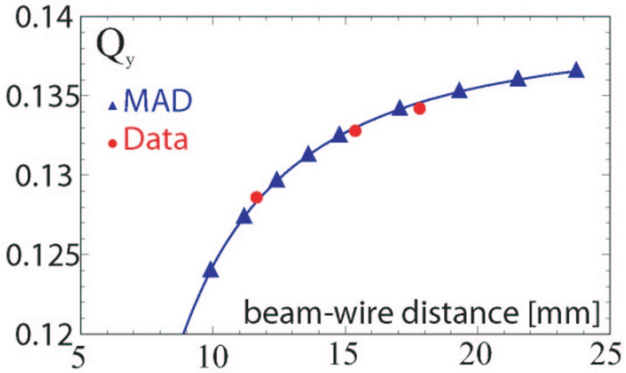

Figure 16: Vertical tune change as a function of beam-wire distance, comparing data and measurements [14] [J. Wenninger].

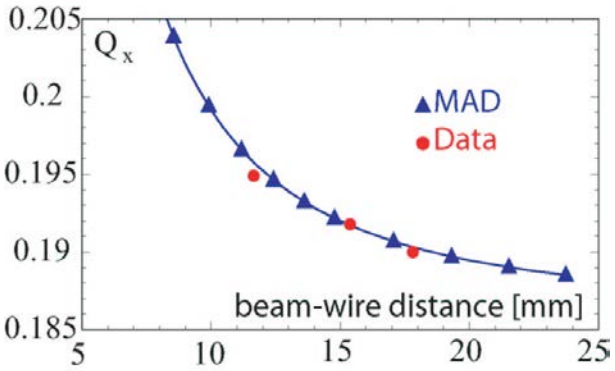

Figure 17: Horizontal tune change as a function of beam-wire distance, comparing data and measurements [14] [J. Wenninger].

The change in the beam orbit at the compensator follows from the self-consistent equation

$$\Delta d = \frac{\beta_y I_{wire} l_{wire} r_p}{\gamma ec(d+\Delta d)\tan\left(\pi\left(Q_y+\Delta Q_y\right)\right)},$$

while the tune changes are given by

$$\Delta Q_{x,y} = \mp \frac{r_p \beta_{x,y} I_{wire} l_{wire}}{2\pi\gamma ec} \frac{1}{(d+\Delta d)^2}.$$

In most of the later studies only the tune change was monitored.

The effect of the compensator on the nonlinear optics has also been studied, by acquiring turn-by-turn beam-position monitor (BPM) data after kicking the beam. The nonlinearity of the wire field led to a reduced decoherence time, to a tune shift with amplitude, and (additional) spectral resonance lines. The measured tune shift was consistent with the theoretical predictions

$$\Delta Q_x \approx \frac{3}{4} \frac{I_{wire} l_{wire} r_p}{\gamma ec} \frac{\beta_x}{d^4} \hat{y}^2$$

and

$$\Delta Q_y \approx -\frac{3}{8} \frac{I_{wire} l_{wire} r_p}{\gamma ec} \frac{\beta_x}{d^4} \hat{y}^2$$

The resonance lines introduced by the BBLR are illustrated in Fig. 18.

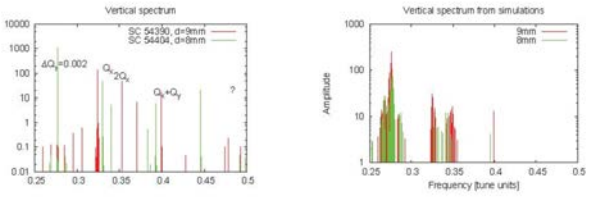

Figure 18: Resonance spectra with wire excitation: experimental data with 240 A wire current at 9 (red) and 8 mm (green) beam-wire distance (left) and the corresponding simulation data (right) [18] [U. Dorda].

A strong effect of chromaticity was noticed when the compensator was excited. Figure 19 shows the beam intensity evolution during $Q_{x,y}'$ scans at 37 GeV/c.

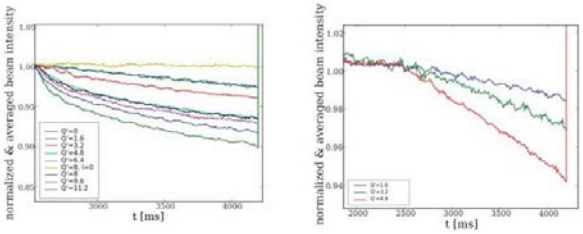

Figure 19: Beam intensity as a function of time for various values of the horizontal (Q_x', left) or vertical chromaticity (Q_y', right) [20]. The wire excitation was 180 A-m, the beam momentum 37 GeV/c and the normalized beam-wire separation about 6.5σ (9 mm).

Figure 20 compares the measured (left) and simulated beam loss (right) for two different values of the vertical chromaticity as a function of the integrated wire strength.

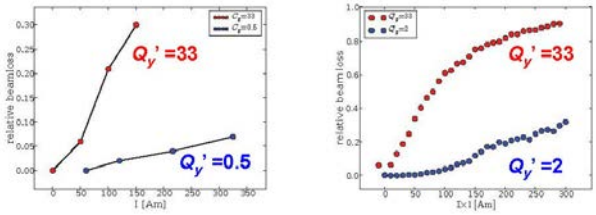

Figure 20: Relative beam loss for two different values of the vertical chromaticity as a function of wire excitation in units of A-m, comparing experimental data (left) and simulations (right) [20] [U. Dorda]. The beam-wire separation was ~6.6 σ.

Various attempts were made to directly measure the 'diffusive' or dynamic aperture. To this end, three types of signals were used: (1) lifetime and background, (2) beam profiles and final emittance, and (3) local diffusion rate inferred by scraper-retraction experiments. Figures 21 and 22 shows some example measurements of lifetime and background at 55 GeV/c. A drop in the lifetime and increased losses are observed for separations less than 9σ; at 7-8σ separation the lifetime decreases to 1-5 h. These results indicated that the LHC nominal separation of 9.5σ (for the encounters between the IP and the first quadrupole Q1) is well chosen, but 'close to the edge'.

Beam profiles before and after wire excitation, measured with an SPS 'wire scanner' (fully unrelated to the wire compensator), reveal that the particles at large transverse amplitude are lost due to the wire excitation; see Fig. 23. These measurements confirmed that the wire compensator or the equivalent set of long-range encounters, acts as a highly effective scraper.

This type of measurement allows for an estimate of the diffusive/dynamic aperture. Specifically, an Abel transformation of the wire-scan data of the form [23, 24]

$$\rho(A) = -2A\int_A^R d\eta \frac{g'(\eta)}{\sqrt{\eta^2 - A^2}}$$

can be used to compute the change in the (normalized) amplitude distribution due to the wire excitation. For the

data of Fig. 23 the results are presented in Fig. 24, indicating that in this particular example (with intentionally small separation) the dynamic aperture is at about 1 σ).

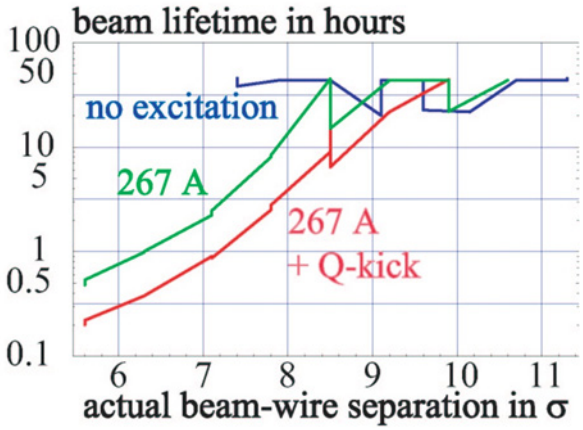

Figure 21: Lifetime as a function of the wire-beam separation in units of rms beam size with (green) and without (blue) wire excitation at 267 A, which corresponds to the nominal total number of LHC long-range encounters at IPs1 and 5. The red data were also taken with the wire excited, while in addition firing the (weak) tune kicker to add a further perturbation.

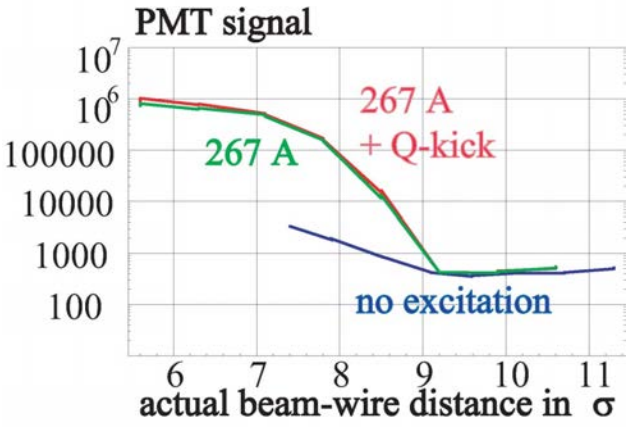

Figure 22: Local relative beam loss rate measured by a photomultiplier as a function of the wire-beam separation in units of rms beam size with (green) and without (blue) a wire excitation of 267 A. As in Fig. 21 for the red data set the (weak) tune kicker was repeatedly fired while the wire was excited.

Figure 25 displays the final emittance inferred from the beam profiles as a function of beam-wire distance without wire excitation and for wire currents of 67 A and 267 A (the latter corresponding to 60 LHC long-range encounters). The reduction of the final emittance without wire excitation at smaller distances is due to mechanical scraping of the beam by the edge of the wire.

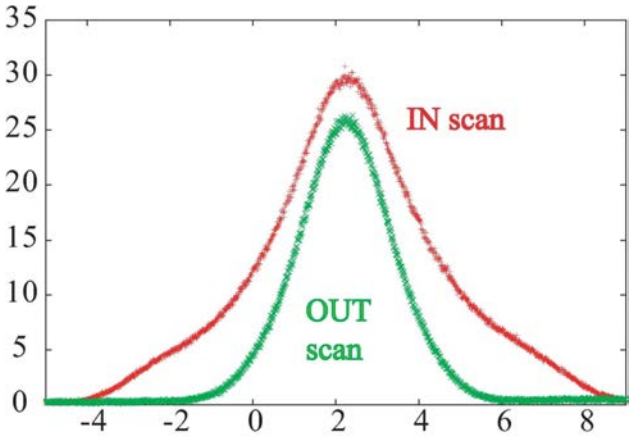

Figure 23: Beam profile before and after wire excitation measured at 26 GeV/*c*. The inferred initial and final emittances were 3.40 μm and 1.15 μm, respectively.

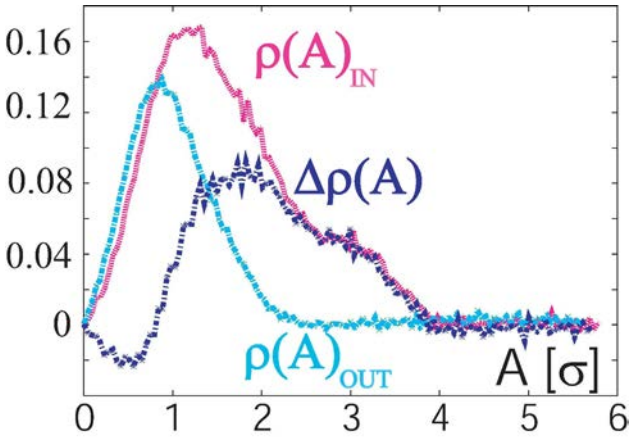

Figure 24: Abel transformation of the beam-profile data from Fig. 23, revealing the change in the (normalized) amplitude distribution.

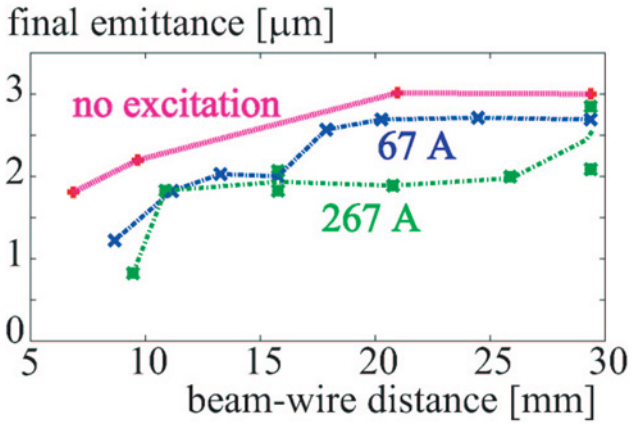

Figure 25: Final emittance without (red) and with wire excitation (blue 67 A, green 267 A) at a beam momentum of 26 GeV/*c* as a function of beam-compensator distance.

With the Abel-transformation technique it was not always possible to obtain a clean result for the diffusive aperture. Therefore, a different technique was also employed to infer the variation of the diffusive/dynamic aperture. Namely, without wire excitation, a known

aperture restriction was introduced using a dedicated mechanical 'scraper,' and wire scans were then executed to determine the 'final emittance' corresponding to a given known aperture determined by the scraper position. This calibration measurement is presented in Fig. 26 – the curve of measured final emittance as a function of scraper position allows estimation of the effective aperture due to the wire excitation from the associated 'final emittance' value.

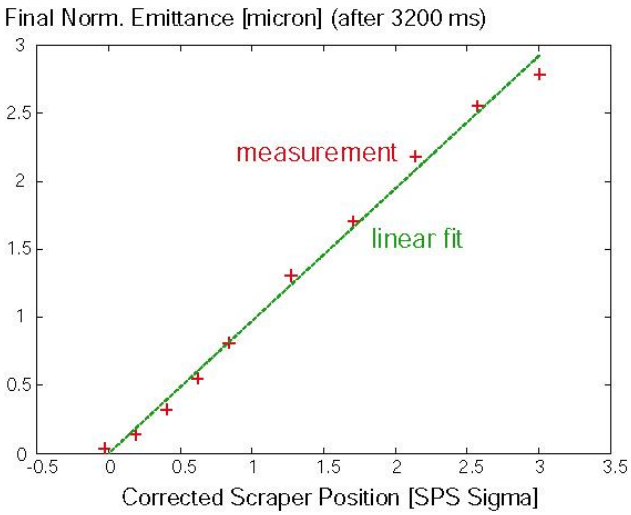

Figure 26: Calibration of the final emittance values by a mechanical scraper.

Following this plan and using the calibration curve of Fig. 26, measurement results for different wire currents were converted into normalized diffusive apertures. The result, shown in Fig. 27, suggests a linear dependence of the dynamic aperture on the square root of the wire current, which is consistent with a scaling law first pointed out by Irwin [4]. In the figure, the measured dynamic aperture is smaller than the simulated diffusive aperture, especially at lower current, hinting at additional effects not included in the simulations or at a systematic error in the calibration method.

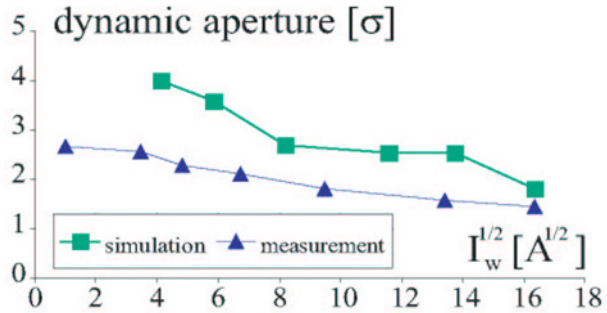

Figure 27: Effect of wire current on SPS dynamic aperture (26 GeV/*c*), inferred from final emittance and the calibration of Fig. 26.

Yet another approach to measuring the diffusive aperture is to directly detect the diffusion rates at various transverse amplitudes, by inserting a scraper to remove particles in a small area around the target amplitude article, then retracting this scraper by a small step, and observing how the loss signal reappears as particles diffuse outwards to the new position of the scraper. This type of measurement was previously used at HERA (and elsewhere) to determine the local diffusion coefficients [25]. Unfortunately, scraper retraction attempts for the SPS wire-compensator studies were not very successful. Figures 28 and 29 present example results. In Fig. 29 the scraper position is about 1σ, and a temporary decrease in the loss rate can be noticed, which might be used to fit a diffusion constant. However, at larger amplitudes (which are of greater interest) the diffusion was much faster than the speed of the SPS scraper. Figure 29 also shows that the scraper moving to its target position, while the wire is not yet excited, already intercepts a significant halo, as evidenced by the elevated background rate prior to the wire excitation.

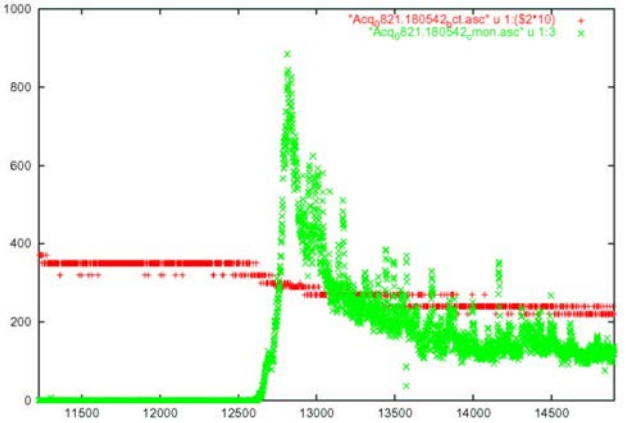

Figure 28: Beam current in units of 10^8 protons (BCT, red) and local loss rate detected by photomultiplier (green) as a function of time during the cycle in units of ms. For these data the wire was excited (at 12725 ms) but no scraping was applied.

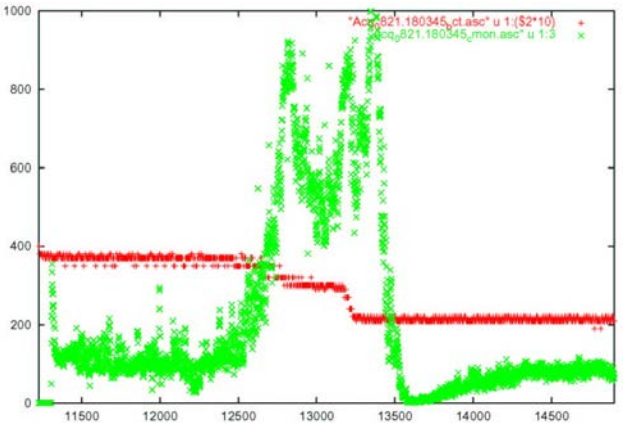

Figure 29: Beam current in units of 10^8 protons (BCT, red) and local loss rate detected by photomultiplier (green) as a function of time during the cycle in units of ms. For these data the wire was excited at 12725 ms; later, at 13225 ms, the scraper was inserted and retracted.

One of the most interesting results from the SPS wire measurements is the measured dependence of the 'beam lifetime' τ_{beam}, as inferred from the beam loss during a cycle at 26 GeV/c, on the beam-wire distance d [15], illustrated in Fig. 30. The measured dependence extremely well follows a 5th order power law as seen from the fitting result embedded in the figure. It has been suggested [26] that a nearby low-order resonance of order n should cause a dependence $\tau_{beam} \sim 1/d^{n+1}$ and that the power in the exponent should, therefore, depend on the betatron tunes. Indeed at the Tevatron (with an electron lens applied as 'wire') [27] and at RHIC [28], operating at other working points in the tune diagram, different power laws were observed (third power and linear dependence, respectively). Figure 31, presenting SPS data for three different sets of tunes, taken several years later at a higher energy, confirms that the losses due to the wire are strongly tune dependent.

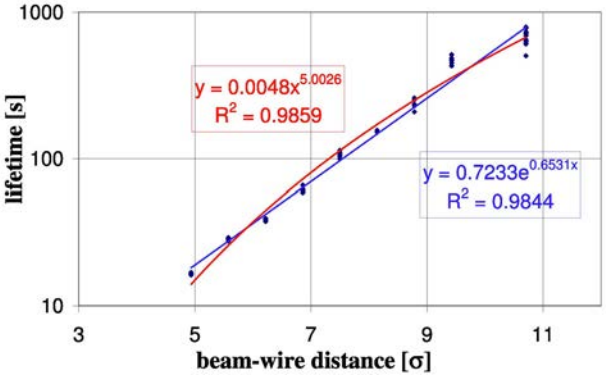

Figure 30: Beam lifetime as a function of beam-wire distance at 26 GeV/c, for betatron tunes of Q_x = 0.321 and Q_y = 0.291 [14].

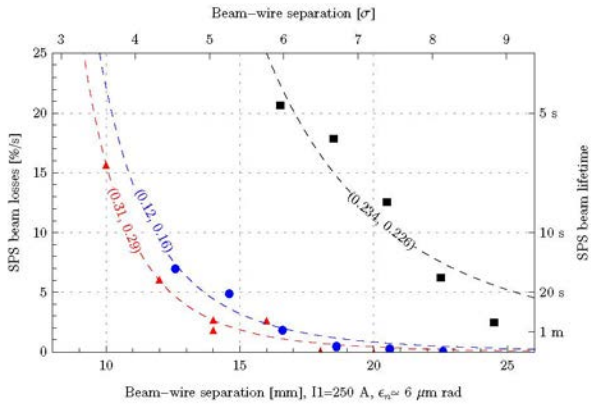

Figure 31: Beam losses as a function of beam-wire distance for three different pairs of tunes at 37 GeV/c with 1.1 s cycle [21] [G. Sterbini]

Extrapolating this measurement to the nominal LHC beam-beam distance, ~9.5σ, predicts a 6 min lifetime. This result was one of the motivations for raising the SPS beam energy and for performing measurements with coasting (non-cycling machine) beams in later studies, where the beam lifetimes were significantly higher.

Figure 32 shows beam losses as a function of wire current I_w for different normalized beam-wire separations (in units of σ) d_n. These later results were fitted as [21]:

$$\text{beam loss (\%)} = 0.07\, e^{-d_n} I_w^2 \,.$$

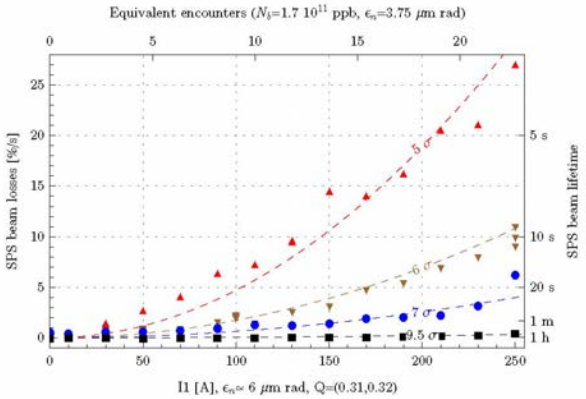

Figure 32: Beam losses as a function of wire current at 37 GeV/c with a 1.1 s cycle, for betatron tunes of Q_x = 0.31 and Q_y = 0.32 (nominal values for LHC collisions) [21].

COMPENSATION STUDIES WITH TWO BBLR WIRE COMPENSATORS

Experiments with two wire devices became possible after the installation of the second SPS wire compensator (Fig. 8) in 2004. The main focus of the two wire studies was the demonstration of compensating the effect of one wire by the second, about 3^o apart in betatron phase advance from the first, and with a slightly different beta function ratio (Fig. 11), and a study of the associated tolerances, making use of the fact that the vertical position of the second wire can be controlled remotely over a 5 mm range. Such a study had been requested by the CERN LHC Technical Committee (LTC) in 2002. Other two-wire studies used the three independent wires of the second device (vertical, horizontal and 45^o wires) to 'model' different crossing schemes at the two main interaction points of the LHC. Results from these latter studies are reported in the appendix.

Figure 33 shows a typical measurement result of the beam lifetime as a function of vertical tune on the SPS injection plateau, with the horizontal tune set to the nominal LHC collision value (0.31). The LHC vertical collision tune is 0.32, near the upper end of the scan range. Three cases are compared: no wire excitation, one wire excited, and both wires excited in compensating configuration. For this measurement the tune and orbit changes due to the wire compensation were corrected at each point. The data demonstrate that the lifetime reduction due to the first wire was recovered by the second wire over a large tune range, except at Q_y<0.285 (close to the 7th-order resonance; see Fig. 34) or when approaching the third integer resonance (including at the nominal tune). Figure 35 shows a later result, taken at a higher beam energy (37 GeV/c), where the natural beam

lifetime, with wires off, was much higher than at injection. Here the compensation worked well over an even larger range, but it still degraded close to the third integer resonance (Q_y > 0.31), and close to the 4th-order resonance (Q_y < 0.27).

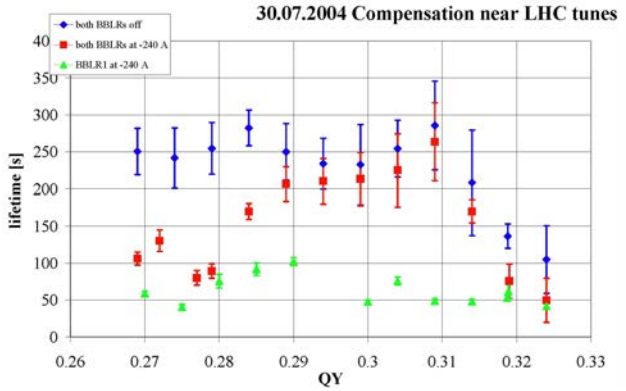

Figure 33: Beam lifetime as a function of vertical tune without wire (blue), with one wire excited at 240 A (green), and with both wires in compensating configuration (red) for a fixed horizontal tune of Qx = 0.31 [14]. The tune scan corresponds to the red line in Fig. 34. This measurement was performed in 2004 at a beam momentum of 26 GeV/c.

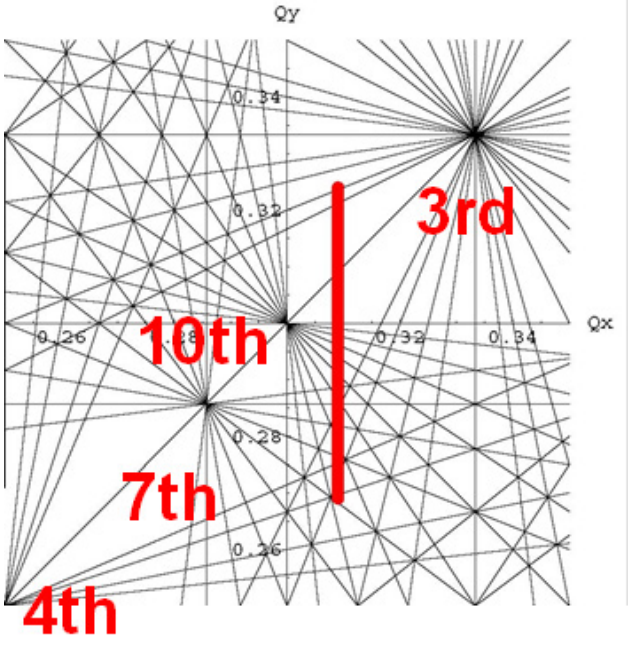

Figure 34: Tune diagram with some low-order resonance lines (incomplete), and the region of a typical vertical tune scan, as used, e.g. for the measurement of Fig. 33.

Figure 36 presents the results of a scan of the vertical position of the second wire compensator with respect to the (fixed) first wire, and the comparison with a simulation using the code BBSIM. The simulation predicts there to be no compensation beyond ~3 mm. The measurement revealed that the compensation was fully lost beyond ~2.5 mm from optimum (equivalent to ≤2σ).

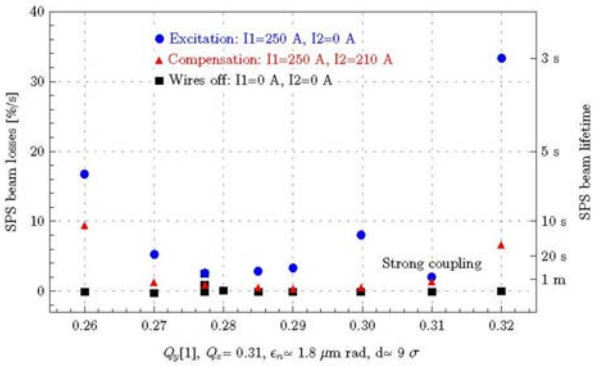

Figure 35: Beam losses (left) and beam lifetime (right) as a function of vertical tune without wire (black), with one wire excited at 250 A (blue), and with both wires in compensating configuration (red) for a fixed horizontal tune of Q_x = 0.31 [21]. The tune scan corresponds to the red line in Fig. 34. This measurement was performed in 2008 at a beam momentum of 37 GeV/c over 1.1 s.

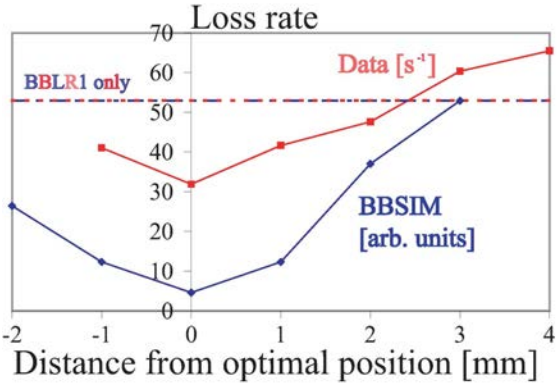

Figure 36: Beam loss rate as a function of vertical distance of second wire with respect to optimum location compared with BBSIM simulations [15].

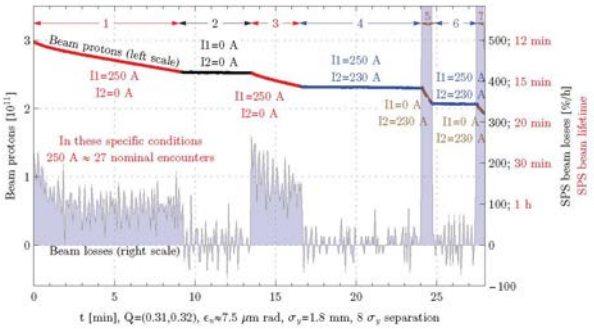

Figure 37: Beam intensity (left), beam loss and lifetime (right) as a function of time while one or two wire compensators at 8σ distance were either turned on (at 250 A and lifetime-optimized 230 A, respectively) or off, in coast at 120 GeV/c (2009) [21]. The normalized transverse emittance had intentionally been blown up to 7.5 μm (twice the nominal).

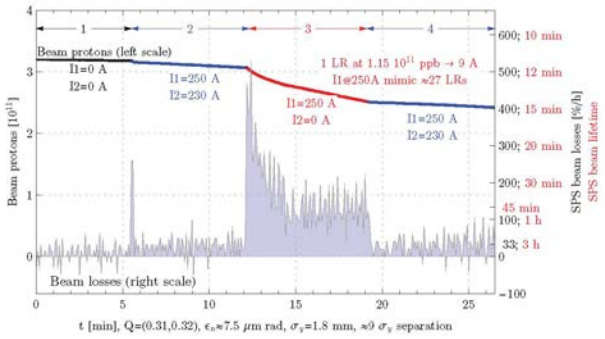

Figure 38: Beam intensity (left), beam loss and lifetime (right) as a function of time while one or two wire compensators at 8σ distance were turned on (at 250 A and lifetime-optimized 230 A, respectively) and off, in coast at 120 GeV/c (2009) [21]. The normalized transverse emittance had intentionally been blown up to 7.5 μm (twice the nominal).

While the compensation measurements reported so far were performed on the cycling machine at fairly low energy, in 2009 machine time was assigned for studies in coast at 120 GeV/c. Results are shown in Figs. 37 and 38.

Another measurement was performed one year later, in 2010, at 55 GeV/c. The results in Fig. 39 reveal that in this year and at this beam energy, the compensation was not as good as in the year before at 120 GeV/c. This could be due to some real energy dependence in the SPS (e.g. changes in field errors, or power-converter stability, etc.) or due to some other change in the machine between 2009 and 2010. Indeed, this and several other SPS beam studies in 2010 and 2011 noticed significant emittance growth (Fig. 40) and low lifetime in coast (Figs. 41 and 42), without wire excitation, at beam energies above the injection plateau (while in earlier years a poor beam lifetime had been noticed only at injection) [29].

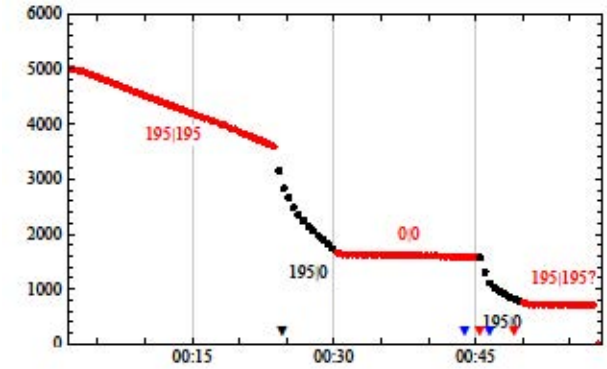

Figure 39: Beam intensity in units of 10^8 protons as a function of time in hours while one or two wire compensators at 9.5σ distance were turned on (at 195 A, which for the given emittance value corresponded to the strength of long-range encounters for two LHC IPs with full beam intensity) and off, in coast at 55 GeV/c (2010) for the nominal LHC collision tune, Q_x=0.31, Q_y=0.32 [R. Calaga].

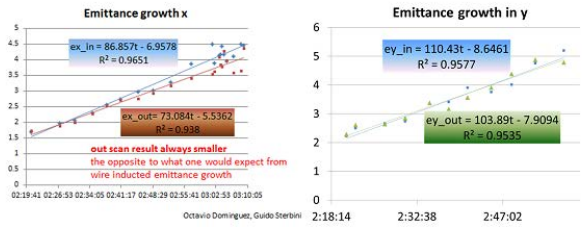

Figure 40: Emittance growth measured by (IN and OUT) wire scans during an SPS coast in 2010 without wire excitation [O. Dominguez, G. Sterbini].

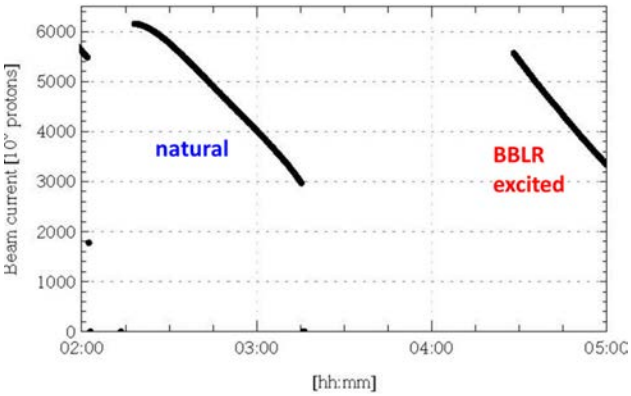

Figure 41: Beam intensity without and with single-wire excitation during an SPS coast in 2010 [O. Dominguez, G. Sterbini].

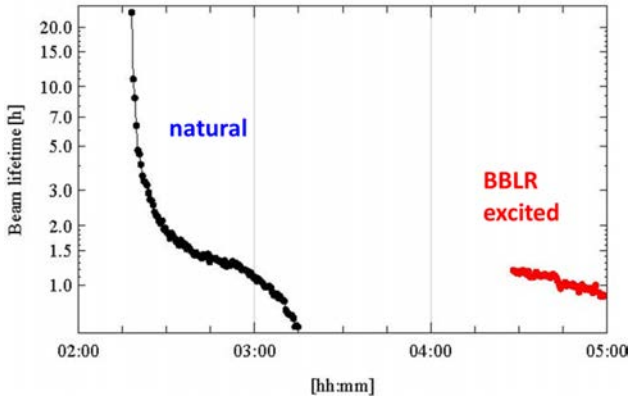

Figure 42: Instantaneous beam lifetime without and with single-wire excitation during an SPS coast in 2010, computed from the intensity data of Fig. 41 [O. Dominguez, G. Sterbini].

ADVANCED BBLR STUDIES

Since different bunches along a train suffer a different number of long-range encounters (the so-called 'PACMAN effect' [1,2]) a dc wire compensator can never offer a perfect compensation. The left picture of Fig. 43 shows the ideal current pattern for PACMAN compensation and the right picture a schematic of an 'RF BBLR' based on a quarter-wave resonator [17, 18]. An experimental test set up (Figs. 44 and 45) has demonstrated the principle, with results as presented in Fig. 46.

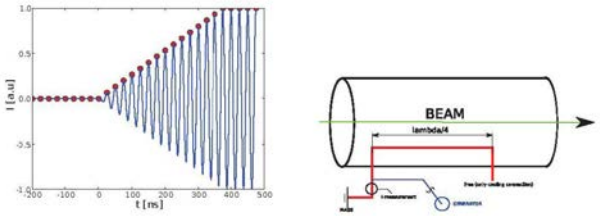

Figure 43: Ideal current pattern for compensation of individual long-range encounters with an amplitude-modulated 40-MHz signal (left) and schematic of an 'RF BBLR' built as a λ/4 resonator [19, 20, 30].

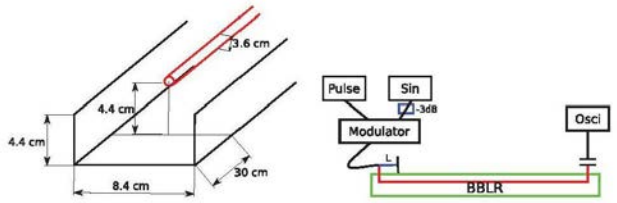

Figure 44: Drawings of 'RF BBLR' test set-up including some dimensions (left) and the cable length L which can be changed for varying the coupling strength (right). Port 2 is connected capacitively in order not to modify the resonator properties [20, 30] [U. Dorda, F. Caspers, T. Kroyer].

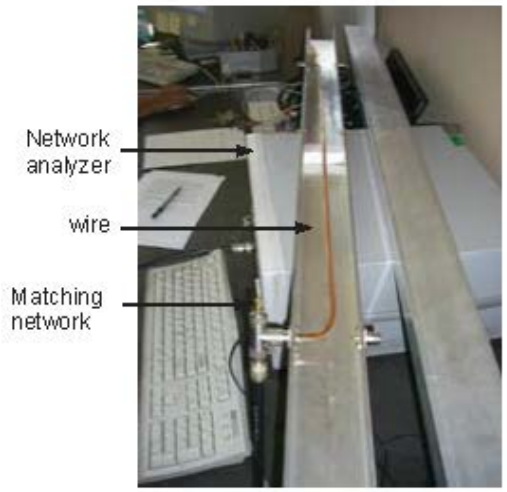

Figure 45: Photograph of 'RF BBLR' test set-up [20] [U. Dorda, F. Caspers, T. Kroyer].

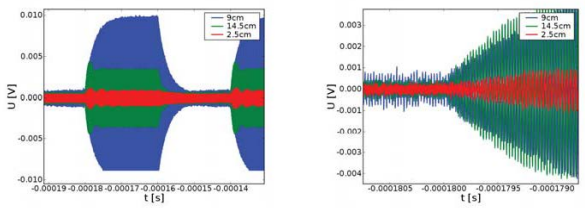

Figure 46: Test measurements showing the effect of varying coupling strength, i.e. the trade-off between rise time and gain: overview illustrating achievable resonator gains (left) and zoomed view showing the rise times for different couplings (right) [20] [U. Dorda, F. Caspers, T. Kroyer].

CONCLUSIONS AND OUTLOOK

Ten years of pioneering wire-compensation studies at the CERN SPS taught many important lessons and gave rise to two PhDs (by G. Sterbini and U. Dorda).

Though the experimental conditions in the SPS were not always ideal (e.g. poor natural lifetime, short cycle times), the compensation of the first wire by a second wire always improved the beam lifetime significantly over a large range of parameters (current, distance, and tune). The results obtained confirm the simulations and strongly suggest that wire compensators will increase the operational flexibility and performance in the LHC.

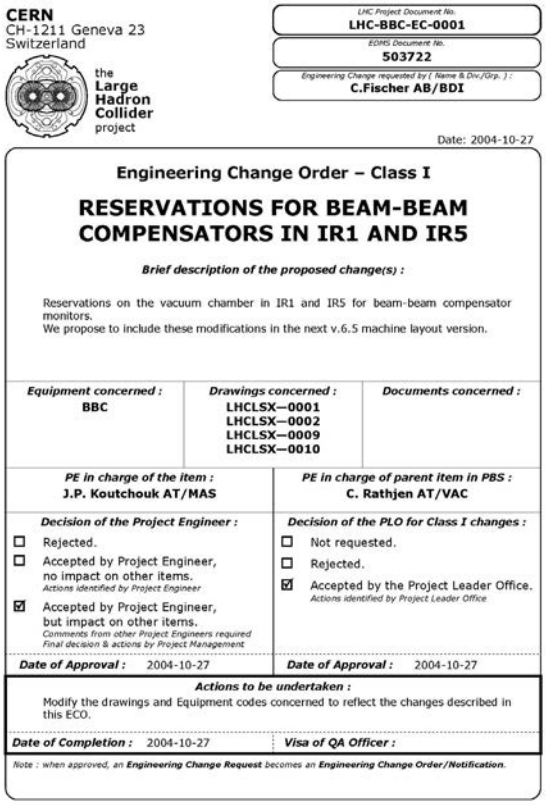

CERN
CH-1211 Geneva 23
Switzerland

the Large Hadron Collider project

LHC Project Document No.: LHC-BBC-EC-0001
EDMS Document No.: 503722
Engineering Change requested by (Name & Div./Grp.) : C.Fischer AB/BDI

Date: 2004-10-27

Engineering Change Order – Class I

RESERVATIONS FOR BEAM-BEAM COMPENSATORS IN IR1 AND IR5

Brief description of the proposed change(s) :

Reservations on the vacuum chamber in IR1 and IR5 for beam-beam compensator monitors.
We propose to include these modifications in the next v.6.5 machine layout version.

Equipment concerned :	Drawings concerned :	Documents concerned :
BBC	LHCLSX—0001 LHCLSX—0002 LHCLSX—0009 LHCLSX—0010	

PE in charge of the item :	PE in charge of parent item in PBS :
J.P. Koutchouk AT/MAS	C. Rathjen AT/VAC

Decision of the Project Engineer :	Decision of the PLO for Class I changes :
☐ Rejected.	☐ Not requested.
☐ Accepted by Project Engineer, no impact on other items. *Actions identified by Project Engineer*	☐ Rejected.
☑ Accepted by Project Engineer, but impact on other items. *Comments from other Project Engineers required Final decision & actions by Project Management*	☑ Accepted by the Project Leader Office. *Actions identified by Project Leader Office*
Date of Approval : 2004-10-27	Date of Approval : 2004-10-27

Actions to be undertaken :
Modify the drawings and Equipment codes concerned to reflect the changes described in this ECO.

Date of Completion : 2004-10-27 | Visa of QA Officer :

Note : when approved, an ***Engineering Change Request*** *becomes an* ***Engineering Change Order/Notification.***

Figure 47: Space reservation for future LHC wire compensators made in 2004 [J.-P. Koutchouk].

For future wire BBLRs in the LHC, 3 m long sections were reserved in the LHC at 103.431 m to 106.431 m from the IP on either side of IP1 and IP5 (Fig. 47). This is close to the place where concrete shielding blocks have been installed (Fig. 48), the latter occupying the distance from 97.075 m to 100.225 m from the IP [31].

Recently, the two BNL wires stored at CERN were declared not useful for future SPS wire tests, as their beam pipe differs from the standard diameter [32].

Figure 48: Concrete shielding block installed in the LHC tunnel close to the reserved wire-compensator location [photo R. Steinhagen].

ACKNOWLEDGEMENTS

The reported SPS wire experiments would not have been possible without the ideas, help and important contributions of Gerard Burtin, Rama Calaga, Jackie Camas, Gijs de Rijk, Octavio Dominguez, Ulrich Dorda, Jean-Pierre Koutchouk, Elias Métral, Yannis Papaphilippou, Federico Roncarolo, Tanaji Sen, Vladimir Shiltsev, Guido Sterbini, Rogelio Tomas, and Jörg Wenninger.

APPENDIX: CROSSING SCHEME STUDIES

The crossing scheme affects the extent of the tune footprint (Fig. 49) as well as the resonance excitation.

On 26 August 2004, an experiment on the crossing planes was conducted for the nominal emittance. Three configurations were implemented (see Fig. 50). Due to constraints imposed by the physical aperture and the different distances of the horizontal and vertical wire from the centre of the chamber (about 55 mm and 20 mm, respectively), a pure alternating crossing could not be realized. Instead a mixed scheme was chosen, modelling horizontal crossing at one wire and 45° crossing at the other, by exciting both wires at the same current. Equal-plane crossings were modelled by exciting only one of the two wires at twice its original strength. For completeness, and to observe a larger effect on the beam lifetime, the first configuration was also tested at twice the strength, which simulates a two times higher beam intensity. The three configurations are shown in Fig. 50.

For all wire configurations, the beam lifetime was measured as a function of the vertical tune, which was varied between 0.26 and 0.33. Figure 52 shows the measurement results, which can be compared with the simulations presented in Fig. 51. Over most of the scanned tune range, the horizontal-horizontal crossing (BBLR2 excited at −240 A) exhibited the best beam lifetime, the pure 45° crossing (BBLR1 at 240 A) the second best, and the mixed crossing (BBLR1 at +120 A, BBLR2 at -120 A) the lowest. At the two ends of the scan range, near the 7th and 3rd integer resonance, respectively, the pure 45° crossing scheme was most robust, while for all others the lifetime strongly decreased here, possibly due to lattice nonlinearities. The lifetime without any wire excitation was comparable to that of the mixed-crossing case. Simulations and experiments are in reasonable agreement. In particular, the simulated diffusive aperture for pure *x*-*x* crossing is 10% larger than for *x*-45° or 45°-45° crossing, which appears consistent with the higher lifetime seen for this case. The larger variation with tune for the experimental data could be attributed to additional machine nonlinearities and/or perturbations, not included in the simulations.

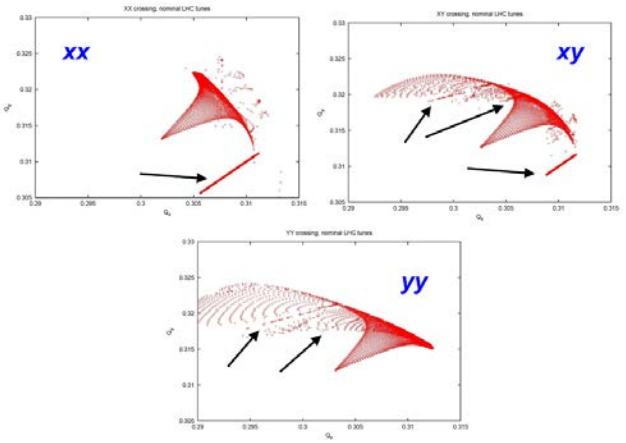

Figure 49: Simulated tune footprints for purely horizontal crossing, (top left), the nominal alternating horizontal-vertical crossing (top right) and purely vertical crossing (bottom) for regular bunches at the LHC collision tunes with collisions in and around the two main IPs. A few important resonances are highlighted by arrows.

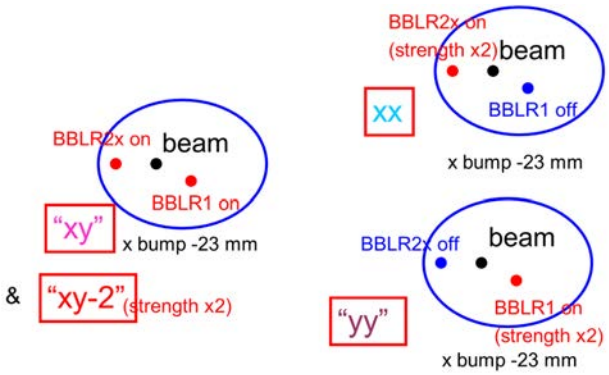

Figure 50: Approximations of different crossing schemes on 09/11/2004. The first configuration (left) models a mixed scheme with horizontal crossing at one wire and 45° crossing at the other, the second (right top) a pure horizontal-horizontal crossing, and the third (right bottom) a pure 45°-45° crossing.

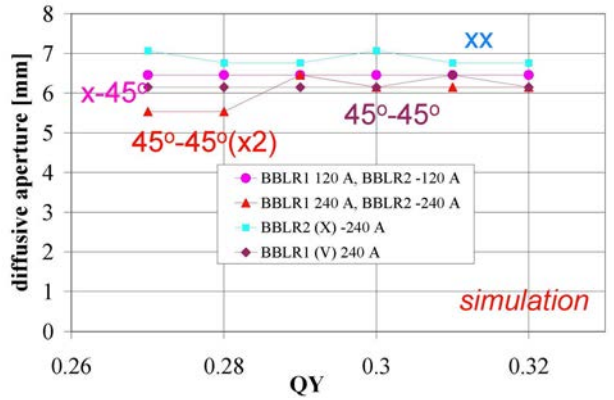

Figure 51: Dynamic aperture simulated by the WSDIFF code [34] (at $\beta \approx 50$ m) as a function of vertical tune keeping $Q_x = 0.31$, for the SPS wire configurations of Fig. 50.

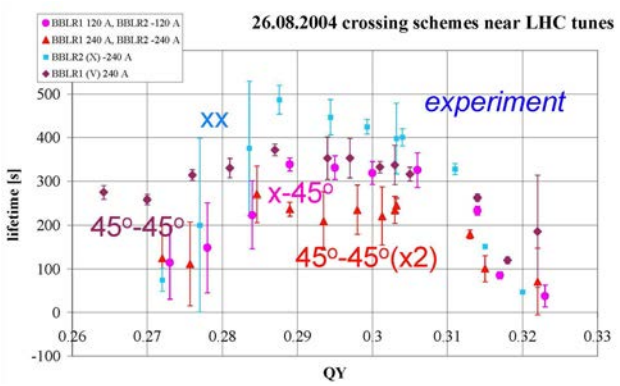

Figure 52: Beam lifetime measured as a function of the vertical tune for the three SPS wire configurations of Fig. 50. The horizontal tune was held constant at $Q_x \approx 0.31$.

On 9 November 2004, a second experiment was performed with reduced beam-wire distance and smaller emittance. One of the wires (BBLR2) had been rotated prior to this experiment, in order to allow for shorter transverse distances. The three configurations of Fig. 53 could then be realized. Again, it was not possible to implement a pure horizontal-vertical crossing. Instead a 45°-135° 'inclined hybrid crossing' [33] was modelled and its performance could be compared with that of a vertical-vertical or 45°-45° crossing.

Figure 54 displays the simulated dynamic aperture for these three configurations. The pure 45°-45° crossing has the smallest dynamic aperture. At vertical tunes of 0.29 or lower the vertical-vertical crossing is best, while at higher tunes the inclined-hybrid scheme yields the largest dynamic aperture. For completeness, the simulation results for a pure horizontal-vertical crossing are also indicated.

The measured beam lifetimes as a function of vertical tune are presented in Fig. 55. The lifetime was lowest for the 45°-45° crossing, the inclined hybrid crossing was best for tunes above 0.3, and the pure vertical-vertical crossing for lower tunes. All these results are consistent with the simulations in Fig. 54.

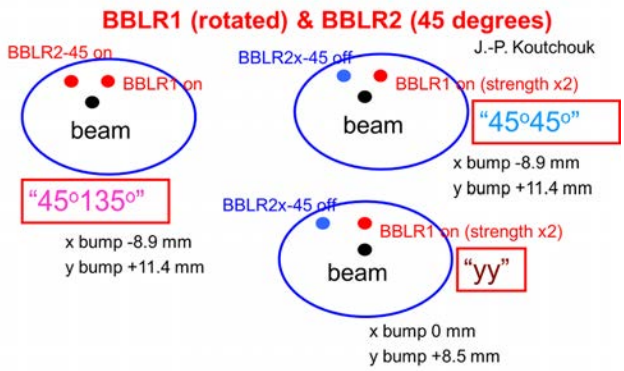

Figure 53: Approximations of different crossing schemes on 09/11/2004. The first configuration (left) models 45°-135° inclined hybrid collision [33], the second (right top) a double 45° hybrid crossing and the third (right bottom) a pure vertical-vertical crossing.

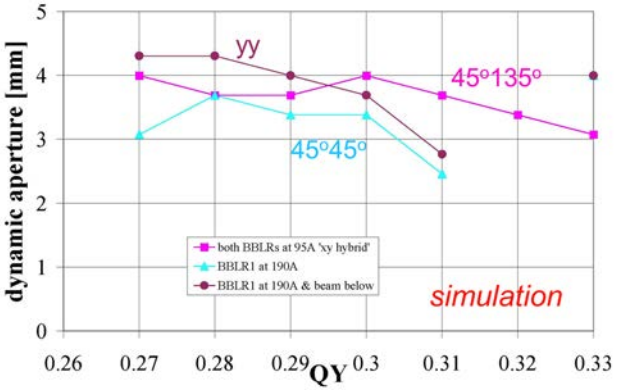

Figure 54: Dynamic aperture simulated by the WSDIFF code [34] (at $\beta \approx 50$ m) as a function of vertical tune keeping $Q_x = 0.31$, for the SPS wire configurations of Fig. 53.

Concluding this appendix, the beam lifetime was shown to vary with the crossing scheme. Experiments and simulations are mostly compatible.

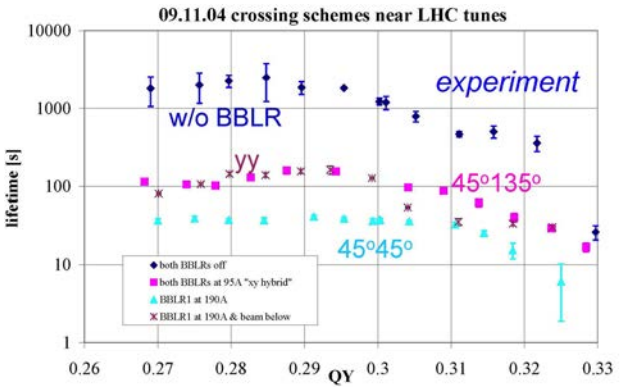

Figure 55: Beam lifetime measured as a function of the vertical tune for the three SPS wire configurations of Fig. 53. The horizontal tune was held constant at $Q_x \approx 0.31$.

REFERENCES

[1] D. Neuffer, S. Peggs, "Beam-Beam Tune Shifts and Spreads in the SSC: Head-On, Long Range and PACMAN conditions," SSC-63 (1986).

[2] W. Herr, "Tune Shifts and Spreads due to the Long-Range Beam-Beam Effects in the LHC," CERN/SL/90-06 (AP) (1990).

[3] W. Chou, D.M. Ritson, "Dynamic aperture studies during collisions in the LHC," CERN LHC Project Report 123 (1998).

[4] J. Irwin, "Diffusive Losses from SSC Particle Bunches due to Long Range Beam-beam Interactions," SSC-223 (1989).

[5] Y. Papaphilippou, F. Zimmermann, "Weak-strong beam-beam simulations for the Large Hadron Collider," Phys. Rev. ST Accel. Beams 2, 104001 (1999).

[6] J.-P. Koutchouk, "Principle of a Correction of the Long-Range Beam-Beam Effect in LHC using Electromagnetic Lenses," LHC Project Note 223 (2000).

[7] J.-P. Koutchouk, "Correction of the Long-Range Beam-Beam Effect in LHC using Electromagnetic Lenses," SL Report 2001-048 (2001).

[8] F. Zimmermann, "Weak-Strong Simulation Studies for the LHC Long-Range Beam-Beam Compensation," Beam-Beam Workshop 2001 FNAL; LHC Project Report 502 (2001).

[9] J. Lin, J. Shi, W. Herr, "Study of the Wire Compensation of Long-Range Beam-Beam Interactions in LHC with a Strong-Strong Beam-Beam Simulation," EPAC 2002, Paris (2002).

[10] Y. Papaphilippou, F. Zimmermann, "Estimates of diffusion due to long-range beam-beam collisions," Phys.Rev.ST Accel.Beams 5 (2002) 074001

[11] CERN Beam-Beam Compensation web site at http://cern-ab-bblr.web.cern.ch/cern-ab-bblr .

[12] The RHIC wires were kindly provided by M. Minty and T. Curcio.

[13] J.-P. Koutchouk, J. Wenninger, F. Zimmermann, "Compensating Parasitic Collisions using Electromagnetic Lenses," presented at ICFA Beam Dynamics Workshop on High-Luminosity e+e- Factories ('Factories'03') SLAC; in CERN-AB-2004-011-ABP (2004) .

[14] J.-P. Koutchouk, J. Wenninger, F. Zimmermann, "Experiments on LHC Long-Range Beam-Beam Compensation in the SPS," EPAC'04 Lucerne (2004).

[15] F. Zimmermann, J.-P. Koutchouk, F. Roncarolo, J. Wenninger, T. Sen, V. Shiltsev, Y. Papaphilippou, "Experiments on LHC Long-Range Beam-Beam Compensation and Crossing Schemes at the CERN SPS in 2004," PAC'05 Knoxville (2005).

[16] F. Zimmermann, „Beam-Beam Compensation Schemes," Proc. First CARE-HHH-APD Workshop (HHH-2004), CERN, Geneva, Switzerland, CERN-2005-006, p. 101 (2005).

[17] F. Zimmermann, U. Dorda, "Progress of Beam-Beam Compensation Schemes," Proc. 2nd CARE-HHH-APD Workshop on Scenarios for the LHC Luminosity Upgrade, Arcidosso, Italy, 2005, CERN-2006-008 (2005).

[18] U. Dorda, J-P. Koutchouk, R. Tomas, J. Wenninger, F. Zimmermann, R. Calaga, W. Fischer, "Wire Excitation Experiments in the CERN SPS," Proc. EPAC08 Genoa (2008).

[19] U. Dorda, F. Zimmermann, "Wire Compensation: Performance, SPS MDs, Pulsed System," Proc. IR07 p. 98 CERN-2008-006 (2007).

[20] U. Dorda, "Compensation of long-range beam-beam interaction at the CERN LHC," PhD Thesis Vienna TU., CERN-THESIS-2008-055 (2008).

[21] G. Sterbini, "An Early Separation Scheme for the LHC Luminosity Upgrade," PhD Thesis EPFL, CERN-THESIS-2009-136 (2009).

[22] G. Sterbini, R. Calaga et al, unpublished; see CERN BBLR web site in Ref. [11].

[23] P.W. Krempl, "The Abel-type Integral Transformation with the Kernel (t2-x2)-1/2 and its Application to Density Distributions of Particle Beams," CERN Note MPS/Int. BR/74-1 (1974).

[24] C. Carli, A. Jansson, M. Lindroos, H. Schönauer, "A Comparative Study of Profile and Scraping Methods for Emittance Measurements in the PS Booster," Particle Accelerators, Vol. 63, pp. 255-277 (2000).

[25] M. Seidel, "The Proton Collimation System of HERA," PhD Thesis U. Hamburg, DESY-94-103 (1994).

[26] V. Shiltsev, private communication, 28 November 2004.

[27] F. Zimmermann, P. Lebrun, T. Sen, V. Shiltsev, X.L. Zhang, "Using the Tevatron Electron Lens as a Wire and Other TEL Studies at FNAL," CERN AB-Note-2004-041 (2004).

[28] W. Fischer, R. Calaga, U. Dorda, J.-P. Koutchouk, F. Zimmermann, V. Ranjbar, T. Sen, J. Shi, J. Qiang, A. Kabel, "Observation of Long-Range Beam-Beam Effect in RHIC and Plans for Compensation," EPAC'06 Edinburgh (2006).

[29] R. Calaga, L. Ficcadenti, E. Métral, R. Tomas, J. Tückmantel, F. Zimmermann, "Proton-beam emittance growth in SPS coasts," Proc. IPAC12 New Orleans (2012).

[30] U. Dorda, F. Caspers, T. Kroyer, F. Zimmermann, "RF Wire Compensator of Long-Range Beam-Beam Effects," Proc. EPAC08 Genoa

[31] J.B. Jeanneret, LHC-LJ-EC-0001; private communication S. Chemli (2013).

[32] H. Schmickler, decision of 21 October 2013.

[33] K. Takayama et al., Phys. Rev. Let. 88, 14, 144801-1 (2002).

[34] WSDIFF web site http://care-hhh-web.cern.ch/CAREHHH/Simulation Codes/Beam-Beam/wsdiff.htm .

Published by CERN in the Proceedings of the ICFA Mini-Workshop on Beam–Beam Effects in Hadron Colliders,
CERN, Geneva, Switzerland, 18–22 March 2013, edited by W. Herr and G. Papotti, CERN–2014–004 (CERN, Geneva, 2014)

FUTURE WISHES AND CONSTRAINTS FROM THE EXPERIMENTS AT THE LHC FOR THE PROTON–PROTON PROGRAMME

R. Jacobsson, CERN, Geneva, Switzerland

Abstract

Hosting six different experiments at four different interaction points and widely different requirements for the running conditions, the LHC machine has been faced with a long list of challenges in the first three years of luminosity production (2010–2012, Run 1), many of which were potentially capable of limiting the performance due to instabilities resulting from the extremely high bunch brightness. Nonetheless, LHC met the challenges and performed extremely well at high efficiency and routinely with beam brightness at twice the design, well over one-third of the time in collision for physics, average luminosity lifetimes in excess of 10 h and extremely good background conditions in the experiments.

While the experimental running configurations remain largely the same for the future high luminosity proton–proton operational mode, the energy and the luminosity should increase significantly, making a prior assessment of related beam–beam effects extremely important to guarantee high performance. Of particular interest is the need for levelling the luminosity individually in the different experiments. Luminosity control as the more general version of 'levelling' has been at the heart of the success for LHCb, and to a large extent also for ALICE, throughout Run 1. With the increasing energy and potential luminosity, luminosity control may be required by all the experiments at some point in the future as a means of controlling the pileup conditions and trigger rates, but possibly also as a way of optimizing the integrated luminosity.

This paper reviews the various motivations and possibilities for controlling the luminosity from the experiments' point of view, and outlines the future running conditions and desiderata for the experiments as they are viewed currently, with the aim of giving guidelines for different options.

INTRODUCTION

The LHC is special in that it has to cater for both direct discovery and precision physics. This means that the outcome of the LHC Run 1 should also be viewed against the backdrop of the rapidly evolving requirements from the different experiments, as the performance parameter space of the machine itself unfolded:

- Up to six experiments taking data simultaneously at four interaction points with instantaneous luminosity ranging from 2×10^{30} cm^{-2} s^{-1} to 8×10^{33} cm^{-2} s^{-1}.
- Luminosity levelling at an intermediate luminosity of 4×10^{32} cm^{-2} s^{-1} in one IP and levelling at a low luminosity of 2×10^{30} cm^{-2} s^{-1} in another IP.
- 50 ns collision scheme with different number of colliding bunches in the different IPs.
- One IP shifted by 11.25 m with respect to the nominal IP.
- Non-colliding bunches and bunches colliding at an offset in only one IP.
- Collision scheme in one IP with main bunches against enhanced satellites from the LHC injectors in the 50 ns gaps.
- Two IPs with experimental spectrometer magnets and need for regular polarity changes.
- A 20° tilted crossing scheme in one IP to assure the same effective crossing angle in both polarities.

All these requirements effectively meant that the preparation for collisions in each fill was a very delicate process and occasional periods with instabilities from collective effects were not easy to deal with. On the other hand, these requirements together with the exceptional performance of the machine allowed exploration of the LHC parameter space for the future. There is a wealth of information available that is still under analyses to help decide on the best options for Run 2 and Run 3 (2015–2017 and 2019–2021, respectively, as the schedule currently stands).

Moreover, the fact that Run 1 already exposed the experiments to very high event pileup has also been very constructive in pushing the experiments to improve on the performance of the current detectors, trigger and reconstruction. It also allowed weaknesses to be revealed and choices to be guided for the successive upgrade programmes for all the experiments. The upgrade programmes are now well underway.

In terms of physics, the Run 1 high luminosity proton–proton programme left us with, on the one hand, the fundamental discovery of the existence of scalars in nature and a compatibility with a 126 GeV/c^2 Standard Model Higgs boson. On the other hand, the absence of a non-Standard Model signal in the precision measurements, in particular in the heavy flavour sector, and in the other direct searches for new particles, strongly indicate that New Physics is either very heavy or is only very weakly coupling to the Standard Model particles.

Of course, all of this does not go without saying that the proton–proton programme also provided vital physics input to the ion physics programme.

While the results above were clearly one of the very likely outcomes of Run 1, it gives a particular significance to the initial scope of Run 2 but leaves the scope beyond Run 2 largely open. That is to say, while the answers found in Run 1 hint at no New Physics but rather an even more well-established Standard Model as low-

978-92-9083-404-5, 0007-8328 –
http://dx.doi.org/10.5170/CERN–2014–004.167

energy effective theory, the unsolved fundamental questions, such as the neutrino oscillations, the baryon asymmetry, the dark matter, dark energy, etc., are still as much in need of New Physics. As it stands now, precision measurements on the newly found boson are likely to be one of the best compasses to suggest the direction on New Physics.

Firstly, the nature of the newly found boson should be determined through precise measurements of the couplings to the vector bosons and the fermions, and its role in the electroweak symmetry breaking and mass generation need to be understood. Of particular importance is the question whether the newly found boson solves the unitarity violations in scattering amplitudes with triple and quartic W and Z boson couplings. This programme of work requires access to all the production and decay modes of the 126 GeV/c^2 boson, some of which are very challenging in an environment with high event pileup.

The other path in the search for New Physics will consist of continued precision measurements on rare heavy flavour decays and CP violation, and direct searches for new particles. The increase of the centre-of-mass energy in LHC to 13 TeV will almost double the heavy flavour production cross-sections with respect to 7–8 TeV, and the parton luminosities for the production of new particles at a mass scale of 1 TeV through gluon–gluon, Σquark–anti-quark, Σgluon–quark(anti-quark) interactions will increase by an order of magnitude and at 2 TeV by two orders of magnitude.

The current physics situation with the high priority on precision measurements means that LHC will be even more challenged to produce the largest possible integrated luminosity at the smallest possible event pileup.

With this in mind, this paper focuses on the options from the experiments' point of view for the future high luminosity proton–proton programme, which currently appears to present the machine with the most involved and the most challenging aspects with respect to beam–beam effects.

Table 1 shows the beam parameters assumed in this paper for discussing the preferred option of 25 ns operation. They stem from the very successful Bunch Compression and Merging Scheme (BCMS) [1,2] that was devised by the LHC injectors in the second half of 2012 to significantly improve the performance with the 25 ns beam. Note that the plots in this paper serve as illustrations. They do not show the ultimate performance. The exact future running conditions of the experiments is currently under study.

Table 1: Assumed beam parameters in the discussion of the preferred option for 25 ns operation [1, 2].

	I_b	ε_N [μm]	N_b (IP1,2,5/IP8)	$\sqrt{s}$ [TeV]	σ_z [cm]
Run 2	1.15×10^{11}	1.9	2500 / 2400	13	10
Run 3	1.4×10^{11}	1.9	2800 / 2600	13	10
HL-LHC	2.2×10^{11}	2.5	2800 / 2600	14	7.5

MOTIVATIONS FOR LUMINOSITY AND PILEUP CONTROL

In the considerations of the strategy to maximize the LHC physics output, obviously neither the peak luminosity nor the delivered integrated luminosity is a good figure-of-merit. Several things may affect the data taking efficiency and the data quality. However, while the experiments use the full good-quality recorded integrated luminosity for physics analyses, not even this is a good figure-of-merit of the physics performance. The physics selection efficiencies and the background rejection, i.e. the physics yields, rely on observables whose resolutions are affected by many things, including in-time event pileup, out-of-time event pileup (also called 'spill-over'), background conditions, etc. The out-of-time pileup is due to the integration time of the detector components and typically implies that a certain fraction of the signal from the previous events is sampled with every event. The yield varies strongly between physics channels, depending on the type of final states and the angular distribution. For instance, final states with muons in the barrel are relatively easy to reconstruct even at very large event pileup, while channels with the need for reconstructing a whole decay chain of hadrons, including π/K identification in the forward region, are much more difficult (Fig. 1). Thus, whichever mode of operation is chosen, the proper figure-of-merit to maximize the physics output is the effective usable integrated luminosity. It will obviously involve a difficult and complicated combination of experimental priorities and compromises, which in the end results in the choice of a running condition and trigger configuration.

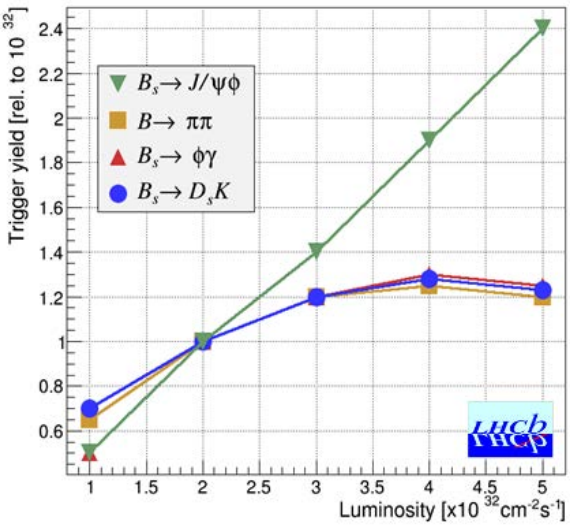

Figure 1: The plot shows the physics yield as a function of luminosity with simple final states such as muons, and the more complicated hadron final states which typically require reconstructing and the decay chain.

The following provides a list of the constraints and the effects which can potentially require limiting or levelling the instantaneous luminosity:

- **Instrumental limitation or instantaneous damage:** An instantaneous luminosity well beyond the design limits of some type of detectors may lead to such important ionization or changes of the dielectric properties that damage follows. For instance, gaseous detectors may receive damage from sparking. In most cases, the detectors will be well protected by current trip thresholds but it obviously involves relatively long recovery times which in turn affect the data taking efficiency and the data quality.
- **Detector ageing** is normally assumed to be linear in instantaneous luminosity and in integrated luminosity but the limits to this assumption is largely an unknown until it has been measured. This means that the detector replacement and upgrade programmes in place are based on experience and expected performance. It also means that the luminosity to which the detector is exposed should ideally be as close as possible to the effective usable luminosity.
- **Detector conditioning:** In some rare cases, detectors have shown a reduced performance or other negative effects at the immediate onset of a high instantaneous luminosity. For this reason, a well-controlled ramp up of instantaneous luminosity may be necessary.
- **Detector performance:** With increased instantaneous luminosity and event pileup, the performance of some sub-detectors degrades due to the effects of out-of-time pileup ('spill-over'), which effectively introduces uncorrelated detector hits in the subsequent bunch crossings and therefore increases the effect of combinatorics and degrades the resolution. Some sub-detectors which are designed for limited channel occupancy may also have intrinsic dead-times at the level of individual channels. At excessive event pileup, this effect acts in the opposite sense of spill-over by introducing detector inefficiencies in the subsequent bunch crossings.
- **Event size:** The event size is proportional to the pileup of physics events together with the hits from background and the spill-over from previous crossings. The readout system may have buffer size limitations which either results in event truncation or dead-time.
- **Trigger rate:** Ideally the trigger rate should just be a product of the physics cross-sections of interest and the instantaneous luminosity. However, at high pileup the trigger selections are strongly affected by the effect of wrongly combining hits or clusters from different events or from spill-over. With increased event pileup, the fake rate at the first level trigger increases rapidly, and the aggravated combinatorics increase very rapidly the average CPU time in the software-based high-level triggers. Some hadronic trigger rates grow exponentially with event pileup (Fig. 2). The excessive rates and processing times ultimately lead to data taking dead-time, which may scale non-linearly with the increased luminosity. Typically, the condition has to be controlled by tightening the selection cuts, often on the requirements on the transverse momentum or energy, with the consequence of decreasing significantly the selection efficiency for the physics. Unlike, for instance, bandwidth limitations which normally affect all physics signals by the same amount, this will affect the efficiency in a physics dependent way. Thus, the additional delivered luminosity offsets the effective usable luminosity by an amount which may be partial, complete, or even worse for low-p_T physics. High trigger efficiency for the Higgs physics while keeping the trigger rate within the budget was one of the biggest challenges for ATLAS and CMS in 2012.

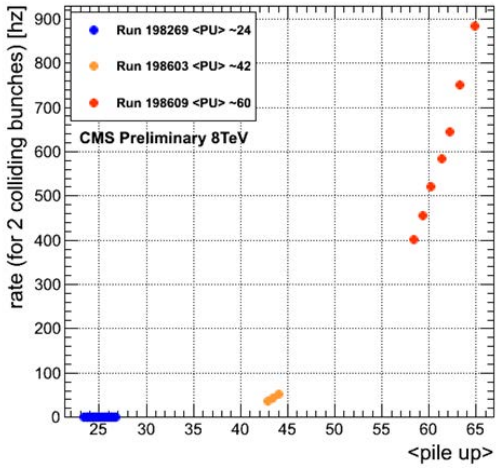

Figure 2: The plot shows the rate per bunch pair of a first level hadron trigger as a function of the pileup. Due to the increasing combinatorics, the fake rate grows exponentially.

- **Readout bandwidth:** The combined effect of increased event size and trigger rates with higher pileup may hit other technical limits related to the readout bandwidth, with similar consequences of introducing dead-time or inefficiencies.
- **Offline processing time:** As in the high-level trigger, the aggravated level of combinatorics with higher pileup increases the reconstruction times almost exponentially. This effect has been mitigated enormously during Run 1 and a lot of work is still in progress to further optimize the code, in particular by profiting efficiently from the parallel architectures of modern CPUs.
- **Machine limitation:** For completeness it should also be mentioned that there could be temporary luminosity limitations introduced by the machine for which it is necessary to operate at a lower instantaneous luminosity than what is potentially available. An example is the current cryogenics limit in IP1 and IP5 with respect to the luminosity debris at an estimated luminosity of $\sim 1.7 \times 10^{34}\,\mathrm{cm}^{-2}\,\mathrm{s}^{-1}$.

- **Luminosity lifetime:** In order to maximize the integrated luminosity, it is interesting to explore the possibility that there may be a potential gain in the luminosity lifetime at the operational limit of the machine by initially levelling the instantaneous luminosity in order to reduce for instance the emittance growth and the collimation burn-off at the peak instantaneous luminosity (Fig. 3). This mechanism should also be combined with the potential increase in physics efficiencies as a consequence of less peak pileup for the trigger, the reconstruction, and the physics resolutions.

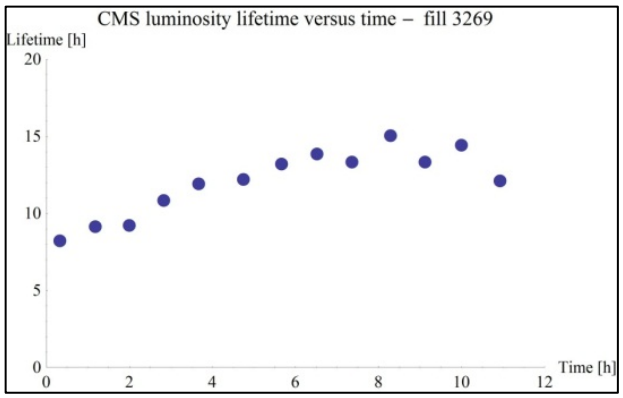

Figure 3: The plot shows an improvement in the luminosity lifetime as the luminosity drops which is partly due to the decreasing rate of collision burn-off. It is interesting to investigate if there are additional effects which may be reduced by levelling the luminosity below its peak value, hence leading to a potential gain in integrated luminosity.

- **Physics:** Even at high pileup, more often than not, the interesting physics event is accompanied by mostly a large number of minimum bias events. Nevertheless, at the limit of the performance, the additional particles from the other primary vertices have the effect of degrading the physics resolutions (vertexing, b-tagging, tracking, momentum, energy [particle-, jet-, missing-], particle identification, etc). The consequences for the physics are reduced background rejection and poorer measurements of the signal. In addition, the systematic errors in precision measurements are often sensitive to changing pileup and temporal variations in the detector performance, trigger, ageing etc. Controlling and levelling the instantaneous luminosity allows working with stable running conditions over months, and makes it easier to monitor and calibrate the detector performance over time.

The last point also elucidates the importance of the size, shape and stability of the luminous region. Each primary vertex is a potential contributor to the usable luminosity. The definition of a usable primary vertex, and the means to immunize the resolutions of the detector observables against pileup, are mainly by associating the hits, energy clusters, tracks and secondary vertices unambiguously to their primary vertices in order to perform pileup suppression and reconstruct each interesting interaction fully. For this reason, a dilution of the primary vertices over the luminous region, typically longitudinally, greatly enhances the situation for the experiment. Obviously the limit in the length of the luminous region at the other extreme is dictated by the finite length of the vertex/inner detectors. A too long luminous region will introduce reconstruction inefficiencies which in turn lead to reduced acceptance. Currently the luminous region is of the order of 50 mm.

Alternatively, the pileup dilution may be enhanced by aiming for a longitudinal flattening of the luminous region away from Gaussian. As a figure of merit for the pileup dilution, the line density as in the average number of events per millimetre is used. However, numerically this number does not reflect well the effect on the usable luminosity with different schemes and shapes. A more appropriate figure of merit should be based on the fraction of the number of primary vertices which may be, or which may not be resolved according to the definition of usable primary vertices above.

In 2012, ATLAS and CMS operated with a peak event pileup of 35 and an average pileup of 20, and LHCb with a constant levelled pileup of 2.1. Significant amount of work went into improving and optimizing the stability of the observables as a function of pileup (Fig. 4).

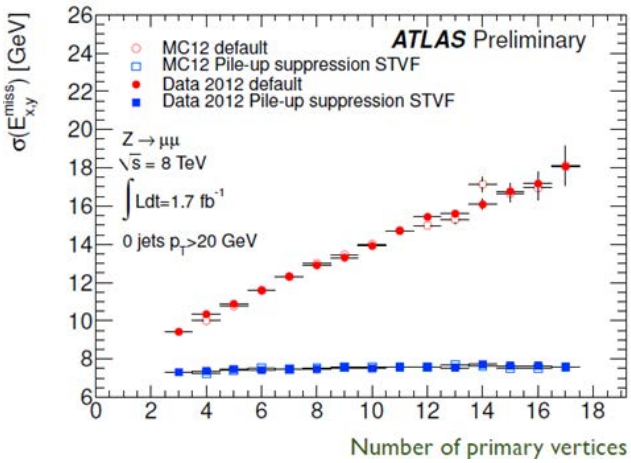

Figure 4: The resolution for missing energy as a function of the pileup. Before applying multivariate techniques to perform pileup suppression, the soft hadrons from the other interactions degraded severely the resolution. Missing energy will play an important role in the characterization of the newly found 126 GeV/c^2 neutral scalar boson.

The future priorities will be even more challenging. For ATLAS and CMS, the studies of the Higgs decay channels to $b\bar{b}$ and $\tau\tau$, and the production modes with couplings to W and Z will require even higher pileup immunity in the resolutions of jets, missing energy and τ-lepton identification.

At a given total instantaneous luminosity L, the average number of interactions per crossing μ is given by $\mu =$

$L\sigma/(f_{\mathrm{rev}}n_{\mathrm{bb}})$, where σ is the cross-section, f_{rev} is the LHC revolution frequency and n_{bb} is the number of colliding bunches. The number of interactions per visible crossings, i.e. pileup, is given by $\mu/(1 - e^{-\mu})$. From this it follows that the difference between running with the maximum LHC filling scheme at 50 ns and 25 ns is a factor of two in the event pileup. Of course, 25 ns operation increases the spill-over effect, but this is overall negligible compared to a factor of two in the event pileup. For all the reasons given above, it is then clear that the only path to maximum physics yield is operating at 25 ns. The only scenario which could temporarily outweigh this strategy is either a strong limitation on the instantaneous luminosity at 25 ns from a total intensity limit, electron cloud, etc., or a severely degraded machine stability, i.e. reduced machine time in collision, requiring some longer-term upgrades. For this case, the 50 ns option is considered a backup and a trigger tuning will be prepared. However, maximizing the physics yield at 50 ns will entail considerable changes in the trigger and reconstruction strategies.

While the 50 ns backup option requires levelling for all the IPs with certainty, 25 ns operation should initially only require levelling for ALICE and LHCb. However, ATLAS and CMS are likely to require levelling, if not before, at the latest in the run with High Luminosity LHC (HL-LHC) [3]. At HL-LHC it is expected that the levelling for ATLAS and CMS should allow reducing the potential luminosity of $2 \times 10^{35}\ \mathrm{cm^{-2}\,s^{-1}}$ by a factor of four.

The next section explores the different options for controlling the luminosity.

LUMINOSITY/PILEUP CONTROL

Writing the luminosity as

$$L = \frac{n_{\mathrm{bb}} \times N^2 \times f_{\mathrm{rev}}}{A} * R(\beta^*, \theta, \sigma_z, \phi_P, \delta_s, \delta_c, \Delta t)$$

where n_{bb} is the number of colliding bunches, N is the number of protons per bunch, f_{rev} is the LHC revolution frequency and A represents the physical head-on beam overlap area. R is an overall luminosity factor from optical and geometrical effects which shows that there are many ways to control the luminosity ('luminosity' is here used to denote both instantaneous luminosity and pileup) at an interaction point. While the luminosity control in the ALICE and in the LHCb experiments was based on adjusting the transversal overlap of the two beams in the plane orthogonal to the crossing plane, i.e. with a beam offset in the separation plane (δ_S), there are a number of reasons to consider the other options for the case where all the experiments require luminosity control. An important reason comes from beam stability with lack of Landau damping from head-on collisions [4].

From the experiments' most exigent point of view, the method by which the luminosity is controlled should be local and individual to the experiment and should have minimal impact on the other experiments. Ideally, even ATLAS and CMS could benefit from a decoupled luminosity. Due to the importance of the size and stability of the luminous region, the method by which the luminosity is controlled should not change its length and position significantly. Ideally it should rather maximize the length. The method should involve a minimum of operational overhead and should not limit the flexibility for the other operational modes. The luminosity control should be performed in a way which is safe to the experiment such that it can be done with the experiments fully switched on in the restricted beam mode which is reserved for the safe physics data taking ('Stable Beams'). Any other way would involve 5–10 min loss of physics data taking for each luminosity re-optimization to put the experiments in a safe state and back operational again. The luminosity control should be stable and relatively fine adjustable to allow the luminosity to be maintained within 5% of the desired instantaneous luminosity. This is particularly important for LHCb, but is somewhat less critical to ALICE, ATLAS and CMS. At the optimal limit of the readout and the trigger capacity, luminosity variations either introduce dead-time if the luminosity exceeds the optimal value, or leads to non-optimal running if it is below. Furthermore, since the optimal luminosity may depend on the data taking configuration and the data taking conditions, and even temporary technical limitations, the luminosity should be remotely controllable. This has been of particular importance to the LHCb experiment. Last but not least, the levelling parameters and the related quantities should be measurable and monitored to allow fast analysis of undesired effects.

With the requirements above in mind, below is a list of methods to control the luminosity together with the main positive and negative implications for the experiments.

- **Bunch crossing frequency:** This is not a method to control the luminosity but since it has been suggested as a means of limiting the event pileup at higher luminosity in the future, the option is included here for completeness. The idea aims at distributing the luminosity on more bunches by reducing the bunch spacing and increasing the total number of bunches n_b in the LHC filling scheme. At the same luminosity, it reduces the pileup by $n_b(>40\ \mathrm{MHz})/n_b(40\ \mathrm{MHz})$, but it also increases the stored energy in the LHC by $\sqrt{n_b(>40\ \mathrm{MHz})/n_b(40\ \mathrm{MHz})}$ as compared to the current configuration. Furthermore, it should be understood that the entire readout systems of the experiments are entirely based on signal processing at the level of 25 ns. It would require a complete remake of the whole electronics system to benefit from a higher bunch crossing rate. Moreover, out-of-time pileup effects will be even more important making the gain unclear. It is not considered a viable option.
- **RF cogging (Δt):** Shifting the RF phase of the beams together with a crossing-angle at the IPs leads to an out-of-time encounter which effectively reduces the

luminosity but which also shifts the longitudinal centre of the luminous region by a fraction of the time difference depending on the beam emittance. However, this is not considered a viable option since it affects the luminosity at all the IPs.

- **Crossing angle (θ):** Changing the crossing-angle allows a very limited lever arm within the acceptable range of angles for controlling the luminosity. In particular at small β^*, the minimum crossing angle is large in order to have sufficient beam separation against long-range interactions. In addition, it is expected that the scheme introduces operational complications with respect to the collimator and orbit management. It is not considered a viable option since it makes the luminous region very short and varying in length during the fill.
- **Bunch rotation with crab cavities (ϕ):** Equivalent to a crossing-angle, the luminosity may be controlled by rotating the bunch [5]. While the crab cavities are necessary to maximize the luminosity at small β^* and maximize the length of the luminous region, their use in levelling is not considered viable since it again reduces strongly the length of the luminous region. For instance, in the nominal 25 ns HL-LHC situation [6], a rotation of 700 μrad would be necessary to reduce the luminosity by a factor four to 5×10^{34} cm^{-2} s^{-1}, resulting in a luminous region length of <20 mm.
- **Piwinski angle ϕ_P (angle θ + bunch length σ_z):** The luminosity may also be controlled by changing the Piwinski angle, which involves both the crossing (or crab rotation) angle and the bunch length according to $L \propto 1/\sqrt{1+[\theta\sigma_z/2\sigma_{x,y}]^2}$. This allows a partial compensation against the length shortening of the luminous region by increasing the bunch length. However, this is not considered a viable option since the lever arm to control the luminosity is very limited together with an insufficient compensation for the shortening of the luminous region. In addition, the increase of the bunch length affects all IPs.

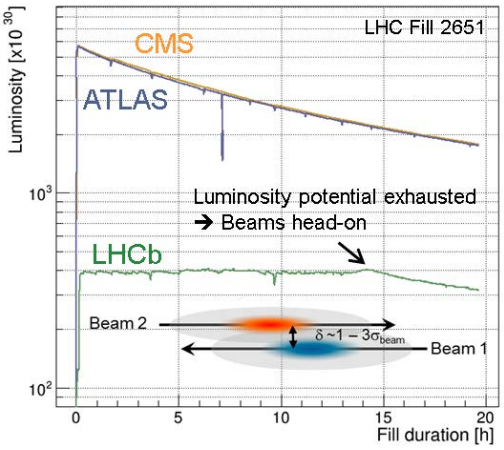

Figure 5: Example of luminosity levelling by separation in LHCb which shows the effect of small orbit drifts and orbit jumps.

- **Beam separation orthogonal to the crossing plane (δ_S):** The luminosity control by adjusting the transversal beam overlap has been successfully used in LHCb and ALICE in Run 1. The operational scheme is simple and the luminous region remains stable both longitudinally and transversally. A drawback is the high sensitivity to orbit drifts and orbit jumps which lead to luminosity instabilities. There is also the risk of accidentally delivering very high instantaneous luminosity head-on. Figure 5 shows an example of the LHCb luminosity in a long fill. While it has been shown that the beam stability tolerates separation of up to a beam sigma [4] even in ATLAS and CMS, and the LHCb and ALICE bunches with larger separation have been stabilized by the head-on Landau damping when colliding in ATLAS and CMS, the main concern is the complete lack of Landau damping if this scheme is applied in all experiments. The required beam separations are not expected to introduce instabilities but the lack of head-on collisions means that there is no Landau damping of instabilities from other sources. In general the scheme is considered a viable option by the experiments.

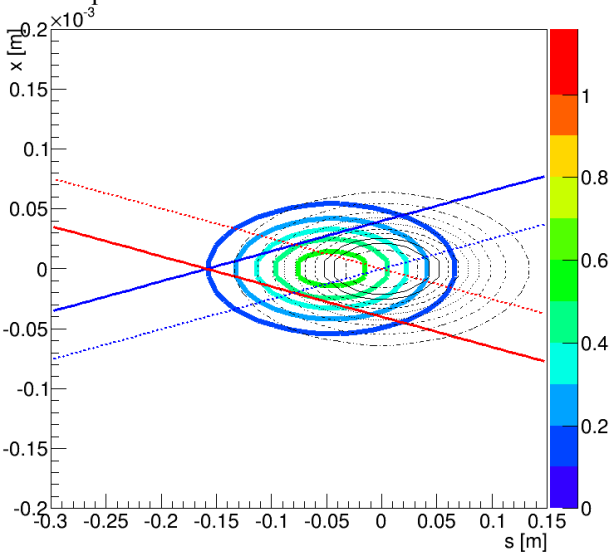

Figure 6: Example of luminosity levelling by separation in the crossing plane. The dashed lines show the luminous region and the geometrical crossing point with head-on collision while the solid lines show the luminous region and the geometrical crossing point in LHCb with the Run 2 beam parameters and a shift of one sigma shift per beam. The shift leads to a luminosity reduction of a factor two and shifts the centre of the luminous region by almost 5 cm.

- **Beam separation in the crossing-plane (δ_c):** Shifting the beams laterally in the crossing-plane also allows controlling the luminosity with a limited length shortening of the luminous region and a limited shift of the longitudinal centre of the luminous region which depends on the angle and the beam emittance. If the beam emittance is very small,

the centre is close to the geometrical crossing point while if the beam emittance is large the centre remains near the beam encounter at $t = 0$. Figure 6 shows an example with the configuration for LHCb in Run 2 and a shift of both beams by a beam sigma resulting in a luminosity reduction of factor of two. Again this option is not preferred since it shifts the centre of the luminous region. Nevertheless it would be interesting to check if the two types of separation have the same effect on the beam stability.

- **Beam focusing (β^*):** Controlling the luminosity by the β^* is clearly a more involved scheme which requires new levels of control and a scheme to manage the optics and the collimators without leaving the 'Stable Beams' condition [7]. However it has the advantage that it imposes no limitation on the luminosity range, it preserves the luminous region longitudinally, and it is relatively immune to orbit variations. The β^* squeeze in Stable Beams to compensate for the emittance growth and the intensity drop could also be performed in only one plane while maintaining the β^* small in the other. This would have the interesting feature of preserving the luminous region transversally in one plane, and supports the idea of the use of flat beams in the future [8]. If the β^* squeeze in Stable Beams cannot be smooth, the scheme could be combined with one of the beam separation schemes above to level the luminosity between the successive β^* steps. The combined scheme could be constructed to maintain the range of separation below one beam sigma to respect the stability diagram. There is some concern about the limit from the total head-on beam–beam tune shift if this scheme is applied in three IPs. However, as of now no limit has been observed and the limit has been demonstrated to be well beyond the design expectations [9].

Table 2 shows a list of examples of luminosity levelling by purely transversal separation and by beam focusing in both planes in the future runs in order to give an indication of the required ranges. The minimum β^* in LHCb has been chosen in order to guarantee a levelling lifetime of >12 h assuming similar emittance and intensity lifetimes to what was achieved in Run 1. The head-on luminosity in ALICE is of concern with separation as it could potentially induce damage. The main background monitor which is connected to the LHC beam dump has thresholds adjusted to a level which dumps the beam in case of excessive luminosity. Furthermore, with levelling by separation in ATLAS and CMS in Run 2, orbit variations of ±1 μm at the IP change the luminosity and pileup by as much as 8%.

All of these arguments appear to favour a combined levelling by beam focusing and a restricted transversal separation. If luminosity levelling by beam focusing is performed in only one plane, the maximum β^* required in the levelling plane is trivially $\beta_l^* = \beta_{\max}^{*2}/\beta_{\min}^*$ as compared to the numbers in Table 2. Clearly, the addition of a combined transversal separation allows reducing the maximum β^* required.

		ATLAS/CMS	LHCb	ALICE
Run 2	Mimimum β*	0.4 m	3 m	10 m
	Head-on luminosity [$cm^{-2}s^{-1}$]	1.5×10^{34}	3×10^{33}	1×10^{33}
	Levelled luminosity [$cm^{-2}s^{-1}$]	No	$4\text{-}6\times10^{32}$	4×10^{30}
	Level by separation δ_s at β^*_{min}	–	$2.8\sigma \rightarrow 0\sigma$	$\sim5\sigma$
	Level by β* at δ_s=0	–	20m → 3m	–
Run 3	Mimimum β*	0.4 m	3 m	10 m
	Head-on luminosity [$cm^{-2}s^{-1}$]	2.5×10^{34} (p.u.~70)	5×10^{33}	1.5×10^{33}
	Levelled luminosity [$cm^{-2}s^{-1}$]	1.5×10^{34} (example)	$1\text{-}2\times10^{33}$	2×10^{31}
	Level by separation δ_s at β^*_{min}	$1.5\sigma \rightarrow 0\sigma$	$2.5\sigma \rightarrow 0\sigma$	$\sim4\sigma$
	Level by β* at δ_s=0	0.8 m → 0.4 m	15 m → 5 m	–
HL-LHC	β*	0.15 m + crab cavity	3 m	10 m
	Head-on luminosity [$cm^{-2}s^{-1}$]	2.4×10^{35}	1×10^{34}	3.5×10^{33}
	Levelled luminosity [$cm^{-2}s^{-1}$]	5×10^{34} (pu~140)	2×10^{33}	2×10^{31}
	Level by separation δ_s at β^*_{min}	$2.5\sigma \rightarrow 0\sigma$	$2.5\sigma \rightarrow 0\sigma$	$\sim4.5\sigma$
	Level by β* at δ_s=0	0.7 m → 0.15 m	16 m → 3 m	–

Table 2: Examples of luminosity levelling by purely transversal separation and by beam focusing in both planes in the future runs assuming the preferred option of 25 ns operation with the parameters in Table 1.

SUMMARY OF EXPERIMENT DESIDERATA FOR THE FUTURE

As a starting point on the running conditions for the future it should be generally noted that already at the same instantaneous luminosity, the event complexity increases naturally when increasing the energy from 8 TeV to 13 TeV due to two effects. The minimum bias cross-section and the associated event pileup is expected to increase by about 15% and the overall multiplicity is expected to increase by ~10–20% depending on the rapidity range. Thus at the same luminosity and the same number of colliding bunches, the events get ~25% more busy in ATLAS and CMS and up to ~40% more busy in LHCb.

For 2015, the experiments assume an initial period of 50 ns operation in order to restart the LHC, commission 13 TeV physics, and for the initial electron cloud scrubbing and the intensity ramp up to a full 50ns machine. The experiments will profit from this phase to perform calibrations and re-commission the detectors and the entire data flow chain. Of particular importance is the commissioning and validation of the triggers and the offline processing which are being extensively revised during LS1 in order to cope with higher pileup. It is expected that the first goal will be to commission the triggers tuned for 25 ns, which in itself may mean limiting the pileup for a short period to the maximum value expected with 25 ns operation. This is obviously only necessary if LHC is potentially already able to deliver significantly higher pileup at 50 ns. It should still be noted that this phase does not fully allow assessing the effect of spill-over in the trigger and reconstruction which introduces some uncertainty in the final tuning. However, this is addressed in parallel by simulation.

Secondly, it is expected that the experiments will be commissioning a backup trigger tuning for 50 ns operation which can then also be used to collect as much integrated luminosity as possible in this first phase.

Nevertheless, the experiments would like to see this phase as short as possible, also implying that no extra time should be spent on optimizing the luminosity in this phase beyond what is necessary to allow the transition to 25 ns operation.

The transition to 25 ns is vital for all the reasons given above and should be the primary goal. It is understood and accepted that this may require a significant amount of commissioning and conditioning time in 2015. It is also clear that the higher stored energy may lead to machine instabilities and may also contribute to limiting the initial instantaneous luminosity at 25 ns.

Clearly the progress will have to be followed closely and some breakpoints for decisions on the strategy will be needed, but in general this phase is considered an investment for the future.

A special case is if the LHC injectors are not able to deliver the 25 ns-BCMS scheme efficiently to fill the entire LHC machine. An instantaneous luminosity limit of $<10^{34}$ cm^{-2} s^{-1} at 25 ns with no prospect for improvement may be considered a tipping point for ATLAS and CMS. Since ALICE and LHCb will be running with a levelled instantaneous luminosity, a tipping point is *only* valid if the machine availability is severely affected at 25 ns. This particular case will therefore require a difficult assessment with all elements at hand on the moment.

In the preferred scenario with 25 ns operation, ATLAS and CMS are not a priori expected to require levelling of the luminosity in Run 2, in particular with the upcoming upgrades. Currently this assumes that the luminosity remains below 2×10^{34} cm^{-2} s^{-1}. This means effectively that ATLAS and CMS expect to be able to cope with a peak pileup of up to 45–60 in Run 2 and Run 3. In this configuration, ATLAS and CMS should be able to collect realistically about 100 fb^{-1} in Run 2 and another 300 fb^{-1} in Run 3 with the upgraded LHC injectors.

In case 50 ns operation turns out to be significantly more productive than 25 ns, luminosity levelling will be needed even with the nominal 50 ns beam parameters. The exact level of pileup at which ATLAS and CMS require levelling of the luminosity is currently under study.

LHCb will require levelling of the instantaneous luminosity from the first day of luminosity production in 2015. In the preferred scenario with 25 ns operation, the LHCb target luminosity is expected to be around 4×10^{32} cm^{-2} s^{-1} for Run 2. After the LHCb upgrade in LS2, LHCb is expecting to be initially running at a levelled luminosity of 1×10^{33} cm^{-2} s^{-1} in Run 3, and later move to a levelled luminosity of 2×10^{33} cm^{-2} s^{-1}. In all cases, the β^* configuration should be such that it allows LHCb to run at constant luminosity with a levelling lifetime which is of the order of the longest typical fill duration (10–15 h). In these conditions, LHCb should be able to collect realistically about 5 fb^{-1} in Run 2 and aim at 50–100 fb^{-1} after the upgrade in LS2. Like with ATLAS and CMS, the studies of the exact conditions for the backup case of 50ns operation has not been completed.

While luminosity levelling is a priori not needed by ATLAS and CMS in the preferred scenario for Run 2, it is strongly felt that a levelling scheme should be prepared. On the one hand, it could be used in case of the unforeseen; on the other hand it allows studying the feasibility for Run 3 and for HL-LHC. For this reason, the choice of levelling method should be the most promising for HL-LHC.

For the reasons outlined in the previous Sections, luminosity levelling by β^* and by transversal separation are considered the two most viable options by the experiments. The levelling by separation is to a large extent already available. It is felt that the levelling by β^* should be studied and implemented, and that the most appropriate option is likely to be a combined levelling by β^* with transversal separation to smoothen the luminosity between the successive β^* steps within a limited range which still provides Landau damping.

Consequently, there is strong interest in putting β^* levelling in operation for LHCb for Run 2. Head-on

collision in LHCb should also allow exploring further the beam–beam limit for the future.

At HL-LHC, the optimal configuration for ATLAS and CMS appears to be a combined β^*/separation levelling scheme with crab cavities providing constantly a bunch rotation that gives a complete bunch-bunch overlap in the crossing plane to maximize the length of the luminous region.

ALICE will need to take proton–proton data yearly for physics normalizations and detector calibrations, but also for operational preparation and verification for the ion runs. In Run 2 with 25ns, ALICE plans to run in two different trigger configurations to collect a minimum of about 3 pb^{-1}/year of barrel triggers at a levelled luminosity of 4×10^{30} cm^{-2} s^{-1} and about 15 pb^{-1}/year of muon triggers at a levelled luminosity of 2×10^{31} cm^{-2} s^{-1}. In the backup case of 50 ns operation, ALICE would request about 45 isolated main–main collisions per turn with a levelled luminosity as the ideal data taking condition. In Run 3 after the upgrade in LS2, ALICE expects to require a minimum of 100 pb^{-1} of proton–proton data per year at a levelled luminosity of 2×10^{31} cm^{-2} s^{-1}. It is expected that the levelling in ALICE will continue to be performed by transversal beam separation. The target luminosity for Run 2 and 25 ns operation implies a separation of about 5 σ at a β^* of 10 m. However, with such a large separation, accidental excessive luminosities are a concern since the beams will be dumped and there is a small risk of detector damage. It seems interesting to investigate the possibility of running at a larger β^* to reduce the maximum potential luminosity.

ATLAS, CMS, LHCb and TOTEM all depend critically on the length of the luminous region to resolve the primary vertices, and on the longitudinal stability. In general the luminous regions should be maintained long and an increase of 10–15% could improve the situation for all experiments. Since the size is a parameter in the physics simulations, the value should be known well in advance and then kept as stable as possible. In addition, in order to improve the acceptance for long-lived B hadrons, LHCb could benefit from a small upstream (anticlockwise) shift of the centre of the luminous region. This may be achieved by a simple small lateral shift of the two beams in the crossing-plane as shown in Fig. 6. Studies of the optimal configuration are underway.

Non-colliding bunches were used by ATLAS, CMS and LHCb in Run 1 to measure single-bunch related physics background and for background subtraction in the luminosity determination. In the nominal 25 ns filling scheme there is no longer room for non-colliding bunches in ATLAS and CMS. Nevertheless, assuming that a stable scheme with negligible impact on luminosity can be found, ATLAS and CMS would still like to have a few non-colliding bunches. LHCb will still get non-colliding naturally at the end of the trains due to the 11.25 m shift from the position of the nominal IP.

LHCb needs to continue operating with the combination of a horizontal internal crossing-angle from the spectrometer magnet and an external vertical angle in order for the effective net crossing-angle to be the same in both polarities. At 25 ns the negative polarity of the spectrometer magnet results in parasitic long-range collisions without the vertical external angle. This means that the tilted crossing scheme has to be set already at injection. This is currently part of a detailed study [10].

As in Run 1, ALICE and LHCb will also require the regular polarity reversals.

In addition to the special high-β^* runs, TOTEM will take data together with CMS during the high-luminosity proton–proton runs in Run 2 and in Run 3. It is hoped that TOTEM will be able to move the horizontal pots to 14σ and the vertical pots to 11 σ in the high-luminosity runs in Run 2. Luminosity levelling by β^* adds a complication to TOTEM in that corrections have to be applied in the analyses for the changes of the optics.

LHCf plans to take data together with ATLAS in Run 2 during the very first phase of proton–proton physics. It will be for a very limited amount of time as the detector ageing is expected to degrade the performance after about 1 fb^{-1}. For this reason, the special runs for LHCf should be scheduled very early in 2015, ideally before 500 nb^{-1} has been accumulated which effectively means during the machine commissioning phase. The requested conditions for the data taking consist of less than 40 colliding bunches and injection optics not to exceed a luminosity of 10^{29} cm^{-2} s^{-1}, and an integrated luminosity of 10 nb^{-1} at several centre-of-mass energies.

CONCLUSION

LHC proved to be an extremely versatile machine in Run 1. While the experiments challenged the machine with a very wide range of requirements, the machine challenged the experiments with unrefusable running conditions which at the end resulted both in physics results of fundamental importance, but also operational prospects of fundamental importance for the future runs.

This paper recapitulates on this outcome, and motivates and outlines the future constraints, requirements and preferences from the experiments which need to be taken into account when defining the future strategy. Many of these requirements are challenging from the point of view of beam–beam effects and will require careful assessment. This is clearly an iterative process between the experiments and the machine which will eventually define a baseline for the running configuration and conditions which maximize the physics performance. Many studies are currently in progress in the experiments to refine the requirements and the limits for the future. It is expected that these studies will be able to deliver more accurate statements at the beginning of 2014.

Nevertheless, it's more than likely that there will be as many surprises and new ideas flowing in the future as in Run 1, which ultimately means that both the experiments and the machine will have to stay flexible.

ACKNOWLEDGMENTS

This paper cannot be concluded without thanking all the colleagues from the LHC and injectors for the exceptional performance of the machines and the fantastic collaboration.

This paper has been presented on the behalf of ALICE, ATLAS, CMS, LHCb, LHCf and TOTEM.

The author would like to thank the organizers of the conference for the invitation to give this talk and thank in particular G. Arduini, O. Bruning, T. Camporesi, M. Chamizo, M. Deile, A. Di Mauro, B. Gorini, W. Herr, M. Lamont, E. Meschi, G. Papotti, T. Pauly, T. Pieloni, G. Rakness, T. Sako and S. Zimmermann for providing input and comments to this paper.

REFERENCES

[1] S.S. Gilardoni, "The High Intensity/Intensity Brightness Upgrade Programme at CERN: Status and Challenges," Proc. 52nd ICFA Advanced Beam Dynamics Workshop on High-Intensity and High-Brightness Hadron Beams, Beijing, 2012.

[2] R. Steerenberg et al., "Post-LS1 25 ns & 50 ns Options from the Injectors," Proc. LHC Beam Operation Workshop, Evian, France, 2012.

[3] HL-LHC, http://hilumilhc.web.cern.ch/HiLumiLHC/

[4] X. Buffat, "Coherent Beam–Beam Modes in the LHC," these proceedings.

[5] G. Sterbini, "Luminosity Levelling with Crabs," Proc. 4th LHC Crab Cavity Workshop, CERN, Geneva, 2010.

[6] O.S. Bruning and F. Zimmermann, "Parameter Space for the LHC Luminosity Upgrade," Proc. IPAC2012, New Orleans, Louisiana, USA.

[7] X. Buffat et al., "Results of β* luminosity levelling," (CERN ATS-Note-2012-071 MD, 2012).

[8] W. Herr et al., "Performance Reach of LHC after LS1," Proc. LHC Performance Workshop, Chamonix, France, 2012.

[9] T. Pieloni et al., "Colliding High Brightness Beams in the LHC," Proc. 52nd ICFA Advanced Beam Dynamics Workshop on High-Intensity and High-Brightness Hadron Beams, Beijing, 2012.

[10] B.J. Holzer, "Spectrometer Operation in IR2 & IR8," Proc. LHC Beam Operation Workshop, Evian, France, 2012.

Published by CERN in the Proceedings of the ICFA Mini-Workshop on Beam–Beam Effects in Hadron Colliders,
CERN, Geneva, Switzerland, 18–22 March 2013, edited by W. Herr and G. Papotti, CERN–2014–004 (CERN, Geneva, 2014)

LUMINOSITY LEVELLING TECHNIQUES FOR THE LHC

B. Muratori*, STFC Daresbury Laboratory, ASTeC and Cockcroft Institute, UK
T. Pieloni†, CERN, Geneva, Switzerland

Abstract

We present the possibilities for doing luminosity levelling at the LHC. We explore the merits and drawbacks of each option and briefly discuss the operational implications. The simplest option is levelling with an offset between the two beams. Crab cavities may also be used for levelling, as may a squeezing of the beam. There is also the possibility of using the crossing angle in order to do luminosity levelling. All of these options are explored, for the LHC and other possible new projects, together with their benefits and drawbacks.

INTRODUCTION

One of the main measures of a collider's performance is its luminosity. However, from the point of view of experiments, what is most important is not the peak luminosity but, rather, the integrated luminosity. For the detection of events, it is also preferable that the luminosity remain constant for as long as possible. Therefore, luminosity levelling can be introduced. This means that the natural decay of the luminosity is pre-empted and the luminosity is spoilt initially with respect to the nominal. Then, as the luminosity decays, it is spoilt less and less in order that it remain constant for as long as possible. While doing this, it is still very much worthwhile to start with as high a luminosity as possible, as this will translate in the luminosity being constant for a longer amount of time after levelling. To explain what is meant by this, we consider the expression for the luminosity in the presence of both an offset and a crossing angle such that the crossing region is illustrated by Fig. 1 (more details can be found in [1, 2]):

$$\mathcal{L} = \frac{N_1 N_2 f N_b}{4\pi\sigma_x\sigma_y} W \mathrm{e}^{\frac{B^2}{A}} \frac{1}{\sqrt{1+(\frac{\sigma_s}{\sigma_x}\tan\frac{\phi}{2})^2}},$$

with

$$A = \frac{\sin^2\frac{\phi}{2}}{\sigma_x^2} + \frac{\cos^2\frac{\phi}{2}}{\sigma_s^2}, B = \frac{(d_2-d_1)\sin\frac{\phi}{2}}{2\sigma_x^2},$$

and

$$W = \mathrm{e}^{-\frac{1}{4\sigma_x^2}(d_2-d_1)^2}.$$

N_1 and N_2 are the number of protons per bunch for Beams 1 and 2, respectively; N_b is the number of colliding bunches per beam; σ_x, σ_y, and σ_s are the transverse and longitudinal bunch dimensions; ϕ is the crossing angle; and d_1 and d_2 are the offsets of Beams 1 and 2 with respect to the nominal.

* bruno.muratori@stfc.ac.uk
† tatiana.pieloni@cern.ch

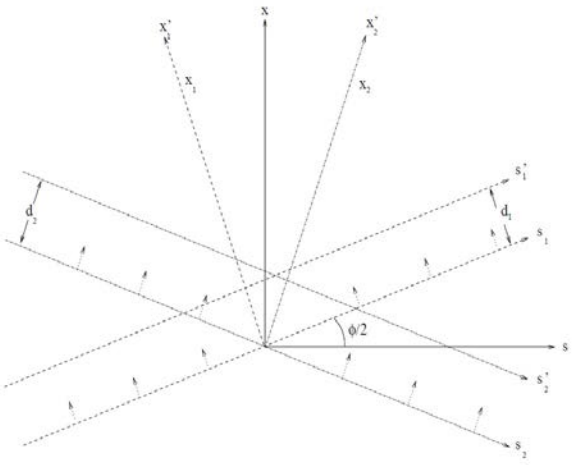

Figure 1: The geometry of the interaction region, with the crossing angle and the offset of the beams.

Various types of luminosity levelling have been suggested. These are explained below, together with an analysis of their merits and drawbacks, as well as a discussion of how they satisfy the requirements, from the point of view of observation, operations, and the LHC experiments [3, 4, 5, 6]. The main types of levelling are separation, crab cavities or crossing angle, and β^* squeeze, as illustrated in Fig. 2.

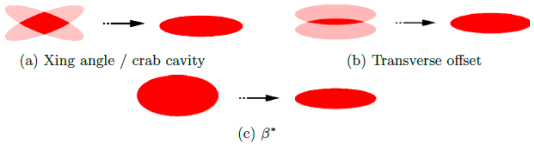

Figure 2: A sketch of the luminous region for different levelling techniques.

LEVELLING WITH OFFSET

The simplest form of levelling is achieved by introducing an offset between the two colliding beams. This is straightforward from an operational point of view, and can be implemented easily and quickly if required. It also makes it possible to do levelling in all IPs independently, as it is done with a local orbit bump, and it gives a smaller tune spread, therefore leading to smaller losses. The average number of p-p collisions per bunch crossing, or pile-up, that experiments can handle is limited, as different events

978-92-9083-404-5, 0007-8328 –
http://dx.doi.org/10.5170/CERN–2014–004.177

need to be distinguished. This is particularly important longitudinally, where the vertex density is critical and levelling with offset allows for this to be kept constant.

Luminosity levelling with offset suffers from several drawbacks. The most obvious one is that a different separation leads to a different beam–beam force being experienced. Therefore, the effect of one beam–beam encounter with a separation of a few orders of the r.m.s. beam size can change the tune spread appreciably, as shown in Fig. 3. This leads to a decrease in the extent of the stability region as a function of the offset, as shown in Fig. 4.

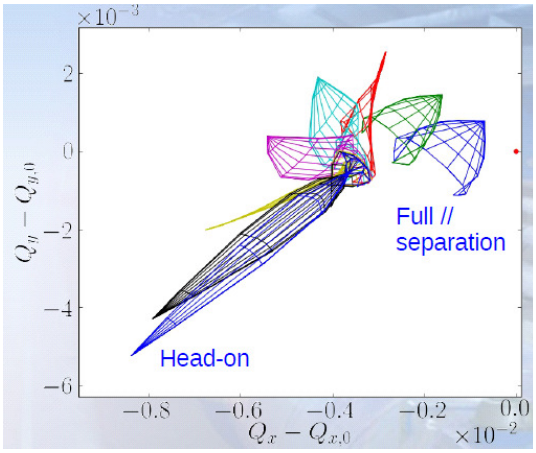

Figure 3: The tune footprints for different separations.

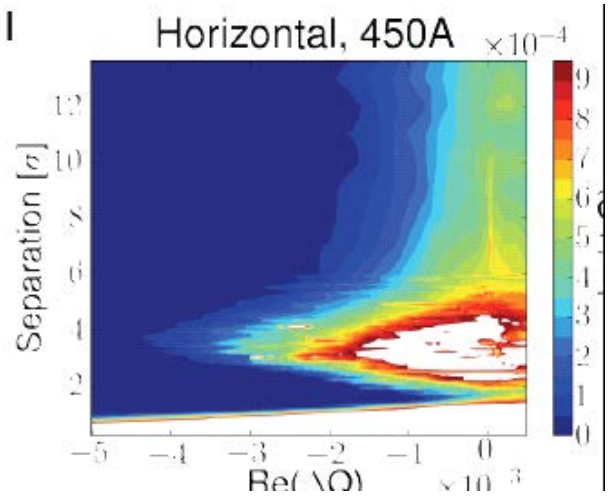

Figure 4: The real tune shift (the extent of the stability region) as a function of the offset.

Note that the minimum is hardly visible and lies just below the big maximum shown in white. The position and amplitude of this minimum depends on the collision schedule, the bunch intensities, emittances, octupole settings, and, in particular, the transverse offset at all the different IPs and the bunches experiencing head-on collisions. The fewer the head-on collisions, the smaller is the stability area shown in Fig. 4. In fact, as can be seen from the figure, there exists a critical separation at which the instability diagram is a minimum. Therefore, it is believed that levelling with transverse offset leads to serious complications in ensuring the stability of all bunches involved. Operationally [7], it is believed that such effects have already been observed in IP8 where, during a few fills, bunches that were colliding only in IP8 were lost and suffered substantial reductions in intensity, as shown in Fig. 5, together with the full separation inferred from the measured luminosity in IP1 and IP8, given in Fig. 6. Clearly, it is expected that this effect will become even worse when bunches collide in more IPs and not all of them experience head-on collisions. Other drawbacks include the fact that the tune shift keeps changing as the beams are brought into and out of collision, and that bunches become more sensitive to instabilities with respect to head-on collisions. The mere fact of going into collision with a separation could in itself give rise to instabilities or maximize their effect. Finally, there is a possible emittance growth resulting from the offsets used, as can be seen in Fig. 7.

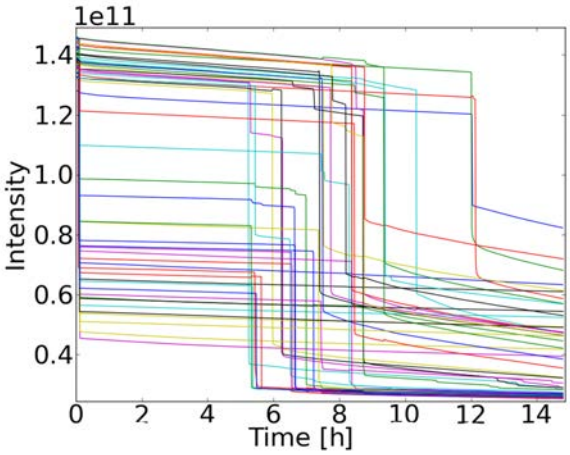

Figure 5: The intensity of the IP8 bunches.

CRAB CAVITY LEVELLING

Crab cavities have been used successfully, in electron colliders, to increase the luminosity back to the nominal value in the presence of a crossing angle. In a similar way, they may be used to perform luminosity levelling by 'spoiling' the luminosity initially, by artificially 'anti'-crabbing the beam, and subsequently by correcting for the natural exponential decrease in luminosity through the usual crabbing of the beam. The main advantages of using crab cavities are that all IPs are independent, and that it is possible to go back and forth easily by just changing the voltage of the cavities.

Luminosity levelling with crab cavities suffers from sev-

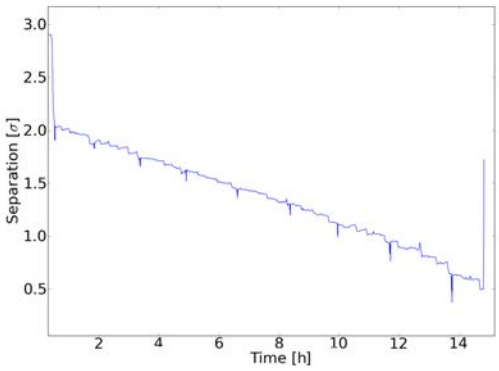

Figure 6: Full separation in IP8.

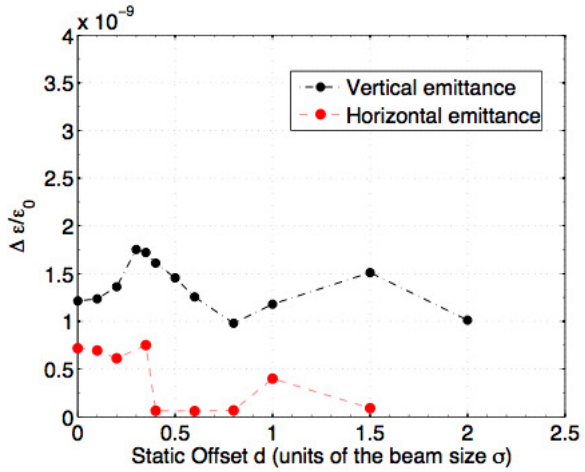

Figure 7: Emittance as a function of beam separation.

eral drawbacks. The most obvious one is that there is, so far, no experience with applying crab cavities to proton bunches at all, and this would most likely lead to additional problems from an operational point of view. The longitudinal vertex density changes with the levelled angle, giving rise to all the problems that were discussed above for offset levelling. Further, the tunes change with the crossing angle, and additional noise could be introduced on the colliding beams, hence reducing the reachable ξ_{bb}. Also, the jitter coming from the cavities needs to be dealt with. Differential phase jitter causes the two bunches to have a height mismatch, which can significantly reduce luminosity or cause the bunches to miss. Phase jitter means that the entry time of the centre of the bunch to is different for the cavities; hence dx is different for the two beams, as may be seen in Fig. 8.

Phase jitter between the cavities causes the two beams to be displaced in the x-plane, which can reduce the luminosity of the collision or even cause the bunches to miss each other completely. Further information about cavity phase jitter for the ILC can be found in [8].

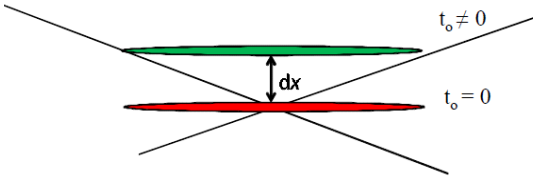

Figure 8: The effect of crab cavity jitter at the IP, where t_0 is the time at which the bunch enters the cavity.

β^* LEVELLING

Another option for doing luminosity levelling is to start with a beam the cross-section of which is larger than the nominal and then gradually squeeze it as the luminosity spontaneously reduces exponentially: this is known as β^* levelling. Now, the stability of the beam relies on impedance modes in the machine being Landau damped. This is done via a tune spread in the presence of beam–beam or other non-linearities in the machine. In the absence of colliding beams, octupoles are used to ensure the required tune spread for damping and, thereby, beam stability [9]. Beam–beam effects may be safely ignored before the β^* squeeze; however, during the squeeze, the β function grows dramatically in the region near the IP. This reduces the separation between the two beams even before they are brought into collision. The stability region before and after the squeeze with two different octupole settings is shown in Fig. 9.

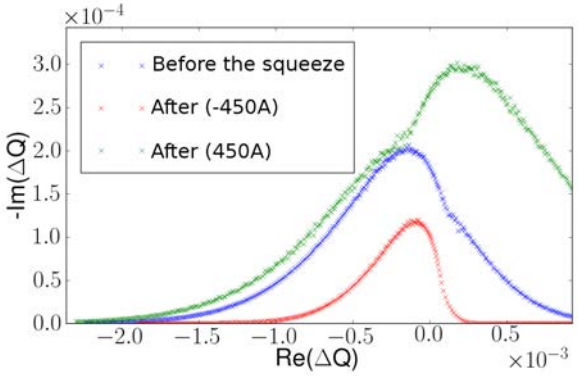

Figure 9: The horizontal stability diagram for different octupole settings before and after the β^* squeeze.

Clearly, it is preferable to use the positive octupole polarity; however, the strength required means that there are some detrimental effects associated with this, namely a reduction in dynamic aperture and feed-down effect. This is avoided if the squeeze is done when the beams are already colliding head on. This ensures a much larger tune spread and hence Landau damping, giving a much larger stability diagram, as shown in Fig. 10.

The principle of β^* levelling is illustrated in Fig. 11,

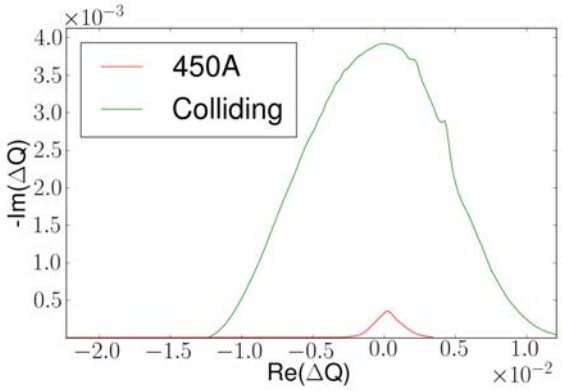

Figure 10: The horizontal stability diagram with and without head-on collision.

for an experiment done in 2012 [7] where the beam was slowly squeezed, as a function of time, and the luminosity increased. Physically, there is no difference between this and keeping the luminosity constant, as it naturally degrades. All parameters, such as beam size, tunes, and orbit, should be monitored while the luminosity is being squeezed. The main advantages are as follows: there is a constant longitudinal vertex density for the experiments; the tunes do not change and are constant over the fill; and it is more stable with the largest area of Landau damping. As

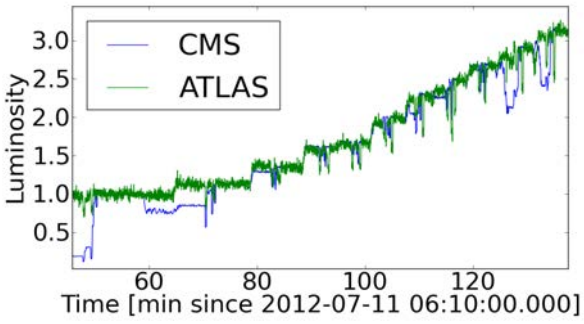

Figure 11: The luminosity evolution during fill 2828.

the tune spread from head-on beam–beam does not depend on β^*, leveling with it would allow a constant stability diagram to be maintained during the procedure, as opposed to what happens when the levelling is done with just offset. Figure 12 shows a comparison of the measured luminosity reduction factors when doing β^* levelling for the experiment performed at the LHC in 2012 [7], both at CMS and ATLAS, as well as the expected reduction. The principal drawbacks are due to the orbit. This has to be kept constant during the squeeze, as the beams must be kept in collision, which means that a feed-forward on it is required for robustness from an operational point of view and could require several changes from normal operations.

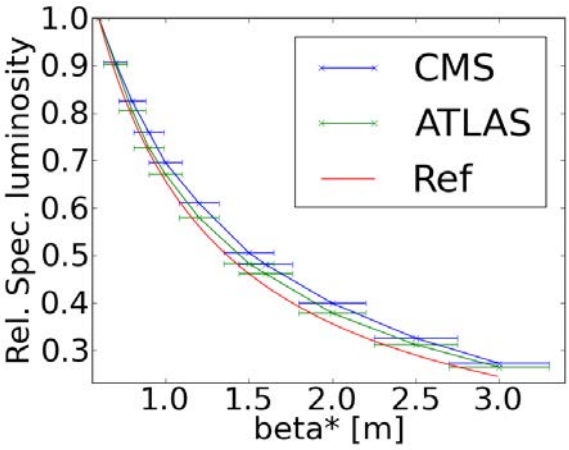

Figure 12: The measured luminosity reduction factor at CMS and ATLAS, compared to expectations.

OTHER LEVELLING POSSIBILITIES

Several other possibilities exist, and these are listed briefly below, Some of them are very new and have not been fully evaluated yet, while others still require experimental verification and further studies of their viability.

- *Longitudinal cogging*: This means introducing a time delay of the order of a couple of RF periods longitudinally, thereby ensuring that there is only a partial overlap of the two colliding bunches at the IP. So far, only 1 or 5 RF periods have been implemented experimentally. It appears to be a relatively easy option to implement; however, it means that levelling is done at all IPs simultaneously and this is very restrictive for the experiments. Longitudinal cogging also moves the luminous region longitudinally.

- *The large crossing (Piwinski) angle option*: This is where the levelling is actually done with a variation of the crossing angle. This option also varies the length of the luminous region according to the crossing angle.

- *The flat beam option*: This has been proposed recently [10] and involves doing the levelling in one plane only, the same as the crossing angle plane. This means that the tune shift in the other plane can be kept constant and the collimators do not have to move much, which could otherwise lead to safety issues.

DISCUSSION

Various scenarios for luminosity levelling, all valid working options, have been presented and their merits and drawbacks have been discussed. The easiest to implement is the offset option; however, this could lead to instabilities. Crab cavities introduce an additional complexity,

which could turn out to be very non-trivial. There is also no experience of crab cavities and proton bunches, and the cavities could also introduce a substantial jitter. Several other options, such as levelling with a crossing angle, flat beam options, or longitudinal cogging, have also been discussed. However, it appears that β^* levelling, possibly together with some offset as well, is the most promising option, as it appears to satisfy most of the requirements, both from the experiments' point of view and operationally. The main problem with β^* levelling is that the orbit has to be kept constant as the levelling is being done, and this may be rather complex from an operational point of view.

Ultimately, the most important thing that will determine exactly how the luminosity shall be levelled, both at the LHC and in possible new projects [11], is the operational simplicity with which the method can be implemented, together with the experimental requirements and constraints.

ACKNOWLEDGEMENTS

The authors would like to thank the Operation group for all the support during the testing of the β^* levelling experiments, in particular W. Herr, J. Wenninger, S. Redaelli, and M. Lamont.

REFERENCES

[1] W. Herr and B. Muratori, "Concept of Luminosity," in Proc. CERN Accelerator School, Intermediate Level Course, Zeuthen, Germany, 2003, CERN-2006-002 (2006).

[2] B. Muratori, "Luminosity and Luminous Region Calculations for the LHC," LHC Project Note 301 (2002).

[3] G. Papotti, "Observations of Beam–Beam Effects in the LHC," these proceedings.

[4] R. Jacobsson, "Needs and Requirements from the LHC Physics Experiments," these proceedings.

[5] D. Jacquet, "Implementation and Experience with Luminosity Levelling with Offset Beams," these proceedings.

[6] R. Giachino, "Diagnostics Needs for Beam–Beam Studies and Optimization," these proceedings.

[7] X. Buffat et al., "Results of β^* Luminosity Leveling MD," CERN-ATS-Note-2012-071 MD (2012).

[8] A. Dexter et al., "ILC Crab Cavity Phase Control System Development and Synchronisation Testing in a Vertical Cryostat Facility," EUROTeV-Report-2008-073 (2008).

[9] J.P. Koutchouk and F. Ruggiero, "A Summary on Landau Octupoles for the LHC," LHC Project Note 163 (1998).

[10] A. Burov, "Circular Modes," these proceedings.

[11] T. Pieloni, "Beam–Beam Studies in the LHC and New Projects," these proceedings.

Published by CERN in the Proceedings of the ICFA Mini-Workshop on Beam–Beam Effects in Hadron Colliders,
CERN, Geneva, Switzerland, 18–22 March 2013, edited by W. Herr and G. Papotti, CERN–2014–004 (CERN, Geneva, 2014)

IMPLEMENTATION AND EXPERIENCE WITH LUMINOSITY LEVELLING WITH OFFSET BEAM

F. Follin, D. Jacquet, CERN, Geneva, Switzerland

Abstract

The practice of luminosity levelling with an offset beam has been used as a routine operation in the LHC since 2011. This paper will describe how it has been implemented and what has been the operational experience with the system.

INTRODUCTION

The LHC has many experiments, all with different objectives and different luminosity needs. CMS and ATLAS are working with a high-luminosity beam (8×10^{33} cm^{-2} s^{-1} in 2012), whereas LHCb's optimal luminosity is 4×10^{32} cm^{-2} s^{-1} and ALICE's working point is around 10^{30} cm^{-2} s^{-1}. Limiting the luminosity and the pile-up in LHCb and ALICE is essential for data quality [1]. High luminosity could also be responsible for premature ageing of their detector. For ALICE, detectors could also be damaged by high luminosity peak.

The β^* value and the number of collisions at each interaction point are optimized for the experiments' needs, but this is not enough to cover for the large range of luminosity needs. In addition, the integrated luminosity for these experiments has to be maximized and the peak luminosity kept under control at the same time. The solution is luminosity levelling.

Among all the possible levelling techniques [2], the levelling by transverse beam offset has been chosen for its flexibility and large range, and the relative simplicity of its implementation. In 2011, the levelling was done manually by the operators before being automated from 2012.

IMPLEMENTATION IN THE LHC[3]

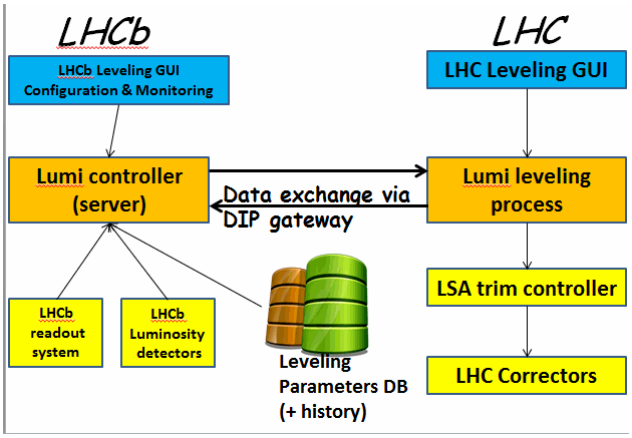

Figure 1: Levelling implementation in LHCb and in LHC.

Control of the levelling has to be implemented, both on the experiment's side and on the LHC side. For example, in the LHCb, a server is responsible for luminosity control. From the LHCb luminosity detectors and LHCb readout system the server publishes the current luminosity to the LHC levelling process, together with the other levelling parameters that are stored in a database with a complete history. A user interface in the LHCb control room has been implemented for levelling monitoring and configuration. The levelling is then completely controlled by the experiments to fulfil their needs (Fig. 1).

Data Exchange Via DIP Gateway

DIP is the data interexchange protocol that is used for all communication between the LHC and the experiments. For the levelling it is used by the experiments to publish the levelling parameters that have to be used by the levelling process. These parameters are the following:

- **Target luminosity** [10^{30} cm^{-2} s^{-1}]: LHCb proton typical target = 400 [10^{30} cm^{-2} s^{-1}]; ALICE pPb typical target = 100 [10^{27} cm^{-2} s^{-1}]
- **Instant luminosity** [10^{30} cm^{-2} s^{-1}]
- **Leveling step size** [σ] (optional): LHCb step size during ramp lumi = 0.2 σ (10.3 μm); LHCb step size when stable lumi= 0.03 σ (1.5 μm)
- **Data quality** (if bad quality, levelling not permitted)
- **Levelling request** (if no request. levelling not permitted)

The LHC levelling application publishes via DIP the levelling status and the status of the crossing plane optimization to LHCb: as long as the crossing is not optimized, LHCb doesn't allow any luminosity levelling.

In the LHC, the luminosity levelling control is part of a more general application that includes also the automation of luminosity scans. The user interface displays the parameters published by the experiments and the instantaneous luminosity and target luminosity evolution with time, as shown in Figs. 2 and 3. The operation team can choose to use either the parameters published by the experiment or the parameters set locally via the user interface.

The levelling algorithm (Fig. 4) is based on a feedback loop on the instantaneous luminosity. The levelling is started by the LHC operation team via the user interface. The instantaneous luminosity is published by the experiments via DIP, the levelling controller does an averaging over several measurements and checks the stability. If the luminosity is in the range defined by the experiments, the measurement loop continues, otherwise a manual action from the LHC operator is requested to changing the separation between the two beams.

978-92-9083-404-5, 0007-8328 –
http://dx.doi.org/10.5170/CERN–2014–004.183

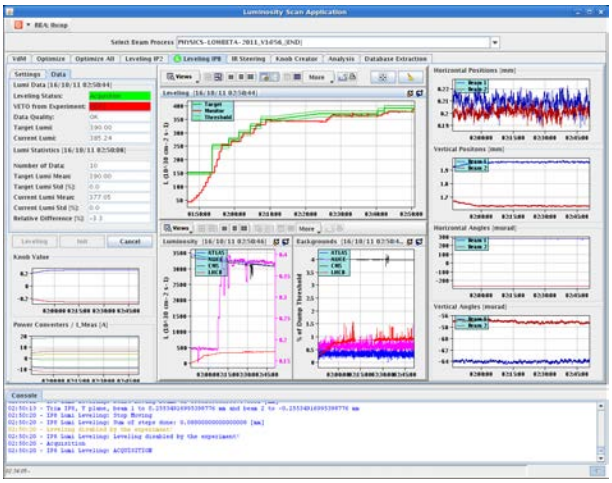

Figure 2: Luminosity scan application.

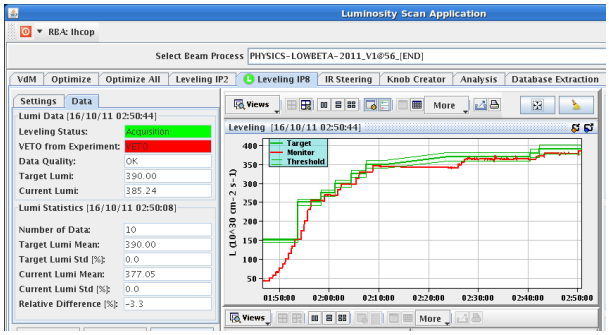

Figure 3: Detail on LHCb levelling control.

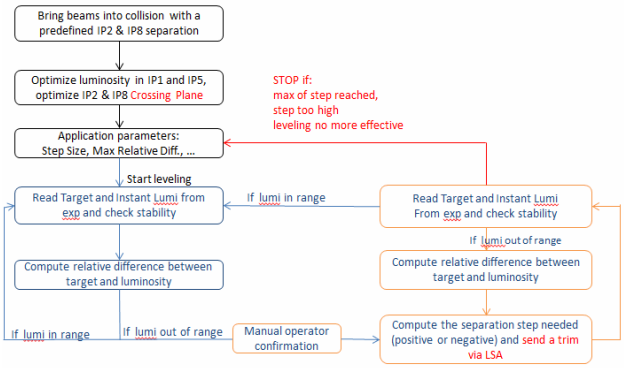

Figure 4: Levelling algorithm.

In current operation, the step size is taken from the experiment's published parameters. After the trim of beam separation, the luminosity reading is checked for stability and whether the value increased or decreased according to the need. If required, the step is undone and inverted. Beams are moved until the luminosity has been pushed within the limits defined by the experiments. When approaching the target, the levelling step is reduced automatically by the algorithm to avoid luminosity overshoot.

The levelling is automatically stopped in the following cases:

- The predefined maximum number of steps has been reached.
- The levelling step is too high
- The levelling is not efficient anymore: beams are in a fully head-on configuration.

Levelling and LSA

LSA is the software infrastructure for CERN accelerator control. In LSA database, all the LHC parameters are defined. A hierarchy system links beam parameters to hardware parameters and the rules to computes their values are programmed in the trim package. High level parameters (i.e. tune, beam position at IPs, chromaticity) are called knobs and represent a property of the beams. Their values are change in operation to optimize the beam or change its property and this trim is propagated to the hardware level, i.e. a new current value for a group of magnets.

To change the luminosity, the levelling process computes the step size from sigma to millimetres. It uses the LSA trim package (Fig. 5) and changes the value of knobs that define the beam position in horizontal and vertical plane.

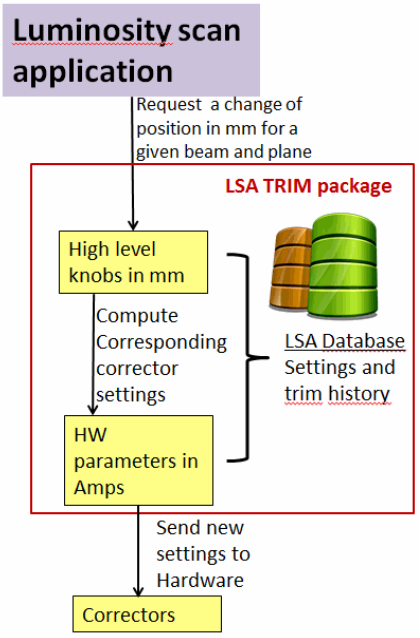

Figure 5: Levelling and LSA trim package.

In LSA, four knobs per IP are defined in units of mm to move each beam in the horizontal or the vertical planes (Fig. 6). Fore correctors are used to control the beam position and angle at the interaction point for a given beam and plane. Each time a new beam position is requested by the levelling, LSA compute the new current in these correctors. Knobs also exist to change the angle in μrad units, but in operation the angle at interaction points is kept to 0. Every settings modification is stored in the LSA database and can be retrieved thanks to the trim history.

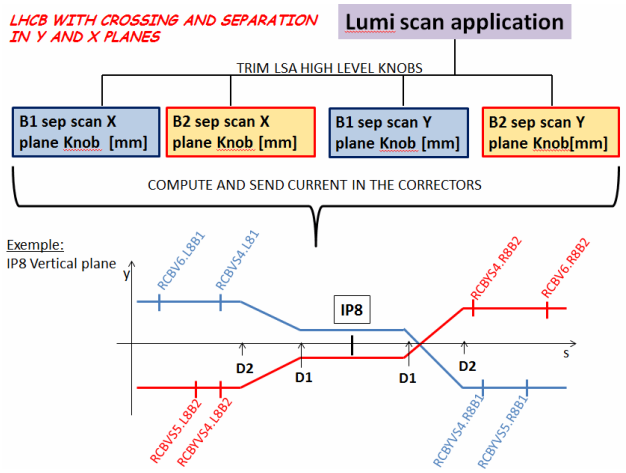

Figure 6: Separation knobs for LHCb.

In 2012, collisions at LHCb were established with a so-called 'tilted' crossing angle to ease the re-setup required at every spectrometer polarity change. The parameter space had to be adapted accordingly, so that higher level knobs were created to move the beams in the crossing and levelling planes. For a given beam, both horizontal and vertical knobs are combined now to move the beam in crossing or levelling plane (Fig. 7).

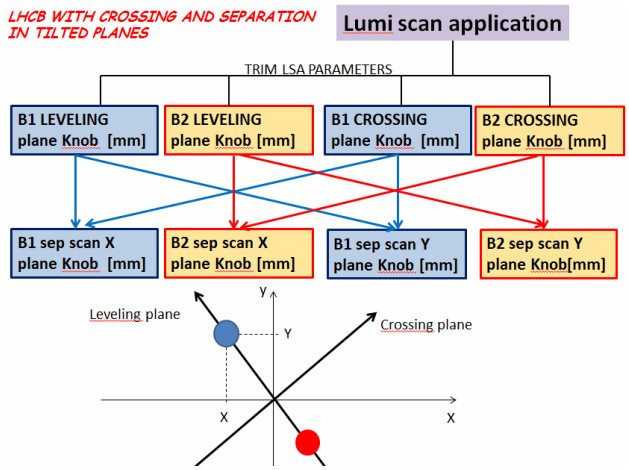

Figure 7: Levelling knobs with LHCb tilted plane.

OPERATIONAL EXPERIENCE

On 21 April 2011, the luminosity levelling in LHCb was used for the first time in operation. It was followed by the ALICE experiment in May 2011. Thanks to the levelling, the year objective of 1 fb^{-1} integrated luminosity for LHCb was already reached in October 2011, well before the end of the proton run.

In 2012, with the increase of the bunch intensity, the levelling in LHCb was needed for each fill. ALICE chose to run on collisions with satellites, to reduce its luminosity. The levelling was nevertheless needed from time to time depending on the satellite intensity.

The levelling was also prepared and tested for ATLAS and CMS in case the high pileup would become a data quality limitation for these experiments.

In 2013, with the proton–ions run, the levelling was used in ALICE, first during the few days of low luminosity run to keep the luminosity very low and constant. Then at the beginning of each fill to ensure that the luminosity stays beyond the limit requested by ALICE.

Weakness

The levelling worked very well with no major issues during two years. Nevertheless, some weakness has been identified:

- The DIP gateway is not always reliable enough and fails sometimes to publish data: this impairs the levelling, as the instantaneous luminosity is not received by the application.
- The luminosity controlled by offset levelling is very sensitive to orbit corrections that are applied regularly during physics to keep the other interaction points at their optimum luminosity. Orbit correction can push the luminosity beyond the limit and in extreme cases trip detectors in LHCb. Even if this is not destructive, this should be avoided, but no preventive mechanism has been implemented on the machine side for now.
- To enable very efficient luminosity control, the experiments have to properly publish the data, e.g. the luminosity target. This was always the case for LHCb, but for ALICE it could have been better managed to gain efficiency.
- For the moment, the algorithm always requires the LHC operator to confirm before starting to move the beams. From time to time this operator response is not immediate and the luminosity continues to go down for several minutes. This could be avoided if the process was fully automated. On the other hand, the operation team needs to check the machine condition before giving the OK for the levelling, for example that no orbit correction is being sent at the same time.

Observed instabilities

As already largely discussed in these proceedings [4,5], at the beginning of 2012 run, bunch-by-bunch instabilities were observed (see Figs. 8 and 9). They occurred either in the process of putting beams into collision or once already in stable beams. These instabilities only affected bunches colliding exclusively in IP8.

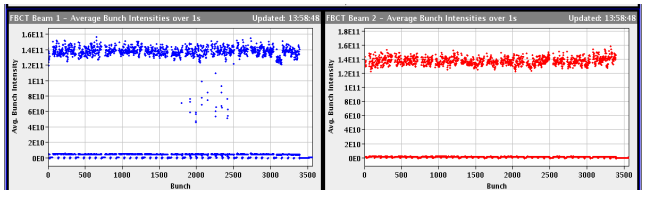

Figure 8: Single bunch instabilities at the beginning of collisions; we see on the bunch-by-bunch intensity plot the intensity drop on Beam 1 bunches colliding in IP8 only.

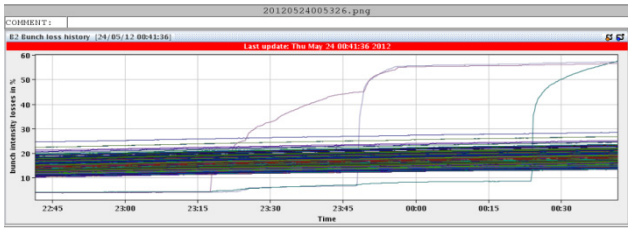

Figure 9: Bunch-by-bunch losses for Beam 2. Beam losses were observed for the three bunches colliding exclusively in IP8 due to instabilities during stable beams.

The first obvious cure that was put in place in operation was to use filling schemes without private bunches for LHCb. Bunches colliding in IP8 are also colliding in IP1 and IP5 and are stabilized by head-on landau damping.

Until the 2012 run, all IPs were put into collision at the same time. To reduce the instabilities observed during this process, this operation was split into two parts. First IP1 and IP5 are put in collision to stabilize the beam as soon as possible. Then the process to tilt the IP8 crossing plane and reduce beam separation in IP8 is played. These solutions have considerably reduced the instabilities.

Example: LHCb Levelling Proton Run

The levelling in IP8 is started after IP1 and IP5 are optimized. IP8 has to be optimized in the crossing plane before LHCb gives the permit to start levelling (Fig.10).

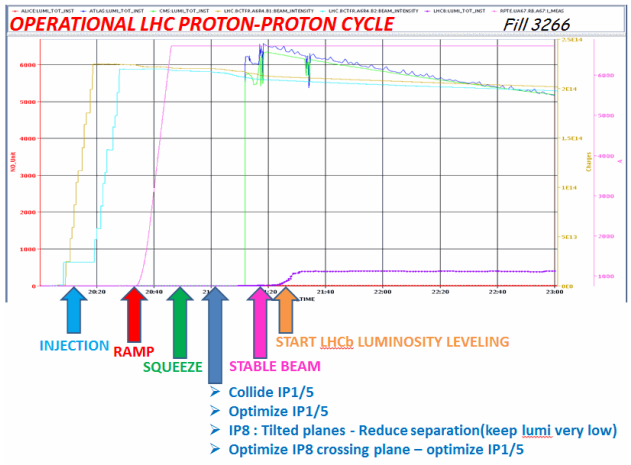

Figure 10: Complete LHC cycle from injection to stable beams.

Figure 11 shows that the initial luminosity of LHCb is very low (less than 10% of the target luminosity). Once the levelling is started, LHCb publishes an intermediate target and request big steps of 0.2 σ in order to reach quickly the target. This time of progressive luminosity increase also allows the conditioning of some detectors. One can also observe that when approaching the target, the application automatically reduces the step size to avoid overshoot.

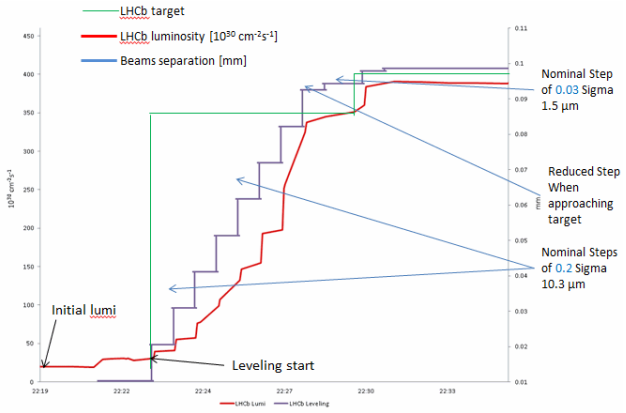

Figure 11: Beginning of levelling process.

After the intermediate target, LHCb publishes the final target that will be used for the rest of the fill. The requested step size is then 0.03 σ to guarantee a maximum stability of the luminosity (Fig. 12).

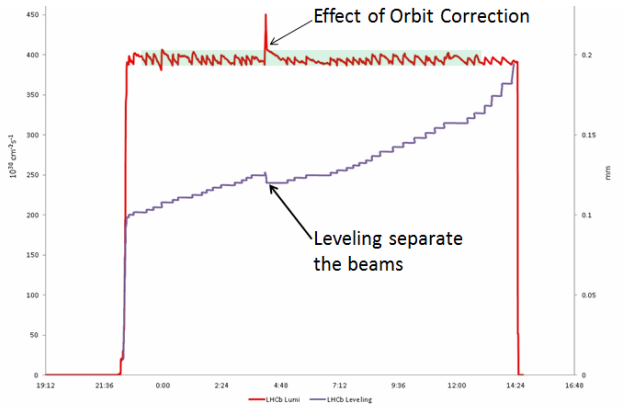

Figure 12: Effect of an orbit correction on the luminosity of LHCb.

Example: ALICE Levelling Proton–ion Run

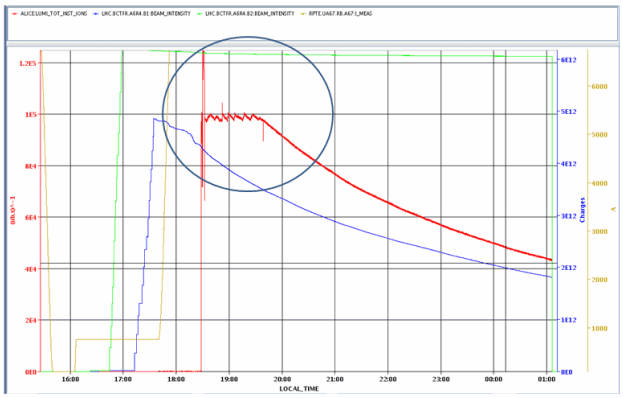

Figure 13: A proton–ion fill and ALICE's luminosity evolution.

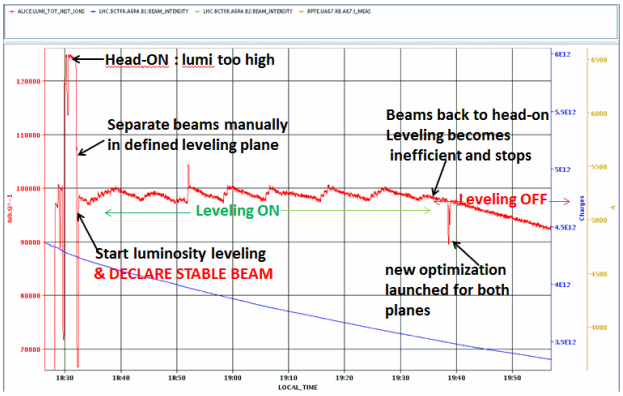

Figure 14: Zoom on ALICE luminosity evolution at the beginning of collisions.

In the example shown in Figs. 13 and 14, during proton–ions physics, ALICE arrives in collision head on with a luminosity higher than the maximum limit. The beams are manually separated until the luminosity is below the target. Then Stable Beams is declared and ALICE levelling started. Luminosity is maintained at the target by the levelling until the beams are back to a head-on configuration, at which time the levelling stops because the luminosity cannot be increased anymore by transversely displacing the beams. The operation team launches a new optimization of IP2 in both planes. The luminosity follows then its natural decay for the rest of the fill.

CONCLUSION

Luminosity levelling with offset beam has been part of the routine operation since 2011. It allows maximization of the integrated luminosity while keeping the peak luminosity and pileup at the optimum value for the detectors performances. Thanks to the levelling, more than 2 fb^{-1} of exploitable data has been delivered to LHCb in 2012. With 2012 operational conditions, the beam–beam instabilities were under control if using filling schemes with no private bunches for LHCb to ensure head-on landau damping.

REFERENCES

[1] R. Jacobsson. “Needs and requirements from the LHC physics experiments,” these proceedings.
[2] B. Muratori and T. Pieloni, “Luminosity levelling techniques for the LHC,” these proceedings.
[3] R. Alemany and F. Follin “Luminosity levelling requirements in IP2 and IP8,” EDMS doc 1133551.
[4] G. Papotti “Observation of beam-beam effects in the LHC,” these proceedings.
[5] X. Buffat. “Consequence of missing collisions – beam stability and landau damping,” these proceedings.

Published by CERN in the Proceedings of the ICFA Mini-Workshop on Beam–Beam Effects in Hadron Colliders,
CERN, Geneva, Switzerland, 18–22 March 2013, edited by W. Herr and G. Papotti, CERN–2014–004 (CERN, Geneva, 2014)

DIAGNOSTICS NEEDS FOR BEAM–BEAM STUDIES AND OPTIMIZATION

R. Giachino, CERN, Geneva, Switzerland

Abstract

During the recent years of LHC operation, we analysed the situation of beam instrumentation and the need to optimize it for beam–beam studies. The most important beam instrumentation devices will be highlighted and modifications or optimizations will be suggested. A complete wish list will be presented to make sure we will be ready after LS1 (Long Shutdown 1) to study the beam–beam effect in a more complete way.

INTRODUCTION

The LHC beam–beam studies during the last three years have been very fruitful, mainly thanks to machine availability and the preparation of the beams at the injectors. The help of experts in the SPS and the CPS complex to obtain very intense bunch with low emittance were the important prerequisites to study the head-on beam–beam phenomena in the LHC. A full set of measurements has taken place in the LHC, for example to study beam–beam losses for decreasing crossing angle [1], to overcome instabilities due to the loss of Landau damping [2, 3] and to have a detailed measurement of the chromaticity and its possible bunch-by-bunch differences.

During these studies, we have heavily used the beam instrumentation devices and we could see that some important instrumentation was missing or not yet operational for beam–beam granularity measurements.

MOTIVATION

Beam instrumentation is extremely important for beam –beam studies, e.g. in dedicated study of instabilities caused by beam–beam effects and data analysis to understand the phenomena. An ambitious target would be to have a bunch-by-bunch measurement of tune, chromaticity, intensity and transverse emittance. In order to control the beam stability we need to measure the turn-by-turn bunch position to determine the rise time and the frequency of the instability. This would allow us to measure and determine which mode is unstable, which instability type is present, as well as whether it is single/coupled bunch, single/coupled beam. An increased control of the stability would also help to understand the cause of the instability, e.g. impedance, electron cloud, beam–beam effect or a combination of the above phenomena. Another important achievement toward a better stability control would be to determine which mode is present. The ADT future development might allow us to measure the two beams synchronized in time (at the turn level). The new head tail monitor could give access to intra-bunch motion and a reliable, continuous chromaticity measurement. Finally, an interesting study could be to look into combined beam–beam/impedance modes (Fig. 1).

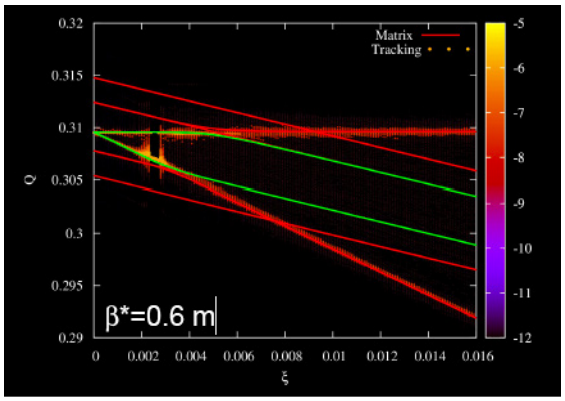

Figure 1: Instability resulting from coupling beam–beam/impedance modes [4].

Another important reason for bunch-by-bunch measurement is to be able to characterize bunch parameters from the beam–beam perspective and correlate them to luminosity lifetime degradation. If we compare this to simulation and try to understand the process, we could reduce the trial and error method and improve optimization of the luminosity lifetime. A working point optimization gave a 15–20% reduced emittance growth over the first 15 minutes in HEP stores in Tevatron Run II as the beam moved away from 5th and 12th order resonance [5]. The parameter space to scan is large, and tune, chromaticity, octupoles and transverse damper settings are the most important candidates to improve beam stability and luminosity lifetime (Fig. 2).

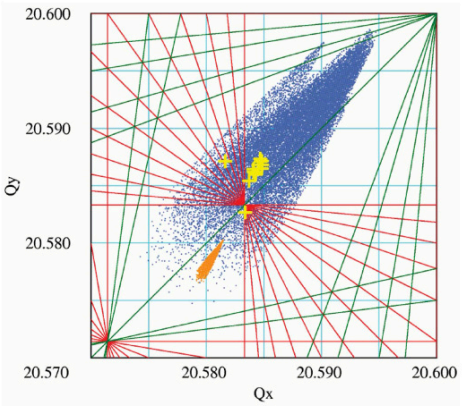

Figure 2: Tevatron tune footprint.

978-92-9083-404-5, 0007-8328
http://dx.doi.org/10.5170/CERN–2014–004.189

During regular operation, the rate of change of beam parameters is slow and therefore measurements with a sampling of a few seconds to one minute would be suitable.

In the squeeze or in the collision beam processes, very fast instabilities can develop. We need a triggered measurement lasting for a few seconds to one minute to record these instabilities. A snapshot of the machine parameters and bunch-by-bunch measurement covering the full collision beam process (of length ~60 s) would be the adequate tool to observe and understand the nature of the instabilities.

If instabilities due to beam–beam effects provoke a beam dump, the only observable signal will be available from the post mortem system (data from different measurement systems is recorded on circular buffers, frozen and exported into a beam dump event in the database). A possible improvement will be to extend the buffer to 1 s.

We stress the need for:

- High resolution, as the instabilities are fast (rise times can be well below 200 turns).
- Large data buffers, to acquire measurements for all bunches for a maximum number of turns.
- A triggering system, to be able to freeze buffers and acquire data from 1 to 2 seconds before the instabilities are detected (for example for tune measurements, BBQ, beam losses, BLMs, etc.), and maximize the chance that useful data to understand the instabilities are recorded when they occur.

OBSERVATION OF INSTABILITIES

In 2012, the optimization of the machine performance was done by using small emittance beams, small β*, tight collimator settings (leading to large impedance) and high intensity per bunch. This brought along instabilities (Fig. 3), which started to limit the LHC efficiency and physics production. If we can measure tune and chromaticity for specific bunches we will be able to understand better the origin of these instabilities and possibly cure them [6].

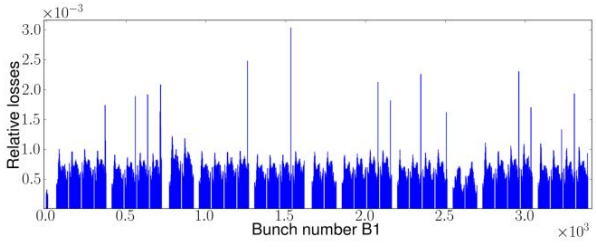

Figure 3: Bunch-by-bunch relative losses during the end of squeeze instability: only some bunches are affected by the instability and suffer losses that are more than twice those suffered by other bunches.

Instabilities in 2012 were essentially observed by BLM, BBQ, MIM (multiband-instability-monitor) and transverse damper beam position signals. The new head–tail monitors will enable measurement of higher frequencies, and thus to look inside the bunch and understand the type of instability by analysing the transverse motion. Its operational development is paramount as it is the only device that can observe the mode of instability (Fig. 4).

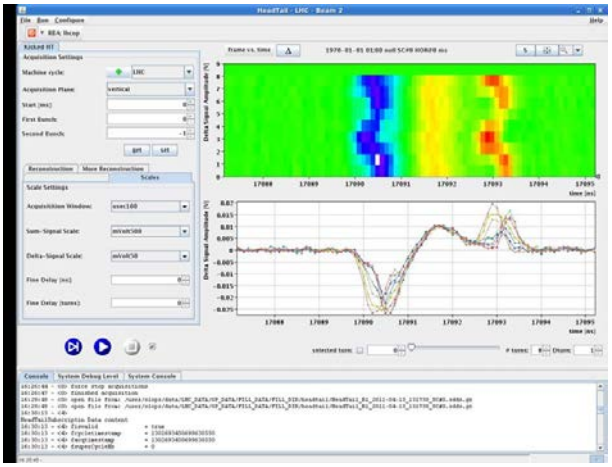

Figure 4: Head–tail monitor.

The tune measurement is vital for beam–beam studies. The BBQ system facilitated a reliable commissioning and operation of the LHC. Single bunch tunes could be measured by both BBQ and Schottky systems. During the 2012 proton run, the Schottky signal was reliable only on B1H for single and multi-bunch measurements at injection and stable beams. Unfortunately, large coherent signals saturated the pre-amplifiers in the other systems, rendering the signals unusable. The Schottky system is one of the systems capable of measuring bunch-by-bunch tune and chromaticity in a non-invasive, independent way. We strongly hope to have reliable tune and chromaticity measurements available after LS1. Schottky systems have been used successfully in other machines in the past (SPS, Tevatron, RHIC).

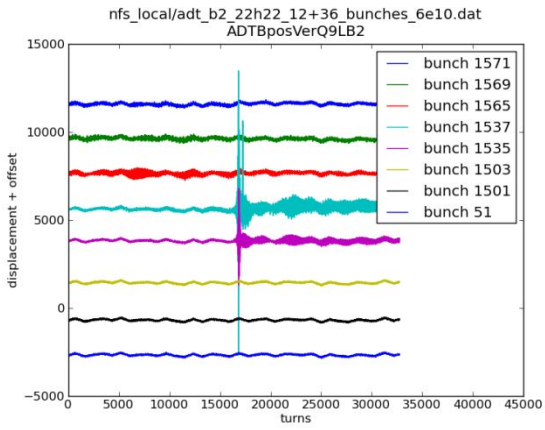

Figure 5: Instability at injection for different bunches during electron-cloud scrubbing studies, as measured by the transverse damper pickups. Only two bunches out of eight are affected by the instability.

The buffer on the transverse damper (ADT) beam position pickups can at present measure only up to 72 turns, but a higher number would be highly appreciated. If we could measure more than 72 turns, we could start to determine the frequency, mode pattern and rise time of the instability (see the example in Fig. 5, where the positions of only eight bunches were recorded to increase the available number of turns).

Chromaticity measurement and control is extremely important in a proton–proton collider. The LHC chromaticity should be nominally set to +2, but to guarantee this we need the chromaticity measurement to be precise within 1 unit to control this important machine parameter. The past LHC run with high-energy instabilities reinforced this need. The BBQ is the only instrument capable of measuring the chromaticity up to this moment, by means of an RF frequency modulation. The Schottky development should be encouraged to obtain reliable and continuous bunch-by-bunch tune and chromaticity measurements at any time to understand the instabilities issues and the differences between bunches (e.g. between Pacman bunches) [7] (Fig. 6).

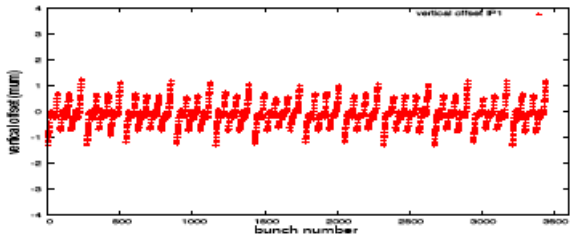

Figure 6: Vertical offset of the luminous region as measured by the ATLAS detector during a physics fill. The offset depends on the position of the bunch in the train [7].

The beam transfer function (BTF) could be useful at LHC to understand the tune spread. For example, at RHIC a BTF measurement is performed in stable beams every 15 minutes (Fig. 7). With this tool, we could study beam–beam coherent modes, normally Landau damped and not visible on BBQ measurement. We have enough simulation knowledge to start exploiting this technique. The LHC PLL could provide similar data after dedicated commissioning.

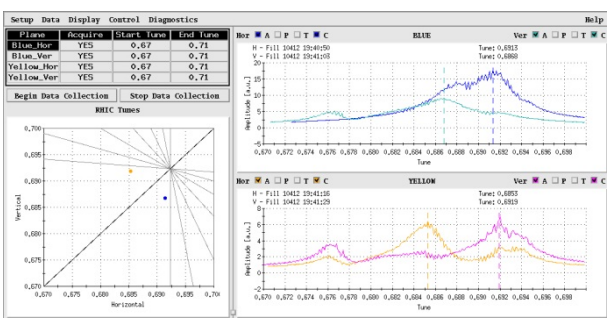

Figure 7: RHIC BTF measurements during stable beams.

Reliable, continuous, bunch-by-bunch emittance measurements are paramount to be able to study the beam–beam phenomena in the LHC.

In 2012. the BSRT (synchrotron light telescopes) was the only instrument capable of performing continuous, non-invasive, bunch-by-bunch measurements. Calibration was done with wire scanners. In the future we should improve the knowledge of the machine optics to reduce the uncertainty of this measurement. Fast scans have been available since May 2012 (1380 bunches can be scanned in 7 minutes) and are very helpful for day-to-day operation and machine studies. A new server that can perform the scans automatically has been available since October 2012.

CONCLUSION

The beam–beam team would like to thank excellent collaboration with the Operation and Beam instrumentation groups. It allowed achievement of important results in the LHC beam–beam studies. To further investigate the origin of instabilities limiting the LHC performance, we would have to upgrade our instrumentation toward more bunch-by-bunch observation. These new tools will allow us to better control the LHC machine parameters, mitigate the instabilities, and optimize its operation and ultimately maximize the integrated luminosity.

LHC after LS1 will be a ‘new’ machine. After this important instrumentation upgrade we will be ready to face this new scenario.

ACKNOWLEDGMENTS

The author would like to thank the following persons for their help in the preparation of this paper: OP group, BI group, ABP group, and in particular G. Arduini, X. Buffat, T. Baer, R. Calaga, D. Jacquet, R. Jacobsoon, R. Jones, W. Herr, W. Hofle, M. Lamont, G. Papotti, T. Pieloni, B. Salvant, R. Steinhagen, G. Trad, D. Valuch and J. Wenninger.

REFERENCES

[1] W. Herr, “Long range beam–beam effects in the LHC,” these proceedings.
[2] G. Papotti, “Observation of beam–beam effects in the LHC,” these proceedings.
[3] X. Buffat, “Coherent beam–beam modes in the LHC,” these proceedings.
[4] S. White, “Beam–beam and impedance.” these proceedings.
[5] V. Shiltsev, “Experience with long range beam–beam effects in the Tevatron,” these proceedings.
[6] X .Buffat, “Operational considerations on the stability of colliding beams,” these proceedings.
[7] M. Schaumann, “Observed beam–beam induced orbit effect at LHC,” these proceedings.

Published by CERN in the Proceedings of the ICFA Mini-Workshop on Beam–Beam Effects in Hadron Colliders,
CERN, Geneva, Switzerland, 18–22 March 2013, edited by W. Herr and G. Papotti, CERN–2014–004 (CERN, Geneva, 2014)

OPERATIONAL CONSIDERATIONS ON THE STABILITY OF COLLIDING BEAMS

X. Buffat, EPFL, Lausanne, Switzerland; CERN, Geneva, Switzerland
W. Herr, T. Pieloni, CERN, Geneva, Switzerland

Abstract

While well studied in the absence of beam–beam and while colliding head-on, the stability of the LHC beams can be very critical in intermediate steps. During the squeeze, the long-range beam–beam interaction becomes a critical component of the beam's dynamics. Also, while the transverse separation at the interaction points is collapsed, the beam–beam forces change drastically, possibly deteriorating the beam's stability. Finally, during luminosity production, the configuration of the LHC in 2012 included few bunches without head-on collision in any of the interaction points having different stability properties. Stability diagrams are being evaluated numerically in these configurations in an attempt to explain instabilities observed in these phases during the 2012 proton run of the LHC.

INTRODUCTION

The LHC configuration changes significantly along a standard operational cycle. These different configurations have different implications from the point of view of beam stability; in particular, the effect of Beam–Beam (BB) interactions can be very different. The approach described in [1] is used to derive stability diagrams in the configurations encountered during the LHC run 2012 and the results are compared to the observations.

BETATRON SQUEEZE

Before the squeeze, BB interactions can be neglected. The stability is ensured by the transverse damper and amplitude detuning from the octupoles. They can be powered with up to $\sim$ 500 A, with either polarity. The resulting stability diagrams for each polarity are shown in Fig. 1. As the expected tune shifts in the LHC have negative real parts [2], the negative polarity is preferable in this configuration and therefore was chosen as the design value. However, going through the squeeze, the effect of the Long-Range BB (LRBB) encounters starts playing a significant role. As can be seen in Fig. 2, at the end of the squeeze, most of the LRBB interactions are already at the separation at which they will stay during luminosity production, the only difference being the separation orbit bump. As can be seen in Fig. 3, the stability diagram changes dramatically during the squeeze, in particular, the negative polarity is no longer preferable. Some instabilities at the end of the squeeze were attributed to this compensation and consequently the polarity was changed [3]. The benefit from the change of polarity could not be properly assessed as this

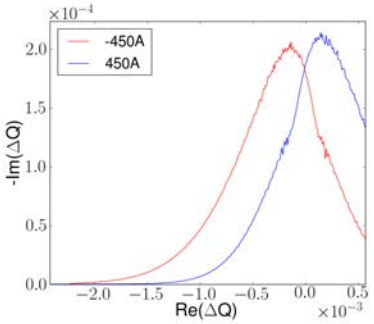

Figure 1: Stability diagrams from octupoles with both polarities.

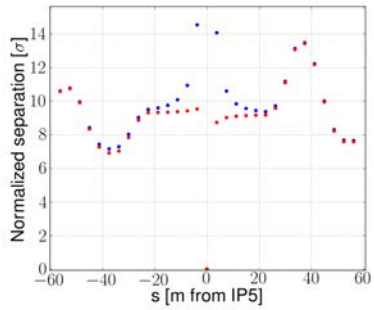

Figure 2: Normalized beam–beam separation in IP5 at the end of the squeeze (blue) and in collision (red).

change in the operational configurations appear alongside a large increase of the chromaticity, from 2 to 15 units, and the transverse feedback gain, from more than 100 turns to 50 turns. While these stabilizing techniques have allowed the machine performance to be increased, by reducing the number of dumps due to beam losses caused by coherent instabilities, they have not cured the instability as it was still clearly visible (Fig. 4). In this new configuration, however, it is clear that the modification of the tune spread due to LRBB can not explain the instabilities observed, as the stability diagram is larger at the end, with respect to the beginning of the squeeze at which the beams are stable.

Several investigations are currently ongoing to understand the instabilities at the end of the squeeze. In particular, the stability diagrams presented are not suited to describing the stability of multibunch modes in the presence bunch dependent amplitude detuning, nor are they suited to coherent beam–beam modes. These effects are currently

978-92-9083-404-5, 0007-8328 –
http://dx.doi.org/10.5170/CERN–2014–004.193

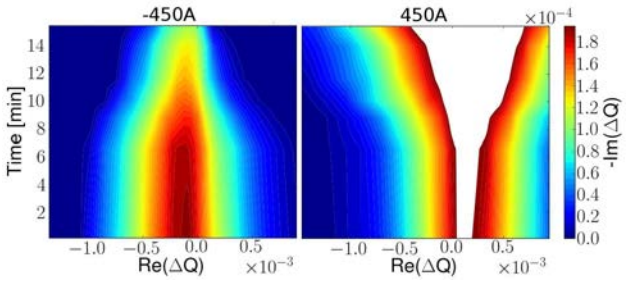

Figure 3: Stability diagram as a function of time during the squeeze for both octupole polarity (± 450 A). The β^*s at $t = 0$ are 11 m in IP1&5 and 10 m in IP2&8, at the end 0.6 m and 3 m respectively. This represents the most common bunch, with the largest number of LRBB interactions; the effect is similar but of lower amplitude for bunches with a lower number of LRBB.

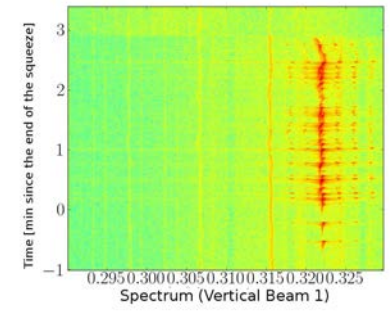

(a) BBQ

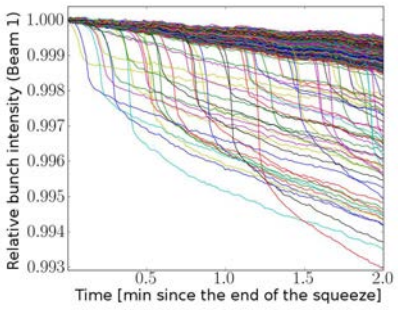

(b) FBCT

Figure 4: Typical observation of an instability at the end of the squeeze during fill 3250. The machine is filled with 1374 bunches per beam with $\sim 1.6 \cdot 10^{11}$ protons per bunch and emittances of $\sim 2.4 \cdot 10^{-6}$ μ m. The chromaticities are set to ~ 10 units, the transverse feedback gain to 50 turns and the octupoles powered with 533A. From $t = 1.8$ to 2.9 the beams are being brought to collision and are fully stabilized once colliding head-on.

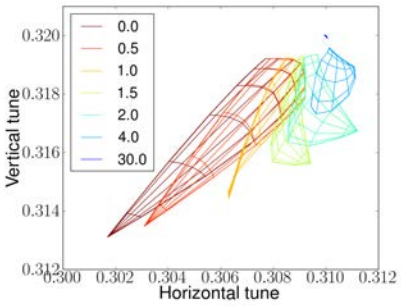

Figure 5: Example of tune footprint of a bunch colliding in IP1 with different separations in the horizontal plane.

studied using multiparticle tracking [4]. Other effects are also under study, such as external noise [1] or optics imperfections.

As in Fig. 4, it has been observed that the instability at the end of the squeeze is always well stabilized once the beams are colliding head-on, therefore it is considered to go through the squeeze with colliding beams in future scenarios [5]. As discussed in the section on luminosity production, this approach not only offers a cure for the instability, but also provides a significant margin for increased impedance or beam brightness.

BRINGING THE BEAMS INTO COLLISION

When the parallel separation is collapsed, in order to bring the beams into collision the tune shift and spread of the colliding bunches change sign as illustrated by Fig. 5, leading to a significant modification of the stability diagram. As shown by Fig. 6(a), the stability diagram is enhanced for separation in the order of 2 to 4σ and drastically reduced around 1.5σ. This minimum of stability depends significantly on the configuration considered and therefore can be very different for bunches having different numbers of LRBB or Head-On BB (HOBB). In this case, the reduction of the stability diagram is however not due to a compensation of tune spread as at the end of the squeeze, it is caused by a change of sign of the tune spread which leads to a systematic cancellation of nearby poles in the dispersion integral. Even if the minimum stability also exists, it is clear from Fig. 6(a) that the positive polarity of the octupole is also favourable in this configuration. One should however not forget that the stability must be ensured for all bunches; in particular, in most LHC configurations there exist some bunches with very few LRBB; the minimum stability for these bunches can still be very critical, as shown by Fig. 6(b).

There have been several observations of coherent instability during the process that brings the beams into collision during the 2012 run of the LHC, a spectrogram during such instability is shown in Fig. 7. The separations at

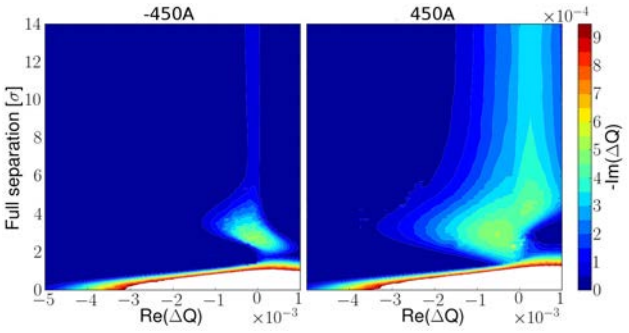

(a) With LRBB

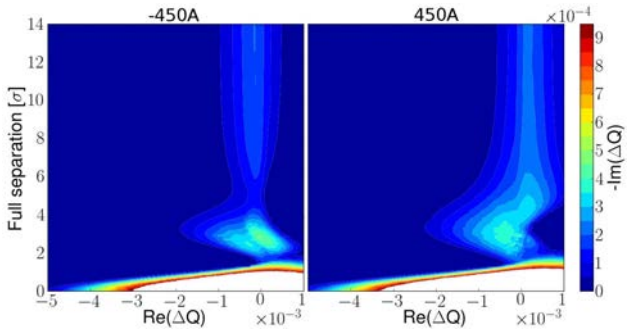

(b) Without LRBB

Figure 6: Stability diagram as a function of beam separation in IP1&5 for a bunch with either maximum number of LRBB or none, and both polarities of the octupoles.

which these instabilities occur is in qualitative accordance with the critical separation discussed above. It is however difficult to make quantitative comparison as many critical observables are not available with sufficient accuracy, such as chromaticities and bunch by bunch emittances. While small separations may be very critical in term of stability, it did not prevent collision in previous years. In addition to the increased impedance due to tighter collimator settings and increased beam brightness, a critical change is the implementation of the process that brings the beams into collision. As can be seen in Fig. 8(a), the implementation of this process included, in early 2012, a change of the crossing angle in IP8 [6], resulting in an extended time spent at critical separations. This could be avoided by a change in the implementation of the process that brings the beams to head-on collision as fast as possible before going through other manipulation (Fig. 8(b)). Other cures to such instability exist; multiparticle tracking simulations suggest that they are well damped by high positive chromaticity or high transverse feedback gain (thanks to a private communication by S. White in 2012). In particular, such instabilities were no longer observed in the LHC after a change of configuration to high chromaticity, high damper gain and positive polarity of the octupole. The short process could only be tested in this new configuration; there would be, however, an interest from the beam lifetime point of view in being able to run with lower chromaticity and damper gain, which, in this case, may be achieved by speeding up the

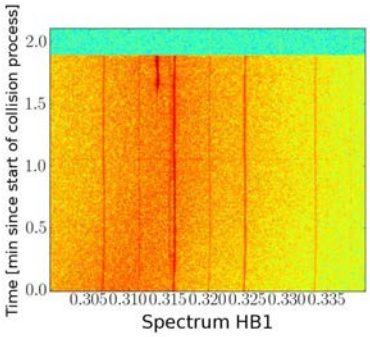

Figure 7: Spectrogram measured by the BBQ in the horizontal plane of Beam 1 during the collision process of fill 2808 (i.e. old implementation). An instability is visible at a time corresponding to separations around 2.3σ, the beams are then dumped due to beam losses.

collision process.

In case this should not suffice, the possibility to go into collision one after the other may be interesting. Indeed, as can be observed in Fig. 9, in this configuration the minimum stability is reached in one plane only. Whereas coupling is assumed to be negligible in our approach, simulation studies suggest that the stability of the two planes could be shared via non-linear coupling of the beam–beam force. It is important to note that even though the beams are separated in one plane only in the model, the machine imperfections create a separation in the other plane. In this configuration, it is important to keep this separation well corrected, as a separation in both planes at one IP would result in a situation similar to both IP1&5 simultaneously.

LUMINOSITY PRODUCTION

While colliding head-on, beam–beam is nominating the non-linearities undergone by the core of the beam and consequently provides the dominant contribution to the stability diagram. Fig. 10 compares stability diagrams from octupole, long-range and head-on; it is clear that HOBB collision is extremely efficient to providing stability, to the point that the stabilization techniques required before bringing the beams into collision are no longer required during luminosity production. This was however not so simple in the LHC configuration used in 2012. Indeed, luminosity in IP2 was provided by bunch-satellite collisions, which lead to an essentially inexistent HOBB contribution and IP8 luminosity was being levelled with a transverse offset. Therefore the only full HOBB collisions were in IP1&5, where non-colliding bunches are requested [7]. The complexity of this configuration is illustrated by Fig. 11, representing the tune footprints of different bunches existing simultaneously in the machine during luminosity production. The stability of each bunch is crucial as the loss of part of a single bunch is enough to create a dump of the whole beam. This enforces the usage of strong stabilizing techniques, in particular high chromaticity, high transverse feedback gain

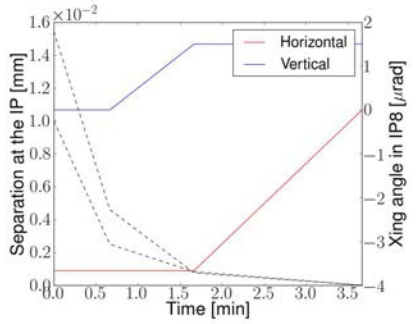

(a) Old process

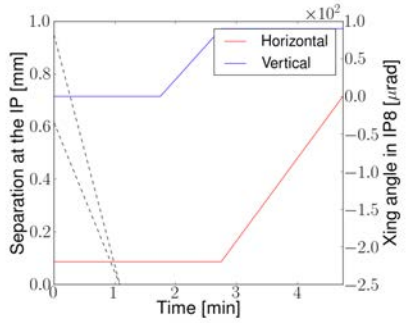

(b) New process

Figure 8: Two implementations of the process that brings the beams into collision and tilts the Xing angle in IP8.

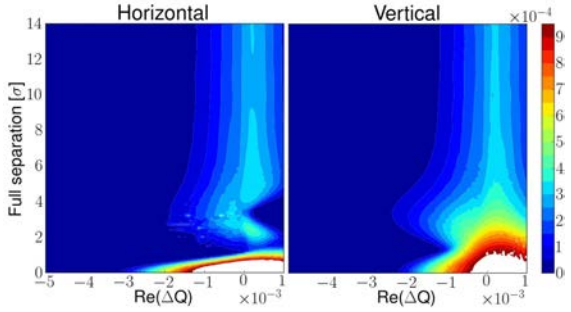

Figure 9: Stability diagram while collapsing the separation in IP1 only (horizontal separation).

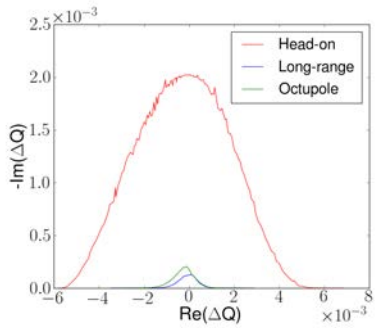

Figure 10: Comparison of stability diagrams from either octupoles powered with -450 A, LRBB in IP1&5 or HOBB in IP1&5.

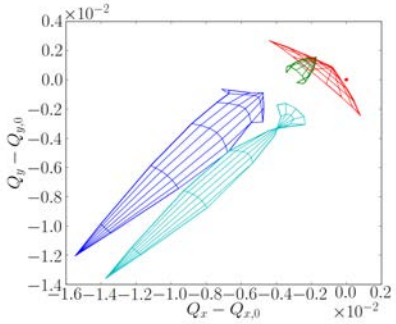

Figure 11: Example of tune footprints of different bunches present simultaneously in the machine during luminosity production.

and high octupole current, during luminosity production in order to stabilize bunches without head-on collision. In order to further optimize luminosity lifetime, it would be advisable to run in a configuration with one head-on collision for each bunch, allowing relaxation of the use of stabilizing techniques which are potentially harmful for the intensity lifetime and emittance growth of all bunches.

Levelling with a Transverse Offset

During the 2012 run of the LHC the luminosity was levelled with a transverse offset in IP8. While not harmful for most bunches having HOBB collision in IP1&5, this technique turned out to be critical for bunches without head-on collision. Indeed, the situation of these bunches is similar to the one described in Fig. 6(a), however the difference with respect to the process of bringing the beams into collision is that, in this case, the separation is varied in small steps and several minutes are spent at each separation, leaving time for a slow instability to develop. One observation of such an instability is shown in Figs. 12 and 13. In particular, when comparing the time at which the instabilities occurred (Fig. 12(a)) with the separation computed from measured luminosities (Fig. 13(b)), it appears that the full separation in IP8 at the time of the instabilities was between 0.9 and 1.6σ, consistent with the critical separations discussed previously. As can be seen in Fig. 12(b), the bunches colliding only in IP8 were located at the end of SPS trains, they were consequently PACMAN bunches, in other words they have a different number of LRBB. Moreover there is bunch-to-bunch variation of the intensity and emittances, which explains why different bunches became unstable at different separations. It is, however, difficult to make quantitative comparison with predications for each individual bunch as many critical parameters are not known to a sufficient precision, in particular the emittances.

CONCLUSION

Stability diagrams corresponding to different operational phases of the LHC were derived. It was found that a com-

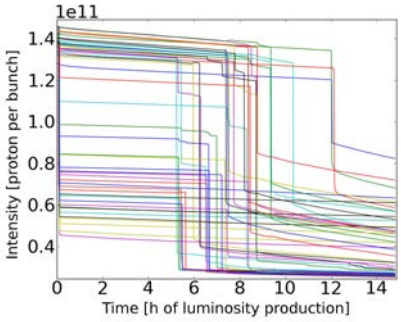

(a) Bunch intensity of IP8 private bunches

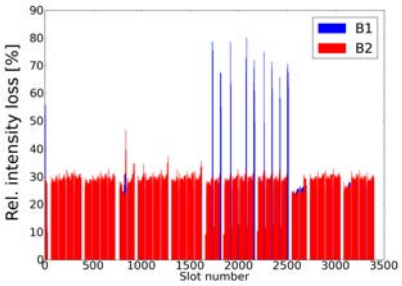

(b) Relative bunch losses during luminosity production

Figure 12: Measured bunch intensities during luminosity production of fill 2646.

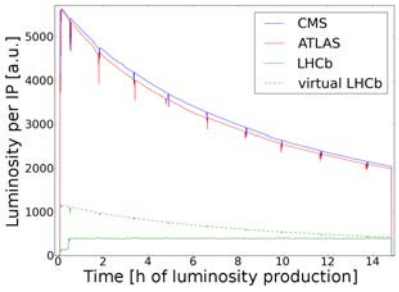

(a) Luminosity per IP

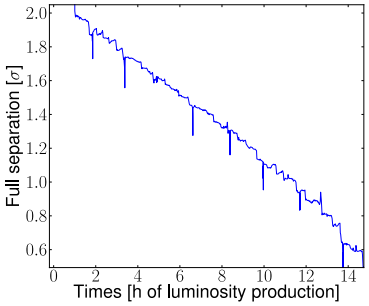

(b) Transverse separation in IP8

Figure 13: Measured luminosities during luminosity production of fill 2646. The virtual luminosity of IP8 is computed from luminosity in IP1&5, the resulting reduction factor is used to compute the full separation in IP8.

promise has to be made when choosing the polarity of the octupoles, the negative polarity providing a better stability at the beginning of the squeeze that degrades during the squeeze due to a partial compensation of the tune spread due to LRBB, as opposed to the positive polarity, which gives less stability at the beginning of the squeeze but rather increases during the squeeze. This effect could not, however, explain instabilities arising at the end of the squeeze, observed in the 2012 run of the LHC with both polarities.

It has been demonstrated that there exists a critical separation, in the order of 1σ, for which the stability diagram can be dramatically reduced. Observations of coherent instabilities while bringing the beams into collision and during luminosity levelling with a transverse offset are consistent with this effect.

HOBB tune spread is not only larger than the one provided by octupoles or LRBB, it is also dominant on the beam core, rather than the tails, which results in significantly larger stability diagrams. The effect of HOBB could be used to ensure the stability of all bunches in most configurations, in particular by going through the squeeze with colliding beams and ensuring at least one HOBB collision per bunch.

ACKNOWLEDGEMENTS

The authors would like to acknowledge G. Arduini, N. Mounet, S. White, B. Salvant, E. Métral, S. Redaelli and J. Wenninger for fruitful collaborations and discussions, as well as the LHC-OP crew, in particular G. Papotti and R. Giachino for their work.

REFERENCES

[1] X. Buffat *et al.*, "Stability Diagrams of Colliding Beams," these proceedings.

[2] N. Mounet, "The LHC Transverse Coupled Bunch Instability," EPFL Thèse No 5305 (2012).

[3] T. Pieloni *et al.*, "Beam Stability with Colliding Beams at 6.5 TeV," Proceedings of the 2012 Evian Workshop on LHC Beam Operation, Evian, 2012. https://indico.cern.ch/event/211614/

[4] S. White *et al.*, "Beam–Beam and Impedance," these proceedings.

[5] X. Buffat *et al.*, "Squeezing With Colliding Beams," Proceedings of the 2012 Evian Workshop on LHC Beam Operation, Evian, 2012. https://indico.cern.ch/event/211614/

[6] B. Holzer, "Spectrometer Operation in IR2&8," Proceedings of the 2012 Evian Workshop on LHC Beam Operation, Evian, 2012. https://indico.cern.ch/event/211614/

[7] R. Jacobsson, "Future Wishes and Constraints from Experiments at LHC," these proceedings.

Published by CERN in the Proceedings of the ICFA Mini-Workshop on Beam–Beam Effects in Hadron Colliders,
CERN, Geneva, Switzerland, 18–22 March 2013, edited by W. Herr and G. Papotti, CERN–2014–004 (CERN, Geneva, 2014)

OBSERVATIONS FROM LHC PROTON–PROTON PHYSICS OPERATION

M. Hostettler,* University of Bern, Switzerland
G. Papotti, CERN, Geneva, Switzerland

Abstract

This paper describes two distinct effects observed during the operation of the LHC in 2012: first, the impacts on beam parameter evolution of the end-of-squeeze instabilities encountered in the second half of the 2012 run; and, second, the very reproducible loss pattern of Beam 1 observed (while a similar pattern was negligible, if present at all, for Beam 2). Statistics for 2012 are provided and the impact on luminosity production is highlighted.

INTRODUCTION

The LHC Operational Cycle

The LHC operational cycle for proton physics consists of injecting beams of proton bunches from the injector complex into both rings, accelerating them from injection energy (450 GeV) to the flat-top energy (4 TeV in 2012), and bringing them into collisions. A full cycle, called a *fill*, is divided into different phases, which are commonly referred to as *beam modes*. This paper covers two effects observed in the part of the cycle after the acceleration phase, which consists of the following beam modes:

- *Squeeze*: The betatron squeeze, in which the currently separated beams are squeezed to the target collision optics (in 2012: $\beta^* = 60$ cm).
- *Adjust*: The phase in which the separation between the beams in the interaction points is made to collapse and the beams are brought into collisions.
- *Stable beams*: The beam mode manually declared by the operators after all adjustments have been made, signalling to the experiments the start of physics data-taking. Physics production fills generally remain in this beam mode for several hours, until the beams are eventually dumped.

The LHC Filling Scheme

The LHC features a 400 MHz RF system corresponding to a bucket length of 2.5 ns and a harmonic number of $h = 35\,640$ [1]. For most proton physics production fills in 2012, the LHC was filled with 50 ns spaced bunches. From the SPS, eight batches of 144 bunches, three batches of 72 bunches, and one batch of six bunches (witness bunches for transfer line verification) were injected into each ring of the LHC, totalling 1374 bunches per beam [2], as shown in Fig. 1.

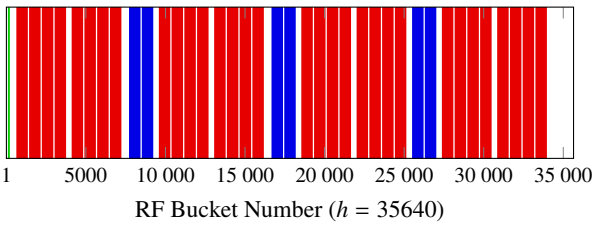

Figure 1: The LHC filling scheme for Beam 1 used in 2012, consisting of eight batches of 144 bunches (red), three batches of 72 bunches (blue), and six witness bunches (green). The filling scheme for Beam 2 is identical apart from the position of the witness bunches.

BEAM PARAMETER EVOLUTION AFTER THE END-OF-SQUEEZE INSTABILITIES

In the second half of 2012, instabilities were frequently observed at the end of the squeeze beam mode [3] in the LHC. Despite not causing significant intensity losses or beam dumps, these instabilities lead to a non-negligible transverse emittance increase of $\sim 0.5\,\mu$m for the affected bunches.

Figure 2 shows, in blue, the horizontal [5] bunch size measurement acquired for a different bunch every second from the scanning Synchrotron Light Telescope (BSRT) system and, in red, the amplitude of the vertical Base-Band-Tune (BBQ) measurement. It can be seen that at ~19:20, the BBQ amplitude increases, indicating the presence of an instability. At the same time, certain bunches develop a higher transverse emittance (the horizontal bunch size measurements separate into two bands).

When the beams that experienced the end-of-squeeze instabilities go into stable beams, two distinct families of bunches can be seen, according to the evolution of their parameters: bunches with a larger emittance develop both higher losses and a shorter bunch length, possibly due to limits in the off-momentum dynamic aperture. This effect has historically been labelled 'Bunch length histogram splitting', as it was visible on the fixed displays in the LHC control room as a double-peaked histogram of Beam 1 bunch lengths. It has been discussed in detail in a previous publication [4], so it will not be treated any further in this paper. The underlying instabilities are subject to current beam–beam studies [3].

* michael.hostettler@cern.ch, michihostettler@students.unibe.ch

978-92-9083-404-5, 0007-8328 –
http://dx.doi.org/10.5170/CERN–2014–004.199

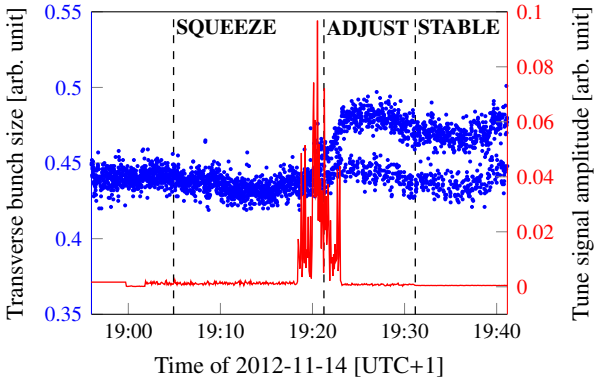

Figure 2: The horizontal bunch sizes of Beam 1 (measured for a different bunch every second by the BSRT) and the amplitude of the vertical tune signal (measured by the BBQ system) for fill 3287, indicating the presence of an instability at ~19:20. Note the two distinct emittance families thereafter.

The impact on the luminosity is mainly emittance-driven: the emittance, derived from the luminosity, at the start of the stable beams period was generally ~2.4 μm in 2012, while the emittance of bunches affected by the instability was ~3 μm, with up to 70% of all bunches affected for particular fills in late 2012. This corresponds to loss of up to 10% in both peak and integrated luminosity; for example, from a peak instantaneous luminosity of more than $7000\,\mu\text{b}^{-1}\cdot\text{s}^{-1}$ for 'good' fills to ~$6500\,\mu\text{b}^{-1}\cdot\text{s}^{-1}$ for fills with ~50% bunches affected.

THE LOSS PATTERN OF BEAM 1 IN STABLE BEAMS

A very reproducible loss pattern was observed during long physics fills in 2012: the integrated losses of the first ~30 bunches of each SPS batch in Beam 1 are up to 10% lower compared to later bunches after 11 h in stable beams, while such a pattern was always negligible, if present at all, for Beam 2. In the following analysis, only the batches of 144 bunches are considered for simplicity, although the batches of 72 bunches show the same behaviour. A similar pattern had already been noticed during 2011 operation [6].

The bunch-by-bunch luminosity published by the main experiments and the total process cross-section [7] allow the intensity lost due to luminosity burn-off to be calculated. Removing the burn-off component from the total losses does not change the overall loss pattern, as depicted in Fig. 3. The cause of the pattern is as yet unknown; in particular, no correlation with the number of long-range interactions has been identified. However, the loss structure of Beam 1 clearly depends on the preceding gaps with no beam (see Fig. 1): after each 36 bunches, a local decrease in losses is visible after the SPS injection kicker gap, and the first bunches in the first SPS batch after the large LHC dump kicker gap lose even less compared to the same bunches in later SPS batches (the lower blue curves in Fig. 3).

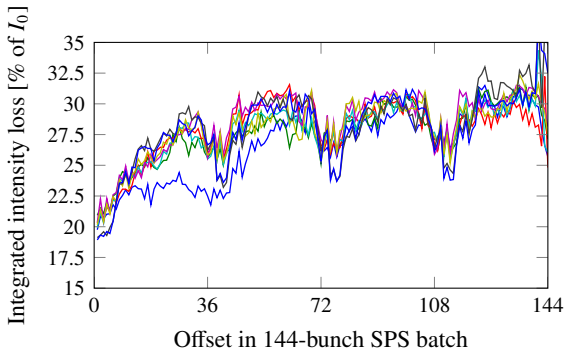

(a) The total intensity losses.

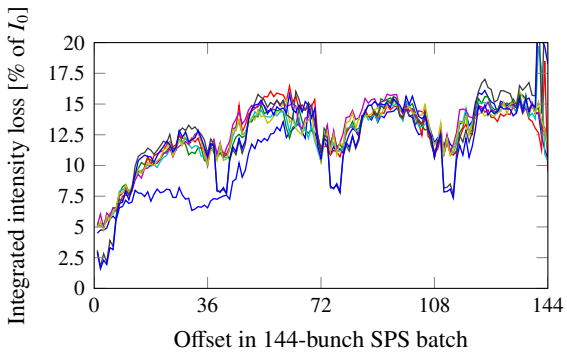

(b) The intensity losses with the burn-off component removed.

Figure 3: The integrated losses of Beam 1 for fill 3363 after 11 h in stable beams, grouped by SPS batches of 144 bunches each (a). Note that removing the burn-off component does not change the loss pattern (b).

Statistics and Correlation to the Bunch Length

Fitting a linear function to the integrated losses of the first 30 bunches of each SPS batch allows the difference in losses among those bunches and therefore the strength of the effect to be quantified; averaging over all 144 bunches of each SPS batch shows the impact on the total losses. This is shown in Fig. 4 for one sample fill.

Figure 5 shows this analysis applied for all 2012 fills that lasted for at least 11 h in stable beams. It is to be noted that Δl, the observed difference over the first 30 bunches, suddenly increases from less than 5% to up to 10% after fill 2875 (see Fig. 5(a)). This is suspected to be correlated with the increase of the bunch length target for the ramp from 1.2 ns to 1.3 ns from fill 2880 onwards, indicating that the pattern is correlated with longitudinal losses. An increase of l_{avg}, the average intensity loss of all bunches, is also observed for the same fills (Fig. 5(b)), while l_0, the intensity loss of the first bunch of each SPS batch, remains at the same level (Fig. 5(c)).

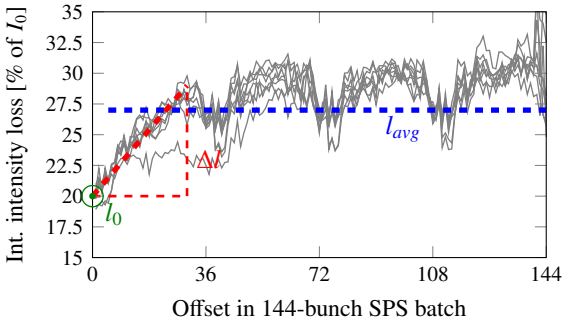

Figure 4: Quantitative analysis of the Beam 1 loss pattern for fill 3363, with the average loss of the first bunch of each 144 SPS batch in green, the average slope over the first 30 bunches of each SPS batch in red, and the total average loss in blue.

Impact on Luminosity

Increased losses lead to a lower total intensity and therefore to a lower integrated luminosity for the same fill duration due to a decreased luminosity lifetime, which is defined as τ in

$$L(t) = L_0 \exp\left(-\frac{t}{\tau}\right). \quad (1)$$

In the bunch-by-bunch luminosity lifetime calculated by fitting Eq. 1 to the luminosity per colliding bunch pair published by the ATLAS experiment for a time window of 2 h set at 8 h after the start of stable beams, the impact of the Beam 1 loss pattern is visible, as depicted in Fig. 6.

The increased total losses after fill 2875 are also visible on the total luminosity lifetime. As shown in Fig. 7, the luminosity lifetime after fill 2875 is on average ~1.5 h lower in the long term compared to earlier fills. Despite the rather large spread of the values, the bunch-by-bunch pattern observed (Fig. 6) indicates a correlation with the loss pattern in question. Assuming the same peak luminosity, this decrease in luminosity lifetime corresponds to a ~7% loss in integrated luminosity for a fill lasting 11 h in stable beams.

CONCLUSIONS

Observations on two distinct effects that affect the LHC luminosity production were studied and presented in this paper. First, instabilities at the end of the betatron squeeze increased the transverse emittances of selected bunches by ~0.5 μm. Up to 70% of all bunches in Beam 1 were affected in late 2012, resulting in a loss of up to 10% of both peak and integrated luminosity.

Second, bunch-by-bunch observations on the integrated intensity losses of Beam 1 bunches showed a very reproducible pattern building up over several hours in stable beams on 144-bunch SPS batches, while no such pattern was observed on Beam 2. A clear cause for the pattern has not been identified yet, but the differences in losses over a SPS batch, as well as the average losses, increased after an increase in bunch length, indicating a correlation with longitudinal losses. The shorter luminosity lifetime due to the increased losses leads to a loss of ~7% of integrated luminosity for long fills.

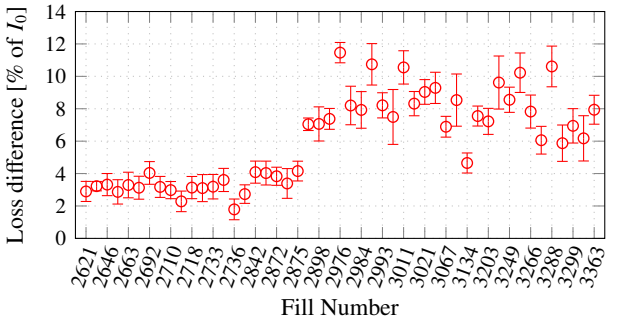

(a) The difference in the average loss, Δl, over the first 30 bunches of each SPS batch. The error bars indicate the fit quality.

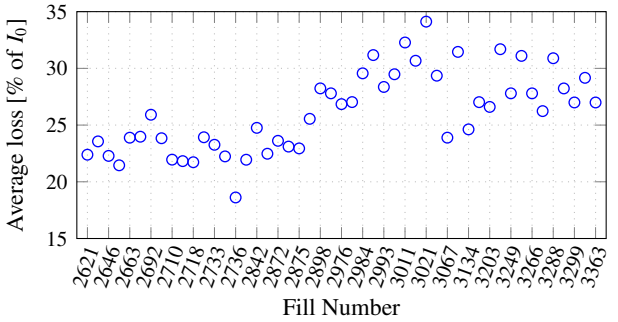

(b) The average loss, l_{avg}, of all bunches.

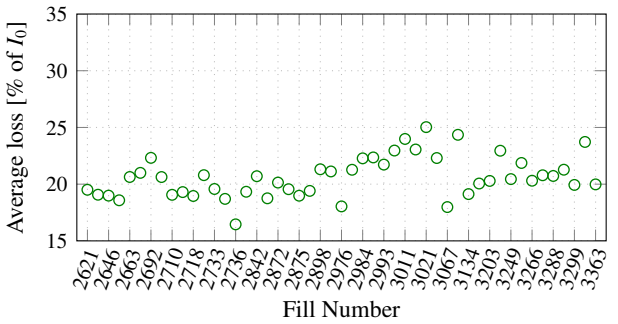

(c) The average loss, l_0, of the first bunch of each SPS batch.

Figure 5: The statistics for the loss pattern of Beam 1 after 11 h in stable beams for 2012. Note the sudden increase of both the slope and the average losses after fill 2875, probably related to an increased bunch length.

ACKNOWLEDGEMENTS

The authors would like to thank G. Arduini, X. Buffat, W. Herr, T. Pieloni, the LHC Beam-Beam Team, and the LHC Beam Operation Committee for fruitful discussions on the topics covered by this paper.

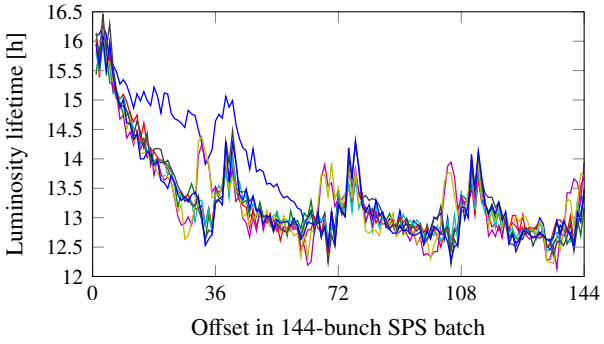

Figure 6: The bunch-by-bunch luminosity lifetime for fill 3363, calculated from ATLAS data after 8 h of stable beams. It shows an inverted image of the Beam 1 loss pattern that was observed.

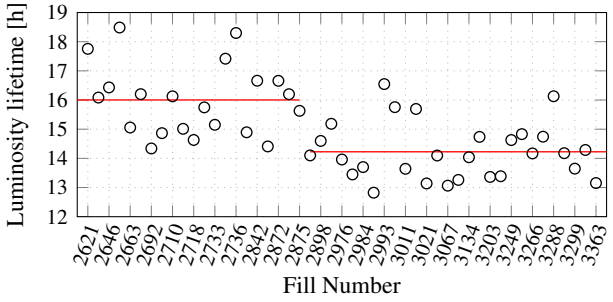

Figure 7: The total luminosity lifetime, calculated using the ATLAS luminosity data after 8 h in stable beams, for the fills considered in Fig. 5. The luminosity lifetime got worse after fill 2875, probably due to the increased total intensity loss. The red lines indicate the average up to and after fill 2875.

REFERENCES

[1] O. Bruening, P. Collier, P. Lebrun, S. Myers, R. Ostojic, J. Poole, and P. Proudlock, "LHC Design Report" (Vol. 1, Ch. 6), CERN-2004-003-V-1 (2004).

[2] Until June 2012, a slightly different filling scheme including 12 witness bunches per beam (and therefore 1380 bunches in total) was used. No change in the loss pattern was observed due to the different filling scheme.

[3] X. Buffat, "Consequences of Missing Collisions – Beam Stability and Landau Damping," these proceedings.

[4] M. Hostettler, G. Arduini, and G. Papotti, "Observations on Bunch Length Histogram Splitting and Selective Emittance Blow-up in LHC Beam 1," CERN-ATS-Note-2013-003 PERF (2003).

[5] No vertical bunch size measurement was available due to technical difficulties.

[6] G. Papotti, A. Gorzawski, M. Hostettler, and R. Schmidt, "Beam Losses through the Cycle," LHC Beam Operation Workshop, Evian (December 2012).

[7] TOTEM Collaboration, "A Luminosity-Independent Measurement of the Proton–Proton Total Cross-Section at $\sqrt{s}$ = 8 TeV," CERN-PH-EP-2012-354 (2012).

Published by CERN in the Proceedings of the ICFA Mini-Workshop on Beam–Beam Effects in Hadron Colliders,
CERN, Geneva, Switzerland, 18–22 March 2013, edited by W. Herr and G. Papotti, CERN–2014–004 (CERN, Geneva, 2014)

DETECTION OF COHERENT BEAM–BEAM MODES WITH DIGITIZED BEAM POSITION MONITOR SIGNALS

G. Stancari*, A. Valishev, Fermi National Accelerator Laboratory, Batavia, IL, USA
S.M. White, Brookhaven National Laboratory, Upton, NY, USA

Abstract

A system for bunch-by-bunch detection of transverse proton and antiproton coherent oscillations in the Fermilab Tevatron collider is described. It is based on the signal from a single beam position monitor located in a region of the ring with large amplitude functions. The signal is digitized over a large number of turns and Fourier-analysed offline with a dedicated algorithm. To enhance the signal, band-limited noise is applied to the beam for about 1 s. This excitation does not adversely affect the circulating beams even at high luminosities. The device has a response time of a few seconds and a frequency resolution of 1.6×10^{-5} in fractional tune, and it is sensitive to oscillation amplitudes of 60 nm. It complements Schottky detectors as a diagnostic tool for tunes, tune spreads, and beam–beam effects. Measurements of coherent mode spectra are presented and compared with models of beam–beam oscillations.

INTRODUCTION

In particle colliders, each beam experiences nonlinear forces when colliding with the opposing beam. A manifestation of these forces is a vibration of the bunch centroids around the closed orbit. These coherent beam–beam oscillation modes were observed in several lepton machines, including PETRA, TRISTAN, LEP, and VEPP-2M [1–4]. Although their observation in hadron machines is made more challenging by the lack of strong damping mechanisms to counter external excitations, they were seen at the ISR, at RHIC, in the Tevatron, and in the LHC [5–11]. Originally, one motivation for the study of coherent beam–beam modes was the realization that their frequencies may lie outside the incoherent tune distribution, with a consequent loss of Landau damping [12]. The goal of the present research is to develop a diagnostic tool to estimate bunch-by-bunch tune distributions, to assess the effects of Gaussian electron lenses for beam–beam compensation [13–16], and to provide an experimental basis for the development of beam–beam numerical codes.

The behaviour of colliding bunches is analogous to that of a system of oscillators coupled by the beam–beam force. In the simplest case, when two identical bunches collide head-on in one interaction region, two normal modes appear: a σ mode (or 0 mode) at the lattice tune, in which bunches oscillate transversely in phase, and a π mode, separated from the σ mode by a shift of the order of the beam–beam parameter, in which bunches are out of phase. In general, the number, frequency, and amplitude of these modes depend on the number of bunches, the collision pattern, the tune separation between the two beams, the transverse beam sizes, and the relative intensities. Coherent beam–beam modes have been studied at several levels of refinement, from analytical linear models to fully three-dimensional particle-in-cell calculations [1, 9, 17–24].

In the Tevatron, 36 proton bunches (identified as P1–P36) collided with 36 antiproton bunches (A1–A36) at the centre-of-momentum energy of 1.96 TeV. There were two head-on interaction points (IPs), corresponding to the CDF and the DZero experiments. Each particle species was arranged in three trains of 12 bunches each, circulating at a revolution frequency of 47.7 kHz. The bunch spacing within a train was 396 ns, or 21 53 MHz RF buckets. The bunch trains were separated by 2.6 μs abort gaps. The synchrotron frequency was 34 Hz, or 7×10^{-4} times the revolution frequency. The machine operated with betatron tunes near 20.58.

The betatron tunes and tune spreads of individual bunches are among the main factors that determine beam lifetimes and collider performance. They are affected by head-on and long-range beam–beam interactions. Three systems were used in the Tevatron to measure incoherent tune distributions: the 21.4 MHz Schottky detectors, the 1.7 GHz Schottky detectors, and the direct diode detection base band tune (3D-BBQ). The latter two systems could be gated on single bunches. Detection of transverse coherent modes complemented these three systems because of its sensitivity, bunch-by-bunch capability, high frequency resolution, and fast measurement time.

The basis for the measurement technique was presented in Ref. [25], and preliminary results can be found in Refs. [26–28]. Several improvements, mainly in the data analysis, were implemented and presented in a concise report [29]. A comprehensive description of the technique and of observations in a wide range of experimental conditions was reported in Ref. [10]. Here, we focus on the detection of coherent beam–beam oscillations and on comparisons with analytical and numerical models.

MODELS

In the Tevatron, transverse coherent oscillations were substantially nonlinear because of properties of the lattice and the beam–beam force. We first used the rigid-bunch approximation for a fast analysis of the expected beam–beam mode frequencies and their dependence on the the betatron tunes Q and on the beam–beam parameter per interaction point ξ. For a more accurate description of the coherent

* stancari@fnal.gov

978-92-9083-404-5, 0007-8328 –
http://dx.doi.org/10.5170/CERN–2014–004.203

mode spectrum, tracking simulations with a strong–strong three-dimensional numerical code were employed.

We used a simple matrix formalism to compute the eigenmode tunes of the system of colliding bunches. Besides the rigid-bunch approximation, one more simplification was used. The complete description of the system would require modelling the interaction of 72 bunches at 138 collision points. The analysis of such a system can be quite complex. Observations and analytical estimates showed that the difference in tunes between individual bunches was small compared to the beam–beam tune shift. Thus, as a first approximation, it is possible to neglect long-range interactions. This reduces the system to six bunches (three in each beam) colliding at two head-on IPs. In the following discussion, we restrict betatron oscillations to one degree of freedom. Because the system has three-fold symmetry, the one-turn map transporting the 12-vector of dipole moments and momenta of the system of six bunches can be expressed as follows:

$$M = M_{\mathrm{BB3}}\, M_{\mathrm{T3}}\, M_{\mathrm{BB2}}\, M_{\mathrm{T2}}\, M_{\mathrm{BB1}}\, M_{\mathrm{T1}},$$

where M_{TN} ($N = 1,2,3$) are the 2×2 block-diagonal, 12×12 matrices transporting phase space coordinates through the accelerator arcs, and $M_{\mathrm{BB}N}$ are the matrices describing thin beam–beam kicks at the IPs. Although there are only two interactions per bunch, three collision matrices are used to describe a one-turn map of the system of six bunches. This construction represents the time propagation of the bunch coordinates through one turn with break points at the CDF (B0), D0 and F0 locations in the machine. If in a given step the bunch is at B0 or D0, its momentum coordinate is kicked according to the distance between the centroids of this bunch and of the opposing bunch. If the bunch is at F0 (1/3 of the circumference from B0 and D0), where the beams are separated, its momentum is unchanged. The eigentunes of the one-turn map can then be computed numerically. We will use the symbols ξ_{p} and ξ_{a} for the beam–beam parameters of protons and antiprotons, respectively; β is the amplitude function at the IP. The Yokoya factor [18, 30] is assumed to be equal to 1.

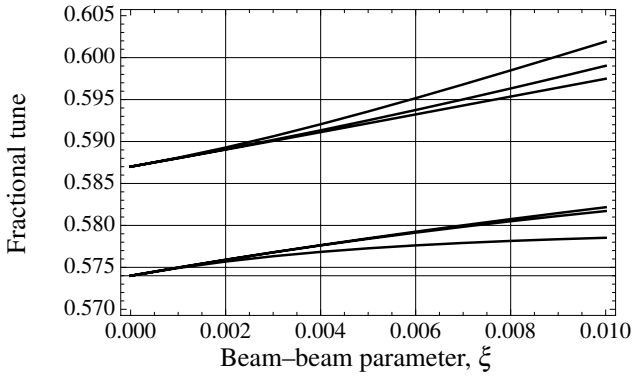

Figure 1: Coherent mode tunes versus the beam–beam parameter per IP, calculated with the linearized model; here $Q_{\mathrm{p}} = 0.587$, $Q_{\mathrm{a}} = 0.574$, and $\xi = \xi_{\mathrm{p}} = \xi_{\mathrm{a}}$.

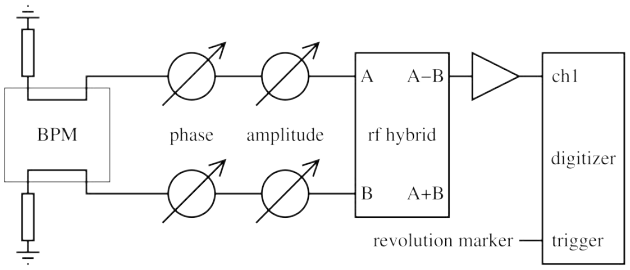

Figure 2: Schematic diagram of the apparatus.

This model provides a quick estimate of the expected values of the coherent beam–beam mode tunes for a given set of machine and beam parameters. In Fig. 1, an example of the dependence of the six eigenfrequencies on the beam–beam parameter per IP is presented. As one would expect, at small values of ξ (uncoupled oscillators) the mode frequencies approach the bare lattice tunes—in this case, 0.587 for protons and 0.574 for antiprotons. When the total beam–beam parameter exceeds the difference between the lattice tunes, the modes are split and their symmetry approaches that of the conventional σ and π modes. The parameters of this calculation are taken to resemble those of the beginning of Tevatron Store 7754, when the beam–beam parameter was $\xi = \xi_{\mathrm{a}} = \xi_{\mathrm{p}} = 0.01$. A comparison with data is given in the Results section (Fig. 4).

A more complete description of coherent oscillations was provided by numerical simulations based on the code BeamBeam3D [22]. BeamBeam3D is a fully parallelized three-dimensional code allowing for self-consistent field calculations of arbitrary distributions and tracking of multiple bunches. Transport from one IP to the other is done through linear transfer maps. The electromagnetic fields generated by the beams are calculated from the Poisson equation using a shifted Green's function method efficiently computed with a fast Fourier transform (FFT) algorithm on a uniform grid.

The measured beam intensities and emittances were used in the simulation. Lattice parameters were measured on the proton orbit. The bare lattice tunes were derived from the main quadrupole currents. Owing to the asymmetry of the collision IPs in the Tevatron, the bunches coupled by groups of three through the head-on interactions. In the simulations, three bunches per beam were therefore tracked to reproduce the spectrum of centroid oscillations. A comparison of the calculated and measured spectra for the case of Tevatron Store 7754 is discussed in the Results section and shown in Fig. 4.

APPARATUS

The system used for the detection of transverse coherent modes (Fig. 2) was based on the signal from a single vertical beam position monitor (BPM) located near the CDF interaction point, in a region where the vertical amplitude function at collisions was $\beta_y = 880$ m. The BPM was a stripline pick-up, with two plate outputs (A and B) for each

of the two counter-propagating beams.

In the Tevatron, protons and antiprotons shared a common vacuum pipe. Outside the interaction regions, their orbits wrapped around each other in a helical arrangement. Therefore, bunch centroids were several millimetres away from the BPM's electrical axis. Typically, the peak-to-peak amplitude of the proton signal was 10 V on one plate and 5 V on the other, whereas the signal of interest was of the order of a few millivolts. For this reason, it was necessary to equalize the A and B signals to take advantage of the full dynamic range of the digitizer. Equalization also reduced false transverse signals due to trigger jitter, as discussed below. The phase and attenuation of each signal was manually adjusted by minimizing the $A-B$ output of the RF hybrid circuit. If necessary, fine-tuning could be done by displacing the beam with a small orbit bump. Orbits at collisions were stable over a time-scale of weeks, and this manual adjustment did not need to be repeated often.

The difference signal from the hybrid was amplified by 23 dB and sent to the digitizer. We used a one-channel, 1 V full range, 10-bit digitizer with time-interleaved analog-to-digital converters (ADCs). It sampled at 8 gigasamples/s (GS/s) and stored a maximum of 1024 megasamples (MS) or 125 000 segments. (Because of a firmware problem, only half of the segments were used in the experiments described below.) The 47.7 kHz Tevatron revolution marker was used as the trigger, so we refer to 'segments' or 'turns' interchangeably. Typically, we sampled at 8 GS/s (with a sample period of 125 ps), i.e. 150 slices for each 19 ns RF bucket. At this sampling rate, one could record waveforms of one bunch for 62 500 turns, of two bunches for 52 707 turns, or of 12 bunches for 12 382 turns, depending on the measurement of interest. A C++ program running on the front-end computer controlled the digitizer settings, including its delay with respect to the Tevatron revolution marker.

The recorded output data contained the raw ADC data together with the trigger time stamps and the delay of the first sample with respect to the trigger. Timing information had an accuracy of about 15 ps, and it was extremely important for the synchronization of samples from different turns.

To enhance the signal, the beam was excited with a few watts of band-limited noise ('tickling') for about 1 s during the measurement. The measurement cycle consisted of the following steps: digitizer setup, tickler turn-on, acquisition start, tickler turn-off, and acquisition stop. The cycle took a few seconds. The procedure was parasitical and did not adversely affect the circulating beams, even at the beginning of regular collider stores, with luminosities around 3.5×10^{32} events/(cm^2 s). When repeating the procedure several times, the Schottky monitors occasionally showed some activity, but no beam loss was observed.

DATA ANALYSIS

Data was analysed offline using the multi-platform, open-source R statistical package [31]. The distribution of differences between trigger time stamps from consecutive turns was used to obtain the average revolution frequency (47713.11 Hz at 980 GeV). From it, the nominal or 'ideal' trigger time stamps for each turn were calculated. The distribution of trigger offsets, i.e. the differences between measured and nominal time stamps, is a measure of the jitter in the revolution marker. The root mean square of the distribution was usually less than 0.2 ns. The delay between the trigger time and the time stamp of the first sample was also recorded with an accuracy of 15 ps. The sum of the trigger offset and the first-sample delay is the correction by which each sample in a segment is to be shifted in time to be aligned with the other segments. For each turn and each bunch, the signal was interpolated with a natural spline and shifted in time according to this correction. One undesirable effect of this synchronization algorithm is that a few slices (usually no more than three) at each edge of the bucket become unusable, as they cannot be replaced with real data. The synchronization of turns is extremely important, as the jitter in trigger time translates into a false transverse oscillation where the difference signal has a slope. If the BPM plates are not perfectly balanced, jitter of even a fraction of a nanosecond can raise the noise floor by several decibels and compromise the measurement.

Bunch oscillations were dominated by low-frequency beam jitter attributable to mechanical vibrations [32, 33]. The range of amplitudes was inferred from comparisons with the regular Tevatron BPM system and corresponds to about ±25 μm. This low-frequency jitter did not affect the measurements of coherent beam–beam modes directly, but it reduced the available dynamic range. A high-pass filter and more amplification may be used to improve the system.

For each bunch, the signal of each individual slice versus the turn number was Fourier-transformed. The frequency resolution is determined by the number of bins in the FFT vector and is limited to 62 500 turns, corresponding to 1.6×10^{-5} of the revolution frequency or 0.8 Hz. The data was multiplied by a Slepian window of rank 2 to confine leakage to adjacent frequency bins and suppress it to below 10^{-5} in farther bins [34]. When the full frequency resolution was not needed, the FFT vectors were overlapped by about one-third of their length to reduce data loss from windowing, and the resulting spectral amplitudes were averaged. Calculations took about 20 s per bunch for 62 500 turns and 150 slices per bunch on a standard laptop computer. Processing time was dominated by the synchronization algorithm.

The noise level was estimated by observing the spectra without beam. The spectra exhibited a few sharp lines in all slices. These lines were attributed to gain and offset differences between the time-interleaved ADCs themselves and to timing skew of their clocks. To improve the signal-to-noise ratio and to suppress backgrounds unrelated to the beam, such as the spurious lines from the digitizer, a set of signal slices (near the signal peaks) and a set of background slices (before the arrival of the bunch) were defined. Amplitude spectra were computed for both signal and back-

ground slice sets, and their ratio was calculated. The ratios are very clean, with some additional variance at the frequencies corresponding to the narrow noise spikes. Results are presented in terms of these signal-to-background amplitude ratios.

Figure 3 shows an example of analysed antiproton data in two regions of the frequency spectrum: a low-frequency region with the horizontal axis expressed in hertz (top two plots), and a high-frequency region, expressed in terms of the revolution frequency or fractional tune (bottom two plots). The two-dimensional colour plots show the amplitude distribution for each of the 150 125 ps slices in logarithmic scale. In this example, the signal slices are numbers 41–95 and 99–147. They are defined as the slices for which the amplitude is above 10% of the range of amplitudes. Background slices are numbers 3–31 (with amplitude below 2% of the range). The black-and-white one-dimensional plots show the ratio between signal and background amplitudes. From the upper two plots of Fig. 3, one can appreciate the strength of the low-frequency components; the 60 Hz power-line noise and its harmonics are also visible. The lines around 34 Hz and 68 Hz are due to synchrotron oscillations leaking into the transverse spectrum. The lower two plots of Figure 3 show the spectra of transverse coherent oscillations. The vertical lines present in all slices in the two-dimensional plot, attributed to digitizer noise, are eliminated by taking the ratio between the signal and background slices. One can also observe the small variance of the noise level compared to the amplitude of the signal peaks.

In the two-dimensional plots of Fig. 3, one may notice patterns in the oscillation amplitude as a function of position along the bunch. These may be an artefact of the imperfect synchronization between the *A* and *B* signals, but they could also be related to the physical nature of the coherent modes (i.e. rigid- versus soft-bunch, head-on versus long-range). The phase of the oscillations as a function of frequency and bunch number may also provide physical insight.

RESULTS

Transverse coherent mode spectra were measured for both proton and antiproton bunches under a wide range of experimental conditions [10]. In this section, we focus on

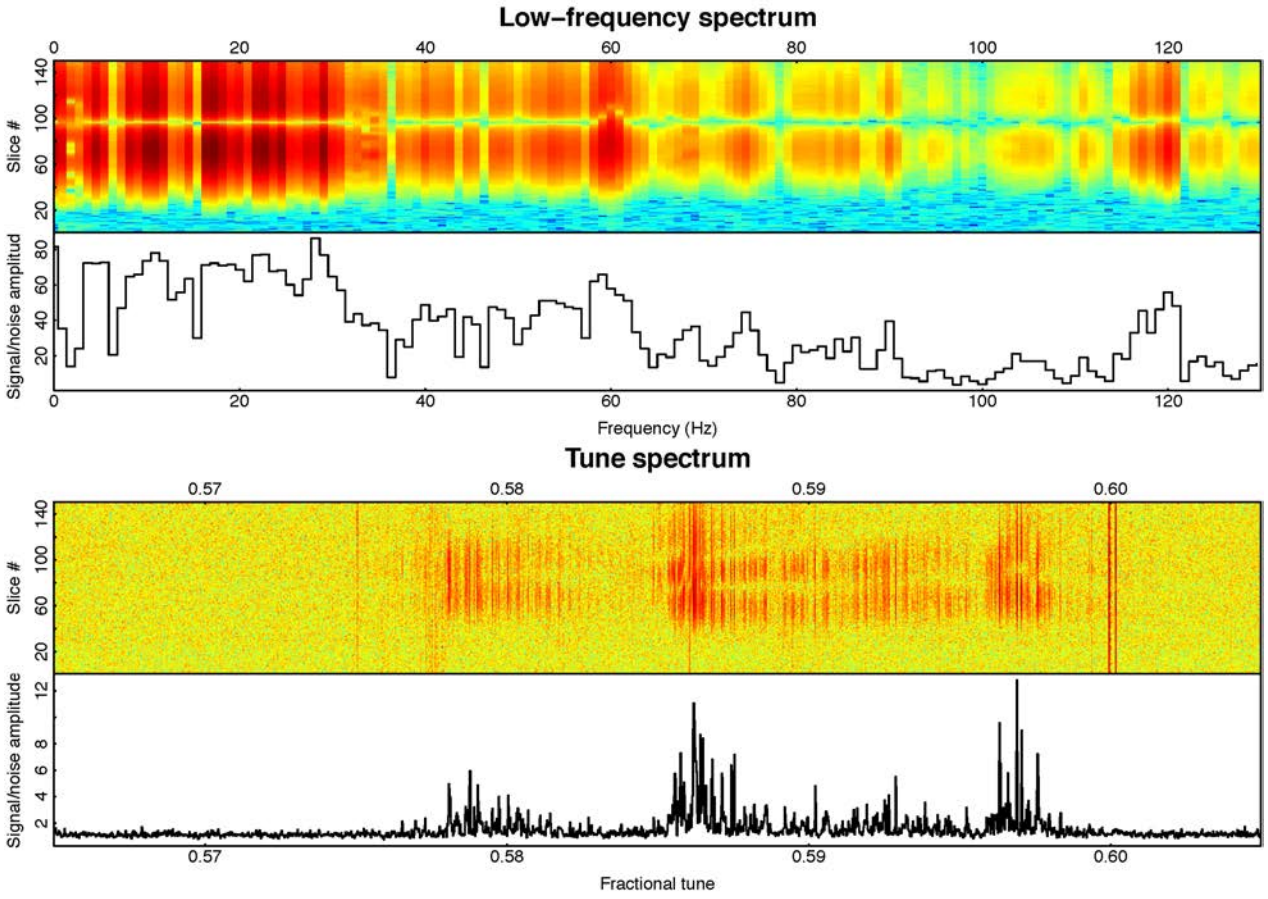

Figure 3: Example of frequency spectra for antiprotons from data taken during Store 7754. Two selected regions of the spectrum are shown: below 130 Hz (top two plots) and around $(47.7\ \text{kHz}) \times (1 - 0.585) = 20$ kHz (bottom two plots). The colour plots show the Fourier amplitude (in logarithmic scale) versus the frequency for each of the 150 125 ps slices. The black traces represent the average amplitudes of the signal slices divided by those of the background slices.

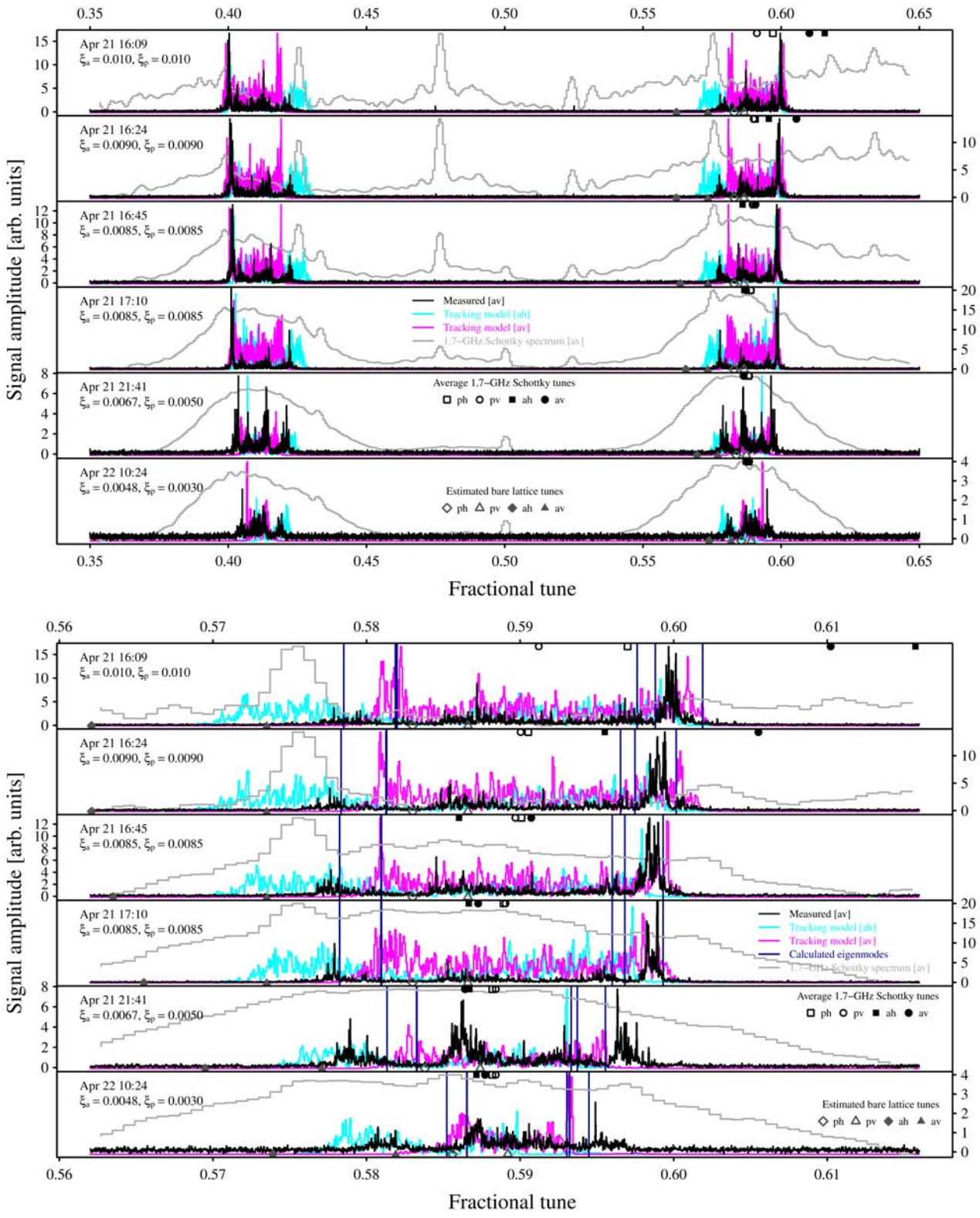

Figure 4: Evolution of vertical coherent beam–beam modes for antiproton bunch A13 during the course of Store 7754.

the observation of coherent beam–beam modes, their evolution over the course of a collider store, and comparisons with analytical and numerical models.

An illustration of the evolution of transverse coherent modes during a collider store is shown in Fig. 4 for vertical antiproton oscillations. The top panel covers a wide range of fractional tunes, while the bottom one shows the details near the betatron frequencies. In each plot, the black line represents the measured spectra, the grey histogram shows the measured 1.7 GHz antiproton vertical Schottky spectra for comparison, and the cyan and magenta traces are the antiproton horizontal (ah) and antiproton vertical (av) spectra calculated with the BeamBeam3D code. The bottom panel shows the six calculated rigid-bunch modes as vertical dark-blue lines. Markers are used to indicate the average Schottky tunes (black) and the estimated bare lattice tunes (dark grey) for protons and antiprotons, both horizontally and vertically (ph, pv, ah, and av). The first four spectra were acquired within about an hour after the beams were brought into collision; the fifth plot was taken after about six hours, whereas the last plot was taken at the end of the store, just before the beams were dumped. The calculated beam–beam parameters per IP, ξ_a and ξ_p, are printed on the left side of each plot.

Over the course of a store, the lattice tunes need to be periodically adjusted to keep the average incoherent tune close to the desired working point. Except for the last two measurements, which may be affected by the evolving linear coupling and by a slight miscalibration of the tune settings, the estimated lattice tune (dark-grey triangles) lies below the first group of eigenmodes, as expected.

One can clearly see how, as the beam–beam force weakens, the spread in coherent modes decreases, as does the amplitude of the π mode (near 0.60). The asymmetries between the beams, the large number of bunches, and the multiple collision points give rise to a rich spectrum of oscillations.

A comparison with the Schottky spectra reveals many common coherent spikes. The ones at 0.475/0.525, visible in both the Schottky spectrum and the digitized BPM spectrum, are unexplained. Because of the distortions of the Schottky spectrum at the beginning of the store, the present system provides a better indication of the tune distribution under these conditions.

The predicted eigenfrequencies of the simplified rigid-bunch model are close to the measured peaks. Obviously, the measured spectra are richer than those predicted by the simplified model, and a complete explanation requires a more detailed description of the beam dynamics, such as one based on the three-dimensional strong–strong code. The results of the BeamBeam3D simulations are very similar to the data. The comparison between data (vertical) and simulations (both horizontal and vertical) suggests that the effect of coupling, not included in simulations, is non-negligible and may account for some of the discrepancies.

CONCLUSIONS

A system was developed to measure the spectra of coherent beam–beam oscillations of individual bunches in the Fermilab Tevatron collider. It is based on the analysis of the digitized signal from a single beam position monitor. It requires applying band-limited noise to the beam, but an extension of its dynamic range is possible, if needed, so as to operate without excitation.

The device has a response time of a few seconds and a frequency resolution of 1.6×10^{-5} in fractional tune, and it is sensitive to oscillation amplitudes of 60 nm. In terms of sensitivity, resolution, and background level, it provides a very clean measurement of coherent oscillations in hadron machines. The system is complementary to Schottky detectors and transfer-function measurements as a diagnostic tool for tunes, tune spreads, and beam–beam effects. At the beginning of a collider store, when strong coherent lines distort the incoherent Schottky tune spectrum, the present system may provide a more accurate indication of betatron tunes.

Coherent oscillations in the Tevatron were stable, probably thanks to the different intensities of the two beams, their tune separation, and chromaticity. The average amplitude of the oscillations around the ring was estimated to be of the order of 20 nm. Patterns in the oscillation amplitude as a function of position along the bunch were observed. They may be related to the physical nature of the coherent modes. The phase of the oscillations as a function of frequency and bunch number may also provide physical insight, but it was not considered in this analysis.

A simplified collision model was used to calculate normal mode frequencies and to show their dependence on beam–beam coupling. Some scenarios were simulated using the self-consistent three-dimensional strong–strong numerical code BeamBeam3D. Models were compared with observations made over the course of a collider store, as the strength of the beam–beam force decreased with time. Some discrepancies were observed, but the overall agreement was satisfactory, considering the uncertainties in the antiproton parameters, such as lattice tunes and coupling, and their variation over time.

ACKNOWLEDGMENTS

The authors thank V. Kamerdzhiev (Forschungszentrum Jülich, Germany), F. Emanov (Budker Institute for Nuclear Physics, Novosibirsk, Russia), Y. Alexahin, B. Fellenz, V. Lebedev, G. Saewert, V. Scarpine, A. Semenov, and V. Shiltsev (Fermilab) for their help and insights.

Fermi Research Alliance, LLC, operates Fermilab under contract no. DE-AC02-07-CH-11359 with the United States Department of Energy (US DOE). Brookhaven National Laboratory is operated by Brookhaven Science Associates, LLC, under contract no. DE-AC02-98-CH-10886 with the US DOE. This work was partially supported by the US LHC Accelerator Research Program (LARP).

REFERENCES

[1] A. Piwinski, IEEE Trans. Nucl. Sci. 26 (1979) 4268.

[2] T. Ieiri, T. Kawamoto, and K. Hirata, Nucl. Instrum. Methods Phys. Res. A 265 (1988) 364.

[3] E. Keil, K. Cornelis, and K. Hirata, Proc. 15th Int. Conf. High Energy Accelerators, Hamburg, Germany, p. 1106 (1992).

[4] I.N. Nesterenko, E.A. Perevedentsev, and A.A. Valishev, Phys. Rev. E 65 (2002) 056502.

[5] J.P. Koutchouk, CERN Report No. ISR-OP/JPK-svw (19 March 1982).

[6] J.P. Koutchouk, CERN Report No. ISR-OP/JPK-bm (15 June 1982).

[7] W. Fischer et al., BNL Report No. C-AD/AP/75 (2002).

[8] W. Fischer et al., Proc. 2003 Particle Accelerator Conf. (PAC03), Portland, Oregon, USA, 12–16 May 2003, p. 135.

[9] T. Pieloni, PhD Thesis, École Polytechnique Fédérale de Lausanne, Switzerland (2008).

[10] G. Stancari and A. Valishev, Phys. Rev. ST Accel. Beams 15 (2012) 041002.

[11] X. Buffat et al., Proc. 2011 Int. Particle Accelerator Conf. (IPAC11), San Sebastián, Spain, 4–9 September 2011, p. 1870.

[12] Y. Alexahin, Part. Accel. 59 (1998) 43.

[13] V .Shiltsev et al., Phys. Rev. ST Accel. Beams 2 (1999) 071001.

[14] V. Shiltsev et al., New J. Phys. 10 (2008) 043042.

[15] V. Shiltsev et al., Phys. Rev. ST Accel. Beams 11 (2008) 103501.

[16] A. Valishev and G. Stancari, Proc. 2011 Particle Accelerator Conf. (PAC11), New York, USA, 28 March–1 April 2011, p. 67.

[17] R.E. Meller and R.H. Siemann, IEEE Trans. Nucl. Sci. 28 (1981) 2431.

[18] K. Yokoya and H. Koiso, Part. Accel. 27 (1990) 181.

[19] W. Herr, M.P. Zorzano, and F. Jones, Phys. Rev. ST Accel. Beams 4 (2001) 054402.

[20] Y. Alexahin, Nucl. Instrum. Methods Phys. Res. A 480 (2002) 253.

[21] T. Pieloni and W. Herr, Proc. 2005 Particle Accelerator Conf. (PAC05), Knoxville, Tennessee, USA, 16–20 May 2005, p. 4030.

[22] J. Qiang et al., Phys. Rev. ST Accel. Beams 5 (2002) 104402.

[23] J. Qiang et al., Nucl. Instrum. Methods Phys. Res. A 558 (2006) 351.

[24] E.G. Stern et al., Phys. Rev. ST Accel. Beams 13 (2010) 024401.

[25] J.-P. Carneiro et al., Fermilab Report No. Beams-doc-1911-v1 (unpublished).

[26] A. Semenov et al., Proc. 2007 Particle Accelerator Conf. (PAC07), Albuquerque, New Mexico, USA, 25–29 June 2007, p. 3877.

[27] V. Kamerdzhiev, V. Lebedev, and A. Semenov, Proc. 2008 Beam Instrumentation Workshop (BIW08), Tahoe City, California, 4–8 May 2008, p. 300.

[28] A. Valishev et al., Proc. 2008 European Particle Accelerator Conf. (EPAC08), Genoa, Italy, 23–27 June 2008, p. 3158.

[29] G. Stancari, A. Valishev, and A. Semenov, Proc. 2010 Beam Instrumentation Workshop (BIW10), Santa Fe, New Mexico, USA, 2–6 May 2010, p. 363.

[30] K. Yokoya, Phys. Rev. ST Accel. Beams 3 (2000) 124401.

[31] R Development Core Team, *R: A Language and Environment for Statistical Computing* (Vienna: R Foundation for Statistical Computing, 2010), ISBN 3-900051-07-0.

[32] B. Baklakov et al., Proc. 1999 Particle Accelerator Conf. (PAC99), New York, USA, 29 March–2 April 1999, p. 1387.

[33] V. Shiltsev, G. Stancari, and A. Valishev, J. Instrum. 6 (2011) P08002.

[34] W.H. Press et al., *Numerical Recipes: The Art of Scientific Computing*, 3rd edition (Cambridge: Cambridge University Press, 2007).

Published by CERN in the Proceedings of the ICFA Mini-Workshop on Beam–Beam Effects in Hadron Colliders,
CERN, Geneva, Switzerland, 18–22 March 2013, edited by W. Herr and G. Papotti, CERN–2014–004 (CERN, Geneva, 2014)

BTF MEASUREMENTS WITH BEAM–BEAM INTERACTIONS

P. Görgen, O. Boine-Frankenheim, TEMF, TU-Darmstadt, Germany
W. Fischer, Brookhaven National Laboratory, Upton, NY, USA

Abstract

We present considerations about the transverse beam transfer function (BTF) of beams under the influence of two effects: The strong–strong beam–beam effect and the influence of a Gaussian electron lens. The BTF are investigated using two methods: BTF excitation is simulated in a particle-in-cell (PIC) code. The BTF model is verified using a known analytic expectation. Analytic expectations for BTF of beams under a stationary electron lens are derived by extending BTF from the formalism of Berg and Ruggiero. Finally we compare the analytic BTF results for a stationary Gaussian lens to both the PIC simulation for split tune conditions and to PIC simulations for a beam influenced by an electron lens. We conclude that the formalism represents the electron lens well and can be applied to a limited extend to the beam–beam effect under split tune conditions. The analytic formalism allows us to recover the strength of an electron lens by means of fitting and can give clues regarding the strength of the beam–beam effect under split tune conditions.

RECONSTRUCTION OF TUNE SPREAD FROM BTF

For a long time there has been a desire at BNL to recover the beam–beam parameter and with it the tune spreads from BTF of beams undergoing the beam–beam effect. Recently this desire has been intensified by the construction and installation of the electron lens [1]. Normally the machine is run in conditions with the two rings tuned to identical or near-identical tunes. We refer to these conditions as *normal conditions*. Under these circumstances, the coherent beam–beam modes often dominate the BTF. When observed, the distance between π and σ modes can be used to determine the beam–beam parameter and with it one can estimate the tune spread. For diagnosing the tune spread due to the electron lens we can not expect π and σ modes outside the incoherent spectrum: The electron beam is dumped after usage and not fed back into the system. However, running the electron lens will lead to a tune spread similar to the one caused by the beam–beam effect (but with a positive tune shift). This tune spread in turn will lead to a deformation of the betatron peak. We would like to be able to recover the strength of the electron lens from this deformation in the absence of beam–beam interactions.

A similar situation can be hoped for in runs with split tunes. We talk about split tunes when the tunes are, unlike normal conditions, offset in the two rings; for example, during the 2012 split tunes run they were typically separated by about 0.04 and located on either side of the 7/10 resonance line. In this case the coherent lines can move into the incoherent spectrum where they can be landau-damped. The resulting beam heating has been observed in measurement [2]. In simulation, the incoherent spectrum of the beam–beam effect of split tunes leads to BTF similar to those of an electron lens. However, due to the opposite sign of the force of the beam–beam and the electron lens the betatron peak is located on the other side of the lattice tune.

When talking about BTF we should specify what we mean exactly. The BTF system at RHIC uses the direct diode detection technique [3] developed at CERN together with a coherent excitation signal fed onto the beams. The complex response amplitude as a fraction of excitation amplitude gives the BTF at the frequency of the excitation. The excitation signal is swept over a range of frequencies around the fractional tune to obtain the BTF as a function of frequency. Commonly the complex BTF is separated into phase and amplitude and the result is shown as a function of frequency.

BTF OF COASTING BEAMS

The BTF of coasting beams have been studied in detail in the past, as they give, for example, information on the stability limits for beams under space charge. Examples of such studies can be found in [4, 5]. We think that the machine conditions in RHIC during pp-operation allow us to apply coasting beam considerations for the bunched beams in RHIC: the synchrotron period with the 28 MHz radio frequency (RF) system and the time used to take one frequency sample in the baseband-Q (BBQ) BTF system are about the same ($\sim$30 ms). For this reason, from the point of view of the BTF measurement, the beam might be expected to resemble a coasting beam. Longitudinal motion is very slow on the timescale of the BTF measurement. Simulations include chromaticity and synchrotron motion. It will be shown later that they agree with a coasting-beam description.

Application to the BTF of Beams Under Beam–Beam or an Electron Lens

To account for an electron lens or a beam–beam effect where the coherent modes lie inside the incoherent spectrum, we use the theory developed by Berg and Ruggiero in [6]. We only have to extend the BTF they give by replacing the tune change due to an octupole with the tune change due to a Gaussian lens. The BTF by Berg and Ruggiero is

$$R(\Omega) = \int_0^\infty \int_0^\infty \frac{1}{\Omega - \omega_x\left(J_x, J_y\right)} \frac{J_x \, \mathrm{d}\psi_x}{\mathrm{d}J_x} \psi_y \, \mathrm{d}J_x \, \mathrm{d}J_y, \tag{1}$$

where J_x and J_y are the transverse action angle variables, ψ_x, ψ_y are the distribution functions in action angle vari-

978-92-9083-404-5, 0007-8328 –
http://dx.doi.org/10.5170/CERN–2014–004.211

ables, separated into the contribution of x and y direction, $\omega_x(J_x, J_y)$ is betatron frequency as a function of these variables, and Ω is the frequency at which the BTF is calculated.

For the distribution functions ψ_x, ψ_y, we use the distribution of a Gaussian transverse distribution in action angle variables as found for example in [7] (we can also simply split the ψ_0 we find in [6] to get ψ_x, ψ_y). We also need the formula for the single particle tune shift due to a Gaussian lens ΔQ_{lens} which as a function of the action-angle amplitudes of the particles $J_{x,y}$ and the peak tune shift ΔQ_0 is [4]

$$\Delta Q_{\mathrm{lens}} = \Delta Q_0 \int_0^1 \frac{\left(I_0\left(\frac{J_x z}{2}\right) - I_1\left(\frac{J_x z}{2}\right)\right) I_0\left(\frac{J_y z}{2}\right)}{\exp(z(J_x + J_y)/2)}\,\mathrm{d}z. \tag{2}$$

Because the Bessel functions are slow to evaluate when one tries to calculate eq. (1) numerically, instead of this analytic expression we use a well-behaved replacement that is friendlier for numerics and was developed for the treatment of space charge in [4]. With $a_{x,y} = \sqrt{2J_{x,y}}$, the approximation for our ΔQ_{lens} is now

$$\Delta Q_0 \frac{192 - 11a_x - 18\sqrt{a_x a_y} + 3a_y^2}{192 - 11a_x - 18\sqrt{a_x a_y} + 3a_y^2 + 36a_x^2 + 24a_y^2}. \tag{3}$$

For the longitudinal distribution we assume a Gaussian momentum spread with the tune shift according to chromaticity resulting in a tune deviation $\Delta Q_{\mathrm{chrom}}$. It can be taken into account by modifying $R(\Omega)$ to include also the tune shift due to chromaticity, the resulting $R(\Omega)$ is

$$\int_{-\infty}^{\infty}\int_0^{\infty}\int_0^{\infty} \frac{1}{\Omega - \omega_x\left(J_x, J_y, p\right)} \frac{J_x\,\mathrm{d}\psi_x}{\mathrm{d}J_x}\psi_{yp}\,\mathrm{d}J_x\,\mathrm{d}J_y\,\mathrm{d}p, \tag{4}$$

where $\psi_{yp} = \psi_y(y)\psi_p(p)$ contains the combined densities in the vertical and momentum plane. The resulting ω_x is‘

$$\omega_x(J_x, J_y, p) = \omega_0\left(Q_0 + \Delta Q_{\mathrm{lens}}(J_x, J_y) + \Delta Q_{\mathrm{chrom}}(p)\right) \tag{5}$$

with ω_0 the revolution frequency, Q_0 the lattice tune and $\Delta Q_{\mathrm{chrom}}(p)$ the tune shift due to chromaticity. The chromaticity usually plays a minor role for the BTF of realistic beams because RHIC runs at low chromaticity.

SIMULATION MODEL

For the investigation of BTF of beams undergoing the beam–beam effect in RHIC, a simulation model was implemented on top of the particle tracking code PATRIC [8]. For the tracking between interaction points (IPs), matrices from madx are used. The translation between IPs is done by one single matrix multiplication with the linear one-turn map computed using the one-turn map on the 2012 100 GeV polarized proton lattice [9]. For synchrotron motion the respective parts of the madx result are ignored and replaced by a more versatile model which is present in the code; this allows us to take into account different RF waveforms. One instance of the code is run for each of the typically six (in the case of two IPs) or two (in the case of one IP) coupling bunches. The beam–beam interaction is taken into account by exchanging the two-dimensional electric fields between the bunches at the interaction points and kicking the particles accordingly. The fields are calculated using a two-dimensional fast-Fourier-transform-based Poisson solver with open boundary conditions [10]. The beam–beam implementation reproduces the expected behaviour, especially the π an σ modes are found at the expected positions of Q and $Q - \lambda_{\mathrm{yokoya}} \cdot \xi_{\mathrm{bb}}$ with Q the tune, ξ_{bb} the beam–beam parameter and $\lambda_{\mathrm{yokoya}}$ the Yokoya factor [11]. The maximum single particle tune shift in simulation equals the beam–beam parameter as expected.

BTF Implementation

The BTF is implemented as follows. A particle ensemble of typically between 10^5 and 10^7 macroparticles is initialized as a matched Gaussian distribution and left coasting for a few thousand turns to equilibrate possible matching errors. After this initial equilibration the equilibrium distribution is cached. Then, a coherent excitation is carried out by adding a sinusoidal excitation signal $a(t) = \sin(\omega t)$ to the momentum component of the particle vectors at each passing of the exciter. Because the excitation frequency is chosen around the fractional tune, it is assumed that a whole bunch sees the same excitation signal. After each turn the transverse position of the centre of charge of the beam and the excitation signal amplitude is stored. In post-processing the BTF is calculated as the fraction of the complex amplitudes of the response and the exciting signal. The amplitudes are determined using the discrete Fourier transformation (DFT) at the chosen excitation frequency. After each excitation frequency the PIC-code re-initializes with the equilibrium particle distribution to reduce transient modes. To make sure we look primarily at the steady state of the excited beam, not at the transients, the first few hundred turns at the excitation frequency are ignored.

In the case of multiple bunches in one ring, the BTF excitation signal takes into account the phase between the bunches to replicate the situation in the real machine where all bunches are excited by the same excitation signal.

Test of the BTF model Before considering BTF of more complex situations we needed to validate our simulation model to make sure we agree with known analytic results. A good benchmark is the BTF of a beam with a Gaussian velocity profile and a tune spread solely due to chromaticity. We consider the single particles as harmonic oscillators around their betatron frequency ω. In the derivation we follow [7]. A harmonic oscillator driven off-frequency at a frequency of Ω carries out a beating at an amplitude A which is proportional to $\frac{1}{\omega^2 - \Omega^2}$. To determine the response of an ensemble of harmonic oscillators to a driving frequency Ω the intuitive approach is to integrate amplitude over the density $\psi(\omega)$ of eigenfrequencies. To make things simpler, A can be approximated by $\frac{1}{2\omega_\beta(\omega - \Omega)}$ where $\omega \simeq \Omega \simeq \omega_\beta$ (which is the case around the betatron

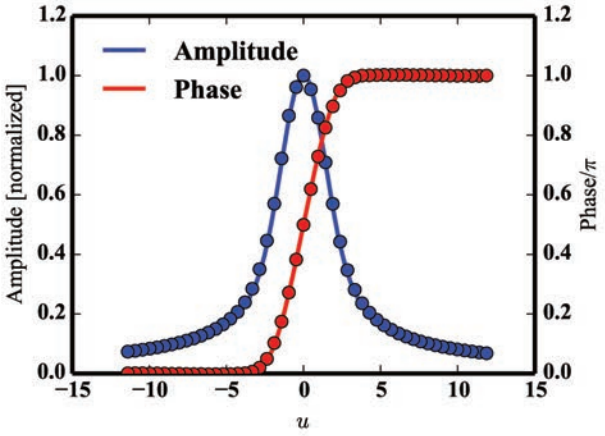

Figure 1: Comparison of amplitude and phase of the analytic prediction for the BTF of a beam with Gaussian tune spread (line) and the PIC BTF simulation results (points); u is the normalized frequency coordinate given in eq. (7). The simulation agrees well with analytic predictions.

lines). Taking out constant factors, the BTF behaves as

$$R(\Omega) \propto \int \frac{1}{\omega - \Omega} \psi(\omega)\, \mathrm{d}\omega. \tag{6}$$

This equation has an analytic solution for different forms of frequency distributions [7]. We look at the result for a Gaussian frequency spread. The normalized frequency u can be defined as a function of the mean particle betatron frequency $\overline{\omega}$, the driving frequency Ω and the frequency width of the distribution $\Delta\omega$ via the equation,

$$u = \frac{\overline{\omega} - \Omega}{\Delta\omega}. \tag{7}$$

Then the real and imaginary parts of the BTF are proportional to f and g, as below [7]:

$$f(u) = \sqrt{\frac{2}{\pi}} e^{-u^2/2} \int_0^\infty \frac{\mathrm{d}y}{y} e^{-y^2/2} \sinh(uy), \tag{8}$$

$$g(u) = \sqrt{\frac{\pi}{2}} e^{-u^2/2}. \tag{9}$$

The analytic BTF compares well to our PIC code as shown on example data in Fig. 1. It is also noteworthy that eq. (4) simplifies to eq. (6) in the absence of the lens.

Tune Distribution

The tune distributions in simulation are computed by running the simulation without BTF excitation for (2000 to 8000) turns. The particle coordinates are stored for a subset of typically (10^4 to 10^5) particles. In post-processing, DFT is used to find the peak of the oscillation frequency. The analytic tune distributions are computed by numerically evaluating particle density over the distribution and binning the resulting fractions into bins depending on the corresponding tune change according to eq. (2).

Electron-lens Model

To model the electron lens, the code uses the analytic expressions for the fields of a round Gaussian beam to kick the particles at one of the interaction points. The intensity of the field is adjusted to correspond to a chosen beam–beam parameter. The electron lens in simulation can be run as a *positron lens* by simply changing the sign of the beam–beam parameter, which we did most of the time to be able to easily make a comparison between BTF with stationary Gaussian lens and BTF with split tunes.

SIMULATION STUDY

First we ran simulations of a beam undergoing an interaction solely with a Gaussian lens. At the beginning it appeared as though the BTF from simulation and the analytic expectation were in disagreement: the first simulations for both split tunes and electron-lens type configuration showed a double peak structure not present in the analytic expectation. However, as shown in a sweep of excitation amplitudes in Fig. 2 on the example of a split tunes simulation, a significant reduction in exciter amplitude led to results in which no double peaks were observed any more. After amplitude reduction, the simulation results for a Gaussian lens were in good agreement with the analytic formula from eq. (4).

Recovery of the Beam–Beam Parameter

To test whether fitting to measured BTF of a beam interacting with an electron lens would enable us to recover the beam–beam parameter, we ran simulations of beams with Gaussian lenses of different beam–beam parameters. We fitted the analytic formula for the BTF to simulated BTF. Because the evaluation of the analytic BTF is rather costly, we calculate analytic BTF in MATHEMATICA for a reasonable range of parameters and use an interpolating function to fit the simulation data. An example fit is shown in Fig. 3. The beam–beam parameters to which the fits converge lie within three percent of the actual beam–beam parameter chosen for the simulation. Our test set consisted of simulated BTF with beam–beam parameters between 0.0025 and 0.0145.

Split Tune Conditions

We conducted part of the simulation study on split tune conditions because during the current run the hopes for a running electron lens are not high. The BTF of beams under split tune conditions looked similar to the analytic expectation for a defocussing Gaussian lens.

We ran simulations for split tune conditions for the same range of beam–beam parameters as we did previously for the electron lens. Again we tried to recover the beam–beam parameters using our fitting routine. For the split tunes we observed a slight deviation of the analytic result from the BTF even though overall agreement was visually still acceptable, as shown in Fig. 4. The beam–beam parameters recovered from the fits are given in the figure and were slightly underestimating the actual beam–beam parameter

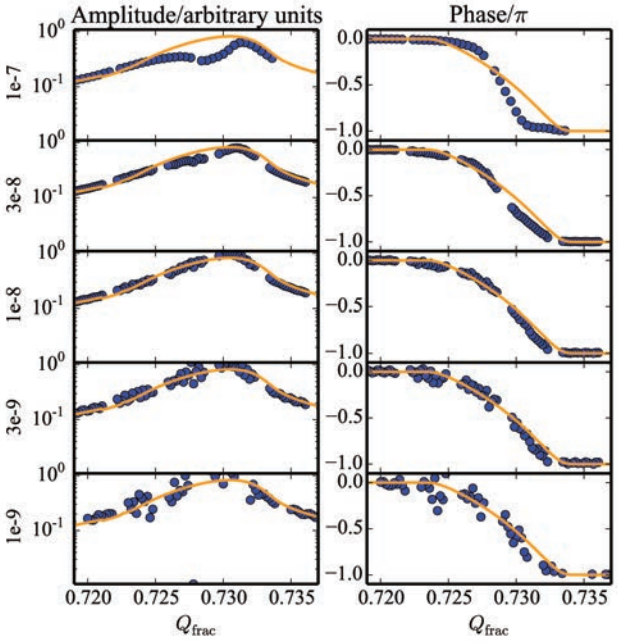

Figure 2: Comparison of numeric BTF (dots) from PIC simulation with split tunes and one IP to the analytic expectation (line). Normalized amplitudes are on the left, and values of phase/π are on the right. The excitation amplitude (the amplitude of the sinusoidal signal added to the x' component of the particle vector) is given on the left of the plots. We see good agreement for medium amplitudes. For higher amplitudes we observe a deviation, possibly due to particles in the tails of the distribution or due to coherent modes. For lower amplitudes the numerical noise is higher than the signal but can be reduced by increasing particle number.

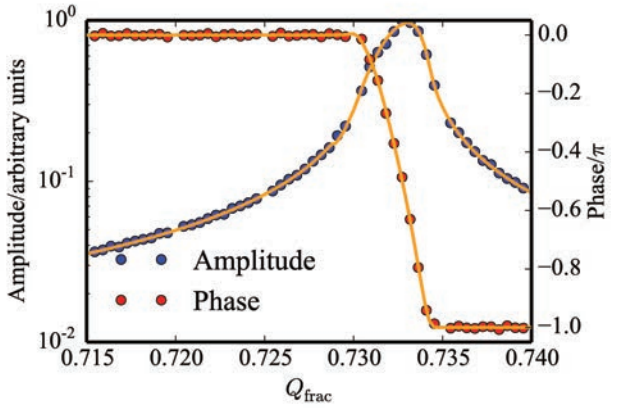

Figure 3: Comparison of analytic expectation (orange) with simulation amplitude (blue dots) and phase (red dots) for a Gaussian lens. We see very good agreement.

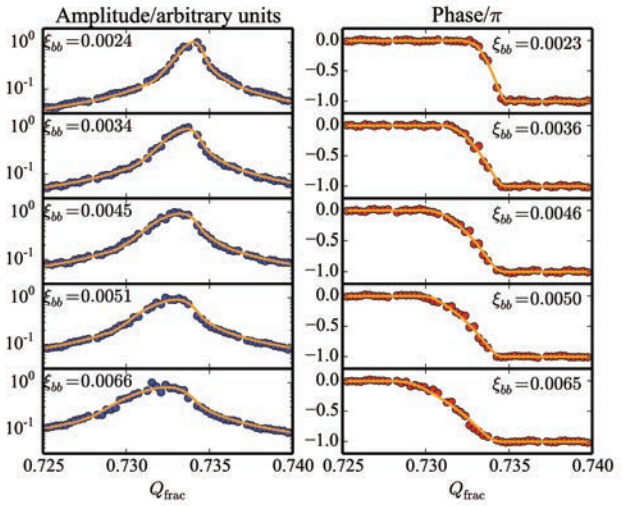

Figure 4: BTF from PIC simulations with 1 IP and split tunes (dots) in amplitude (left) and phase (right) for different beam–beam parameters in comparison with fits of the analytic BTF. The result of the fit is given in the individual plots. We see good agreement between the fits to phase and amplitude. Note that the fit results seem to scale linearly with the beam–beam parameter chosen in the simulation but are slightly lower. The dependence of fit result on simulation input is shown in Fig. 5.

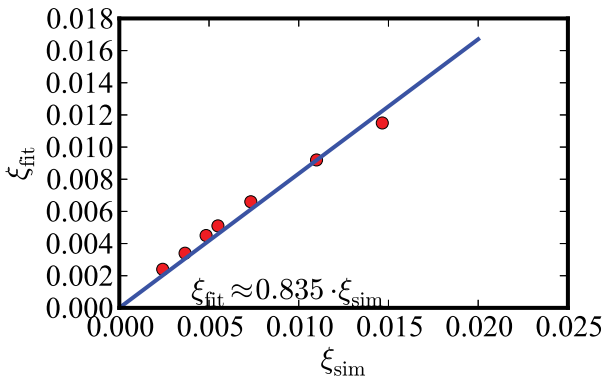

Figure 5: Relation between ξ_{bb} from fit to BTF simulations of split tunes and from simulation input. The dependence is approximately linear for our range of parameters.

used in the simulation. We blame this on the coherent modes to be expected within the incoherent spectrum and possibly leading to a narrowing of the peak. A plot of the beam–beam parameter from the fit over the actual beam–beam parameter from the simulation can be found in Fig. 5. The relation between fit result and actual beam–beam parameter appears to be scaling linearly with a factor of about 0.8. This result might, however, be dependent on the tune splitting.

Comparison with Measurement

The BTF that are available of split tunes measured in the machine do unfortunately not all replicate the analytic ex-

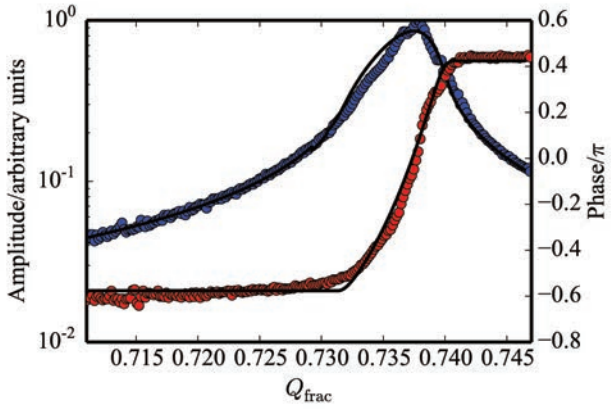

Figure 6: Comparison of the fits of the analytic result to measurement data in the yellow horizontal plane. Dots in red are measurement data and those in blue are phase data; the black line is the analytic fit.

pectation. There may be several reasons for that. Firstly the split tunes fills were full machines (instead of the simulation situation of only two or six coupling bunches). During the 2012 run the BTF system was measuring the centre-of-mass motion of all the bunches in the machine and combining them into a single BTF. For conditions with differing bunch parameters this may lead to a deformation of the signal so that we cannot expect it to follow our clean simulation data anymore. Furthermore the coherent modes in the incoherent tune distribution can lead to a deformation of the bunches and a resulting deformation of the BTF not covered by our assumption of round Gaussian beams. For this reason we decided to look at the BTF of the best-behaved fills among the split tunes. Best-behaved means, in this case, no multipeak-structures in the individual planes, low heating compared to the other fills, and rather round beams. The beams were, however, still slightly asymmetrical (normalized 6 σ emittances were, for yellow, $\varepsilon_x = 20, \quad \varepsilon_y = 17.5$, and, for blue, $\varepsilon_x = 22.5, \quad \varepsilon_y = 21.5$) at an average of $1.8 \cdot 10^{11}$ particles per bunch. Nevertheless we tried to apply the fitting algorithm for round beams demonstrated above on simulated BTF. In the horizontal plane according to the beam properties we would expect a beam–beam parameter of 0.012 to 0.014. We found a reasonable approximation of the measurement by the analytic result. The beam–beam parameters obtained from the fits to yellow and blue horizontal BTF measurement data are $\xi_{\mathrm{fit,yellow}} = 0.012$ and $\xi_{\mathrm{fit,blue}} = 0.012$ when one takes into account the factor of 0.835 between ξ_{fit} and ξ obtained from simulation. Furthermore the fits to amplitude and phase deviate only by a few percent. In the vertical plane, the peaks looked distorted, on which basis we reason that here other effects might be at work. On top of that, in the vertical plane, coherent modes were observed for some fills. Example fits in the horizontal plane can be found in Fig. 6.

CONCLUSION AND OUTLOOK

Currently our analytic model is restricted to round Gaussian beams, as is typically the case in RHIC. However, it should be feasible to generalize the analytic theory for arbitrary aspect ratios by adjusting ΔQ_{lens}. In absence of an electron lens a possible test scenario for the fitting method could be found in weak–strong beam–beam interactions, where a strong beam could be modelled as the electron lens and the measurement would be done on the weak beam. For the 2013 run, the BTF system has been upgraded and is now able to measure BTF of single bunches, which would enable running different intensity strong–weak BTF in one fill. Furthermore, once the electron lenses are up and running, we can test whether the BTF of an electron lens agrees with the BTF according to eq. (4), as is to be expected according to our simulation. In this case we would be able to give a good estimate for the strength of the electron lens from the BTF alone.

ACKNOWLEDGMENTS

Paul Görgen would like to thank Simon White for his support.

REFERENCES

[1] W. Fischer et al., "Construction Progress of the RHIC Electron Lenses," Proc. International Particle Accelerator Conference, New Orleans, May 2012.

[2] S. White et al., "Coherent Beam–Beam Effects Observation and Mitigation at the RHIC Collider," Proc. International Particle Accelerator Conference, New Orleans, May 2012.

[3] M. Gasior and R. Jones, "The Principle and First Results of Betatron Tune Measurement by Direct Diode Detection," LHC-Project-Report 853 (2005).

[4] A. Burov and V. Lebedev, "Transverse Instabilities of Coasting Beams with Space Charge," Phys. Rev. ST Accel. Beams 12, 034201 (2009).

[5] V. Kornilov and O. Boine-Frankenheim, "Stability of Transverse Dipole Modes in Coasting Ion Beams with Nonlinear Space Charge, Octupoles, and Chromaticity," Phys. Rev. ST Accel. Beams 1, 074202 (2008).

[6] J. Berg and F. Ruggiero, "Landau Damping with Two-dimensional Betatron Tune Spread," CERN SL-AP-96-71.

[7] K.Y. Ng, *Physics of Intensity Dependent Beam Instabilites* (World Scientific, Singapore, 2006).

[8] O. Boine-Frankenheim and V. Kornilov, "Implementation and Validation of Space Charge and Impedance Kicks in the Code PATRIC for Studies of Transverse Coherent Instabilities in FAIR Rings," Proc. International Computational Accelerator Physics Conference, Chamonix, October 2006.

[9] S. Tepikian, private communication.

[10] V. Kapin, Proc. European Particle Accelerator Conference, Paris, June 2002, p. 1637.

[11] K. Yokoya and K.Haruyo, "Tune Shift of Coherent Beam–Beam Oscillations," Part. Accel. **27** (1990) 181.

Published by CERN in the Proceedings of the ICFA Mini-Workshop on Beam–Beam Effects in Hadron Colliders,
CERN, Geneva, Switzerland, 18–22 March 2013, edited by W. Herr and G. Papotti, CERN–2014–004 (CERN, Geneva, 2014)

BEAM–BEAM AND IMPEDANCE*

S. White, Brookhaven National Laboratory, Upton, NY, USA
X. Buffat, EPFL, Lausanne, Switzerland; CERN, Geneva, Switzerland

Abstract

As two counter-rotating beams interact they can give rise to coherent dipole modes. Under the influence of impedance these coherent beam–beam modes can couple to higher order head–tail modes and lead to strong instabilities. A fully self-consistent approach including beam–beam and impedance was used to characterize this new coupled mode instability and study possible cures such as a transverse damper and high chromaticity.

INTRODUCTION

In a high-energy, high-brightness hadron collider, the coherent dynamics of colliding beams is dominated by beam–beam interactions. The non-linearities of the beam–beam force introduce a tune spread largely exceeding the one from other sources, such as non-linear fields, and provide sufficient stability for any pure impedance instabilities. When they interact with each other, the two beams will couple, resulting in coherent oscillations. In the case of equal beams and tunes these coherent oscillations can be described by two eigenmodes, corresponding to either in-phase or out-of-phase oscillation, respectively the σ- and π-modes. The frequency of these modes may be well separated from the incoherent tune spread and consequently they do not profit from the large intrinsic Landau damping properties of the beam–beam interactions. Such coherent beam–beam modes are generally not self-excited and require some external mechanism to become unstable, such as the machine impedance. When studying the stability of colliding beams, it is therefore necessary to consider both processes simultaneously.

Past studies have shown that the combination of beam–beam interactions and impedance could lead to coherent instabilities. However, these studies were performed either using a linearized model [1] or for very specific cases applied to the Tevatron [2]. During the 2012 proton run of the LHC, coherent instabilities were routinely observed [3], triggering a renewed interest to pursue these studies. In this paper, we present a refined model allowing one to study the interplay of beam–beam and impedance using the full LHC impedance model [4]. We will concentrate mostly on single-bunch effects and associated stabilization techniques and present preliminary results for multibunch effects.

* Work partially supported by Brookhaven Science Associates, LLC under Contract No. DE-AC02-98CH10886 with the U.S. Department of Energy, and in part by the U.S. LHC Accelerator Research Program.

MODELS

Two models were used to characterize the interplay of beam–beam and impedance:

- An analytical model based on the circulant matrix approach used in Ref. [1]
- A fully self-consistent multiparticle tracking model. Single-bunch effects were studied with the code BeamBeam3D [5] and multibunch effects with the code COMBI [6]

The circulant matrix model (CMM) allows one to compute the complex tune shift in the presence of six-dimensional beam–beam interactions, impedance, chromaticity and transverse damper. The bunches are sliced in the longitudinal phase space and the beam–beam kicks are computed with the linearized approximation. Landau damping is not included in this model but the computation of the eigenmodes is very fast allowing for extensive parameter scans. This provides an excellent tool for understanding the coherent beam dynamics in the presence of various physics processes. This approach is very fast and most appropriate for extensive parameter scans, which provide a good understanding of the coherent dynamics in the presence of various processes.
While much more demanding in terms of computing power, tracking simulations are a necessary complement to the CMM. Indeed, the CMM is not a self-consistent approach, giving rise to differences in the frequencies of beam–beam coherent modes. In simple cases, the beam–beam parameter can be re-scaled in order to compensate for the change of frequency of the modes due to lack of self-consistency. In more complex configurations, this approximation needs to be tested against a self-consistent model. Also, the CMM is not suited to study any non-linear effect, in particular Landau damping. Indeed, even though the complex tune shift can be computed, the dispersion integral used to derive the stability of a pure impedance mode is not valid for a beam–beam coherent mode. An analytical derivation of a dispersion integral in LHC-type configurations promises to be a great challenge, in particular in the multibunch regime, i.e. in the presence of PACMAN effects. A numerical approach, by the means of self-consistent multiparticle tracking codes, allows one to address these issues. Moreover, such approach allows one to treat any other non-linear effects, e.g. transverse feedback imperfections or external noise. BeamBeam3D and COMBI (COherent Multi-Bunch Instabilities) are two similar implementations of such model, based on different

978-92-9083-404-5, 0007-8328 –
http://dx.doi.org/10.5170/CERN–2014–004.217

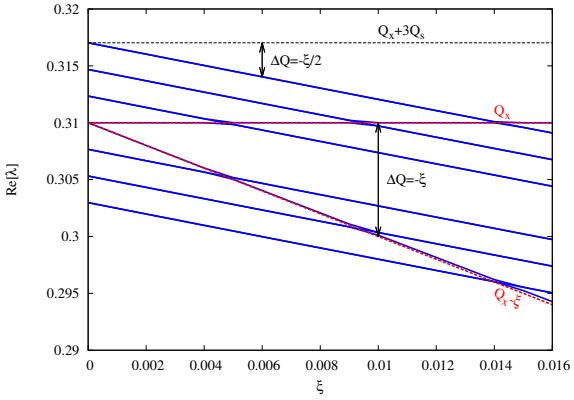

Figure 1: Synchro–betatron modes as a function of the beam–beam parameter for $Q' = 0.0$ and $\beta^*/\sigma_s \approx 100$. Impedance was not included in this case. The σ- and π-modes are shown in red.

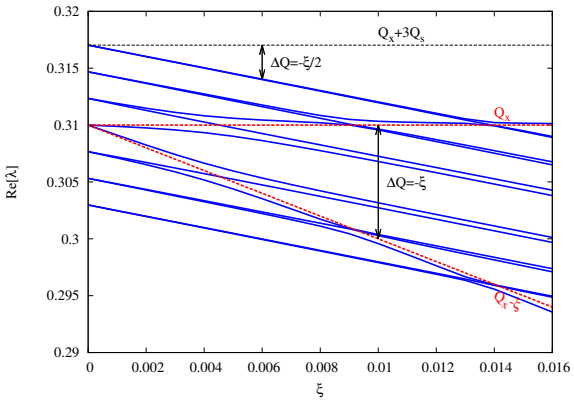

Figure 2: Synchro–betatron modes as a function of the beam–beam parameter for $Q' = 0.0$ and $\beta^*/\sigma_s \approx 1$. Impedance was not included in this case. The σ- and π-modes are shown in red.

multicore parallelization concepts.

Figures 1 and 2 show the tunes of the synchro–betatron modes up to the third sideband in the presence of a six-dimensional beam–beam interaction. When the synchro–betatron coupling introduced by the beam–beam interaction is negligible ($\beta^*/\sigma_s >> 1$), there is no cross talk between higher order head–tail modes and the coherent beam–beam σ- and π-modes. The tune of the sidebands is shifted by the coherent beam–beam tune shift, which is approximately equal to $\xi/2$ in this case. When the synchro–betatron coupling becomes important ($\beta^*/\sigma_s \approx 1$), the synchrotron sidebands are now deflected when their frequency approaches the frequency of the coherent beam–beam modes, indicating possible coupling between the coherent beam–beam dipolar modes and higher order head–tail modes. In both cases, the imaginary part of the tune shifts of all modes is equal to zero: in the presence of beam–beam interactions only, the system is always stable.

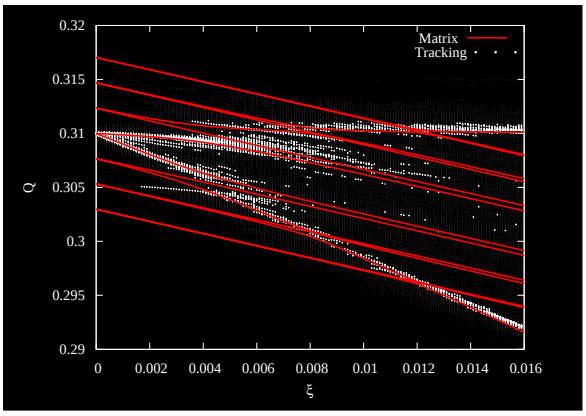

Figure 3: Synchro–betatron modes as a function of the beam–beam parameter for $Q' = 0.0$ and $\beta^*/\sigma_s \approx 1$. Comparison between the CMM and BeamBeam3D. Impedance was not included in this case.

Figure 3 shows a comparison between the tracking code BeamBeam3D and the CMM for $\beta^*/\sigma_s \approx 1$. The CMM was re-scaled by the Yokoya factor to match the tracking results. An excellent agreement is observed and one can see that the frequency of the modes is modified when the beam–beam coherent modes cross the first sidebands. The frequency components between the σ- and π-modes observed in the tracking correspond to the beam–beam tune spread.

The implementation of impedance in BeamBeam3D was fully benchmarked with the HEADTAIL code [7]. In order to validate the implementation of the LHC impedance model into the the CMM, we compared the rise times as a function of chromaticity for an airbag distribution. The results are shown in Fig. 4, where an excellent agreement is observed. The implementation of the LHC impedance model in COMBI was also benchmarked against multi-bunch HEADTAIL [4]; nevertheless, this development is rather recent and only preliminary results are presented.

MODE COUPLING INSTABILITY OF COLLIDING BEAMS

We start by looking at the simple case of two single bunches colliding head-on in one interaction point (IP). The impedance model used in the following simulations was derived using the 2012 LHC lattice and collimator settings [4]. The beam–beam interactions are computed with a full six-dimensional model taking into account the synchro–betatron effects and eventual non-Gaussian transverse distributions. In order to estimate the beam stability for a large number of beam parameters, multiparticle tracking is performed over 10000 turns and each case is analysed using an interpolated FFT algorithm. The beam stability of any

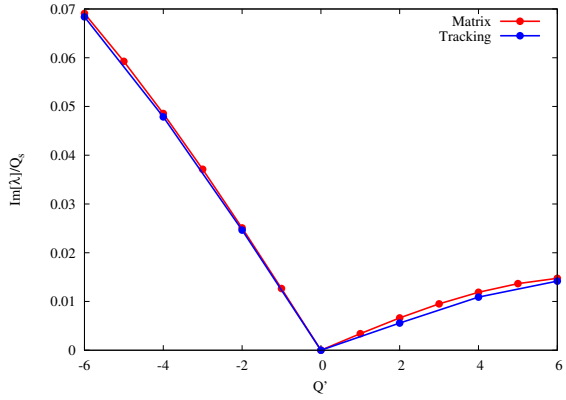

Figure 4: Imaginary part of the tune shift as a function of chromaticity for the CMM and BeamBeam3D. In both models an airbag distribution was used.

given mode can then be assessed by looking at the amplitude of its corresponding spectral line.

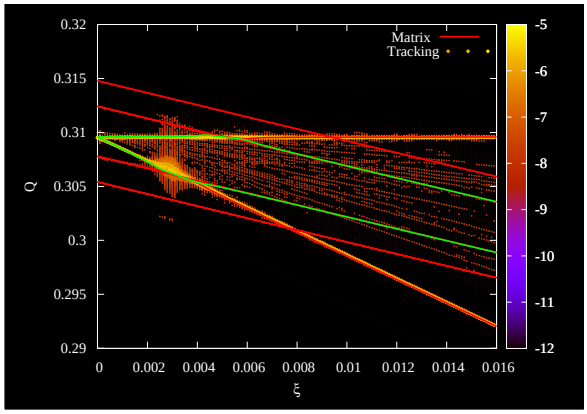

Figure 5: Synchro–betatron modes as a function of the beam–beam parameter for $Q' = 0.0$ and $\beta^*/\sigma_s \approx 90$. The colours correspond to the amplitude of the spectral line. Impedance was set to be constant over the whole scan.

Figures 5 and 6 show a scan in the beam–beam parameter at constant impedance. As the beam–beam π-mode approaches the head–tail mode –1 ($\xi \approx 0.003$), they become coupled, leading to a strong instability with similar rise times and characteristics to the impedance-driven TMCI (Transverse Mode Coupling Instability). This is observed in both the tracking and CMM with comparable rise times. The CMM also indicates a coupling between the σ-mode and the head–tail mode +1. This is not observed in the tracking simulations; the reasons for this discrepancy are under investigation but could be related to Landau damping, which is not taken into account in the CMM. The strength of this coupling instability and the range in terms of ξ over which the modes couple are determined by the strength of the wake and the β-function at the IP.

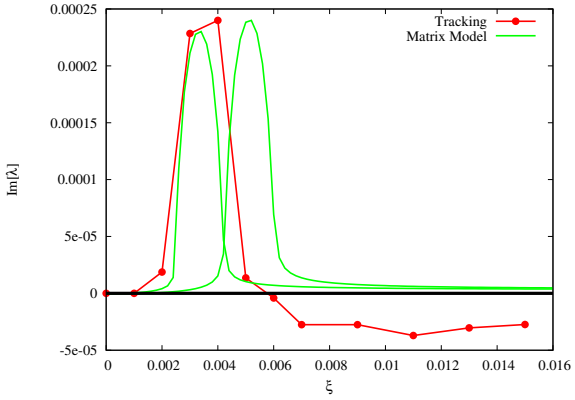

Figure 6: Imaginary part of the tune shift of the most unstable modes as a function of the beam–beam parameter for $Q' = 0.0$ and $\beta^*/\sigma_s \approx 90$. Impedance was set to be constant over the whole scan.

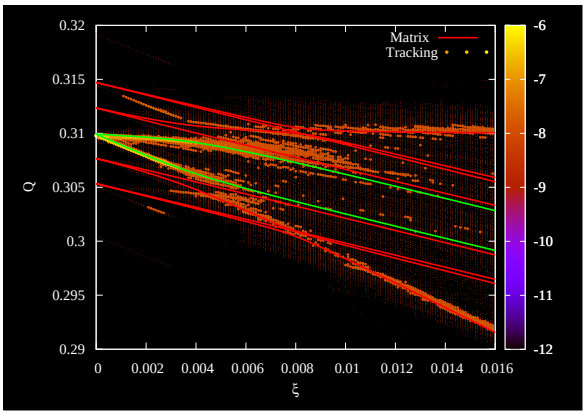

Figure 7: Synchro–betatron modes as a function of the beam–beam parameter for $Q' = 0.0$ and $\beta^*/\sigma_s \approx 1$. The colours correspond to the amplitude of the spectral line. Impedance was set to be constant over the whole scan.

Figure 7 shows a scan in the beam–beam parameter using the same beam parameters as in Fig. 5 except for the ratio β^*/σ_s. A ratio $\beta^*/\sigma_s \approx 1$ introduces synchro–betatron coupling from the beam–beam interaction itself. In this case, as was shown in Fig. 2, the synchrotron sidebands can be deflected by the beam–beam modes. For strong synchro–betatron coupling the most unstable modes involved in the coupling instability (shown in green in Figs. 5 and 7) are not overlapping any higher order head–tail modes. This results in a suppression of the mode coupling instability observed for higher β^*/σ_s ratios. Synchro–betatron coupling also increases the Landau damping introduced by the beam–beam interactions. It was shown in Ref. [8] that when the synchrotron tune is of the order of the beam–beam parameter and significant synchro–betatron coupling is present, the tune spread of the lower order sidebands can overlap the π-mode and damp it. This

effect could be reproduced in simulations [9] and may be useful in the case where coherent beam–beam mode stability becomes an issue for machines operating at low β^*/σ_s ratio.

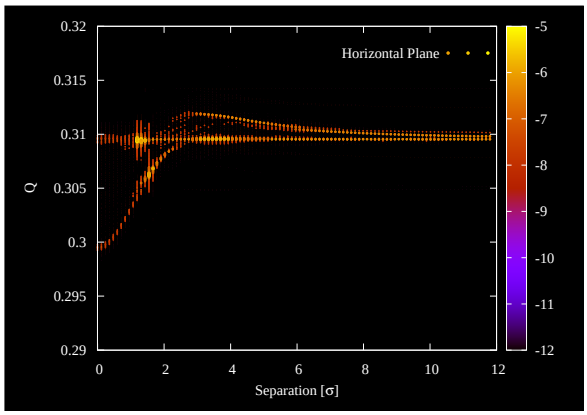

Figure 8: Synchro–betatron modes as a function of the transverse separation for $Q' = 0.0$ and $\beta^*/\sigma_s \approx 90$. The colours correspond to the amplitude of the spectral line. Impedance and beam–beam parameters were set to be constant over the whole scan.

Colliding with transverse offsets changes the frequency of the beam–beam coherent modes and modifies the stability diagram [10]. Offset collisions can occur while bringing the beam into collisions, in the first moments of a physics store before the luminosity is optimized or when levelling the luminosity, as was routinely done at the LHC in 2012 [11]. Figure 8 illustrates a scan in separation (only the separation plane is shown) including coherent beam–beam and impedance. The mode coupling instability is observed when either the π-mode overlaps the head–tail mode –1 or the σ-mode overlaps the head–tail mode +1 at separations between 1.0 and 2.0 σ. These instabilities also occur when the stability diagram reaches its minimum [10]. This was tested in a dedicated experiment [12] during which instabilities were observed at small separations while the beam was fully stable when colliding head-on. Weak–strong simulations with single-plane offset indicate that the stability can be shared between the horizontal and vertical planes preventing any loss of Landau damping and consequently any impedance-only-driven instabilities to rise. This experiment, although not fully conclusive, appears to confirm the existence of the mode coupling instability involving coherent beam–beam modes. Experimental data and detailed analysis can be found in Ref. [12].

It is worth mentioning that mode coupling instabilities can also occur for long-range interactions when the tune shift is sufficiently high. In the case of the LHC, the β-functions at the location of the long-range interactions can reach several kilometers, discarding any benefits from synchro–betatron coupling, and this therefore represents the worst-case scenario for this specific mode coupling instability. With the 2012 LHC beam parameters the tune shift at which the instability occurs is reached for approximately 10 long-range interactions, as shown in Fig. 9. This number has to be compared to 16 long-range interactions per IP in the case of nominal LHC bunches, indicating that PACMAN bunches are the most critical ones. The instability observed for 15 long-range interactions is originating from the other plane.

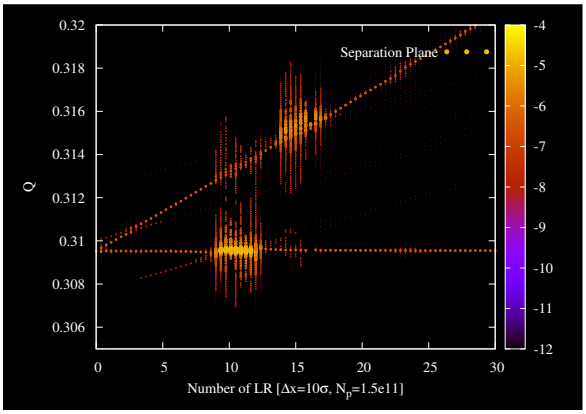

Figure 9: Synchro–betatron modes as a function of the number of long-range interactions for a single colliding IP. All the long-range interactions were lumped in one location for which a separation of 10 σ was assumed.

Figure 9 represents the simplified case of a single IP colliding, where all the interactions were lumped in one place. In reality, multibunch effects and the phase advance between consecutive IPs will modify the situation and should be considered in any realistic simulations of the LHC.

STABILIZATION OF SINGLE-BUNCH INSTABILITIES

Chromaticity combined with tune spread (to provide Landau damping) is generally used to cure transverse instabilities. In the specific case of the LHC, the bunch-by-bunch transverse damper can also be used for this purpose. In order get a better understanding of how these parameters affect the coherent beam dynamics, we start with the CMM. All the following simulations were performed using beam parameters corresponding to the most critical configuration, where the transverse mode coupling instability is the strongest.

Figure 10 shows the real and imaginary tune shifts for a single bunch colliding head-on computed using the CMM for increasing chromaticity. At $Q' = 0.0$, the modes are fully coupled and the instability develops similarly to what was previously shown in Figs. 5 and 6. As the chromaticity is increased the frequencies of the modes involved in the instability are separated until they fully decouple for $Q' = 10.0$. Chromaticity should therefore help mitigating the mode coupling instability. However, the larger the ratio β^*/σ_s, the higher the chromaticity required to decouple

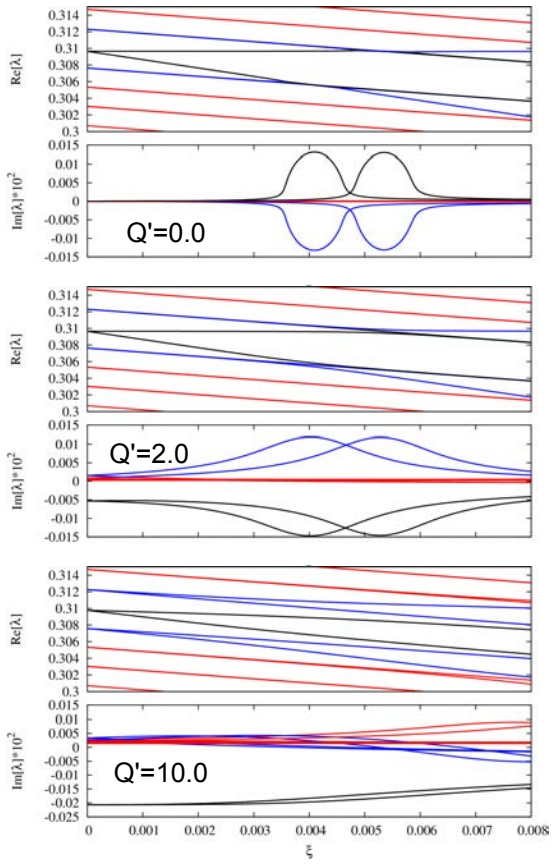

Figure 10: Real and imaginary parts of the tune shift as a function of the beam–beam parameters for a single bunch colliding head-on at $Q' = 0.0$ (top), $Q' = 2.0$ (middle) and $Q' = 10.0$ (bottom). Here the ratio $\beta^*/\sigma_s \approx 70$.

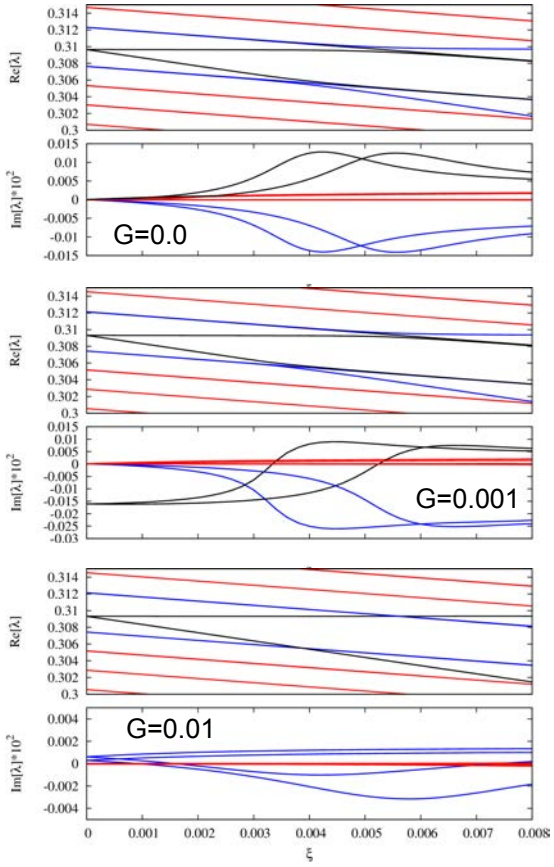

Figure 11: Real and imaginary parts of the tune shift as a function of the beam–beam parameters for a single bunch colliding head-on at $G = 0.0$ (top), $G = 0.001$ (middle) and $G = 0.01$ (bottom). Here the ratio $\beta^*/\sigma_s \approx 8$. The gain G is specified in 1/turns.

the modes. Operating with too large chromaticity may degrade beam lifetime. For very large ratio β^*/σ_s, which is typically the case for long-range interactions, using chromaticity only may therefore not be appropriate to cure this instability.

Figure 11 shows the real and imaginary tune shifts for a single bunch colliding head-on computed using the CMM for increasing transverse damper gain. The damper is assumed to be an ideal rigid bunch damper for which the gain is defined in 1/turns. The damper is most efficient on modes with a significant dipolar component, such as head–tail mode 0. If Landau damping is sufficient to damp higher order modes, which is generally the case for colliding beams, the transverse damper should be a very efficient means to cure the instability without having to run at unrealistically high gain.

As mentioned before, the CMM does not include Landau damping. In order to assess beam stability including Landau damping, multiparticle simulations are required. Figures 12 and 13 show the impact of chromaticity on the mode coupling instability for a single bunch colliding head-on in one IP. For low β^*/σ_s ratio chromaticity alone is sufficient to damp the instability. As the ratio is increased, chromaticity alone reduces the rise time but does not completely cure the instability up to $Q' = 6.0$. Comparing the cases with $\beta^*/\sigma_s \approx 30$ and $\beta^*/\sigma_s \approx 110$, it seems that the rise time as a function of chromaticity converges for large β^*/σ_s ratios. This confirms the results from the CMM and indicates possible issues with long-range interactions when using chromaticity only as a cure to the mode coupling instability.

Figure 14 shows the impact of the transverse damper on the mode coupling instability for a single bunch colliding head-on in one IP with $\beta^*/\sigma_s \approx 100$ and $Q' = 0.0$. It is seen that even for a very low gain of 0.001 the beam is rendered stable by the transverse damper. This benefit of the transverse damper was experimentally demonstrated with offset collisions. It was shown that the beams were strongly unstable when the damper was turned off and stable with the damper on for a separation of approximately $1.0\,\sigma$ [12] and with $Q' \approx 5.0$. This strong instability with offset collisions and damper off is a good candidate for the mode coupling instability mentioned before.

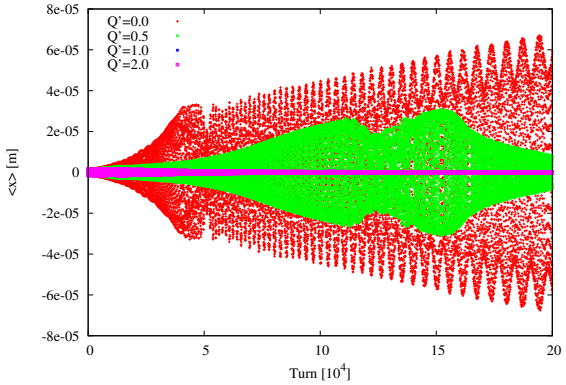

Figure 12: Centre of mass motion for a single bunch colliding head-on with $\beta^*/\sigma_s \approx 8$ and increasing Q'.

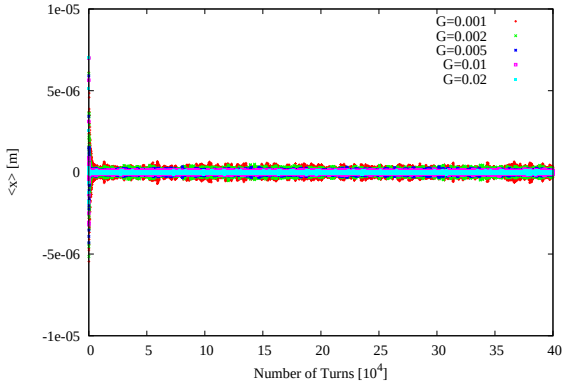

Figure 14: Centre of mass motion for a single bunch colliding head-on with $\beta^*/\sigma_s \approx 100$ and $Q' = 0.0$ as a function of the damper gain.

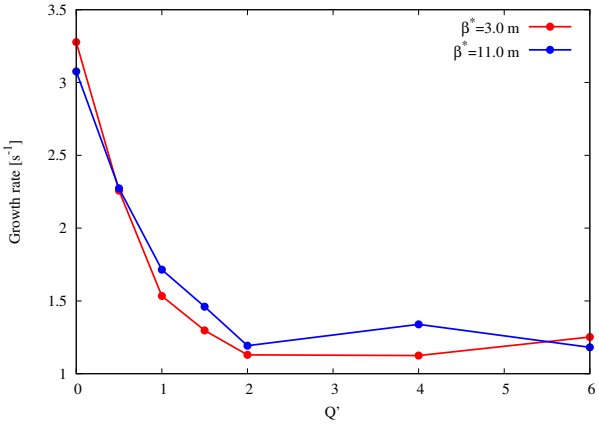

Figure 13: Instability rise time for a single bunch colliding head-on with $\beta^*/\sigma_s \approx 30$ and $\beta^*/\sigma_s \approx 110$ as a function of Q'.

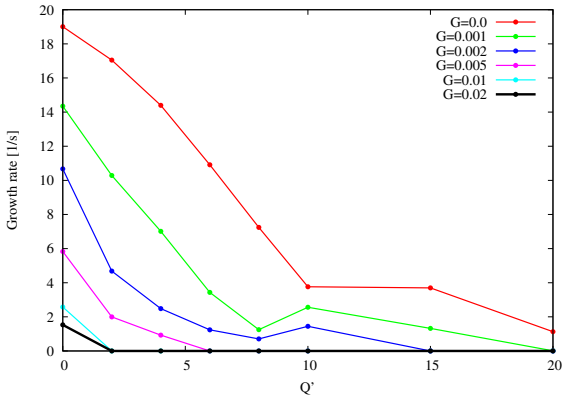

Figure 15: Instability rise time as a function of chromaticity for different damper gains, in the single-bunch approximation of a configuration with 10 long-range interactions separated by $10\,\sigma$.

Although it seems that any instability involving head-on interactions could be cured with the transverse damper, the situation is more complicated when looking at offset collisions and even more for long-range interactions. Two mechanisms can degrade the situation: the reduction of the tune spread and the absence of synchro–betatron coupling in the case of long-range interactions. Figure 15 shows the instability rise time as a function of transverse damper gain and chromaticity in the case of long-range interactions. All the interactions are lumped in one location and the tune shift was set to be equivalent to 10 long-range interactions with a separation of $10\,\sigma$. In this case, either chromaticity or damper only is not sufficient to damp the instability. There is however a correlated dependence: the higher the gain the lower the chromaticity required to stabilize the beams and inversely. In 2012, the LHC was operated with both high gain and chromaticity. Both these parameters are known to degrade beam lifetime and emittance; these results indicate that there should be room for optimization of these parameters which should be considered during LHC recommissioning in 2015.

Adding a full head-on interaction significantly increases the tune spread and consequently damps all long-range types of instabilities. This is consistent with experimental observations [3] and indicates that operating the transverse damper during physics stores may not be required as long as sufficient tune spread is provided and tune shifts at which the coupled mode instability occurs are avoided.

MULTIBUNCH EFFECTS

Previous results were produced using the single-bunch approximation. In the LHC, the filling pattern, long-range interactions and symmetry of the collision points should be considered to give a more realistic picture of the coherent beam dynamics. In such configuration, each bunch encounters a different set of beam–beam interactions, leading

to significantly different incoherent and coherent effects. In particular, the coupling between bunches along a single beam through the machine impedance and to bunches of the other beam through beam–beam interactions becomes different for each bunch. The CMM was extended to multi-bunch in order to properly take into account the real beam–beam configuration and coupled bunch impedance.

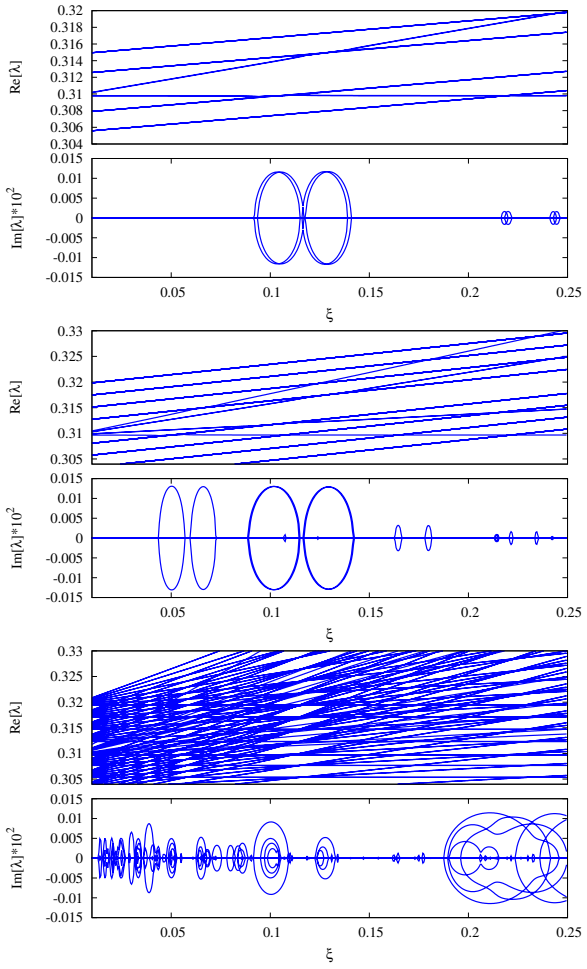

Figure 16: Real and imaginary parts of the tune shift as a function of the beam–beam parameter. In this case only long-range interactions in a single IP were considered. The top plot is for two bunches in each beam, the middle plot for three bunches in each beam and the bottom plot for eight bunches in each beam colliding only on one side of the IP to enhance PACMAN effects. The modes of all bunches are shown in these plots.

Figure 16 shows how the complexity of the collision pattern can modify the coherent beam dynamics. In these cases only long-range interactions in a single IP were considered. The top plot shows the case of two bunches per beam, each bunch colliding only once on either side of the IP, and is therefore similar to the single-bunch case. The only difference between the bunches comes from the coupled bunch impedance. The coupled mode instabilities are clearly observed when the beam–beam modes cross the head–tail modes ± 1. Although much weaker, this instability is also observed when the beam–beam modes cross the head–tail modes ± 2. This is an interesting feature which deserves further investigation, as the effect of the damper on such higher order mode coupling instabilities is unclear. As the number of bunches is increased, and hence the complexity of the collision pattern, a lot of modes with different frequencies appear and consequently mode coupling instabilities occur for most beam–beam parameters. In particular, the different modes do not necessarily involve the whole beam, but only a subset of bunches, as also shown by self-consistent simulations in Fig. 18. It is rather clear from this picture that PACMAN effects and the overall complexity of the LHC collision pattern cannot be neglected when looking at coherent beam dynamics.

Figure 17 shows a comparison of simulations with the CMM and COMBI in an identical configuration (nominal 2012 LHC running condition with $Q_s = 0.002$), indicating a good agreement between the models. In particular, mode coupling instabilities are observed for separations from 11 to 16 σ at frequencies around the horizontal tune, 0.31. The separation at which the instabilities occur depends on the beam–beam parameter and synchrotron tune. The instabilities observed in the tracking code only, at frequencies between 0.316 and 0.325, originate from the vertical plane and therefore do not appear in the CMM, which models one plane only. It is foreseen to further extend the CMM to take this into account.

The complex tune shift of each mode is evaluated by singular value decomposition of the turn-by-turn position of each bunch. The singular vectors associated with the most unstable mode at separations of 9 and 10 σ are shown in Fig. 18. In particular, one observes that, in the configuration with 10 σ separation, bunches at the edge of the train are stable, while the bunches at the centre of the train are unstable. The opposite is true at 9 σ. Moreover, the rise time associated with these two modes are significantly different, respectively 1800 and 3800 turns. This observation provides another indication of the importance of PACMAN effects on the coherent dynamics and therefore motivates further studies of the effect of the different stabilization techniques in configurations as close as possible to the real LHC.

SUMMARY AND OUTLOOK

During the 2012 proton run of the LHC, coherent instabilities were routinely observed in the LHC at the end of the squeeze and with beams colliding with a transverse offset, triggering a renewed interest to pursue studies of the interplay of beam–beam and impedance. For this purpose two models were developed:

- An analytical model based on the circulant matrix approach used in Ref. [1]

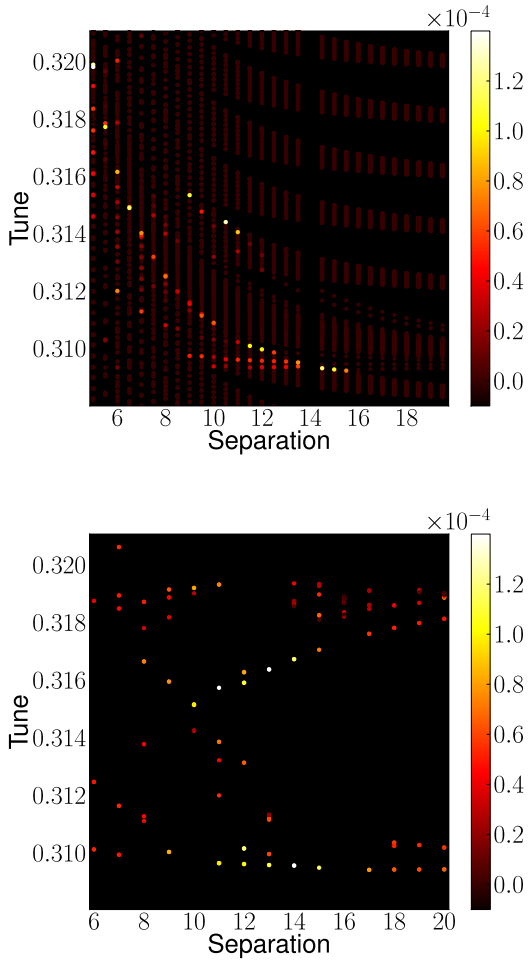

Figure 17: Coherent mode frequencies and rise times (colour) as a function of the normalized separation in the horizontal plane at the long-range location for two trains of 36 bunches colliding in one IP with 16 long-range interactions. The upper plot shows the result from CMM and the lower from COMBI. The synchrotron tune in this case was set to 0.002.

- A fully self-consistent multiparticle tracking model. Single-bunch effects were studied with the code BeamBeam3D [5] and multibunch effects with the code COMBI [6]

A full benchmarking campaign with existing code was done to validate the implementation of impedance in these different models and excellent agreement was reached for both the analytical model and tracking codes.

Single-bunch effects were studied in detail for various cases. It was shown that the coherent beam–beam modes can couple with higher order head–tail modes giving rise to strong instabilities with similar characteristics to the impedance-driven TMCI. Possible cures were considered and it was demonstrated that, in the case of the single-bunch approximation, a combination of chromaticity and

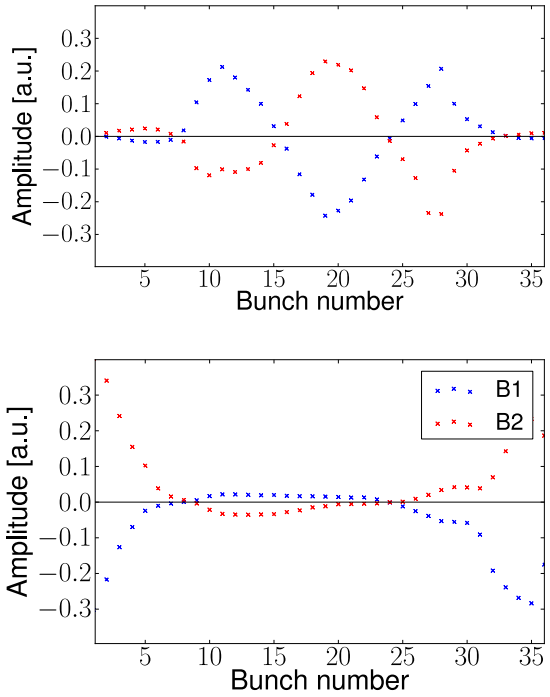

Figure 18: Oscillation amplitude of each bunch of the two beams for an unstable mode in the presence of impedance and 16 long-range beam–beam interactions in one IP with separations of $10\,\sigma$ (upper plot) and $9\,\sigma$ (lower plot).

transverse damper should stabilize the beams in all cases. Specific cases should be studied in detail to optimize the values of the gain and chromaticity. Nevertheless, due to its complex collision pattern, the LHC beams can hardly be approximated with a single bunch. PACMAN effects and coupled bunch impedance have to be considered in any attempt to realistically model the LHC. Both analytical and tracking models were developed to study multibunch effects. Preliminary results show good agreement and tend to confirm the invalidity of the single-bunch approximation for the case of the LHC. Further efforts should be pursued in this direction to provide a better understanding of LHC observations.

ACKNOWLEDGMENTS

The authors would like to thank T. Pieloni and N. Mounet for their help and support regarding these studies.

REFERENCES

[1] E.A. Perevedentsev and A.A. Valishev, Phys. Rev. Spec. Top. Accel. Beams 4 (2001) 024403.

[2] E. Stern et al., Phys. Rev. Spec. Top. Accel. Beams 13 (2010) 024401.

[3] G. Papotti, "Observation of Beam–Beam Effects in the LHC," these proceedings.

[4] N. Mounet, PhD thesis, CERN-THESIS-2012-055, (2012).

[5] J. Qiang et al., Phys. Rev. Spec. Top. Accel. Beams 5 (2002) 104402.

[6] T. Pieloni, PhD thesis, CERN-THESIS-2010-056 (2010).

[7] G. Rumolo et al., Phys. Rev. Spec. Top. Accel. Beams 5 (2002) 121002.

[8] Y. Alexahin, Nucl. Instrum. Methods A 480 (2002) 253.

[9] S. White et al., "Synchro–Betatron Effects in the Presence of Large Piwinski Angle and Crab Cavities at the HL-LHC," Proceedings of IPAC12, Shanghai, China, (2012).

[10] X. Buffat, "Stability Diagrams of Colliding Beams," this workshop.

[11] B. Muratori and T. Pieloni, "Luminosity Leveling Techniques: Implications for Beam–Beam Interactions," this workshop.

[12] X. Buffat, "Coherent Beam–Beam Modes in the LHC," this workshop.

Published by CERN in the Proceedings of the ICFA Mini-Workshop on Beam–Beam Effects in Hadron Colliders,
CERN, Geneva, Switzerland, 18–22 March 2013, edited by W. Herr and G. Papotti, CERN–2014–004 (CERN, Geneva, 2014)

COHERENT BEAM–BEAM MODE IN THE LHC

X. Buffat, EPFL, Lausanne, Switzerland; CERN, Geneva, Switzerland
R. Calaga, R. Giachino, W. Herr, G. Papotti, T. Pieloni, CERN, Geneva, Switzerland
S. White, BNL, Upton, NY, USA

Abstract

Observations of single bunch beam–beam coherent modes during dedicated experiments in the LHC are presented. Their role in standard operation for physics is discussed and, in particular, candidates of beam–beam coherent mode driven unstable by the machine impedance are presented.

INTRODUCTION

Two colliding beams are strongly coupled by the Beam–Beam (BB) interaction, be it Head-On (HO) or Long-Range (LR). This coupling can cause the two beams to oscillate coherently in different eigenmodes. When considering one bunch per beam colliding in one Interaction Point (IP), the beams can oscillate in phase, known as the σ-mode, or out of phase, known as the π-mode. In such simple configurations, self-consistent tracking simulations with BB and linear lattice transport show that the new eigenmodes, having different frequencies, are not damped in the incoherent spectrum generated by BB (Fig. 1), as already studied in [1]. The complexity increases significantly when considering real LHC cases, with four interaction regions and several LR interactions around each IP. Previous studies indicate that in such complex configurations, the BB coherent modes tend to be brought inside the incoherent spectrum and are therefore naturally damped [2]. These statements are investigated based on observations during dedicated experiments and during luminosity production in the LHC.

Recent studies suggest that coherent BB modes play an important role in the development of impedance driven instabilities [3]. A dedicated experiment aiming at probing this effect is presented.

STABLE COHERENT MODES

Dedicated Experiment

A series of experiments was performed with single bunches, at injection energy (450 GeV), to probe the maximum BB tune shift achievable in the LHC [4]. Some of these tests were done with a single bunch and without transverse feedback. This configuration is ideal to study BB coherent mode, as the Base Band Tune (BBQ) system allows turn by turn measurement of the bunch position. A Singular Value Decomposition (SVD) of this data revealed the presence of BB coherent motion, as indicated by Figs 2 and 3. Indeed, not only do the frequencies of the mode observed clearly match the self-consistent simulations, but also the oscillation of the two beams is clearly correlated, in the expected in/out of phase manner. Such behaviour was observed in all experiments performed in this configuration.

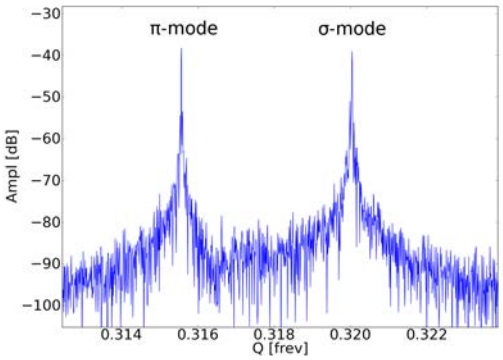

Figure 1: Self-consistent simulation of the beam spectrum of two bunches undergoing one HO BB interaction. The σ-mode lies on the lattice tunes whereas the π-mode is shifted down by $Y \cdot \xi$, where Y is the Yokoya factor and ξ the BB parameter [5].

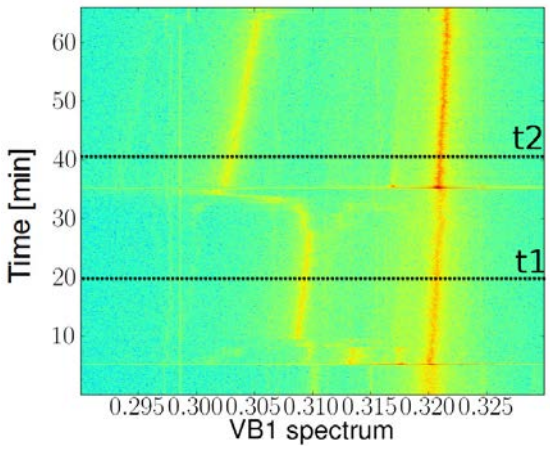

Figure 2: Spectrogram in the vertical plane of Beam 1, measured by the BBQ, during an experiment aiming at probing high BB parameters, at injection energy; $\xi \sim 0.01$ per IP. At $\sim$ 10 minutes, the movement of the lower line marks the start of HO collision in IP1, and IP5 at $\sim$ 35 minutes. The spectrums at t_1 and t_2 are shown in Fig. 3.

Similar experiments were performed, aiming at providing the highest pile-up in the experiments [4], with a few bunches at 4 TeV. Having more than one bunch per beam, turn by turn and bunch by bunch measurement of the position is required to perform an SVD analysis. The pickups used by the transverse feedback can provide such data, as

978-92-9083-404-5, 0007-8328 –
http://dx.doi.org/10.5170/CERN–2014–004.227

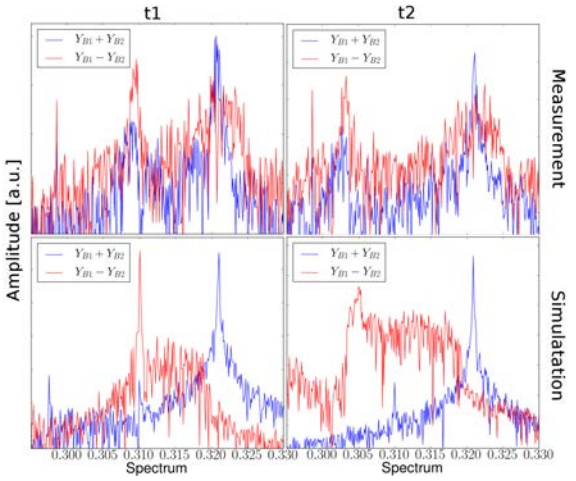

Figure 3: The SVD of turn by turn data of both measurement and simulation gives two singular vectors corresponding to the addition (blue) and subtraction (red) of both beams' data, the spectrum of the associated singular vectors are plotted. The two columns correspond to the time defined on Fig. 2, i.e. one IP colliding and two IPs colliding. The upper row shows measurement from the BBQ and the lower row self-consistent tracking with COMBI [2] using measured intensity and emittances.

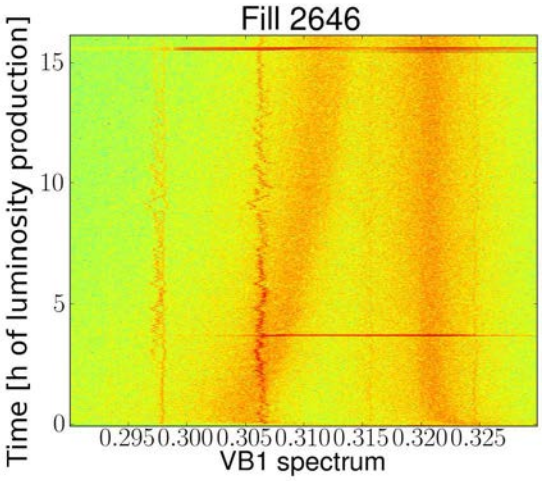

Figure 4: Spectrogram in the vertical plane of Beam 1, measured by the BBQ, during luminosity production. The blurred line at ~ 0.321 is the machine tune Q_v, the sharp lines at ~ 0.307 and ~ 0.298 are noise lines and the blurred line starting at ~ 0.305 and moving towards the machine tune is consistent with $Q_v - \xi$, ξ being the BB parameter of the most common bunch, which decays during the fill with the beam brightness.

opposed to the BBQ, which cannot. However, the acquisition buffer limits the number of consecutive turns measurable and the sensitivity of these pickups is lower. Nevertheless, they can be used to detect BB coherent mode in dedicated experiments such as these. Unfortunately, a significant coherent signal could not be observed in these experiments, due to the transverse feedback, which, as opposed to previous experiments, was kept on.

Luminosity Production

The configuration during luminosity production is very complex; all 1374 bunches are coupled together via either HO or LR interactions in the four interaction regions. Consequently, there exist a variety of modes, with different frequencies, most of them laying inside the incoherent spectrum. Also, the damper is always kept on during luminosity production, which, as mentioned previously, prevents the observation of any coherent mode. For these reasons, no BB coherent modes have been observed during luminosity production. Nevertheless, as shown by Fig. 4, there are lines in the BBQ signal at frequencies consistent with both incoherent or coherent motion due to BB interactions. However, without further diagnostics, it is not possible to distinguish between the two.

UNSTABLE COHERENT MODES

At the end of the experiment presented in Fig. 2, a coherent mode, previously demonstrated to be a π-mode, became unstable (Fig. 5). The beams stabilize themselves naturally at the expense of large intensity loss and emittance growth; the frequency of the mode after the instability reflects the reduction of beam brightness. Beam–beam modes are not self-excited; in this case, the driving force is unknown. In particular, the lack of chromaticity measurement during the experiment and the large uncertainties of the LHC impedance model at injection energy [6] do not allow quantitative comparison with models including BB and impedance. Such instability was never observed with colliding beams at top energy.

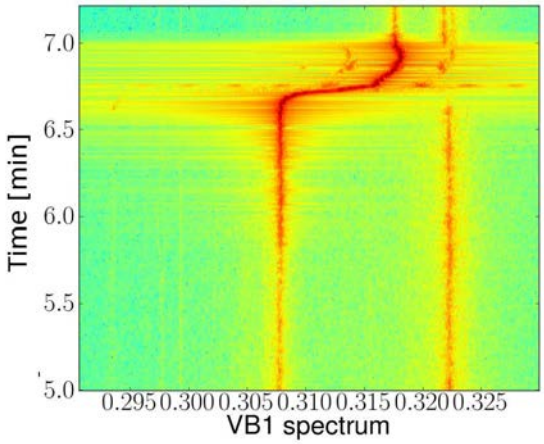

Figure 5: Unstable π-mode observed during a dedicated experiment aiming at probing large HO BB parameters at injection energy with one high brightness bunch per beam colliding in IP1&5.

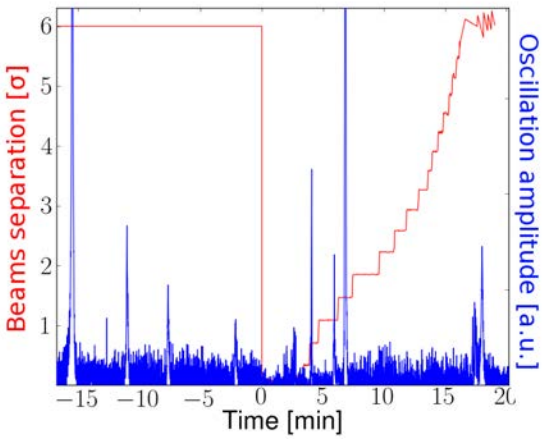

(a)

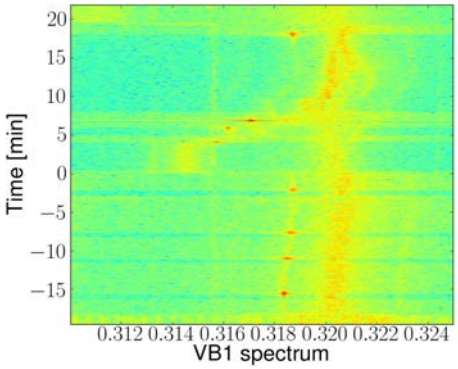

(b)

Figure 6: Spectrogram, vertical plane of Beam 1.

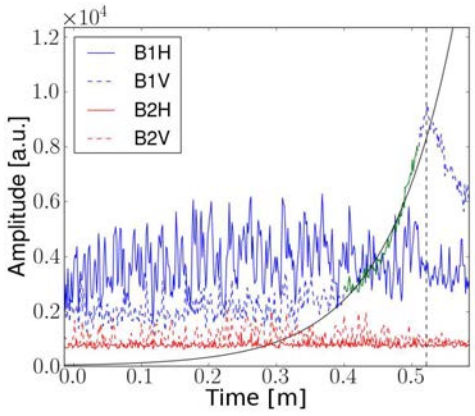

(a) The measured rise time is 5.9 s at 6 σ separation. Only Beam 1 is unstable in the vertical plane.

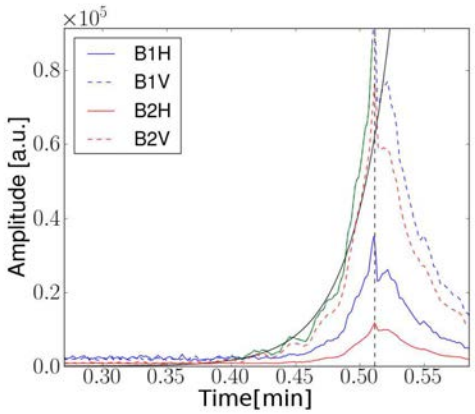

(b) The measured rise time is 1.8 s at 1.4 σ separation. Both beams are unstable in the vertical plane.

Figure 7: Measured oscillation amplitude in both planes of both beams, with an exponential fit to measure the rise time. The instability is damped before a significant degradation of the beam brightness by turning the transverse feedback on, marked by a vertical dashed line.

During luminosity production, there have been plenty of observations of instabilities when the beams were colliding with a transverse offset, despite the presence of a strong transverse feedback. In some cases, the instability was observed in one beam only and could be explained by a lack of Landau damping of pure impedance mode [7]. In some others, the instability is observed on both beams. These observations could be consistent with a single beam instability going with an incoherent transmission of the signal to the other beam. Nevertheless, a coherent beam–beam instability is not excluded.

These observations motivated theoretical developments and a dedicated experiment at the end of a special fill [8]. After the squeeze, two bunches per beam were colliding in IP1&5. First, the beams were re-separated by 6 σ, the r.m.s. beam size, in both IPs and the chromaticity was set to ~ 5 units. Before $t = 0$, in Fig. 6(a), a series of spikes in the oscillation amplitude mark a few tests of the beams' stability without transverse feedback, by turning it off and on again when an instability is observed. The octupole strength is increased after each tentative; it was found that the maximum strength was not sufficient to stabilize the beams. At $t = 0$, the beams were brought into collision in IP5 with the feedback on. Once the beams were colliding HO, the feedback was no longer required to maintain the beams' stability. The beams were then re-separated in steps, visible in Fig. 6(a). At each step, the stability without transverse feedback is tested, as previously. It was observed that the beams are stable for separations below 0.7 σ and from 1.8 to 6 σ, whereas unstable from 0.7 to 1.8 σ and at 6 σ. Also, the instabilities at intermediate separations have different characteristics than for the 6 σ separation. As shown by Fig. 7, at intermediate separations both beams are unstable, as opposed to 6 σ. Moreover the rise times are significantly different (Table 1).

Due to the lack of time, the scan in separation is extremely coarse; moreover, important parameters, such as chromaticity and emittances, are poorly know. These factors render a quantitative comparison with theoretical models difficult. Nevertheless, the existence of a critical separa-

Table 1: Measured rise time at different separations

Full separation [σ]	Rise time [1/s]
0.7	2.7
1.1	6.7
1.4	1.8
6	5.9

tion, in the order of 1 to 2 σ, is in accordance with a lack of Landau damping due to the modification of the tune spread caused by the beam–beam force [7], as well as a coupled beam–beam and impedance mode [3]. The experimental evidence does not allow us to distinguish between these two models, which are not mutually exclusive. Nevertheless, the fact that both beams became unstable simultaneously, with identical rise times (Fig. 7(b)) is a indication that the two beams oscillate coherently.

It is important to stress that, as predicted in [3], the transverse feedback was efficient at stabilizing the beams. Indeed, during this experiment, no instabilities were observed while the transverse feedback was active. This is different with respect to what is observed during luminosity production, as instabilities are observed while the transverse feedback is on. The configuration is nevertheless very different, in particular the presence of multiple bunches is expected to have a strong impact on the dynamic. The models are therefore being extended to assess the full LHC complexity in the multibunch regime.

CONCLUSION

Beam–beam coherent modes have been observed in the LHC, during experiments with single bunches and without transverse feedback. Their frequency and the corresponding eigenvectors follow theoretical models and simulations. Some frequencies observed in the beam spectrum, while running with multibunch and with the transverse feedback on, could be attributed to coherent beam–beam modes. Nevertheless, the instrumentation available could not measure the correlation between the beams, and thus do not allow demonstration of the presence of coherent motion.

Recent developments suggest that the stability of beams colliding with a transverse offset can be critical. An experiment was performed, the results being in qualitative agreement with the models. In particular, it was shown that beams, being unstable when separated, can be stabilized by HO collision, removing the need for the transverse feedback in this configuration. Also, it was shown that there exists a critical separation at which the beams' stability is reduced. The two beams were strongly coupled during instabilities observed while colliding with a transverse offset in the order of 1 to 2 σ. Unfortunately, as in the previous case, the lack of diagnostics prevents demonstration of the presence of coherent motion.

While the frequency and eigenvectors of the beam–beam coherent modes are well understood and agree well with observations, the stability of these modes, in particular in the presence of the machine impedance, still requires both theoretical and experimental investigations to fully assess the LHC complex configurations.

REFERENCES

[1] Y. Alexahin, "On the Landau Damping and Decoherence of Transverse Dipole Oscillations in Colliding Beams," CERN SL-96-064 AP (1996).

[2] T. Pieloni,"A Study Of Effects in Hadron Collider with Large Number of Bunches," EPFL thèse No 4211 (2009).

[3] S. White *et al.*, "Beam–Beam And Impedance," these proceedings.

[4] G. Trad *et al.*, "Beam–Beam Effects with a High Pile-Up Test in the LHC," these proceedings.

[5] K. Yokoya *et al.*, "Tune Shift Of Coherent Beam–Beam Oscillations," Part. Accel. 27 (1990).

[6] N. Mounet *et al.*, "Impedance Effects on Beam Stability," Proceedings of the 2011 Workshop on LHC Beam Operation, Evian, 2011, CERN-ATS-2012-083 (2012).

[7] X. Buffat *et al.*, "Stability Diagram of Colliding Beams," these proceedings.

[8] X. Buffat *et al.*, "Stability of Beams Colliding with a Transverse Offset", CERN-ATS-Note-2013-016 MD (2013).

Published by CERN in the Proceedings of the ICFA Mini-Workshop on Beam–Beam Effects in Hadron Colliders,
CERN, Geneva, Switzerland, 18–22 March 2013, edited by W. Herr and G. Papotti, CERN–2014–004 (CERN, Geneva, 2014)

BEAM–BEAM-INDUCED ORBIT EFFECTS AT LHC

M. Schaumann, RWTH Aachen, Aachen, Germany
R. Alemany Fernandez, CERN, Geneva, Switzerland

Abstract

For high bunch intensities the long-range beam–beam interactions are strong enough to provoke effects on the orbit. As a consequence the closed orbit changes. The closed orbit of an unperturbed machine with respect to a machine where the beam–beam force becomes more and more important has been studied and the results are presented in this paper.

INTRODUCTION

In the LHC (Large Hadron Collider) the beam–beam electromagnetic force is experienced as a localized, periodic distortion when the two beams interact with each other at the collision points. This force is most important for high-brightness beams, which is the case at the LHC, and it can be classified into two types: head-on and long-range. The effects of the beam–beam force manifest themselves in very different ways. In this paper the closed-orbit effects due to long-range beam–beam interactions are studied. Long-range interactions distort the beams much less than head-on interactions. However, there is a large number of them due to the large number of bunches per beam (2808 bunches per beam in the nominal LHC). In nominal conditions, up to 30 long-range interactions per experiment have to be expected. Experimental data are presented in order to validate the simulation studies about the beam–beam effects at the LHC [1–3] performed during recent years. More details of the analysis presented here can be found in Refs. [4, 5].

LONG-RANGE BEAM–BEAM KICK

When the beams are separated, as is the case for long-range beam–beam interactions, the beams will exert a kick to each other whose coherent dipole component leads to orbit changes. The change in angle (kick) can be computed with the following equation [1]:

$$\Delta r' = -\frac{2Nr_0}{\gamma} \cdot \frac{1}{r} \cdot \left[1 - \exp(-\frac{r^2}{4\sigma^2})\right], \qquad (1)$$

where r is the beam separation, σ is the beam size at the interaction point and γ is the relativistic Lorentz factor.

Analysis and Results

During a dedicated machine study period with only one bunch circulating per beam, a horizontal orbit scan in steps of 100 μm was performed in ATLAS (IP1) and a vertical one in CMS (IP5) to measure the orbit kick due to the beam–beam force. The scan went far enough to reach the non-linear regime of the force.

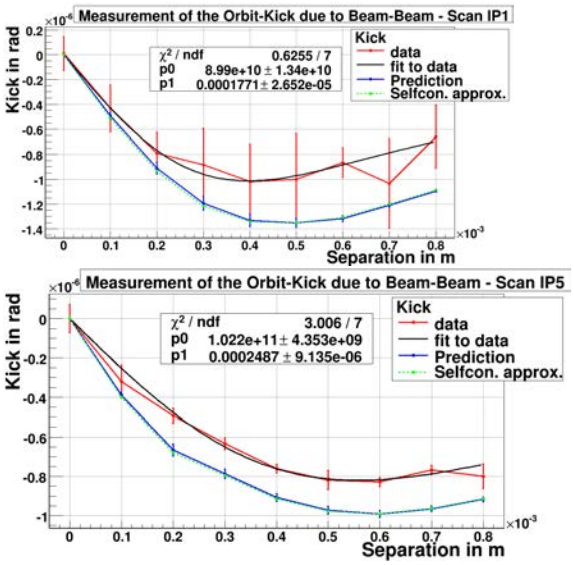

Figure 1: Measurement and prediction of the orbit kick due to beam–beam force during an orbit scan. The vertical axis is given in units of 10^{-6} rad and the horizontal axis in units of 10^{-3} m.

To avoid additional effects arising from the trim of the separation bumps, only beam 1 was moved and beam 2 was untouched. In this way beam 2 is only perturbed by the beam–beam kick and a clean signal should be measured.

The result is illustrated in Fig. 1, where the red line indicates the kick determined by an orbit correction of the taken data and the solid blue line was calculated using Eq. (1).

For the calculation, the values of σ and N were varied at each separation step according to the measured values. The shape of the measured curve fits to the expectation, but the measured strength is lower than the prediction. The black line is a fit to the data using Eq. (1); the intensity $N = p_0$ and the beam size $\sigma = p_1$ were left as free but constant parameters. The obtained value for σ is in agreement with the measurement, but the obtained N is too small compared to the measured one; thus, the origin of the discrepancy must be different. Therefore, the green dashed line tries to approximate the self-consistent effect which is not considered in Eq. (1) and arises from the effect of the interaction itself. If the orbit is changed due to a bunch crossing, the positions of the beams will be different after one turn, which implies a variation of the force, leading again to a different orbit until an equilibrium is found. The dashed line shows that this effect is too small to explain the gap. Further investigation is needed to identify the discrepancy.

978-92-9083-404-5, 0007-8328 –
http://dx.doi.org/10.5170/CERN–2014–004.231

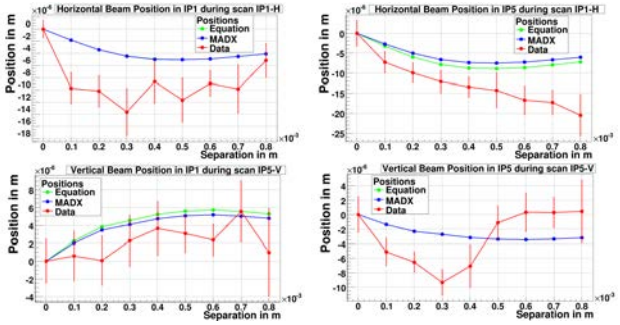

Figure 2: Measurement and prediction of the positions at IP1 and IP5 due to beam–beam force during an orbit scan. The vertical axis is given in units of 10^{-6} m and the horizontal one in units of 10^{-3} m.

Figure 2 shows in red the beam positions at IP1 and IP5 during the scans as a function of the separation, where the error bars show the standard deviation. A prediction was calculated and simulated with the MADX program. Here a discrepancy between prediction and measurement is also found. Nevertheless, the positions at the IPs were interpolated from the data of the two closest beam-position monitors (BPMs) on the left- and right-hand sides of the IPs only. Those BPMs have a resolution of around 5 μm, which is larger than the standard deviation and the observed discrepancy. As expected, the shape of the curves agree with the prediction (except for the beam position in IP5 during the scan of IP5, which needs further investigation). However, the source of the gap will be explained when the gap in Fig. 1 is understood.

BUNCH-BY-BUNCH ORBIT DIFFERENCES

The study of the orbit effects due to the coherent dipolar kick of the beam–beam force performed in the previous section shows that the expected orbit variations are in the order of a few micrometers. It is interesting to analyse this effect on a bunch-by-bunch basis, since the so-called PACMAN effect introduces differences bunch-to-bunch: bunches at the head or tail of a bunch train encounter fewer long-range interactions since they cross empty buckets. This leads to differences in the long-range orbit kicks for those bunches w.r.t. to the core of the train [3]. Three ways of measuring the position variations are analysed in the following.

ATLAS Luminous Region Reconstruction

The analysis presented in the following uses the microvertex detector of the ATLAS experiment. A total of five luminosity fills with different filling schemes have been analysed to investigate the dependence on the number of bunches.

In Fig. 3 the reconstructed luminous region in the vertical (crossing-angle) plane and horizontal (separation) plane of

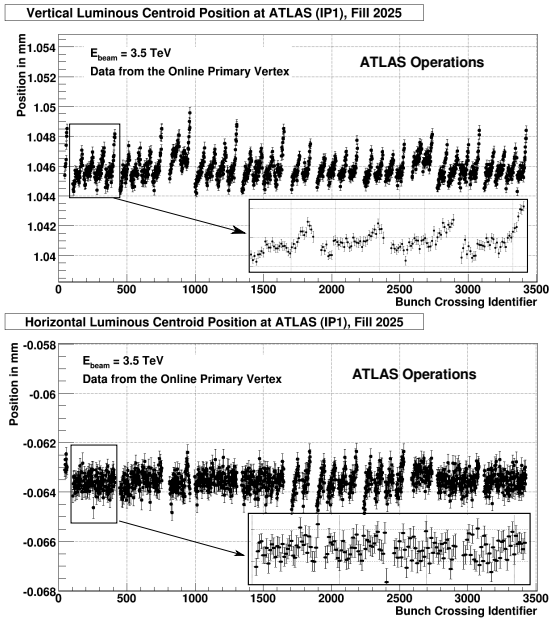

Figure 3: Luminous centroid position in ATLAS. Top (bottom) figure shows the vertical (horizontal) luminous region position and a zoom over the first four trains of 36 bunches.

ATLAS is plotted as a function of the bunch-crossing identifier for fill 2025 with 1380 bunches spaced by 50 ns. As predicted by the simulations [3], the orbits at the interaction point of all bunches are slightly different and this is more evident for PACMAN bunches in the vertical plane.

The luminous centroid reconstruction can only give the convoluted position of both beams. But, since the orbits of both beams are almost identical at the interaction point in the vertical plane (simulations [3] show that they are slightly different due to the intensity variations bunch-by-bunch, in the order of 15% in this fill), most of the bunches collide head-on, although not all of them in the central orbit. In particular, the PACMAN bunches show offsets w.r.t. the core of the train of (2.0 ± 0.3) μm due to the different number of long-range interactions. There are two types of them, the ones close to an eight-bunch gap (between trains), and the ones close to a 36/56-bunch gap (between groups of two or four trains). In Fig. 3 a zoom over the first four 36-bunch trains is illustrated. The bunches at the core of the train show a different structure than the bunches close to a gap. This is due to the different number of long-range interactions. While the bunches at the core of the train have on average 74 long-range interactions, the PACMAN bunches have in the order of 10 long-range interactions fewer. The different number of long-range interactions implies a different amount of coherent dipolar kicks, and therefore different orbits. The effect is even more clear for the PACMAN bunches close to the 36/56-bunch gap; those have on average 40 long-range interactions fewer and the orbit difference is, consequently, bigger.

The orbit offset due to beam–beam kicks in the vertical plane is (5.0 ± 0.3) μm peak to peak. This is a factor of

2.5 bigger than the offsets presented in the simulations of Ref. [3]. Nevertheless, it has to be taken into account that the simulations are done for nominal LHC parameters, i.e. 2808 bunches spaced by 25 ns; therefore, the bunch pattern is different. As a continuation of this study, new simulations will be done with the parameters of this fill to be able to assess the data in a more quantitative way.

The orbit offsets in the horizontal plane of IP1 do not show a particular structure, as in the case of the vertical plane. If the orbit could be reconstructed for both beams separately, simulations predict that the positions of the beams are symmetric to the central orbit and offset by a few micrometers (see Ref. [3], Figs. 14–16). The PACMAN bunch effect appears as well, but in the horizontal plane it arises from the long-range interactions in the vertical (crossing) plane of IP5. Since the effect in this plane is global and travels through the ring, it appears with a different shape as the local effect in the crossing-angle plane of the considered IP. But, since we are using the luminous region, only the convolution of both beams is visible, and the effect is cancelled because of its symmetry. There are, however, some trains which show a structure compatible with the beam–beam effect of the vertical plane. The source of this structure should come from extra coherent dipole kicks happening in the horizontal plane somewhere else for those bunches, but this effect needs further investigation.

No dependence on the number of bunches was found for the filling schemes analysed with the same number of long-range interactions, as could be expected.

Luminosity Optimization

During every luminosity run, once the beams are brought into collision, every interaction point undergoes a luminosity scan in the horizontal and vertical planes to find the full beam overlap and therefore the maximum luminosity. This process is done by integrating the luminosity over the whole beam, and assuming an average position over all bunches. However, since we have demonstrated that there are bunch-by-bunch orbit differences, it is interesting to look at the variation in the maximum of the luminosity as a function of the bunch number. Figure 4 displays the relative position of the two colliding bunches where the maximum luminosity is found during the scan. The plots show IP1 in the horizontal plane (top plot) and vertical plane (bottom plot).

To understand this structure, the position of each beam should be reconstructed. Since this is not possible with the BPMs, simulations have to be referenced again (see Ref. [3], Figs. 14–16): the PACMAN bunch positions are offset w.r.t. the core of the train and have a mirror-like structure to the opposite beam. When the scan is performed, the luminosity maximum is first found for those bunches and afterwards for the core of the train. Thus, in Fig. 4 (top) the Gaussian fit mean position is closer to the zero displacement for the PACMAN bunches.

No structure is visible in the vertical plane, because in IP5 the vertical plane is the separation plane where there are no long-range effects. Moreover, the local long-range effects in IP1 cannot be seen as in Fig. 3, since as explained above the orbits for both beams are nearly identical and as both beams are moved symmetrically in opposite directions the effect is not visible using this measurement method, since the separation is the same for all bunches.

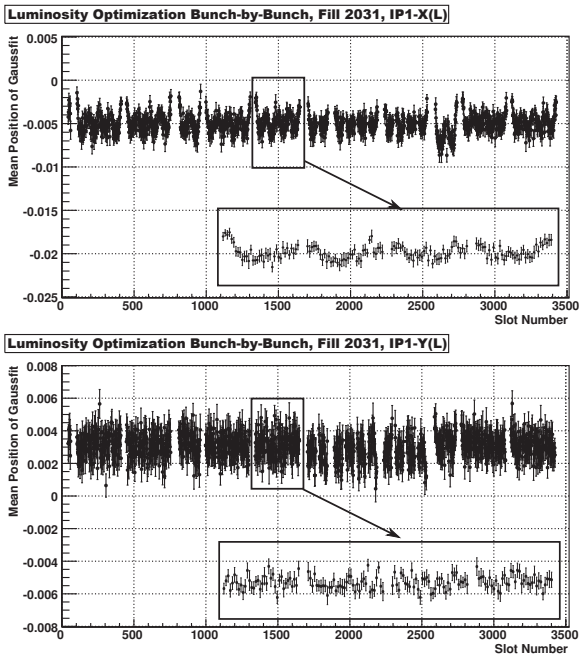

Figure 4: Position of the maximal luminosity (total bunch overlap) as a function of the bunch number. Top (bottom) figure shows the horizontal (vertical) mean position of the luminosity maximum in units of millimeters w.r.t. the beam position before the scan.

Beam-position Monitors

An exhaustive analysis of the data measured by the LHC BPM system during a typical luminosity run was performed to assess the feasibility of those instruments to measure closed-orbit deviations in bunch-by-bunch mode in the order of a few micrometers.

From the analysis one can conclude that the BPM system has a bunch-by-bunch orbit measurement able to give a relative bunch-to-bunch resolution in the 5 μm range. Yet the non-linearity in the bunch-by-bunch mode for different global positions limits this resolution to $\pm 50\,\mu$m when comparing along the train for different mean positions. The current LHC BPM system, therefore, does not have sufficient linearity or resolution to resolve the bunch-by-bunch orbit variations at the few-micrometer level expected from beam–beam interaction orbit effects during normal operation.

However, if the separation at the parasitic encounters is decreased, the long-range beam–beam force is enhanced

and the orbit distortion becomes strong enough to be measured with the BPM system. In a dedicated experiment [5,6] the crossing angle was reduced simultaneously in IP1 and IP5 by the same amount and bunch-by-bunch orbit data were taken during every step of the experiment.

The bunch-by-bunch orbit measurement is the sum of many components, e.g. common motions of all bunches, like betatron oscillation and initial orbit differences between bunches; moreover, electronic and temperature effects influence the absolute position measured between bunches and BPMs. In this experiment the interest lies in the observation of the orbit changes introduced by the enhanced long-range kick and not in the absolute position of the beam. Therefore, all those effects influencing the absolute beam position have to be filtered out to resolve the small effects of the changing beam–beam force from the BPM measurement.

In the following, only the data of beam 1, consisting of three trains with 12, 36 and 36 bunches, are plotted. The 12 bunches of train 1 were all non-colliding and train 3 only collides in IP8. Train 2 collides in IP1 and IP5, where the crossing angle was varied, and additionally in IP2. Bunches in train 2 had up to 16 long-range interactions per IP.

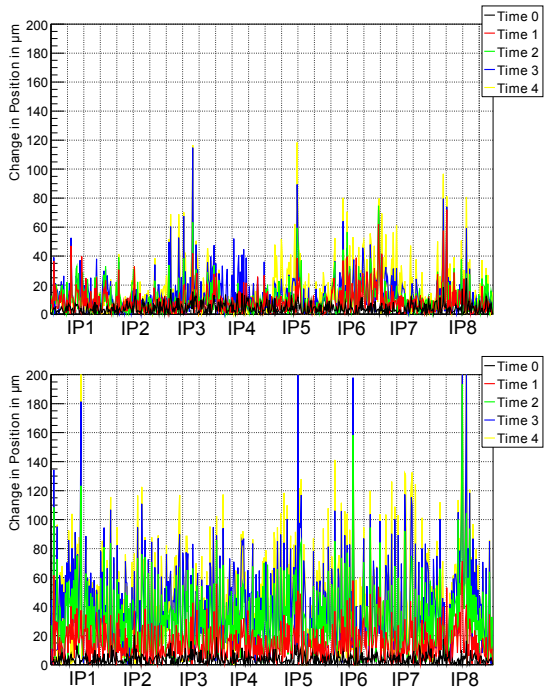

Figure 5: Horizontal absolute change in position of beam 1 as a function of the location in the ring for five different crossing angles. Top: bunch with zero head-on and long-range interactions, bottom: three head-on, 16 long-range interactions.

Figure 5 shows the changes in relative position (after filtering) for different crossing angles (times 0 to 4) as a function of the location around the ring. In the top plot a non-colliding bunch (with zero head-on and zero long-range interactions) is shown with respect to a reference bunch with the same properties. Since this bunch does not experience any long-range interactions, it is not expected to change its position when the crossing angle is decreased from times 0 to 4. A noise floor of $\propto$ 20–40 μm is clearly visible, which limits the resolution. This is in agreement with the value found during normal operation.

The bottom plot shows a bunch of train 2 with three head-on and 16 long-range interactions with respect to the same reference bunch. In this case a clear systematic structure above the noise level develops which increases when the crossing angle is decreased, giving a qualitative measurement of the enhancement of the long-range beam–beam force.

In Fig. 6 the relative position change at varying crossing angles is shown at a particular BPM (BPM.6L1.B1) on the left-hand side of IP1 for all bunches in the machine. Train 2 shows the typical PACMAN bunch behaviour: bunches in the core of the train experience the largest number of long-range kicks and therefore show the largest change in position while reducing the crossing angle. With decreasing number of long-range interactions to the ends of the train, the effect on the orbit is also reduced. Since only the crossing angles in IP1 and IP5 were varied, trains 1 and 3, which do not have collisions in those IPs, are not affected.

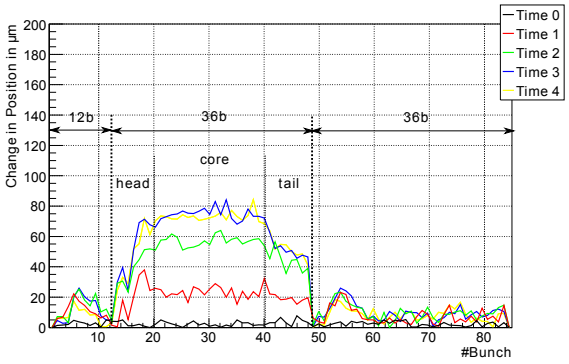

Figure 6: Horizontal absolute change in position of beam 1 as a function of the bunch number for a particular BPM around IP1.

ACKNOWLEDGEMENTS

The authors would like to thank the LHC Operations Group and the Beam–Beam Working Group for their support during the machine development studies and J. Wenniger, M. Favier, R. Jones, E. Calvo, T. Bär, G. Müller, W. Herr and B. Holzer for their fruitful discussions during the analysis of the data. We thank the ATLAS Collaboration for providing the beam-spot information from their data. In particular, we are grateful to R. Bartoldus, J. Cogan, C. Gwilliam, E. Strauss and C. Rembser for their help.

REFERENCES

[1] T. Pieloni, CERN-THESIS-2010-056 (2008).

[2] W. Herr, CERN-2006-002 (2006), pp. 379ff.

[3] W. Herr, LHC Project Report 628 (2003).

[4] M. Schaumann, CERN-THESIS-2011-138 (2011).

[5] M. Schaumann et al., CERN-ATS-Note-2012-021 MD (2012).

[6] R. Alemany et al., CERN-ATS-Note-2011-120 MD (2011).

[7] M. Schaumann, IPAC12, WEPC081 (2011).

Published by CERN in the Proceedings of the ICFA Mini-Workshop on Beam–Beam Effects in Hadron Colliders,
CERN, Geneva, Switzerland, 18–22 March 2013, edited by W. Herr and G. Papotti, CERN–2014–004 (CERN, Geneva, 2014)

SIMULATION OF BEAM–BEAM INDUCED EMITTANCE GROWTH IN THE HL-LHC WITH CRAB CAVITIES*

S. Paret, J. Qiang, LBNL, Berkeley, CA, USA

Abstract

The emittance growth in the HL-LHC due to beam–beam effects is examined by virtue of strong–strong computer simulations. A model of the transverse damper and the noise level have been tuned to simulate the emittance growth in the present LHC. Simulations with projected HL-LHC beam parameters and crab cavities are discussed. It is shown that with the nominal working point, the large beam–beam tune shift moves the beam into a resonance that causes substantial emittance growth. Increasing the working point slightly is demonstrated to be very beneficial.

INTRODUCTION

The force between two colliding beams applies a coherent kick to the colliding bunches if they have a finite offset. At the same time, due to its non-linear nature, the beam–beam force damps coherent transverse motion at the cost of the emittance. Noise on the transverse bunch positions at Interaction Points (IPs) can therefore lead to emittance growth. This effect is more pronounced for higher beam intensity and therefore of particular interest for the High-Luminosity Large Hadron Collider (HL-LHC).

In addition to the extreme beam parameters, a new feature of the HL-LHC may impact the emittance. The HL-LHC layout is based on Crab Cavities (CCs) to compensate the geometric luminosity loss due to large crossing angles. Large crossing angles are required to mitigate long-range beam–beam effects. Noise in the phase of the CCs' field imparts a transverse offset on to the colliding bunches. Hence noise in the CCs may accelerate the emittance growth [1]. A prediction of the emittance growth, depending on the noise, is of considerable interest for HL-LHC planning.

Simulations to predict the impact of CC noise on the emittance have been carried out for years (see, e. g., Refs. [1, 2, 3]). But over time the anticipated beam parameters in the future LHC have changed, and recently a detailed model of the LHC's transverse damper has been implemented in the code BeamBeam3D [4]. The damper has a significant impact on the evolution of the emittance, because it suppresses coherent dipolar motion – ideally without contributing to the emittance growth. However, in reality, noise in the damper – in particular, due to the uncertainty of the beam position measurements – has a detrimental effect on the emittance. The measurement uncertainty is included in the damper model.

Since the noise properties of the future CCs and their control system are not known yet, reasonable models and parameter ranges have to be explored. Common noise models are white noise, coloured noise with a specific correlation time, and a mono-frequent perturbation [5]. White noise is the easiest to model and has only one free parameter, the r.m.s. amplitude, but tends to be too pessimistic. Correlated noise features an additional parameter, the correlation time. A sinusoidal perturbation is described by an amplitude, frequency, and phase. In addition, the phase relation between the perturbation on a CC before and after an IP (in a local crabbing scheme) is assumed to play a role. In this paper, only white CC phase noise is considered. The examination of the other noises is work in progress.

The set-up of the simulations is described in Section 1. The first case that we consider here is a LHC run from last year. The set of measured beam parameters was used in simulations to reproduce the measured emittance growth. The purpose of this study was to validate the code and to determine the noise level in the damper, which is not precisely known. Assuming that the damper hardware does not change, a similar noise level is expected to be present in the HL-LHC. Section 2 describes the simulation of the recent LHC performance. In the following section, we examine the impact of CCs on last year's beam.

The focus then turns towards the HL-LHC. As yet, a definite plan for the HL-LHC set-up does not exist. Two HL operational scenarios based on different bunch spacing have been specified [6], and although luminosity levelling is a key element of both HL-LHC scenarios, the means to achieve it have not yet been defined. As a consequence, only studies for possible HL-LHC conditions can be run at this point. Section 4 is dedicated to various case studies with HL beam parameters, mainly referring to the 50 ns bunch spacing scenario. The paper closes with a conclusion and an outlook.

COMPUTATIONAL SET-UP

All of the simulations presented in this paper were done using a strong–strong collision model implemented in the code BeamBeam3D [7]. In order to avoid numerically induced emittance growth, and to gain computation speed, the fields were computed assuming a Gaussian particle distribution instead of a self-consistent approach [4]. This assumption is justified by the fact that the particle distribution is Gaussian initially and does not change significantly in a short period of time under stable conditions.

The main objective of the simulations was to quantify

*This work was partially supported by the US LHC Accelerator Research Program and the National Energy Research Scientific Computing Center of the US Department of Energy under contract No. DE-AC02-05CH11231

978-92-9083-404-5, 0007-8328 –
http://dx.doi.org/10.5170/CERN–2014–004.237

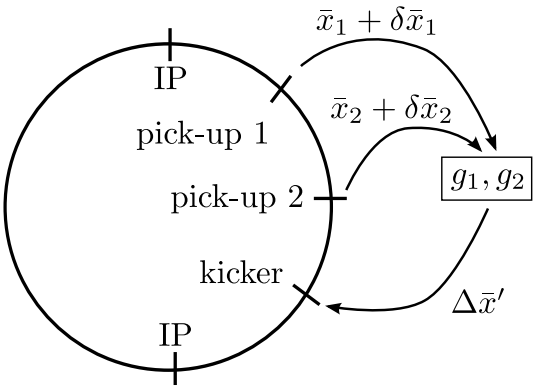

Figure 1: The scheme of the damper model.

the beam–beam induced emittance growth. As shown in the next section, the emittance in the LHC increased in the order of 10 %/h in operation in the year 2012, which results in very small changes in a simulation that is limited to a few seconds of real storage time. In order to keep the residual noise level low, 8×10^6 macro-particles were used. The longitudinal space was discretized into eight slices.

The nominal tunes, $Q_x = 64.31$ and $Q_y = 59.32$, were initially set for the simulation of the present LHC as well as the HL-LHC. Linear transfer maps, calculated using the working point, were employed to transfer the beams between collisions. Two collisions per turn, corresponding to IP1 and IP5 in the LHC, were simulated. Following the original, the crossing plane was horizontal in one IP and vertical in the other IP. BeamBeam3D was modified to allow for changing collision planes, with the CC kicks and CC noise being applied correspondingly.

The damper model uses a Hilbert-notch filter and two pick-ups per beam and plane, just as does the actual system in the LHC [8, 9]. The correction kick at turn n due to one pick-up is given by

$$\Delta\bar{x}'_n = \frac{a_0 g}{\sqrt{\beta_p \beta_k}} \sum_{m=1}^{7} H_m(\varphi_H) \times (\bar{x}_{n-d+1-m} - \bar{x}_{n-d-m}), \tag{1}$$

where H_m are the coefficients of the Hilbert filter, φ is a phase that needs to be determined as a function of the tune and damper gain, and d is the delay of the damper. The actual kick is the superposition of two terms associated with different pick-ups. Authentic values were used for the phase advance between the pick-ups and the kicker, and the phases in the Hilbert filter φ_H. The gain of the damper was set to 0.1. Noise is inserted by adding random numbers, $\delta\bar{x}_n$, to the measurement; that is, replacing $\bar{x}_n \to \bar{x}_n + \delta\bar{x}_n$ in Eq. 1. A scheme of the damping system is shown in Fig. 1. In BeamBeam3D, the damper noise has a white spectrum and a Gaussian amplitude distribution.

THE 2012 BEAM

During regular operation, the luminous region in the detectors is measured, as well as the beam intensity. The LHC operators provided a set of beam parameters from a 'normal' long fill in June 2012 (fill 2710) [10]. These parameters are only coarsely representative for the general LHC performance. Notable variations of the emittance evolution and other parameters were observed in different fills. However, detailed information about the overall performance is not yet available.

Table 1: Beam parameters in the simulation of the LHC in 2012 and in the future.

	2012	**HL**
N	1.5×10^{11}	3.5×10^{11}
ϵ_n [μm]	2.3	3.0
β^* [m]	0.6	1.02
Q_x	64.31	64.31
Q_y	59.32	59.32
θ [mrad]	0.29	0.59
$g_1 + g_2$	0.1	0.1
f_{CC} [MHz]	-	400.8
Collisions per turn	1 hor., 1 ver.	1 hor., 1 ver.

Assuming two equal bunches with Gaussian profiles colliding head-on, the beam width was calculated using

$$\sigma_x = \sqrt{2} \cos\frac{\phi}{2} \sigma_{Lx}, \tag{2}$$

where ϕ is the crossing angle and σ_{Lx} is the width of the luminous region. The initial half cross-section of the beams found in that way is about 18 μm in the horizontal and vertical directions. (The actual difference between the horizontal and vertical beam sizes was neglected.) With the beta function at the IP, $\beta^* = 0.6$ m, the emittance was deduced from the measured beam size. Table 1 lists the beam parameters used in the simulation of the LHC in 2012.

Due to the computational cost, only a few tens of seconds of storage time can be simulated with more than a million macro-particles. Hence only the initial emittance growth of the hour-long storage is of interest. Due to the limited time resolution of the measurements, a linear fit to the emittance during the first 6 h after injection was performed to assess the initial growth. Figure 2 shows that the emittance growth in the horizontal and vertical plane is linear for several hours to a very good approximation. The growth rates according to the fits are roughly 13 %/h in the horizontal plane and 4 %/h in the vertical plane. Here and in what follows, we provide the average emittance of the two beams in either plane, because they are usually quite similar.

In the horizontal plane, intra-beam scattering contributes significantly to the emittance growth. Simulations have been carried out to quantify its impact on the beams [11]. For conditions similar to the ones considered here, an intra-beam scattering driven, horizontal emittance growth of about 5 %/h was found. Therefore, we have assumed that the emittance growth due to the collisions amounts to about 8 %/h.

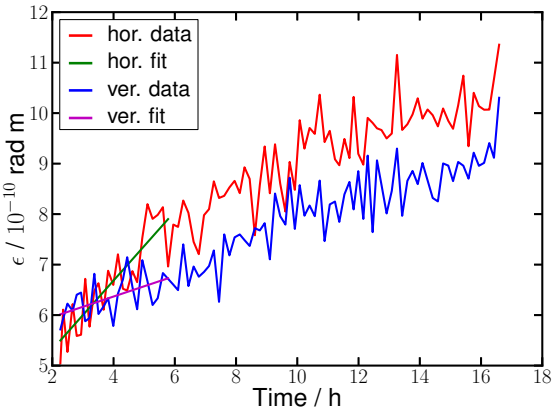

Figure 2: Transverse emittances in the LHC during a physics run in 2012.

Simulations with different noise levels were run in order to reproduce the emittance growth attributed to the collisions with the actual beam and machine parameters. The damper noise was adjusted to match the measured emittance growth. Figure 3 displays the simulated emittance that approximates the measured data. The emittance of both beams is shown for both planes. Two straight thick lines indicate the slope corresponding to 8 %/h and 5 %/h, respectively. The r.m.s. fluctuation of the beam centroid amounts 0.11 μm and 0.09 μm, horizontally and vertically respectively, at an IP. This fluctuation level is on the scale of observations in the LHC [12].

At this point, we have demonstrated that BeamBeam3D is able to reproduce the measured data of actual LHC beams. Assuming that the damper noise does not depend on beam parameters, the r.m.s. noise level fed into the damper in this simulation was used as a reference in other simulations. The impact of crab cavities on the emittance of the LHC beams in 2012 is studied next.

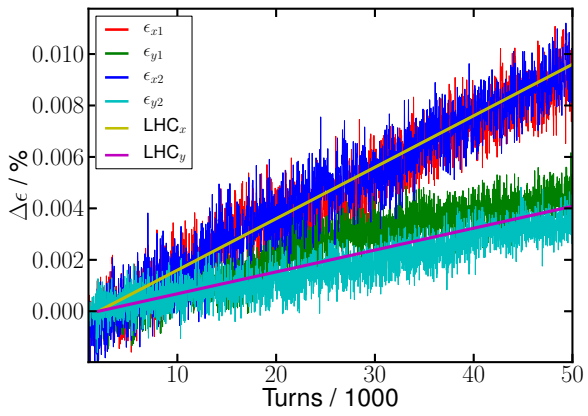

Figure 3: The emittance growth in a simulation of the LHC as operated in 2012. The straight solid lines visualize the fit to the measured data (Fig. 2) after correction for intra-beam scattering.

THE 2012 BEAM WITH CRAB CAVITIES

Before switching to the HL-LHC parameters, crab cavities were virtually added to the 2012 LHC. The set-up that has been measured and simulated provides a good reference with which to compare the simulation with CCs. For the HL parameters, it will take years before experimental data will be available, so the impact of CCs on HL beams can only be studied by comparing simulations with and without crab cavities.

In the first run, the beam and general machine parameters were kept as described in the previous section. As the only change, CCs were added around both IPs, with to a phase advance of $\frac{\pi}{2}$ between the CC and the IP. The CCs were assumed to be perfect; that is, the only noise source taken into account was the damper system. The resulting emittance growth differs only weakly from the case without CCs. Horizontally, we find 9 %/h and vertically only 2.4 %/h.

In order to get a first impression of the impact of CC noise on the emittance, a simulation without damper noise but with CC noise was done. Since the noise in the future CCs is not known, the accelerating cavities in the LHC were taken for an estimation. The power spectrum of the phase noise in these cavities has been measured and used to assess an approximate white noise level. The white noise that contains the same power in all betatron sidebands as the actual spectrum corresponds to 2×10^{-4} rad r.m.s. [13].

The evolution of the emittance with damper noise or CC noise is shown in Figs. 4 and 5, respectively. As far as damper noise is concerned, the CCs have little effect on the emittance. Phase noise with the estimated level, on the other hand, has a severe impact on the emittance, increasing the growth to 60 %/h horizontally and 17 %/h vertically.

The emittance growth simulated with white noise is not

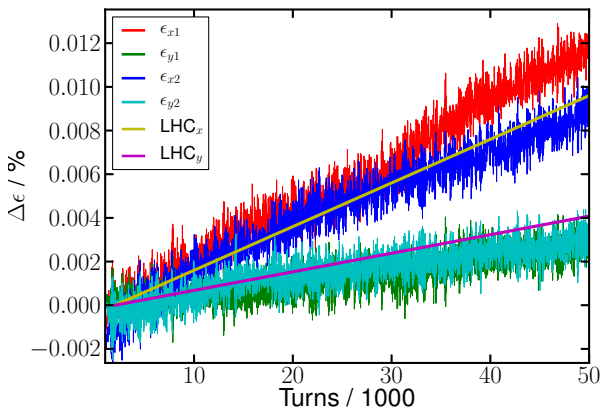

Figure 4: Emittances with the last 2012 beam parameters and CCs with damper noise only.

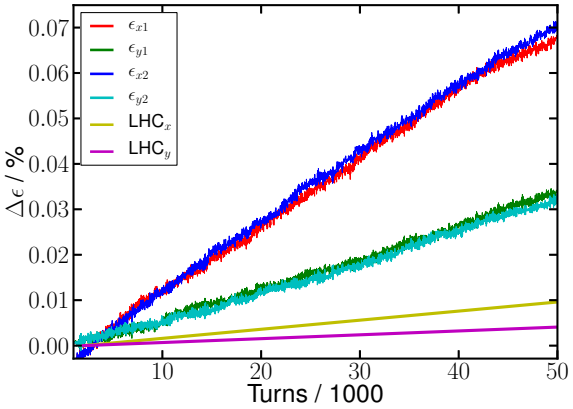

Figure 5: Emittances with the last 2012 beam parameters and CCs with CC noise only.

an accurate prediction for the perturbation caused by CCs, however, for several reasons. First, in the real system, no white noise is expected. Simulations with more realistic noise spectra should give more accurate results. A spectrum with lower noise at higher frequencies is expected to produce less emittance growth. Second, the noise in the present accelerating cavities is only an upper boundary for the expected noise level. Third, a filter to suppress the noise at the betatron sidebands is foreseen to further reduce the perturbation of the beam [12].

What we have learned so far is that even at a moderate beam intensity and crossing angle, the emittance is very sensitive to noise. Noise in the damper plays only a marginal role. In the next section, the same noise will be applied to HL beams.

HL-LHC BEAMS

Now the HL beam parameters and noise are examined. At present, two HL-LHC scenarios are considered [6]. The primary difference is the number of bunches stored in the LHC. The other beam parameters are adapted to match the luminosity goal and take other constraints, such as mitigation of long-range effects, into account. Here, we focus on the 50 ns bunch spacing option (with one exception). The relevant beam parameters for our simulations are summarized in Table 1.

A key feature of the HL-LHC is luminosity levelling; that is, the maintenance of a certain luminosity, well below the achievable peak luminosity, for as long as possible [6]. Different approaches to achieve levelling are under consideration, and they may affect the emittance in different ways [14]. In this paper, we consider levelling by means of β^*, and therefore we have increased it from 15 cm (the reference value in [6]) to 1.02 m. Due to the small absolute emittance growth within the short time span covered by our simulations, an adjustment of β^* to compensate the luminosity loss due to the emittance growth is not necessary.

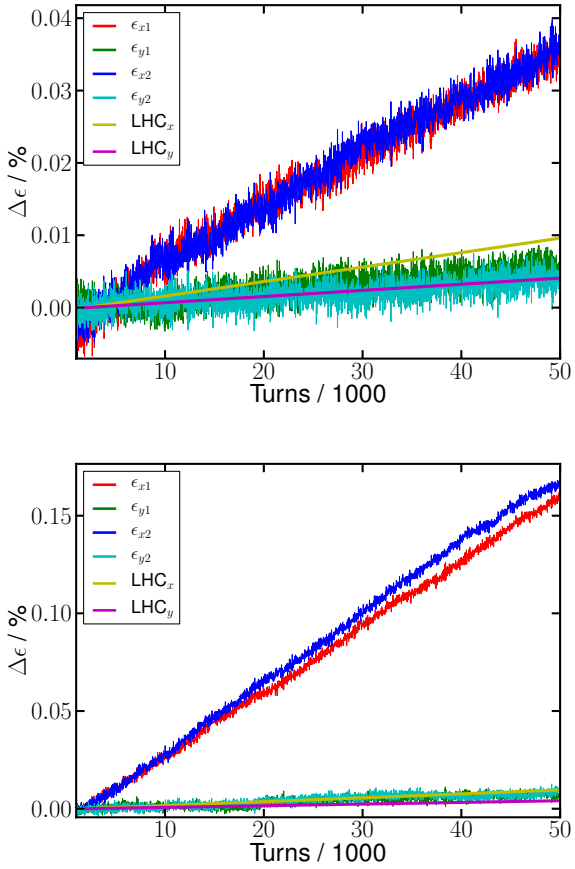

Figure 6: The emittance growth in the HL beams with damper noise (upper) and CC noise (lower).

Allowing for damper noise only, the emittance growth amounts to about 31 %/h horizontally and only 4 %/h vertically. Compared to the numbers from 2012, the horizontal growth is considerably enhanced, while vertically a small suppression is observed. Switching to CC noise exclusively, the horizontal emittance is blown up much more strongly, by 140 %/h. In the horizontal plane, the growth is still at a moderate 7 %/h. Figure 6 visualizes the emittance as a function of time.

In order to determine how much the CCs contribute to the observed emittance growth, a simulation was run without CCs and setting the crossing angle to 0, such that the luminosity and the beam–beam parameter remained unchanged. The resulting emittance growth agreed very well with the simulation with CCs and damper noise. It should be pointed out, however, that chromatic effects were not included in the simulations shown here.

The observed asymmetry between the two transverse planes motivated a more detailed investigation of the role of the tunes. Exchanging the tunes of the horizontal and the vertical plane, as well as the damper parameters (which depend on the tune) led approximately to an exchange of the growth rates in the two planes. A look at the tune diagram

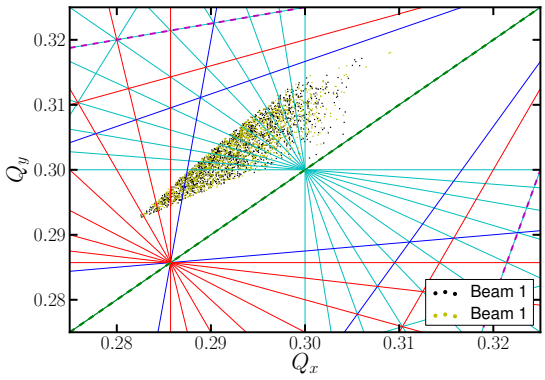

Figure 7: The tune diagram of the HL beams: red lines, seventh-order resonances; blue lines, ninth-order resonances; cyan lines, tenth-order resonances.

helps us to understand the reason. The beam–beam force in HL collisions gives rise to a considerable tune shift and spread, spreading the tune over several seventh- and tenth-order lines and one ninth-order resonance line, as displayed in Fig. 7.

Increasing the working point by 0.005 horizontally avoids the seventh- and ninth-order resonances, as Fig. 8 reveals. A simulation with $Q_x = 64.315$ was run and yielded 16 %/h horizontal and 8 %/h vertical emittance growth with damper noise only. Shifting the working point further to $Q_x = 64.32$ produced still better results. The emittance growth dropped to 8 %/h horizontally and 11 %/h vertically after adjusting the phases of the Hilbert filter to the new working point. The emittances for this run are shown in Fig. 9. The coupling due to the equal fractional tunes leads to a rapid emittance exchange, which looks like noise. However, as the lower part of Fig. 9 demonstrates, the averages of the transverse emittances in both beams increase linearly to a very good approximation.

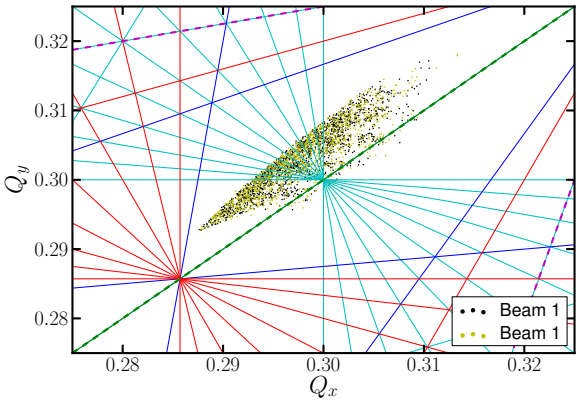

Figure 8: The tune diagram with $Q_x = 64.315$. The colour code of the resonances is the same as in Fig. 7.

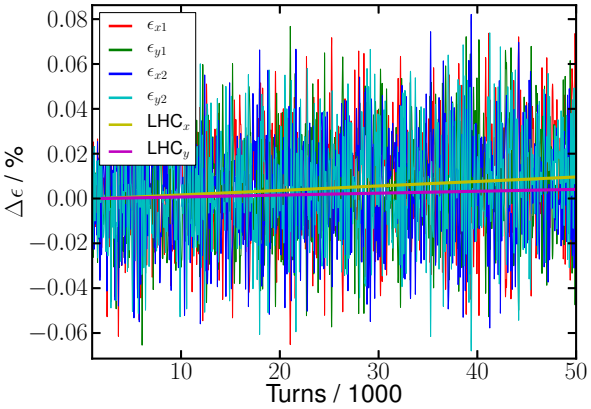

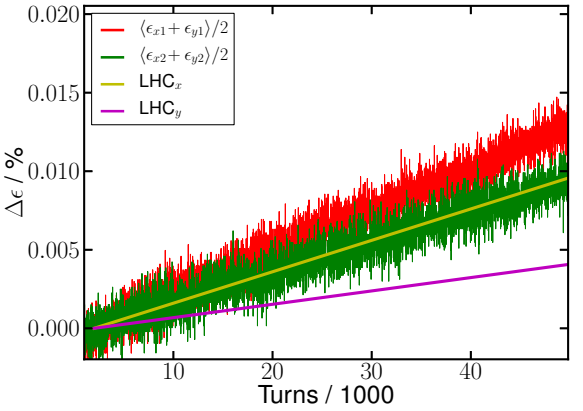

Figure 9: The emittance growth with $Q_x = 64.32$ and damper noise. Upper: all four emittances. Lower: the average of the horizontal and vertical emittance for each beam. Note that the data in the upper figure have been smoothed by a Gaussian convolution.

CONCLUSION

A simulation based on actual LHC beam parameters has allowed us to reproduce the observed emittance growth by adjusting the noise level in the transverse damper. This noise level provides a reference for simulations of the HL-LHC. Simulations with CCs have shown that the beam is very sensitive to white noise in the CC phase. A significant emittance growth has been found in simulations with HL beam parameters and the nominal working point. Increasing the horizontal tune, so as to avoid some higher-order resonances, substantially reduced the emittance growth. Noise in the damper has only a moderate effect on the emittance. Further studies are required to produce more accurate data.

OUTLOOK

After gaining some insights into the emittance evolution with realistic noise in the damper, and with less realistic noise in the CC phase, correlated noise and sinusoidal per-

turbations are of interest. The modelling of the beam dynamics will be refined to account for effects that have been ignored so far; for example, chromaticity. Furthermore, the simulation parameters need to be updated as the projected parameters change over time and estimations of the performance of future hardware become more precise. In particular, having collisions at a third IP (without CCs), which may become the regular operational scenario, will have a tremendous effect on the beam dynamics. The strong dependence of the emittance growth on the working point motivates an optimization of the working point for the HL beams. Also the 25 ns bunch spacing scenario, which is preferred by the experimenters at the LHC, is going to be studied.

ACKNOWLEDGEMENTS

The authors acknowledge the support of W. Höfle, G. Trad, and M. Schaumann, all from CERN, by providing important information about the damper, the LHC beam parameters, and intra-beam-scattering, respectively.

REFERENCES

[1] K. Ohmi et al., "Beam–Beam Effect with an External Noise in LHC," PAC07, Albuquerque, TUPAN048 (2007).

[2] R. Calaga et al., "Small Angle Crab Compensation for LHC IR upgrade," PAC07, Albuquerque, TUPAS089 (2007).

[3] J. Qiang, "Strong–strong beam–beam simulation of crab cavity compensation at LHC", PAC09, Vancouver, WE6PFP038 (2009).

[4] S. Paret and J. Qiang, "Simulation of Colliding Beams with Feedback in LHC," IPAC2012, New Orleans, TUPPC091 (2012).

[5] K. Ohmi, "Beam–Beam Effects under the Influence of External Noise," these proceedings.

[6] O.S. Brüning and F. Zimmermann, "Parameter Space for the LHC Luminosity Upgrade," IPAC2012, New Orleans, MOPPC005 (2012).

[7] J. Qiang et al., "A Parallel Particle-in-Cell Model for Beam–Beam Interaction in Energy Ring Colliders," J. Comput. Phys. 198 (2004) 278-94.

[8] W. Höfle et al., "LHC Damper," CERN-ATS-Report-2012-0? MD (LHC) (2012).

[9] V.M. Zhabitsky, "Beam Stability in Synchrotrons with Digital Transverse Feedback Systems in Dependence on Beam Tunes," E9-2011-95, JINR (2011).

[10] G. Trad, CERN, private communication.

[11] M. Schaumann and J.M. Jowett, "Predictions of Bunch Intensity, Emittance and Luminosity Evolution for p-p Pperation of the LHC in 2012," CERN-ATS-Note-2012-044 PERF (2012).

[12] W. Höfle, CERN, private communication.

[13] P. Baudrenghien, "LLRF for Crab Cavities," 2nd Joint HiLumi LHC-LARP Annual Meeting (2012), http://indico.cern.ch/conferenceDisplay.py?confId=183635

[14] B. Muratori et al., "Luminosity Levelling Techniques: Implications for Beam–Beam Interactions," these proceedings.

Published by CERN in the Proceedings of the ICFA Mini-Workshop on Beam–Beam Effects in Hadron Colliders,
CERN, Geneva, Switzerland, 18–22 March 2013, edited by W. Herr and G. Papotti, CERN–2014–004 (CERN, Geneva, 2014)

BEAM–BEAM STUDY OF ERL BASED eRHIC

Y. Hao, V.N. Litvinenko, V. Ptitsyn, BNL, Upton, NY, USA

Abstract

Beam–beam effects in eRHIC, the proposed ERL-based Electron–Ion Collider (EIC) at BNL, have several unique features distinguishing them from those in hadron-colliders and lepton-colliders. Taking the advantage of the fact that the electron beam is used only once, we expect the luminosity to be 10 times greater than for the ring–ring collision scheme with similar parameters. However, without instituting proper treatments, the quality of electron and hadron beams can undergo degradation or even beam loss, driven by the beam–beam interactions. We will discuss the harmful effects, including the disruption and mismatch effect of the electron beam, the kink instability and the noise heating of the ion beam and the possible countermeasures.

INTRODUCTION

The main advantage of an energy recovery linac (ERL) based electron–ion collider (EIC) compared with a ring–ring collider is the higher achievable luminosity of the former. In an ERL-based EIC, which we also call a linac-ring scheme, the electron bunch collides only once with the ion bunch and thereafter is recycled. Hence, the beam–beam parameter for the electrons in ERL scheme can exceed by a large margin (as in Table 1) that permissible for electron circulating in a ring. While the beam–beam parameter for the ions remains the same in both schemes, the luminosity achieved in the linac-ring collision scheme exceeds that of the ring–ring collider scheme between 10 and 100 times [1]. Figure 1 illustrates the layout of eRHIC, the EIC proposed in Brookhaven National Laboratory. Table 1 lists its design parameters.

In the new parameter range of eRHIC, the electron beam is subject to a very strong beam–beam effects that create a new set of beam dynamics effects. First, the electron beam experiences significant disruption and mismatch effects due to the beam–beam interaction. Second, the collective motion of the electron beam inside the ion beam during their collision can cause a new head–tail type of instability, named 'kink instability'. And the ion beam can be heated up by the noise of the fresh electron beam each turn. In this paper, we will report our studies on those individual effects and carry out countermeasures to the harmful ones.

ELECTRON DISRUPTION EFFECTS

The electron beam experiences very strong beam–beam force from the ion beam in the interaction region. The force will make the electron beam oscillate inside the ion beam and deform the distribution of the electron beam, as studied

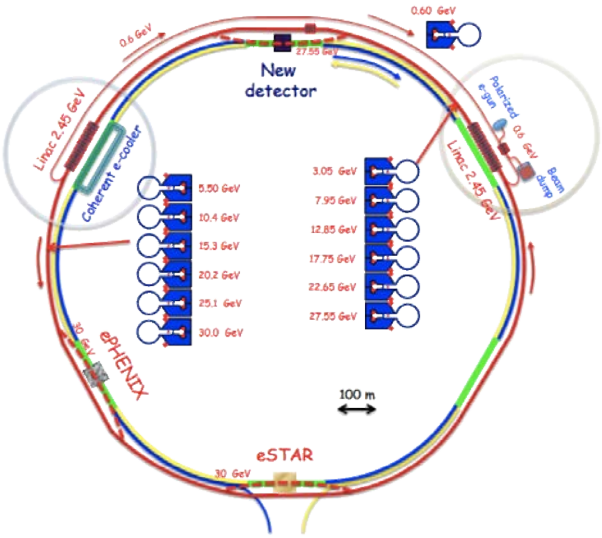

Figure 1: eRHIC design layout. The blue and yellow curves represent the existing blue and yellow rings of RHIC. The red curve illustrates the new ERL accelerator for the electron beam.

Table 1: Parameter range of eRHIC

Parameters	Range
Electron beam energy (GeV)	5-30
Ion beam energy (GeV) (proton)	50-250
Electron beam disruption parameter	5-142
Ion beam–beam parameter	0.015
Ion bunch length (cm)	8.3
Electron bunch length (cm)	0.2-0.4
Electron and ion β^* (cm)	5
Ion synchrotron tune	0.004

in [2]. We found that the disruption parameter $d_e = l_{i,z}/f_e$ is convenient to characterize the oscillation of the electron beam, where $l_{i,z}$ is the ion bunch length and f_e is the focal length of the linearized beam–beam interaction. For an ion beam with Gaussian longitudinal distribution, the number of oscillations n of the electron beam inside the ion beam is

$$n = \frac{\sqrt{d_e}}{(2\pi)^{3/4}} \approx \frac{\sqrt{d_e}}{4}.$$

Thus, for the eRHIC parameters, a single electron will oscillates up to 3 full oscillations in the ion beam.

We use simulation code, EPIC [3], to calculate the elec-

978-92-9083-404-5, 0007-8328 –
http://dx.doi.org/10.5170/CERN–2014–004.243

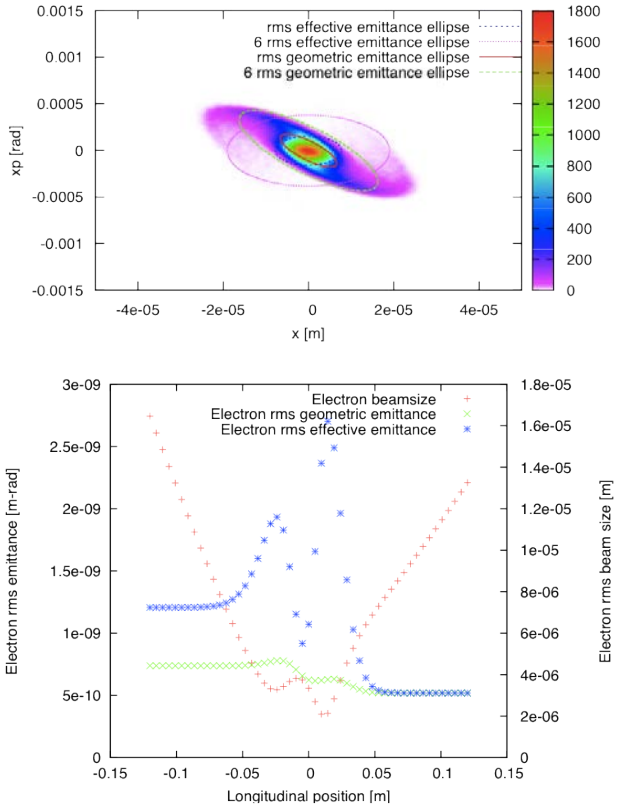

Figure 2: The top figure shows the phase space distribution of the electron beam after collision, and bottom figure shows the evolution of the electron beam size and emittance, for $d_e = 27$. In the top figure, the r.m.s. and 6 r.m.s. ellipses for both geometric and effective emittance, respectively, are plotted.

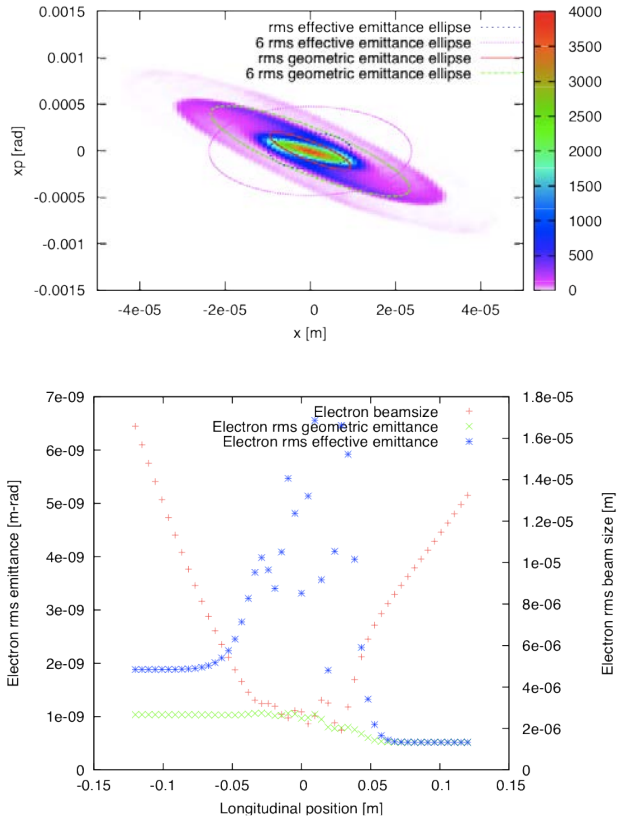

Figure 3: The top figure shows the phase space distribution of the electron beam after collision, and bottom figure shows the evolution of the electron beam size and emittance, for $d_e = 150$. In the top figure, the r.m.s. and 6r.m.s. ellipses for both geometric and effective emittance, respectively, are plotted.

tron beam evolution inside the opposing ion beam. Figure 2 and Fig. 3 illustrate the examples of the electron beam distribution after the collision and the e-beam evolution inside the ion beam. The former correspond to the case of $d_e = 27$, and latter for $d_e = 150$. In the electron beam distribution plots, the nonlinear force deform its initial Gaussian distribution completely. The electrons with larger betatron amplitude rotate slower than those in the core. Therefore the distribution after collision forms a spiral shape. We use 2 different definitions of beam emittance to characterize the occupied phase space area. One is the r.m.s. geometric emittance obtained from the beam distribution, written as

$$\varepsilon_x = \sqrt{\left\langle (x-\bar{x})^2 \right\rangle \left\langle (x'-\bar{x}')^2 \right\rangle - \langle (x-\bar{x})(x'-\bar{x}') \rangle^2}. \quad (1)$$

The other emittance uses the design optics function and is called effective emittance. It is defined as the half of the average value of the Courant–Snyder invariant of all macroparticles based on the design lattice

$$C(\tilde{x}, \tilde{x}') = \gamma \tilde{x}^2 + 2\alpha \tilde{x}\tilde{x}' + \beta \tilde{x}'^2. \quad (2)$$

In the e-beam distribution plots of Fig. 2 and Fig. 3, both emittances are represented as ellipses of 1 r.m.s. value and 6 r.m.s. value. The evolution plots illustrate the evolution of the 2 r.m.s. emittance and the r.m.s. beam size. These plots clearly show the mismatch between the beam distribution and the design optics due to the beam–beam interaction. The effective emittance will determine the aperture requirement of the magnet downstream of interaction point (IP), as shown in Fig. 4. The calculated aperture shows that the small-gap magnet designed for eRHIC is suitable for the ERL energy recovery passes.

KINK INSTABILITY AND ITS MITIGATION METHODS

The kink instability develops due to the electron beam passes the imperfection of the head of the ion beam to its tail. Therefore, for the ion beam, the beam–beam interaction behaves as an effective wake field. If we assume both beams have only infinitesimal offsets, the wake field

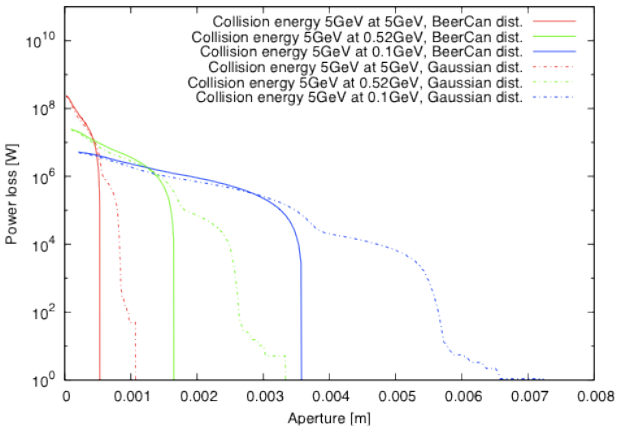

Figure 4: The aperture requirement is shown of the energy recovery pass downstream IP. A maximum 10 m β^* is assumed in all arcs.

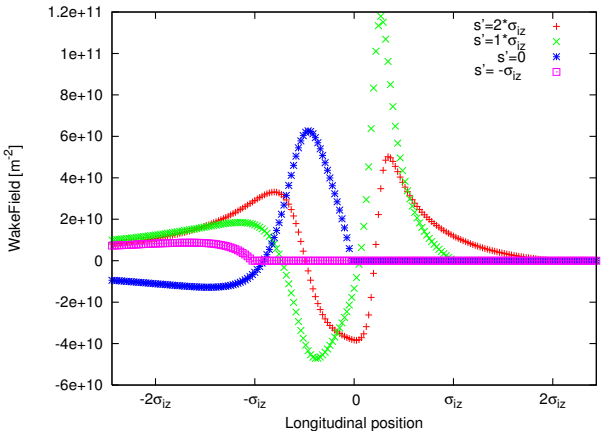

Figure 5: The example of the kink wake field with the beam–beam parameter of the ion beam $\xi_p = 0.015$ is shown. The electron beam has disruption parameter $d_e = 27$. In the figure, the electron beam travels from the positive s to negative. The symbol $s^{'}$ denotes the location of the introduced offset.

$$W\left(s,s'\right)=\frac{\gamma_i}{Z^2N_{ib}r_i}\frac{\Delta x'\left(s\right)}{\Delta x\left(s'\right)} \tag{3}$$

can be retrieved from simulation, where N_{ib} is the number of ions in the slice, γ_i is the energy of the ion beam and r_i is the classical radius of the ion beam. The wake field is illustrated in Fig. 5.

The threshold of the strong head–tail instability (the kink instability) can be calculated using the 2-particle model or the multi-particle model[4]. Both models are based on linearized beam–beam forces. For a 2-particle model, the threshold is simply: $\xi_i d_e < 4\nu_s/\pi$. However, to model the electron beam correctly in the high disruption parameter case, the multi-particle model should be used, predicting the threshold as in Fig. 6.

Both linear models predict that the parameter of the eRHIC exceeds the threshold. A simulation using nonlinear beam–beam forces is required to confirm this understanding. Figure 7 shows the emittance growth associated with the kink instability at different disruption parameters of the electron beam. Even with the lowest disruption parameter, $d_e = 5$, the system is not stable at +2 chromaticity (the nominal value of RHIC operation), although the emittance growth in this case is much less than those with higher d_e. If we increase the chromaticity to stabilize the emittance growth, it requires unreasonable values. Therefore, a dedicate feedback system is desired as a countermeasure.

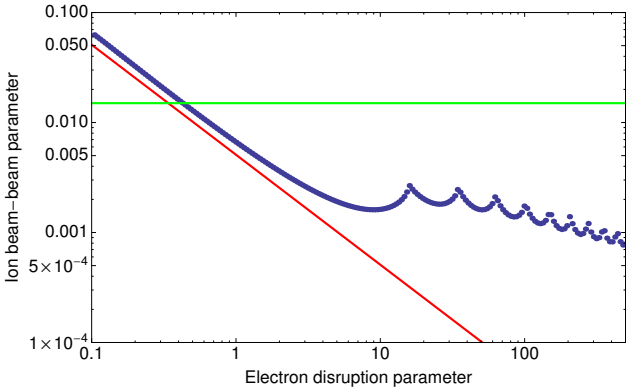

Figure 6: The threshold of kink instability, with the choice of the synchrotron tune 0.004, is shown. The blue dots denote the threshold calculated from the 51 macro-particles circulant matrix method. The red line represents the simple threshold form from equation $\xi_i d_e < 4\nu_s/\pi$. The green line corresponds to $\xi_i = 0.015$, which is the design beam–beam parameter of ion beam in eRHIC.

The first feedback system [4], shown in Fig. 8, takes full advantage of flexibility of a linac-ring scheme, which has the following procedures. We steer the fresh electron bunch before collision based on the transverse offset of the last-used electron bunch that collides with the same ion bunch. Then the centroid of the new electron bunch will oscillate within the opposing ion bunch due to the focusing beam–beam force. We are expecting that oscillation of the centroid of the electron bunch gives the ion bunch proper kicks to correct the offset of the ion bunch before the visible adverse effect, such as emittance growth and luminosity loss, due to the kink instability.

Mathematically, we introduce the offset by modifying the motion of the centroid of the electron bunch based on the information from the last one:

$$\begin{pmatrix}\bar{x}_e\\ \bar{x}'_e\end{pmatrix}_{n+1,i}=M_f\begin{pmatrix}\bar{x}_e\\ \bar{x}'_e\end{pmatrix}_{n,f}. \tag{4}$$

Here, the subscript n denotes the electron–ion collision in n^{th} turn, and the subscripts i and f respectively represent the bunch centroid before and after collision. Map M_f defines the algorithm of the feedback system. Here, for simplicity and easier realization, we limit M_f to be a matrix.

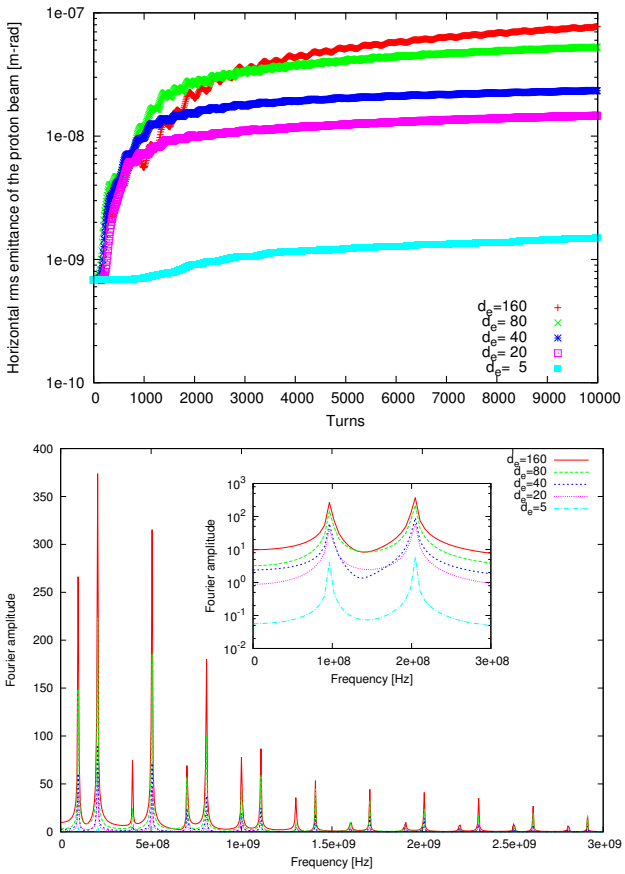

Figure 7: The top figure shows the proton beam emittance growth due to the kink instability at different disruption parameters with the chromaticity of both transverse directions set at $+2$ units, and the beam–beam parameter of the proton beam at 0.015. The bottom figure shows Fourier spectrum of the turn by turn proton slice centroid data. The proton beam is cut to 100 longitudinal slices for this calculation.

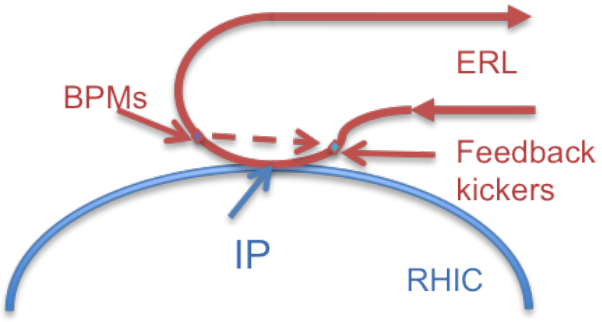

Figure 8: The schematic layout is shown of the feedback system I for mitigating the kink instability in eRHIC.

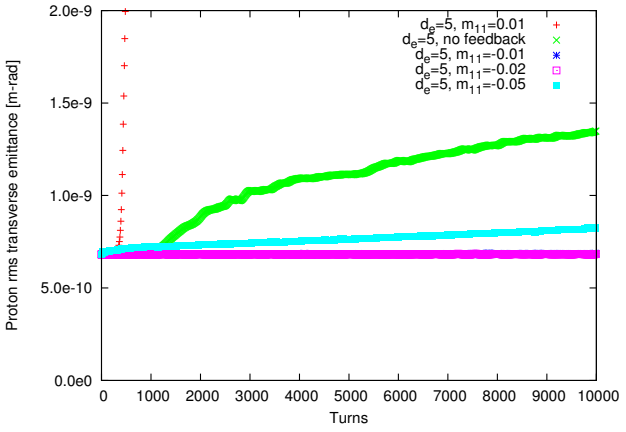

Figure 9: The effect of the feedback system at disruption parameter 5 is shown.

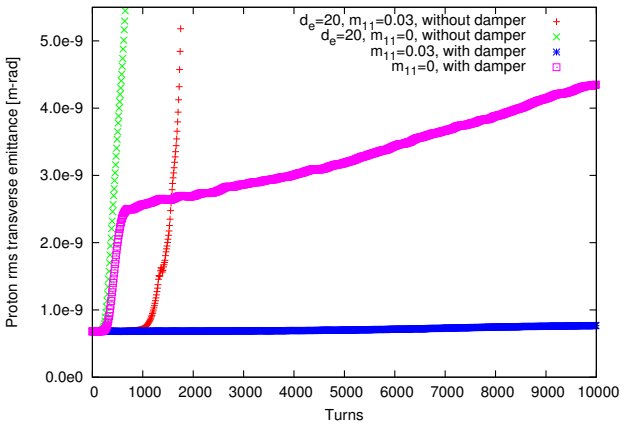

Figure 10: The effect of the feedback system at disruption parameter 20 is shown.

Figure 9 shows the effect of this feedback system at disruption parameter 5. In this case, the emittance growth due to the kink instability is suppressed with proper amplitude of the feedback gain m_{11} (-0.01 or -0.02) without a noticeable decreasing in luminosity. An incorrect sign of the gain may boost the instability, as shown by the red dots in Fig. 9.

When the disruption parameter exceeds 15, this feedback system itself can not stabilize the emittance, because the system will excite the instability of the rigid mode while it can correct the head–tail mode of the ion beam. Therefore we have to add the transverse bunch-by-bunch damper to damp the rigid mode of the ion beam simultaneously. The result for $d_e = 20$, as an example, is shown in Fig. 10. The red dots show the case with the feedback gain of $m_{11} = 0.03$ without transverse damper. The centroid of the ion bunch becomes unstable and causes fast emittance growth due to the offset of two beams. By applying the bunch-by-bunch feedback in the simulation, the ion centroid is stable and the emittance growth is prevented (blue curve).

The simple feedback loses its efficiency when $d_e > 25$. In this range, the electron beam oscillate too fast and the

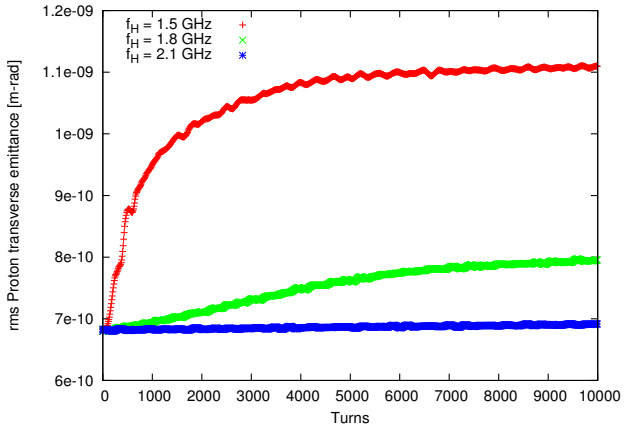

Figure 11: The comparison is shown of kink instability dampings with different high frequency limits f_H when the disruption parameter $d_e = 150$. The gain of the feedback is selected to minimize the emittance growth ion beam.

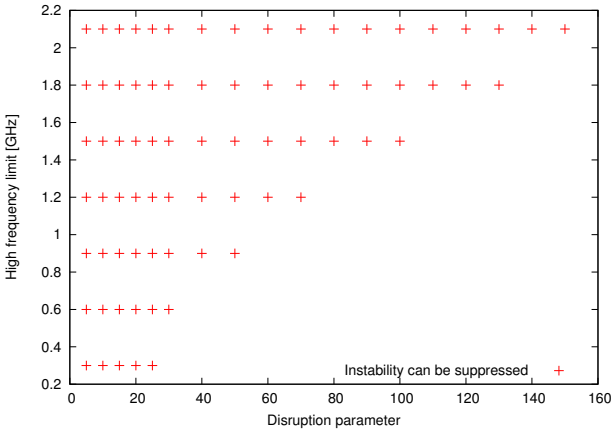

Figure 12: The relation is shown between the required high frequency limit f_H and the electron disruption parameter d_e. Each point shows where the instability can be suppressed in the corresponding parameter (f_H and d_e) with proper amplitude. For all calculations, the low frequency limit is set at 50 MHz

frequency of the oscillation does not match that of the lowest instability mode. We need an alternative feedback scheme for this disruption parameter range, such as a traditional pick-up and kicker system in the ion beam, to suppress the instability coherently [5].

For the pickup–kicker system, the effect can also be modelled as a wake field. If we assume the system has a uniform frequency response with low and high frequency limits f_L and f_H, the corresponding wake field of this system is [6]

$$W(\tau) = R \int_{f_L}^{f_H} \cos(2\pi f \tau)\, df, \qquad (5)$$

where R is related to gain of the amplifier between the pickup and the kicker.

We fix the low frequency limit to 50 MHz, which is below the first peak in the bottom figure of Fig. 7. Then we vary the high frequency limit to find the requirement for the individual disruption parameter.

Figure 11 shows that the required f_H is at least 2.1 GHz to suppress the kink instability when d_e is 150. For other d_e, as shown in Fig. 12, the required f_H is a monotonically increasing function of d_e. Therefore, we demonstrated that the kink instability will be suppressed by a pickup and kicker system with whole electron beam disruption parameter range (5–150), if the required frequency bandwidth is selected.

NOISE HEATING EFFECT OF THE ION BEAM

Since the ion beam always collides with fresh electron bunches, the electron beam parameter fluctuation will affect the ion beam through the beam–beam interaction. The fluctuations can be classified as two types. The first is dipole errors due to the electron beam transverse position offset; the second is quadrupole error due to the fluctuation of the electron beam intensity or transverse beam size.

If the noise of the electron beam is considered as white noise, i.e. a uniform spectrum in frequency domain, the effect of both dipole error and quadrupole errors can be evaluated analytically. For the quadrupole errors, the r.m.s. beam size of the ion beam is expected to grow exponentially, with the rising time

$$\tau = \frac{T}{4\pi^2 \xi_i^2} \frac{1}{(\delta f/f)^2},$$

where ξ_i is the beam–beam parameter of the ion beam, T is the revolution period and $\delta f/f$ is the r.m.s. error of the beam–beam focal length. For eRHIC parameters, to get a slow rising time (~10 hours), the relative error of the electron beam parameter should be better than 2×10^{-4}. A Lorentz frequency spectrum $g(\omega) = 1/(\omega^2 + \alpha^2 \omega_0^2)$ is considered, where α is a free parameter much less than 1 and ω_0 is the angular revolution frequency of the ion ring. In this case, the rising time τ is lengthened to $\tau/R(\alpha)$, where

$$\begin{aligned} R(\alpha) &= \frac{1 - \exp(-2\alpha)}{1 + \exp(-2\alpha) - 2\cos(4\pi\nu)\exp(-\alpha)} \\ &= \frac{\alpha}{1 - \cos(4\pi\nu)} + O(\alpha^3). \end{aligned}$$

For the dipole errors, the ion beam is kicked turn by turn due to the electron beam random offset. By following the well-known random walk formulas, the ion beam displacement gives $\sqrt{< x_i^2 > (t)} = \sqrt{t/\tau + < x_i^2 > (0)}$ and $1/\tau = 8\pi^2 \xi_i^2 < d_n^2 > /T$, where d_n is the n^{th} turn electron beam displacement at IP. We need a bunch-by-bunch transverse damper in the ion ring to compensate the dipole heating up effect.

CONCLUSION

We report on the key finding for distinct beam–beam effects in the ERL based eRHIC. Our study identified the challenges as well as possible countermeasures for both the electron and the ion beams.

A dedicated feedback system is required to suppress the emittance growth caused by the kink instability. We proposed two possible feedback systems. The feedback applied to the electron beam works for moderate values of the disruption parameter, e.g. $d_e < 25$. A traditional broadband pickup and kicker feedback system can damp the instability for the whole range of the disruption parameter expected in eRHIC.

We report on the requirement for the intensity and beam size stability of the electron beam to avoid the hadron beam emittance growth caused by noise in beam–beam interactions. We also established a need for a transverse bunch-by-bunch damper to compensate for the possible heating effect caused by random noise in the transverse displacement in the electron beam.

REFERENCES

[1] V. Ptitsyn *et al.*, eRHIC Accelerator Position Paper, Tech. Rep. (C-AD, BNL, 2007).

[2] Y. Hao and V. Ptitsyn, *Phys. Rev. ST Accel. Beams* **13** (2010) 071003.

[3] Y. Hao, Beam-Beam Interaction Study in ERL based eRHIC, Ph.D. thesis, Indiana University, 2008.

[4] Y. Hao, V. N. Litvinenko and V. Ptitsyn, *Phys. Rev. ST Accel. and Beams* **16** (2013) 101001.

[5] Y. Hao *et al.*, Kink Instability Suppression with Stochastic Cooling Pickup and Kicker, Proc. Int. Particle Accelerator Conf., New Orleans, NM, 2012.

[6] M. Blaskiewicz and J.M. Brennan, WEM2105, Proc.COOL, Bad Kreuznach, 2007.

Published by CERN in the Proceedings of the ICFA Mini-Workshop on Beam–Beam Effects in Hadron Colliders,
CERN, Geneva, Switzerland, 18–22 March 2013, edited by W. Herr and G. Papotti, CERN–2014–004 (CERN, Geneva, 2014)

SUMMARY OF THE WORKING GROUP ON 'BEAM–BEAM EXPERIENCE IN HADRON COLLIDERS'

O. Bruning, G. Sterbini, CERN, Geneva, Switzerland

Abstract

There were four presentations given during the session 'Beam–beam experience in hadron colliders', reporting the beam–beam observations in SPS [1], Tevatron [2], RHIC [3] and HERA [4]. Presentations were followed by discussions. Below we summarize the major observations, findings and results.

BEAM–BEAM EFFECTS IN THE SPS PROTON–ANTIPROTON COLLIDER

A rich set of observations and data were collected during the SP**Error! Bookmark not defined.**S proton–antiproton collider run [1].

Without the pretzel separation, only three bunches per beam could be stored in the machine. Using the pretzel separation the number of bunches per beam doubled (6+6). The average beam–beam long-range separation was 3 σ at injection and 6 σ at collision.

The beam–beam effect was a crucial ingredient of the collider beam dynamics. In fact, without separation and with 6+6 bunches, the antiproton beam was lost in less than 5 s.

The tune spread at injection was dominated by space charge in the proton beam and by beam–beam effects in the antiproton beam. The space charge issue was cured with longer bunches in the 200 MHz bucket and by installing a 100 MHz RF system.

During the squeeze it was difficult to keep the tunes constant and the working point of the machine had a strong dependence on the temperature of the final focusing quadrupoles.

From dedicated experiments it was observed that equal geometrical sizes for the colliding beams minimize the beam losses. Colliding beams with different sizes reduce significantly the beam lifetimes and increase the background in the detectors.

Diffusion studies with scrapers during collision showed that the high-order (HO) resonances had almost no effect on the particles with small amplitudes.

Halving the beam separation increased the experiment background by up to a factor 5, whilst no significant effect was observed by varying the crossing angle.

In addition, distance scans were performed to quantify the effect of bunch miss-crossing: it was observed that maximum losses occurred at a separation of 0.2–0.3 σ.

All sources of tune modulation (energy jitter and chromaticity, power supply ripple, etc.) coupled with beam–beam effects had a significant impact and had to be minimized. Using this argument, it was explained that reducing the chromaticity improved the overall machine performance.

Discussion

During the discussion it was clarified that, in the past, experiment background was used as the main observable to quantify the beam–beam effect since the detector performance was driven by this figure. Nowadays, with higher peak luminosity achievable, it is no longer a convenient figure of merit and it is replaced mainly by the luminosity lifetime. E. Métral asked if the electrostatic separators used for the pretzel separation are still available at CERN. K. Cornelis answered that this has to be checked, adding that this hardware cannot operate in PPM mode and therefore they are not compatible with the standard SPS supercycle.

OVERVIEW OF BEAM–BEAM EFFECTS IN THE TEVATRON

The Tevatron has run for more than two decades, constantly pushing its performance beyond the design luminosity [2].

It was already clear in Tevatron Run I that the beam–beam effects would put the beam on dangerous resonances. In fact, already during the 6+6 operation the antiproton emittance blew up; there were halo formation and beam losses, entangling and significant reduction of the luminosity lifetime.

With the installation of the HV separators, helical separation became possible. Orbit and tune variation along the train was observed and it was in very good agreement with simulations.

In Tevatron Run II, the bunches were 36+36. The operations were much more involved. The long-range interaction was critical during injection, ramp and squeeze. The chromaticity played an important role and, as for the SPS, it was important to minimize it. The minimum beam separation at the parasitic beam encounters had to be larger than 5–6 σ.

The total measured HO tune shift went up to 0.04, but the best integrated luminosity could be generated for HO tune shifts around 0.02 and the more dangerous resonances were the 5th, 12th and 7th order. In order to reduce the beam losses, the beam sizes were matched (blow-up of antiproton emittance). A semi-empirical model of integrated luminosity was set up to compute the different contributions to the machine performance: at the end of Run II, the beam–beam effect induced losses accounted for 22–32% of the integrated luminosity.

Several solutions have been adopted over the years to alleviate the beam–beam effect:

- increase the beam separation,
- reduce the Q' and Q'',

978-92-9083-404-5, 0007-8328 –
http://dx.doi.org/10.5170/CERN–2014–004.249

- use the transverse damper (at injection) and the octupoles all along the cycle,
- stabilize the orbit and the tune of the machine,
- improve the diagnostics,
- use e-lens compensation.

Discussion

During the discussion, there was a question on the limiting factor of the chromaticity correction. A. Valishev answered that the limit was due to the number of sextupole families (driven by the cost of cables). R. Giachino asked to comment on the potential of the Schottky tune monitor. V. Shiltsev answered that it was a valuable tool during operation. O. Bruning asked about the main sources of noise. V. Shiltsev answered that the main contributors were vacuum pumps and bus stability. A. Chao asked about the chromatic effect due to the beam–beam long-range separation. V. Shiltsev answered that was simulated to be ~6 units.

BEAM–BEAM OBSERVATIONS IN RHIC

The relativistic heavy ion collider (RHIC) at Brookhaven National Laboratory has been in operation since 2000. Over the past decade the luminosity in the polarized proton (p–p) operations has increased by more than one order of magnitude. However, the figure of merit for the p-p operation in RHIC is given by the luminosity times the fourth power of the proton beam polarization. The total peak luminosity therefore plays only a secondary role compared to the beam polarization. The maximum total beam–beam tune shift with two collision points has reached 0.018. The beam–beam interaction leads to large tune spread, emittance growth and short beam and luminosity lifetimes. The longitudinal bunch profiles have large tails due to the re-bunching with a higher RF system and the beam lifetime is therefore sensitive to the non-linear chromaticity.

The main limits to the beam lifetime in the RHIC p-p runs are the beam–beam interaction, the non-linear magnetic field errors in the interaction regions (IRs), the non-linear chromaticities with low-beta, the horizontal and vertical third-order betatron resonances and the machine and beam parameter modulations.

The luminosity decay is fitted with a double exponential: a short and a long time constant were observed (respectively ~1 and ~100 h). Just after the first collisions, a shortening of the longitudinal emittance and a shrinking of the transverse emittance take place systematically, together with beam losses. This effect is higher in bunches with two HO collisions than in bunches with one HO.

From studies and simulation it was concluded that the beam–beam effect reduces the off-momentum transverse dynamic aperture and the fast losses at the start of the physics run are dominated by this mechanism.

During the second part of the run, the present IBS model can fully justify the observed luminosity decay.

To increase the machine performance, chromatic effects of the low-beta played an important role together with the 10 Hz oscillations of the triplets. To attack these issues, several correction techniques of non-linear chromaticities have been tested and implemented in RHIC together with a 10 Hz orbit feedback successfully tested in the 2011 p–p run.

To reduce the large beam–beam tune spread from high bunch intensities, electron lenses are being installed in RHIC.

Discussion

A. Valishev asked if local or global chromatic correction was implemented. Y. Luo answered that the correction was local.

BEAM–BEAM EFFECTS IN HERA

Differently to the three machines previously described, HERA was a hadron–lepton collider (920 GeV p colliding with 27.6 GeV e±) [4].

Due to the filling scheme and to the machine layout there were no long-range encounters, no Pacman bunches, no crossing angle between the beams and the same bunches were crossing at the two Interaction Points, IPs, (one-on-one configuration, no multibunch beam–beam coupling).

Matching the transverse beam sizes at the IPs was mandatory in order to obtain good beam lifetimes (elliptical beams). Due to the induced tune spread, the beam–beam interaction negatively affected the e± polarization.

The choice of the tunes was crucial and the collision tunes for e^+, e^- and p were different in order to avoid the second- and third-order sideband resonances and to optimize the lepton polarization.

For HERA beams, partial separation at the IPs was observed to be very problematic.

Strong–strong beam–beam theories do not predict an unstable mode for the HERA parameters. Nevertheless, beam–beam instabilities were observed: this is thought to be due to the driven coherent oscillation on the lepton beam and not to a coherent beam–beam mode.

Discussion

A. Burov asked if the damper was used during operation. M. Vogt answered that it was not used for the proton since it was too noisy. W. Fischer asked if there had been attempts to further increase the HO tune shift. M. Vogt replied that there had been few attempts, without positive results.

CONCLUSIONS

In past hadron colliders it has been observed that:

- The mismatch between the beam sizes can significantly increase the beam–beam detrimental effect.
- Reducing the beam–beam long-range separation below 6 σ had a severe impact on the beam lifetime.

- A crucial way to reduce the beam–beam induced losses is to lower chromaticity and to limit its non-linear component.
- Regarding the HO tune shift limit, it is not possible to extract a general rule since it depends strongly on the observable chosen to define it (experiment background, luminosity lifetime) and on the noise and tune stability of the single machine.

ACKNOWLEDGEMENTS

The chairman acknowledges all the speakers for the high quality of their presentations.

REFERENCES

[1] K. Cornelis, "Beam–beam effect in the SPS proton-antiproton collider", these proceedings.
[2] V. Shiltsev, "Overview of beam-beam effect in the Tevatron", these proceedings.
[3] Y. Luo, "Beam–beam observations in RHIC", these proceedings.
[4] M. Vogt, "Beam–beam effects in HERA", these proceedings.

Published by CERN in the Proceedings of the ICFA Mini-Workshop on Beam–Beam Effects in Hadron Colliders,
CERN, Geneva, Switzerland, 18–22 March 2013, edited by W. Herr and G. Papotti, CERN–2014–004 (CERN, Geneva, 2014)

SUMMARY OF THE WORKING GROUP ON 'SINGLE PARTICLE EFFECTS: PARASITIC LONG-RANGE BEAM-BEAM INTERACTIONS' *

V. Shiltsev#, FNAL, Batavia, IL, U.S.A.; E. Métral, CERN, Geneva, Switzerland

Abstract

There were three presentations given at the session "Single particle effects: parasitic long-range beam-beam interactions" [1, 2, 3] which were followed by discussions. Below we summarize major findings and discussions.

TEVATRON AND LHC OBSERVATIONS

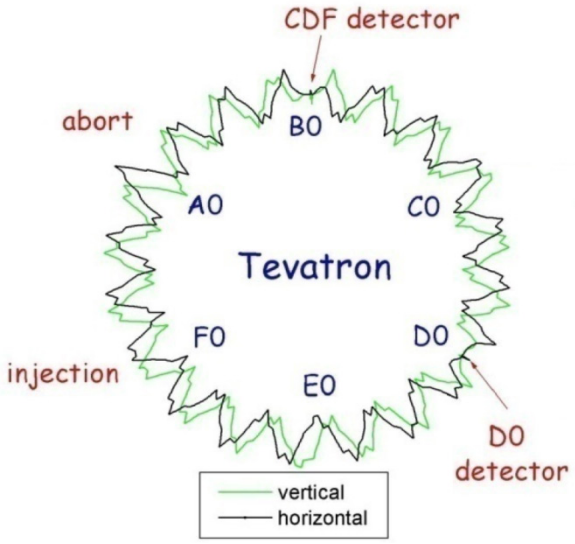

Figure 1: The pattern of the Tevatron helical orbits at the collision stage.

There are similarities and differences in the observations of the long-range beam-beam effects in the Tevatron and in the LHC. They start with the patterns of the parasitic interactions.

During the Tevatron Collider Run II 36 x 36 bunch operation, each bunch experienced 72 long-range interactions per revolution at injection, but at collision there were 70 long-range interactions and two head-on collisions per bunch at the CDF and D0 detectors (see Fig. 1). At the bunch spacing of 396 ns, the distance between the neighbor interaction points was 59 m. In total, there were 138 locations around the ring where beam-beam interactions occurred. The sequence of 72 interactions out of the 138 possible ones differed for each bunch, hence the effects varied from bunch to bunch. Notably, the long-range interactions occurred at the different betatron phases.

*Fermi Research Alliance, LLC operates Fermilab under contract No.. DE-AC02-07CH11359 with the U.S. Department of Energy
#shiltsev@fnal.gov

The locations of these interactions and the beam separations changed from injection to collision because of the antiproton cogging (relative timing between antiprotons and protons).

At the LHC, where the beams are separated with a crossing angle, there are up to 120 long range encounters which are lumped at the betatron phases of main interaction points (see Fig. 2). Consequently, the issues are very different from the helical (or pretzel) separation scheme.

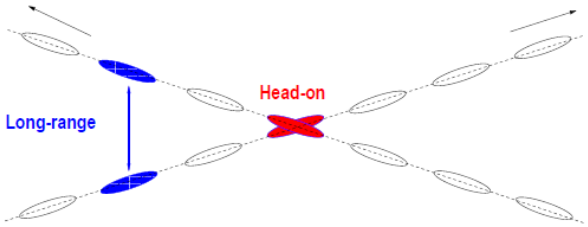

Figure 2: Schematic of proton-proton collisions in the LHC.

Besides the difference in the separation schemes and the total number of the parasitic interaction points, one should note that the LHC has larger separation – of about 9-10 σ - in all interaction points, except one (LHC-b at the interaction point 8) where the separation varies during the collision runs from few to one σ in order to level the luminosity at some 10% of the main low-beta interaction points (at CMS and ATLAS). During the Tevatron collision stores most of the long-range interactions were at 8-10 σ but they were less essential than 4 near interaction point crossings at 5.8-6 σ separation. In low-beta squeeze the beams briefly (2 s) came within 2-2.5 σ at 1 parasitic interaction point and that usually caused sharp loss spikes. So, here the first unresolved question – why one such small-separation interaction point was so harmful in the Tevatron and seemingly is of no concern in the LHC? One can point to the difference in the single bunch intensities (1.2-1.5 10^{11} protons per bunch in the LHC and some 3 10^{11} protons per bunch in the Tevatron) but at this moment it is not clear whether that is sufficient for full explanation.

It was shown that in the Tevatron, the long-range beam-beam interactions occur at all stages (injection, ramp, squeeze, collisions) and affected both proton and antiproton beams. They resulted in beam losses, and emittance blow-ups, which occurred in remarkable bunch-to-bunch dependent patterns. Of notice is that these phenomena were a) thoroughly studied experimentally; b) described by phenomenological models indicating quantitative dependencies of the beam loss rates and the emittance growth rates on the machine and beam parameters (tunes, chromaticities, separations, beam

978-92-9083-404-5, 0007-8328 –
http://dx.doi.org/10.5170/CERN–2014–004.253

intensities and emittances, etc); c) modeled in Lifetrac [4] simulations which not only described the observations but were used to make quantitative predictions (which were later confirmed in operation).

Studies of the beam-beam effects in the LHC are currently at the stage of compilation of the experimental evidences and analysis of parametric dependencies (on the crossing angle, intensities, tunes, bunch spacing, etc.). Collider operation and machine performance analysis tools are being developed, and the Tevatron SDA software (Software for Data Analysis) and on-line store analysis programs are being used as an example. The LHC beam diagnostic suite is being steadily expanding and improving with the goal of having several trustable, cross-calibrated monitors of all beam parameters working in bunch-by-bunch measurements modes.

Given detrimental consequences of the beam-beam effects (including long-range) on the Tevatron performance, the beam-beam issues have been seriously addressed and eventually corrected to the operational satisfaction. In particular, the long-range effects were mitigated by: i) an increase of separation by installation of additional HV separators; ii) a rearrangement of the helical orbits; iii) an optimization of the machine optics - linear and nonlinear; iv) pulsed e-lenses; v) a large number of incremental improvements (there was no "silver bullet"). In the LHC some of the most obvious operationally harmful beam-beam effects were corrected by proper adjustment of the beam loading schemes to equalize at least the number of the head-on collisions for all the bunches.

SIMULATION OF LONG-RANGE AND HEAD-ON BEAM-BEAM EFFECTS

There are several approaches to the simulations of the beam-beam effects: i) the fastest is analytical calculations of the resonance driving terms [5] or similar method of calculating "smears" [3]; ii) fast tracking – by, e.g. Sixtrack [6] or frequency map analyses [7] – to find the dynamic aperture; iii) slow ("comprehensive") tracking of the long-term dynamics, e.g. with Lifetrac as described in [8]. The later method was shown to be very useful, adequate, having valuable quantitative predictive and provide results which can be directly compared to observables (lifetime, emittance growth, etc.). For instance, for most of the Collider Run II the modified Lifetrac weak-strong beam-beam code was used to study the beam-beam effects in the Tevatron. It correctly described all observed beam dynamics effects, had predictive power and had been particularly useful for supporting and planning changes of the machine configuration.

Methods i) and ii) are very practical and (relatively) very fast but their result – dynamic aperture – though potentially "measurable" in dedicated beam studies, does not provide quantitative description of the observables. Still, the dynamic aperture (DA) analysis is helpful as it gives qualitative estimates, e.g. the scaling laws for the LHC:

$$DA \propto \frac{1}{n_b}$$

$$DA \propto \frac{1}{\sqrt{\varepsilon}}$$

$$DA \propto d_{sep} \propto \alpha$$

$$DA \propto d_{sep} \propto \sqrt{\beta^*}$$

$$DA \propto \frac{1}{N}$$

where, n_b is the number of bunches, ε is the transverse emittance, d_{sep} is the beam separation, α is the crossing angle, β^* is the betatron function at the interaction point and N is the bunch intensity.

OTHER DISCUSSIONS

There also was an interesting discussion on the "complexity" of accelerators, understood in the mathematically defined terms of the *CPT theorem* [9]. At the very general level, it was pointed out – see [3] and Fig. 3 – that the hadron beam machines seems to be more "complex" (problematic, "not-that-easy to work with") than the electron ones; that the colliders are more "complex" than one beam machines; and that, seemingly, the most complex systems are those that involve more beams, e.g. 4-lepton-beams DCI collider [10], or 3-beam systems such as "beam-beam-beam" or "three beam instability" (two colliding hadron beams interacting with electron cloud) [11] or the beam-beam effects in hadron colliders compensated by electron lenses.

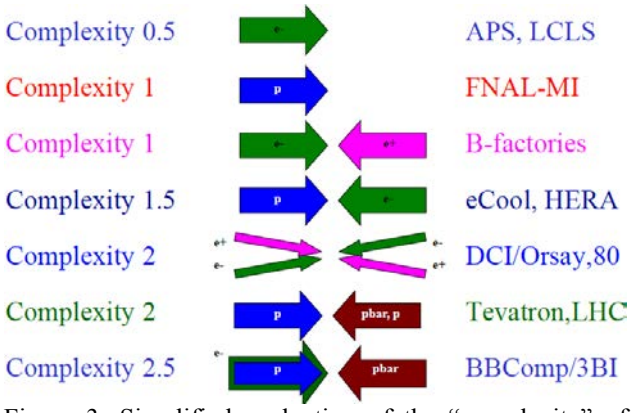

Figure 3: Simplified evaluation of the "complexity" of accelerators [3].

REFERENCES

[1] W.Herr, these proceedings.
[2] D.Kaltchev, these proceedings.
[3] V.Shiltsev, these proceedings.

[4] D. Shatilov, Proceedings of the 2005 Particle Accelerator Conference, Knoxville, Tennessee, USA.
[5] Y. Alexahin, FERMILAB-TM-2148 (2001).
[6] F. Schmidt, CERN/SL/94–56 (AP).
[7] J. Laskar, Proceedings of the 2003 Particle Accelerator Conference, Portland, Oregon, USA.
[8] A. Valishev et al., JINST **7** (2012) P12002.
[9] V. Shiltsev, Mod.Phys.Lett. A, **26** (2011) 761.
[10] G. Arzelia et al., HEACC, 1971.
[11] A. Burov, these proceedings.

Participants

Name	Institution	E-mail
ALESSIO Federico	CERN	federico.alessio@cern.ch
ARDUINI Gianluigi	CERN	gianluigi.arduini@cern.ch
BAER Tobias	University of Hamburg	tobias.baer@cern.ch
BANFI Danilo	EPFL-CERN	danilo.banfi@cern.ch
BRUNING Oliver	CERN	oliver.bruning@cern.ch
BUFFAT Xavier	EPFL	xavier.buffat@cern.ch
BURKHARDT Helmut	CERN BE	helmut.burkhardt@cern.ch
BUROV Alexey	Fermilab	alexey.burov@cern.ch
CALAGA Rama	CERN	rama.calaga@cern.ch
CHAO Alex	SLAC	achao@slac.stanford.edu
CIMINO Roberto	LNF-INFN	roberto.cimino@lnf.infn.it
CORNELIS Karel	CERN	karel.cornelis@cern.ch
DE MARIA Riccardo	CERN	riccardo.de.maria@cern.ch
FISCHER Wolfram	BNL	wolfram.fischer@bnl.gov
FITTERER Miriam	CERN	mfittere@cern.ch
FUNAKOSHI Yoshihiro	KEK	yoshihiro.funakoshi@kek.jp
GIACHINO Rossano	CERN	rossano.giachino@cern.ch
GIOVANNOZZI Massimo	CERN	massimo.giovannozzi@cern.ch
GOERGEN Paul	TEMF TU Darmstadt	goergen@temf.tu-darmstadt.de
HAO Yue	BNL	yhao@bnl.gov
HERR Werner	CERN	werner.herr@cern.ch
HOSTETTLER Michi	CERN	michael.hostettler@cern.ch
JACOBSSON Richard	CERN	richard.jacobsson@cern.ch
JACQUET Delphine	CERN	delphine.duchastelle@cern.ch
JOWETT John	CERN	john.jowett@cern.ch
KALTCHEV Dobrin	TRIUMF	kaltchev@triumf.ca
KOZANECKI Witold	CEA-Saclay	witold.kozanecki@cern.ch
LUO Yun	BNL	yluo@bnl.gov
METRAL Elias	CERN	elias.metral@cern.ch
MILARDI Catia	LNF-INFN	catia.milardi@lnf.infn.it
MONTAG Christoph	BNL	montag@bnl.gov
MOUNET Nicolas	CERN	nicolas.mounet@cern.ch
MURATORI Bruno	STFC	bruno.muratori@stfc.ac.uk
OHMI kazuhito	KEK	ohmi@post.kek.jp
OIDE Katsunobu	KEK	katsunobu.oide@kek.jp
PAPOTTI Giulia	CERN	giulia.papotti@cern.ch
PARET Stefan	LBNL	sparet@lbl.gov
PIELONI Tatiana	CERN	tatiana.pieloni@cern.ch
QIN Qing	IHEP Beijing	qinq@ihep.ac.cn
REINE Versteegen	CERN	reine.versteegen@cern.ch
RIJOFF Tatiana Libera	CERN	tatiana.rijoff@cern.ch
RIVKIN Leonid	EPFL and PSI	leonid.rivkin@psi.ch
SALVANT Benoit	CERN	benoit.salvant@cern.ch
SCHAUMANN Michaela	RWTH Aachen	michaela.schaumann@cern.ch

SEEMAN John	SLAC	seeman@slac.stanford.edu
SHILTSEV Vladimir	Fermilab	shiltsev@fnal.gov
SHWARTZ Dmitry	BINP	d.b.shwartz@inp.nsk.su
STANCARI Giulio	Fermilab	stancari@fnal.gov
STERBINI Guido	CERN	guido.sterbini@gmail.com
TRAD Georges	CERN	georges.trad@cern.ch
VALISHEV Alexander	Fermilab	valishev@fnal.gov
VOGT Mathias	DESY	vogtm@mail.desy.de
WENNINGER Jorg	CERN	jorg.wenninger@cern.ch
WHITE Simon	BNL	smwhite@bnl.gov
ZHANG Yuan	IHEP Beijing	zhangy@ihep.ac.cn
ZHANG Yuhong	JLab	yzhang@jlab.org
ZIMMERMANN Frank	CERN	frank.zimmermann@cern.ch
ZOBOV Mikhail	INFN LNF	mikhail.zobov@lnf.infn.it